NASA/CR-1998 206838

FINAL
IN-02-CR
OCIT

Final Technical Report on

NASA-Langley Award # NAG-1-194

Effects of Suction on Swept-Wing Transition

16 December 1995 to 31 March 1998

To

Michael J. Walsh
National Aeronautics and Space Administration
Langley Research Center, FLDMD
Mail Stop 163, Building 1247A
Hampton, VA. 23681-0001

By

William S. Saric
Professor

Mechanical and Aerospace Engineering
Arizona State University
Box 87-6106
Tempe, AZ. 85287-6106

February 1998

ABSTRACT

Stability experiments are conducted in the Arizona State University Unsteady Wind Tunnel on a 45° swept airfoil. The pressure gradient is designed to provide purely crossflow-dominated transition; that is, the boundary layer is subcritical to Tollmien-Schlichting disturbances. The airfoil surface is hand polished to a 0.25 μm rms finish. Under these conditions, stationary crossflow disturbances grow to nonuniform amplitude due to submicron surface irregularities near the leading edge. Uniform stationary crossflow waves are produced by controlling the initial conditions with spanwise arrays of micron-sized roughness elements near the attachment line. Hot-wire measurements provide detailed maps of the crossflow wave structure, and accurate spectral decompositions isolate individual-mode growth rates for the fundamental and harmonic disturbances. Roughness spacing, roughness height, and Reynolds number are varied to investigate the growth of all amplified wavelengths. The measurements show early nonlinear mode interaction causing amplitude saturation well before transition. Comparisons with nonlinear parabolized stability equations calculations show excellent agreement in both the disturbance amplitude and the mode-shape profiles.

TABLE OF CONTENTS

	Page
LIST OF TABLES	x
LIST OF FIGURES	xi
NOMENCLATURE	xxxiv
1 INTRODUCTION	1
1.1 Background and Motivation	1
1.1.1 Boundary-Layer Transition	2
1.1.2 Transition Prediction	3
1.2 Three-Dimensional Boundary Layers	5
1.2.1 Swept-Wing Flows	5
1.2.2 Crossflow Instability	6
1.3 Review of Recent Results	8
1.3.1 Literature Surveys	8
1.3.2 Experimental Investigations	9
1.3.3 Theoretical Developments	13
1.4 Experimental Goals	15
1.5 Outline	16
2 WIND-TUNNEL FACILITY	19
2.1 Unsteady Wind Tunnel	19
2.2 Computer Systems	22
2.3 Instrumentation	25
2.4 Traverse and Sting	26
3 TEST MODEL AND EXPERIMENTAL DESIGN	31
3.1 Background	31

Page

3.2 Model Configuration 32
3.2.1 Airfoil 32
3.2.2 Test-Section and Wall Liners 33
3.3 Test Conditions 34
3.3.1 Angle of Attack 35
3.3.2 Reynolds Number 36
3.3.3 Roughness Elements 36
3.4 Coordinate Systems 38
3.5 Theoretical Predictions 41
3.5.1 Basic State 41
3.5.2 Linear Stability Calculations 43
4 EXPERIMENTAL METHODS 49
4.1 Special Considerations 49
4.1.1 Stationary Disturbances 49
4.1.2 Wind-Tunnel Heating 50
4.2 Hot-Wire Techniques 51
4.2.1 Velocity Calibration 51
4.2.2 Temperature Compensation 52
4.3 Wind-Tunnel Speed Control 54
4.4 Disturbance Measurement Techniques 55
4.4.1 Boundary-Layer Profile Scans 55
4.4.2 Spanwise Scans at Constant Y 58
4.5 Flow Visualization 65
5 RESULTS PART 1: BASELINE CONFIGURATION 67
5.1 Overview 67

Page

5.2 Flow Visualization 69

5.3 Basic State 72

5.3.1 C_p Measurements 72

5.3.2 Boundary-Layer Profiles 73

5.4 Natural Surface Roughness 76

5.5 Distributed Roughness 78

5.5.1 Vortex Structure and Mean-Flow Distortion 78

5.5.2 Disturbance Profiles and Mode Shape 80

5.5.3 Total Disturbance Amplitude Distribution 82

5.5.4 Mode-Shape Comparisons 84

5.5.5 Wavelength Separation 86

5.6 Summary 90

6 RESULTS—PART 2: PARAMETRIC STUDY 93

6.1 Reynolds Number Variation 93

6.1.1 Effect of Decreasing Re_c 94

6.1.2 Effect of Increasing Re_c 95

6.1.3 Disturbance Amplitude Comparison 97

6.2 Multiple-Mode Crossflow Waves 98

6.2.1 Disturbance Structure 98

6.2.2 Wavelength Separation 100

6.3 Initial Amplitude Variation 102

6.3.1 Data Set $\mathcal{E}$ 103

6.3.2 Data Set $\mathcal{F}$ 104

6.3.3 Disturbance Amplitude Comparison 106

6.4 Special Considerations 107

Page

6.4.1 Which Wavelength Is Conserved? 107

6.4.2 Effect of Acoustic Forcing 110

7 CONCLUSIONS 113

7.1 Summary of Key Results 113

7.2 Closing Remarks 117

REFERENCES 118

LIST OF TABLES

Table		Page
2.1	Unsteady Wind Tunnel computer systems.	23
2.2	Traverse system capabilities.	28
3.1	Roughness element measures at $x/c = 0.023$.	39
3.2	Boundary-layer hot-wire probe rotation angles.	41
5.1	Experimental data set configuration.	68
5.2	Approximate transition location determined by naphthalene flow visualization.	71
6.1	Effect of freestream acoustic forcing on transition location for $Re_c = 2.4 \times 10^6$ and [48|12] roughness.	111

LIST OF FIGURES

Figure		Page
2.1	Plan view of the ASU Unsteady Wind Tunnel.	126
2.2	Side view of traverse carriage.	127
2.3	Front view of traverse carriage.	128
2.4	Plan view of hot-wire sting.	129
3.1	Unswept NLF(2)-0415 airfoil and free-air C_p for $\alpha = 0°$ and $\delta_F = 0°$.	130
3.2	Test-section end liners and NLF(2)-0415 airfoil for $\alpha = -4°$.	131
3.3	Unswept NLF(2)-0415 airfoil and upper-surface free-air C_p for $\alpha = -4°$ and $\delta_F = 0°$.	132
3.4	Profilometer measurement of NLF(2)-0415 surface finish.	133
3.5	Schematic plan view of swept wing showing coordinate systems and curved inviscid streamline.	134
3.6	Schematic cross section of swept wing showing coordinate systems.	135
3.7	Schematic of swept wing boundary-layer profile showing the tangential, crossflow, and total velocity profile.	136
3.8	Instrumentation sting showing probe rotations required by local surface curvature effects.	137
3.9	Swept NLF(2)-0415 airfoil and upper-surface C_p for $\alpha = -4°$ and $\delta_F = 0°$. The C_p is computed with the wind-tunnel walls in place.	138
3.10	Theoretical basic-state boundary-layer profiles for $\alpha = -4°$, $Re_c = 2.4 \times 10^6$. Tangential (u_t) component.	139
3.11	Theoretical basic-state boundary-layer profiles for $\alpha = -4°$, $Re_c = 2.4 \times 10^6$. Crossflow (w_t) component.	140
3.12	Theoretical basic-state boundary-layer profiles for $\alpha = -4°$, $Re_c = 2.4 \times 10^6$. Streamwise (u) component.	141
3.13	Theoretical crossflow Reynolds numbers for $\alpha = -4°$.	142

Figure Page

3.14 Linear theory N-factors for stationary crossflow disturbances. $Re_c = 2.4 \times 10^6$. 143

4.1 Typical hot-wire velocity calibration. 144

4.2 Typical hot-wire temperature compensation. 145

4.3 Comparison of inferred hot-wire velocity with and without temperature compensation. 146

4.4 Wind tunnel "cruise control" program. 147

4.5 Typical boundary-layer profile scan. 148

4.6 Typical spanwise hot-wire scan at constant Y. 149

4.7 Typical spanwise traverse-alignment scan. 150

5.1 Naphthalene flow visualization for $Re_c = 2.2 \times 10^6$, [6|12] roughness. . . 151

5.2 Naphthalene flow visualization for $Re_c = 3.2 \times 10^6$, [6|12] roughness. . . 152

5.3 Naphthalene flow visualization for $Re_c = 2.2 \times 10^6$, [6|36] roughness. . . 153

5.4 Naphthalene flow visualization for $Re_c = 3.2 \times 10^6$, [6|36] roughness. . . 154

5.5 Comparison of experimental and theoretical pressure distribution for $Re_c = 1.6 \times 10^6$. 155

5.6 Comparison of experimental and theoretical pressure distribution for $Re_c = 2.4 \times 10^6$. 156

5.7 Comparison of experimental and theoretical pressure distribution for $Re_c = 3.2 \times 10^6$. 157

5.8 Variation of measured pressure distribution with Reynolds number. Upper ports. 158

5.9 Variation of measured pressure distribution with Reynolds number. Lower ports. 159

5.10 Spanwise array of 100 mean-flow boundary-layer profiles covering a span of 99 mm at $x/c = 0.20$. $Re_c = 1.6 \times 10^6$, no artificial roughness. . 160

5.11 Spanwise array of 100 mean-flow boundary-layer profiles covering a span of 99 mm at $x/c = 0.60$. $Re_c = 1.6 \times 10^6$, no artificial roughness. . 161

Figure Page

5.12 Experimental basic-state boundary-layer profiles for $Re_c = 1.6 \times 10^6$, no artificial roughness. 162

5.13 Comparison of experimental and theoretical basic-state boundary-layer profile at $x/c = 0.05$. $Re_c = 1.6 \times 10^6$. 163

5.14 Comparison of experimental and theoretical basic-state boundary-layer profile at $x/c = 0.10$. $Re_c = 1.6 \times 10^6$. 164

5.15 Comparison of experimental and theoretical basic-state boundary-layer profile at $x/c = 0.15$. $Re_c = 1.6 \times 10^6$. 165

5.16 Comparison of experimental and theoretical basic-state boundary-layer profile at $x/c = 0.20$. $Re_c = 1.6 \times 10^6$. 166

5.17 Comparison of experimental and theoretical basic-state boundary-layer profile at $x/c = 0.25$. $Re_c = 1.6 \times 10^6$. 167

5.18 Comparison of experimental and theoretical basic-state boundary-layer profile at $x/c = 0.30$. $Re_c = 1.6 \times 10^6$. 168

5.19 Comparison of experimental and theoretical basic-state boundary-layer profile at $x/c = 0.35$. $Re_c = 1.6 \times 10^6$. 169

5.20 Comparison of experimental and theoretical basic-state boundary-layer profile at $x/c = 0.40$. $Re_c = 1.6 \times 10^6$. 170

5.21 Comparison of experimental and theoretical basic-state boundary-layer profile at $x/c = 0.45$. $Re_c = 1.6 \times 10^6$. 171

5.22 Comparison of experimental and theoretical basic-state boundary-layer profile at $x/c = 0.50$. $Re_c = 1.6 \times 10^6$. 172

5.23 Comparison of experimental and theoretical basic-state boundary-layer profile at $x/c = 0.55$. $Re_c = 1.6 \times 10^6$. 173

5.24 Comparison of experimental and theoretical basic-state boundary-layer profile at $x/c = 0.60$. $Re_c = 1.6 \times 10^6$. 174

5.25 Comparison of experimental and theoretical displacement thickness for basic-state boundary layers. $Re_c = 1.6 \times 10^6$. 175

5.26 Comparison of experimental and theoretical momentum thickness for basic-state boundary layers. $Re_c = 1.6 \times 10^6$. 176

Figure Page

5.27 Comparison of experimental and theoretical shape factor for basic-state boundary layers. $Re_c = 1.6 \times 10^6$. 177

5.28 Streamwise velocity contours at $x/c = 0.45$. $Re_c = 3.0 \times 10^6$, no artificial roughness. 178

5.29 Streamwise velocity contours at $x/c = 0.45$. $Re_c = 2.4 \times 10^6$, [6|12] roughness. 179

5.30 Single stationary crossflow vortex isolated from figure 5.29 and plotted on a 1:1 scale. 180

5.31 Effect of combined (v', w') disturbance motion on the streamwise boundary layer velocity at $x/c = 0.20$. $Re_c = 2.4 \times 10^6$, [6|12] roughness. 181

5.32 Effect of combined (v', w') disturbance motion on the streamwise boundary layer velocity at $x/c = 0.30$. $Re_c = 2.4 \times 10^6$, [6|12] roughness. 182

5.33 Effect of combined (v', w') disturbance motion on the streamwise boundary layer velocity at $x/c = 0.45$. $Re_c = 2.4 \times 10^6$, [6|12] roughness. 183

5.34 Spanwise array of 100 mean-flow boundary-layer profiles covering a span of 99 mm at $x/c = 0.45$. $Re_c = 2.4 \times 10^6$, [6|12] roughness. 184

5.35 Spanwise array of 100 disturbance profiles covering a span of 99 mm at $x/c = 0.45$. $Re_c = 2.4 \times 10^6$, [6|12] roughness. 185

5.36 Disturbance velocity contours at $x/c = 0.45$. $Re_c = 2.4 \times 10^6$, [6|12] roughness. 186

5.37 Stationary crossflow mode shape at $x/c = 0.45$. $Re_c = 2.4 \times 10^6$, [6|12] roughness. 187

5.38 Streamwise velocity contours at $x/c = 0.05$. $Re_c = 2.4 \times 10^6$, [6|12] roughness. 188

5.39 Streamwise velocity contours at $x/c = 0.10$. $Re_c = 2.4 \times 10^6$, [6|12] roughness. 189

5.40 Streamwise velocity contours at $x/c = 0.15$. $Re_c = 2.4 \times 10^6$, [6|12] roughness. 190

5.41 Streamwise velocity contours at $x/c = 0.20$. $Re_c = 2.4 \times 10^6$, [6|12] roughness. 191

Figure Page

5.42 Streamwise velocity contours at $x/c = 0.25$. $Re_c = 2.4 \times 10^6$, [6|12] roughness. 192

5.43 Streamwise velocity contours at $x/c = 0.30$. $Re_c = 2.4 \times 10^6$, [6|12] roughness. 193

5.44 Streamwise velocity contours at $x/c = 0.35$. $Re_c = 2.4 \times 10^6$, [6|12] roughness. 194

5.45 Streamwise velocity contours at $x/c = 0.40$. $Re_c = 2.4 \times 10^6$, [6|12] roughness. 195

5.46 Spanwise array of 100 mean-flow boundary-layer profiles covering a span of 99 mm at $x/c = 0.05$. $Re_c = 2.4 \times 10^6$, [6|12] roughness. 196

5.47 Spanwise array of 100 mean-flow boundary-layer profiles covering a span of 99 mm at $x/c = 0.10$. $Re_c = 2.4 \times 10^6$, [6|12] roughness. 197

5.48 Spanwise array of 100 mean-flow boundary-layer profiles covering a span of 99 mm at $x/c = 0.15$. $Re_c = 2.4 \times 10^6$, [6|12] roughness. 198

5.49 Spanwise array of 100 mean-flow boundary-layer profiles covering a span of 99 mm at $x/c = 0.20$. $Re_c = 2.4 \times 10^6$, [6|12] roughness. 199

5.50 Spanwise array of 100 mean-flow boundary-layer profiles covering a span of 99 mm at $x/c = 0.25$. $Re_c = 2.4 \times 10^6$, [6|12] roughness. 200

5.51 Spanwise array of 100 mean-flow boundary-layer profiles covering a span of 99 mm at $x/c = 0.30$. $Re_c = 2.4 \times 10^6$, [6|12] roughness. 201

5.52 Spanwise array of 100 mean-flow boundary-layer profiles covering a span of 99 mm at $x/c = 0.35$. $Re_c = 2.4 \times 10^6$, [6|12] roughness. 202

5.53 Spanwise array of 100 mean-flow boundary-layer profiles covering a span of 99 mm at $x/c = 0.40$. $Re_c = 2.4 \times 10^6$, [6|12] roughness. 203

5.54 Spanwise array of 100 disturbance profiles covering a span of 99 mm at $x/c = 0.05$. $Re_c = 2.4 \times 10^6$, [6|12] roughness. 204

5.55 Spanwise array of 100 disturbance profiles covering a span of 99 mm at $x/c = 0.10$. $Re_c = 2.4 \times 10^6$, [6|12] roughness. 205

5.56 Spanwise array of 100 disturbance profiles covering a span of 99 mm at $x/c = 0.15$. $Re_c = 2.4 \times 10^6$, [6|12] roughness. 206

Figure Page

5.57 Spanwise array of 100 disturbance profiles covering a span of 99 mm at $x/c = 0.20$. $Re_c = 2.4 \times 10^6$, [6|12] roughness. 207

5.58 Spanwise array of 100 disturbance profiles covering a span of 99 mm at $x/c = 0.25$. $Re_c = 2.4 \times 10^6$, [6|12] roughness. 208

5.59 Spanwise array of 100 disturbance profiles covering a span of 99 mm at $x/c = 0.30$. $Re_c = 2.4 \times 10^6$, [6|12] roughness. 209

5.60 Spanwise array of 100 disturbance profiles covering a span of 99 mm at $x/c = 0.35$. $Re_c = 2.4 \times 10^6$, [6|12] roughness. 210

5.61 Spanwise array of 100 disturbance profiles covering a span of 99 mm at $x/c = 0.40$. $Re_c = 2.4 \times 10^6$, [6|12] roughness. 211

5.62 Stationary crossflow mode shapes for $Re_c = 2.4 \times 10^6$ and [6|12] roughness. 212

5.63 Total disturbance amplitude and amplification factor N for $Re_c = 2.4 \times 10^6$ and [6|12] roughness. 213

5.64 Comparison of experimental and theoretical total disturbance amplification factor N for $Re_c = 2.4 \times 10^6$ and [6|12] roughness. 214

5.65 Comparison of experimental and theoretical crossflow mode shape at $x/c = 0.10$. $Re_c = 2.4 \times 10^6$, [6|12] roughness. 215

5.66 Comparison of experimental and theoretical crossflow mode shape at $x/c = 0.15$. $Re_c = 2.4 \times 10^6$, [6|12] roughness. 216

5.67 Comparison of experimental and theoretical crossflow mode shape at $x/c = 0.20$. $Re_c = 2.4 \times 10^6$, [6|12] roughness. 217

5.68 Comparison of experimental and theoretical crossflow mode shape at $x/c = 0.25$. $Re_c = 2.4 \times 10^6$, [6|12] roughness. 218

5.69 Comparison of experimental and theoretical crossflow mode shape at $x/c = 0.30$. $Re_c = 2.4 \times 10^6$, [6|12] roughness. 219

5.70 Comparison of experimental and theoretical crossflow mode shape at $x/c = 0.35$. $Re_c = 2.4 \times 10^6$, [6|12] roughness. 220

5.71 Comparison of experimental and theoretical crossflow mode shape at $x/c = 0.40$. $Re_c = 2.4 \times 10^6$, [6|12] roughness. 221

5.72 Comparison of experimental and theoretical crossflow mode shape at $x/c = 0.45$. $Re_c = 2.4 \times 10^6$, [6|12] roughness. 222

Figure Page

5.73 Spanwise hot-wire scan at $x/c = 0.05$, $Y = 0.3$ mm. $Re_c = 2.4 \times 10^6$, [6|12] roughness. 223

5.74 Spanwise hot-wire scan at $x/c = 0.10$, $Y = 0.6$ mm. $Re_c = 2.4 \times 10^6$, [6|12] roughness. 224

5.75 Spanwise hot-wire scan at $x/c = 0.15$, $Y = 0.75$ mm. $Re_c = 2.4 \times 10^6$, [6|12] roughness. 225

5.76 Spanwise hot-wire scan at $x/c = 0.20$, $Y = 0.85$ mm. $Re_c = 2.4 \times 10^6$, [6|12] roughness. 226

5.77 Spanwise hot-wire scan at $x/c = 0.25$, $Y = 0.9$ mm. $Re_c = 2.4 \times 10^6$, [6|12] roughness. 227

5.78 Spanwise hot-wire scan at $x/c = 0.30$, $Y = 0.9$ mm. $Re_c = 2.4 \times 10^6$, [6|12] roughness. 228

5.79 Spanwise hot-wire scan at $x/c = 0.35$, $Y = 0.9$ mm. $Re_c = 2.4 \times 10^6$, [6|12] roughness. 229

5.80 Spanwise hot-wire scan at $x/c = 0.40$, $Y = 0.9$ mm. $Re_c = 2.4 \times 10^6$, [6|12] roughness. 230

5.81 Spanwise hot-wire scan at $x/c = 0.45$, $Y = 0.9$ mm. $Re_c = 2.4 \times 10^6$, [6|12] roughness. 231

5.82 Power spectral density of spanwise hot-wire scan at $x/c = 0.05$, $Y = 0.3$ mm. $Re_c = 2.4 \times 10^6$, [6|12] roughness. 232

5.83 Power spectral density of spanwise hot-wire scan at $x/c = 0.10$, $Y = 0.6$ mm. $Re_c = 2.4 \times 10^6$, [6|12] roughness. 233

5.84 Power spectral density of spanwise hot-wire scan at $x/c = 0.15$, $Y = 0.75$ mm. $Re_c = 2.4 \times 10^6$, [6|12] roughness. 234

5.85 Power spectral density of spanwise hot-wire scan at $x/c = 0.20$, $Y = 0.85$ mm. $Re_c = 2.4 \times 10^6$, [6|12] roughness. 235

5.86 Power spectral density of spanwise hot-wire scan at $x/c = 0.25$, $Y = 0.9$ mm. $Re_c = 2.4 \times 10^6$, [6|12] roughness. 236

5.87 Power spectral density of spanwise hot-wire scan at $x/c = 0.30$, $Y = 0.9$ mm. $Re_c = 2.4 \times 10^6$, [6|12] roughness. 237

Figure Page

5.88 Power spectral density of spanwise hot-wire scan at $x/c = 0.35$, $Y = 0.9$ mm. $Re_c = 2.4 \times 10^6$, [6|12] roughness. 238

5.89 Power spectral density of spanwise hot-wire scan at $x/c = 0.40$, $Y = 0.9$ mm. $Re_c = 2.4 \times 10^6$, [6|12] roughness. 239

5.90 Power spectral density of spanwise hot-wire scan at $x/c = 0.45$, $Y = 0.9$ mm. $Re_c = 2.4 \times 10^6$, [6|12] roughness. 240

5.91 Individual-mode disturbance amplitude and amplification factor N for $Re_c = 2.4 \times 10^6$ and [6|12] roughness. 241

5.92 Total and individual-mode disturbance amplitude and amplification factor N for $Re_c = 2.4 \times 10^6$ and [6|12] roughness. 242

6.1 Streamwise velocity contours at $x/c = 0.05$. $Re_c = 1.6 \times 10^6$, [6|12] roughness. 243

6.2 Streamwise velocity contours at $x/c = 0.10$. $Re_c = 1.6 \times 10^6$, [6|12] roughness. 244

6.3 Streamwise velocity contours at $x/c = 0.15$. $Re_c = 1.6 \times 10^6$, [6|12] roughness. 245

6.4 Streamwise velocity contours at $x/c = 0.20$. $Re_c = 1.6 \times 10^6$, [6|12] roughness. 246

6.5 Streamwise velocity contours at $x/c = 0.25$. $Re_c = 1.6 \times 10^6$, [6|12] roughness. 247

6.6 Streamwise velocity contours at $x/c = 0.30$. $Re_c = 1.6 \times 10^6$, [6|12] roughness. 248

6.7 Streamwise velocity contours at $x/c = 0.35$. $Re_c = 1.6 \times 10^6$, [6|12] roughness. 249

6.8 Streamwise velocity contours at $x/c = 0.40$. $Re_c = 1.6 \times 10^6$, [6|12] roughness. 250

6.9 Streamwise velocity contours at $x/c = 0.45$. $Re_c = 1.6 \times 10^6$, [6|12] roughness. 251

6.10 Streamwise velocity contours at $x/c = 0.50$. $Re_c = 1.6 \times 10^6$, [6|12] roughness. 252

Figure Page

6.11 Streamwise velocity contours at $x/c = 0.55$. $Re_c = 1.6 \times 10^6$, [6|12] roughness. 253

6.12 Streamwise velocity contours at $x/c = 0.60$. $Re_c = 1.6 \times 10^6$, [6|12] roughness. 254

6.13 Spanwise array of 100 mean-flow boundary-layer profiles covering a span of 99 mm at $x/c = 0.05$. $Re_c = 1.6 \times 10^6$, [6|12] roughness. 255

6.14 Spanwise array of 100 mean-flow boundary-layer profiles covering a span of 99 mm at $x/c = 0.10$. $Re_c = 1.6 \times 10^6$, [6|12] roughness. 256

6.15 Spanwise array of 100 mean-flow boundary-layer profiles covering a span of 99 mm at $x/c = 0.15$. $Re_c = 1.6 \times 10^6$, [6|12] roughness. 257

6.16 Spanwise array of 100 mean-flow boundary-layer profiles covering a span of 99 mm at $x/c = 0.20$. $Re_c = 1.6 \times 10^6$, [6|12] roughness. 258

6.17 Spanwise array of 100 mean-flow boundary-layer profiles covering a span of 99 mm at $x/c = 0.25$. $Re_c = 1.6 \times 10^6$, [6|12] roughness. 259

6.18 Spanwise array of 100 mean-flow boundary-layer profiles covering a span of 99 mm at $x/c = 0.30$. $Re_c = 1.6 \times 10^6$, [6|12] roughness. 260

6.19 Spanwise array of 100 mean-flow boundary-layer profiles covering a span of 99 mm at $x/c = 0.35$. $Re_c = 1.6 \times 10^6$, [6|12] roughness. 261

6.20 Spanwise array of 100 mean-flow boundary-layer profiles covering a span of 99 mm at $x/c = 0.40$. $Re_c = 1.6 \times 10^6$, [6|12] roughness. 262

6.21 Spanwise array of 100 mean-flow boundary-layer profiles covering a span of 99 mm at $x/c = 0.45$. $Re_c = 1.6 \times 10^6$, [6|12] roughness. 263

6.22 Spanwise array of 100 mean-flow boundary-layer profiles covering a span of 99 mm at $x/c = 0.50$. $Re_c = 1.6 \times 10^6$, [6|12] roughness. 264

6.23 Spanwise array of 100 mean-flow boundary-layer profiles covering a span of 99 mm at $x/c = 0.55$. $Re_c = 1.6 \times 10^6$, [6|12] roughness. 265

6.24 Spanwise array of 100 mean-flow boundary-layer profiles covering a span of 99 mm at $x/c = 0.60$. $Re_c = 1.6 \times 10^6$, [6|12] roughness. 266

6.25 Spanwise array of 100 disturbance profiles covering a span of 99 mm at $x/c = 0.05$. $Re_c = 1.6 \times 10^6$, [6|12] roughness. 267

Figure Page

6.26 Spanwise array of 100 disturbance profiles covering a span of 99 mm at $x/c = 0.10$. $Re_c = 1.6 \times 10^6$, [6|12] roughness. 268

6.27 Spanwise array of 100 disturbance profiles covering a span of 99 mm at $x/c = 0.15$. $Re_c = 1.6 \times 10^6$, [6|12] roughness. 269

6.28 Spanwise array of 100 disturbance profiles covering a span of 99 mm at $x/c = 0.20$. $Re_c = 1.6 \times 10^6$, [6|12] roughness. 270

6.29 Spanwise array of 100 disturbance profiles covering a span of 99 mm at $x/c = 0.25$. $Re_c = 1.6 \times 10^6$, [6|12] roughness. 271

6.30 Spanwise array of 100 disturbance profiles covering a span of 99 mm at $x/c = 0.30$. $Re_c = 1.6 \times 10^6$, [6|12] roughness. 272

6.31 Spanwise array of 100 disturbance profiles covering a span of 99 mm at $x/c = 0.35$. $Re_c = 1.6 \times 10^6$, [6|12] roughness. 273

6.32 Spanwise array of 100 disturbance profiles covering a span of 99 mm at $x/c = 0.40$. $Re_c = 1.6 \times 10^6$, [6|12] roughness. 274

6.33 Spanwise array of 100 disturbance profiles covering a span of 99 mm at $x/c = 0.45$. $Re_c = 1.6 \times 10^6$, [6|12] roughness. 275

6.34 Spanwise array of 100 disturbance profiles covering a span of 99 mm at $x/c = 0.50$. $Re_c = 1.6 \times 10^6$, [6|12] roughness. 276

6.35 Spanwise array of 100 disturbance profiles covering a span of 99 mm at $x/c = 0.55$. $Re_c = 1.6 \times 10^6$, [6|12] roughness. 277

6.36 Spanwise array of 100 disturbance profiles covering a span of 99 mm at $x/c = 0.60$. $Re_c = 1.6 \times 10^6$, [6|12] roughness. 278

6.37 Disturbance velocity contours at $x/c = 0.15$. $Re_c = 1.6 \times 10^6$, [6|12] roughness. 279

6.38 Disturbance velocity contours at $x/c = 0.20$. $Re_c = 1.6 \times 10^6$, [6|12] roughness. 280

6.39 Stationary crossflow mode shapes for $Re_c = 1.6 \times 10^6$ and [6|12] roughness. 281

6.40 Total disturbance amplitude and amplification factor N for $Re_c = 1.6 \times 10^6$ and [6|12] roughness. 282

6.41 Streamwise velocity contours at $x/c = 0.05$. $Re_c = 3.2 \times 10^6$, [6|12] roughness. 283

Figure Page

6.42 Streamwise velocity contours at $x/c = 0.10$. $Re_c = 3.2 \times 10^6$, [6|12] roughness. 284

6.43 Streamwise velocity contours at $x/c = 0.15$. $Re_c = 3.2 \times 10^6$, [6|12] roughness. 285

6.44 Streamwise velocity contours at $x/c = 0.20$. $Re_c = 3.2 \times 10^6$, [6|12] roughness. 286

6.45 Streamwise velocity contours at $x/c = 0.25$. $Re_c = 3.2 \times 10^6$, [6|12] roughness. 287

6.46 Streamwise velocity contours at $x/c = 0.29$. $Re_c = 3.2 \times 10^6$, [6|12] roughness. 288

6.47 Spanwise array of 100 mean-flow boundary-layer profiles covering a span of 99 mm at $x/c = 0.05$. $Re_c = 3.2 \times 10^6$, [6|12] roughness. 289

6.48 Spanwise array of 100 mean-flow boundary-layer profiles covering a span of 99 mm at $x/c = 0.10$. $Re_c = 3.2 \times 10^6$, [6|12] roughness. 290

6.49 Spanwise array of 100 mean-flow boundary-layer profiles covering a span of 99 mm at $x/c = 0.15$. $Re_c = 3.2 \times 10^6$, [6|12] roughness. 291

6.50 Spanwise array of 100 mean-flow boundary-layer profiles covering a span of 99 mm at $x/c = 0.20$. $Re_c = 3.2 \times 10^6$, [6|12] roughness. 292

6.51 Spanwise array of 100 mean-flow boundary-layer profiles covering a span of 99 mm at $x/c = 0.25$. $Re_c = 3.2 \times 10^6$, [6|12] roughness. 293

6.52 Spanwise array of 100 mean-flow boundary-layer profiles covering a span of 99 mm at $x/c = 0.29$. $Re_c = 3.2 \times 10^6$, [6|12] roughness. 294

6.53 Spanwise array of 100 disturbance profiles covering a span of 99 mm at $x/c = 0.05$. $Re_c = 3.2 \times 10^6$, [6|12] roughness. 295

6.54 Spanwise array of 100 disturbance profiles covering a span of 99 mm at $x/c = 0.10$. $Re_c = 3.2 \times 10^6$, [6|12] roughness. 296

6.55 Spanwise array of 100 disturbance profiles covering a span of 99 mm at $x/c = 0.15$. $Re_c = 3.2 \times 10^6$, [6|12] roughness. 297

6.56 Spanwise array of 100 disturbance profiles covering a span of 99 mm at $x/c = 0.20$. $Re_c = 3.2 \times 10^6$, [6|12] roughness. 298

Figure Page

6.57 Spanwise array of 100 disturbance profiles covering a span of 99 mm at $x/c = 0.25$. $Re_c = 3.2 \times 10^6$, [6|12] roughness. 299

6.58 Spanwise array of 100 disturbance profiles covering a span of 99 mm at $x/c = 0.29$. $Re_c = 3.2 \times 10^6$, [6|12] roughness. 300

6.59 Stationary crossflow mode shapes for $Re_c = 3.2 \times 10^6$ and [6|12] roughness. 301

6.60 Total disturbance amplitude and amplification factor N for $Re_c = 3.2 \times 10^6$ and [6|12] roughness. 302

6.61 Spanwise hot-wire scan at $x/c = 0.05$, $Y = 0.3$ mm. $Re_c = 3.2 \times 10^6$, [6|12] roughness. 303

6.62 Spanwise hot-wire scan at $x/c = 0.10$, $Y = 0.45$ mm. $Re_c = 3.2 \times 10^6$, [6|12] roughness. 304

6.63 Spanwise hot-wire scan at $x/c = 0.15$, $Y = 0.65$ mm. $Re_c = 3.2 \times 10^6$, [6|12] roughness. 305

6.64 Spanwise hot-wire scan at $x/c = 0.20$, $Y = 0.7$ mm. $Re_c = 3.2 \times 10^6$, [6|12] roughness. 306

6.65 Spanwise hot-wire scan at $x/c = 0.25$, $Y = 0.7$ mm. $Re_c = 3.2 \times 10^6$, [6|12] roughness. 307

6.66 Spanwise hot-wire scan at $x/c = 0.29$, $Y = 0.65$ mm. $Re_c = 3.2 \times 10^6$, [6|12] roughness. 308

6.67 Power spectral density of spanwise hot-wire scan at $x/c = 0.05$, $Y = 0.3$ mm. $Re_c = 3.2 \times 10^6$, [6|12] roughness. 309

6.68 Power spectral density of spanwise hot-wire scan at $x/c = 0.10$, $Y = 0.45$ mm. $Re_c = 3.2 \times 10^6$, [6|12] roughness. 310

6.69 Power spectral density of spanwise hot-wire scan at $x/c = 0.15$, $Y = 0.65$ mm. $Re_c = 3.2 \times 10^6$, [6|12] roughness. 311

6.70 Power spectral density of spanwise hot-wire scan at $x/c = 0.20$, $Y = 0.7$ mm. $Re_c = 3.2 \times 10^6$, [6|12] roughness. 312

6.71 Power spectral density of spanwise hot-wire scan at $x/c = 0.25$, $Y = 0.7$ mm. $Re_c = 3.2 \times 10^6$, [6|12] roughness. 313

6.72 Power spectral density of spanwise hot-wire scan at $x/c = 0.29$, $Y = 0.65$ mm. $Re_c = 3.2 \times 10^6$, [6|12] roughness. 314

Figure Page

6.73 Individual-mode disturbance amplitude and amplification factor N for $Re_c = 3.2 \times 10^6$ and [6|12] roughness. 315

6.74 Total and individual-mode disturbance amplitude and amplification factor N for $Re_c = 3.2 \times 10^6$ and [6|12] roughness. 316

6.75 Reynolds number effect on the total disturbance amplitude and amplification factor N. [6|12] roughness. 317

6.76 Streamwise velocity contours at $x/c = 0.05$. $Re_c = 2.4 \times 10^6$, [6|36] roughness. 318

6.77 Streamwise velocity contours at $x/c = 0.10$. $Re_c = 2.4 \times 10^6$, [6|36] roughness. 319

6.78 Streamwise velocity contours at $x/c = 0.15$. $Re_c = 2.4 \times 10^6$, [6|36] roughness. 320

6.79 Streamwise velocity contours at $x/c = 0.20$. $Re_c = 2.4 \times 10^6$, [6|36] roughness. 321

6.80 Streamwise velocity contours at $x/c = 0.25$. $Re_c = 2.4 \times 10^6$, [6|36] roughness. 322

6.81 Streamwise velocity contours at $x/c = 0.30$. $Re_c = 2.4 \times 10^6$, [6|36] roughness. 323

6.82 Streamwise velocity contours at $x/c = 0.35$. $Re_c = 2.4 \times 10^6$, [6|36] roughness. 324

6.83 Streamwise velocity contours at $x/c = 0.40$. $Re_c = 2.4 \times 10^6$, [6|36] roughness. 325

6.84 Streamwise velocity contours at $x/c = 0.45$. $Re_c = 2.4 \times 10^6$, [6|36] roughness. 326

6.85 Spanwise array of 100 mean-flow boundary-layer profiles covering a span of 99 mm at $x/c = 0.05$. $Re_c = 2.4 \times 10^6$, [6|36] roughness. 327

6.86 Spanwise array of 100 mean-flow boundary-layer profiles covering a span of 99 mm at $x/c = 0.10$. $Re_c = 2.4 \times 10^6$, [6|36] roughness. 328

6.87 Spanwise array of 100 mean-flow boundary-layer profiles covering a span of 99 mm at $x/c = 0.15$. $Re_c = 2.4 \times 10^6$, [6|36] roughness. 329

Figure Page

6.88 Spanwise array of 100 mean-flow boundary-layer profiles covering a span of 99 mm at $x/c = 0.20$. $Re_c = 2.4 \times 10^6$, [6|36] roughness. 330

6.89 Spanwise array of 100 mean-flow boundary-layer profiles covering a span of 99 mm at $x/c = 0.25$. $Re_c = 2.4 \times 10^6$, [6|36] roughness. 331

6.90 Spanwise array of 100 mean-flow boundary-layer profiles covering a span of 99 mm at $x/c = 0.30$. $Re_c = 2.4 \times 10^6$, [6|36] roughness. 332

6.91 Spanwise array of 100 mean-flow boundary-layer profiles covering a span of 99 mm at $x/c = 0.35$. $Re_c = 2.4 \times 10^6$, [6|36] roughness. 333

6.92 Spanwise array of 100 mean-flow boundary-layer profiles covering a span of 99 mm at $x/c = 0.40$. $Re_c = 2.4 \times 10^6$, [6|36] roughness. 334

6.93 Spanwise array of 100 mean-flow boundary-layer profiles covering a span of 99 mm at $x/c = 0.45$. $Re_c = 2.4 \times 10^6$, [6|36] roughness. 335

6.94 Spanwise array of 100 disturbance profiles covering a span of 99 mm at $x/c = 0.05$. $Re_c = 2.4 \times 10^6$, [6|36] roughness. 336

6.95 Spanwise array of 100 disturbance profiles covering a span of 99 mm at $x/c = 0.10$. $Re_c = 2.4 \times 10^6$, [6|36] roughness. 337

6.96 Spanwise array of 100 disturbance profiles covering a span of 99 mm at $x/c = 0.15$. $Re_c = 2.4 \times 10^6$, [6|36] roughness. 338

6.97 Spanwise array of 100 disturbance profiles covering a span of 99 mm at $x/c = 0.20$. $Re_c = 2.4 \times 10^6$, [6|36] roughness. 339

6.98 Spanwise array of 100 disturbance profiles covering a span of 99 mm at $x/c = 0.25$. $Re_c = 2.4 \times 10^6$, [6|36] roughness. 340

6.99 Spanwise array of 100 disturbance profiles covering a span of 99 mm at $x/c = 0.30$. $Re_c = 2.4 \times 10^6$, [6|36] roughness. 341

6.100 Spanwise array of 100 disturbance profiles covering a span of 99 mm at $x/c = 0.35$. $Re_c = 2.4 \times 10^6$, [6|36] roughness. 342

6.101 Spanwise array of 100 disturbance profiles covering a span of 99 mm at $x/c = 0.40$. $Re_c = 2.4 \times 10^6$, [6|36] roughness. 343

6.102 Spanwise array of 100 disturbance profiles covering a span of 99 mm at $x/c = 0.45$. $Re_c = 2.4 \times 10^6$, [6|36] roughness. 344

Figure Page

6.103 Disturbance velocity contours at $x/c = 0.45$. $Re_c = 2.4 \times 10^6$, [6|36] roughness. 345

6.104 Stationary crossflow mode shapes for $Re_c = 2.4 \times 10^6$ and [6|36] roughness. 346

6.105 Total disturbance amplitude and amplification factor N for $Re_c = 2.4 \times 10^6$ and [6|36] roughness. 347

6.106 Spanwise hot-wire scan at $x/c = 0.10$, $Y = 0.4$ mm. $Re_c = 2.4 \times 10^6$, [6|36] roughness. 348

6.107 Spanwise hot-wire scan at $x/c = 0.15$, $Y = 0.8$ mm. $Re_c = 2.4 \times 10^6$, [6|36] roughness. 349

6.108 Spanwise hot-wire scan at $x/c = 0.20$, $Y = 0.9$ mm. $Re_c = 2.4 \times 10^6$, [6|36] roughness. 350

6.109 Spanwise hot-wire scan at $x/c = 0.25$, $Y = 1.0$ mm. $Re_c = 2.4 \times 10^6$, [6|36] roughness. 351

6.110 Spanwise hot-wire scan at $x/c = 0.30$, $Y = 1.0$ mm. $Re_c = 2.4 \times 10^6$, [6|36] roughness. 352

6.111 Spanwise hot-wire scan at $x/c = 0.35$, $Y = 1.0$ mm. $Re_c = 2.4 \times 10^6$, [6|36] roughness. 353

6.112 Spanwise hot-wire scan at $x/c = 0.40$, $Y = 0.95$ mm. $Re_c = 2.4 \times 10^6$, [6|36] roughness. 354

6.113 Spanwise hot-wire scan at $x/c = 0.45$, $Y = 0.9$ mm. $Re_c = 2.4 \times 10^6$, [6|36] roughness. 355

6.114 Power spectral density of spanwise hot-wire scan at $x/c = 0.10$, $Y = 0.4$ mm. $Re_c = 2.4 \times 10^6$, [6|36] roughness. 356

6.115 Power spectral density of spanwise hot-wire scan at $x/c = 0.15$, $Y = 0.8$ mm. $Re_c = 2.4 \times 10^6$, [6|36] roughness. 357

6.116 Power spectral density of spanwise hot-wire scan at $x/c = 0.20$, $Y = 0.9$ mm. $Re_c = 2.4 \times 10^6$, [6|36] roughness. 358

6.117 Power spectral density of spanwise hot-wire scan at $x/c = 0.25$, $Y = 1.0$ mm. $Re_c = 2.4 \times 10^6$, [6|36] roughness. 359

6.118 Power spectral density of spanwise hot-wire scan at $x/c = 0.30$, $Y = 1.0$ mm. $Re_c = 2.4 \times 10^6$, [6|36] roughness. 360

Figure Page

6.119 Power spectral density of spanwise hot-wire scan at $x/c = 0.35$, Y = 1.0 mm. $Re_c = 2.4 \times 10^6$, [6|36] roughness. 361

6.120 Power spectral density of spanwise hot-wire scan at $x/c = 0.40$, Y = 0.95 mm. $Re_c = 2.4 \times 10^6$, [6|36] roughness. 362

6.121 Power spectral density of spanwise hot-wire scan at $x/c = 0.45$, Y = 0.9 mm. $Re_c = 2.4 \times 10^6$, [6|36] roughness. 363

6.122 Power spectral density of spanwise hot-wire scan at $x/c = 0.45$, Y = 0.9 mm. $Re_c = 2.4 \times 10^6$, [6|36] roughness. Enhanced view showing amplitude of small-wavelength disturbances. 364

6.123 Individual-mode disturbance amplification factor N for $Re_c = 2.4 \times 10^6$ and [6|36] roughness. 365

6.124 Individual-mode disturbance amplitude for $Re_c = 2.4 \times 10^6$ and [6|36] roughness. 366

6.125 Streamwise velocity contours at $x/c = 0.05$. $Re_c = 2.4 \times 10^6$, [18|12] roughness. 367

6.126 Streamwise velocity contours at $x/c = 0.10$. $Re_c = 2.4 \times 10^6$, [18|12] roughness. 368

6.127 Streamwise velocity contours at $x/c = 0.15$. $Re_c = 2.4 \times 10^6$, [18|12] roughness. 369

6.128 Streamwise velocity contours at $x/c = 0.20$. $Re_c = 2.4 \times 10^6$, [18|12] roughness. 370

6.129 Streamwise velocity contours at $x/c = 0.25$. $Re_c = 2.4 \times 10^6$, [18|12] roughness. 371

6.130 Streamwise velocity contours at $x/c = 0.30$. $Re_c = 2.4 \times 10^6$, [18|12] roughness. 372

6.131 Streamwise velocity contours at $x/c = 0.35$. $Re_c = 2.4 \times 10^6$, [18|12] roughness. 373

6.132 Streamwise velocity contours at $x/c = 0.40$. $Re_c = 2.4 \times 10^6$, [18|12] roughness. 374

6.133 Streamwise velocity contours at $x/c = 0.45$. $Re_c = 2.4 \times 10^6$, [18|12] roughness. 375

Figure Page

6.134 Spanwise array of 100 mean-flow boundary-layer profiles covering a span of 99 mm at $x/c = 0.05$. $Re_c = 2.4 \times 10^6$, [18|12] roughness. . . . 376

6.135 Spanwise array of 100 mean-flow boundary-layer profiles covering a span of 99 mm at $x/c = 0.10$. $Re_c = 2.4 \times 10^6$, [18|12] roughness. . . . 377

6.136 Spanwise array of 100 mean-flow boundary-layer profiles covering a span of 99 mm at $x/c = 0.15$. $Re_c = 2.4 \times 10^6$, [18|12] roughness. . . . 378

6.137 Spanwise array of 100 mean-flow boundary-layer profiles covering a span of 99 mm at $x/c = 0.20$. $Re_c = 2.4 \times 10^6$, [18|12] roughness. . . . 379

6.138 Spanwise array of 100 mean-flow boundary-layer profiles covering a span of 99 mm at $x/c = 0.25$. $Re_c = 2.4 \times 10^6$, [18|12] roughness. . . . 380

6.139 Spanwise array of 100 mean-flow boundary-layer profiles covering a span of 99 mm at $x/c = 0.30$. $Re_c = 2.4 \times 10^6$, [18|12] roughness. . . . 381

6.140 Spanwise array of 100 mean-flow boundary-layer profiles covering a span of 99 mm at $x/c = 0.35$. $Re_c = 2.4 \times 10^6$, [18|12] roughness. . . . 382

6.141 Spanwise array of 100 mean-flow boundary-layer profiles covering a span of 99 mm at $x/c = 0.40$. $Re_c = 2.4 \times 10^6$, [18|12] roughness. . . . 383

6.142 Spanwise array of 100 mean-flow boundary-layer profiles covering a span of 99 mm at $x/c = 0.45$. $Re_c = 2.4 \times 10^6$, [18|12] roughness. . . . 384

6.143 Spanwise array of 100 disturbance profiles covering a span of 99 mm at $x/c = 0.05$. $Re_c = 2.4 \times 10^6$, [18|12] roughness. 385

6.144 Spanwise array of 100 disturbance profiles covering a span of 99 mm at $x/c = 0.10$. $Re_c = 2.4 \times 10^6$, [18|12] roughness. 386

6.145 Spanwise array of 100 disturbance profiles covering a span of 99 mm at $x/c = 0.15$. $Re_c = 2.4 \times 10^6$, [18|12] roughness. 387

6.146 Spanwise array of 100 disturbance profiles covering a span of 99 mm at $x/c = 0.20$. $Re_c = 2.4 \times 10^6$, [18|12] roughness. 388

6.147 Spanwise array of 100 disturbance profiles covering a span of 99 mm at $x/c = 0.25$. $Re_c = 2.4 \times 10^6$, [18|12] roughness. 389

6.148 Spanwise array of 100 disturbance profiles covering a span of 99 mm at $x/c = 0.30$. $Re_c = 2.4 \times 10^6$, [18|12] roughness. 390

Figure Page

6.149 Spanwise array of 100 disturbance profiles covering a span of 99 mm at $x/c = 0.35$. $Re_c = 2.4 \times 10^6$, [18|12] roughness. 391

6.150 Spanwise array of 100 disturbance profiles covering a span of 99 mm at $x/c = 0.40$. $Re_c = 2.4 \times 10^6$, [18|12] roughness. 392

6.151 Spanwise array of 100 disturbance profiles covering a span of 99 mm at $x/c = 0.45$. $Re_c = 2.4 \times 10^6$, [18|12] roughness. 393

6.152 Stationary crossflow mode shapes for $Re_c = 2.4 \times 10^6$ and [18|12] roughness. 394

6.153 Total disturbance amplitude and amplification factor N for $Re_c = 2.4 \times 10^6$ and [18|12] roughness. 395

6.154 Spanwise hot-wire scan at $x/c = 0.05$, $Y = 0.4$ mm. $Re_c = 2.4 \times 10^6$, [18|12] roughness. 396

6.155 Spanwise hot-wire scan at $x/c = 0.10$, $Y = 0.6$ mm. $Re_c = 2.4 \times 10^6$, [18|12] roughness. 397

6.156 Spanwise hot-wire scan at $x/c = 0.15$, $Y = 0.75$ mm. $Re_c = 2.4 \times 10^6$, [18|12] roughness. 398

6.157 Spanwise hot-wire scan at $x/c = 0.20$, $Y = 0.8$ mm. $Re_c = 2.4 \times 10^6$, [18|12] roughness. 399

6.158 Spanwise hot-wire scan at $x/c = 0.25$, $Y = 0.85$ mm. $Re_c = 2.4 \times 10^6$, [18|12] roughness. 400

6.159 Spanwise hot-wire scan at $x/c = 0.30$, $Y = 0.85$ mm. $Re_c = 2.4 \times 10^6$, [18|12] roughness. 401

6.160 Spanwise hot-wire scan at $x/c = 0.35$, $Y = 0.85$ mm. $Re_c = 2.4 \times 10^6$, [18|12] roughness. 402

6.161 Spanwise hot-wire scan at $x/c = 0.40$, $Y = 0.85$ mm. $Re_c = 2.4 \times 10^6$, [18|12] roughness. 403

6.162 Spanwise hot-wire scan at $x/c = 0.45$, $Y = 0.85$ mm. $Re_c = 2.4 \times 10^6$, [18|12] roughness. 404

6.163 Power spectral density of spanwise hot-wire scan at $x/c = 0.05$, $Y = 0.4$ mm. $Re_c = 2.4 \times 10^6$, [18|12] roughness. 405

Figure Page

6.164 Power spectral density of spanwise hot-wire scan at $x/c = 0.10$, $Y =$ 0.6 mm. $Re_c = 2.4 \times 10^6$, [18|12] roughness. 406

6.165 Power spectral density of spanwise hot-wire scan at $x/c = 0.15$, $Y =$ 0.75 mm. $Re_c = 2.4 \times 10^6$, [18|12] roughness. 407

6.166 Power spectral density of spanwise hot-wire scan at $x/c = 0.20$, $Y =$ 0.8 mm. $Re_c = 2.4 \times 10^6$, [18|12] roughness. 408

6.167 Power spectral density of spanwise hot-wire scan at $x/c = 0.25$, $Y =$ 0.85 mm. $Re_c = 2.4 \times 10^6$, [18|12] roughness. 409

6.168 Power spectral density of spanwise hot-wire scan at $x/c = 0.30$, $Y =$ 0.85 mm. $Re_c = 2.4 \times 10^6$, [18|12] roughness. 410

6.169 Power spectral density of spanwise hot-wire scan at $x/c = 0.35$, $Y =$ 0.85 mm. $Re_c = 2.4 \times 10^6$, [18|12] roughness. 411

6.170 Power spectral density of spanwise hot-wire scan at $x/c = 0.40$, $Y =$ 0.85 mm. $Re_c = 2.4 \times 10^6$, [18|12] roughness. 412

6.171 Power spectral density of spanwise hot-wire scan at $x/c = 0.45$, $Y =$ 0.85 mm. $Re_c = 2.4 \times 10^6$, [18|12] roughness. 413

6.172 Individual-mode disturbance amplitude and amplification factor N for $Re_c = 2.4 \times 10^6$ and [18|12] roughness. 414

6.173 Total and individual-mode disturbance amplitude and amplification factor N for $Re_c = 2.4 \times 10^6$ and [18|12] roughness. 415

6.174 Streamwise velocity contours at $x/c = 0.05$. $Re_c = 2.4 \times 10^6$, [48|12] roughness. 416

6.175 Streamwise velocity contours at $x/c = 0.10$. $Re_c = 2.4 \times 10^6$, [48|12] roughness. 417

6.176 Streamwise velocity contours at $x/c = 0.15$. $Re_c = 2.4 \times 10^6$, [48|12] roughness. 418

6.177 Streamwise velocity contours at $x/c = 0.20$. $Re_c = 2.4 \times 10^6$, [48|12] roughness. 419

6.178 Streamwise velocity contours at $x/c = 0.25$. $Re_c = 2.4 \times 10^6$, [48|12] roughness. 420

Figure Page

6.179 Streamwise velocity contours at $x/c = 0.30$. $Re_c = 2.4 \times 10^6$, [48|12] roughness. 421

6.180 Streamwise velocity contours at $x/c = 0.35$. $Re_c = 2.4 \times 10^6$, [48|12] roughness. 422

6.181 Streamwise velocity contours at $x/c = 0.40$. $Re_c = 2.4 \times 10^6$, [48|12] roughness. 423

6.182 Streamwise velocity contours at $x/c = 0.45$. $Re_c = 2.4 \times 10^6$, [48|12] roughness. 424

6.183 Spanwise array of 100 mean-flow boundary-layer profiles covering a span of 99 mm at $x/c = 0.05$. $Re_c = 2.4 \times 10^6$, [48|12] roughness. . . . 425

6.184 Spanwise array of 100 mean-flow boundary-layer profiles covering a span of 99 mm at $x/c = 0.10$. $Re_c = 2.4 \times 10^6$, [48|12] roughness. . . . 426

6.185 Spanwise array of 100 mean-flow boundary-layer profiles covering a span of 99 mm at $x/c = 0.15$. $Re_c = 2.4 \times 10^6$, [48|12] roughness. . . . 427

6.186 Spanwise array of 100 mean-flow boundary-layer profiles covering a span of 99 mm at $x/c = 0.20$. $Re_c = 2.4 \times 10^6$, [48|12] roughness. . . . 428

6.187 Spanwise array of 100 mean-flow boundary-layer profiles covering a span of 99 mm at $x/c = 0.25$. $Re_c = 2.4 \times 10^6$, [48|12] roughness. . . . 429

6.188 Spanwise array of 100 mean-flow boundary-layer profiles covering a span of 99 mm at $x/c = 0.30$. $Re_c = 2.4 \times 10^6$, [48|12] roughness. . . . 430

6.189 Spanwise array of 100 mean-flow boundary-layer profiles covering a span of 99 mm at $x/c = 0.35$. $Re_c = 2.4 \times 10^6$, [48|12] roughness. . . . 431

6.190 Spanwise array of 100 mean-flow boundary-layer profiles covering a span of 99 mm at $x/c = 0.40$. $Re_c = 2.4 \times 10^6$, [48|12] roughness. . . . 432

6.191 Spanwise array of 100 mean-flow boundary-layer profiles covering a span of 99 mm at $x/c = 0.45$. $Re_c = 2.4 \times 10^6$, [48|12] roughness. . . . 433

6.192 Spanwise array of 100 disturbance profiles covering a span of 99 mm at $x/c = 0.05$. $Re_c = 2.4 \times 10^6$, [48|12] roughness. 434

6.193 Spanwise array of 100 disturbance profiles covering a span of 99 mm at $x/c = 0.10$. $Re_c = 2.4 \times 10^6$, [48|12] roughness. 435

Figure Page

6.194 Spanwise array of 100 disturbance profiles covering a span of 99 mm at $x/c = 0.15$. $Re_c = 2.4 \times 10^6$, [48|12] roughness. 436

6.195 Spanwise array of 100 disturbance profiles covering a span of 99 mm at $x/c = 0.20$. $Re_c = 2.4 \times 10^6$, [48|12] roughness. 437

6.196 Spanwise array of 100 disturbance profiles covering a span of 99 mm at $x/c = 0.25$. $Re_c = 2.4 \times 10^6$, [48|12] roughness. 438

6.197 Spanwise array of 100 disturbance profiles covering a span of 99 mm at $x/c = 0.30$. $Re_c = 2.4 \times 10^6$, [48|12] roughness. 439

6.198 Spanwise array of 100 disturbance profiles covering a span of 99 mm at $x/c = 0.35$. $Re_c = 2.4 \times 10^6$, [48|12] roughness. 440

6.199 Spanwise array of 100 disturbance profiles covering a span of 99 mm at $x/c = 0.40$. $Re_c = 2.4 \times 10^6$, [48|12] roughness. 441

6.200 Spanwise array of 100 disturbance profiles covering a span of 99 mm at $x/c = 0.45$. $Re_c = 2.4 \times 10^6$, [48|12] roughness. 442

6.201 Stationary crossflow mode shapes for $Re_c = 2.4 \times 10^6$ and [48|12] roughness. 443

6.202 Total disturbance amplitude and amplification factor N for $Re_c = 2.4 \times 10^6$ and [48|12] roughness. 444

6.203 Spanwise hot-wire scan at $x/c = 0.05$, $Y = 0.45$ mm. $Re_c = 2.4 \times 10^6$, [48|12] roughness. 445

6.204 Spanwise hot-wire scan at $x/c = 0.10$, $Y = 0.6$ mm. $Re_c = 2.4 \times 10^6$, [48|12] roughness. 446

6.205 Spanwise hot-wire scan at $x/c = 0.15$, $Y = 0.75$ mm. $Re_c = 2.4 \times 10^6$, [48|12] roughness. 447

6.206 Spanwise hot-wire scan at $x/c = 0.20$, $Y = 0.75$ mm. $Re_c = 2.4 \times 10^6$, [48|12] roughness. 448

6.207 Spanwise hot-wire scan at $x/c = 0.25$, $Y = 0.8$ mm. $Re_c = 2.4 \times 10^6$, [48|12] roughness. 449

6.208 Spanwise hot-wire scan at $x/c = 0.30$, $Y = 0.8$ mm. $Re_c = 2.4 \times 10^6$, [48|12] roughness. 450

Figure Page

6.209 Spanwise hot-wire scan at $x/c = 0.35$, $Y = 0.85$ mm. $Re_c = 2.4 \times 10^6$, [48|12] roughness. 451

6.210 Spanwise hot-wire scan at $x/c = 0.40$, $Y = 0.85$ mm. $Re_c = 2.4 \times 10^6$, [48|12] roughness. 452

6.211 Spanwise hot-wire scan at $x/c = 0.45$, $Y = 0.85$ mm. $Re_c = 2.4 \times 10^6$, [48|12] roughness. 453

6.212 Power spectral density of spanwise hot-wire scan at $x/c = 0.05$, $Y =$ 0.45 mm. $Re_c = 2.4 \times 10^6$, [48|12] roughness. 454

6.213 Power spectral density of spanwise hot-wire scan at $x/c = 0.10$, $Y =$ 0.6 mm. $Re_c = 2.4 \times 10^6$, [48|12] roughness. 455

6.214 Power spectral density of spanwise hot-wire scan at $x/c = 0.15$, $Y =$ 0.75 mm. $Re_c = 2.4 \times 10^6$, [48|12] roughness. 456

6.215 Power spectral density of spanwise hot-wire scan at $x/c = 0.20$, $Y =$ 0.75 mm. $Re_c = 2.4 \times 10^6$, [48|12] roughness. 457

6.216 Power spectral density of spanwise hot-wire scan at $x/c = 0.25$, $Y =$ 0.8 mm. $Re_c = 2.4 \times 10^6$, [48|12] roughness. 458

6.217 Power spectral density of spanwise hot-wire scan at $x/c = 0.30$, $Y =$ 0.8 mm. $Re_c = 2.4 \times 10^6$, [48|12] roughness. 459

6.218 Power spectral density of spanwise hot-wire scan at $x/c = 0.35$, $Y =$ 0.85 mm. $Re_c = 2.4 \times 10^6$, [48|12] roughness. 460

6.219 Power spectral density of spanwise hot-wire scan at $x/c = 0.40$, $Y =$ 0.85 mm. $Re_c = 2.4 \times 10^6$, [48|12] roughness. 461

6.220 Power spectral density of spanwise hot-wire scan at $x/c = 0.45$, $Y =$ 0.85 mm. $Re_c = 2.4 \times 10^6$, [48|12] roughness. 462

6.221 Individual-mode disturbance amplitude and amplification factor N for $Re_c = 2.4 \times 10^6$ and [48|12] roughness. 463

6.222 Total and individual-mode disturbance amplitude and amplification factor N for $Re_c = 2.4 \times 10^6$ and [48|12] roughness. 464

6.223 Stationary crossflow mode shapes at $x/c = 0.10$ and $x/c = 0.45$ for $Re_c = 2.4 \times 10^6$ and [k|12] roughness. 465

6.224 Total disturbance amplitude for $Re_c = 2.4 \times 10^6$ and [k|12] roughness. . 466

Figure Page

6.225 Total disturbance amplification factor N for $Re_c = 2.4 \times 10^6$ and $[k|12]$ roughness. 467

6.226 Chordwise variation of fundamental crossflow mode wavelength. 468

NOMENCLATURE

A	disturbance amplitude
A_o	reference disturbance amplitude
C	= 1.83 m, airfoil streamwise chord (along X axis)
C_p	pressure coefficient
C_{p_2}	unswept pressure coefficient
C_{p_3}	swept pressure coefficient
C_T	hot-wire temperature-compensation coefficient
c	= 1.29 m, airfoil normal chord (along x axis)
E	hot-wire anemometer output voltage
E_c	equivalent anemometer output voltage at the hot-wire calibration temperature
f	frequency [Hz]
f_c	Nyquist critical frequency [Hz]
H	shape factor
h_{10}	larger of two heights where crossflow velocity w_t is 10% of maximum [m]
k	roughness height [m]
M	Mach number; number of FFT averages
m	mode number
N	= $\ln(A/A_o)$, amplification factor; number of samples
n	curve-fit order
p	static pressure [Pa]
p_∞	freestream static pressure [Pa]

Re_c	$= U_\infty C/\nu$, streamwise chord Reynolds number
Re_{cf}	$= w_{t_{\max}} h_{10}/\nu$, crossflow Reynolds number based on maximum crossflow velocity and second 10% point in crossflow profile
Re_k	$= U(k)k/\nu$, roughness Reynolds number based on total velocity at top of roughness and roughness height
Re_θ	$= u_t\theta/\nu$, attachment-line Reynolds number based on edge velocity and momentum thickness of attachment-line boundary layer
S	length (in time [s] or space [m]) of a data set; spanwise extent of a hot-wire scan [m]
T	temperature [°C]
T_c	hot-wire calibration temperature [°C]
U	$= (u^2 + w^2)^{1/2} = U(y)$, magnitude of total velocity [m/s]
U_e	boundary-layer edge velocity along X axis [m/s]
U_∞	freestream velocity along X axis [m/s]
u, v, w	velocity components in global (X, Y, Z) coordinates [m/s]
u', v', w'	disturbance velocity components in (X, Y, Z) coordinates [m/s]
u_n, v_n, w_n	velocity components in model-oriented (x, y, z) coordinates [m/s]
u_t, v_t, w_t	velocity components in boundary-layer (x_t, y_t, z_t) coordinates [m/s]
X, Y, Z	global test-section coordinates: X is along the upstream flow axis, Y is normal to test-section side wall, Z is unswept spanwise coordinate (positive down)
x, y, z	model-oriented coordinates: x is chordwise, y is normal to chord line, z is spanwise (parallel to leading edge)
x_t, y_t, z_t	boundary-layer coordinates: x_t is along outer streamline, y_t is normal to model surface, z_t is crossflow direction
α	airfoil angle of attack; chordwise (x) wavenumber
β	spanwise (z) wavenumber

Δ	change or difference, e.g., ΔT is a temperature difference
Δ_s	sampling interval
Δf	spectral frequency resolution
$\Delta\lambda$	spectral wavelength resolution
δ	boundary-layer thickness [m]
δ^*	displacement thickness [m]
δ_F	flap deflection angle
Λ	sweep angle
λ	wavelength [m]
λ_{cf}	crossflow disturbance wavelength measured normal to vortex axis [m]
λ_s	$= \lambda_z$
λ_z	wavelength measured in swept span (z) direction [m]
ν	kinematic viscosity [m^2/s]
θ	momentum thickness [m]
ρ	density [kg/m^3]
ω	frequency [rad/s]
ξ, ζ, z	body-intrinsic coordinates: ξ is chordwise and tangent to airfoil surface, ζ is normal to airfoil surface, z is spanwise (parallel to leading edge)

CHAPTER 1

Introduction

1.1 Background and Motivation

The understanding, prediction, and eventual control of the processes that cause a boundary layer to transition from laminar to turbulent flow are in the group of the most important unsolved problems in fluid mechanics. This is due in large part to the vast array of practical engineering applications that depend strongly on the state of the boundary layer. These include, but certainly are not limited to, nose cone and heat shield requirements on reentry vehicles, efficiency and performance of turbine cascades and turbomachinery systems, convective heat transfer and temperature control, and skin-friction drag reduction. The last of these areas has profound implications for civil and commercial aviation. Several estimates indicate that a 25% reduction in fuel consumption would be achieved by maintaining laminar flow on the wings of modern transport aircraft (Pfenninger 1977; Thomas 1985; Saric 1994b). In light of this, it is no surprise that boundary-layer stability and transition have received considerable attention throughout this century. Yet in spite of all the theoretical and experimental efforts, no mathematical model exists that can predict the transition Reynolds number for a zero-pressure-gradient flow over a smooth flat plate (Saric 1994c). This is not to

say, however, that significant progress in Laminar Flow Control (LFC) has not been made. Wall suction, heating (in water) or cooling (in gases), and careful shaping of the pressure distribution can delay transition by limiting the growth of unstable disturbances. Thus, while important advances in transition research have been made, the ultimate success of transition prediction and LFC requires a more fundamental understanding of the processes that lead to transition.

1.1.1 Boundary-Layer Transition

Although the transition from laminar to turbulent flow is complicated by many factors, the process for boundary layers in external flows is usually divided into three phases. The first involves the mechanisms by which freestream disturbances enter the boundary layer and is called *receptivity* (Morkovin 1969). This process is still not well understood, but is arguably the most important in boundary-layer transition as it provides the critical initial amplitude, frequency, and phase for unstable waves (Saric 1994c). The initial conditions are known to come from external disturbances in the form of freestream fluctuations (both acoustic and vortical), surface roughness, and surface vibration. The appearance of a particular instability mode, however, is also influenced by several other factors including Reynolds number, wall curvature, wing sweep, and pressure gradient. The combination of these factors can cause a variety of instabilities to occur, and the receptivity of the boundary layer to these various modes can dramatically affect the details of transition.

The second phase of the transition process concerns the initial growth of small disturbances in the boundary layer and is described by *linear stability theory*. The growth of unstable waves is modeled with a set of linear, unsteady, disturbance equations obtained from the governing nonlinear Navier-Stokes equations. The well-known Orr-Sommerfeld equation for incompressible, parallel basic states is the best example, however similar equations can be derived for more general flows. The linear regime is

the most studied stage of boundary-layer transition and is, at least conceptually, well understood for two-dimensional flows (Saric 1992b). Three-dimensional flows, however, exhibit fundamentally different stability characteristics (Reed and Saric 1989) and have proven a greater challenge for linear theory.

The third and final phase of boundary-layer transition is characterized by *nonlinear interactions* among multiple instability modes. This occurs when the disturbances becomes large enough to interact with each other through the nonlinear terms in the Navier-Stokes equations. These interactions can distort the basic-state boundary layer leading to the rapid growth of secondary instabilities and the onset of turbulence. Because the nonlinear interactions are initially characterized by double exponential growth (Saric 1992b), it is generally believed that transition occurs very quickly after the development of nonlinear effects. As we will see in chapters 5 and 6, this is not necessarily true.

1.1.2 Transition Prediction

True transition prediction must account for all three stages of the transition process described above. However, due to the relative simplicity and computational efficiency of the linear disturbance equations, transition prediction schemes are typically based on linear theory. By far the most popular of these techniques is the celebrated e^N method of Smith and Gamberoni (1956) and van Ingen (1956). Complete reviews can be found in Arnal (1984, 1992, 1994), Mack (1984), and Saric (1992b, 1994c). The basic assumptions of the method are (1) there is some uniform norm of initial amplitude, (2) there exists a critical disturbance amplitude at transition, and (3) this amplitude is achieved through the exponential growth described by linear theory. Within this framework, the disturbance growth rates computed from linear theory are integrated from the initial point of instability to the transition location (as provided by experimental data) to give the amplitude ratio A/A_o. The natural log of this

ratio is the amplification factor N (commonly called the N-factor). For a known flow situation, the N-factor will have some value (say, 9) at transition. In unknown flow situations or those for which experimental data are not available, the growth rates are integrated up to the location where $N = 9$ (or whatever value of N was deemed appropriate), at which point transition is assumed to occur. In this regard, the e^N method would be better described as providing transition correlations rather than transition predictions.

The e^N method finds its greatest utility when used as a comparative measure of the role of stabilizing or destabilizing effects within the boundary layer; i.e., heating/cooling, suction/blowing, pressure gradients, curvature, etc. As a transition-prediction scheme, however, the limitations of the e^N method are obvious. Since linear theory can only calculate the amplitude ratio between two locations, initial conditions cannot be taken into account and the receptivity process is entirely ignored. Moreover, nonlinear interactions are not considered. Thus, the e^N method can be expected to fail for flows in which these effects are important. For example, Radeztsky et al. (1993a) show that small changes in the surface roughness on a swept airfoil can dramatically change the transition location as well as the N-factor at transition. In general, e^N correlations work within some error limits only for flows with identical disturbance environments, and the use of this method without the support of experimental data is particularly dangerous (Saric 1994c).

For flows in which the e^N method is known to fail (such as crossflow-dominated boundary layers), the recently developed parabolized stability equations (PSE) promise to be an effective tool for transition modeling. Herbert (1994) gives a comprehensive analysis of the PSE. The formulation results in an initial-boundary-value problem that can be solved by numerical marching. The initial conditions must be prescribed, hence the PSE do not address the receptivity problem. However, nonparallel effects

are taken into account and the nonlinear terms can be retained. Thus, the PSE can analyze the nonlinear response of forced modes. This represents a major step toward the goal of modeling all three phases of the transition process. At the same time, the lack of initial conditions underscores the need for accurate and detailed experiments.

1.2 Three-Dimensional Boundary Layers

1.2.1 Swept-Wing Flows

The study of three-dimensional boundary layers is motivated by the need to understand the fundamental instability mechanisms that cause transition in swept-wing flows. Research has identified four types of instabilities for these flows: attachment line, streamwise, centrifugal, and crossflow. The attachment-line problem is caused by a basic instability of the attachment-line boundary layer or by its contamination with turbulent disturbances and develops, in general, on swept wings with a large leading-edge radius (Poll 1979, 1984, 1985; Hall et al. 1984; Hall and Malik 1986). The streamwise instability is not unlike the familiar Tollmien-Schlichting wave in two-dimensional flows. This mechanism is associated with the chordwise velocity component and is generally stabilized by a favorable pressure gradient. Centrifugal instabilities can appear over concave regions on the surface and result in the development of Görtler vortices (Floryan 1991; Benmalek and Saric 1994; Saric 1994a). Crossflow waves, on the other hand, are an inviscid instability mechanism caused by the combined effect of wing sweep and pressure gradient. All of these instabilities can appear individually or together depending on the combination of Reynolds number, wall curvature, wing sweep, pressure gradient, and external disturbances (including surface roughness). Thus, the swept wing provides a rich environment in which to study the stability behavior of three-dimensional boundary layers.

1.2.2 Crossflow Instability

The present experiment focuses on the crossflow instability that occurs on swept wings in regions of strong, favorable pressure gradient. The physical mechanism for the instability is described as follows. The potential-flow streamlines are highly curved near the leading edge due to the combined effect of wing sweep and pressure gradient. These streamlines are deflected as they pass over the airfoil, first inboard near the leading edge, then outboard in the pressure recovery region downstream of the pressure minimum. Because of the loss of streamwise momentum near the surface, the deflection is greater within the boundary layer and the total boundary-layer flow is not in the direction of the inviscid streamline. The component of flow perpendicular to the inviscid streamline is called the *crossflow* velocity. The crossflow velocity satisfies the no-slip condition and asymptotically vanishes at the boundary-layer edge, thus the profile contains an inflection point and is subject to an inviscid instability. This crossflow instability manifests itself as co-rotating vortices whose axes are aligned roughly with the potential-flow direction.

Unlike Tollmien-Schlichting instabilities, the crossflow problem exhibits stationary ($f = 0$) as well as traveling disturbances that are amplified. Linear theory predicts much larger growth rates for the traveling waves, however in many experiments transition is dominated by the stationary disturbances. Whether transition is controlled by the stationary or traveling waves is intimately tied to the receptivity problem. Müller and Bippes (1989), Bippes (1990, 1991), and Bippes et al. (1991) have shown that traveling waves are observed in environments rich in unsteady freestream disturbances, whereas stationary waves dominate transition in low-disturbance environments. Since the low-disturbance environment is more characteristic of flight, the stationary waves are expected to be more important. Under these conditions, the disturbance amplitude can be modulated by changing the surface roughness charac-

teristics of the model (Kachanov and Tararykin 1990; Radeztsky et al. 1993a, 1994). In light of this, one should be very suspicious of simple transition prediction schemes (such as the e^N method) that do not account for initial conditions.

The stationary waves (that is, the v' and w' disturbances) are typically very weak, hence many theoreticians insist that they can be accurately modeled with linear theory. However, experiments often show evidence of strong nonlinear effects (Dagenhart et al. 1989, 1990; Bippes and Nitschke-Kowsky 1990; Bippes et al. 1991; Deyhle et al. 1993; Radeztsky et al. 1994). The resolution of this apparent paradox lies in the understanding of the physical mechanism by which the stationary waves disturb the boundary layer. The key to the stationary disturbance is that the wave fronts are fixed with respect to the model and nearly aligned with the potential-flow direction (i.e., the wavenumber vector is nearly perpendicular to the inviscid streamline). Consequently, although the (v', w') motion of the wave is weak, its stationary nature produces an *integrated effect* that causes a strong u' distortion in the streamwise boundary-layer profile. In simple terms, the weak stationary wave "works" on the same fluid to produce a large u' disturbance by convecting low-speed fluid away from the surface (where $v' > 0$) and high-speed fluid toward the surface (where $v' < 0$). This integrated effect and the resulting distortion of the mean boundary layer leads to the modification of the basic state and the early development of nonlinear effects.

An interesting side effect of the stationary crossflow waves is the destabilization of secondary instabilities. The u' distortions created by the stationary wave are *spatial*, resulting in a spanwise modulation of the mean streamwise velocity profile. As the distortions grow, the boundary layer develops an alternating pattern of accelerated, decelerated, and doubly inflected profiles. The inflected profiles are inviscidly unstable and, as such, are subject to a high-frequency secondary instability (Kohama et al. 1991). This secondary instability is highly amplified and leads to rapid local

breakdown. Because transition develops locally, the transition front is nonuniform in span and characterized by a saw-tooth pattern of turbulent wedges.

1.3 Review of Recent Results

The need to better understand the transition processes for swept-wing flows has sparked strong interest in three-dimensional boundary layers over the last 50 years. Significant theoretical advancements have been made, however there have been relatively few experiments detailed enough to validate the theory. The combination of complex geometries, multiple instability mechanisms, and observed nonlinear effects has proven a formidable challenge and hence many issues are still unresolved.

1.3.1 Literature Surveys

There is no shortage of publications in the field of boundary-layer stability and transition; certainly more than can be discussed in detail here. Comprehensive reviews for both two- and three-dimensional flows are given by Arnal (1984, 1986), Mack (1984), Poll (1984), Saric (1992b), and Reshotko (1994). Reed et al. (1996) give an up-to-date discussion of effectiveness and limitations of linear theory in describing boundary-layer instabilities. The reader is referred to these reports for overviews of much of the early work in stability and transition. In particular, the treatise of Mack (1984) provides the primary source of fundamental information on stability theory.

Several key papers provide in-depth reviews of stability and transition research in three-dimensional boundary layers and, in particular, swept-wing flows. Much of the early theoretical and experimental work is discussed by Reed and Saric (1989). Swept-wings, rotating disks, axisymmetric bodies (rotating cones and spheres), corner flows, and attachment-line instabilities are reviewed, as well as the stability of flows for other three-dimensional geometries. This paper gives an excellent overview of the unique

stability problems in three-dimensional flows. For swept wings, a historical account of the early investigations concerning the crossflow instability is given, along with a detailed literature survey. Poll (1984) and Arnal (1986) also give extensive reviews of transition in three-dimensional flows. Arnal (1992) and Dagenhart (1992) focus on swept-wing flows and give updated references for the period between 1989 and 1992. Radeztsky (1994) gives a detailed review of the latest developments related to the crossflow problem. Recent theoretical and experimental efforts concerning nonparallel and curvature effects, nonlinear techniques, secondary instabilities, and receptivity issues are discussed. Radeztsky concentrates heavily on the work since 1990, and as such his review is still current.

These references (Poll 1984; Arnal 1986, 1992; Reed and Saric 1989; Dagenhart 1992; Radeztsky 1994) combine to provide a thorough review of the literature on stability theory and transition with emphasis on three-dimensional flows and the crossflow instability. Instead of repeating this material here, the following discussion will highlight the important developments directly related to the specifics of this experiment.

1.3.2 Experimental Investigations

Although crossflow disturbances have been observed experimentally since the early 1950s (Gray 1952), much of the important experimental investigations have occurred in the last ten years. Saric and Yeates (1985) studied crossflow waves on a 25° swept flat plate using a "wall bump" to generate the necessary pressure gradient. In other experiments, Poll (1985) used a variable-sweep cylinder and Michel et al. (1985) used a swept wing with a high aspect ratio to approximate an infinite span in the measurement region. The Saric and Yeates work is significant in that the first superharmonic of the fundamental stationary mode was observed, providing early experimental evidence of nonlinear effects.

The DLR experiments of Bippes and co-workers provide important results concerning nonlinear effects and initial conditions. The primary findings are reported by Nitschke-Kowsky and Bippes (1988), Müller and Bippes (1989), Bippes (1990, 1991), Bippes and Müller (1990), Bippes and Nitschke-Kowsky (1990), Müller (1990), Müller et al. (1990), and Bippes et al. (1991). Recent results are summarized by Deyhle et al. (1993), Lerche and Bippes (1995), and Deyhle and Bippes (1996). These experiments measure both stationary and traveling crossflow waves, however their relative importance in influencing the details of transition is found to depend on the freestream turbulence level. Müller and Bippes (1989) describe a series of comparative experiments using the same swept flat plate in both low- and high-turbulence tunnels. The stationary waves are found to dominate transition in the low-disturbance environment, however in the high-turbulence tunnel both the growth rate and final amplitude of the stationary disturbance are reduced. At the same time, the traveling waves show larger growth rates and dominate transition. It is interesting that transition is reported to occur at slightly higher Reynolds numbers in the higher-turbulence environment.

In these experiments, the growth of the stationary and traveling waves shows initial qualitative agreement with linear theory, however the disturbance amplitude saturates due to nonlinear effects. Also, the amplitude of the traveling waves shows a spanwise modulation indicating nonlinear interactions with the stationary modes. The observed wavelength for the stationary wave is in general agreement with linear theory and is independent of the freestream turbulence level. However, it is reported that superposing a spanwise periodicity on the flow fixes the wavelength of the stationary disturbance. Another important result is that the stationary waves are observed to remain fixed relative to the model. This indicates that the stationary instability is sensitive to initial conditions provided by surface roughness, and provides a precursor

to the ASU experiments (discussed below).

The swept-wing experiment of Arnal et al. (1984) provides important information regarding the chordwise evolution of the stationary wavelength. In this investigation, the crossflow wavelength is observed to increase with increasing distance from the leading edge, forcing individual vortices to "drop-out" or vanish in order to accommodate the growth in wavelength. Other crossflow experiments at ONERA/CERT are reviewed in Arnal and Juillen (1987) and Arnal et al. (1990). In the latter work, the difficulties of applying the e^N method to three-dimensional flows are discussed.

Using a swept flat plate and wall bump essentially identical to the experimental configuration of Saric and Yeates (1985), Kachanov and Tararykin (1990) investigated the effect of various surface disturbances on the growth of stationary crossflow waves. Spanwise periodic (but constant in time) blowing/suction as well as isolated and periodic roughness were observed to enhance the local distortion of the streamwise boundary-layer velocity. Increasing the height of isolated roughness increased the local disturbance amplitude. Some agreement with linear theory was achieved by superposing the computed solutions for the fundamental and its first three harmonics.

Continued investigations concerning the effects of initial conditions are reported by Ivanov and Kachanov (1994), Kachanov and Michalke (1994), Gaponenko et al. (1995a, 1995b), and Kachanov (1995). Gaponenko et al. (1995b) concentrate on the receptivity of crossflow disturbances to surface vibrations produced with a metallic membrane oscillated by a variable magnetic field. A complex receptivity function is defined, and it is found that the receptivity "amplitudes" are about twice as large for the most unstable crossflow modes as for the quasi-two-dimensional modes. Kachanov (1995) reports that the disturbance frequencies, spanwise wavenumbers, and propagation angles are independent of the properties of the disturbance generators (i.e., suction/blowing or roughness). Nonlinear interactions between the stationary and

traveling crossflow waves are also examined, and a "pumping" of energy either to both modes or to the stationary disturbance is observed prior to transition.

A comprehensive study of stationary crossflow waves is contained in the experiments of Saric and co-workers at Arizona State University. Saric et al. (1990) review the design of the experiments, which use a low-aspect-ratio, 45° swept wing. Wall contours in the test section are used to simulate an infinite span, and the low-turbulence wind tunnel (see chapter 2) ensures that the stationary crossflow waves dominate transition. Dagenhart et al. (1989, 1990) and Dagenhart (1992) report the findings for the original investigations. In these experiments, measurements are obtained for both stationary and traveling waves in a crossflow-dominated boundary layer under the conditions of natural surface roughness. Both the growth rates and wavelengths for the stationary disturbances are found to be smaller than predicted by linear theory. In contrast to Arnal et al. (1984), no "drop-outs" or other adjustments to the stationary vortex spacing are observed.

Later work by Radeztsky et al. (1993a) investigates the sensitivity of stationary crossflow waves to roughness-induced initial conditions by introducing micron-sized artificial roughness elements near the leading edge. These experiments show that a single three-dimensional roughness element can cause early local transition and dramatically decrease the transition Reynolds number. Radeztsky et al. (1994) continued this work under conditions where the natural roughness did not induce measurable stationary crossflow waves. In these experiments, spanwise arrays of distributed roughness are used to control the disturbance wavenumber spectrum. Even for these weak waves, no agreement is found with linear theory predictions. The experimental setup, however, was such that very large roughness ($k = 70\ \ 150\ \mu$m) were required to excite the stationary instability. Since the large roughness ($Re_k \approx 100$) probably produced local nonlinearities, the disparity between the experimental and linear growth

rates is perhaps no surprise.

In other experiments at ASU, Kohama et al. (1991) showed that when the boundary layer is dominated by the stationary crossflow instability, transition is caused by a high-frequency secondary instability. This instability results from the local distortion of the mean streamwise boundary-layer profile by the stationary disturbance. Thus, in contrast to the conjecture of Müller and Bippes (1989) who argued for the importance of the traveling wave, the stationary wave provides the important physical mechanism that ultimately leads to transition in low-disturbance environments.

1.3.3 Theoretical Developments

One common theme runs through all of the experiments discussed above: the importance of nonlinear effects and receptivity/initial conditions. These characteristics of swept-wing instabilities have motivated extensive theoretical and computational efforts in an attempt to provide improved transition prediction for three-dimensional flows. Several recent advances have been made that have a direct impact on crossflow-dominated boundary layers. These developments address nonparallel effects, streamline and body curvature, nonlinear growth, secondary instabilities, and receptivity. The reader is referred to Radeztsky (1994) for a general review of recent theoretical and computational efforts in these areas. The present discussion concentrates on nonlinear techniques and receptivity issues as they apply to the present experiment.

An important theoretical result concerning stationary crossflow waves is reported by Reed (1988), who included the primary distortion of the basic state and predicted the spanwise wavenumber doubling observed in the Saric and Yeates (1985) experiments. More recently, direct numerical simulations (DNS) and the parabolized stability equations (PSE) represent important advances in stability and transition modeling. These methods account for nonparallel and nonlinear effects, which allow for the correct spatial evolution of the stationary crossflow wave as well as its

distortion of the basic state.

DNS have historically been constrained by computer resources and algorithmic limitations, however some successes have been achieved in relation to the stationary crossflow problem. Reed and Lin (1987) and Lin (1992) performed numerical simulations for stationary waves on an infinite-span swept wing similar to the ASU experiments discussed above. Meyer and Kleiser (1990) investigated the disturbance interactions between stationary and traveling crossflow modes using Falkner-Scan-Cooke similarity profiles for the basic state. The results were compared to the experiments of Müller and Bippes (1989). With an appropriate initial disturbance field, the nonlinear development of stationary and traveling crossflow modes was simulated reasonably well up to transition. Wintergerste and Kleiser (1995) continue this work by using DNS to investigate the breakdown of crossflow vortices in the highly nonlinear final stages of transition.

With the continued development of new and powerful computers and numerical methods, DNS are playing an increasingly important role in transition modeling. Kleiser (1991) reviews the literature and Reed (1994) discusses the details of spatial DNS. Reed covers nonparallel, nonlinear, and three-dimensional effects, as well as considerations for compressibility, pressure gradient, and surface geometry. Important discussions concerning receptivity are also included.

The recently developed PSE appear poised to replace traditional linear theory as the state-of-the-art tool for boundary-layer stability analyses. Herbert (1994) gives a detailed description of the PSE. The formulation results in a system of parabolic differential equations describing the disturbance motion. This allows for the proper spatial evolution of disturbance modes as opposed to the traditional patching of local solutions. Moreover, the nonlinear terms can be retained to provide full nonlinear stability analyses. The parabolic nature of the PSE allows the use of computationally

efficient marching algorithms, hence PSE solutions are generated in a fraction of the time required by DNS. On the down side, the initial conditions must be specified, thus the PSE do not address the receptivity problem. However, the nonlinear response of forced modes can by studied by varying the initial conditions. With proper guidance from careful experiments, the PSE have the ability to accurately model nonlinear effects in three-dimensional boundary layers. For swept-wing flows, nonlinear PSE calculations exhibit the disturbance amplitude saturation characteristic of the DLR and ASU experiments. Wang et al. (1994) investigate both stationary and traveling crossflow waves for the swept airfoil used in the ASU experiments and predict nonlinear amplitude saturation for both types of disturbances. It is suggested that the interaction between the stationary and traveling waves is an important aspect of the transition process. Other examples of PSE applied to swept wings can be found in Stuckert et al. (1993), Schrauf et al. (1995), and Haynes and Reed (1996).

1.4 Experimental Goals

As the discussions in this chapter have illustrated, stability and transition in three-dimensional boundary layers is a complicated process with many unanswered questions. In crossflow-dominated flows, the importance of nonlinear effects and their dependence on initial conditions is not well understood. These issues must be addressed for the future development of transition prediction techniques and, ultimately, LFC. Thus, the goals of the present investigation are (1) to study the fundamental physics of the stationary crossflow instability that leads to transition on swept wings in low-disturbance environments, and (2) to provide a detailed and accurate experimental database for the development of current analytical tools such as the nonlinear PSE.

The focus of the present investigation is to study the effects of distributed sur-

face roughness on the (nonlinear) development of stationary crossflow waves. Not only will this provide important input for receptivity studies, but the controlled initial conditions and detailed disturbance measurements will supply theoreticians with critical experimental data for code validation. The airfoil model and test conditions (discussed in chapter 3) are chosen so that the boundary layer is subcritical to attachment-line, Tollmien-Schlichting, and Görtler instabilities, while crossflow waves are strongly amplified. The extremely low turbulence levels of the ASU Unsteady Wind Tunnel ensure that the stationary waves dominate the transition process. In order to investigate the effects of controlled roughness, the aluminum surface of the model is hand polished to a 0.25 μm rms finish. This allows the use of micron-sized artificial roughness elements to control the wavenumber spectrum of the stationary disturbance without saturating the initial disturbance amplitude.

The experimental methods are designed with two objectives in mind. The first is to document the detailed structure of the stationary waves. This provides important information on the global flowfield, including total disturbance mode shapes and amplitude distributions. The second objective of the measurements is to isolate and track the growth of individual crossflow modes. These data are used to investigate nonlinear interactions among various modes, and allow accurate comparisons with single-wavelength stability calculations.

1.5 Outline

The details of the current experiment are presented in the remaining chapters. Chapter 2 describes the ASU Unsteady Wind Tunnel facility, including the instrumentation and measurement devices used for data acquisition. Details of the experimental design and configuration are presented in chapter 3. This chapter also discusses the test conditions, for which basic-state and linear stability calculations are presented.

The measurement techniques used to acquire and process the data are described in chapter 4. Hot-wire calibration techniques and wind-tunnel control methods are also discussed. Chapters 5 and 6 present the experimental data in detail and discuss the results. Chapter 5 focuses on the baseline experimental configuration and includes comparisons with both linear and nonlinear theoretical predictions. Transition data and basic-state measurements are also presented. The effect of Reynolds number, roughness spacing, and roughness height on the growth of the stationary waves are investigated in chapter 6. Chapter 7 gives the conclusions.

CHAPTER 2

Wind-Tunnel Facility

2.1 Unsteady Wind Tunnel

The present experiment is conducted in the Unsteady Wind Tunnel at Arizona State University. The tunnel was originally built in 1970 by Dr. Philip Klebanoff and calibrated by Dr. James McMichael at the National Bureau of Standards in Gaithersburg, Maryland. In 1984, the wind tunnel was relocated to Arizona State University under the direction of Dr. William Saric. It became operational in 1987, after extensive modifications designed to improve the flow quality. In its present configuration (figure 2.1), the facility operates as a low-speed, low-turbulence, closed-circuit, atmospheric wind tunnel in which the stability and transition of laminar boundary layers are investigated. Saric (1992a) gives a detailed description of the facility.

A 150 hp, variable-speed, DC motor powers the wind-tunnel fan. The 1.83 m-diameter, single-stage, axial fan (Buffalo Forge model G300F) has nine adjustable-pitch blades and eleven stators. The maximum rated fan speed is 1350 rpm, giving a maximum test-section velocity of 35 m/s for this experiment. The motor is controlled by a Mentor II digital DC drive. This controller is equipped with a RS/232 serial interface, which is converted to GPIB for digital communication with the wind-tunnel computers (discussed below). The desired rotational speed is set by writing into a

16-bit register, giving a speed resolution of 0.02 rpm for the G300F fan. Once this register is loaded, the speed reference is *exact* and the accuracy is determined by the feedback system. With a 1000-line optical encoder and a PID control loop, the Mentor II maintains the motor speed to within 0.01% of the set point.

Several key design features result in very low freestream turbulence levels. The tunnel is lengthened by 5 meters over the original design, allowing the primary diffuser to be extended. The return loop is contoured to provide a smooth transition into the fan inlet. All four corners are fitted with turning vanes (item 'a' in figure 2.1). The turning vanes are circular-arc airfoils with a 50 mm chord and 40 mm spacing. Upstream of the contraction cone the flow passes through a 76 mm-thick aluminum honeycomb "wall" (item 'b' in figure 2.1). The honeycomb consists of 6.35 mm hexagonal cells. Immediately downstream of the honeycomb are seven stainless steel screens (item 'c' in figure 2.1). The first five screens have an open-area ratio of 0.7; the last two are seamless with a 0.65 open-area ratio. The screens are constructed with 0.165 mm wire on a 30/inch mesh and are separated by 230 mm. (Additional screens are placed in the diffuser and test-section recovery region to prevent stall.) Following the screens is a 1.64 m settling chamber where viscosity dissipates the small-scale turbulent fluctuations. The steel-reinforced contraction cone (5.33:1 contraction ratio) follows a 5th-order polynomial to eliminate curvature discontinuities at the contraction entrance and exit.

Special precautions are taken to minimize the motor- and fan-generated turbulence. The aft end of the motor is fitted with a nacelle to reduce wake turbulence. Behind the nacelle are splitter plates, which reduce the large-scale vortical motion created by the fan. Screens are placed immediately after the splitter plates and at the downstream end of the diffuser. These measures are necessary to prevent a diffuser stall. To minimize mechanical vibrations, the fan housing is connected to the wind

tunnel with flexible rubber couplings and is supported on a concrete pad that is isolated from the building foundation. Similar measures isolate the test section. Finally, the fan/motor and test section are on opposite sides of a sound-insulated wall that divides the building.

These design features reduce the test-section turbulence to exceptionally low levels. Hot-wire measurements in the freestream show that $u'/U_\infty < 0.02\%$ (20 m/s, 2 Hz high-pass). More information on the calibration of the Unsteady Wind Tunnel is given by Saric et al. (1988) and Mousseux (1988).

The Unsteady Wind Tunnel is equipped with two complete and interchangeable test sections, each measuring 1.4 m $\times$ 1.4 m $\times$ 4.9 m. As mentioned above, flexible couplings provide the only physical connection between the test section and the wind tunnel. By simply removing these couplings, the test section can be easily rolled out of the tunnel and the second test section can be rolled into place with a different experiment. Thus, one experiment can be configured in the work area while another is in the tunnel.

Unsteady flows are generated using a unique double-duct design. Opening a trap door in the plenum diverts air from the primary duct (i.e., contraction cone and test section) into a secondary duct located above the test section. These passages recombine in the recovery region downstream of the test section. Immediately before this point, each duct contains a set of rotating shutters. The shutters in the secondary duct lag those in the primary by 90°, allowing up to 100% velocity fluctuations at 25 Hz while maintaining (relatively) steady loading on the fan. Any number of shutters in either duct can be disengaged to reduce the unsteady amplitude. To function as a steady wind tunnel, the primary shutters are locked open and the secondary duct is closed. The present experiment operates in this steady configuration.

2.2 Computer Systems

Every effort is made to automate the experimental procedures at the Unsteady Wind Tunnel. This improves operational efficiency and increases consistency and reliability by minimizing the ever-present subjectivity of the researcher. Central to this task are several computer systems, which oversee all wind-tunnel operations.

Table 2.1 lists the features and capabilities of the Unsteady Wind Tunnel computer systems. All wind-tunnel operations are controlled by the Sun SPARCstation 20. This multiprocessor workstation is equipped with a GPIB interface board, National Instruments model GPIB-SPRC-B. This versatile device-communication bus allows the Sun to interface with all computer-controlled instrumentation while retaining the flexibility and expansibility to grow with changing needs. With this arrangement, all instrumentation devices are "external" in that they do not reside within the computer but communicate with it digitally via the GPIB. Consequently, signal degradation is minimized since the data-acquisition equipment is placed close to the experiment, thereby eliminating the need for long analog cables between the wind-tunnel room and the control room. Moreover, the modularity of the entire system allows virtually any component, including the computer, to be replaced or upgraded independently.

The SPARCstation runs version 2.4 of the Solaris operating system: Sun's UNIX based on AT&T's System V, Release 4. This multiuser, multitasking environment allows simultaneous data acquisition, analysis, wind-tunnel control, and program development. OpenWindows provides a modern, X Windows-based, graphical user interface displayed on a 20 inch, 256-color console terminal.

All data-acquisition, analysis, and wind-tunnel-control programs are written "in house" using C, C++, or LabVIEW. A set of custom object-code libraries simplifies the programming task by providing a standardized interface to the acquisition and control instruments (Reibert 1996). Tecplot is available for plotting, and LaTeX

Table 2.1: Unsteady Wind Tunnel computer systems.

Feature	**Sun**	**PC**	**Digital**	**Macintosh**
System and Operating Environment				
System	SPARC 20	ACT486	DEC 5000	Quadra
Model	612MP	50	200	650
OS	Solaris	SCO UNIX	Ultrix	Mac OS
OS Version	2.4	2.0	4.41	7.5.3
GUI	OpenWindows	OSF/Motif	OSF/Motif	N/A
Processor				
CPU	SuperSPARC+	80486DX	R3000	MC68040
No. of CPU	2	1	1	1
Speed [MHz]	60	50	25	33
MIPS	167[a]	12[b]	24	8[b]
MFLOPS	36.6[a]	2[b]	3[c]	N/A
Graphics				
System	TurboGX	Trident 8900	8-plane	Built-in
Monitor [inch]	20	17	19	17
Resolution	1024 × 768	1024 × 768	1024 × 864	832 × 624
Colors	256	256	256 (gray)	65536
Memory and Storage				
RAM [MB]	64	20	16	8
Disk [MB]	3150	425	2430	230
Tape [MB]	5000	2000	100	8000
Floppy	•	•		•
CD-ROM	•			•
I/O Buses and Connectivity				
SCSI	•	•	•	•
GPIB	•	•		
Ethernet	•	•	•	•

[a] Value for each SuperSPARC+ processor in a single-CPU system.

[b] Estimated.

[c] Double precision.

(along with the standard complement of supporting programs) is installed for technical document production. The SPARCstation also functions as a server on the World Wide Web. The ASU Wind Tunnel Complex home page can be reached at http://wtsun.eas.asu.edu.

A PC compatible serves as a back-up data-acquisition system. This computer runs the Santa Cruz Operation's Open Desktop Server System version 2.0. This multiuser UNIX environment is based on AT&T's System V, version 3.2.4. The system features OSF/Motif X Windows graphics displayed on a 17 inch, 256-color console terminal. This machine is also equipped with a GPIB controller, National Instruments model AT-GPIB/TNT. This allows the PC to take over all data-acquisition and wind-tunnel-control functions simply by moving the GPIB cable from the SPARCstation to the PC. To facilitate this, the custom programming libraries used to access the wind-tunnel instrumentation devices are maintained on the PC. Thus, the researcher needs only to move the GPIB cable from the SPARCstation to the PC and recompile his programs to bring the back-up data-acquisition computer on line.

A DECstation 5000 provides additional workstation capabilities and data storage space. This unit runs Ultrix version 4.41: Digital's UNIX based on BSD. The OSF/Motif X Windows graphics system is displayed on a 19 inch, 256-shade, gray-scale console terminal.

A Macintosh Quadra 650 is available for general-purpose computing. This computer runs System 7.5.3 of the Macintosh OS displayed on a 17 inch, 64k-color terminal. A wide array of software is installed including drafting and word-processing applications.

High-quality printed output is provided by a Hewlett-Packard HP4M 600 dpi PostScript laser printer. A Hewlett-Packard 1200C/PS 300 dpi PostScript inkjet printer is available for color output.

All wind-tunnel computers and printers are connected via the Ethernet. A subnet router connects the Unsteady Wind Tunnel to the campus backbone, which is in turn connected to the world-wide Internet. The router functions as a gateway by differentiating between local transmissions and those intended for machines outside the Unsteady Wind Tunnel. This creates a fast local network by isolating local traffic from the global network.

2.3 Instrumentation

Freestream flow conditions are determined by pressure and temperature measurements near the test-section entrance plane. A 10 torr differential pressure transducer (MKS model 398HD) measures dynamic pressure from a Pitot-static tube. The static side of the probe is also connected to a MKS 390HA 1000 torr absolute pressure transducer. Both temperature-compensated transducers are connected to MKS 270B 14-bit signal conditioners. These provide visual displays as well as digital and analog output signals, the latter of which are interfaced with the data-acquisition system. The test-section temperature is measured with a thin-film RTD. The calibrated analog output is also wired into the data-acquisition system.

Hot-wire anemometry provides accurate boundary-layer velocity measurements. The system consists of Dantec 55P15 boundary-layer probes and two Dantec 55M01 constant-temperature anemometers equipped with 55M10 CTA standard bridges. The hot-wire probes use 5 μm platinum-plated tungsten wires. The probe tines are 1.25 mm apart and are offset 3 mm from the probe axis to facilitate measurements close to the model surface.

A two-channel filter/amplifier (Stewart model VBF44) provides analog signal conditioning for AC measurements. This unit has two high-pass and two low-pass filter responses. The low-pass filters have an AC-couple option. Cutoff frequencies range

from 1 Hz to 255 kHz, and pre- and post-filter gains provide a maximum amplification of 70 dB. All features are remotely programmable through a RS/232 serial interface. A three-channel Tektronix AM502 filter/amplifier provides additional analog filtering, and a GPIB-controlled Stanford Research Systems SR530 lock-in amplifier measures amplitude and phase data.

All analog signals are digitized with two IOtech ADC488/8SA analog-to-digital (A/D) converters. Each A/D converter can simultaneously sample and hold up to eight differential signals with 16-bit resolution. Connected in a master/slave arrangement, the two units use a common clock trigger to provide a total of sixteen channels of simultaneous A/D conversion. The input voltage range for each channel is independently programmable between ± 1 and ± 10 volts, thus "small" signals can be resolved to 33 μV. The aggregate sampling rate varies discretely from 0.02 Hz to 100 kHz. These external A/D converters communicate with the data-acquisition computer via the GPIB.

An IOtech DAC488HR/4 digital-to-analog converter is available for source signal generation. This four-channel, 16-bit unit provides synchronous analog output at a maximum update rate of 100 kHz per channel. The unit can also operate as a waveform generator and a precision DC voltage source. All options are remotely accessible via the GPIB.

Other typical laboratory electronic equipment is available, including an eight-channel Tektronix 5440 oscilloscope, Fluke 8050A digital multimeters, and various signal generators and power supplies.

2.4 Traverse and Sting

A computer-controlled, three-dimensional instrumentation traverse allows accurate positioning of the hot-wire probes within the test section. A detailed description of

the system is given by Radeztsky (1994). The important features are highlighted below.

The traverse carriage (figures 2.2 and 2.3) is located outside the test section and moves in the X (streamwise) direction on two stainless steel Thompson rails. Only the instrumentation sting penetrates the flowfield. This is a critical design feature necessary to minimize the intrusiveness of the measurement system. A moving traverse within the test section will cause local pressure field variations and global flow adjustments that can dramatically alter the results of boundary-layer stability experiments (Saric 1990).

The hot-wire sting reaches into the measurement region through a slotted plexiglass window contained within the test-section wall. A zipper automatically opens and closes the slot around the sting when the carriage moves in the X direction. An air-tight plexiglass outer wall (item 'f' in figure 2.2) encloses the entire system in a pressure box. This equalizes the pressure across the interior test-section wall, virtually eliminating any transverse loading on the slotted window. Mass transfer through the small gaps in the slot surrounding the sting is also minimized.

The Y (wall-normal) and Z (vertical) motion subsystems are entirely contained on the traverse carriage. The sting mounts to a small aluminum sub-carriage (item 'd' in figures 2.2 and 2.3), which is supported on two parallel rails. A high-resolution lead screw moves the Y carriage normal to the test-section wall. Vertical motion is provided by moving the Y carriage with twin lead screws and rails, shown as items 'b' and 'c' in figure 2.3. Another set of twin lead screws and rails moves the slotted window in conjunction with the vertical motion of the Y carriage. These movements are coordinated to ensure the sting is always centered in the slotted window.

All lead screws are driven by high-resolution Compumotor microstepping motors. 1000-line Renco optical encoders provide digital position feedback for all axes includ-

Table 2.2: Traverse system capabilities.

Direction	X	Y	Z
Total Travel	1.25 m	100 mm	175 mm
Minimum Step	12 μm	0.7 μm	1.3 μm

ing the slotted window. Quadrature increases the effective encoder resolution by a factor of four, giving the minimum step sizes shown in table 2.2. A four-axis digital motion controller (Compumotor model CM4000) directs all traverse movements. This microprocessor-based controller internally governs all aspects of the motion control including the encoder feedback loop.

New software algorithms have been implemented that greatly improve the accuracy and reliability of the traverse system. The CM4000 firmware contains a BASIC-like programming language. Although awkward to use for complex motion control, it is sufficient to communicate with the data-acquisition computer via the GPIB. During an experiment, a resident program on the CM4000 waits for commands indicating a traverse move is desired. When these commands are received, the controller initiates the motion, monitors the encoder feedback and applies any necessary "correction moves", then indicates to the computer when all axes are within the dead-band tolerance. This process repeats until the computer, at the end of the experiment, tells the CM4000 to shutdown the traverse system. The essential feature of this method is the resident program on the CM4000. Without it, the controller cannot monitor the encoder feedback and position accuracy is potentially compromised. This was the case with all previous experiments.

The hot-wire sting (figure 2.4) is the same used in earlier swept-wing experiments at the Unsteady Wind Tunnel (Dagenhart et al. 1989, 1990; Kohama et al. 1991; Radeztsky et al. 1993a, 1994). The streamlined, carbon-composite body attaches to the traverse via an aluminum mounting strut. Two Dantec probe tubes are mounted

on the composite section. The probe mount at the tip of the sting allows rotation about the Z axis. This motion, coupled with probe rotation about the tube axis, is necessary to accurately position the hot-wire relative to the three-dimensional surface of the swept wing. Radeztsky (1994) gives further details concerning the sting.

CHAPTER 3

Test Model and Experimental Design

This chapter reviews the experimental design and setup. The swept-wing test model and its configuration within the test section are described. The test conditions are chosen, and stability calculations are presented for those conditions.

3.1 Background

As discussed in section 1.3, the early ASU experiments (Dagenhart et al. 1989, 1990; Saric et al. 1990) investigated the stability and transition of swept-wing boundary layers dominated by the crossflow instability mechanism. In these experiments, the initial conditions for the disturbance amplitude came from the unknown natural roughness of the surface. Later experiments by Radeztsky et al. (1993a) studied the sensitivity to isolated leading-edge roughness. This work, however, focused on transition location and in large part ignored the details of the disturbance growth. It was not until the experiments of Radeztsky et al. (1994) that a detailed and systematic investigation of the effects of distributed surface roughness on (very weak) stationary crossflow waves was documented.

The present investigation returns to the configuration of the original experiments in order to study the effects of distributed surface roughness in a crossflow-dominated boundary layer. The following sections discuss the details of the experimental design.

3.2 Model Configuration

3.2.1 Airfoil

The NLF(2)-0415 airfoil (Somers and Horstmann 1985) is the same used in all previous swept-wing work at the Unsteady Wind Tunnel (Dagenhart et al. 1989, 1990; Saric et al. 1990; Kohama et al. 1991; Radeztsky et al. 1993a, 1994). The NLF(2)-0415 is designed as an unswept, natural-laminar-flow airfoil for use on general aviation aircraft. The airfoil cross section and pressure distribution for the design angle of attack of 0° are shown in figure 3.1. The favorable pressure gradient back to the pressure minimum at $x/c = 0.71$ is designed to maintain laminar flow on the upper surface by controlling the Tollmien-Schlichting (T-S) instability.

The airfoil is swept 45° for the ASU experiments, creating a test model well-suited for the study of three-dimensional boundary layers. The small leading-edge radius eliminates attachment-line instabilities for the Reynolds number range of the Unsteady Wind Tunnel ($Re_\theta = 44$ at $\alpha = -4°$ and $Re_c = 2.4 \times 10^6$), and the absence of concave regions on the upper surface suppresses the Görtler instability. The result is a nearly ideal platform for the investigation of crossflow and/or T-S instabilities. At small negative angles of attack, the favorable pressure gradient from the attachment line to the pressure minimum at $x/c = 0.71$ produces strong crossflow and stabilizes the T-S modes. At $\alpha = 0°$, the pressure gradient is weakly favorable back to $x/c = 0.71$. Under these conditions, both crossflow and T-S disturbances are weakly amplified. At small positive angles of attack, the pressure minimum moves forward to $x/c = 0.02$, and the adverse pressure gradient leads to strong growth of T-S waves. A 20%-chord, trailing-edge flap with a maximum deflection of ±20° allows further contouring of the pressure distribution. Dagenhart (1992) gives a detailed review of the operating range for the NLF(2)-0415.

3.2.2 Test-Section and Wall Liners

The swept NLF(2)-0415 airfoil is mounted vertically in a dedicated test section measuring 1.4 m × 1.4 m × 4.9 m. The vertical orientation simplifies instrumentation access since the test surface (i.e., airfoil upper surface) faces the front wall of the test section. The model attaches to the test section via a shaft and thrust bearing. The axis of the shaft is parallel to the leading edge and is located at $x/c = 0.25$. This combination allows angle-of-attack rotations about the 1/4-chord line from $-4°$ to $+4°$ in $1°$ increments. Since it is good experimental practice to avoid symmetry planes, the thrust bearing is positioned 76 mm off center placing the pivot point 610 mm from the test-section front wall and 760 mm from the rear wall. In addition, moving the model closer to the front wall reduces the span of the instrumentation sting, which helps minimize probe vibration.

In the interest of detailed measurements, the swept airfoil chord of 1.83 m is chosen to allow significant boundary-layer growth ($\delta \approx 4$ mm in the mid-chord region for moderate chord Reynolds numbers). Of course, wall-interference effects cannot be ignored when a model this size is placed in a 1.4 m-square test section. One way to handle these effects is to include the test-section walls in all theoretical models. This is relatively straightforward for the front and rear walls (i.e., those opposite the airfoil upper and lower surfaces). However, including the effects of the test-section floor and ceiling significantly complicates the computational effort. The simplifying assumption of spanwise invariance cannot be used, and a fully three-dimensional code is required for both the basic state and the stability calculations. On the other hand, the flowfield is spanwise invariant (i.e., the boundary-layer and stability characteristics are invariant along lines of constant chord) if the airfoil is infinite in span. Under these conditions, the problem can be modeled in two dimensions with the addition of a constant spanwise velocity $U_\infty \sin(\Lambda)$ in the z direction. This results in dramatically

more efficient computational methods. Just as important, the infinite-span swept wing produces a benchmark configuration for crossflow studies (not unlike the flat plate for Tollmien-Schlichting instabilities).

In light of this, the challenge now falls to the experimentalist to create an infinite-span airfoil in a finite test section. At the Unsteady Wind Tunnel, this is accomplished by contouring the test-section floor and ceiling with end liners. These liners create a stream surface that follows the inviscid streamlines for an infinite-span airfoil. This experiment uses the same end liners constructed for the previous experiments at $\alpha = -4°$. The reader is referred to Dagenhart (1992) for a discussion the liner design and Radeztsky (1994) for a detailed description of the construction technique. The NLF(2)-0415 airfoil and end liners for the present configuration are shown in figure 3.2.

The floor and ceiling liners are 130 mm thick at the test-section entrance. This necessitates the installation of contraction-cone fairings, which reduce the contraction exit area to match the smaller test-section entrance. The fairings begin at the inflection point in the original contraction contour and follow a 5th-order polynomial to avoid curvature discontinuities. The contraction ratio is 6.55:1 with the fairings installed. Symmetric entrance flow is maintained since the floor and ceiling liners are the same thickness at the test-section entrance.

3.3 Test Conditions

Many factors influence the choice of the experimental test conditions, but by far the most important are the stability characteristics of the boundary layer. Consequently, stability calculations are an integral part of the design process for this type of experiment. Traditionally, an exhaustive study is performed in which the boundary-layer behavior is analyzed over the entire parameter space of the proposed experiment. The

test conditions are then chosen to provide the desired stability features. After the experiment is conducted, the results are compared to the predictions and conclusions are drawn as to the applicability of the theoretical model.

The original experiments of Dagenhart et al. (1989, 1990), as well as those of Radeztsky et al. (1993a, 1994), proceeded in this fashion. The basic state was computed with the Kaups and Cebeci (1977) boundary-layer code, with edge conditions supplied by the MCARF code (Stevens et al. 1971). Linear, parallel stability predictions were then obtained using the SALLY (Srokowski and Orszag 1977) and MARIA (Dagenhart 1981) codes, from which the test conditions were chosen. However, the disturbance measurements from these experiments bear little resemblance to the theoretical predictions. While this is certainly instructive in its own right, the failure of linear theory under these conditions does little to assist the experimentalist in designing future tests.

Fortunately, the present work has the benefit of hindsight, and can rely on the previous experiments for assistance in choosing appropriate test conditions. When used in conjunction with theoretical predictions, this dramatically improves the ability of the experimentalist to pick operating conditions that exhibit the desired boundary-layer stability characteristics. For the present experiment, this means that the combination of angle of attack, Reynolds number, and surface roughness distribution can be chosen *a priori* with little or no "guesswork".

3.3.1 Angle of Attack

Since the present investigation focuses on the crossflow instability, the angle of attack is set to $-4°$ and the flap is not deflected ($\delta_F = 0°$). Figure 3.3 shows the unswept airfoil contour and upper-surface C_p distribution for this configuration. With the continuously negative pressure gradient from the attachment line to $x/c = 0.71$, the boundary layer is subcritical to T-S waves and transition is dominated by the

stationary crossflow instability. This is predicted by Dagenhart (1992) and confirmed experimentally by Dagenhart et al. (1989, 1990) and Kohama et al. (1991). These early experiments show that the 45°-swept NLF(2)-0415 at $\alpha = -4°$ is a near perfect crossflow generator.

3.3.2 Reynolds Number

Although several factors influence the choice of Reynolds number, the final decision represents a tradeoff between crossflow disturbance growth, transition location, and wind-tunnel heating. With the present configuration, the maximum chord Reynolds number is 3.6×10^6, however this cannot be sustained over long runs due to wind-tunnel heating (see section 4.1.2). Fortunately, at $\alpha = -4°$ the crossflow disturbance growth is strong even at moderate chord Reynolds numbers so it is not necessary to maximize the tunnel speed. The baseline Reynolds number for this experiment is $Re_c = 2.4 \times 10^6$. This is large enough to generate significant crossflow, yet small enough to minimize wind-tunnel heating effects. Moreover, the disturbance growth can be analyzed in detail since laminar flow is maintained beyond 50% chord. When the effect of Reynolds number on the disturbance amplitude is desired, measurements are also taken at $Re_c = 1.6 \times 10^6$ and 3.2×10^6.

3.3.3 Roughness Elements

Whereas traveling crossflow disturbances are influenced by freestream turbulence (Müller and Bippes 1989; Müller 1990; Bippes et al. 1991; Deyhle et al. 1993; Deyhle and Bippes 1996), the development of stationary waves depends strongly on surface roughness near the attachment line (Radeztsky et al. 1993a, 1994). As outlined in chapter 1, the primary goal of this experiment is to study the growth of stationary crossflow disturbances and their dependence on initial conditions. It is therefore essential to carefully control and document the surface roughness distribution.

The first step in this process is to reduce the natural roughness of the model, thus the aluminum surface of the NLF(2)-0415 airfoil is highly polished. Figure 3.4 shows a profilometer measurement of the surface finish. The 0.12 μm rms finish is typical of the roughness level near the mid-chord region. Near the leading edge the roughness level is 0.25 μm rms. This very smooth surface provides an ideal environment within which the effect of roughness on stationary crossflow waves is investigated.

Following Radeztsky et al. (1993a), the initial conditions are controlled by applying roughness elements to the airfoil surface near the attachment line. The ability of artificial roughness to induce stationary crossflow waves is well-documented by Radeztsky et al. (1993a, 1994). Two different roughness elements are used. The first are Geotype #GS-104 circular "rub-down" dots common in the graphic arts industry. These 3.7 mm-diameter, dry-transfer dots produce a 6 μm-thick roughness element when rubbed onto the airfoil surface. Although the surface of the element is somewhat uneven, the edges are clean and the dots can be stacked with little compression of the lower layers. Careful profilometer measurements indicate a mean thickness of 6 μm per layer. The practical limit on stacking the dots is 3 to 4 layers based on the ability to maintain a well-defined edge. For the present experiment, one- and three-layer dots are used to produce $k = 6$ μm and 18 μm roughness. Thicker roughness elements are die-cut from 3M #850 industrial polyester tape. The diameter of these elements is also 3.7 mm, and the total height including the adhesive is 48 μm (measured with a profilometer). When stamped carefully from the #850 tape, these circular roughness elements have exceptionally clean edges and an absolutely uniform thickness.

The dots are applied in full-span arrays along the z axis at $x/c = 0.023$. This location is near the neutral point for the stationary crossflow instability, and has been shown by Radeztsky et al. (1993a) to maximize the influence of the roughness. The fundamental disturbance wavelength is fixed by the spanwise spacing of the elements.

Two different spacings are used for this experiment: 12 mm and 36 mm. As shown in chapter 5, the 12 mm spacing is chosen to amplify the dominant wavelength that appears in the absence of artificial roughness. The 36 mm spacing allows the study of the interaction between the fundamental and multiple harmonic disturbances.

The size of the elements with respect to the boundary layer is measured by the roughness Reynolds number:

$$Re_k = \frac{U(k)k}{\nu}, \tag{3.1}$$

where k is the dimensional roughness height and $U(k)$ is the total boundary-layer velocity at the top of the element. Clearly, Re_k depends on the freestream velocity and the roughness location. Since the boundary layer is too thin to measure at $x/c = 0.023$, the theoretical boundary-layer solution is used to calculate Re_k. Table 3.1 lists the Re_k values for the conditions of this experiment. Also listed is the roughness height normalized by the boundary-layer thickness δ and displacement thickness δ^* at $x/c = 0.023$. The Re_k values are well below the Braslow limit for three-dimensional roughness (von Doenhoff and Braslow 1961; Juillen and Arnal 1990), hence the elements do not trip the boundary layer or induce a local turbulent wedge.

3.4 Coordinate Systems

The correct interpretation of the theoretical and experimental results requires an understanding of the coordinate systems in which the data are presented. Figures 3.5 and 3.6 show the common coordinate systems used to describe a swept wing. The freestream flow is from left to right as indicated. The global test-section coordinates (X, Y, Z) are aligned with the tunnel. The streamwise coordinate X is in the flow

Table 3.1: Roughness element measures at $x/c = 0.023$.

Roughness Configuration			k/δ	k/δ^*	Re_k
Type	Layers	k [μm]			
$Re_c = 1.6 \times 10^6$ ($\delta = 0.92$ mm, $\delta^* = 0.30$ mm)					
GS-104	1	6	0.0065	0.0203	0.061
GS-104	3	18	0.0196	0.0610	0.55
3M 850	1	48	0.0522	0.1627	3.8
$Re_c = 2.4 \times 10^6$ ($\delta = 0.75$ mm, $\delta^* = 0.24$ mm)					
GS-104	1	6	0.0080	0.0249	0.11
GS-104	3	18	0.0240	0.0749	1.0
3M 850	1	48	0.0640	0.1992	7.0
$Re_c = 3.2 \times 10^6$ ($\delta = 0.65$ mm, $\delta^* = 0.21$ mm)					
GS-104	1	6	0.0092	0.0288	0.17
GS-104	3	18	0.0277	0.0865	1.5
3M 850	1	48	0.0738	0.2308	10.7

direction, Y is normal to the front wall of the test section, and the vertical coordinate Z completes the right-handed system. The velocity components in this system are denoted by (u, v, w). The model-oriented coordinate system (x, y, z) is attached to the wing-chord plane. The x coordinate is normal to the leading edge, y is normal to the chord line, and z is parallel to the leading edge in the swept span direction. The velocity components in this system are (u_n, v_n, w_n). The third system is the boundary-layer coordinates (x_t, y_t, z_t). In this system, x_t is tangent to the inviscid streamline, y_t is normal to the model surface, and z_t completes the right-handed orthogonal system. The velocity components in the boundary-layer system are (u_t, v_t, w_t). The *crossflow* direction is defined by z_t, and w_t is the crossflow velocity component. Figure 3.7 shows a typical swept-wing boundary layer in the boundary-layer coordinate system.

With Λ positive as shown in figure 3.5, the crossflow component is negative upstream of the pressure minimum. Body-intrinsic coordinates (ξ, ζ, z), shown in figure 3.6, represent yet another coordinate system often used in computational analyses. This system is similar to model-oriented coordinates, except the origin is attached to the airfoil surface rather than the wing-chord plane. The ξ coordinate is tangent to the model surface and normal to the leading edge. The coordinate $\zeta = y_t$ is normal to the surface.

The differences in these coordinate systems must be considered when comparing theoretical and experimental results. Computations are typically performed in model-oriented or body-intrinsic coordinates, however, the axes of the instrumentation traverse are aligned with the global (X, Y, Z) coordinates. While it is certainly possible to program the three-dimensional traverse to move in another coordinate system, practical limits on the step size may prevent this. For instance, a step $\Delta\zeta$ normal to the airfoil surface decomposes into the steps $\Delta X = \Delta\zeta \sin(\phi)$ and $\Delta Y = \Delta\zeta \cos(\phi)$, where ϕ is the angle between ζ and Y (see figure 3.6). However, over most of the model ϕ is only a few degrees. Thus, a reasonably small $\Delta\zeta$ (say, 30 μm) would require a ΔX that is smaller than the minimum step size in the X direction. On the other hand, moves in the z direction pose no problems since the step sizes are typically much larger and decompose equally into the X and Z directions.

Because of these restrictions, no adjustments are made to the Y motion of the traverse. Consequently, the hot-wire scanning techniques discussed in section 4.4 acquire data in the (Y, z) plane. Within this plane, the boundary-layer hot-wire probe support is rotated about the Z axis by an angle β to account for local surface curvature effects. The hot-wire probe itself must then be rotated about its longitudinal axis by an angle σ so that the tines are equidistant from the model surface. These rotations are shown in figure 3.8, and the angles β and σ are listed in table 3.2 for

Table 3.2: Boundary-layer hot-wire probe rotation angles.

x/c	β [°]	σ [°]	x/c	β [°]	σ [°]
0.05	30	16	0.35	12	6
0.10	25	12	0.40	10	6
0.15	20	10	0.45	10	5
0.20	18	9	0.50	8	4
0.25	15	8	0.55	5	3
0.30	15	7	0.60	5	2

all measurement locations. The hot wire measures the total velocity normal to the element after both rotations. Accurate comparisons with theory depend strongly on the ability of the computational results to be cast in this field. For example, if the computations are generated in body-intrinsic coordinates, the velocity profile in the (ξ, ζ) plane must be projected onto the plane normal to the hot-wire element and then interpolated from ζ to Y. Only then can the boundary-layer profiles and disturbance measurements be consistently compared with this experiment. The computational results to which the experimental data are compared are transformed in this manner.

3.5 Theoretical Predictions

This section describes the theoretical basis for the experimental test conditions. The basic-state boundary-layer solutions are presented, as are stability calculations for the stationary crossflow disturbances.

3.5.1 Basic State

The first step in a stability analysis is to compute the basic-state boundary layer. This requires appropriate edge conditions, which for this experiment are generated by the MCARF code (Stevens et al. 1971). MCARF computes the C_p for an unswept

airfoil in a duct, hence it correctly handles the flat front and rear walls of the test section. The effect of wing sweep is accounted for by transforming the MCARF pressure distribution into a "three-dimensional" or "swept" C_p according to

$$C_{p_3} = C_{p_2} \cos^2(\Lambda). \tag{3.2}$$

This represents a renormalization by the dynamic pressure in the freestream (X) direction. Figure 3.9 shows the swept airfoil contour and upper-surface C_p for the NLF(2)-0415 at $\alpha = -4°$ and $\delta_F = 0°$ in the Unsteady Wind Tunnel. There are three differences between this plot and figure 3.3.

1. The airfoil cross section is viewed in the (X, y) plane and nondimensionalized by the swept chord C, hence it appears thinner. (In the coordinate systems described in section 3.4, x/c and X/C are equivalent but y/c and y/C are not.)

2. The swept C_{p_3} defined by equation (3.2) is plotted.

3. The pressure distribution is computed with the front and rear test-section walls in place.

The primary effect of the wind-tunnel walls is to accelerate the flow to a slightly lower minimum pressure. This will increase—although not dramatically—the crossflow disturbance growth rates.

The MCARF code is run in an inviscid mode, i.e., no corrections for displacement thickness are applied. The cross-sectional area of the Unsteady Wind Tunnel test section increases by 3.7% to account for wall and model boundary-layer growth. Although only approximate, Dagenhart (1992) has shown that this correction is sufficiently accurate for this experiment.

Using the C_p distribution of figure 3.9, the laminar boundary layers are computed with the boundary-layer code of Haynes (Haynes and Reed 1996). This code is designed for infinite-span swept wings and employs the conical-flow assumption. The boundary-layer profiles at several chord locations for $Re_c = 2.4 \times 10^6$ are shown in figures 3.10–3.12. The velocity component tangent to the inviscid streamline (figure 3.10) accelerates continuously under the presence of the favorable pressure gradient. The crossflow component (figure 3.11) shows rapid initial growth due to the large pressure gradient near the leading edge, followed by a more moderate and sustained development in the mid-chord region. The streamwise velocity component measured by the hot wires is plotted in figure 3.12. These boundary-layer profiles are typical for swept-wing flows.

The crossflow Reynolds number is based on the maximum crossflow velocity and the larger of the two heights where the crossflow velocity is 10% of the maximum, thus

$$Re_{\mathrm{cf}} = \frac{w_{t_{\max}} h_{10}}{\nu}. \tag{3.3}$$

Historically, the crossflow Reynolds number has been used for transition correlations based purely on basic-state boundary-layer characteristics (see, for example, Reed and Haynes 1994). For the present experiment, Re_{cf} varies from 5.7 at $x/c = 0.005$ to 270 at $x/c = 0.60$ for $Re_c = 2.4 \times 10^6$. Figure 3.13 shows the streamwise variation of Re_{cf} for several chord Reynolds numbers.

3.5.2 Linear Stability Calculations

The linear stability behavior of the above boundary layers aids in the choice of experimental test conditions and provides a benchmark to which the experimental results are compared. Traditional analyses of this type involve solving the Orr-Sommerfeld

equation for the disturbance growth rates and normal modes (discussed below). Many codes such as SALLY (Srokowski and Orszag 1977) and COSAL (Malik 1982) are generally available for this task. More recently, the parabolized stability equations (PSE) have become very popular as an alternate method for predicting stability behavior (see the discussion in section 1.3.3).

Although the experimental results are compared to both linear and nonlinear PSE calculations in chapter 5, the present discussion focuses on spatial stability analysis using linear, parallel theory. While these restrictions certainly limit the class of flows to which the analysis applies, they allow us to effectively illustrate the fundamental ideas of stability theory. Complete reviews of this topic can be found in many places. In particular, the reader is referred to Mack (1984), Arnal (1992, 1994), and Saric (1992b, 1994c) for detailed discussions. The summary presented here follows that of Saric (1994c).

The analysis begins by assuming a *parallel* basic state given by

$$U = U(y), \quad V = 0, \quad W = W(y), \tag{3.4}$$

where y is normal to the surface and U, V, and W are the chordwise (x), wall-normal (y), and spanwise (z) velocity components, respectively. This assumption immediately forces a local analysis in that the stability characteristics at each streamwise location—determined using the local velocity distributions—are obtained independently of all others.

The total field quantities consist of the basic state plus small, three-dimensional

disturbances and are written as

$$u = U + u'(x, y, z, t) \tag{3.5a}$$

$$v = v'(x, y, z, t) \tag{3.5b}$$

$$w = W + w'(x, y, z, t) \tag{3.5c}$$

$$p = P + p'(x, y, z, t) \tag{3.5d}$$

Equations 3.5 are substituted into the incompressible Navier-Stokes equations, the basic-state solution is removed (the basic state itself satisfies the Navier-Stokes equations), and products of the small disturbance quantities are neglected (e.g., $u'u'_x \ll u'$). The resulting linear disturbance equations are

$$u'_x + v'_y + w'_z = 0 \tag{3.6}$$

$$u'_t + Uu'_x + U_y v' + Wu'_z + p'_x - \nabla^2 u'/R = 0 \tag{3.7}$$

$$v'_t + Uv'_x + Wv'_z + p'_y - \nabla^2 v'/R = 0 \tag{3.8}$$

$$w'_t + Uw'_x + W_y v' + Ww'_z + p'_z - \nabla^2 w'/R = 0 \tag{3.9}$$

where subscripts denote partial differentiation and the equations have been appropriately nondimensionalized (R is the Reynolds number).

Equations (3.6)–(3.9) are reduced to ordinary differential equations with the introduction of the *normal mode*

$$q'(x, y, z, t) = q(y)\, e^{i(\alpha x + \beta z - \omega t)} + C.C., \tag{3.10}$$

where q' represents any one of the disturbance quantities and $C.C.$ stands for complex conjugate. The form of the normal mode is suggested by the linearity of the

disturbance equations and the fact that the coefficients (i.e., basic-state velocities) are functions only of y. Equation (3.10) represents a single sinusoidal wave (i.e., one Fourier mode) with chordwise wavenumber α, spanwise wavenumber β, and frequency ω. The amplitude function $q(y)$ is complex but q' is real by the inclusion of the complex conjugate.

Substituting equation (3.10) into equations (3.6)–(3.9) produces a 6th-order system of ordinary differential equations describing the disturbance motion. This system can be combined into a single 4th-order equation known as the *Orr-Sommerfeld* equation:

$$\left\{\left(D^2-k^2\right)^2 - iR\left[(\alpha U+\beta W-\omega)\left(D^2-k^2\right)-\alpha\left(D^2U\right)-\beta\left(D^2W\right)\right]\right\}\phi = 0, \tag{3.11}$$

where $k^2 = \alpha^2 + \beta^2$, $D \equiv d/dy$, and $\phi = v$ represents the normal-mode amplitude function for the v' disturbance. (The variable change is simply to remain consistent with conventional notation.) The disturbances are zero at the wall and must vanish in the farfield, hence the boundary conditions are

$$\phi(0) = D\phi(0) = 0 \quad \text{and} \quad \phi \xrightarrow[y\to\infty]{} 0. \tag{3.12}$$

The condition $D\phi = 0$ is a statement of the no-slip condition [$Dv = 0$ in equation (3.6)].

Equations (3.11) and (3.12) form a linear, homogeneous system for the normal-mode amplitude function ϕ ($= v$) in terms of the basic-state velocity profiles and the parameters α, β, ω, and R. The system defines an eigenvalue problem (by virtue of its linearity and homogeneity), thus solutions to equation (3.11) are obtained only for certain combinations of the parameters. This combination is expressed by the

dispersion relationship

$$\mathcal{F}(\alpha, \beta, \omega, R) = 0. \tag{3.13}$$

For spatial stability analysis, α and β are complex and ω is real. Thus, equation (3.13) represents two equations in six unknowns. Actually, the Reynolds number is known and the frequency is typically specified, leaving the wavenumbers (α_r and β_r) and the growth rates (α_i and β_i) as the four undetermined quantities. Consequently, additional constraints on α and/or β are required in order to solve equation (3.13). Many such constraints have been proposed and are reviewed by Arnal (1994). Typically they involve a somewhat *ad hoc* assumption concerning the direction of growth, the direction of propagation, or the disturbance wavelength. The present analysis follows Mack (1988) and assumes, quite simply, that β_r is fixed (and specified) and $\beta_i = 0$. This amounts to nothing more than a statement of the infinite-span assumption and is verified experimentally in chapter 6. With $\omega = 0$ for stationary disturbances and β_r input, equation (3.13) is solved for the chordwise wavenumber α_r and growth rate $-\alpha_i$. The solution is strictly local, and must be re-evaluated at each chord location using the new local conditions as input.

The disturbance amplitude ratio between two locations is computed by integrating the spatial growth rate, giving

$$\frac{A}{A_o} = e^N \tag{3.14}$$

where the amplification factor or integrated growth rate N (also called the "N-factor") is given by

$$N = \int_{x_o}^{x} \sigma \, dx. \tag{3.15}$$

In general, the growth rate σ is some combination of α_i and β_i meant to represent the total amplification of the disturbance. As mentioned above, however, $\beta_i = 0$ for the infinite-span airfoil. In this case, the integrated growth rate N reduces to

$$N = \int_{x_o}^{x} -\alpha_i \, dx = \ln \frac{A}{A_o}. \tag{3.16}$$

The N-factor provides the basis for the celebrated e^N transition correlation method (Smith and Gamberoni 1956; van Ingen 1956). See Saric (1992b) and Arnal (1992, 1994) for current reviews.

Using these techniques, linear stability predictions for stationary crossflow disturbances are computed for the experimental test conditions outlined in section 3.3. The calculations are generated with the stability code of Haynes (Haynes and Reed 1996). Figure 3.14 shows N versus x/c for $Re_c = 2.4 \times 10^6$. Amplitude curves are shown for several values of the spanwise wavelength $\lambda_z = 2\pi/\beta_r$. The N-factors are computed relative to $x/c = 0.05$. The data show typical linear behavior for stationary crossflow modes in a swept-wing boundary layer. Short wavelength disturbances grow early in the region of rapid boundary-layer growth, while long-wavelength modes are amplified at larger x/c after a region of initial decay. The modes with the largest N-factor are those that are short enough to grow early but long enough to remain unstable until the pressure minimum at $x/c = 0.71$. In agreement with the SALLY calculations used by Dagenhart (1992) and Radeztsky (1994), the $\lambda_z = 12$ mm mode is the most unstable.

CHAPTER 4

Experimental Methods

The experimental procedures at the Unsteady Wind Tunnel are designed to provide high-quality, reliable data in each test. This requires a clear understanding of the stability problem, as well as certain wind-tunnel effects that may influence the results. This chapter discusses these issues, and describes the specific data-acquisition and post-processing techniques used for the present experiment.

4.1 Special Considerations

4.1.1 Stationary Disturbances

The stationary crossflow problem on a swept wing presents several unique challenges to the experimentalist. Unlike the rotating disk analogue, the stationary waves are fixed in space. Thus, the measurement probe must be moved through the flowfield to capture the stationary structure. This requires special steps to ensure the positioning accuracy of the instrumentation traverse system, and corrective actions are usually needed to compensate for misalignment between the traverse and the model.

Stationary disturbances also require mean-flow, or DC, measurements. At a given measurement point in the boundary layer, the time-dependent u' fluctuations are due to *traveling* disturbances, whereas the mean of the measurement represents the stationary component. Consequently, one cannot AC-couple the signal and amplify

the fluctuations. This process would remove the stationary component of interest and leave only the traveling waves. Instead, the stationary disturbance component must be determined by looking for spatial variations in the total boundary-layer velocity u. This works well downstream where the distortions of the mean boundary layer are large, however near the leading edge it becomes increasingly difficult to extract small disturbance quantities from $O(1)$ measurements. Unfortunately, the critical initial disturbance amplitude must be determined under these conditions, which underscores the need for accurate measurements.

4.1.2 Wind-Tunnel Heating

Additional complications are caused by the fan-generated and frictional heating of a closed-circuit wind tunnel. This problem can be minimized or even removed by the introduction of a heat exchanger. These systems, however, add mechanical complexities to the tunnel, create a large drag penalty, and may alter the flow quality (Rae and Pope 1984). In addition, the large thermal time constant characteristic of large wind tunnels may affect the accuracy to which the test-section temperature can be controlled. Thus, active cooling systems are not necessarily the panacea for wind-tunnel heating.

The Unsteady Wind Tunnel is not equipped with a cooling system, hence the test-section temperature is at the mercy of the natural heating effects. The warm desert environment at Arizona State University compounds the problem. The ambient temperature frequently reaches 45 °C during the summer months. As a result, the test-section temperature can increase by 20 °C during a high-Reynolds-number experiment. On the other hand, low-speed runs that continue into the evening are often characterized by an initial increase, then decrease in the test-section temperature. Velocity measurements using hot-wire anemometry must account for these temperature fluctuations.

4.2 Hot-Wire Techniques

Experiments at the Unsteady Wind Tunnel use hot-wire anemometry for all quantitative velocity measurements within the boundary layer. This topic is well studied, with no dearth of publications describing various calibration and signal-analysis techniques. The approach at the Unsteady Wind Tunnel focuses on empirical accuracy. Although the methods account for the dominant behavior of the hot wire, no particular physical model for the velocity or temperature response is used. Computer analysis and automated procedures are emphasized. This eliminates the need for analog equipment (such as temperature compensators and linearizers), but requires additional software development.

4.2.1 Velocity Calibration

For low-speed flows, the voltage output from a constant-temperature anemometer (CTA) is dominated by the fluid velocity and temperature difference between the hot-wire element and the fluid (Perry 1982). Thus,

$$U = \mathcal{F}(E, \Delta T), \tag{4.1}$$

where the velocity is isolated as the dependent variable since it is the desired quantity. Assume for now the temperature difference between the wire and the fluid (ΔT) is fixed. Then the classic model of the anemometer's velocity response is given by King's Law (King 1914, 1915):

$$U = \left(P + QE^2\right)^2, \tag{4.2}$$

where P and Q are parameters involving the physical properties of the hot-wire element and the fluid. The Unsteady Wind Tunnel model generalizes King's Law by

using a simple polynomial fit:

$$U = \sum_{k=0}^{n} A_k E^k. \tag{4.3}$$

The coefficients A_k are determined such that equation (4.3) best fits (in the least-squares sense) a moderate number of voltage/velocity data points. A 4th-order fit ($n = 4$) is chosen to match King's Law to leading order. The polynomial fit, however, is more general in that the E and E^3 terms not present in King's Law allow a more robust approximation of the data points.

The hot wires are calibrated *in situ* by monitoring the anemometer output and Pitot-static velocity as the tunnel is increased though a set of predetermined calibration speeds. Figure 4.1 shows a typical calibration curve fit. The calibration points must entirely encompass the operating speeds of the hot wire since extrapolating a polynomial fit is potentially unstable. The procedure is fully automated and takes less than 5 minutes, allowing the hot wires to be calibrated at virtually any time during the experiment. As a standard practice, the calibration is repeated each morning to protect against possible "calibration drift" experienced by tungsten hot wires (Perry 1982).

4.2.2 Temperature Compensation

The above discussion has neglected the effect of fluid temperature changes on the CTA output. This cannot be ignored since the test-section temperature varies during an experiment (see section 4.1.2).

Numerous methods for CTA temperature compensation have been proposed. The current Unsteady Wind Tunnel approach follows Bearman (1971), and improves the technique of Radeztsky et al. (1993b) to include the velocity dependence of the temperature-compensation coefficient. As with the velocity calibration, the emphasis

is on empirical data fits and computer automation. The model assumes the square of the CTA voltage varies linearly with temperature for a fixed velocity, that is

$$E_c^2 = E^2 + C_T(T_c - T), \tag{4.4}$$

where E_c is the CTA "equivalent" voltage at the calibration temperature T_c. The *compensation coefficient* C_T is a function of velocity, as indicated in figure 4.2. These data are obtained by monitoring the test-section temperature, anemometer output, and Pitot-static velocity while the tunnel is pre-heated. (The pre-heat also minimizes temperature changes during the experiment.) The speed dependence of the compensation coefficient is modeled well with a 2nd-order polynomial curve fit,

$$C_T = \sum_{j=0}^{2} B_j U^j, \tag{4.5}$$

whose coefficients B_j are determined by the least-squares technique. It is important to note that the compensation coefficients are obtained before the velocity calibration discussed in the preceding section. This allows the velocity calibration to be corrected for any temperature changes, effectively producing a constant-temperature hot-wire calibration.

For data-acquisition purposes, equations (4.5) and (4.3) are substituted into equation (4.4) to give an implicit relation for the temperature-compensated CTA voltage:

$$E_c^2 = E^2 + \sum_{j=0}^{2} \left[B_j \left(\sum_{k=0}^{n} A_k E_c^k \right)^j \right] (T_c - T). \tag{4.6}$$

Given a temperature T and an anemometer voltage E, equation (4.6) is implicitly solved for E_c. This corrected voltage is then converted to an accurate hot-wire velocity using equation (4.3). Figure 4.3 illustrates the accuracy obtainable with this method.

The test-section temperature is more than 10 °C above the calibration temperature for all speeds, and the uncorrected hot-wire velocities are plagued with errors exceeding 15%. On the other hand, the error in the temperature-compensated measurements is less than 1% over the entire speed range.

The calibration and data-acquisition techniques outlined above are implemented through a custom set of programming libraries (Reibert 1996). In addition to standardizing the methods, this allows acquisition program to be developed and updated efficiently.

4.3 Wind-Tunnel Speed Control

Wind-tunnel heating can also affect the freestream velocity during an experiment. More precisely, changes in kinematic viscosity caused by wind-tunnel heating (or cooling) may necessitate a change in freestream velocity in order to keep a relevant nondimensional parameter constant. For example, consider an experiment in which the test-section temperature rises from 30 °C to 50 °C (not uncommon at the Unsteady Wind Tunnel). If the velocity remains fixed, the Reynolds number will decrease by 11% (air at 1 atmosphere). This may have a significant impact on the stability characteristics of the experiment. Consequently, the freestream velocity must be increased to compensate for the increase in the kinematic viscosity.

To coordinate these velocity adjustments, the Unsteady Wind Tunnel is controlled from the Sun SPARCstation data-acquisition computer using a "cruise control" program (figure 4.4). This custom LabVIEW virtual instrument continually monitors the tunnel conditions (test-section static pressure, dynamic pressure, temperature, and fan/motor rpm) and adjusts the motor speed to maintain the desired *control value*. Three *control parameters* are available: freestream velocity, Reynolds number, and nondimensional frequency. When the control parameter or control value

is changed, the program commands the data-acquisition system to provide continuous updates as tunnel approaches the new conditions. When the difference between the measured and target freestream velocity is within tolerance (1% of the target or 0.1 m/s, whichever is smaller), the program enters a "slow maintenance" mode in which the tunnel conditions are updated less frequently (typically every 15 seconds). This has two benefits. First, the fan motor is not unnecessarily chasing continuous but insignificant rpm adjustments. Instead, the program simply applies a "drift correction" to compensate for the slowly varying temperature. Second, the A/D system is available for other tasks. This is essential since the A/D converters are a shared system resource and must be available for experimental data acquisition.

The present work uses the Reynolds number control parameter to maintain a constant chord Reynolds number during each experiment.

4.4 Disturbance Measurement Techniques

The majority of the data presented in chapters 5 and 6 are obtained using the two measurement techniques discussed below. Although each methods is optimized for a specific task, the common goal is to quantify the stationary crossflow disturbance amplitude by accurately measuring spatial variations in the mean boundary-layer velocity.

4.4.1 Boundary-Layer Profile Scans

Multiple wall-normal boundary-layer scans provide a detailed, two-dimensional map of the stationary structure. These maps are constructed by taking a spanwise series of mean-flow boundary-layer profiles at constant x/c. A typical set consists of 100 profiles, each separated by 1 mm in the swept span direction. The technique is similar to that of Radeztsky (1994).

Before the scan begins, the "BL" hot wire (positioned at the end of the sting, see figure 2.4) is adjusted for local surface curvature effects. This is necessary since the hot wires are aligned to measure the streamwise velocity u and not the component u_n normal to the leading edge. The adjustment involves moving the hot wire very close to the model and, under magnification, rotating the probe about its axis so that the tines are equidistant from the surface. This ensures that the hot wire element is not averaging across the boundary layer. The probe is then moved to the edge of the boundary layer and the scan is started.

Each individual profile is fully self contained. The BL hot wire measures the boundary-layer velocity and the "FS" hot wire (located mid-span on the sting, see figure 2.4) tracks the external-flow velocity at the same x/c.[1] The scan starts with the BL hot wire positioned at the edge of the boundary layer. This reference point is acquired, and the boundary-layer-edge-to-external-flow velocity ratio is recorded. The probes are then stepped toward the model, acquiring the mean velocity from both hot wires at each point. The boundary-layer velocity is normalized by the instantaneous edge velocity U_e. This is computed by scaling the FS hot-wire velocity by the edge-to-external-flow velocity ratio from the initial reference point. This instantaneous local normalization is essential since the tunnel speed is, in general, changing due to heating effects (see section 4.3). As the scan progresses, the step size is scaled with u/U_e to provide finer resolution near the airfoil surface. When u/U_e reaches a predetermined threshold, the profile is terminated and the hot wires are moved to the boundary-layer edge at the next span location. A new boundary-layer-edge-to-external-flow velocity ratio is obtained, and the entire procedure is repeated. Figure 4.5 shows a typical profile.

[1] The FS hot wire measures the velocity in the external flowfield approximately 150 mm "above" the boundary-layer probe.

Once the profiles are acquired, the data produce a two-dimensional map of the mean-flow boundary layer, complete with any amplified stationary disturbance structure. From this velocity field it is relatively straightforward to generate velocity contours, disturbance profiles, and stationary wave mode shapes from which the disturbance amplitude is obtained.

Like all experimental measurement techniques, this method has both advantages and disadvantages. On the plus side, the individual profiles are self-consistent and self-aligning. The location of the airfoil surface is determined by extrapolating each profile to zero velocity. The slight pressure-gradient-induced curvature of the boundary layer is ignored, and a straight line is fit through the lower portion of the profile. Dagenhart (1992) and Radeztsky (1994) successfully used this technique in earlier swept-wing experiments at ASU. With a known reference point for each profile, the scans are easily assembled to produce the two-dimensional velocity field. Moreover, traverse/model alignment concerns virtually disappear since each profile is aligned with the airfoil surface independently.

The foremost disadvantage of this method is the time required for a complete set of profiles. The $O(1)$ spanwise gradients make it impossible to use the highly optimized technique of Radeztsky (1994), hence each individual boundary-layer profile is obtained without assistance from the previous scan. Moreover, the strong distortion of the boundary-layer flow demands high resolution in the wall-normal direction. A typical profile in the mid-chord region ($\delta \approx 4$ mm) contains on average 60 data points. Each data point, in turn, requires approximately 3 seconds to acquire (2 seconds of sampling at 1 kHz and 1 second for the traverse move and overhead). Thus, 5 hours are needed to obtain 100 profiles. Consequently, this technique can quickly become prohibitively time consuming.

4.4.2 Spanwise Scans at Constant Y

One of the primary goals of this experiment is to accurately determine the wavenumber content of the amplified stationary crossflow disturbances. This will not only provide single-wavelength growth rates for comparison with linear theory, but will also guide nonlinear PSE computations by providing initial conditions for individual modes. To quantify this analysis, some sort of spectral decomposition must be applied to the data. The spectral method, in turn, will impose certain restrictions on the data that will ultimately require a second measurement technique.

Spectral Considerations

As with any experiment that involves analysis in the spectral domain, frequency resolution issues are of paramount importance. For discrete experimental data, the sampling parameters must be chosen appropriately to yield the desired spectral characteristics. The present experiment adds a slight twist: the acquired signal is a function of space rather than time. In this context, inverse wavelength takes on the role of "frequency", and the sampling parameters determine the wavelength resolution in the *spatial* power spectrum. The translation from the time domain to the spatial domain illuminates the requirements that must be satisfied by the measurement technique. This is briefly reviewed below. A complete discussion of discrete spectral methods can be found in many sources. In particular, Press et al. (1992) give a succinct explanation of several techniques.

In general, a discrete signal contains N evenly spaced measurements over a length S (in time or space). The sampling interval Δ_s is

$$\Delta_s = \frac{S}{N-1}. \tag{4.7}$$

The sampling frequency $f = 1/\Delta_s$. For a time-domain signal, f is in Hertz. If, on

the other hand, S (and therefore Δ_s) are spatial quantities, f is in cycles per length. This corresponds to inverse wavelength (not wavenumber).

The one-sided power spectral density (PSD) is defined at the $N/2 + 1$ discrete frequencies

$$f_k = \frac{k}{N\Delta_s}, \quad k = 0, \ldots, \frac{N}{2}, \tag{4.8}$$

giving a frequency resolution of $\Delta f = 1/(N\Delta_s)$. The Nyquist critical frequency is $f_c = 1/(2\Delta_s)$. For a spatial spectrum, the wavelength resolution $\Delta\lambda$ is more important. Since $\lambda = 1/f$,

$$\Delta\lambda = \left|\frac{d\lambda}{df}\right| \Delta f = \frac{\Delta f}{f^2} = \frac{\lambda^2}{N\Delta_s} \approx \frac{\lambda^2}{S}. \tag{4.9}$$

Several key features of the spatial spectrum are exposed by equation (4.9).

1. The wavelength resolution is a function of λ, and increases with the square of the wavelength. Thus, small wavelengths are resolved better than large wavelengths.

2. Increasing the length of the data set S decreases the wavelength resolution. Thus, all wavelengths are best resolved by maximizing the spatial extent of the sample. Increasing the number of samples N without changing S does not affect $\Delta\lambda$; the "extra" information goes into increasing the Nyquist frequency by reducing the sampling interval Δ_s.

3. The smallest wavelength for which a power estimate is obtained is $\lambda = 2\Delta_s$. This is used to determine the sampling interval for the measurements.

In short, one must sample longer to improve the spectral frequency resolution. Sampling faster only serves to increase the Nyquist frequency.

Another important issue is the choice of kernel used to generate the PSD. The Fourier transform is certainly the most common, due in no small part to the advent of the fast Fourier transform (FFT). However, many alternate methods are available, each with characteristic advantages and disadvantages (Kay and Marple 1981). Previous ASU swept-wing experiments (Radeztsky et al. 1994) used the maximum entropy method (MEM), which generates the PSD in terms of a Laurent series. The result is a continuous spectrum that is well-suited for "peaky" spectra and small data sets. The major drawback, however, is that the user must (somewhat arbitrarily) choose the number of poles in the Laurent series expansion. If too few are chosen, certain features in the spectrum may be suppressed. On the other hand, too many poles can create spurious peaks or even split sharp peaks. In addition, spectral peaks can shift frequency depending on the phase. As pointed out by Radeztsky (1994), practical application of the MEM requires subjective interaction from the user and is therefore difficult to automate.

To avoid these problems, the present analysis relies strictly on FFT-based spectral methods. The subjectivity of the MEM is removed, allowing the PSD generation to be automated. However, a new set of concerns arises as a result of the discrete spectrum:

1. How much confidence does one have in the FFT-based power estimates, i.e., is the PSD estimate for each frequency "bin" correct on average?

2. Can the frequency (or wavelength) resolution be improved when the length of the data series is limited?

In general, these are nontrivial issues that are discussed in-depth in the literature (see, for example, Press et al. 1992 and Kay and Marple 1981). Here the topics will be briefly addressed in the context of the present experiment.

The first problem is cast in terms of spectral leakage and variance. Leakage (of

energy into adjacent frequency "bins") is caused by the abrupt turning on and off of the data series. The solution to this problem is to *window* the data with a transfer function that changes more gradually from zero to a maximum and back to zero over the length of the data. Many standard windows are commonly available (Press et al. 1992). The Welch window is used for this experiment. This quadratic window is computationally efficient and provides a reasonable trade-off between the sidelobe fall-off and the highest sidelobe level. The variance issue is handled by averaging. This process involves splitting the data series into smaller segments, computing the PSD for each segment, then averaging the individual spectra to form the final power spectrum. This presents little difficulty in the time domain, where it is easy to acquire multiple back-to-back data segments by simply sampling longer. For spatial spectra, however, the length of the sample is typically fixed by the physical constraints of the system. In this case, one can repeat the experiment multiple times, but this is often too time consuming due to overhead associated with setting up each run. A better approach is to increase the sampling frequency by a factor M representing the desired number of averages. The data stream can then be demultiplexed into M data segments—each covering the total length S—which provide the necessary averages. This technique preserves the desired wavelength resolution since the spatial extent of each data segment is not compromised.

The second point concerns improving the wavelength (or frequency) resolution without increasing the sample length S. This is particularly important for spatial spectra due to the physical limits of the measurement region. At issue here is whether or not the data or the FFT can be modified so that the PSD estimates better approximate the "true" power spectrum of the (windowed) data. The answer is, quite simply, yes and no. The pessimist will point out that once the data are acquired, the "information content" of the signal is fixed and cannot be magically increased by the

FFT procedure. In particular, the fundamental frequency resolution is entirely determined by the number of samples and the sampling interval, and cannot be altered by the FFT. However, all hope is not lost. It is entirely possible to increase the number of discrete spectral modes used in the Fourier expansion. This does not improve the fundamental frequency resolution, but instead allows the FFT to interpolate additional PSD estimates to better approximate the *available* information contained within the data (Kay and Marple 1981). This is accomplished by zero-padding each data segment before it is converted by the FFT. Care must be taken to add the zeros after the window has been applied, else the effect of the window will be seriously compromised. When applied correctly, zero-padding has the quite desirable effect of "smoothing" an otherwise coarse power spectrum.

All spectra used in this work have mean square power spectral density plotted on the ordinate. Thus, by Parseval's theorem the square root of the integral of the spectrum equals the rms of the original signal.

Scanning Technique

Spatial spectra for stationary crossflow waves are best obtained from a single spanwise trace of u/U_e at constant Y. The sampling requirements for these measurements are obtained directly from the previous discussion. The velocity profile must cover the entire spanwise extent of the measurement region in order to provide the best possible wavelength resolution in the spectral domain. For the present experiment, that distance is 240 mm. With 256 data points along this span, the wavelength resolution will be $\Delta\lambda = 0.6$ mm at $\lambda = 12$ mm, and wavelengths between 1.9 mm and 240 mm will be resolved by the spectrum. Four-times over-sampling (acquiring 1024 points along the total span) allows four averages, each with 256 points covering the total span of 240 mm.

One way to generate the u/U_e versus span profile is to take a spanwise slice

(at constant Y) across a set of wall-normal boundary-layer profiles. This has the distinct advantage that all heights within the boundary layer are available for analysis. Unfortunately, at nearly 3 minutes per boundary layer it would take over two days of continuous data acquisition to obtain the 1024 profiles needed to meet the spectral requirements! Consequently, this approach is abandoned.

To reduce the data-acquisition time, the measurements are limited to a single spanwise scan at a constant height above the airfoil surface. As with the wall-normal profiles, the spanwise scan begins with the BL hot wire positioned at the edge of the boundary layer. This reference point is acquired, and the boundary-layer-edge-to-external-flow velocity ratio is recorded. The probes are then stepped toward the model until the BL hot wire is a user-specified distance from the surface. The scan proceeds with the probes being moved in the swept span (z) direction, acquiring the mean velocity at 1024 points along the 240 mm span. The boundary-layer velocity is nondimensionalized with the instantaneous edge velocity in the same manner as the wall-normal scans. At each measurement point, the Y position of the hot wires is adjusted to compensate for any misalignment between the model and the traverse (more on this later). Figure 4.6 shows a typical scan. This velocity profile is well-suited for the spatial spectral techniques discussed above, and the peaks in the PSD are integrated to obtain the disturbance energy in individual crossflow modes.

Traverse Alignment

The stationary crossflow disturbance amplitude is a strong function of Y. It is therefore critical to remain a fixed distance above the airfoil surface during a spanwise scan. This is accomplished by prefacing the spanwise scan with a traverse-alignment scan. The purpose of this preliminary scan is to locate the airfoil surface in the coordinate system in which the traverse moves.

In previous ASU experiments, Radeztsky (1994) aligned the traverse by moving

along the span and recording the Y position (in traverse coordinates) corresponding to $u/U_e = 0.75$. This method is relatively fast and works well provided $Y = Y(u/U_e)$ is one-to-one at all span locations. The primary disadvantage is that the physical location of the model surface is never actually determined. Only a relative correction is obtained allowing the spanwise scan to proceed at a nominal u/U_e. For the present experiment, disturbance amplitudes computed from the spanwise scans will be directly compared to those obtained from wall-normal boundary-layer profiles. The quality of these comparisons depends strongly on being able to specify the exact height above the airfoil surface for the spanwise scan. Moreover, $Y = Y(u/U_e)$ is not necessarily one-to-one due to the large distortions of the mean boundary layer. Consequently, the technique of Radeztsky cannot be used.

The location of the model surface can be accurately determined, however, by extrapolating a boundary-layer profile to zero velocity. This idea—borrowed from the wall-normal scanning technique—provides the basis for the traverse-alignment procedure. A small number of wall-normal boundary-layer profiles (usually 25) are taken over the 240 mm extent of the spanwise scan. These profiles are optimized to concentrate data points near the airfoil surface at the expense of detail high in the boundary layer. This minimizes the time required for each profile while maintaining an accurate extrapolation to zero velocity. The surface coordinate is recorded at each span location, and the data are fit with a low-order polynomial. Figure 4.7 shows a typical traverse-alignment profile. The curve fit effectively represents the physical location of the model surface as a function of span. This relation is used by the spanwise scan to maintain the desired height above the airfoil surface, resulting in the velocity profile shown in figure 4.6.

4.5 Flow Visualization

Stationary crossflow waves, through a spanwise modulation of the mean boundary-layer flow, produce a surface shear stress pattern that can be identified with a shear-stress-sensitive flow-visualization technique. Naphthalene is an effective medium for this type of visualization; at room temperature it sublimes at a rate proportional to shear stress.

To apply the naphthalene to the wing, it is first dissolved in 1,1,1-trichloroethane. The saturated solution is sprayed onto the airfoil surface using a compressed-air sprayer. The solvent quickly evaporates, leaving a thin coating of naphthalene on the model. Care must be taken to avoid spraying the leading edge since the naphthalene adds roughness to the surface. As a general rule, the naphthalene is not applied forward of $x/c = 0.20$. According to Radeztsky et al. (1993a), this is well beyond the point where surface roughness influences the stationary crossflow instability.

With the naphthalene coating on the airfoil, the wind tunnel is started and brought to the desired test condition. The naphthalene quickly sublimes in regions of high shear, but remains where the shear stress is low. The stationary crossflow waves are visible as streaks of naphthalene. This pattern is caused by the transposition of high- and low-momentum fluid within the boundary layer resulting in the spanwise modulation of the surface shear stress. The naphthalene also quickly sublimes in the turbulent region, leaving a clear picture of the transition front.

CHAPTER 5

Results—Part 1: Baseline Configuration

5.1 Overview

The experimental results and discussion are divided into two chapters, of which this is the first. Stationary crossflow disturbance measurements for the baseline test condition (described below) are presented in detail. For this data set, comparisons with theoretical predictions provide valuable assistance not only in analyzing the data, but in understanding the underlying physical mechanisms of the crossflow instability. Transition data and basic-state measurements are also presented in this chapter.

The following chapter continues the investigation by describing the experimental results under varying freestream and surface-roughness conditions. From the reference condition discussed in this chapter, the chord Reynolds number, roughness spacing, and roughness height are varied independently to cover the parameter space. Chapter 6 concludes by addressing several summary topics and specific questions raised during the experiment.

In both this and the next chapter, all of the crossflow disturbance amplitude measurements are acquired using the two hot-wire scanning techniques described in section 4.4. The results are grouped into the six data sets summarized in table 5.1. The chord Reynolds number is shown in the column marked Re_c, while the roughness

Table 5.1: Experimental data set configuration.

Data Set	$Re_c/10^6$	Roughness		Scan Type	
		k [μm]	λ_z [mm]	BL	Span
$\mathcal{A}$	2.4	6	12	•	•
$\mathcal{B}$	1.6	6	12	•	
$\mathcal{C}$	3.2	6	12	•	•
$\mathcal{D}$	2.4	6	36	•	•
$\mathcal{E}$	2.4	18	12	•	•
$\mathcal{F}$	2.4	48	12	•	•

height and spanwise spacing are given in the k and λ_z columns, respectively. Data are obtained using the wall-normal boundary-layer profile and spanwise scan at constant Y^+ techniques as indicated by a bullet (•) in the BL or Span column. This chapter concentrates on the baseline or control configuration defined by data set $\mathcal{A}$. Data sets $\mathcal{B}$ through $\mathcal{F}$ are presented in chapter 6.

The roughness elements are applied in full-span arrays at $x/c = 0.023$ as outlined in section 3.3.3. Different roughness configurations are achieved by varying the height or spanwise spacing of the elements, but the chord location remains fixed and the roughness always covers the entire span. Therefore, a statement of the element height and spanwise spacing unambiguously defines the roughness configuration. The shorthand notation $[k|\lambda_z]$ will be used for this purpose. Thus, [6|36] denotes $k = 6$ μm roughness with a 36 mm spanwise spacing, while [48|12] means the roughness elements are 48 μm thick and 12 mm apart. The absence of artificial roughness is denoted by [0|0].

Following the convention commonly used in CFD, crossflow modes are expressed as (f, m). In this notation, f is the disturbance frequency (zero for stationary waves) and m is the mode number defined as the disturbance wavenumber normalized by the wavenumber of the fundamental mode. Thus, $m = 1$ denotes the fundamental

disturbance, while $m = 2$ represents the first superharmonic with a wavenumber equal to twice that of the fundamental (i.e., half the wavelength). The spanwise-invariant disturbance—usually called the "mean-flow distortion" mode—is denoted by $(0, 0)$. This should not be confused with the local distortions of the mean boundary layer caused by the stationary crossflow waves. Where ambiguity in the terminology may result, the meaning should be clear from the context.

5.2 Flow Visualization

Surface shear-stress patterns and transition locations are obtained using naphthalene flow visualization (see section 4.5). This technique has been calibrated against hot-wire and hot-film measurements (Dagenhart 1992) and has been successfully used by Dagenhart et al. (1989, 1990) and Radeztsky et al. (1993a) as a transition indicator. One of the more significant results to come out of Radeztsky et al. (1993a) was the fact that micron-sized roughness is not effective beyond 10% chord. Thus, the inherent roughness associated with the deposition of naphthalene is benign if applied away from the attachment line.

Figures 5.1 and 5.2 show the naphthalene pattern at $Re_c = 2.2 \times 10^6$ and 3.2×10^6. The roughness configuration is [6|12] for both cases. The flow is left to right, and the photographs show the airfoil upper surface as viewed through a glass window in the test-section front wall. Lines of constant chord drawn on the model with a felt-tipped pen appear as black lines parallel to the leading edge. The white numerals indicate x/c in percent. The stationary crossflow vortex pattern is clearly indicated by the alternating light and dark streaks. Strictly speaking, these streaks show the spanwise modulation of the surface shear stress caused by the transposition of high- and low-momentum fluid within the boundary layer (more on this later). In this sense, the naphthalene pattern provides a visual image of the "footprint" of the stationary wave

structure.

The region within which the boundary layer is turbulent is marked by the absence of naphthalene.[1] The jagged transition front that develops as a series of turbulent wedges is typical for swept-wing boundary layers dominated by the stationary cross-flow instability. It is interesting to note that the turbulent wedge pattern is somewhat nonuniform is span even when the initial conditions are carefully controlled with artificial roughness. This feature becomes more pronounced as the growth rates are decreased (i.e., the transition pattern is more regular for $Re_c = 3.2 \times 10^6$ than for $Re_c = 2.2 \times 10^6$). Without a detailed receptivity study, it is unclear whether this nonuniformity is caused by submicron imperfections in the height or edges of the roughness elements or is due to small perturbations in the spanwise spacing (or both).

Some light is shed on this phenomenon by repeating the flow visualizations with a different roughness spacing. Figures 5.3 and 5.4 show the same experiments with the roughness spacing increased to 36 mm (i.e., [6|36] roughness). As with the 12 mm spacing, the turbulent wedge pattern is more uniform for the larger Reynolds number. However, for both $Re_c = 2.2 \times 10^6$ and 3.2×10^6, the jagged transition front is strikingly more regular for the 36 mm roughness spacing than for the 12 mm spacing. Clearly, the spectral content of the surface roughness distribution can significantly influence the *local* transition characteristics of the boundary layer. It is also evident that the 36 mm spacing excites multiple disturbance modes. In both figures 5.3 and 5.4, the turbulent wedges are 36 mm apart corresponding to the roughness spacing, but the naphthalene clearly shows vortex streaks at larger spanwise wavenumbers (i.e., smaller wavelengths).

Although the turbulent wedges that comprise the transition front are well-defined,

[1] This does not apply to the leading-edge region, where the naphthalene sublimes quickly due to the high shear of the thin, laminar boundary layer. Moreover, naphthalene is not applied upstream of $x/c \approx 0.20$ to avoid adding surface roughness in this region.

Table 5.2: Approximate transition location determined by naphthalene flow visualization.

Roughness		Transition Location $[x/c]$	
k [μm]	λ_z [mm]		
6	12	0.52	0.32
6	36	0.49	0.30
18	12	0.51	0.30
48	12	0.49	0.28
	$Re_c =$	2.4×10^6	3.2×10^6

the jagged pattern and potential spanwise nonuniformity create some ambiguity in determining the transition location. Dagenhart (1992) defined the transition location as the average of the beginning and ending locations of the turbulent wedges. This was necessitated by the random distribution of "natural" surface roughness that influenced transition in his experiments. The present work ignores the downstream edge of the saw-tooth pattern, and defines the transition location as the average starting location of the turbulent wedges. This definition is based on the simple premise that the *onset* of transition signifies the loss of laminar flow. In addition, considering only the vertices of the wedges helps remove some of the ambiguity when the transition front is nonuniform in span. With this in mind, the average transition location for several test conditions is shown in table 5.2. As indicated in figures 5.1–5.4, increasing the roughness spacing moves transition *forward*. On the other hand, fixing the spanwise spacing at 12 mm and increasing the roughness height from 6 μm to 48 μm (an Re_k increase of nearly two orders of magnitude) has surprising little effect on the transition location. This is in contrast to the results of Radeztsky et al. (1993a), which show that the vertex of the transition wedge behind an isolated roughness element moves forward by nearly 10% chord when the roughness height is increased from 6 μm to 18 μm.

5.3 Basic State

The basic state is documented with pressure measurements and boundary-layer profiles. The former provide information on the global flowfield, while the latter allow specific details of the basic-state boundary layer to be analyzed.

5.3.1 C_p Measurements

The pressure distribution is measured with two rows of pressure ports mounted in the test surface of the NLF(2)-0415. Each row consists of 23 pressure taps aligned with the freestream (X) direction. The ports extend from $x/c = 0$ to $x/c = 0.78$ and are clustered near the leading edge. One row of ports is located near the ceiling or "upper" end of the model, while the other is located near the floor or "lower" end. The ports are 647 mm (measured parallel to the leading edge) from the center span of the model. The pressure coefficient is determined by measuring $p - p_\infty$ with a differential pressure transducer and dividing by the freestream dynamic pressure $\rho U_\infty^2/2$. This normalization generates the swept C_{p_3} defined by equation (3.2).

Figures 5.5–5.7 show the pressure distribution obtained from both sets of pressure ports for $Re_c = 1.6 \times 10^6$, 2.4×10^6, and 3.2×10^6. Also plotted is the theoretical C_p computed using the MCARF code (Stevens et al. 1971). As discussed in section 3.5.1, the computations account for the front and rear test-section walls but do not apply any displacement thickness corrections. The MCARF solution under-predicts the measured C_p for all Reynolds numbers. For the upper ports, the difference is largest in the range $0.05 \leq x/c \leq 0.35$. Dagenhart (1992) indicates that the test-section ceiling liner is slightly too thin in this region, to which he attributes the difference in pressure. For the lower ports, the difference between the measured and theoretical C_p increases with increasing x/c. This may be caused by the inclined floor of the test section, which drops by 50 mm over its length (4.9 m) to approximately account for

wall boundary-layer growth (see section 3.5.1). The proximity of the pressure ports to the test-section end liners also compromises the comparison with MCARF. All of the ports are within 50–150 mm of the liner surface, which magnifies the effect of small errors in the end liners with respect to their influence in the mid-span region. Boundary-layer profiles presented in the following section confirm that the basic state is spanwise independent in the test region of the model.

The pressure distribution has a slight Reynolds-number dependence as shown in figures 5.8 and 5.9. This is not a compressibility effect ($M < 0.1$ for all operating speeds), but instead is due to changes in the displacement thickness of the boundary layers on the test-section walls and the airfoil model. This is not unexpected since the inclination of the test-section floor is technically optimum for only one operating condition. The Reynolds-number effect, however, is weak and can be ignored without loss of accuracy.

In short, although there are slight differences between the measured and theoretical pressure distribution, the generally good agreement shows that the experimental flowfield reasonably matches the CFD design.

5.3.2 Boundary-Layer Profiles

As discussed in chapter 3, the 45°-swept NLF(2)-0415 airfoil at $\alpha = -4°$ produces large-amplitude stationary crossflow waves for moderate chord Reynolds numbers. While ideal for the study of this instability mechanism, the strong distortions of the mean boundary layer make it impossible to measure the basic-state profiles for most of the test conditions of this experiment. Even in the absence of artificial surface roughness, the nonlinear mean-flow distortion [$(0,0)$ mode] is observed for $Re_c \geq 1.8 \times 10^6$. In light of this, basic-state boundary layers are measured only at $Re_c = 1.6 \times 10^6$. At this Reynolds number, the stationary wave growth rates are sufficiently small and the mean-flow distortion is negligible. Although this does

not allow a direct comparison with theory for the majority of the test cases, it does provide a reference point at which the agreement between theory and experiment can be assessed.

Basic-state profiles are obtained with the boundary-layer scanning technique described in section 4.4.1. Figure 5.10 shows the profiles at $x/c = 0.20$. The plot actually contains 100 profiles each separated by 1 mm in the swept span (z) direction. Each profile contains approximately 45 measurement points in the wall-normal direction. The profiles are virtually identical, and show no evidence of stationary crossflow waves. More importantly, the absence of any variation confirms that the flowfield is spanwise invariant in the test region of the model. Thus, the infinite-span assumption is verified. This plot also answers two questions about the measurement technique. First, the boundary layer is sufficiently linear near the wall to allow a straight-line extrapolation to locate the airfoil surface. Second, because the airfoil surface is located by each profile independently, the method is "self-aligning" in that the scans are well-matched at the wall and the boundary-layer edge.

The boundary-layer profiles acquired under the same conditions at $x/c = 0.60$ are plotted in figure 5.11. These 100 mean-flow profiles show a very slight spanwise modulation due to the presence of weak stationary crossflow waves. Because the spanwise variation is small (less than 1% rms), the average of the 100 profiles is taken as the basic-state boundary layer. In fact, at all chord locations the basic-state profile is defined as the spanwise average of 100 mean-flow boundary-layer scans taken over 99 mm of span. These profiles are shown in figure 5.12 for $0.05 \leq x/c \leq 0.60$. The number of measurement points in the wall-normal direction varies with x/c, but ranges from about 30 data points at $x/c = 0.05$ to more than 60 at $x/c = 0.60$.

The measured profiles are compared to the theoretical basic-state solutions in figures 5.13 -5.24. The computational results are provided by Haynes using the

boundary-layer code of Haynes and Reed (1996). It is important to note that the dots are used simply to differentiate between the experimental and computed profiles. The experimental data are actually obtained with much higher resolution than indicated by the symbols. The theoretical profiles are projected onto the experimental measurement plane (as discussed in section 3.4) to allow an accurate comparison. Displacement thickness, momentum thickness, and shape factor comparisons (figures 5.25–5.27) indicate that the computed profile is slightly decelerated with respect to the measured boundary layer at all chord locations. This effect may be caused by any number of factors, ranging from experimental flow misalignment to the breakdown of the boundary-layer equations near the leading edge.

Similar basic-state differences were noted in the previous ASU experiments involving the NLF(2)-0415 model (Dagenhart 1992; Radeztsky 1994). In these cases, an *ad hoc* adjustment to the angle of attack and/or Reynolds number was applied in order to bring the theoretical basic state in line with the experimental data. While it can be argued that these adjustments may increase the validity of disturbance-amplitude comparisons, the present work makes no attempt to "fix" the differences in the computed and measured basic-state profiles for the following reasons.

1. Due to experimental constraints, any flowfield adjustments would be based solely on comparisons of the streamwise velocity u. In terms of the cross-flow velocity component, however, the validity of these adjustments cannot be ascertained.

2. The C_p measurements indicate that the experimental flowfield agrees well with the CFD design. The difference in the *level* of the C_p (see figure 5.6) could be due to a slight angle-of-attack misalignment, however any adjustment to the angle of attack or sweep angle is unwarranted in light of the good agreement between the measured and computed pressure *gradient*.

3. The NLF(2)-0415 at $\alpha = -4°$ generates almost no lift when placed in the Unsteady Wind Tunnel test section. Consequently, the upstream or forward influence of the model is minimized. Flowfield calculations indicate that the test-section velocity at the location of the Pitot-static probe is within 0.5% of the velocity in the farfield. Thus, a Reynolds-number adjustment would be insignificant.

Simply stated, although comparisons of the measured and theoretical boundary-layer profiles indicate a slight disagreement in the basic state, there is simply no experimental data available that conclusively justify a contrived adjustment to the flowfield parameters. Moreover, whereas linear stability calculations are sensitive to small changes in the basic state, the strong nonlinear characteristics of this problem appear to make the actual stability behavior more forgiving of basic-state discrepancies. This will be highlighted in the following sections, where disturbance amplitudes computed with nonlinear parabolized stability equations agree remarkably well with the experimental results.

5.4 Natural Surface Roughness

From the conditions of the basic-state scans discussed above, one needs only to increase the Reynolds number to generate measurable distortions of the mean boundary layer. Figure 5.28 is a contour plot of the normalized boundary-layer velocity at $x/c = 0.45$ for $Re_c = 3.0 \times 10^6$. No artificial roughness is placed on the airfoil surface. The figure shows the streamwise velocity u/U_e in the (Y, z) plane. (The Y axis is magnified by a factor of 10 with respect to the z axis in order to provide more detail.) The flow is toward the reader (i.e., the observer is looking upstream into the oncoming boundary-layer flow), and the stationary vortices are turning in the right-handed sense. The velocity contours are constructed from 100 mean-flow

boundary-layer profiles acquired using the technique described in section 4.4.1. It is important to note that the wave-like structure of figure 5.28 represents the integrated effect of the weak *stationary* vortices on the streamwise velocity. The vortices themselves are co-rotating (v', w') disturbances that are too weak to measure directly.

In the absence of artificial surface roughness, the naturally occurring stationary crossflow waves are nonuniform in span. Considering the near mirror finish of the airfoil surface (see figure 3.4), this underscores the extreme sensitivity to roughness-induced initial conditions provided by submicron surface irregularities near the leading edge.

Figure 5.28 displays a dominant feature at a 12 mm spanwise spacing, which is approximately the most amplified stationary wavelength according to linear theory. At the same time, the richness in the spectral content is evident and indicates nonlinear interaction among many modes. This is typical of all the early experiments (Müller and Bippes 1989; Dagenhart et al. 1989, 1990; Bippes and Nitschke-Kowsky 1990; Bippes et al. 1991), and leads to two undesirable side effects.

1. The spanwise nonuniformity creates some ambiguity in determining the disturbance amplitude. For example, Dagenhart (1992) measured the disturbance amplitude by acquiring data over a single vortex wavelength. Clearly the growth rates obtained with this method depend strongly on which vortex is chosen (i.e., which wave in figure 5.28), as well as the ability to accurately track the same vortex at all chord locations.

2. Even a nonlinear stability calculation that includes only a single mode would be inappropriate to characterize the disturbance motion. Instead, the computations would need to include the potentially infinite number of modes that are excited by the random surface roughness.

Thus, the unknown natural roughness of the airfoil surface renders the comparison with theory unnecessarily difficult.

5.5 Distributed Roughness

In order to generate spanwise-uniform stationary crossflow waves with a fixed spectral content, initial conditions are controlled with artificial surface roughness as outlined in section 3.3.3. The roughness elements are distributed in full-span arrays at $x/c = 0.023$. This location—near the first neutral point of the stationary instability—has been shown to maximize the influence of the roughness (Radeztsky et al. 1993a). Applying the elements along the entire span produces a disturbance field that is invariant along lines of constant chord, i.e., the infinite-span assumption is preserved.

This section presents the results for the baseline configuration defined by data set $\mathcal{A}$ in table 5.1. The roughness height is 6 μm and the spanwise spacing between the elements is 12 mm (i.e., [6|12] roughness). This spacing is chosen to excite the dominant stationary wavelength that appears in the absence of artificial surface roughness. The data are acquired at $Re_c = 2.4 \times 10^6$. The roughness Reynolds number $Re_k = 0.1$ for this configuration.

5.5.1 Vortex Structure and Mean-Flow Distortion

Figure 5.29 shows the streamwise velocity contours at $x/c = 0.45$ for the conditions described above. The primary difference between this plot and figure 5.28 is the addition of the artificial roughness. (The only other difference is the lower Reynolds number, which was decreased because of the increase in the disturbance strength.) The dominance and uniformity of the $\lambda_z = 12$ mm mode is striking. The disturbance amplitude is well defined under these conditions (as will be demonstrated in the following section), and meaningful comparisons with both linear and nonlinear

theoretical predictions are possible. The dramatic change in the disturbance motion resulting from such small roughness continues to highlight the sensitivity of the stationary waves to initial conditions provided by leading-edge surface roughness.

The streamwise velocity contours due to a single stationary vortex are isolated in figure 5.30 and plotted on a 1:1 scale. The integrated effect of the combined (v', w') motion of the crossflow vortex produces regions of upwelling and downwelling that transport low- and high-momentum fluid within the boundary layer. The asymmetry of the co-rotating vortices distorts this momentum transfer giving the apparent rollover of low-momentum fluid that appears above high-momentum fluid. The v' and w' components are actually very weak, but because the vortices are stationary and nearly aligned with the potential flow direction, they act on the same streamwise fluid to produce the $O(1)$ u' distortions. This process is described in figures 5.31–5.33, which schematically display the (v', w') motion of two stationary vortices above the measured streamwise velocity contours. The measurements are obtained at $Re_c = 2.4 \times 10^6$ with [6|12] roughness. One can clearly see how the u' distortion develops under the continuous presence of the vortices.

Figure 5.34 shows the 100 mean boundary-layer profiles from which figure 5.29 is generated. These profiles are obtained at 1 mm intervals in the swept span (z) direction using the measurement technique described in section 4.4.1. The dots mark the spanwise average of the profiles, which accounts for the basic state plus the $(0, 0)$ mean-flow distortion mode. Each individual profile contains approximately 60 measurement points. Each measurement point, in turn, represents a two-second average velocity. It is worth emphasizing that these time-averaged profiles represent a spanwise modulation of the mean flow and not an unsteady oscillation in the boundary layer. One can clearly see how the momentum transfer caused by the stationary vortices has distorted the mean boundary layer, resulting in accelerated, decelerated,

and doubly-inflected profiles existing millimeters apart. The presence of the mean-flow distortion mode (indicated by the distortion of the spanwise-averaged profile) shows the effect of strong nonlinear interactions.

An important but often overlooked aspect of this instability is dramatically illustrated by figure 5.34. Quite simply, the mean boundary layer looks nothing like the undisturbed basic state. Even the spanwise-averaged profile is distorted and inflectional due to strong nonlinearities. This is a fundamental consequence of the stationary nature of the disturbance. Although the crossflow vortex itself is a weak (v', w') motion, its integrated effect produces an $O(1)$ u' disturbance resulting in a spanwise-varying mean flow subject to different secondary instability mechanisms depending on the local characteristics of the boundary layer. Consequently, it is *physically* incorrect to model the stationary disturbance as the zero-frequency limit of a traveling wave (although, of course, this is *mathematically* correct with the framework of linear theory). By its very definition, the traveling wave cannot produce the integrated effect that allows a weak disturbance to cause the strong distortion of the streamwise boundary layer. In light of this, the continued failure of linear theory to accurately model the disturbance growth (Dagenhart et al. 1989, 1990; Müller and Bippes 1989; Bippes et al. 1991; Radeztsky et al. 1994) should not be unexpected. By ignoring the mean-flow distortion, linear theory is computing the stability characteristics of boundary layers that do not exist. These ideas will be revisited later in this chapter when the experimental disturbance amplitude is compared to various theoretical predictions.

5.5.2 Disturbance Profiles and Mode Shape

Disturbance profiles are generated by subtracting the basic state plus mean-flow distortion (i.e., the spanwise-averaged profile) from each of the 100 individual boundary-layer profiles. These are shown in figure 5.35 for the boundary-layer profiles of fig-

ure 5.34. The wave-like nature of the spatial disturbance is indicated by the smooth phase change between the profiles. The distortions reach a maximum of 36% near $Y = 1$ mm and are asymmetric due to the rollover phenomenon displayed in figure 5.30. The disturbance velocity is viewed as a contour plot in figure 5.36. (As with the total velocity contours, the Y axis is magnified by a factor of 10 to provide more detail.) Only two contour levels are plotted to highlight the surplus and deficit in the streamwise boundary-layer velocity. It should be emphasized that the contours do not represent the vorticity of the stationary vortices. This data-presentation format accentuates the rollover of the low- and high-momentum fluid and explains the streaks in the naphthalene flow visualization, but otherwise adds no information that cannot be ascertained from the total velocity contours and disturbance profiles. Consequently, disturbance velocity contours will be presented only for select cases.

The stationary wave mode shape is obtained by computing the spanwise rms of the 100 disturbance profiles at each Y location in the boundary layer. Since the stationary disturbance creates a spatially varying wave, this is equivalent to a time-domain rms computed for a traveling fluctuation. Figure 5.37 shows the mode shape for the disturbance profiles of figure 5.35. The rms amplitude reaches a maximum of 19% at $Y = 0.9$ mm, decays to a second local maximum of 9% at $Y = 2.7$ mm, then smoothly vanishes at the boundary-layer edge. The second lobe occurring high in the boundary layer corresponds to the inflectional distortion of the spanwise-averaged profile in figure 5.34, and indicates the presence of nonlinear effects. This points out an important but subtle distinction between the stationary wave mode shape and a classic linear theory eigenmode. In the presence of nonlinearities, the disturbance mode profile will contain *all amplified disturbance modes* [except the $(0,0)$ mean-flow distortion mode], whereas the eigenfunction from linear theory always contains a single disturbance mode. This means the stationary wave mode shape as calculated

here represents the amplitude of the total disturbance.

5.5.3 Total Disturbance Amplitude Distribution

The measurements described above for $x/c = 0.45$ are obtained at 5%-chord intervals from $x/c = 0.05$ to $x/c = 0.45$. Figures 5.38–5.45 show the streamwise velocity contours for the additional measurement locations. As with the velocity contour at $x/c = 0.45$ (figure 5.29), the Y-to-z aspect ratio of 10:1 is chosen to enhance the detail in the plots. The mean boundary-layer profiles from which the contour plots are constructed are shown in figures 5.46–5.53. Figures 5.54–5.61 display the corresponding disturbance profiles, which are plotted on a consistent scale of $\pm 40\%$ to accentuate the disturbance growth. The mode-shape profiles are presented in figure 5.62 for $0.10 \leq x/c \leq 0.45$. This series of plots clearly shows the development of the mean boundary-layer distortion caused by the stationary crossflow waves. The disturbance is too weak to measure near the leading edge, but by 10% chord a very small distortion of the mean boundary layer is detected (figure 5.39). This distortion grows quickly up to $x/c = 0.25$, where the disturbance profiles (shown in figure 5.58) begin to exhibit the asymmetric shape characteristic of the downstream locations. The beginning of the "second lobe" distortion of the mode shape is apparent at $x/c = 0.30$ ($Y \approx 1.6$ mm), confirming the presence of early nonlinear effects. The nonlinear features continue to develop to the final measurement location of $x/c = 0.45$.

The data at $x/c = 0.05$ highlight the accuracy of the measurement technique as well as the difficulty in acquiring data in a thin boundary layer. The complete set of 100 boundary-layer scans (figure 5.46) contains approximately 3500 distinct measurement points covering 99 mm of span within a 1.2 mm-thick boundary layer. Each measurement point, in turn, represents the time average of 2000 instantaneous analog-to-digital conversions for each of five different quantities (test-section static pressure, temperature, dynamic pressure, and two hot wires). The entire scan takes

three hours to complete. The straight-line extrapolation to find the airfoil surface has worked remarkably well, resulting in profiles that are consistently matched at the wall and the boundary-layer edge.[2] In fact, all 100 profiles are buried beneath the dots of the spanwise-averaged profile. The method is not perfect, however, and the large dimensional du/dY gradient of the thin boundary layer magnifies any small errors in the traverse movement. Measurements presented later will show that the stationary-wave-induced distortions of the mean boundary layer are too small to be extracted from the background noise under these conditions. Therefore, the disturbance profiles and mode shape at $x/c = 0.05$ are rejected for this data set ([6|12] roughness at $Re_c = 2.4 \times 10^6$), and $x/c = 0.10$ is taken as the initial measurement position for which experimental data are available.

The total stationary disturbance amplitude is computed from the mode-shape profiles of figure 5.62. Three different measures of the mode shape are used to characterize the disturbance amplitude: the maximum, average, and rms of the mode with respect to Y. The average of the mode corresponds to the integral of $|u'|$, and the rms measure essentially gives the integral of $|u'|^2$. Figure 5.63 shows the disturbance amplitude distribution for [6|12] roughness at $Re_c = 2.4 \times 10^6$. The dashed lines mark the absolute size of the mode shapes as computed by each of the three measures. The solid lines show the corresponding amplification factor N. The initial disturbance amplitude at $x/c = 0.10$ is used as the reference amplitude for each N-factor curve [A_o in equation (3.16)]. The ability of the N-factor to collapse the data onto a single curve is typical. By equation (3.14), the roughly constant slope of the N-factor curves indicates that the disturbance growth is approximately exponential for $x/c \leq 0.25$. For $x/c \geq 0.30$, the local spatial growth rate decreases and the disturbance ampli-

[2]The straight-line extrapolation is strictly valid only for a zero-pressure-gradient flow with no disturbances. However, the profile curvature at the wall is negligible for this experiment and the technique is justified *a posteriori* by figure 5.10.

tude saturates due to nonlinear effects. This nonlinear amplitude saturation occurs well before the transition location of $(x/c)_{\rm tr} = 0.52$. It is important to note that the quantitative value of N is not relevant because of the arbitrariness in choosing the normalizing amplitude. Only the slope is important as it provides the local spatial growth rate.

Figure 5.64 compares the experimental N-factor (as computed from the maximum of the mode shape profiles) with various theoretical predictions of Haynes (Haynes and Reed 1996). The nonlinear parabolized stability equations (PSE) results are computed using initial amplitudes provided by the experiment, and great care is taken to ensure the computations are presented in the coordinate system to which the measurements are restricted (see section 3.4). The agreement is excellent, especially in predicting the amplitude saturation. (At this time, the Haynes and Reed formulation does not contain curvature, which is known to be stabilizing and may account for the small differences in the disturbance growth.) In contrast, the Orr-Sommerfeld and linear PSE results fail to predict the details of the disturbance growth. The early qualitative agreement with the linear PSE computations indicates that the nonlinear effects are initially weak up to $x/c = 0.25$, at which time the growth rates depart from linear behavior. The saturation of the disturbance amplitude is dramatic for $x/c \geq 0.30$. In this region the $(0,0)$ mean-flow-distortion mode is observed in the spanwise-averaged boundary-layer profile, and the mode shapes exhibit the characteristic second lobe indicative of strong nonlinear effects. Figure 5.64 absolutely and conclusively removes all doubt about the importance of nonlinear effects for the stationary crossflow instability.

5.5.4 Mode-Shape Comparisons

The ability of the nonlinear PSE to capture the details of the disturbance growth can be assessed by comparing the measured and computed mode shapes. These

comparisons are shown in figures 5.65–5.72 for $0.10 \leq x/c \leq 0.45$. The theoretical mode shapes provided by Haynes (Haynes and Reed 1996) are appropriately projected onto the experimental measurement plane as outlined in section 3.4. The dots simply differentiate between the experimental and computed results and do not indicate actual measurement points. The initial conditions for the nonlinear PSE are chosen so the calculations match the experiment at the first location for which measurements are available. This means the disturbance amplitudes are equal by definition at $x/c = 0.10$ (figure 5.65). The mean boundary-layer distortions are initially very weak, which explains the noise in the experimental data at 10% chord.

The nonlinear PSE result overpredicts the maximum amplitude by 0.3% at $x/c = 0.15$ (figure 5.66), and their is evidence of some stretching in the Y direction. These trends continue downstream, and explain the slight difference between the experimental and nonlinear PSE N-factor curves in figure 5.64. At $x/c = 0.30$, both the measured and computed mode shapes begin to exhibit the second lobe indicating the presence of strong nonlinearities (figure 5.69). The nonlinear features continue to develop until the final measurement location at $x/c = 0.45$.

It is important to focus on the "shape" of the mode as well its "size" when comparing the experimental and theoretical data. Although the computations slightly overestimate the measured data, all of the essential features of the stationary disturbance are captured by the nonlinear PSE. In particular, the development of the nonlinear second lobe is predicted remarkably well. The success of the nonlinear PSE and its agreement with the experiment underscores the significance of the mean boundary-layer distortion as the dominant aspect of the stationary crossflow instability.

5.5.5 Wavelength Separation

Spanwise Scans at Constant Y

As pointed out previously, disturbance amplitudes computed from mode-shape profiles contain all amplified stationary modes. However, the mode shapes provide no information concerning the wavenumber content of the disturbance. These data are important in light of the sustained region of nonlinear interaction shown in figure 5.64, hence the spanwise scan at constant Y technique (section 4.4.2) is used to obtain individual-mode growth rates. At each chord position, the scan is performed at the height corresponding to the peak of the total disturbance mode shape. This allows the amplitude of the individual modes to be directly compared to the total disturbance amplitude computed from the maximum of the mode-shape profile.

Figures 5.73–5.81 show the hot-wire surveys for $0.05 \leq x/c \leq 0.45$. The data are acquired for $Re_c = 2.4 \times 10^6$ with [6|12] roughness. These plots show the spanwise distribution of the normalized streamwise velocity at a fixed height in the boundary layer. The velocity trace is equivalent to that which would be obtained by taking a spanwise slice across a set of wall-normal boundary-layer profiles at a constant height above the airfoil surface. The primary difference is that the data cover the entire spanwise extent of the available measurement region (240 mm) at better than four times the spanwise resolution of the boundary-layer scans. This allows accurate decomposition in the spectral domain.

The development of the stationary-wave-induced distortion of the mean boundary layer is clearly evident for $x/c \geq 0.15$. At $x/c = 0.45$ (figure 5.81), the velocity fluctuations range from $u/U_e = 0.30$ to $u/U_e = 0.88$, and the rms of the signal (computed by first subtracting the mean velocity of $u/U_e = 0.67$) is 18.5%. This value agrees well with the maximum of the mode-shape profile (figure 5.37), indicating the scan proceeded at the desired height in the boundary layer. The lack of any overrid-

ing DC trend confirms that the traverse-alignment technique sufficiently models the misalignment between the airfoil surface and the hot-wire traverse. Moreover, the uniformity of the disturbance over the entire span verifies the spanwise independence of the instability, and once again validates the infinite-span assumption.

The velocity profiles are not as clean near the leading edge. The nominal u/U_e at $x/c = 0.10$ drops slightly as the scan progresses (from left to right in figure 5.74), and the data appear contaminated by background noise. These features are exaggerated at $x/c = 0.05$ (figure 5.73). This is not caused by a failure of the traverse-alignment technique, but instead results from the magnification of small traverse errors by the increasingly large du/dY gradient of the thin boundary layer. (Recall that this effect was observed in the total disturbance profiles discussed previously.) Fortunately, the disturbance amplitude is not a strong function of Y near the leading edge, as indicated by the relative "flatness" of the mode-shape profile for small x/c (shown in figure 5.62). Therefore, the "drift" in the scan can be tolerated without rendering the data useless.

Spectral Analysis

The spatial power spectra for the spanwise scans are shown in figures 5.82 5.90. These plots show the power spectral density (PSD) as a function of spanwise wavelength λ_z (note the equivalent label λ_s in the figures). The power estimates are generated with the FFT-based power spectrum technique described in section 4.4.2. With 64 times spectral smoothing through zero padding, the method accurately extracts the peaky spectra with sufficient resolution to allow disturbance amplitude calculations by integration of the PSD.

The data for $0.20 \leq x/c \leq 0.45$ are plotted on the same scale to highlight the disturbance growth. The spectra are dominated by a 12 mm component corresponding to the spacing of the roughness elements. However, a clear contribution from the $(0, 2)$

mode at $\lambda_z = 6$ mm appears for $x/c \geq 0.35$. Careful examination of these data reveals that the 6 mm component first becomes measurable at $x/c = 0.30$. Moreover, a very weak 4 mm component is detected for $x/c \geq 0.35$. (These features are too small to appear on the scale of the plots.) This wave doubling was observed by Saric and Yeates (1985) and predicted by Reed (1988). Thus, the growth of the $(0, 2)$ and $(0, 3)$ harmonics and their nonlinear interaction with the fundamental mode leads to the amplitude saturation observed in figure 5.64.

The power axis is magnified to show the small disturbance levels for $x/c \leq 0.15$ (figures 5.82 5.84). The 12 mm component continues to dominate the PSD at $x/c = 0.15$, however a small peak appears at $\lambda_z = 7.2$ mm and a tiny bump can be seen at $\lambda_z = 6$ mm. Although the 6 mm feature is arguably the $(0, 2)$ mode, it is rejected since its amplitude is dangerously close to the noise floor of the spectrum. At $x/c = 0.10$ the fundamental mode at $\lambda_z = 12$ mm is smaller (but still measurable), the 6 mm feature has disappeared, and the 7.2 mm component is larger. At $x/c = 0.05$ the disturbance energy is almost entirely contained in the 7.2 mm wavelength and its harmonic at $\lambda_z = 3.6$ mm. In particular, there is no evidence of the fundamental crossflow mode ($\lambda_z = 12$ mm) or its harmonics. These trends are caused by two separate phenomena:

1. The lack of any measurable crossflow modes for small x/c is simply due to the infinitesimal amplitude of the stationary disturbance near the leading edge. This underscores the ability of the $k = 6$ μm roughness to provide uniform stationary waves without excessive initial amplitudes.

2. The emergence of the 7.2 mm component, as well as the increased noise in the PSD, is caused by the magnification of small traverse errors in the thin boundary layer near the leading edge. This has been discussed previously, and results from the increase in the dimensional wall-normal velocity gradient du/dY. The

7.2 mm wavelength itself comes from a small, once-per-revolution eccentricity of the traverse vertical motion (Z) lead screws (Radeztsky 1994).

It should be emphasized that the traverse motion is highly accurate (as shown in table 2.2), and resolution issues are a concern only under the influence of the large velocity gradient of a thin boundary layer. Fortunately, the accuracy of the spectral decomposition technique allows the crossflow modes to be separated from the noise even when the disturbance amplitude is very small.

Individual-Mode Disturbance Amplitudes

By Parseval's theorem, the square root of the integral of the PSD equals the rms amplitude of the signal. Thus, the disturbance energy for a single mode is computed by integrating the corresponding peak in the spectrum.[3] The extent of the peak is defined by the first local minimum on each side.

Figure 5.91 shows the disturbance amplitude as a function of x/c for $Re_c = 2.4 \times 10^6$ with [6|12] roughness. As with the total disturbance amplitude (figure 5.63), the dashed lines represent the rms amplitude of the individual modes, while the amplification factor N is plotted with solid lines. The N-factors are relative to the point at which the mode is first detected. The fundamental ($\lambda_z = 12$ mm) mode contains most of the disturbance energy, however the $(0, 2)$ and $(0, 3)$ modes are also amplified in the region of nonlinear amplitude saturation.

Recall that at each chord location the spanwise scan is taken at the boundary-layer height corresponding to the maximum of the mode-shape profile. This permits us to compare the amplitude of the individual modes with that of the total disturbance computed from the maximum of the mode shape. Figure 5.92 shows this comparison. It is a remarkable verification of the two vastly different measurement techniques

[3]Actually, the PSD is converted from mean-square to sum-square power, and the power estimates in each peak are summed to provide the disturbance energy. This avoids introducing error with an approximate integration technique.

that the amplitude of the total and fundamental ($\lambda_z = 12$ mm) disturbances agree for $x/c < 0.30$. In particular, this validates the spectral decomposition technique and highlights the ability of the FFT—when correctly implemented—to extract peaky spectra from a limited data series. Both the total and fundamental disturbances exhibit the characteristic nonlinear amplitude saturation at $x/c = 0.30$. At this location, the amplitude of the fundamental diverges from the total disturbance and the $(0, 2)$ harmonic at $\lambda_z = 6$ mm becomes measurable. The 6 mm component contains significant energy and the $(0, 3)$ mode ($\lambda_z = 4$ mm) becomes unstable in the region of strong nonlinear interaction ($x/c \gtrsim 0.35$). It is interesting to note that the amplitude saturation is not limited to the fundamental disturbance, but is also observed in the 6 mm mode. Clearly, the amplitude saturation phenomenon is caused by the nonlinear interaction between the fundamental disturbance and its harmonics.

5.6 Summary

The data presented in this chapter provide detailed experimental measurements and theoretical calculations for the baseline configuration defined as $Re_c = 2.4 \times 10^6$ with [6|12] roughness. These results provide important insight into the fundamental nature of the stationary crossflow instability. When the initial conditions are governed by "natural" surface roughness, the stationary waves are nonuniform in span and contain many disturbance modes. Micron-sized artificial roughness elements placed near the leading edge generate uniform stationary waves with a controlled wavenumber content. Detailed hot-wire measurements show early departure from linear behavior and saturation of the disturbance amplitude. Spectral analysis shows that this saturation phenomenon is caused by the nonlinear growth of harmonic disturbances and their interaction with the fundamental mode. The nonlinear effects are observed well before transition. PSE computations agree remarkably well with the experiment and

confirm the importance of nonlinear effects.

These measurements continue to highlight the sensitivity to roughness-induced initial conditions and the importance of the receptivity process for this instability mechanism. With this in mind, the following chapter presents a parametric study in which the disturbance growth is investigated under varying freestream and surface-roughness conditions.

CHAPTER 6

Results—Part 2: Parametric Study

This chapter discusses the experimental results for data sets $\mathcal{B}$ through $\mathcal{F}$ defined in table 5.1, which is repeated on the following page for convenience. Along with data set $\mathcal{A}$, data sets $\mathcal{B}$ and $\mathcal{C}$ examine the effects of varying the chord Reynolds number. Multiple-mode crossflow waves are produced with data set $\mathcal{D}$. Finally, data sets $\mathcal{E}$ and $\mathcal{F}$ combine with data set $\mathcal{A}$ to investigate the dependence on initial disturbance amplitude.

6.1 Reynolds Number Variation

Measurements for data sets $\mathcal{B}$ and $\mathcal{C}$ are presented in this section. The roughness configuration remains at $k = 6$ μm with 12 mm spanwise spacing (i.e., [6|12] roughness) for these investigations. Transition occurs somewhere past the pressure minimum for data set $\mathcal{B}$ ($Re_c = 1.6 \times 10^6$), and a complete set of boundary-layer profile scans are taken from $x/c = 0.05$ to $x/c = 0.60$ in 5%-chord increments. For data set $\mathcal{C}$ ($Re_c = 3.2 \times 10^6$), transition occurs at $x/c = 0.32$ with some turbulent wedges near $x/c = 0.30$. In this case, boundary-layer profile scans and spanwise scans at constant Y are obtained for $0.05 \leq x/c \leq 0.29$. The last measurement location is chosen to ensure that no data are acquired in a turbulent boundary layer. The roughness Reynolds numbers (Re_k) are 0.061 and 0.17 for $Re_c = 1.6 \times 10^6$ and 3.2×10^6, respectively.

Table 5.1: Experimental data set configuration.

Data Set	$Re_c/10^6$	Roughness		Scan Type	
		k [μm]	λ_z [mm]	BL	Span
$\mathcal{A}$	2.4	6	12	•	•
$\mathcal{B}$	1.6	6	12	•	
$\mathcal{C}$	3.2	6	12	•	•
$\mathcal{D}$	2.4	6	36	•	•
$\mathcal{E}$	2.4	18	12	•	•
$\mathcal{F}$	2.4	48	12	•	•

6.1.1 Effect of Decreasing Re_c

The streamwise velocity contours, boundary-layer profiles, and disturbance profiles for $Re_c = 1.6 \times 10^6$ are shown in figures 6.1–6.12, 6.13–6.24, and 6.25–6.36, respectively. As with the earlier contour plots, the 10:1 Y-to-z aspect ratio is chosen to enhance the detail. (From this point forward, the 10:1 aspect ratio will be assumed unless otherwise noted.) The disturbance profiles are plotted on a consistent scale of $\pm 40\%$ to facilitate direct comparisons with data set $\mathcal{A}$. The data look qualitatively similar to the results for $Re_c = 2.4 \times 10^6$, except the disturbance amplitudes are smaller as expected. This is a consequence of the reduction in Re_k and growth rate with the lower chord Reynolds number.

A careful analysis of the disturbance motion shows that stationary crossflow waves are not measurable for $x/c \leq 0.15$. This is illustrated by comparing the disturbance velocity contours at $x/c = 0.15$ and $x/c = 0.20$ (figures 6.37 and 6.38). The periodicity of the velocity surplus and deficit clearly indicates a stationary wave at $x/c = 0.20$. However, at $x/c = 0.15$ no definite structure stands out above the background noise of the measurements. Thus, the data for $x/c \leq 0.15$ are not considered.

The mode-shape profiles for $0.20 \leq x/c \leq 0.60$ are shown in figure 6.39. It is worth emphasizing that the symbols simply identify the curves and do not represent

measurement points. The strong distortion and second lobe that dominate the $Re_c = 2.4 \times 10^6$ data are missing, although the mode shapes at $x/c = 0.55$ and $x/c = 0.60$ are beginning to "push out" near $Y = 2.3$ mm in an early sign of nonlinear effects. Tracking the maximum, average, and rms of the mode shapes yields the amplitude distribution shown in figure 6.40. As noted earlier, the amplification factor N collapses the three measures to a single curve. It is interesting that a slight amplitude saturation is observed for $x/c \geq 0.50$ even though the disturbance amplitude is relatively small. This reaffirms the importance of nonlinear effects for boundary layers dominated by the stationary crossflow instability.

6.1.2 Effect of Increasing Re_c

Increasing the chord Reynolds number to 3.2×10^6 provides a third data set with [6|12] roughness. Figures 6.41–6.46, 6.47–6.52, and 6.53–6.58 show the streamwise velocity contours, boundary-layer profiles, and disturbance profiles, respectively. The data look very similar to those obtained for $Re_c = 2.4 \times 10^6$. The distortion of the mean boundary layer, however, develops much more quickly due to the increased growth rates.

The disturbance remains too weak to measure at $x/c = 0.05$ (figures 6.41, 6.47, and 6.53) even though the roughness Reynolds number (Re_k) is 50% larger under these conditions than for $Re_c = 2.4 \times 10^6$. (This will be confirmed by the spanwise scans presented below.) Thus, the disturbance amplitudes are computed for $x/c \geq 0.10$. Figure 6.59 shows the mode-shape profiles for these chord locations. The mode shape first begins to distort at $x/c = 0.20$, and along with the asymmetry of the disturbance profiles at this location (figure 6.56), indicates that nonlinearities are present. From $x/c = 0.20$ to $x/c = 0.29$ the mode shape quickly develops the second lobe characteristic of strong nonlinear effects. Figure 6.60 shows the total disturbance amplitude and amplification factor N computed from the mode shapes. Nonlinear

behavior is observed for $x/c \geq 0.20$, with strong amplitude saturation occurring for $x/c \geq 0.25$.

Data set $\mathcal{C}$ also contains a full set of spanwise scans suitable for spectral analysis. Figures 6.61 6.66 show the velocity profiles for $0.05 \leq x/c \leq 0.29$. The corresponding spectra are presented in figures 6.67–6.72. The scans are contaminated by noise for small x/c due to the magnification of small traverse errors by the large wall-normal gradient du/dY. This effect was observed for $Re_c = 2.4 \times 10^6$, but is intensified for $Re_c = 3.2 \times 10^6$ because of the increase in freestream velocity and decrease in boundary-layer thickness. Consequently, the hot-wire scan at $x/c = 0.05$ is overwhelmed by the $\lambda_z = 7.2$ mm traverse eccentricity discussed in section 5.5.5, and no crossflow modes can be extracted (figure 6.67).

The background noise level is smaller at $x/c = 0.10$, and figure 6.68 shows that there is measurable energy in the fundamental mode ($\lambda_z = 12$ mm). The $(0, 2)$ harmonic at $\lambda_z = 6$ mm also appears to be amplified, but we are forced to ignore it since it is arguably the same level as the background noise. By $x/c = 0.15$, the fundamental crossflow wavelength dominates and the $(0, 2)$ mode contains significant energy (figure 6.69). In fact, the $\lambda_z = 6$ mm component can be clearly seen in the velocity profile (figure 6.63). This trend continues downstream until the last measurement location at $x/c = 0.29$. The $(0, 3)$ mode ($\lambda_z = 4$ mm) becomes unstable at $x/c = 0.25$ and undergoes strong growth until $x/c = 0.29$. Unlike the $Re_c = 2.4 \times 10^6$ case, the data at $x/c = 0.29$ show evidence of a weak $(0, 4)$ mode ($\lambda_z = 3$ mm) just before transition. Its amplitude, however, is an order of magnitude below that of the $(0, 3)$ mode and is barely detectable above the background noise level of the spectrum.

These features are encapsulated in figure 6.73, which shows the disturbance amplitude and corresponding amplification factor N for the dominant stationary crossflow

modes. These data are computed by integrating the appropriate peaks in the spectra. As with the results for $Re_c = 2.4 \times 10^6$ (figure 5.91), the amplitude of the fundamental mode saturates in the region where the harmonics contain significant disturbance energy. However, in contrast to figure 5.91 the amplitude of the fundamental actually decreases at the last measurement location and the $(0, 2)$ and $(0, 3)$ modes show no evidence of amplitude saturation.

Figure 6.74 compares the amplitude of the individual modes to that of the total disturbance computed from the maximum of the mode-shape profiles. (Recall that the spanwise scans proceed at the height corresponding to the maximum of the mode shape.) This plot displays features similar to the results for $Re_c = 2.4 \times 10^6$ (shown in figure 5.92). In particular, the nonlinear amplitude saturation is characterized by the decrease in the amplitude of the fundamental mode (with respect to the total disturbance) and the corresponding growth of the harmonics. The accuracy of the two measurement techniques is indicated by the excellent agreement between the total and fundamental disturbances for $x/c \leq 0.20$.

6.1.3 Disturbance Amplitude Comparison

The data presented above are combined with the results for $Re_c = 2.4 \times 10^6$ (presented in section 5.5) to investigate the effect of chord Reynolds number on the stationary crossflow instability.

Figure 6.75 shows the total disturbance amplitude distribution for $Re_c = 1.6 \times 10^6$, 2.4×10^6, and 3.2×10^6 with [6|12] roughness. These curves are generated from the maximum of the mode-shape profiles. As before, the dashed lines show the absolute disturbance amplitude and the solid lines represent the amplification factor N. Amplitude saturation is evident for all Reynolds numbers. Recall that transition is occurring at $x/c = 0.32$ for $Re_c = 3.2 \times 10^6$, at $x/c = 0.52$ for $Re_c = 2.4 \times 10^6$, and somewhere past the pressure minimum for $Re_c = 1.6 \times 10^6$. It is interesting to note

that the amplitude of the stationary crossflow disturbance is approximately equal at transition for the two largest Reynolds number cases. The N-factors are different, but this is due to the difference in the reference amplitude at $x/c = 0.10$. It appears there may exist an equilibrium amplitude toward which the disturbance grows. This idea will be revisited later in this chapter.

6.2 Multiple-Mode Crossflow Waves

Flow visualizations presented in section 5.2 indicate that increasing the spanwise spacing of the roughness elements generates stationary crossflow waves containing multiple disturbance modes. Moreover, the characteristic saw-tooth pattern of the transition front becomes more regular and the average transition location moves forward when the roughness spacing is increased. Clearly, changing the initial conditions by altering the surface roughness distribution affects the stability characteristics and warrants further investigation.

This section describes the measurements for data set $\mathcal{D}$ in table 5.1. The roughness height remains at 6 μm, but the spanwise spacing is increased to 36 mm. This is denoted as [6|36] roughness in the shorthand notation described in section 5.1. The chord Reynolds number is 2.4×10^6. The disturbance structure is mapped for $0.05 \leq x/c \leq 0.45$ using the boundary-layer profile technique. Spanwise scans at constant Y provide individual-mode growth rates for $0.10 \leq x/c \leq 0.45$.

6.2.1 Disturbance Structure

The streamwise velocity contours for $0.05 \leq x/c \leq 0.45$ are plotted in figures 6.76 6.84. Figures 6.85–6.93 show the boundary-layer profiles from which the contours are generated. The corresponding disturbance profiles are presented in figures 6.94–6.102. As with the previous data sets, no stationary-wave-induced distortions of the mean

boundary layer are measurable at $x/c = 0.05$ (figure 6.76). In addition, figure 6.77 shows no measurable stationary disturbance at $x/c = 0.10$. This is in contrast to the data for [6|12] roughness (section 5.5), which contain measurable energy in the fundamental crossflow mode at 10% chord.

The data at $x/c = 0.15$ (figures 6.78, 6.87, and 6.96) show the first indication of unstable crossflow modes. Figure 6.79 clearly exhibits the distortion of the mean boundary layer at $x/c = 0.20$, and there is an apparent 36 mm feature corresponding to the roughness spacing. The disturbance profiles become asymmetric at $x/c = 0.25$ due to the nonlinear interaction among the various modes (figure 6.98). By $x/c = 0.30$, the velocity contour (figure 6.81) displays a more complicated structure indicating the presence of multiple stationary modes. This pattern develops downstream into the quite dramatic distortion of the mean boundary layer at $x/c = 0.45$ (figure 6.84). The primary features are 36 mm apart and represent the fundamental crossflow mode. Unlike the 12 mm forcing, however, there is clear evidence of significant energy in the harmonic wavelengths. These features are accentuated in the contour plot of the velocity surplus/deficit shown in figure 6.103. The ability of the artificial roughness to provide uniform initial conditions even for large spanwise spacing is indicated by the periodicity of the boundary-layer distortions.

The mode-shape profiles for $0.15 \leq x/c \leq 0.45$ are plotted in figure 6.104. Once again, the symbols are used to identify the curves but do not indicate measurement points. The nonlinear distortion appears at $x/c = 0.35$, after which the mode shape quickly develops the now-familiar second lobe indicating the presence of strong nonlinear effects. As a measure of the total disturbance energy, the profiles look qualitatively similar to those obtained with [6|12] roughness. However, one should be cautioned against placing too much emphasis on this comparison. The velocity contours clearly show the dramatic difference in the disturbance field for the two roughness spacings.

Figure 6.105 shows the chordwise distribution of the total disturbance amplitude and amplification factor N. These curves are computed from the maximum, average, and rms of the mode-shape profiles. Amplitude saturation occurs for $x/c \geq 0.35$.

6.2.2 Wavelength Separation

The rich modal content of the disturbance structure for [6|36] roughness is illuminated by spanwise scans and spectral analysis. The scans are performed at the boundary-layer height corresponding to the maximum of the mode shapes for $0.10 \leq x/c \leq 0.45$. The hot-wire surveys are presented in figures 6.106–6.113. Figures 6.114–6.122 show the power spectral density for these cases. Unstable crossflow modes are first detected at $x/c = 0.15$. The spectrum at this location (figure 6.115) shows energy in the $(0, 3)$, $(0, 4)$, and $(0, 5)$ modes (λ_z = 12 mm, 9 mm, and 7.2 mm). The $(0, 5)$ mode must be ignored since 7.2 mm happens (quite coincidentally) to be the exact wavelength of the traverse-related disturbance discussed in section 5.5.5. A small amount of energy appears in the $(0, 2)$ mode (λ_z = 18 mm), however this is disregarded as it is essentially within the noise of the spectrum. It is interesting that the fundamental mode (λ_z = 36 mm) is too weak to measure at $x/c = 0.15$ even though several harmonics are amplified.

The velocity profile at $x/c = 0.20$ (figure 6.108) shows the first sign of a 36 mm feature corresponding to the roughness spacing. However, the spectrum (shown in figure 6.116) indicates the energy in the fundamental mode is infinitesimal compared to the $(0, 2)$–$(0, 5)$ modes. In fact, based on a consistent definition of the spectral noise, the 36 mm "peak" must be ignored even though its effect is evident in the velocity profile. It appears that the fundamental mode, although tiny in amplitude, is providing enough energy to "pump" the more unstable wavelengths on a 36 mm scale. The fundamental mode itself becomes measurable at $x/c = 0.25$ (figure 6.117), although the harmonics—especially at λ_z = 12 mm and 9 mm—contain most of the

disturbance energy.

The higher harmonics become unstable at $x/c = 0.30$. The spectrum at this location, plotted in figure 6.118, shows the emergence of the $(0,6)$-$(0,8)$ modes ($\lambda_z = 6$ mm, 5.1 mm, and 4.5 mm). These modes continue to grow downstream until the last measurement position at $x/c = 0.45$. At this location the velocity profile (figure 6.113) clearly shows the effect of multiple unstable modes, which are well-defined in the spectrum (figure 6.121). It is important to note that the broadening of the PSD with increasing λ is an artifact of plotting the spectrum in the wavelength versus the wavenumber domain. Focusing on the small-wavelength disturbances (figure 6.122) shows unstable harmonics up to and including the $(0,9)$ mode ($\lambda_z = 4$ mm). There appear to be no amplified subharmonics (wavelength doubling) of the roughness spacing.

Integrating the spectral power in each peak provides the disturbance amplitude for each unstable mode. Figure 6.123 shows the amplification factor N for all wavelengths amplified by the 36 mm forcing. The $(0,5)$ mode ($\lambda_z = 7.2$ mm) is not plotted because of its contamination by the vertical traverse motion. The fundamental disturbance is not detected until $x/c = 0.25$, but has the largest growth rate. The harmonics at $\lambda_z = 18$ mm, 12 mm, and 9 mm are detected *before* the fundamental, yet display smaller growth rates. Amplitude saturation occurs for the $\lambda_z = 12$ mm, 9 mm, 6 mm, and 5.1 mm disturbances. Although the amplitude of the short wavelength disturbances ($\lambda_z = 4.5$ mm and 4 mm) is very small, they are growing as we move toward transition.

Since the individual modes are detected at different locations with different initial amplitudes, the reference amplitude for the N-factor calculations is different for each wavelength. Consequently, direct comparisons between the value of N are not meaningful. In this case it is instructive to consider the disturbance amplitude distribution

shown in figure 6.124. This plot shows the rms amplitude of the amplified disturbances as a function of x/c, and can be used to compare the relative disturbance energy in individual modes.

Based on preliminary nonlinear PSE calculations, it appears the 36 mm forcing is providing initial energy for several harmonics as well as the fundamental disturbance. This explains the early growth of the $(0,3)$ and $(0,4)$ modes ($\lambda_z = 12$ mm and 9 mm), which are near the most unstable wavelength for this experiment. The importance of the spectral content of the roughness distribution may also indicate that the roughness excite the stationary instability through a wave-like pressure disturbance and not a local injection of vorticity. However, one should be cautioned that a more detailed receptivity study is required to fully address this topic.

6.3 Initial Amplitude Variation

The height of the artificial roughness elements has been fixed at 6 μm in all the results presented up to this point. In this section, the effect of increasing the initial disturbance amplitude by changing the roughness height is investigated.

Data sets $\mathcal{E}$ and $\mathcal{F}$ defined in table 5.1 contain measurements for two additional roughness heights: 18 μm and 48 μm. The details of the elements are described in section 3.3.3. In both cases, the spanwise spacing of the elements is 12 mm and the data are obtained for $Re_c = 2.4\times10^6$. Under these conditions, the roughness Reynolds numbers are 1.0 and 7.0 for $k = 18$ μm and 48 μm, respectively. The measurements presented in this section are combined with the results for [6|12] roughness at $Re_c = 2.4 \times 10^6$ (data set $\mathcal{A}$) to provide disturbance amplitudes covering a nearly two-order-of-magnitude change in Re_k.

6.3.1 Data Set $\mathcal{E}$

Figures 6.125–6.133 show the streamwise velocity contours for [18|12] roughness at $Re_c = 2.4 \times 10^6$. The mean boundary-layer profiles used to construct the contour plots are presented in figures 6.134–6.142, and figures 6.143–6.151 show the corresponding disturbance profiles. In contrast to the [6|12] roughness at the same Reynolds number, measurable stationary crossflow waves are detected at $x/c = 0.05$ (this will be confirmed by spectral analysis). The distortion of the mean boundary layer is clearly evident in the velocity contour at $x/c = 0.10$ (figure 6.126). The asymmetry of the disturbance profiles at $x/c = 0.20$, shown in figure 6.146, indicates the early "rollover" of the streamwise velocity component due to the distortions of the mean boundary layer.

The stationary wave mode-shape profiles are plotted in figure 6.152 for $0.05 \leq x/c \leq 0.45$. The nonlinear distortion leading to the second lobe occurs by $x/c = 0.25$ and continues to develop downstream. Figure 6.153 shows the total disturbance amplitude computed from the maximum, average, and rms of the mode shapes. Although qualitatively similar to the [6|12] roughness case (figure 5.63), there are several important differences:

1. The initial disturbance amplitude is larger and can be measured at $x/c = 0.05$.

2. The amplitude saturation is more pronounced and occurs earlier, at $x/c \approx 0.25$ (saturation occurs at $x/c \approx 0.3$ for the $k = 6$ μm roughness).

3. The saturation amplitude at $x/c = 0.45$ is comparable to the 6 μm roughness case. (This will be discussed in detail later.)

4. The disturbance amplitude shows a "dip" at $x/c = 0.35$ which is not present for the [6|12] roughness. In fact, the amplitude measures show a "two-stage"

saturation process described by an initial amplitude saturation at $x/c = 0.35$, followed by second growth to $x/c = 0.40$ and a final saturation at $x/c = 0.45$.

Spanwise scans and spectral decomposition provide important information regarding the two-stage amplitude saturation. The velocity profiles and corresponding power spectra are shown in figures 6.154–6.162 and 6.163–6.171. The scans are performed at the boundary-layer height corresponding to the maximum of the mode shapes. The spectrum at $x/c = 0.05$ (figure 6.163) displays the familiar $\lambda_z = 7.2$ mm traverse-induced noise, however the fundamental crossflow mode ($\lambda_z = 12$ mm) is clearly amplified at this location. Figure 6.164 indicates that the $(0, 2)$ harmonic ($\lambda_z = 6$ mm) becomes unstable by $x/c = 0.10$. The $(0, 3)$ mode ($\lambda_z = 4$ mm) is detected at $x/c = 0.25$.

The disturbance amplitude and amplification factor N for the unstable crossflow modes are plotted in figure 6.172. Figure 6.173 shows the same data combined with the total disturbance amplitude computed from the maximum of the mode-shape profiles. The fundamental mode exhibits the same two-stage amplitude saturation that characterizes the total disturbance. Moreover, this behavior is also observed in the harmonic wavelengths. The $\lambda_z = 6$ mm mode shows early growth, saturates at $x/c = 0.25$, then grows again only to saturate a second time at $x/c = 0.45$. Even the $(0, 3)$ mode ($\lambda_z = 4$ mm) shows the same general trend. It is no surprise that the strong nonlinear effects beginning at $x/c = 0.25$ correlate with the resurgence of the 6 mm component and emergence of the 4 mm wavelength.

6.3.2 Data Set $\mathcal{F}$

The measurements presented above are repeated for [48|12] roughness. The streamwise velocity contours, mean boundary-layer profiles, and disturbance profiles for $0.05 \leq x/c \leq 0.45$ are shown in figures 6.174–6.182, 6.183–6.191, and 6.192–6.200,

respectively. The total disturbance mode-shape profiles are plotted in figure 6.201. As with the corresponding plots for the previous data sets, the symbols do not indicate measurement points, but are simply used as curve identifiers. The data are very similar to those obtained for [18|12] roughness. However, there are two notable differences. First, the distortion of the mode shape and development of the second lobe begins at $x/c = 0.20$, compared to $x/c = 0.25$ for the $k = 18$ μm roughness. This indicates that nonlinear effects develop more quickly with increased initial disturbance amplitude, as expected. Second, the disturbance-layer thickness--defined as the height at which the mean boundary-layer distortions vanish--has increased by approximately 0.5 mm at $x/c = 0.45$ (about a 1 mm increase with respect to the [6|12] roughness).

The total disturbance amplitude and amplification factor N determined from the mode-shape profiles are plotted in figure 6.202. The trends noted for the $k = 18$ μm roughness continue to develop. The initial amplitude is larger and saturation occurs earlier, now at $x/c \approx 0.20$. The two-stage saturation phenomenon still appears at $x/c = 0.35$, and the saturation amplitude remains relatively unchanged from both the [6|12] and [18|12] roughness cases. In contrast to these previous measurements (figures 5.63 and 6.153), the disturbance amplitude actually decreases from $x/c = 0.40$ to $x/c = 0.45$.

Spanwise scans performed at the boundary-layer height corresponding to the maximum of the mode-shape profiles give the disturbance amplitude in individual crossflow modes. The velocity profiles are shown in figures 6.203-6.211. The corresponding spectra are plotted in figures 6.212-6.220. Integrating the spectral peaks provides the individual-mode rms amplitude and N-factor curves shown in figure 6.221. The fundamental crossflow mode exhibits the two-stage saturation phenomenon, however the $(0, 2)$ harmonic ($\lambda_z = 6$ mm) no longer displays this feature. Moreover, the

6 mm-wavelength disturbance is not detected until $x/c = 0.15$, whereas it contains measurable energy at $x/c = 0.10$ for [18|12] roughness. On the other hand, the $(0, 3)$ mode ($\lambda_z = 4$ mm) becomes unstable earlier but otherwise behaves similarly to that for $k = 18$ μm roughness. Comparing these data to the total disturbance amplitude (figure 6.222) shows the typical trends. The region of nonlinear amplitude saturation is characterized by a decrease in the amplitude of the fundamental mode (with respect to the total disturbance) and the corresponding growth of the harmonic disturbances.

6.3.3 Disturbance Amplitude Comparison

The total disturbance mode-shape profiles offer the opportunity to quantify the effects of roughness height on the growth and structure of the stationary waves. Figure 6.223 shows the mode shapes at $x/c = 0.10$ and $x/c = 0.45$ for [6|12], [18|12], and [48|12] roughness. The larger roughness generates a much larger initial amplitude, however the disturbance profiles relax downstream to a similar mode shape. The disturbance energy is redistributed higher in the boundary layer with increasing initial amplitude, actually increasing the disturbance-layer thickness as noted earlier.

Figure 6.224 shows the total disturbance amplitude distributions for the three roughness heights. These curves are simply the maximum measures of the mode-shapes extracted from figures 5.63, 6.153, and 6.202. As indicated above, the initial amplitude and growth rate increase with larger roughness. However, the amplitude prior to transition remains essentially unchanged. It appears that once the nonlinear effects are strong enough to cause saturation, the saturation amplitude is fixed.

Figure 6.225 shows the amplification factor N for the amplitude distributions of figure 6.224. The N-factors are computed relative to $x/c = 0.10$ since this is the first location at which measurements are available for all roughness heights. Because of the larger initial amplitude and growth rate, the disturbance amplitude reaches the saturation level earlier for the larger roughness. Consequently, the relative growth

decreases with increased roughness height and the amplitude saturation becomes more pronounced. When analyzing figure 6.225, it is important to bear in mind that the numerical value of N is irrelevant because the initial conditions are different for each roughness configuration. Only the slope is important as it provides the local spatial growth rate.

Recall that transition occurs at $x/c \approx 0.50$ for all roughness heights considered (section 5.2). In light of this, figure 6.225 shows that for distributed surface roughness, nonlinear effects can dominate the stationary crossflow instability well before transition. In the case of [48|12] roughness, for example, strong nonlinear interactions and amplitude saturation are observed over 60% of the extent of the laminar boundary layer. The insensitivity of the transition location to the height of distributed roughness is in contrast to Radeztsky et al. (1993a), who showed that a single roughness element induces an isolated transition wedge whose location is a strong function of the roughness height. Moreover, when compared with Radeztsky et al. (1993a), the transition location in the case of distributed roughness is at a larger x/c than for isolated roughness. Clearly there are many receptivity issues that warrant further investigation.

6.4 Special Considerations

6.4.1 Which Wavelength Is Conserved?

In section 3.5.2 it was noted that linear, parallel stability analyses require certain constraints on one or more of the parameters of equation (3.13) in order to obtain solutions to the Orr-Sommerfeld equation. Many so-called integration strategies have been proposed, each attempting to choose appropriate constraints based on some

assumed physical behavior of the instability.[1] Arnal (1994) reviews the common strategies, which typically involve an assumption concerning the direction of growth, the direction of propagation, and/or the wavelength of the unstable disturbance.

No single integration strategy is universally accepted as providing the most applicable results for the general three-dimensional flowfield. However, it is possible to choose physically meaningful constraints for infinite-span swept wings. In this case the disturbance field must be the same at each spanwise location, from which it follows that the spanwise growth rate $\beta_i = 0$ (Mack 1988). This means the disturbance grows only in the chordwise direction, hence the need to impose an *ad hoc* constraint on the growth direction is removed. The experimental evidence supporting $\beta_i = 0$ is provided by any of the streamwise velocity contours and spanwise scans presented earlier in this chapter. For example, figures 5.29 and 5.81 clearly show a spanwise-invariant disturbance field.

The appropriate constraint concerning the crossflow wavelength (or equivalently the direction of propagation of the disturbance) is not so obvious. In early experiments at ASU, Dagenhart (1992) measured the stationary disturbance wavelength by counting the number of light and dark streaks that appear in a naphthalene flow visualization. To within the resolution of this technique, the crossflow wavelength normal to the vortex axis (λ_{cf}) appeared to remain constant over the model. In addition, no "drop-outs" or other adjustments to the vortex spacing were observed. Thus, Dagenhart concluded that the appropriate wavelength constraint for the linear, parallel stability calculations on infinite-span wings is constant λ_{cf}. These early results, however, were restricted by certain fundamental limitations of the technique:

1. With naphthalene flow visualization, the edges of the vortex streaks are not

[1] The term "integration strategies" comes from the ultimate goal of computing the amplification factor N via equation (3.15).

always well defined and can be obscured by inconsistency in the concentration and application of the naphthalene. Moreover, the wavelength measurements were obtained under the conditions of natural surface roughness, which has been shown to generate a complicated stationary structure containing many disturbance modes (figure 5.28). Consequently, measurements of the separation between the vortex streaks are rather subjective and open to the interpretation of the observer.

2. As discussed in section 4.5, the naphthalene sublimes quickly near the leading edge due to the high shear of the thin, laminar boundary layer. As a result, Dagenhart's measurements were confined to the mid-chord region of the model, in which the direction of propagation of the stationary wave is nearly constant. In light of this, it is no surprise that vortex drops-outs or adjustments to the spanwise spacing were not observed.

With a high-resolution instrumentation traverse and improved measurement techniques, the present experiment is much better equipped to objectively analyze the wavenumber distribution for the stationary crossflow instability. In fact, the power spectra for the spanwise scans contain all the necessary information. By virtue of the measurement technique, the location of each peak in the spectrum gives the spanwise wavelength $\lambda_z = 2\pi/\beta_r$ of the corresponding unstable crossflow mode. Tracking this spectral peak at each chord location gives the wavelength distributions shown in figure 6.226. This plot shows the spanwise wavelength (λ_z) of the fundamental crossflow mode [i.e., the $(0,1)$ mode] as a function of x/c for all experimental data sets with 12 mm roughness spacing. Also plotted is the variation of λ_z predicted by linear theory (data provided by Haynes) using the constant *crossflow* wavelength constraint. The value of $\lambda_{cf} = 8.5$ mm is chosen because it gives $\lambda_z = 12$ mm at $x/c = 0.05$, corresponding to the initial roughness forcing. Clearly, fixing λ_{cf} fails to produce the

correct spanwise wavelength. Instead, the spanwise wavelength remains constant as proposed by Mack (1988). It should be noted, however, that λ_z does not dramatically change when λ_{cf} is fixed, which explains why the qualitative measurements of Dagenhart produced the incorrect conclusion.

In summary, the spanwise growth rate β_i is zero and the spanwise wavenumber β_r is constant for infinite-span swept wings.

6.4.2 Effect of Acoustic Forcing

As discussed in section 1.3, Müller and Bippes (1989), Bippes (1990, 1991), and Bippes et al. (1991) have shown that the growth of traveling crossflow waves depends strongly on the freestream turbulence level. However, in these experiments the initial conditions for the stationary waves came from the unknown natural roughness of the model surface. What is not well understood is the importance of freestream disturbances (acoustic and vortical) in relation to surface roughness and their combined effect on transition. At issue here is the receptivity of the boundary layer to various types of disturbances, both in the freestream and on the airfoil. While this problem is far from being solved and continues to evade a robust theory, the experimentalist can provide valuable information concerning the response of the boundary layer under varying environmental conditions.

With this in mind, the present work also investigates the interaction between freestream acoustic disturbances and artificial surface roughness in relation to their effect on transition in crossflow-dominated flows. The study ignores the details of the instability growth, concentrating instead on the transition location as a global measure of the stability of the boundary layer. The transition location is determined from naphthalene flow visualization using the technique described in section 4.5.

The tests are performed with the [48|12] surface roughness distribution (i.e., k = 48 μm roughness with a 12 mm spanwise spacing applied at $x/c = 0.023$). Freestream

Table 6.1: Effect of freestream acoustic forcing on transition location for $Re_c = 2.4 \times 10^6$ and [48|12] roughness.

Frequency Range [Hz]	Transition Location $[x/c]$
No Sound	0.49
30–200	0.49
200–1k	0.49
1k–5k	0.49

acoustic disturbances are generated with an array of nine speakers mounted in the plenum wall. The source signal contains bandwidth-limited random noise. Three frequency ranges are chosen: 30–200 Hz, 200–1000 Hz, and 1–5 kHz corresponding to the unstable frequencies for traveling crossflow waves, Tollmien-Schlichting disturbances, and secondary instabilities, respectively. The sound pressure level is held constant at 100 dB (20 μPa reference). Table 6.1 displays the average transition location for $Re_c = 2.4 \times 10^6$ under these conditions. The acoustic forcing has absolutely no effect on the transition location. Moreover, no changes in any detail of the characteristic saw-tooth transition pattern are noted. These results confirm the observations of Takagi et al. (1991) and Radeztsky et al. (1993a), as well as the more recent findings of Deyhle and Bippes (1996), and indicate that acoustic disturbances play only a passive role in the crossflow instability.

CHAPTER 7

Conclusions

7.1 Summary of Key Results

The important results of this experimental investigation are summarized in the following specific conclusions.

1. Stationary crossflow waves dominate the transition process on swept wings in a low-disturbance environment. Even under the conditions of 0.25 μm rms natural surface roughness, the stationary waves cause strong nonlinear distortions of the mean streamwise boundary layer and the jagged transition front (due to a local breakdown caused by secondary instabilities) indicates sensitivity to the randomly distributed roughness.

2. Leading-edge roughness provides the all-important initial conditions for the stationary waves. In the absence of artificial roughness, submicron irregularities in the natural surface finish generate nonuniform disturbance motion containing many modes. Systematic introduction of equally-spaced roughness elements produces an ideal fundamental mode at that spacing. The micron-sized elements introduce known initial conditions without saturating the initial disturbance amplitude, thus providing the necessary database for comparisons with both linear and nonlinear computations.

3. In contrast to the results for isolated roughness elements (Radeztsky et al. 1993a), increasing the height of the distributed roughness has surprisingly little affect on the transition location. Moreover, transition occurs at larger x/c for distributed roughness than for an isolated element of the same height. This behavior is also observed when the spacing of the distributed roughness is increased from 12 mm to 36 mm, in which case transition moves forward and the characteristic saw-tooth transition front becomes dramatically more regular in span. This indicates that, through enhanced nonlinear interactions among multiple modes, the wavenumber content of the stationary disturbance can significantly influence the *local* transition characteristics of the boundary layer.

4. Extensive hot-wire measurements document the detailed structure of the distortion of the mean boundary layer caused by the integrated effect of the stationary waves. Boundary-layer profiles clearly show the growth of the mean-flow distortion [$(0,0)$ mode] and the corresponding development of the nonlinear second lobe in the total disturbance mode-shape profile. This early nonlinear mode interaction causes the total disturbance amplitude to saturate *well before transition.*

5. Accurate spectral decomposition provides individual-mode growth rates for the fundamental crossflow mode and all amplified harmonics. These data show that the amplitude saturation phenomenon is caused by the nonlinear growth of the harmonic disturbances and their interaction with the fundamental mode. The amplitude saturation is not limited to the fundamental mode, but is also observed in the harmonic wavelengths.

6. Uniformly distributed roughness at the most unstable wavelength ($\lambda_z = 12$ mm) produces an ideal fundamental mode and poor excitation of other modes. In

fact, harmonic disturbances are amplified only through nonlinear coupling. In this sense, forcing the most unstable wavelength provides a *minimum* destabilization of the total disturbance.

7. Increasing the spanwise spacing of the roughness elements generates multiple-mode stationary waves that produce an intricate distortion of the mean boundary layer leading to earlier transition. Spectral analysis shows that harmonic disturbances can be amplified before the fundamental mode, indicating that the Fourier decomposition of the roughness distribution is an important aspect of the receptivity process. This suggests that the roughness may excite the stationary instability through a wave-like pressure disturbance and not a local injection of vorticity.

8. Increasing the height of the distributed roughness produces a larger initial disturbance and enhanced nonlinear interaction leading to earlier amplitude saturation. In addition, a "two-stage" saturation is observed for the larger roughness heights. However, the total disturbance relaxes downstream to a similar mode shape profile and the transition location remains largely unaffected. This suggests that once the nonlinear effects are strong enough to cause saturation, the saturation amplitude is fixed.

9. No wavelength doubling (i.e., modes with wavelengths larger than the fundamental) is observed for any roughness configuration. On the other hand, both the 12 mm and 36 mm forcing produce amplified harmonics up to the $\lambda_z = 4$ mm wavelength. It is interesting to note that the diameter of the roughness elements is 3.7 mm. Thus, the measurements show no evidence of unstable harmonics with wavelengths smaller than the roughness diameter (with the exception of the infinitesimal $\lambda_z = 3$ mm disturbance immediately before transition for [6|12]

roughness at $Re_c = 3.2 \times 10^6$). This result is unexplained and illuminates the importance of the receptivity process for stationary crossflow waves.

10. In contrast to Radeztsky et al. (1994), the early disturbance growth shows qualitative agreement with linear theory even though the present distortion of the mean boundary layer is an order of magnitude larger. This shows that there is, in fact, a linear region for the stationary crossflow instability, and may indicate that the large roughness used in the previous experiments caused the linear receptivity regime to be bypassed.

11. Although a region of linear growth is observed, the importance of nonlinear effects as the dominant aspect of the stationary crossflow instability is firmly established and incontrovertible. This is reinforced by the outstanding nonlinear PSE calculations that agree remarkably well with the experimental data. Together these results show that the important physical mechanism is not the weak (v', w') motion of the stationary wave itself, but rather its ability to induce $O(1)$ u' distortions of the mean boundary-layer flow. In light of this, the failure of linear theory to capture the details of the disturbance growth is perhaps no surprise. Linear theory simply cannot account for the distortion of the basic state resulting from the integrated effect of the stationary wave.

12. The secondary instability that leads to transition appears to be most effective in the presence of multiple-mode disturbances. This is suggested by the uniformity of the saw-tooth transition front and the decrease in the transition Reynolds number with increased roughness spacing. Because of these effects, even linear stability analyses of the distorted mean flow are insufficient to describe the transition process.

13. Traditional transition-correlation techniques such as the classic e^N method are ineffective under these conditions. The nonlinear amplitude saturation occurs well before transition, thus the disturbance amplitude is relatively constant over a large extent of the laminar boundary layer. Moreover, increasing the roughness height moves the saturation point forward, while the saturation amplitude and transition location remain unchanged. On the other hand, increasing the roughness height from 6 μm to 48 μm causes a nearly 50% *decrease* in the disturbance amplification factor N at transition. Thus, transition correlations based on N-factor criteria are not possible. In fact, the strong nonlinear saturation and its dependence on initial conditions show that, in a stationary-crossflow-dominated boundary layer, no transition prediction is possible without proper account for the receptivity process.

7.2 Closing Remarks

Whereas transition correlation is often based on semi-empirical observations, accurate transition *prediction* requires an intimate understanding of the physics involved. The present investigation provides this information for swept-wing boundary layers dominated by the stationary crossflow instability. The importance of nonlinear effects is firmly established, and the ability of micron-sized roughness to alter the disturbance growth confirms that receptivity issues cannot be ignored. This experiment provides a detailed database for the development and validation of computational methods concerning three-dimensional boundary-layer stability and transition prediction.

REFERENCES

Arnal, D. 1984. Description and prediction of transition in two-dimensional incompressible flow. In *Special Course on Stability and Transition of Laminar Flows*, AGARD R-709.

Arnal, D. 1986. Three-dimensional boundary layers: Laminar-turbulent transition. In *Special Course on Calculation of Three-Dimensional Boundary Layers with Separation*, AGARD R-741.

Arnal, D. 1992. Boundary-layer transition: Prediction, application to drag reduction. In *Special Course on Skin Friction Drag Reduction*, AGARD R-786. Loughton, Essex: Specialised Printing Services Ltd. ISBN 92-835-0661-8.

Arnal, D. 1994. Boundary-layer transition: Predictions based on linear theory. In *Special Course on Progress in Transition Modelling*, AGARD R-793. Loughton, Essex: Specialised Printing Services Ltd. ISBN 92-835-0742-8.

Arnal, D. and J. C. Juillen. 1987. Three-dimensional transition studies at ONERA-CERT. AIAA Paper 87-1335.

Arnal, D., E. Coustols, and J. C. Juillen. 1984. Experimental and theoretical study of transition phenomena on an infinite swept wing. Rech. Aérosp. No. 1984-4.

Arnal, D., G. Casalis, and J. C. Juillen. 1990. Experimental and theoretical analysis of natural transition on infinite swept wing. In *Laminar-Turbulent Transition* (eds. D. Arnal and R. Michel), vol. 3, pp. 311–325. Berlin: Springer-Verlag. ISBN 3-540-52196-8.

Bearman, P. W. 1971. Corrections for the effect of ambient temperature drift on hot-wire measurements in incompressible flow. DISA Information #11, pp. 25–30.

Benmalek, A. and W. S. Saric. 1994. Effects of curvature variations on the nonlinear evolution of Goertler vortices. *Phys. Fluids* 3(10):3353–3367.

Bippes, H. 1990. Instability feature appearing on swept wing configurations. In *Laminar-Turbulent Transition* (eds. D. Arnal and R. Michel), vol. 3, pp. 419 430. Berlin: Springer-Verlag. ISBN 3-540-52196-8.

Bippes, H. 1991. Experiments on transition in three-dimensional accelerated boundary-layer flows. In *Proc. R.A.S. Boundary Layer Transition and Control*, Cambridge, U.K.

Bippes, H. and B. Müller. 1990. Disturbance growth in an unstable three-dimensional boundary layer. In *Numerical and Physical Aspects of Aerodynamics Flows IV* (ed. T. Cebeci), pp. 345–358. Berlin: Springer-Verlag. ISBN 3-540-52259-X.

Bippes, H. and P. Nitschke-Kowsky. 1990. Experimental study of instability modes in a three-dimensional boundary layer. *AIAA J.* 28(10):1758–1763.

Bippes, H., B. Müller, and M. Wagner. 1991. Measurements and stability calculations of the disturbance growth in an unstable three-dimensional boundary layer. *Phys. Fluids* 3(10):2371–2377.

Dagenhart, J. R. 1981. Amplified crossflow disturbances in the laminar boundary layer on swept wings with suction. TP-1902, NASA.

Dagenhart, J. R. 1992. *Crossflow Stability and Transition Experiments in a Swept-Wing Flow.* Ph.D. diss., Virginia Polytechnic Institute and State University. Also NASA TM-108650.

Dagenhart, J. R., W. S. Saric, M. C. Mousseux, and J. P. Stack. 1989. Crossflow vortex instability and transition on a 45-degree swept wing. AIAA Paper 89-1892.

Dagenhart, J. R., W. S. Saric, J. A. Hoos, and M. C. Mousseux. 1990. Experiments on swept-wing boundary layers. In *Laminar-Turbulent Transition* (eds. D. Arnal and R. Michel), vol. 3, pp. 369–380. Berlin: Springer-Verlag. ISBN 3-540-52196-8.

Deyhle, H. and H. Bippes. 1996. Disturbance growth in an unstable three-dimensional boundary layer and its dependence on environmental conditions. To appear in *J. Fluid Mech.*

Deyhle, H., G. Höhler, and H. Bippes. 1993. Experimental investigation of instability wave propagation in a 3-D boundary-layer flow. *AIAA J.* 31(4):637–645.

Floryan, J. M. 1991. On the Görtler instability of boundary layers. *Prog. Aerospace Sci.* 28:235–271.

Gaponenko, V. R., A. V. Ivanov, and Y. S. Kachanov. 1995b. Experimental study of 3D boundary-layer receptivity to surface vibrations. In *Proc. IUTAM Symposium on the Nonlinear Stability of Three-Dimensional Boundary Layers*, Manchester, U.K.

Gaponenko, V. R., A. V. Ivanov, and Y. S. Kachanov. 1995a. Experimental study of cross-flow instability of a swept-wing boundary layer with respect to travelling waves. In *Laminar-Turbulent Transition* (ed. R. Kobayashi), vol. 4, pp. 373–380. Berlin: Springer-Verlag. ISBN 3-540-59297-0.

Gray, W. E. 1952. The effect of wing sweep on laminar flow. RAE TM Aero 255.

Hall, P. and M. R. Malik. 1986. On the instability of a three-dimensional attachment-line boundary layer: Weakly nonlinear theory and a numerical approach. *J. Fluid Mech.* 163:257–282.

Hall, P., M. R. Malik, and D. I. A. Poll. 1984. On the stability of an infinite swept attachment-line boundary layer. *Phil. Trans. Roy. Soc. Lon. A* 395:229–245.

Haynes, T. S. and H. L. Reed. 1996. Computations in nonlinear saturation of stationary crossflow vortices in a swept-wing boundary layer. AIAA Paper 96-0182.

Herbert, T. 1994. Parabolized stability equations. In *Special Course on Progress in Transition Modelling*, AGARD R-793. Loughton, Essex: Specialised Printing Services Ltd. ISBN 92-835-0742-8.

Ivanov, A. V. and Y. S. Kachanov. 1994. A method of study of the stability of 3D boundary layers using a new disturbance generator. In *Proc. International Conference on the Methods of Aerospace Research*, Institute of Theoretical & Applied Mechanics, Novosibirsk.

Juillen, J. C. and D. Arnal. 1990. Etude expérimentale du déclencement de la transition par rugosités et par ranier sur de bord d'attaque d'une aile en flèche en èncoulement incompressible. Rapport Final 51/5018.35, CERT/ONERA.

Kachanov, Y. S. 1995. Generation, development and interaction of instability modes in swept-wing boundary layer. In *Proc. IUTAM Symposium on the Nonlinear Stability of Three-Dimensional Boundary Layers*, Manchester, U.K.

Kachanov, Y. S. and A. Michalke. 1994. 3D instability of flat-plate boundary layer. theory and experiment. *Eur. J. Mech., B/Fluids* 13(4):401–422.

Kachanov, Y. S. and O. I. Tararykin. 1990. The experimental investigation of stability and receptivity of a swept-wing flow. In *Laminar-Turbulent Transition* (eds. D. Arnal and R. Michel), vol. 3, pp. 499 509. Berlin: Springer-Verlag. ISBN 3-540-52196-8.

Kaups, K. and T. Cebeci. 1977. Compressible laminar boundary layers with suction on swept and tapered wings. *J. Aircraft* 14(7):661–667.

Kay, S. M. and S. L. Marple, Jr. 1981. Spectrum analysis –a modern perspective. *Proc. IEEE* 69(11):1380–1419.

King, L. V. 1914. On the convection of heat from small cylinders in a stream of fluid. *Phil. Trans. Roy. Soc. Lon. A* 214:373–432.

King, L. V. 1915. On the precision measurements of air velocity by means of the linear hot-wire anemometer. *Phil. Mag.* 29:556–577.

Kleiser, L. 1991. Numerical simulation of transition in wall-bounded shear flows. *Ann. Rev. Fluid Mech.* 23:495–537.

Kohama, Y., W. S. Saric, and J. A. Hoos. 1991. A high-frequency secondary instability of crossflow vortices that leads to transition. In *Proc. R.A.S. Boundary Layer Transition and Control*, Cambridge, U.K.

Lerche, T. and H. Bippes. 1995. Experimental investigation of cross-flow instability under the influence of controlled disturbance generation. In *Proc. Colloquium of the Royal Netherlands Academy of Arts and Sciences on Transitional Boundary Layers in Aerodynamics: State-of-the-Art and Future Directions of Research*, Amsterdam. Elsevier.

Lin, R.-S. 1992. *Stationary Crossflow Instability on an Infinite Swept Wing.* Ph.D. diss., Arizona State University.

Mack, L. M. 1984. Boundary-layer linear stability theory. In *Special Course on Stability and Transition of Laminar Flows*, AGARD R-709.

Mack, L. M. 1988. Stability of three-dimensional boundary layers on swept wings at transonic speeds. In *IUTAM Symp. Transsonicum III* (eds. Zierep and Oertel). Berlin: Springer-Verlag.

Malik, M. R. 1982. COSAL—A black box compressible stability analysis code for transition prediction in three-dimensional boundary layers. CR-165952, NASA.

Meyer, F. and L. Kleiser. 1990. Numerical simulation of transition due to crossflow instability. In *Laminar-Turbulent Transition* (eds. D. Arnal and R. Michel), vol. 3, pp. 609–619. Berlin: Springer-Verlag. ISBN 3-540-52196-8.

Michel, R., D. Arnal, E. Coustols, and J. C. Juillen. 1985. Experimental and theoretical studies of boundary layer transition on a swept infinite wing. In *Laminar-Turbulent Transition* (ed. V. V. Kozlov), vol. 2, pp. 553–561. Berlin: Springer-Verlag. ISBN 3-540-15250-4.

Morkovin, M. V. 1969. On the many faces of transition. In *Viscous Drag Reduction* (ed. C. S. Wells), pp. 1–31. New York: Plenum.

Mousseux, M. C. 1988. *Flow-Quality Improvements in the Arizona State University Unsteady Wind Tunnel.* Master's thesis, Arizona State University.

Müller, B. 1990. Experimental study of travelling waves in a three-dimensional boundary layer. In *Laminar-Turbulent Transition* (eds. D. Arnal and R. Michel), vol. 3, pp. 489–498. Berlin: Springer-Verlag. ISBN 3-540-52196-8.

Müller, B. and H. Bippes. 1989. Experimental study of instability modes in a three-dimensional boundary layer. In *Fluid Dynamics of Three-Dimensional Turbulent Shear Flows and Transition*, AGARD CP-438. Loughton, Essex: Specialised Printing Services Ltd. ISBN 92-835-0502-6.

Müller, B., H. Bippes, and F. S. Collier, Jr. 1990. The stability of a three dimensional boundary layer over a swept flat plate. In *Instability and Transition* (eds. M. Y. Hussaini and R. G. Voight), vol. 2, pp. 268–277. New York: Springer-Verlag. ISBN 0-387-97324-9.

Nitschke-Kowsky, P. and H. Bippes. 1988. Instability and transition of a three-dimensional boundary layer on a swept flat plate. *Phys. Fluids* 31(4):786–795.

Perry, A. E. 1982. *Hot-wire Anemometry.* New York: Oxford University Press. ISBN 0-19-856327-2.

Pfenninger, W. 1977. Laminar flow control—laminarization. In *Special Course on Concepts for Drag Reduction*, AGARD R-654.

Poll, D. I. A. 1979. Transition in the infinite swept attachment line boundary layer. *Aeronaut. Q.* 30:607–629.

Poll, D. I. A. 1984. Transition description and prediction in three-dimensional flows. In *Special Course on Stability and Transition of Laminar Flows*, AGARD R-709.

Poll, D. I. A. 1985. Some observations of the transition process on the windward face of a long yawed cylinder. *J. Fluid Mech.* 150:329–356.

Press, W. H., S. A. Teukolsky, W. T. Vetterling, and B. P. Flannery. 1992. *Numerical Recipes in C: The Art of Scientific Computing.* New York: Cambridge University Press, 2nd ed. ISBN 0-521-43108-5.

Radeztsky, R. H. Jr. 1994. *Growth and Development of Roughness-Induced Stationary Crossflow Vortices.* Ph.D. diss., Arizona State University.

Radeztsky, R. H. Jr., M. S. Reibert, W. S. Saric, and S. Takagi. 1993a. Effect of micron-sized roughness on transition in swept-wing flows. AIAA Paper 93-0076.

Radeztsky, R. H. Jr., M. S. Reibert, and S. Takagi. 1993b. A software solution to temperature-induced hot-wire voltage drift. In *Proc. Third International Symposium on Thermal Anemometry*, vol. 167, pp. 49–55. ASME-FED.

Radeztsky, R. H. Jr., M. S. Reibert, and W. S. Saric. 1994. Development of stationary crossflow vortices on a swept wing. AIAA Paper 94-2373.

Rae, W. H. Jr. and A. Pope. 1984. *Low-Speed Wind Tunnel Testing.* New York: John Wiley & Sons, 2nd ed. ISBN 0-471-87402-7.

Reed, H. L. 1988. Wave interactions in swept-wing flows. *Phys. Fluids* 30(11):3419–3426.

Reed, H. L. 1994. Direct numerical simulation of transition: The spatial approach. In *Special Course on Progress in Transition Modelling*, AGARD R-793. Loughton, Essex: Specialised Printing Services Ltd. ISBN 92-835-0742-8.

Reed, H. L. and T. S. Haynes. 1994. Transition correlations in three-dimensional boundary layers. *AIAA J.* 32(5):923–929.

Reed, H. L. and R.-S. Lin. 1987. Stability of three-dimensional boundary layers. SAE Paper 87-1857.

Reed, H. L. and W. S. Saric. 1989. Stability of three-dimensional boundary layers. *Ann. Rev. Fluid Mech.* 21:235–284.

Reed, H. L., W. S. Saric, and D. Arnal. 1996. Linear stability theory applied to boundary layers. *Ann. Rev. Fluid Mech.* 28:389–428.

Reibert, M. S. 1996. *Standard C Libraries and Codes: A Guide to Programming at the ASU Unsteady Wind Tunnel.* Arizona State University. Unsteady Wind Tunnel Internal Documentation.

Reshotko, E. 1994. Boundary layer instability, transition and control. AIAA Paper 94-0001.

Saric, W. S. 1990. Low-speed experiments: Requirements for stability measurements. In *Instability and Transition* (eds. M. Y. Hussaini and R. G. Voight), vol. 1, pp. 162–174. New York: Springer-Verlag. ISBN 0-387-97323-0.

Saric, W. S. 1992a. The ASU transition research facility. AIAA Paper 92-3910.

Saric, W. S. 1992b. Laminar-turbulent transition: Fundamentals. In *Special Course on Skin Friction Drag Reduction*, AGARD R-786. Loughton, Essex: Specialised Printing Services Ltd. ISBN 92-835-0661-8.

Saric, W. S. 1994a. Görtler vortices. *Ann. Rev. Fluid Mech.* 26:379–409.

Saric, W. S. 1994b. Low-speed boundary-layer transition experiments. In *Aspects of Transition to Turbulence: Experiments, Theory & Computations* (eds. M. Hussaini and T. Corke).

Saric, W. S. 1994c. Physical description of boundary-layer transition: Experimental evidence. In *Special Course on Progress in Transition Modelling*, AGARD R-793. Loughton, Essex: Specialised Printing Services Ltd. ISBN 92-835-0742-8.

Saric, W. S. and L. G. Yeates. 1985. Experiments on the stability of crossflow vortices in swept-wing flows. AIAA Paper 85-0493.

Saric, W. S., S. Takagi, and M. C. Mousseux. 1988. The ASU Unsteady Wind Tunnel and fundamental requirements for freestream turbulence measurements. AIAA Paper 88-0053.

Saric, W. S., J. R. Dagenhart, and M. C. Mousseux. 1990. Experiments in swept-wing transition. In *Numerical and Physical Aspects of Aerodynamics Flows IV* (ed. T. Cebeci), pp. 359–371. Berlin: Springer-Verlag. ISBN 3-540-52259-X.

Schrauf, G., T. Herbert, and G. Stuckert. 1995. Evaluation of transition in flight tests using nonlinear PSE analysis. AIAA Paper 95-1801.

Smith, A. M. O. and N. Gamberoni. 1956. Transition, pressure gradient, and stability theory. ES 26388, Douglas Aircraft Company, El Segundo, California.

Somers, D. M. and K. H. Horstmann. 1985. Design of a medium-speed natural-laminar-flow airfoil for commuter aircraft applications. *DFVLR-IB/29-85/26.*

Srokowski, A. J. and S. A. Orszag. 1977. Mass flow requirements for LFC wing design. AIAA Paper 77-1222.

Stevens, W. A., S. H. Goradia, and J. A. Braden. 1971. A mathematical model for two-dimensional multi-component airfoils in viscous flow. CR-1843, NASA.

Stuckert, G. K., T. Herbert, and V. Esfahanian. 1993. Stability and transition on swept wings. AIAA Paper 93-0078.

Takagi, S., W. S. Saric, R. H. Radeztsky, Jr., S. A. Spencer, and D. J. Orr. 1991. Effect of sound and micron-sized roughness on crossflow-dominated transition. *Bull. Am. Phys. Soc.* 36:2630.

Thomas, A. S. W. 1985. Aircraft drag reduction technology--a summary. In *Special Course on Aircraft Drag Prediction and Reduction*, AGARD R-723. Loughton, Essex: Specialised Printing Services Ltd. ISBN 92-835-1507-2.

van Ingen, J. L. 1956. A suggested semi-empirical method for the calculation of the boundary-layer transition region. VTH 71 & 74, Dept. Aero. Eng., Univ. of Techn., Delft, Netherlands.

von Doenhoff, A. E. and A. L. Braslow. 1961. The effect of distributed roughness on laminar flow. In *Boundary-Layer Control* (ed. Lachmann), vol. 2. Pergamon.

Wang, M., T. Herbert, and G. K. Stuckert. 1994. Crossflow-induced transition in compressible swept-wing flows. AIAA Paper 94-2374.

Wintergerste, T. and L. Kleiser. 1995. Direct numerical simulation of transition in a three-dimensional boundary layer. In *Proc. Colloquium of the Royal Netherlands Academy of Arts and Sciences on Transitional Boundary Layers in Aerodynamics: State-of-the-Art and Future Directions of Research*, Amsterdam. Elsevier.

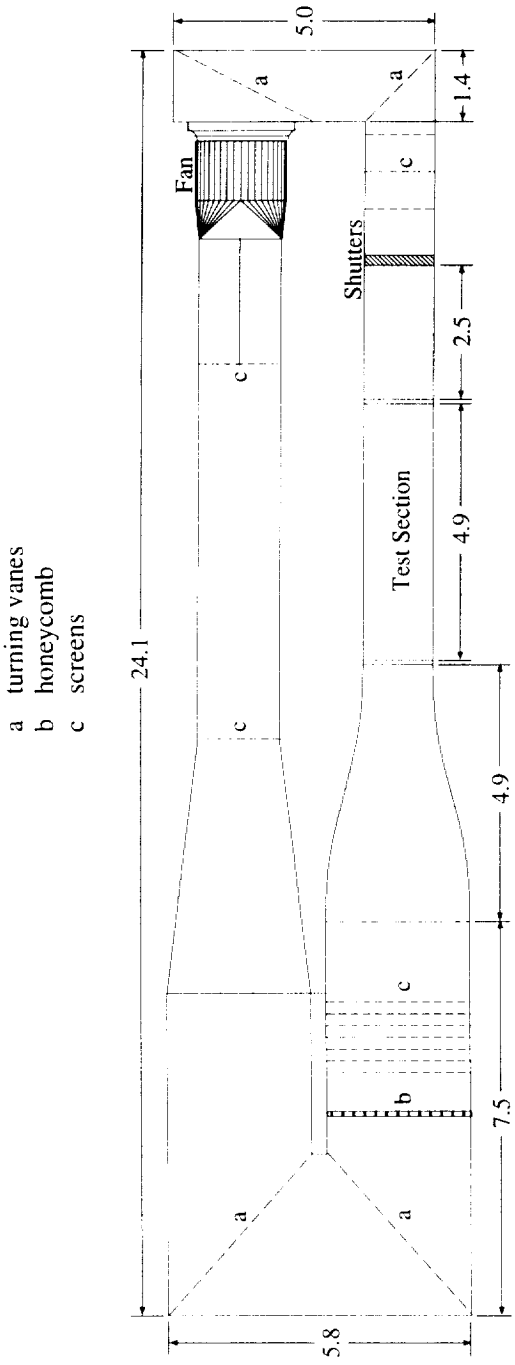

Figure 2.1: Plan view of the ASU Unsteady Wind Tunnel. All dimensions in meters.

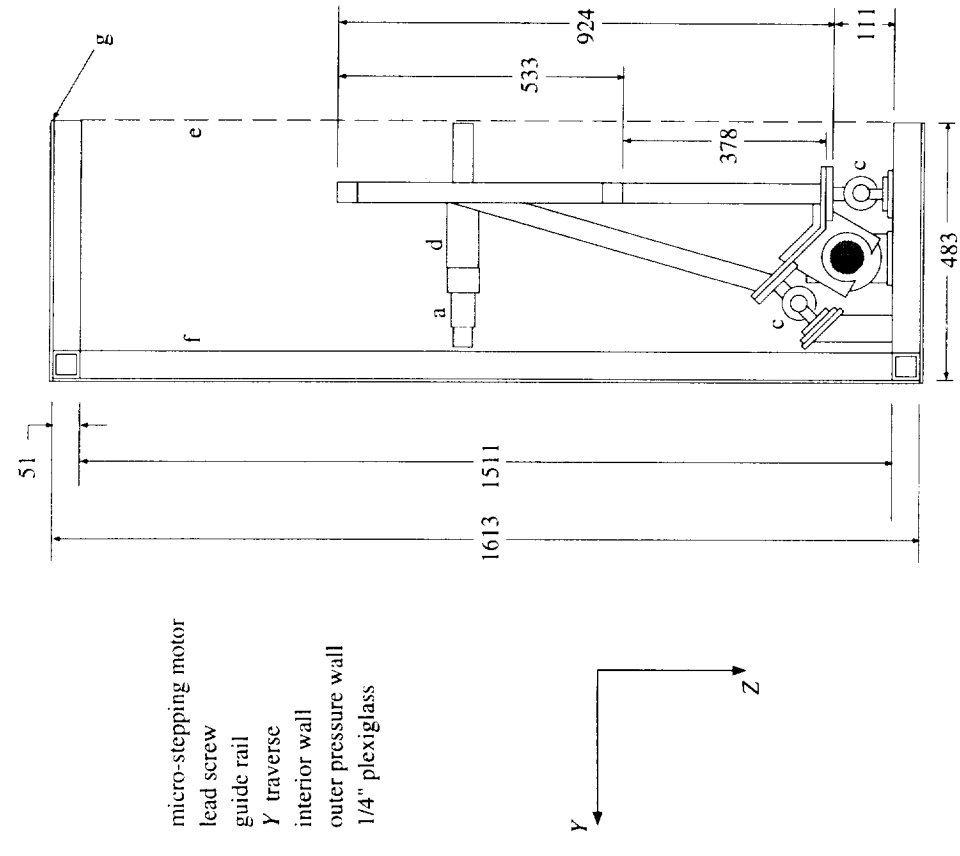

Figure 2.2: Side view of traverse carriage. All dimensions in millimeters.

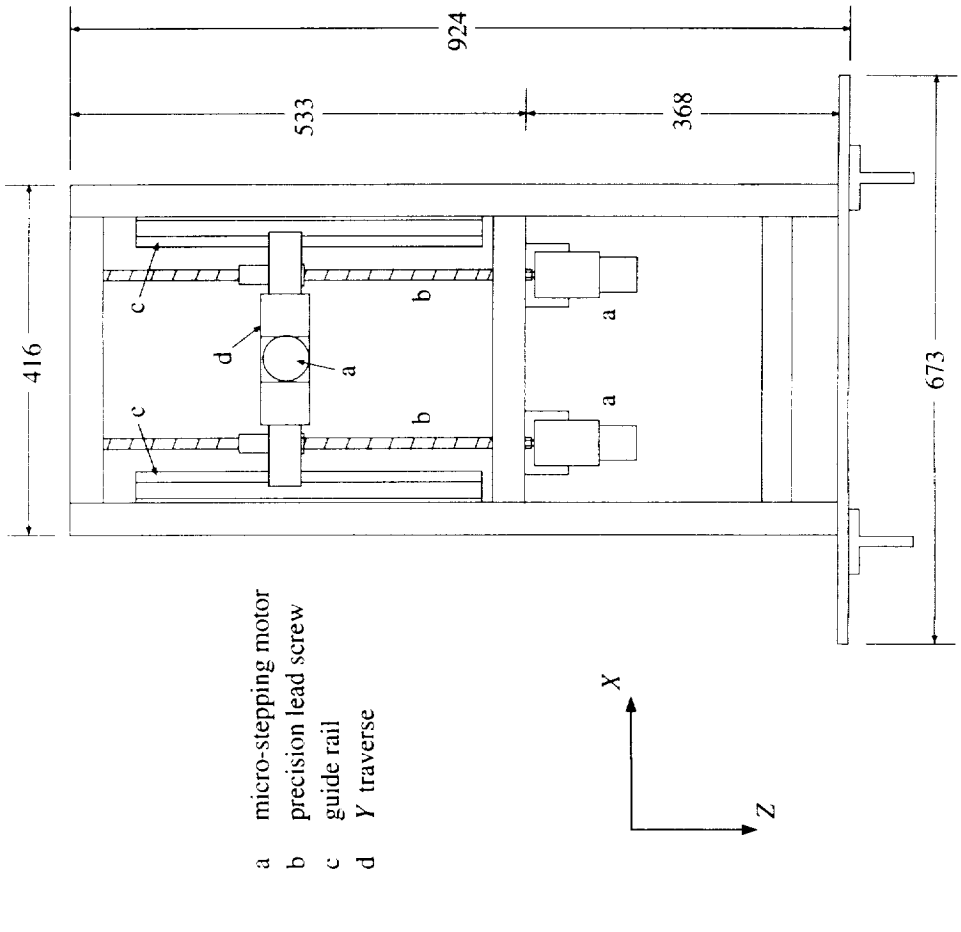

Figure 2.3: Front view of traverse carriage. All dimensions in millimeters.

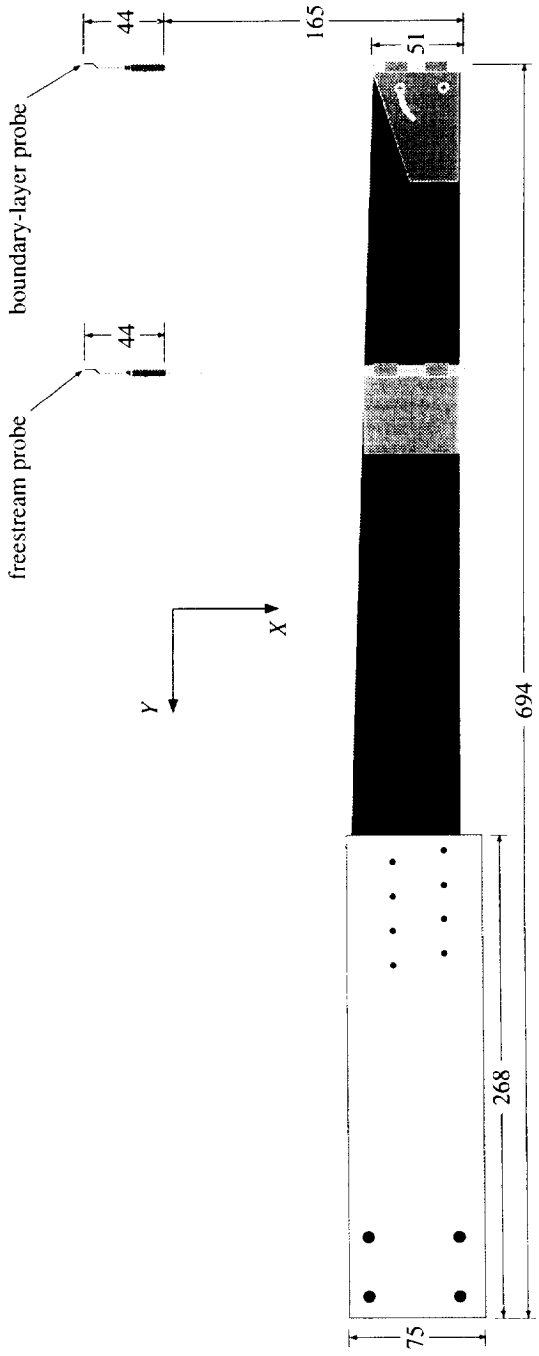

Figure 2.4: Plan view of hot-wire sting. All dimensions in millimeters.

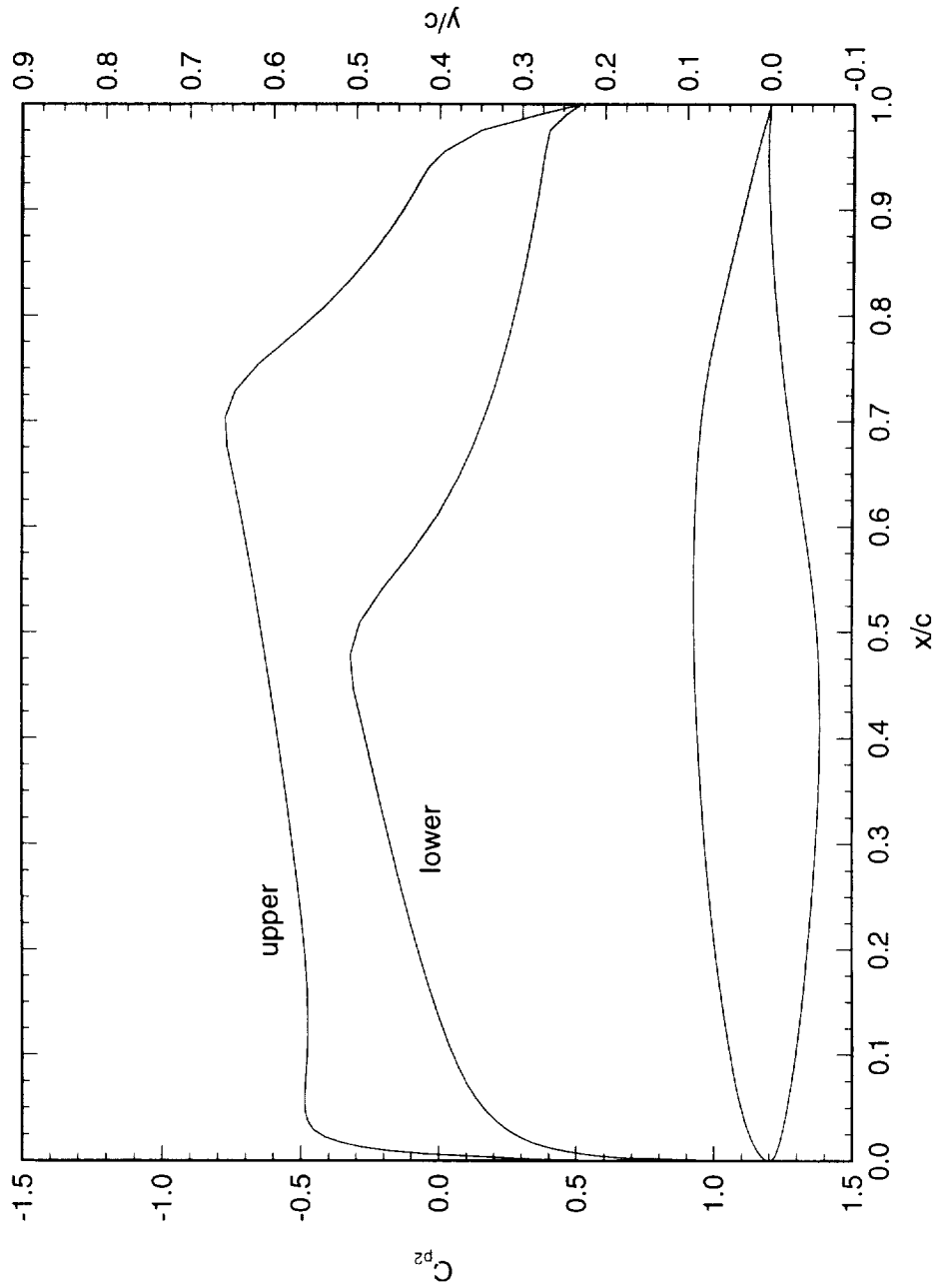

Figure 3.1: Unswept NLF(2)-0415 airfoil and free-air C_p for $\alpha = 0°$ and $\delta_F = 0°$.

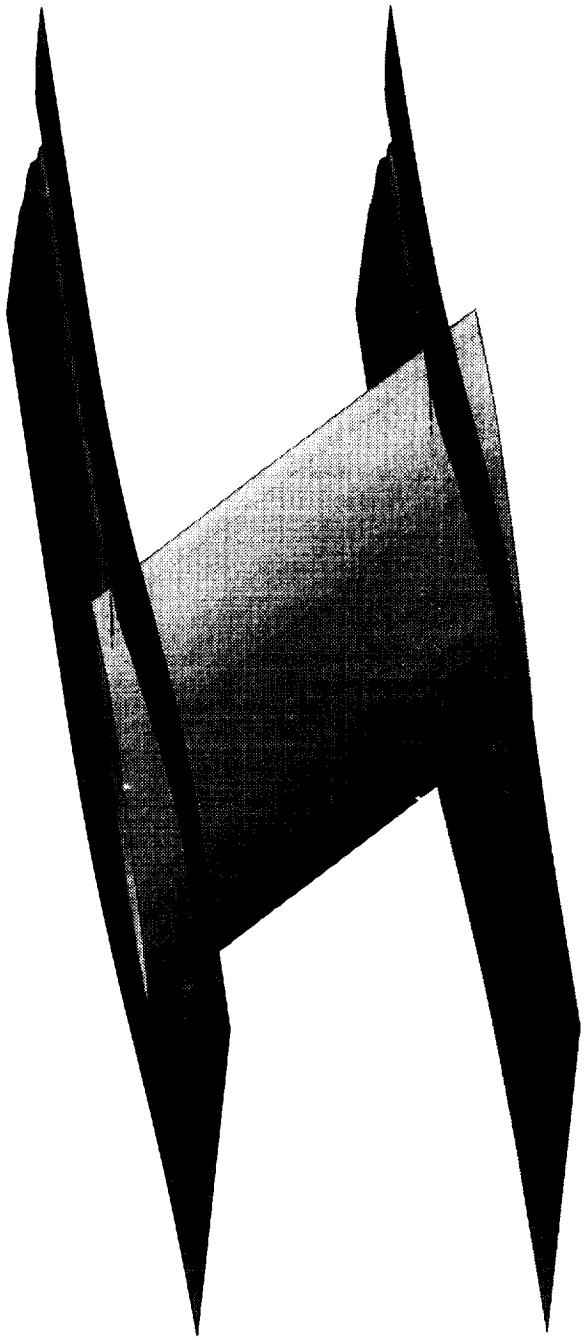

Figure 3.2: Test-section end liners and NLF(2)-0415 airfoil for $\alpha = -4°$.

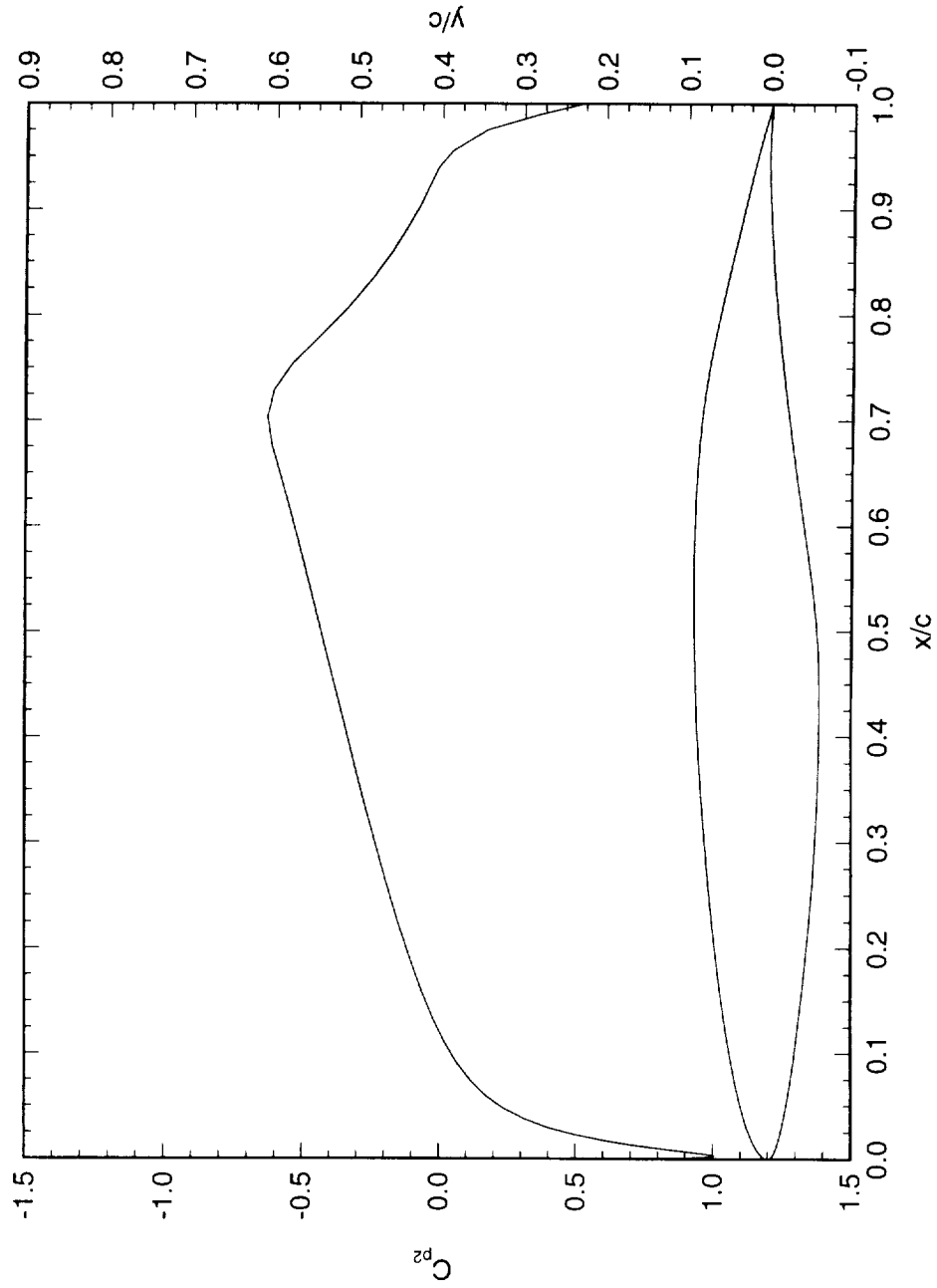

Figure 3.3: Unswept NLF(2)-0415 airfoil and upper-surface free-air C_p for $\alpha = -4°$ and $\delta_F = 0°$.

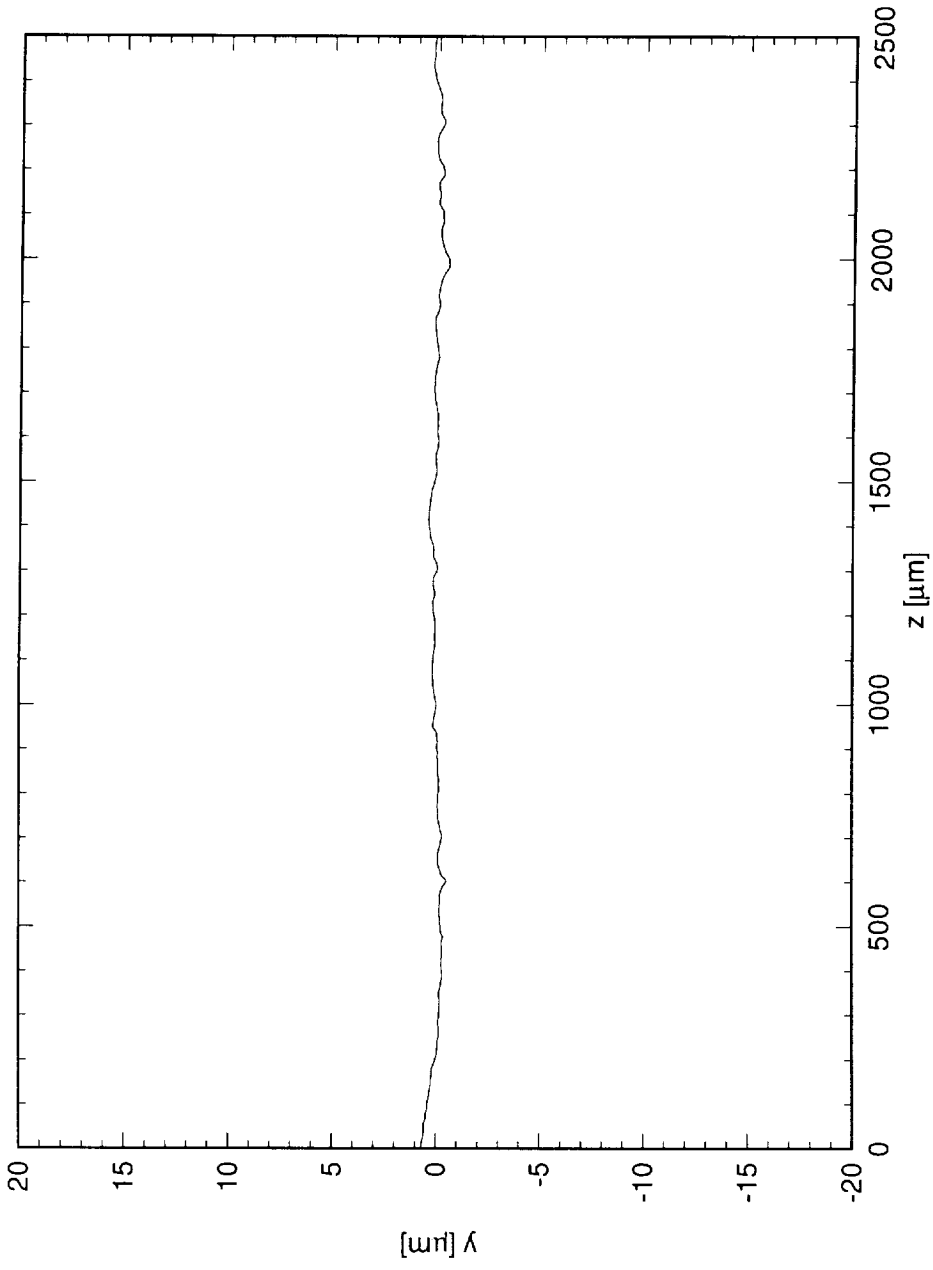

Figure 3.4: Profilometer measurement of NLF(2)-0415 surface finish. Filtered 20–1500 μm, 0.12 μm rms.

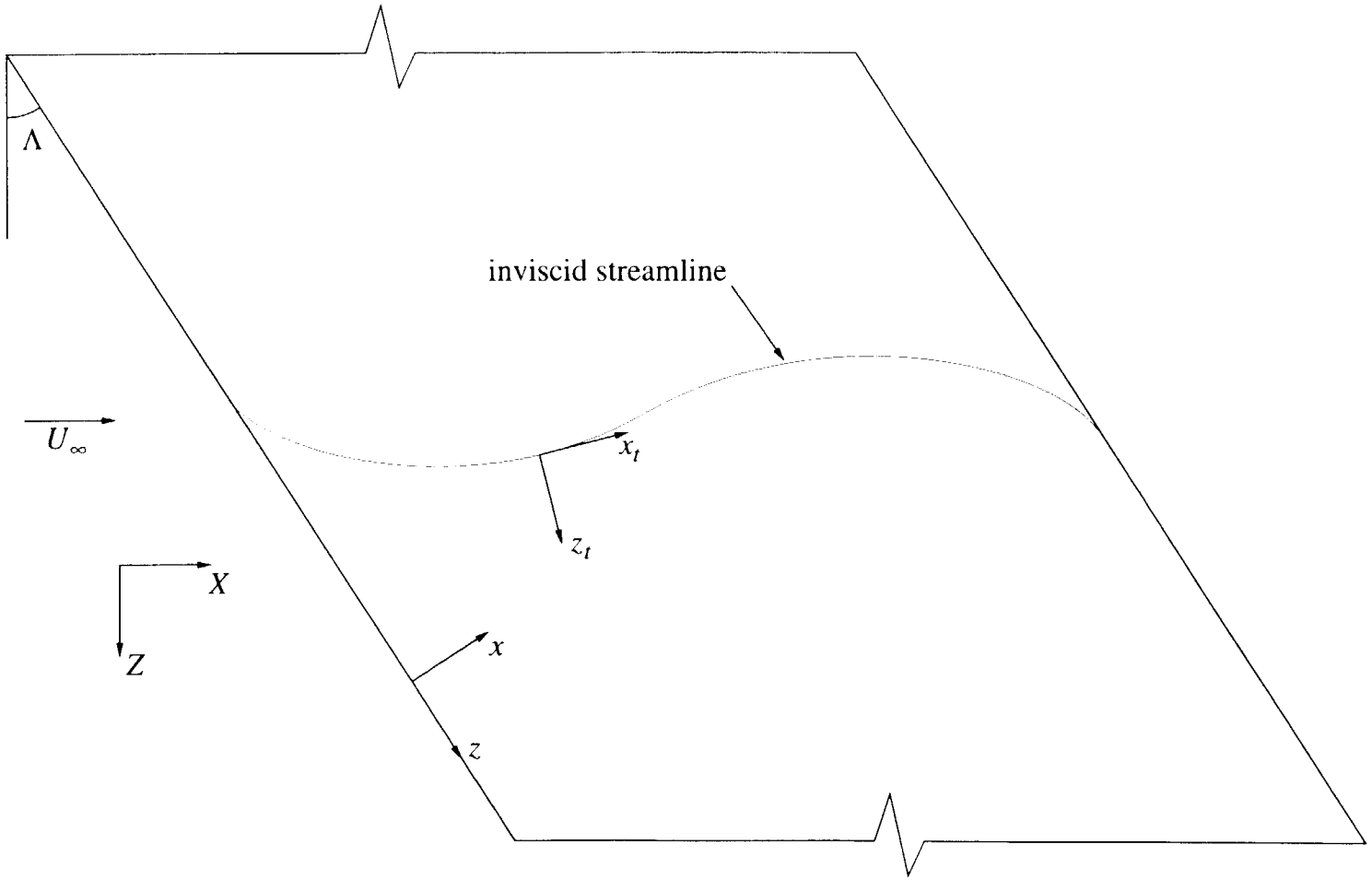

Figure 3.5: Schematic plan view of swept wing showing coordinate systems and curved inviscid streamline.

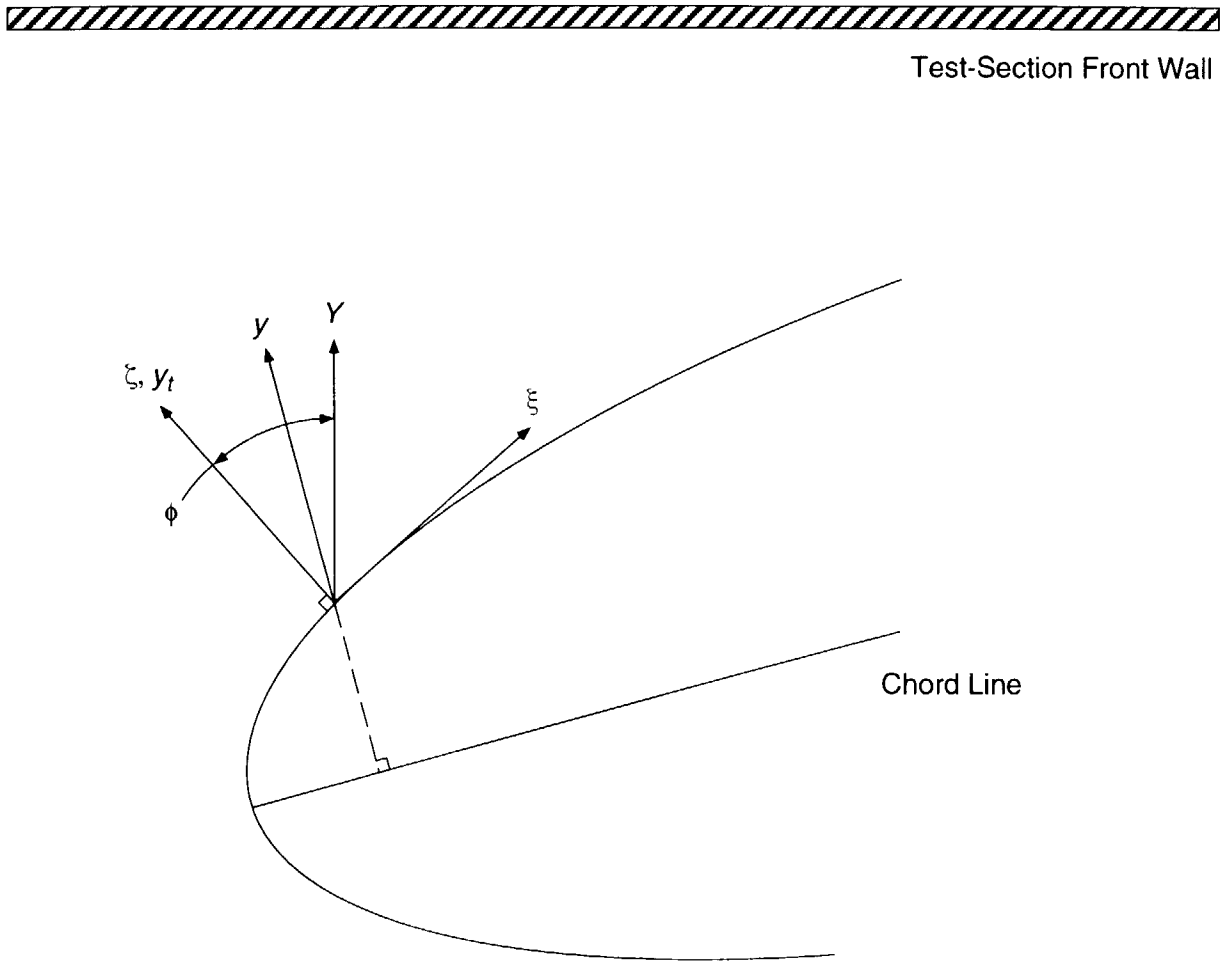

Figure 3.6: Schematic cross section of swept wing showing coordinate systems.

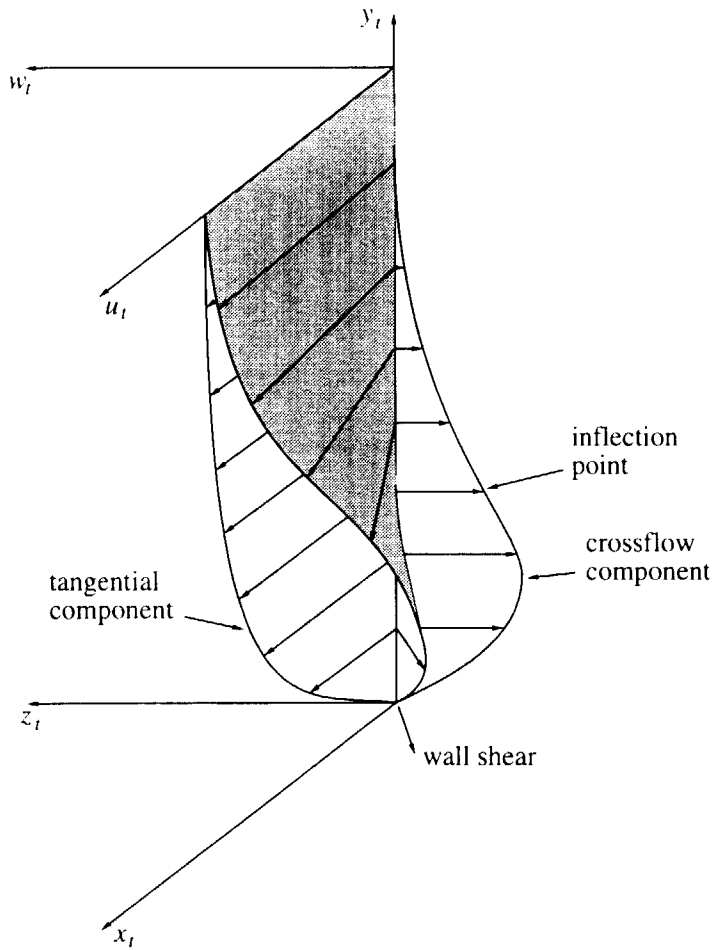

Figure 3.7: Schematic of swept wing boundary-layer profile showing the tangential, crossflow, and total velocity profile.

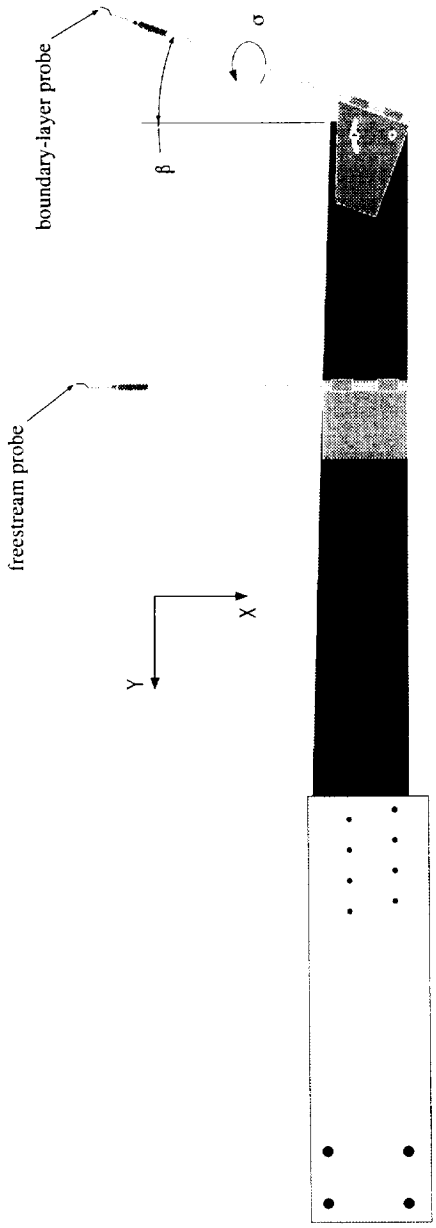

Figure 3.8: Instrumentation sting showing probe rotations required by local surface curvature effects.

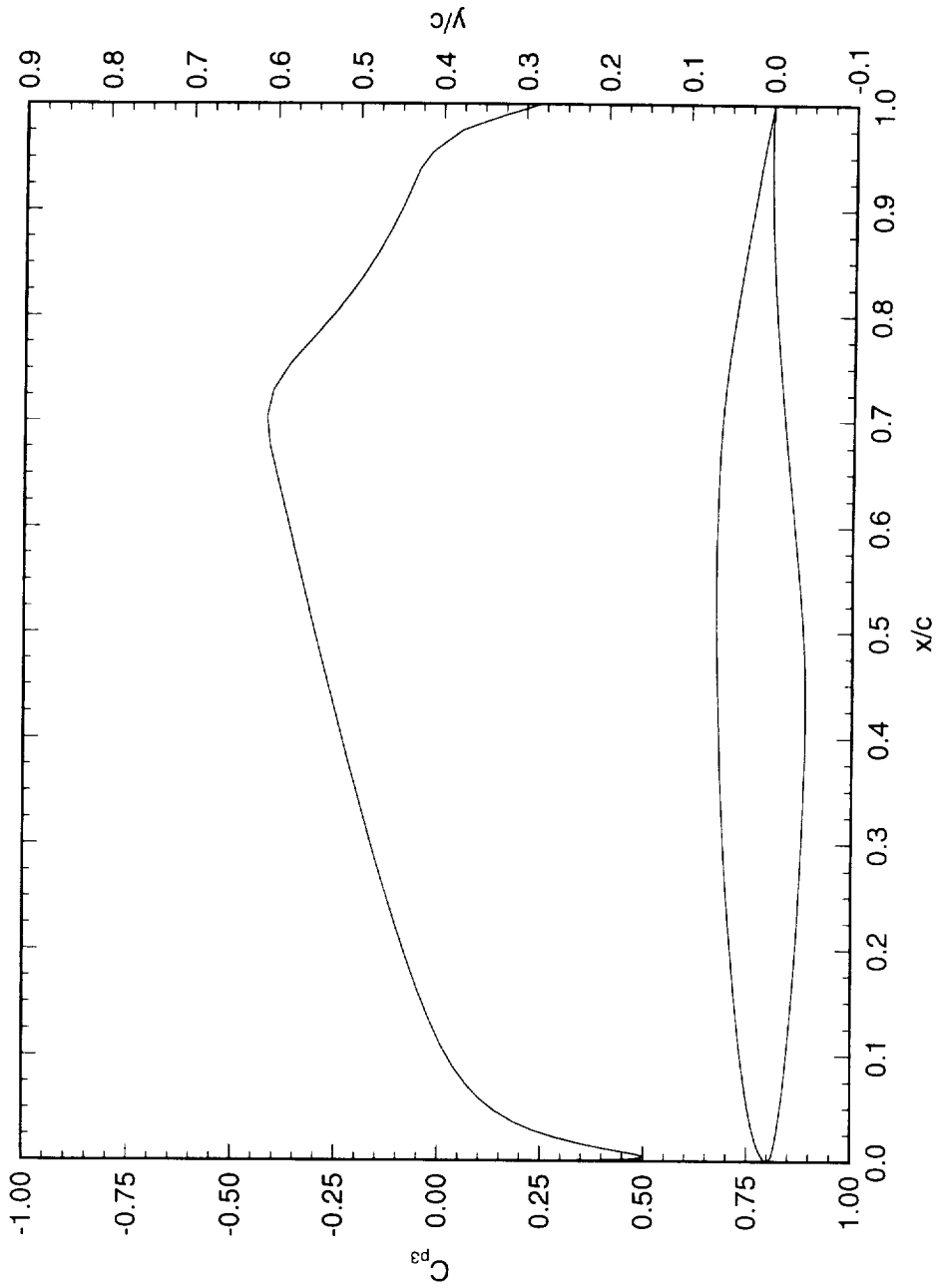

Figure 3.9: Swept NLF(2)-0415 airfoil and upper-surface C_p for $\alpha = -4°$ and $\delta_F = 0°$. The C_p is computed with the wind-tunnel walls in place.

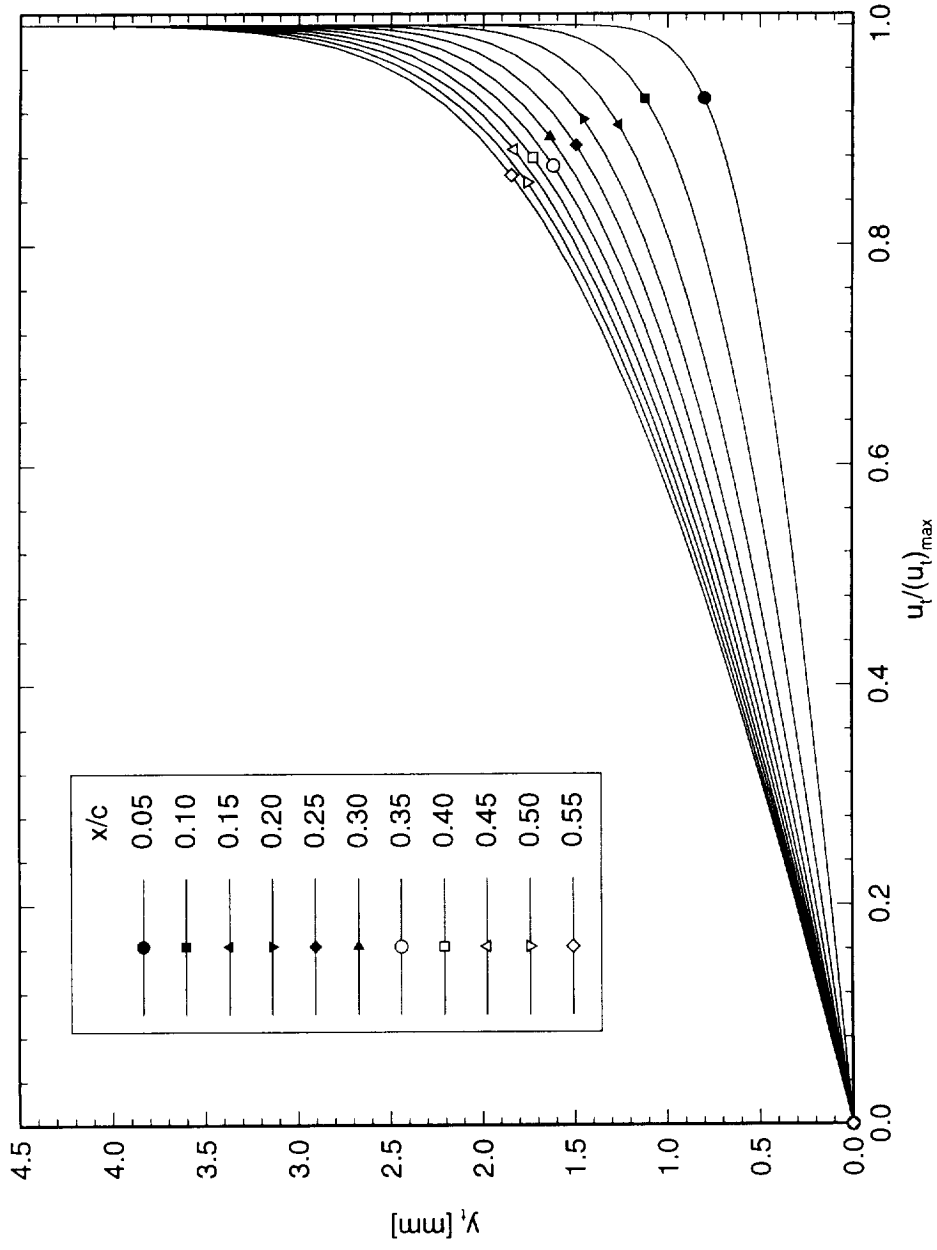

Figure 3.10: Theoretical basic-state boundary-layer profiles for $\alpha = -4°$, $Re_c = 2.4 \times 10^6$. Tangential (u_t) component.

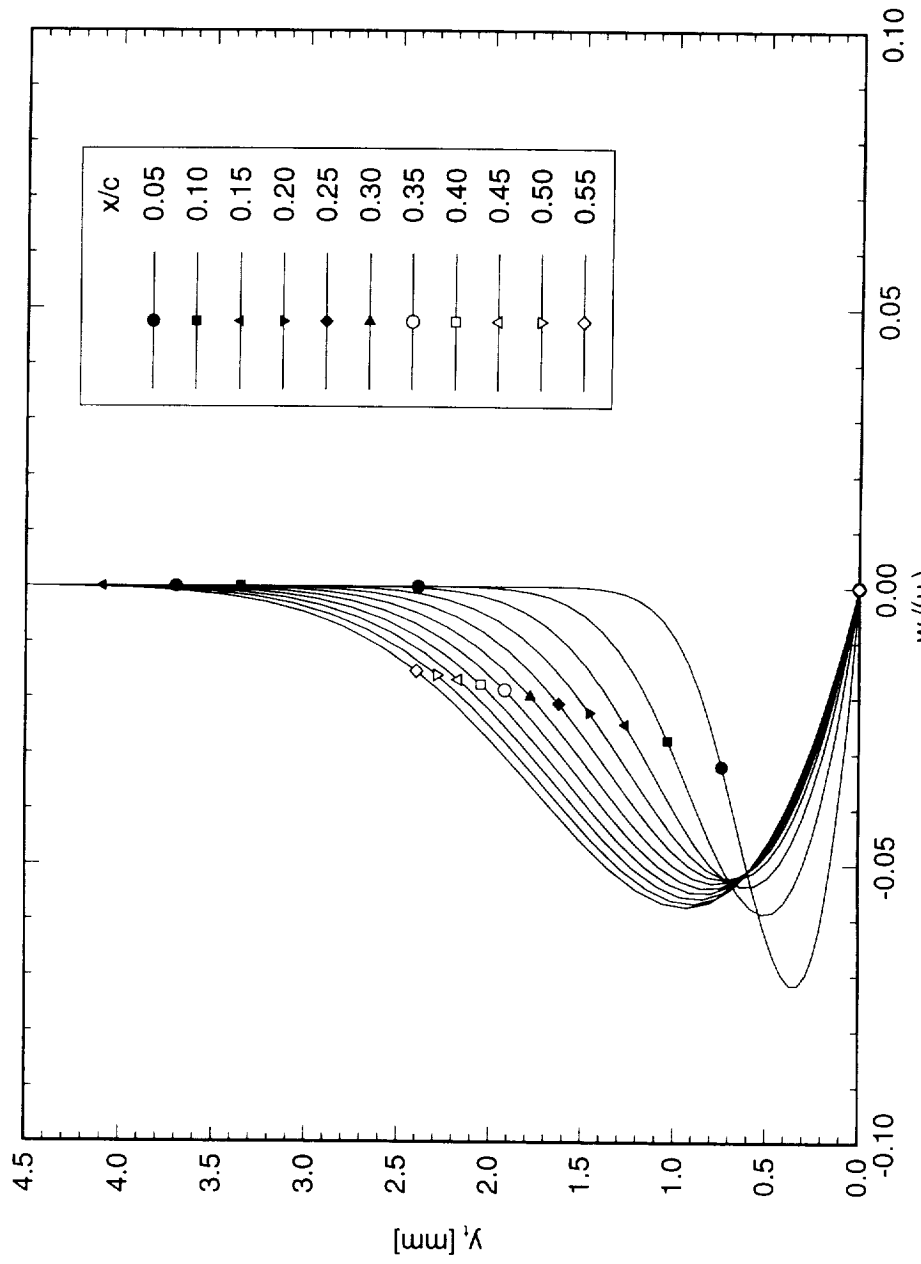

Figure 3.11: Theoretical basic-state boundary-layer profiles for $\alpha = -4°$, $Re_c = 2.4 \times 10^6$. Crossflow (w_t) component.

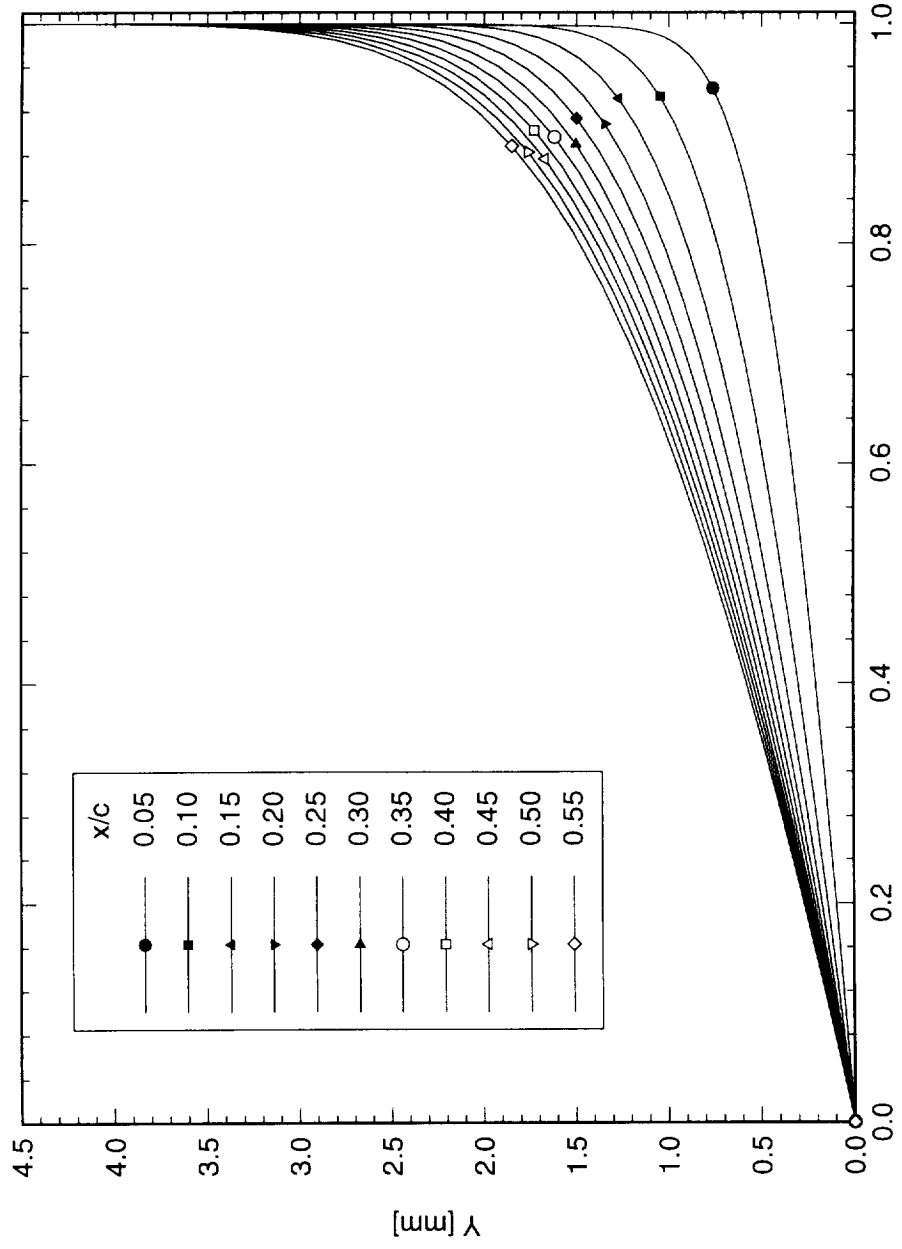

Figure 3.12: Theoretical basic-state boundary-layer profiles for $\alpha = -4^\circ$, $Re_c = 2.4 \times 10^6$. Streamwise (u) component.

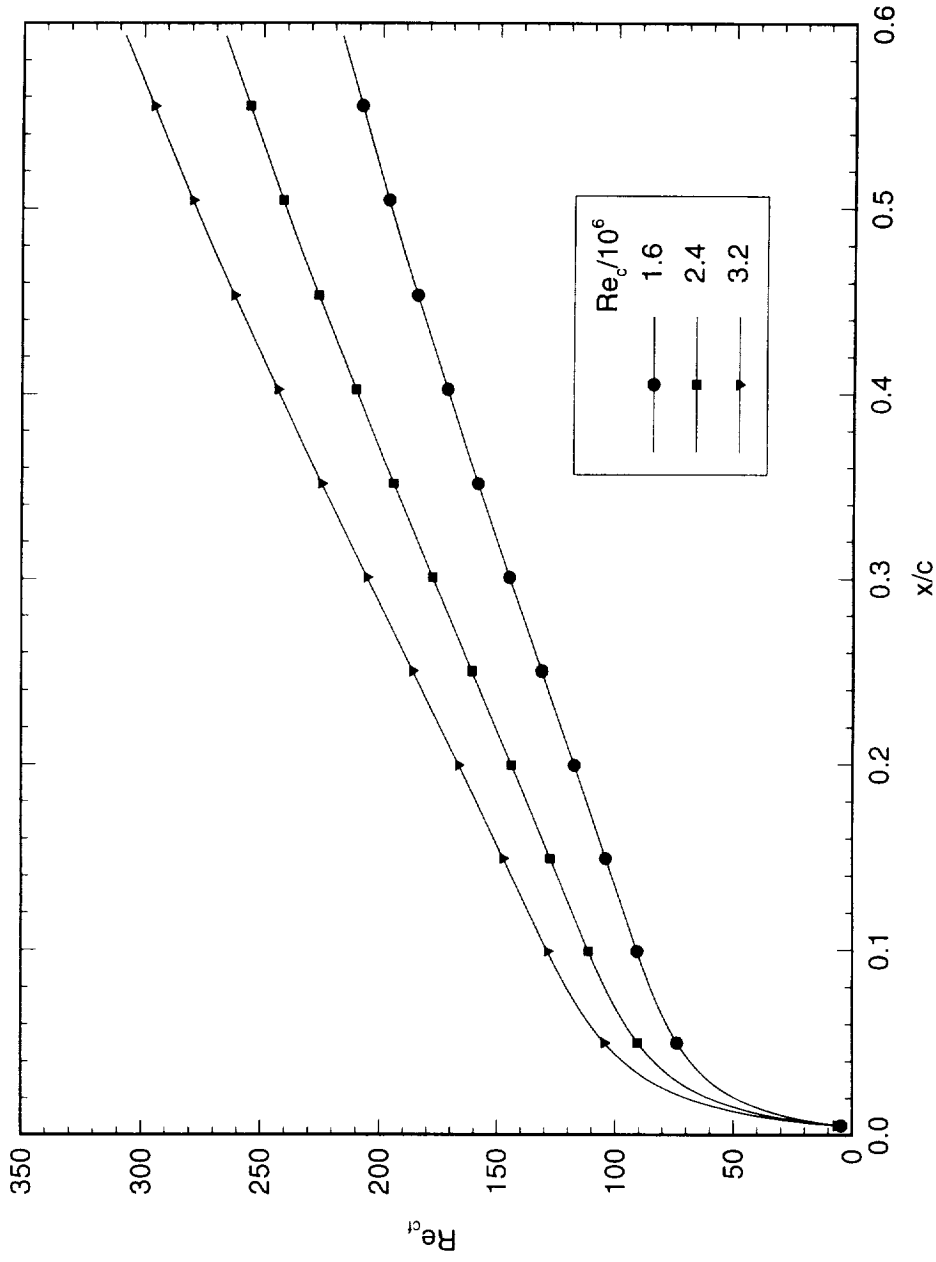

Figure 3.13: Theoretical crossflow Reynolds numbers for $\alpha = -4°$.

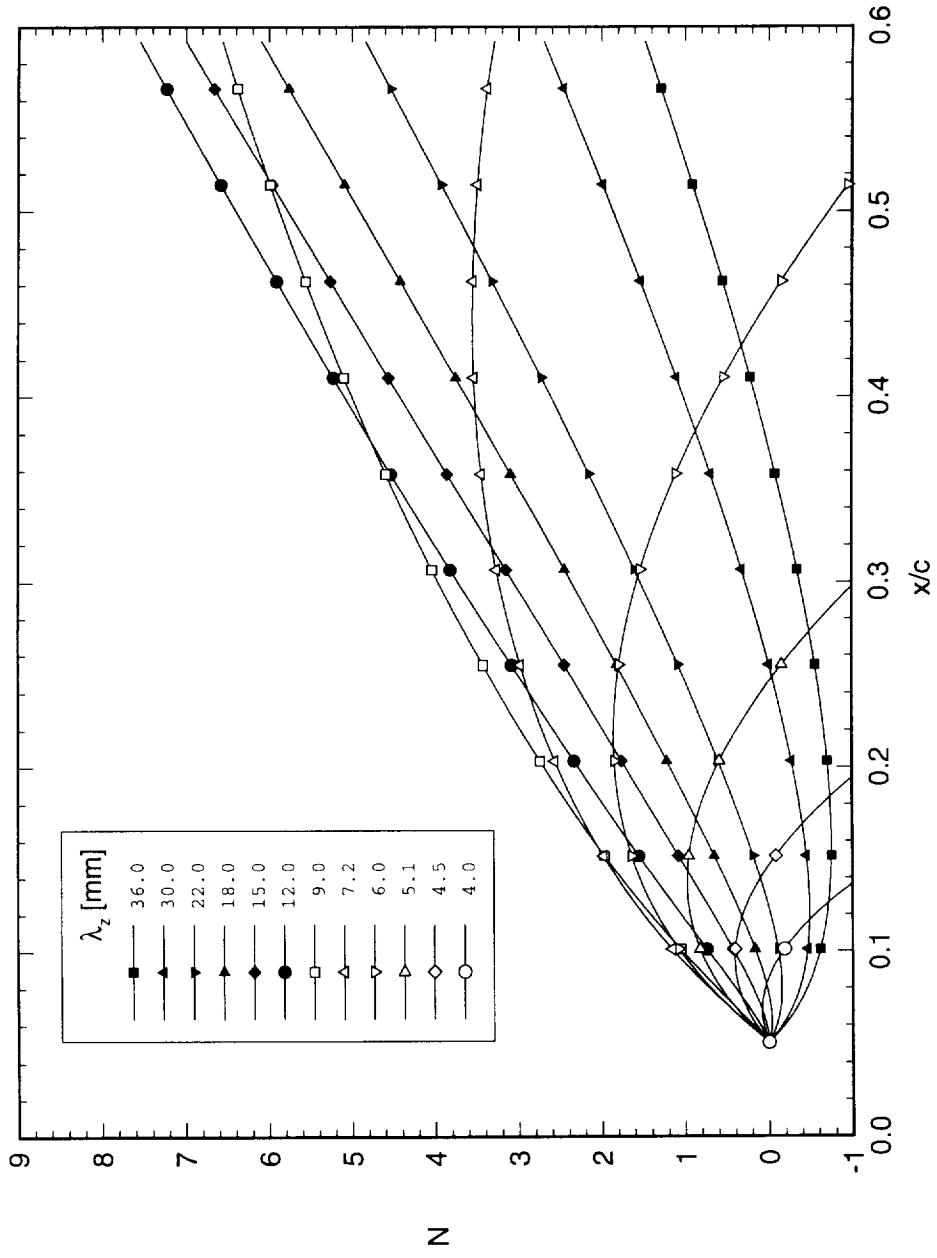

Figure 3.14: Linear theory N-factors for stationary crossflow disturbances. $Re_c = 2.4 \times 10^6$. The reference point for the N-factor calculations is $x/c = 0.05$.

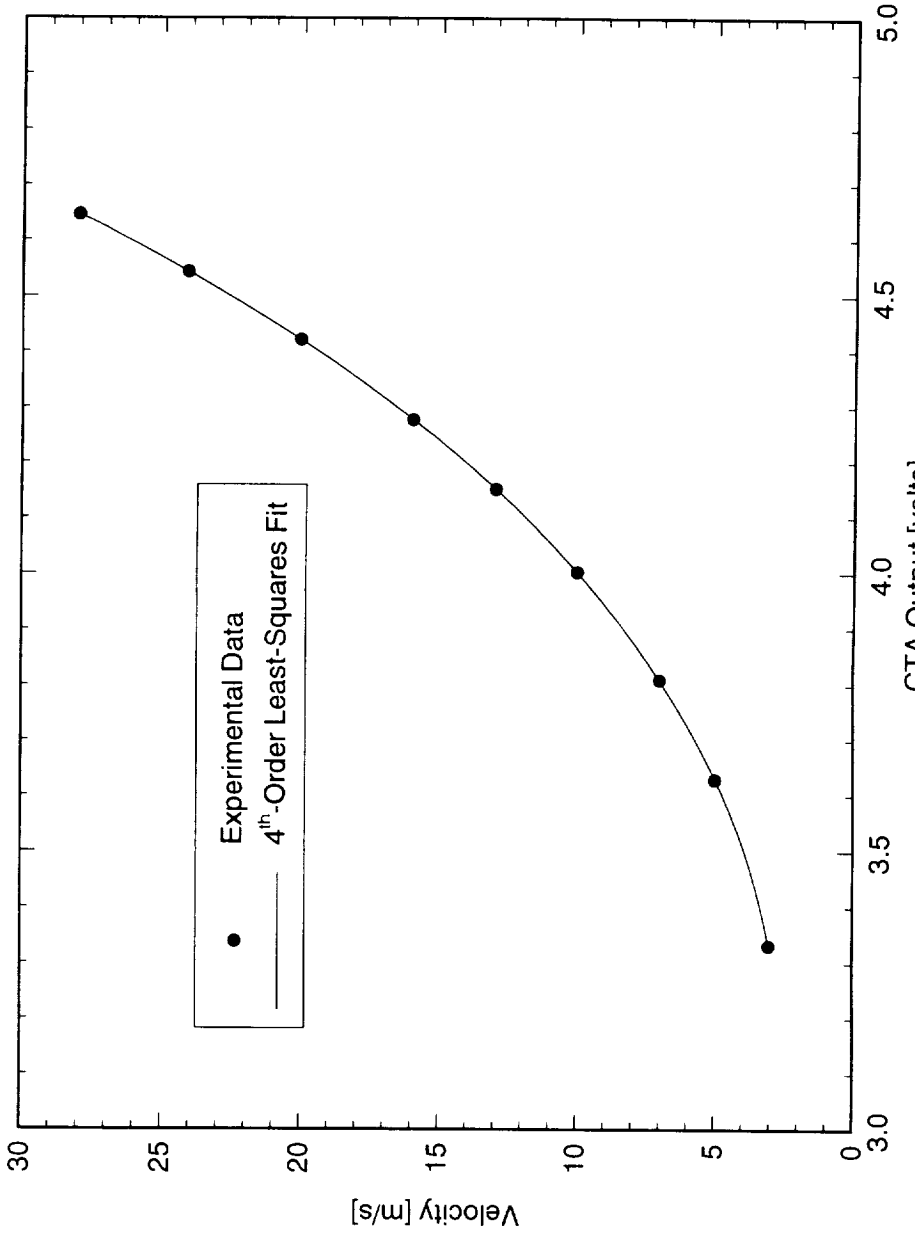

Figure 4.1: Typical hot-wire velocity calibration.

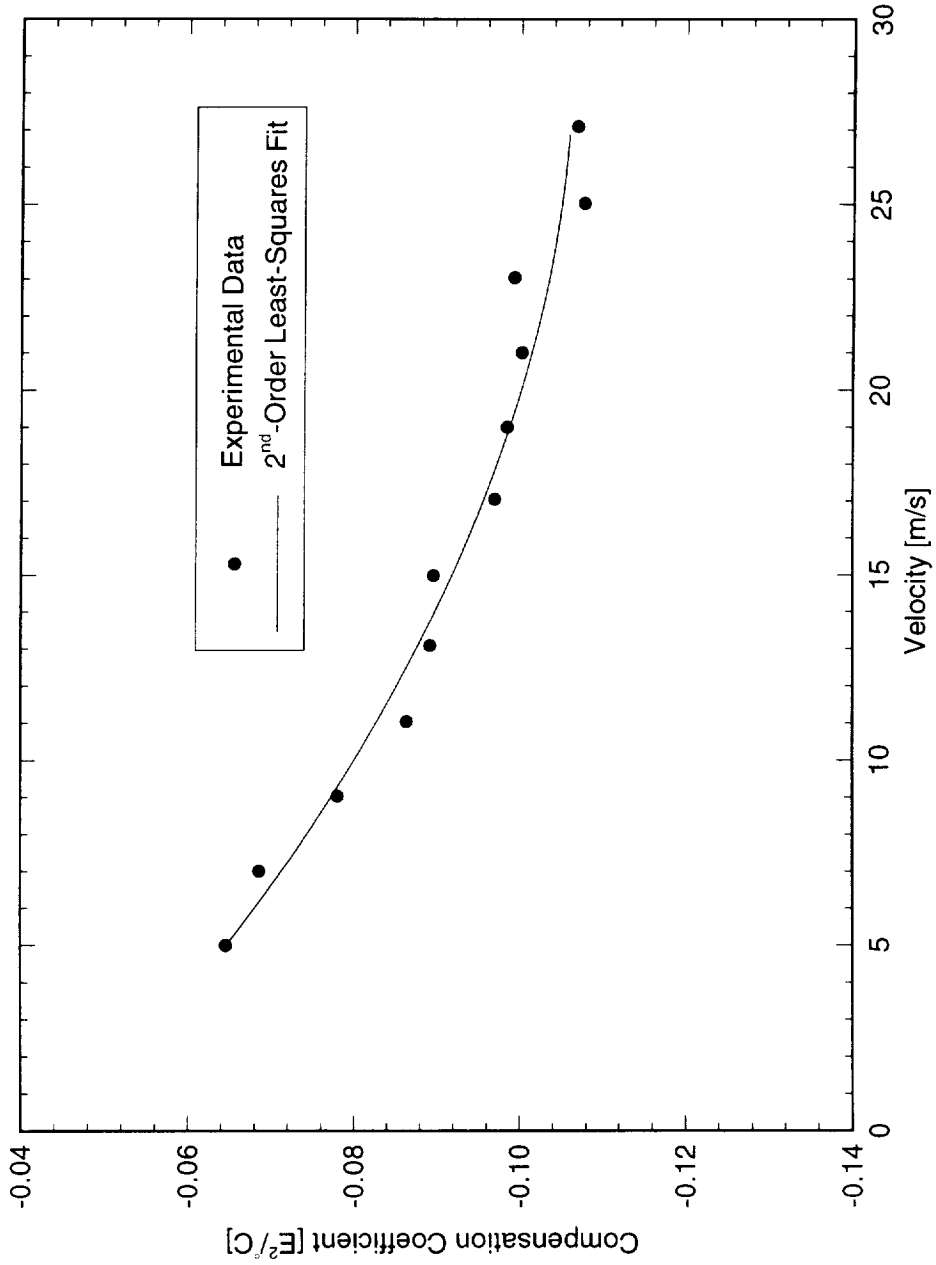

Figure 4.2: Typical hot-wire temperature compensation. The scatter in the data is caused by short sampling times.

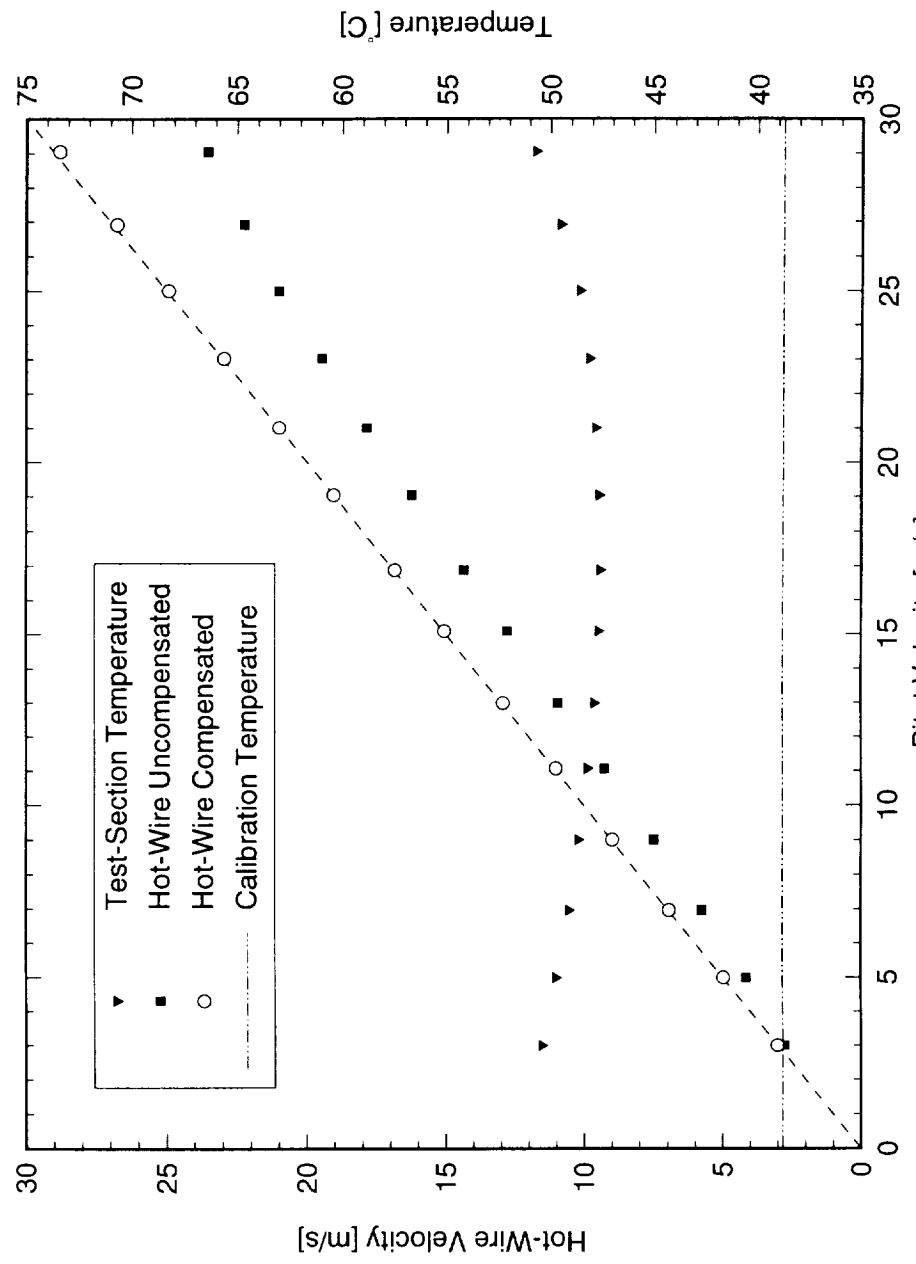

Figure 4.3: Comparison of inferred hot-wire velocity with and without temperature compensation. The uncompensated velocity readings suffer from errors exceeding 15%. With compensation the error is less than 1% over the entire speed range.

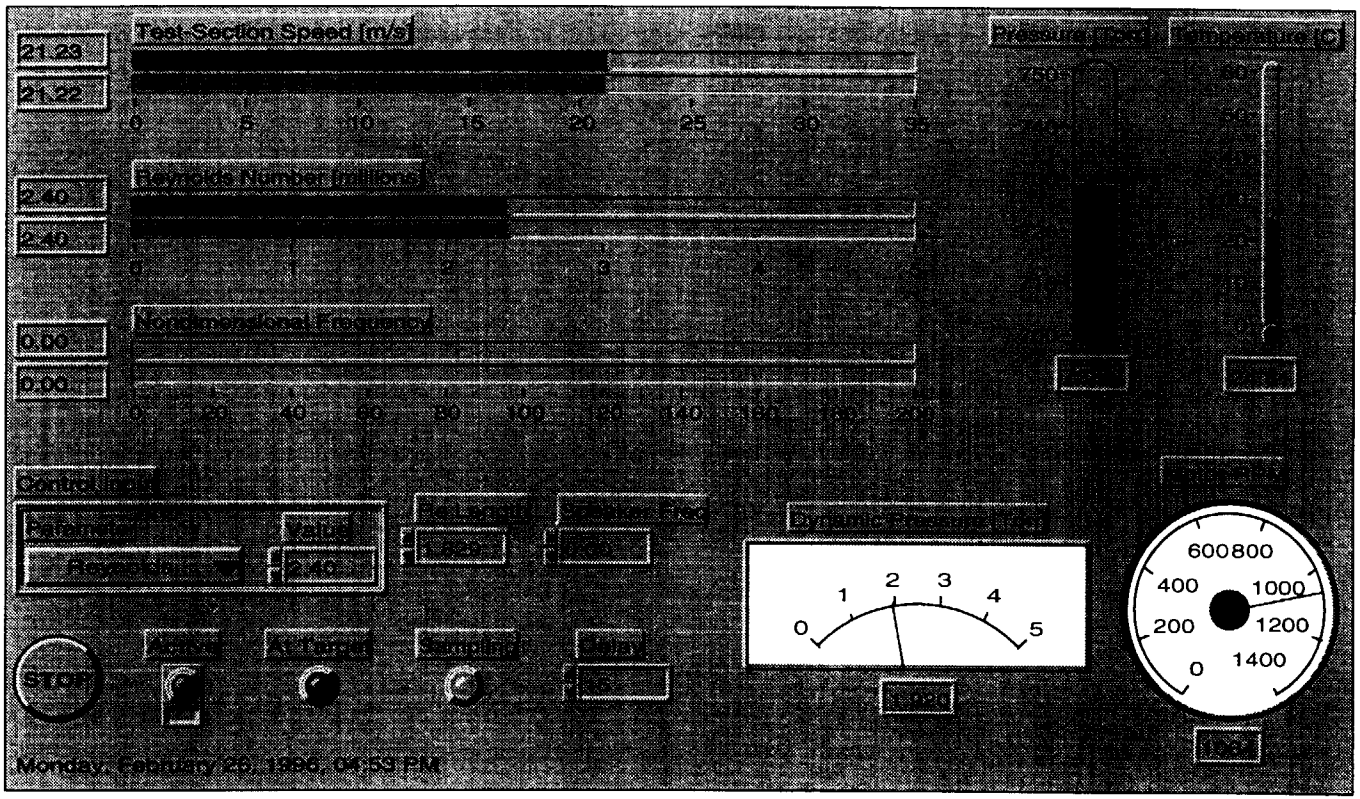

Figure 4.4: Wind tunnel "cruise control" program. The test-section speed, Reynolds number, and nondimensional frequency are represented with dual sliders. For each set, the lower slider is the target and the upper slider is the measured value.

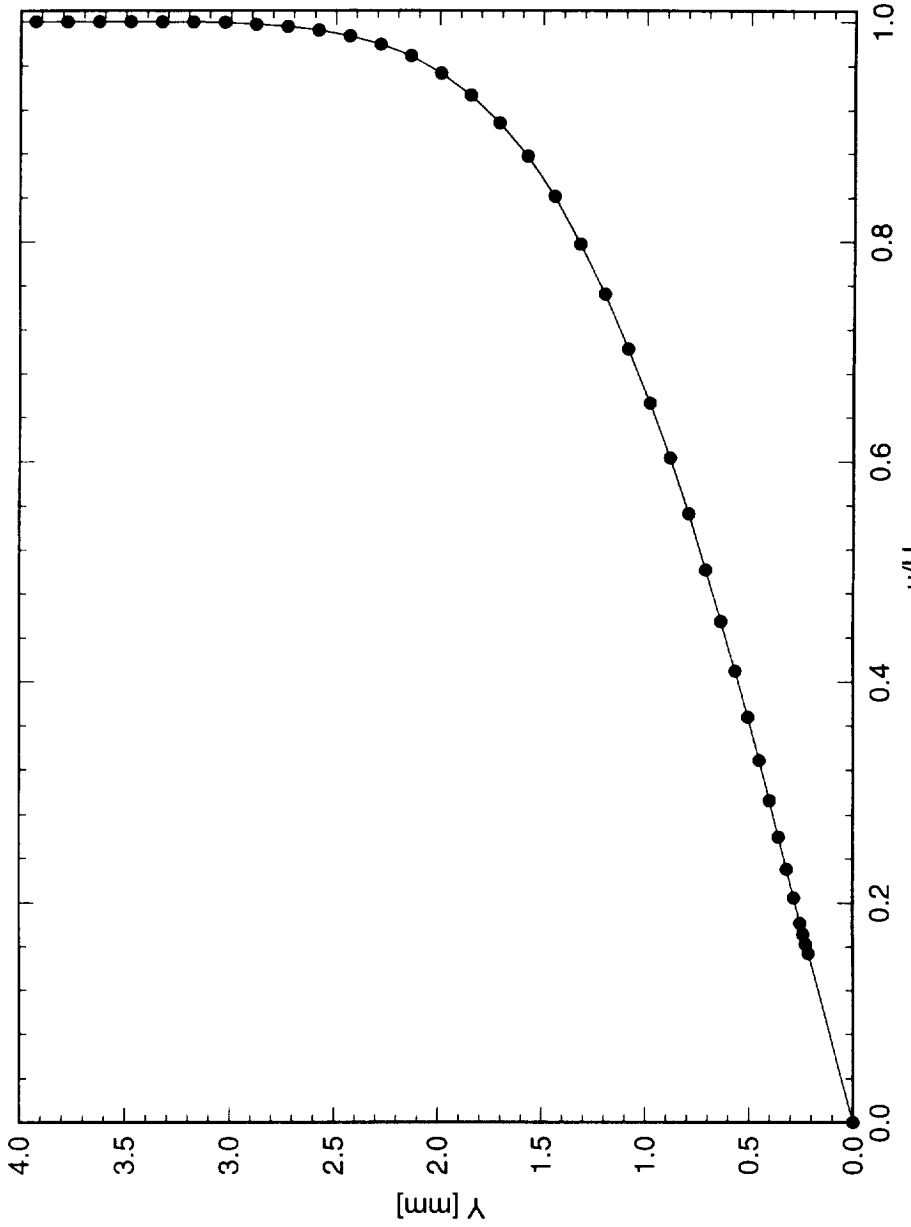

Figure 4.5: Typical boundary-layer profile scan. $Re_c = 1.6 \times 10^6$, $x/c = 0.20$.

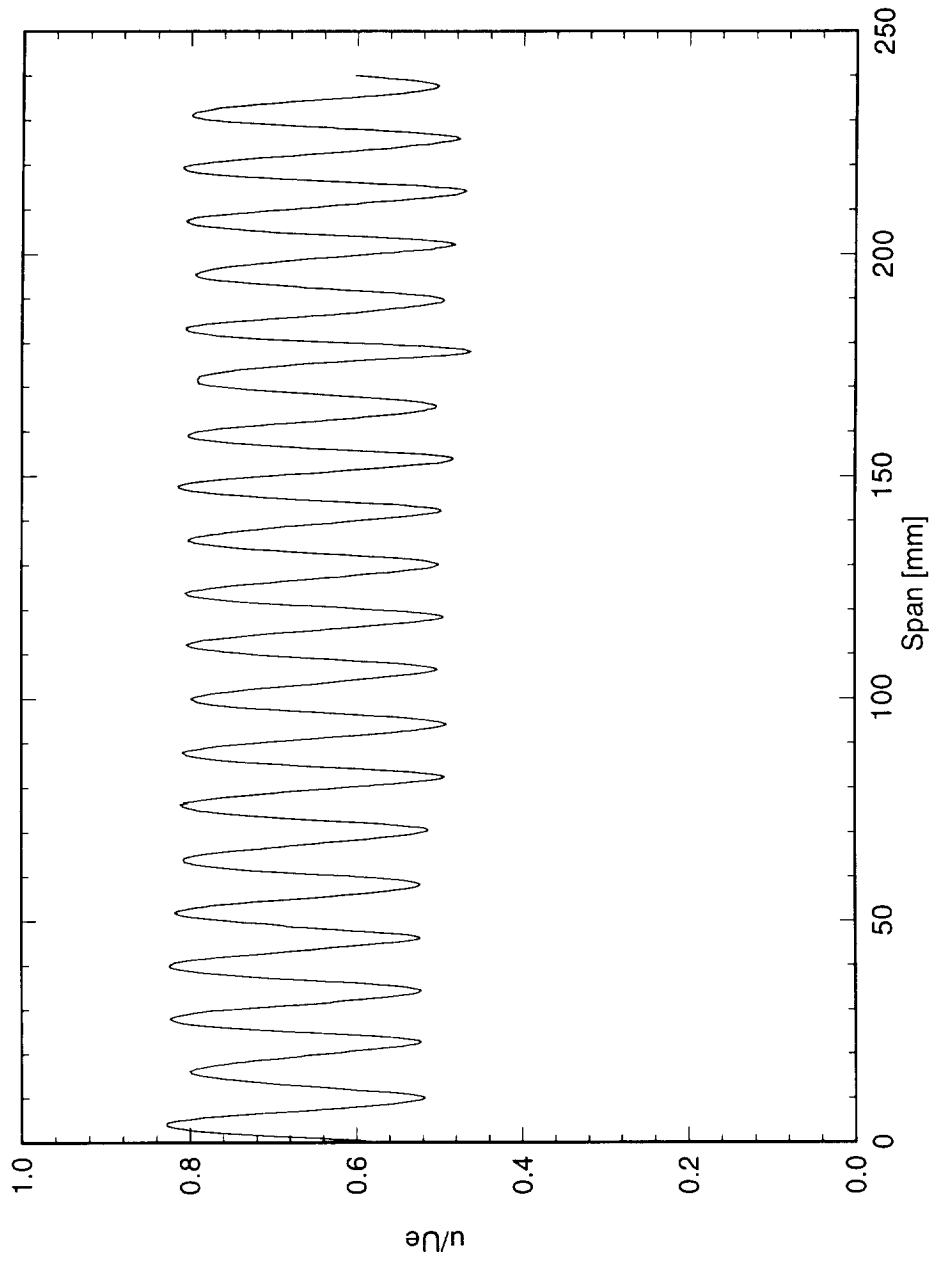

Figure 4.6: Typical spanwise hot-wire scan at constant Y. The velocity profile shows the distortion of the mean boundary-layer flow caused by the stationary crossflow waves. Scan is at $x/c = 0.30$, $Y = 0.9$ mm. $Re_c = 2.4 \times 10^6$. A full-span array of $k = 6$ μm roughness with 12 mm spacing is at $x/c = 0.023$.

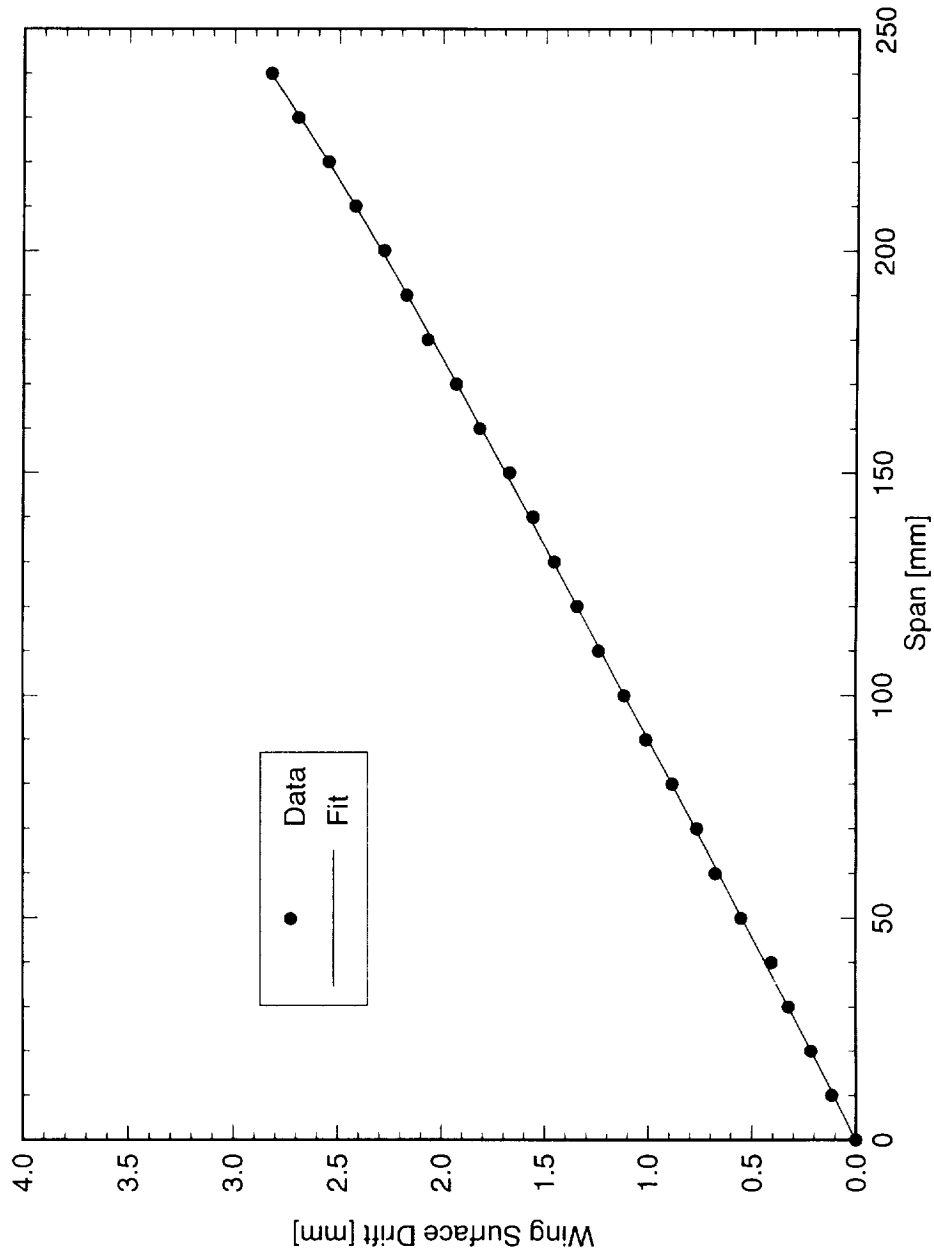

Figure 4.7: Typical spanwise traverse-alignment scan. The misalignment between the hot-wire traverse and the model is indicated by the apparent "drift" in the traverse motion. Scan is at $x/c = 0.30$. $Re_c = 2.4 \times 10^6$.

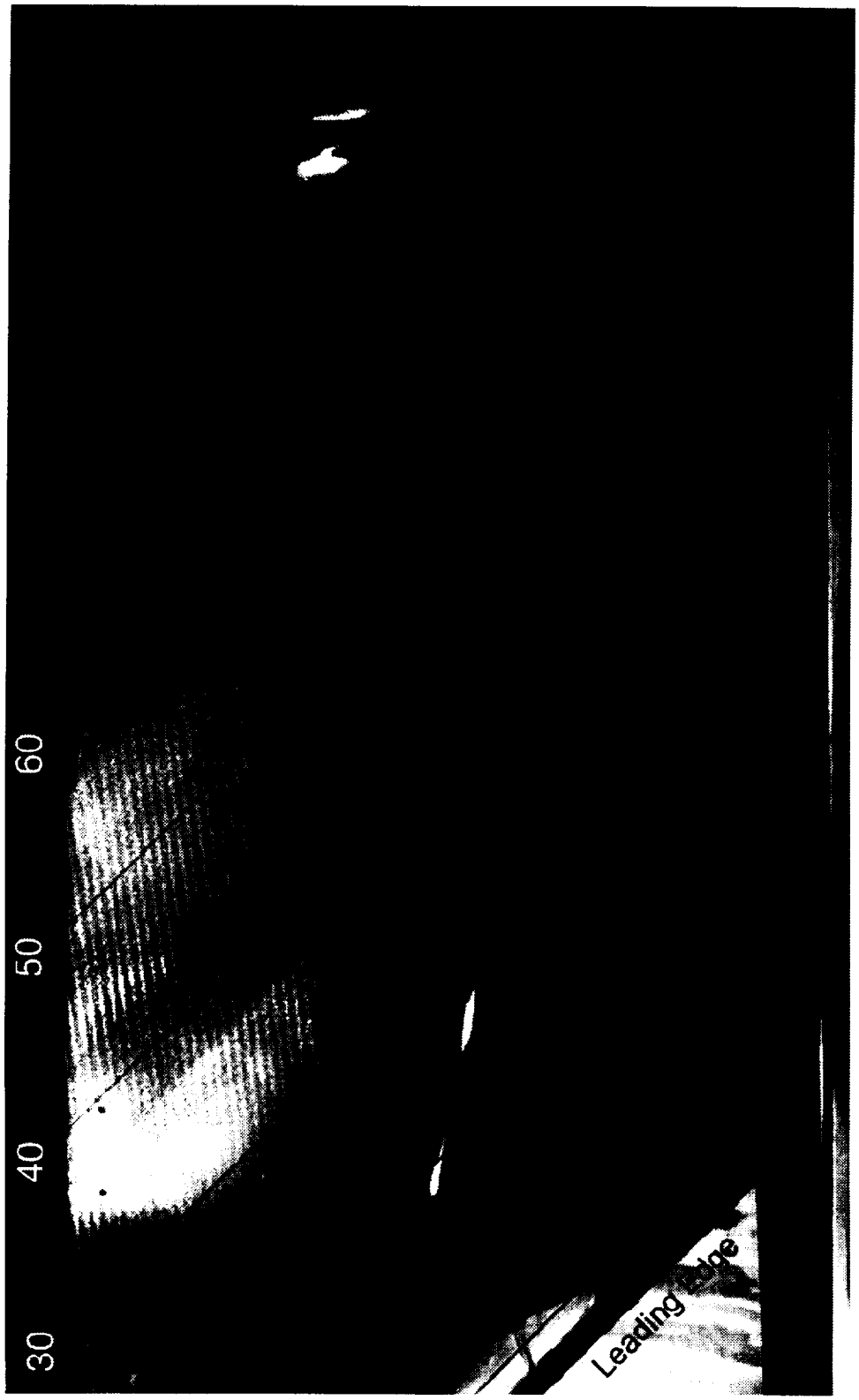

Figure 5.1: Naphthalene flow visualization for $Re_c = 2.2 \times 10^6$, [6|12] roughness.

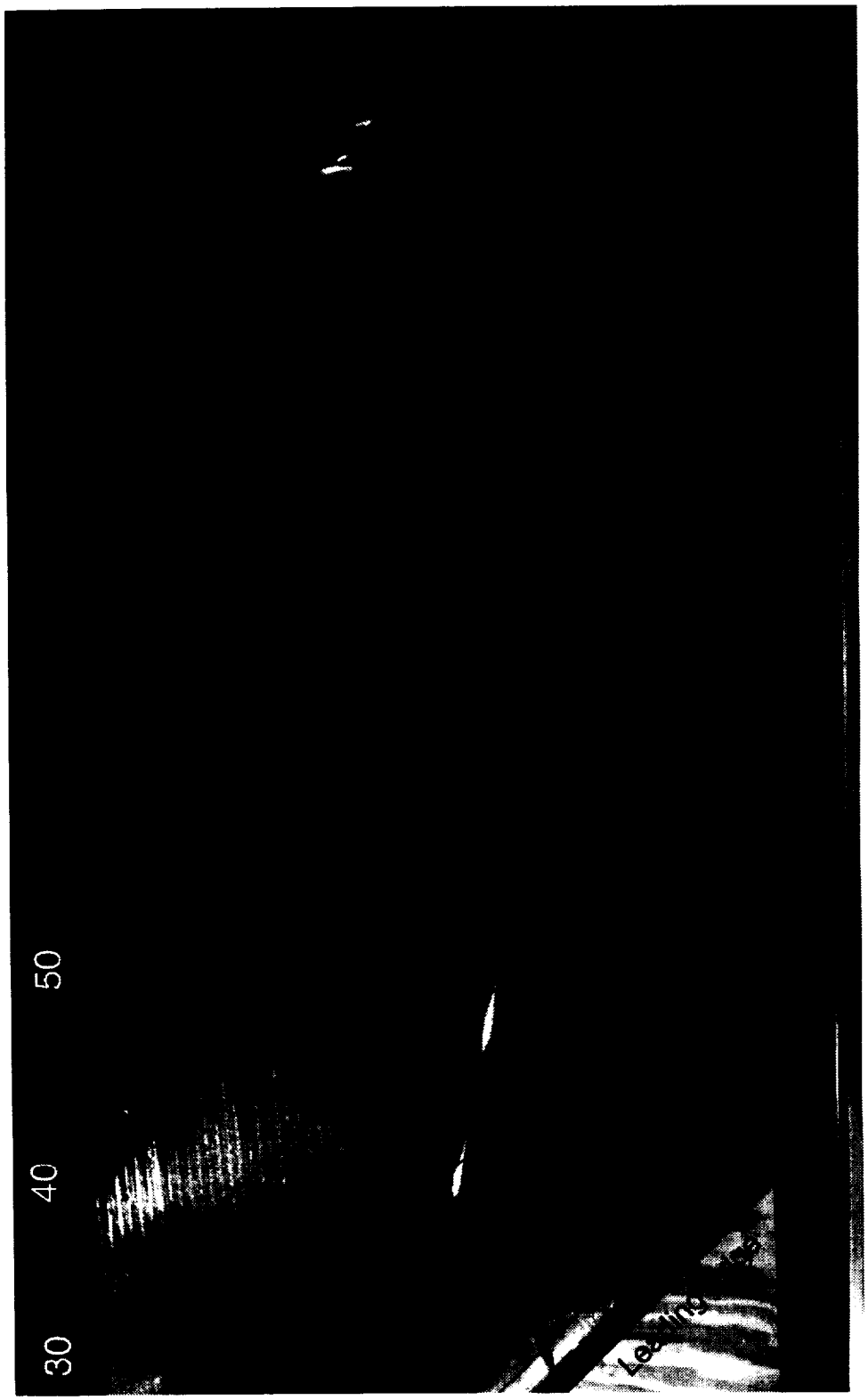

Figure 5.2: Naphthalene flow visualization for $Re_c = 3.2 \times 10^6$, [6|12] roughness.

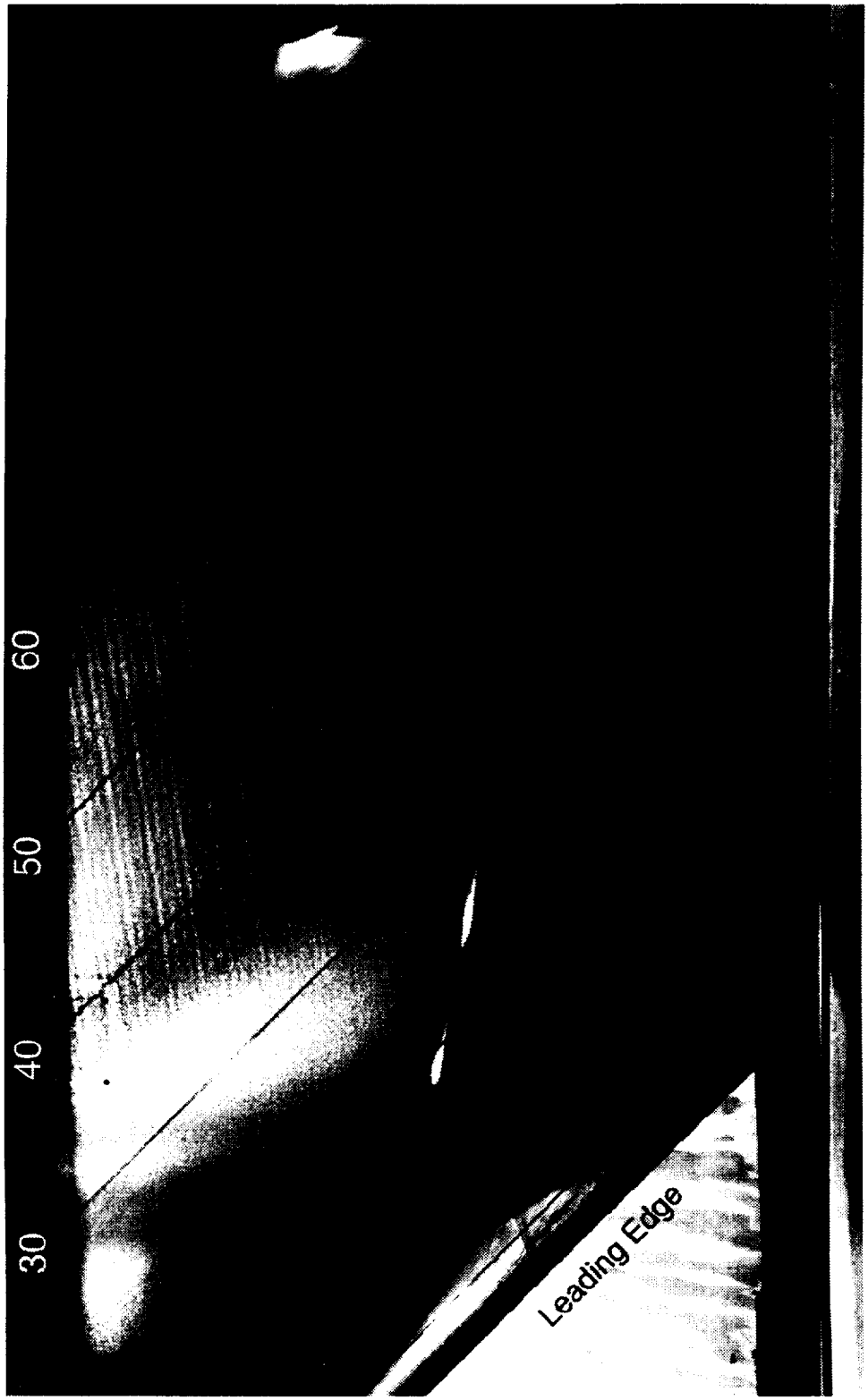

Figure 5.3: Naphthalene flow visualization for $Re_c = 2.2 \times 10^6$, [6|36] roughness.

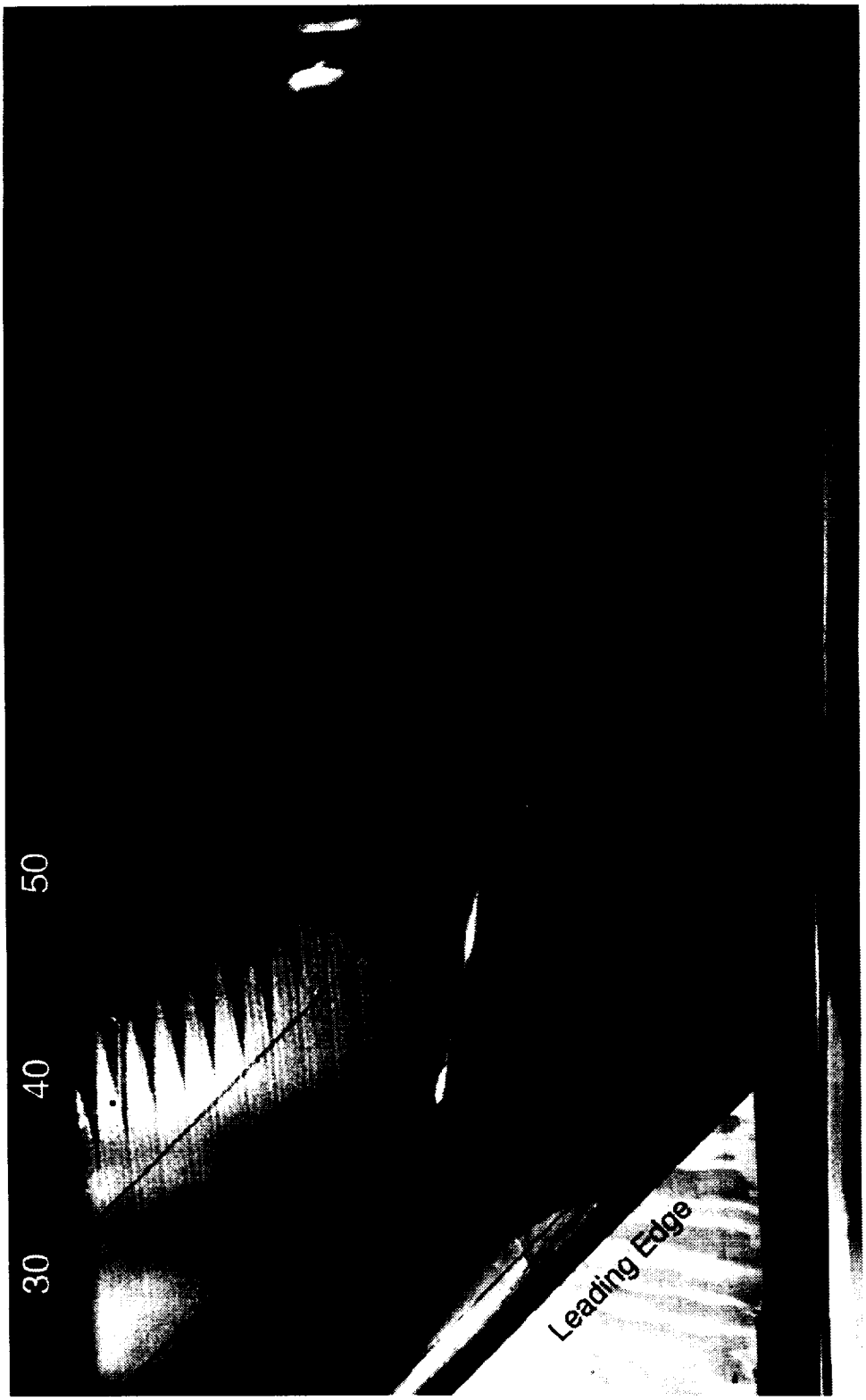

Figure 5.4: Naphthalene flow visualization for $Re_c = 3.2 \times 10^6$, [6|36] roughness.

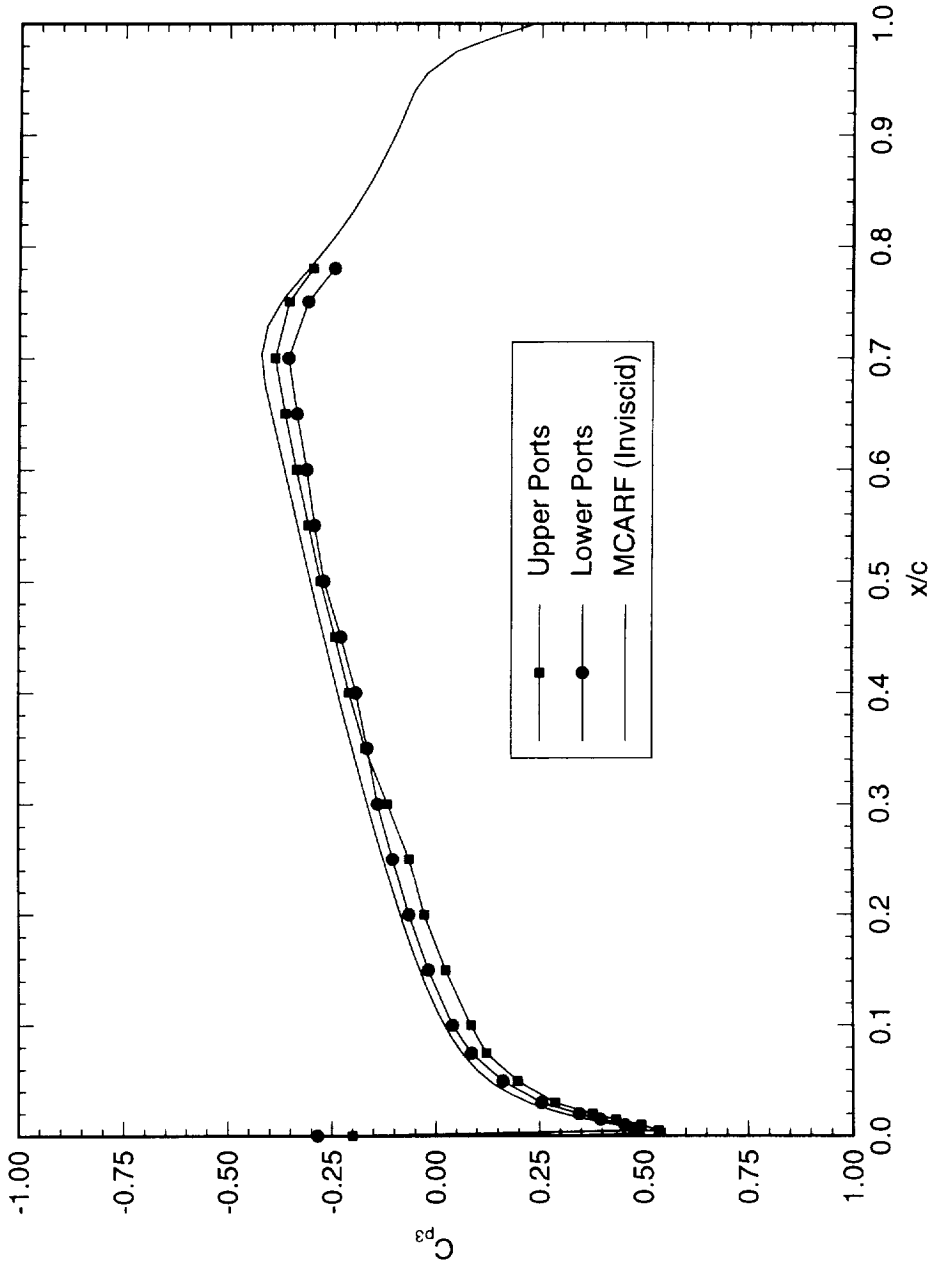

Figure 5.5: Comparison of experimental and theoretical pressure distribution for $Re_c = 1.6 \times 10^6$.

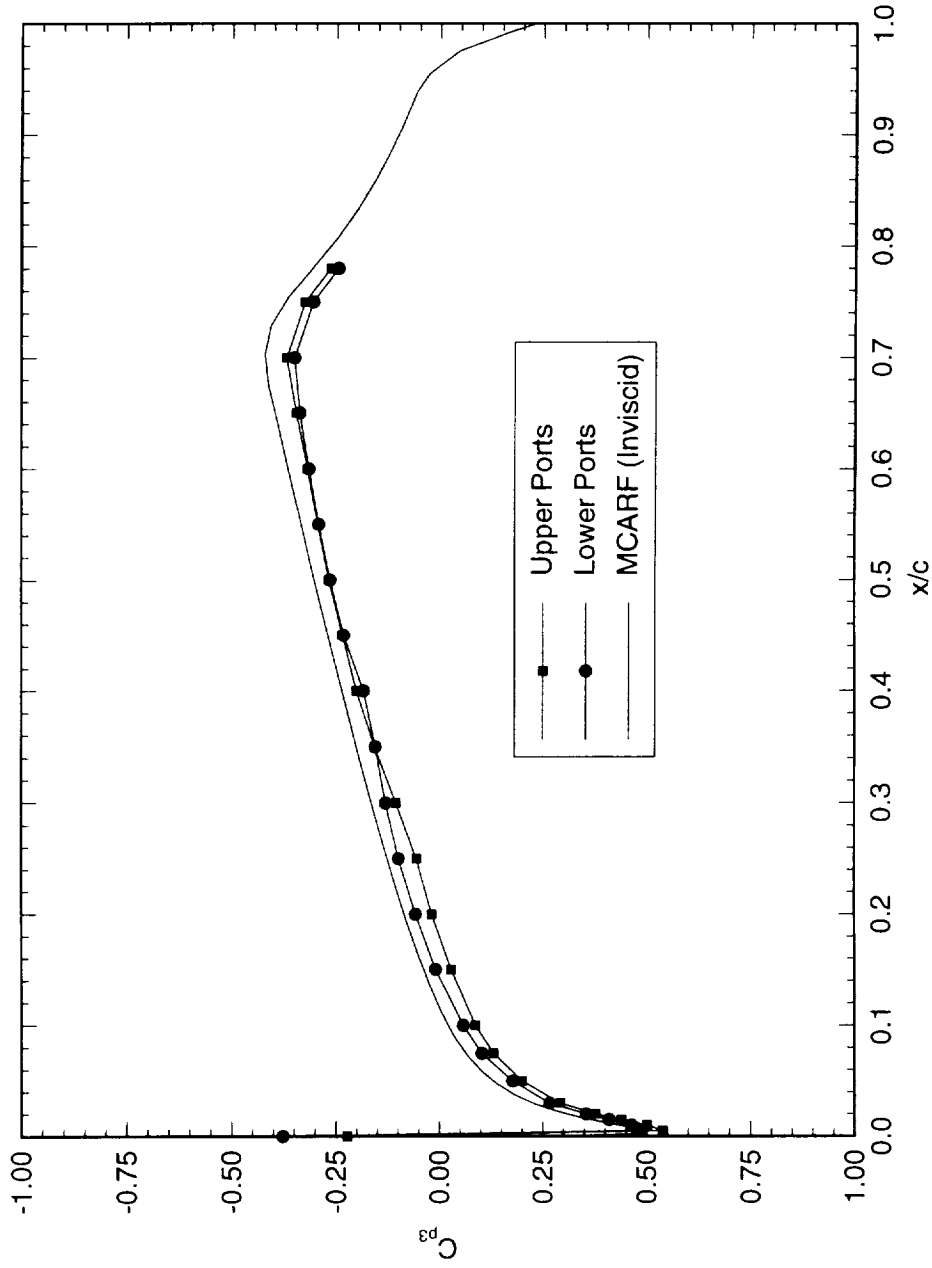

Figure 5.6: Comparison of experimental and theoretical pressure distribution for $Re_c = 2.4 \times 10^6$.

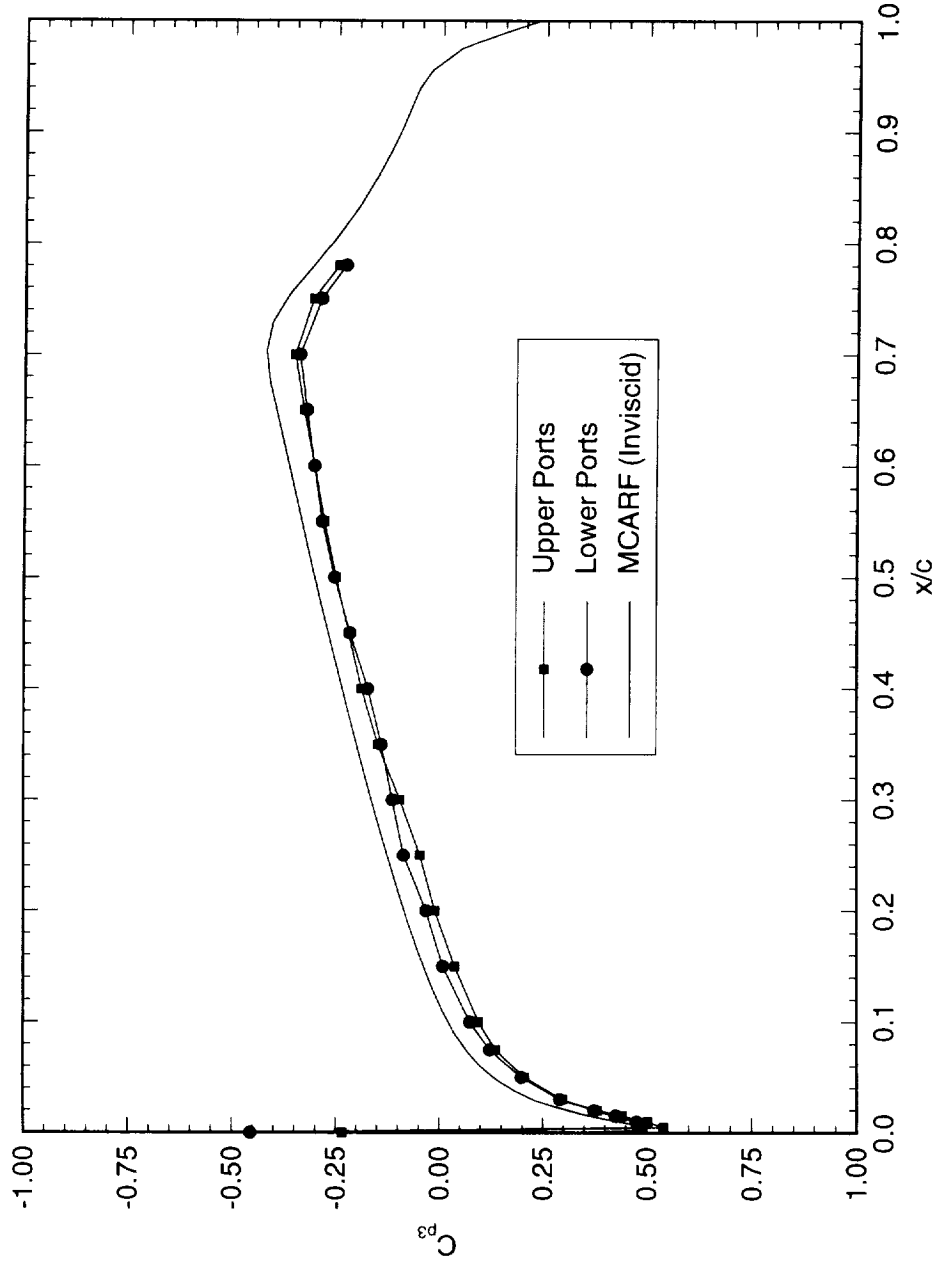

Figure 5.7: Comparison of experimental and theoretical pressure distribution for $Re_c = 3.2 \times 10^6$.

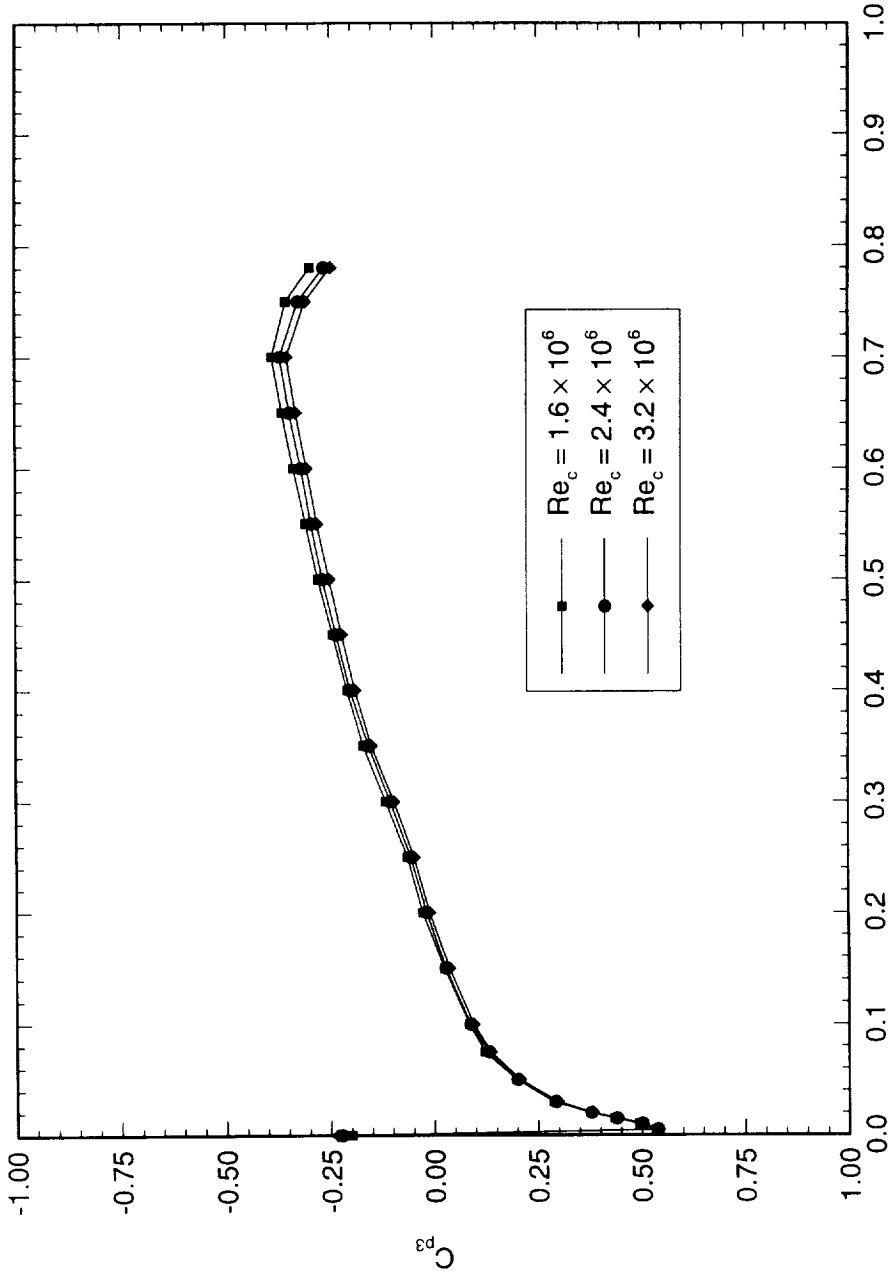

Figure 5.8: Variation of measured pressure distribution with Reynolds number. Upper ports.

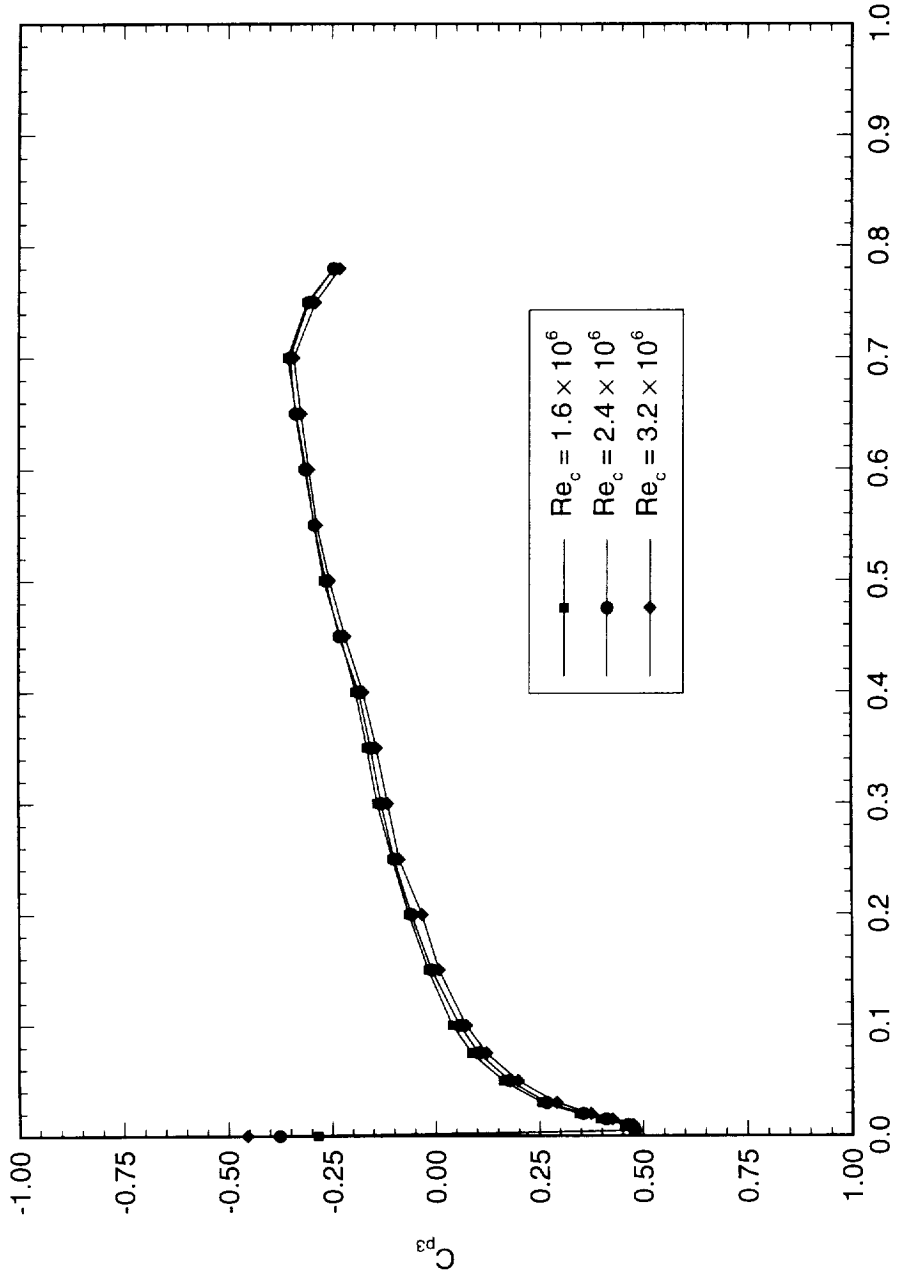

Figure 5.9: Variation of measured pressure distribution with Reynolds number. Lower ports.

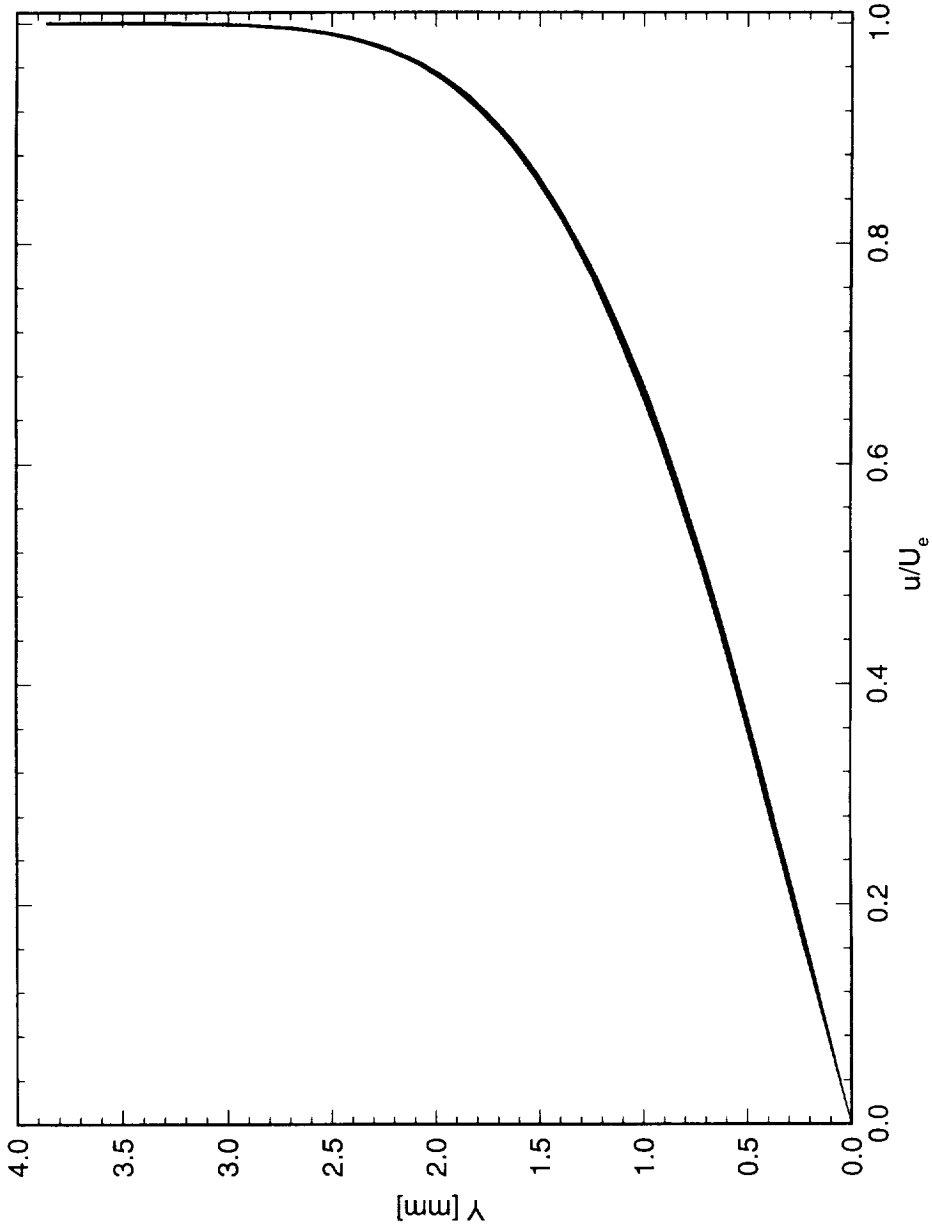

Figure 5.10: Spanwise array of 100 mean-flow boundary-layer profiles covering a span of 99 mm at $x/c = 0.20$. $Re_c = 1.6 \times 10^6$, no artificial roughness.

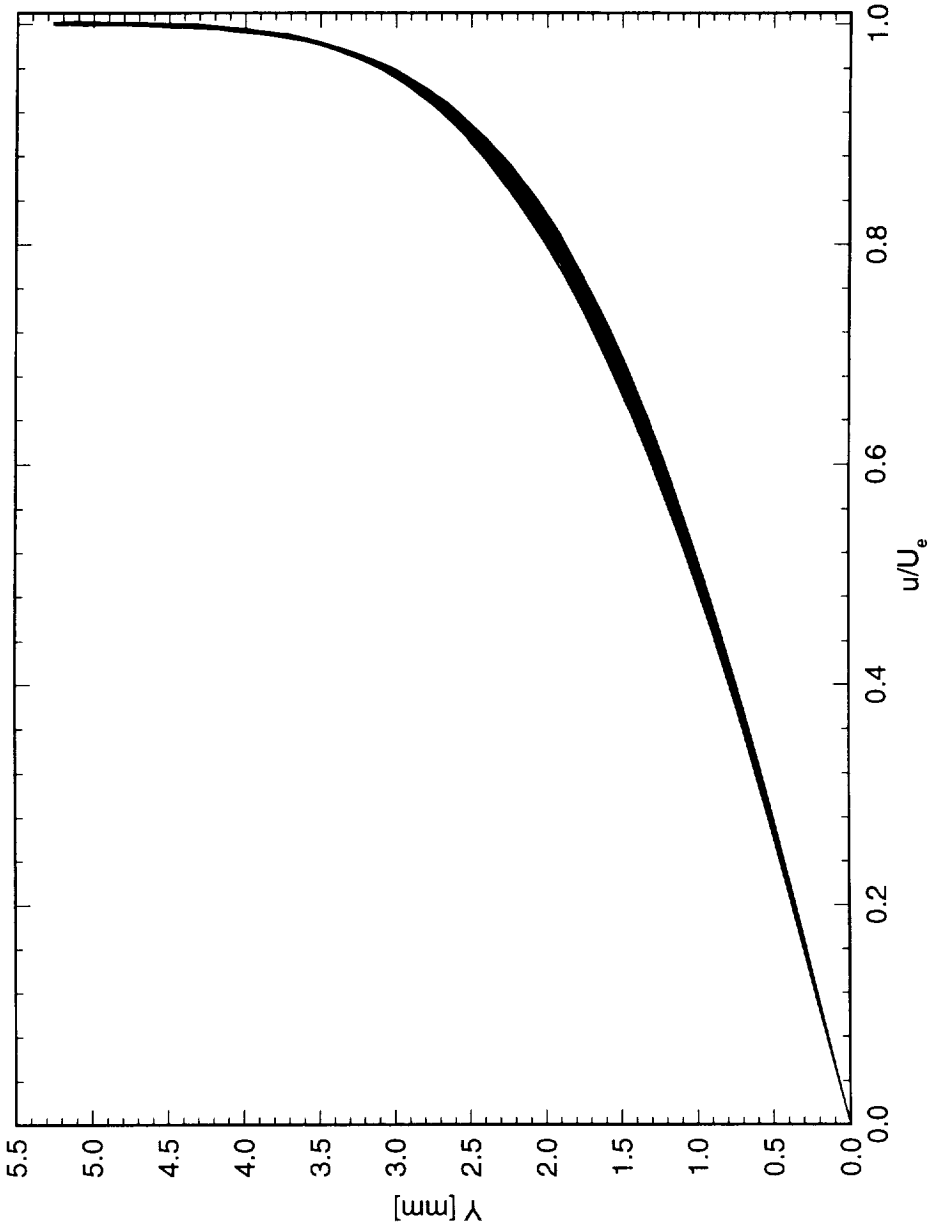

Figure 5.11: Spanwise array of 100 mean-flow boundary-layer profiles covering a span of 99 mm at $x/c = 0.60$. $Re_c = 1.6 \times 10^6$, no artificial roughness.

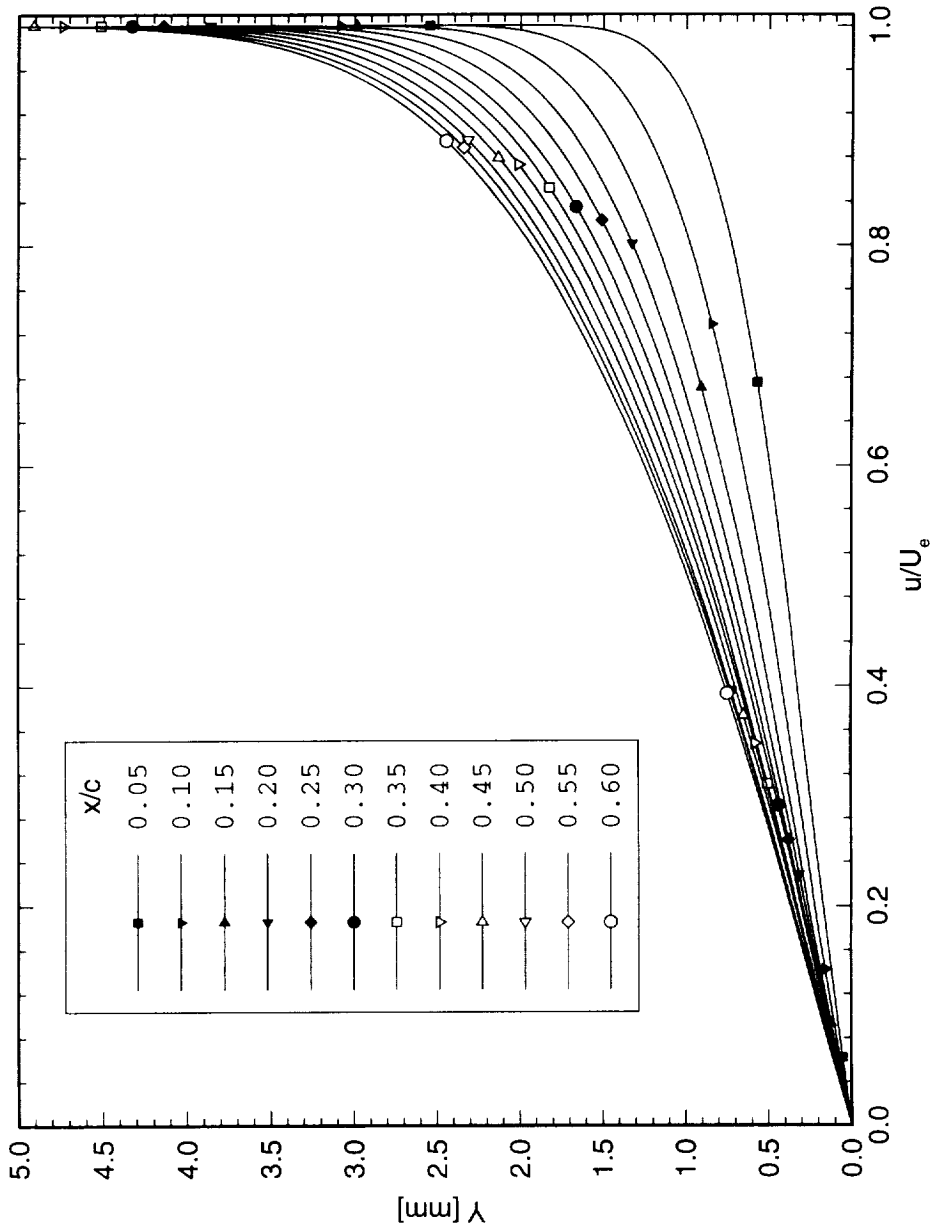

Figure 5.12: Experimental basic-state boundary-layer profiles for $Re_c = 1.6 \times 10^6$, no artificial roughness.

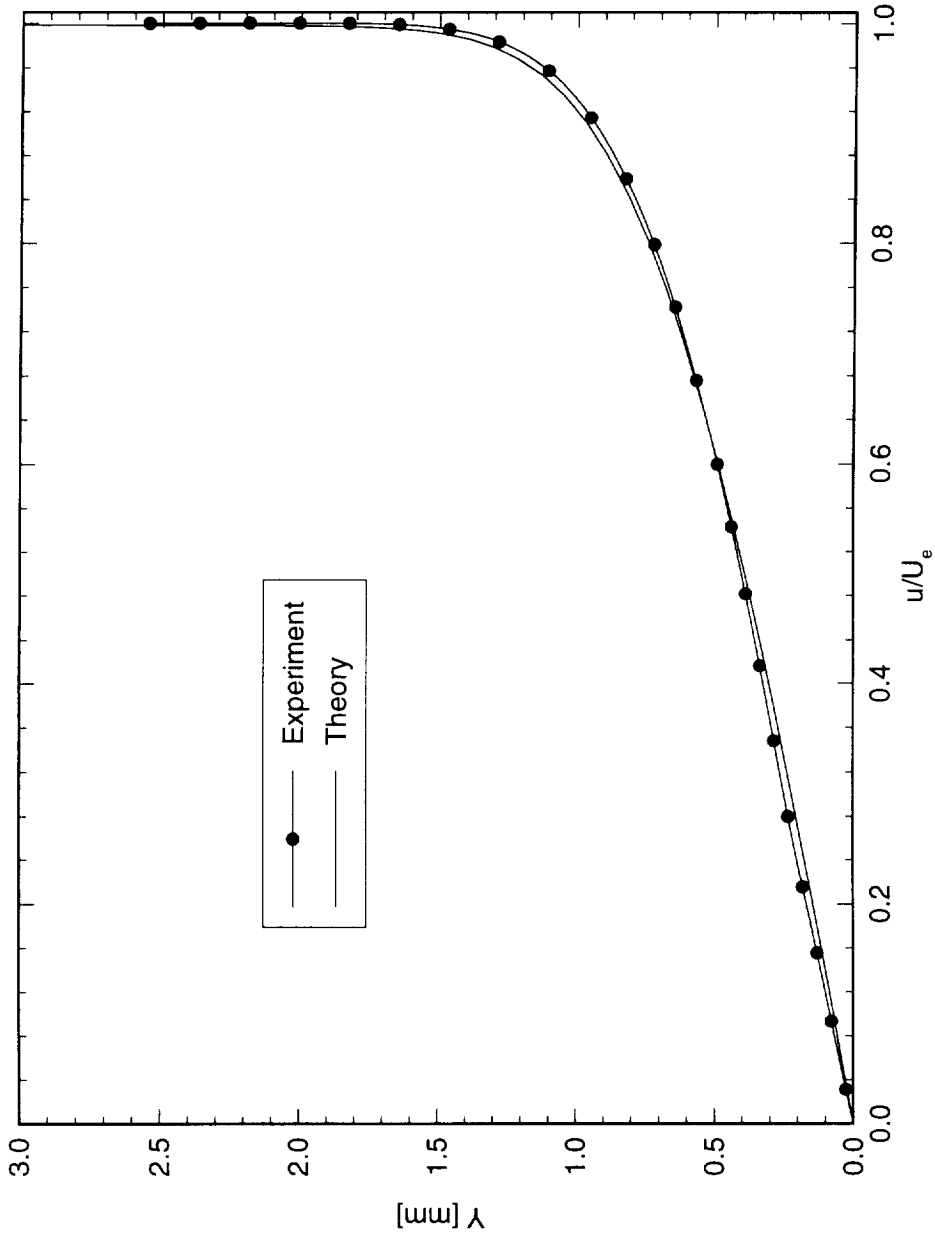

Figure 5.13: Comparison of experimental and theoretical basic-state boundary-layer profile at $x/c = 0.05$. $Re_c = 1.6 \times 10^6$. The dots are simply identifiers and do not represent measurement points.

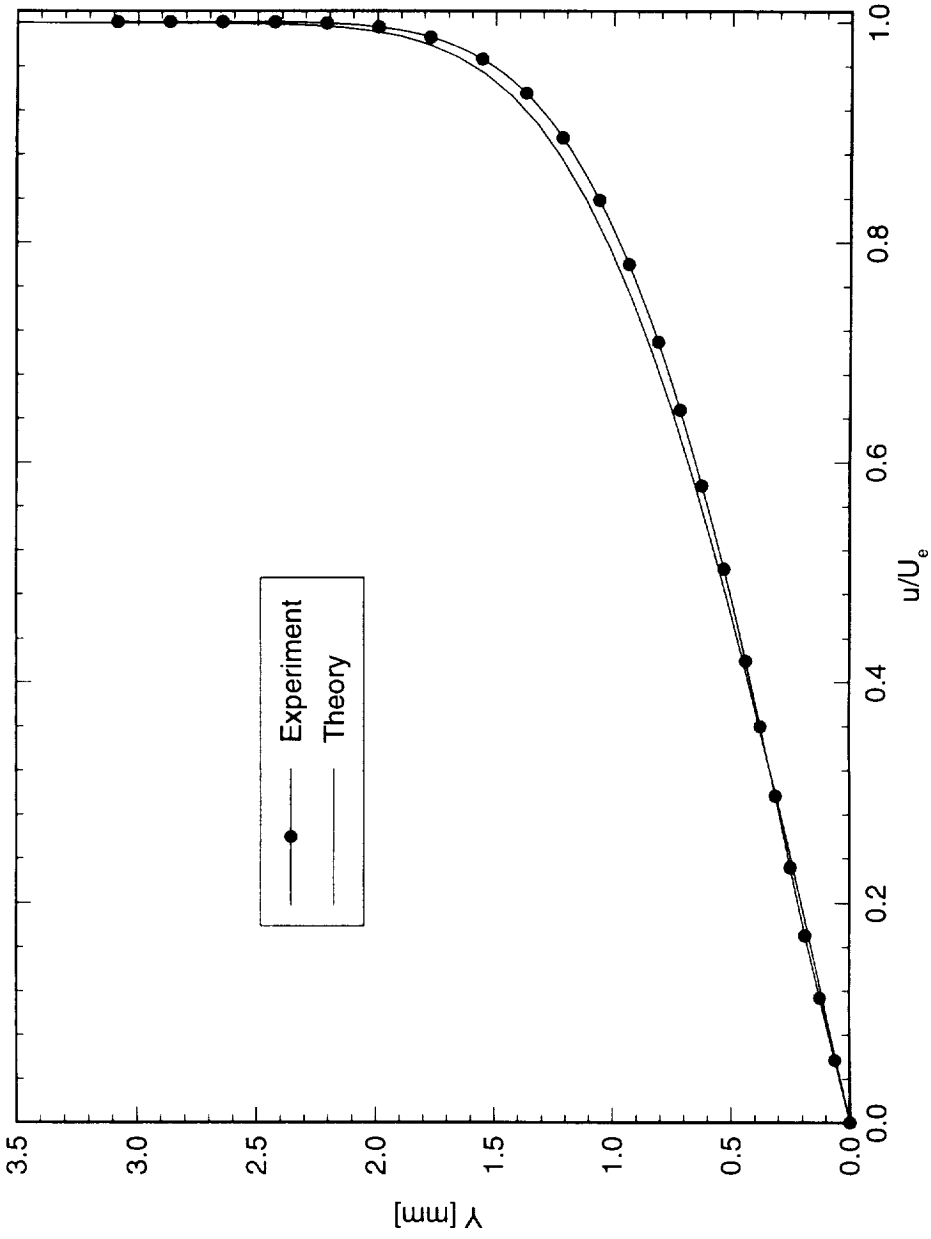

Figure 5.14: Comparison of experimental and theoretical basic-state boundary-layer profile at $x/c = 0.10$. $Re_c = 1.6 \times 10^6$. The dots are simply identifiers and do not represent measurement points.

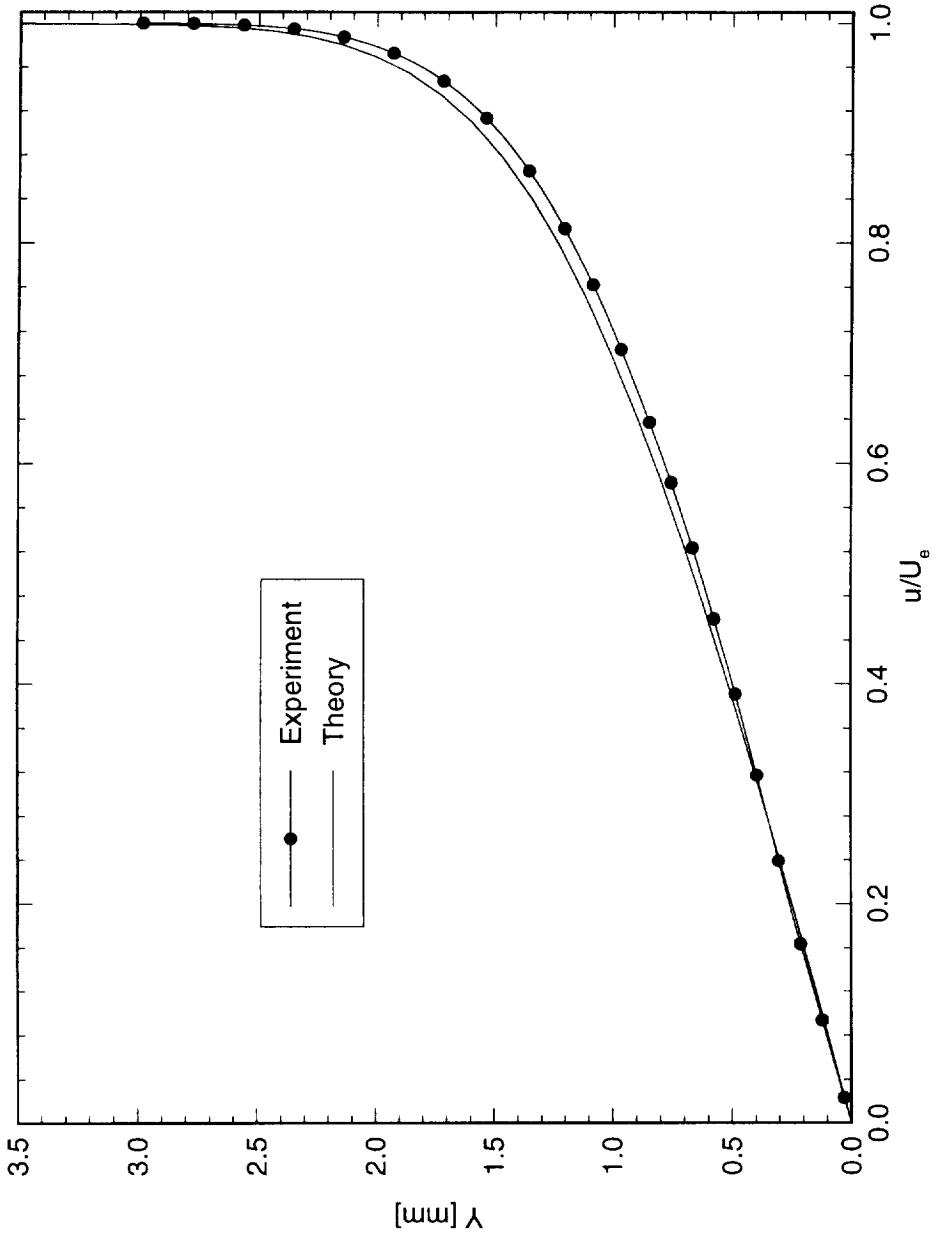

Figure 5.15: Comparison of experimental and theoretical basic-state boundary-layer profile at $x/c = 0.15$. $Re_c = 1.6 \times 10^6$. The dots are simply identifiers and do not represent measurement points.

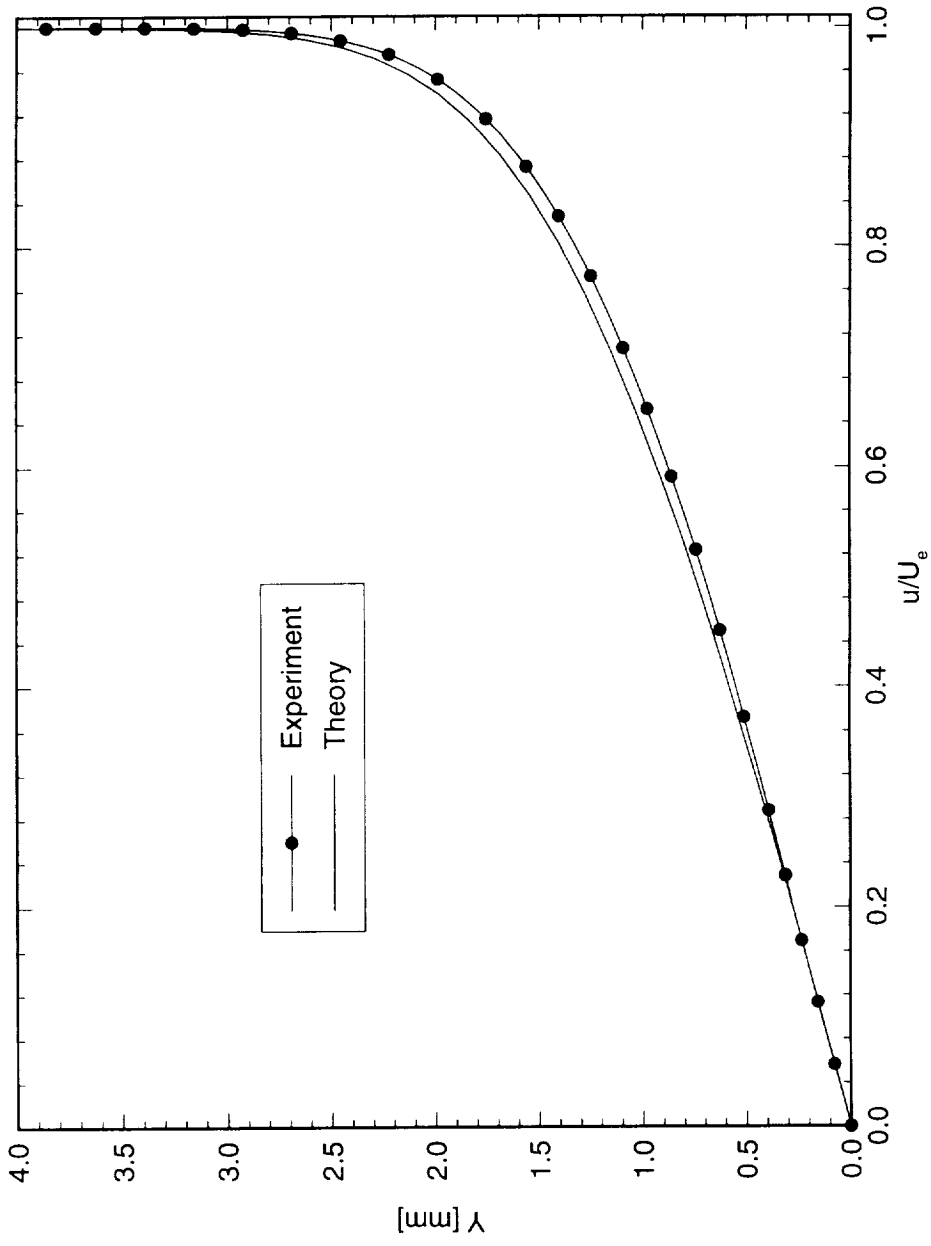

Figure 5.16: Comparison of experimental and theoretical basic-state boundary-layer profile at $x/c = 0.20$. $Re_c = 1.6 \times 10^6$. The dots are simply identifiers and do not represent measurement points.

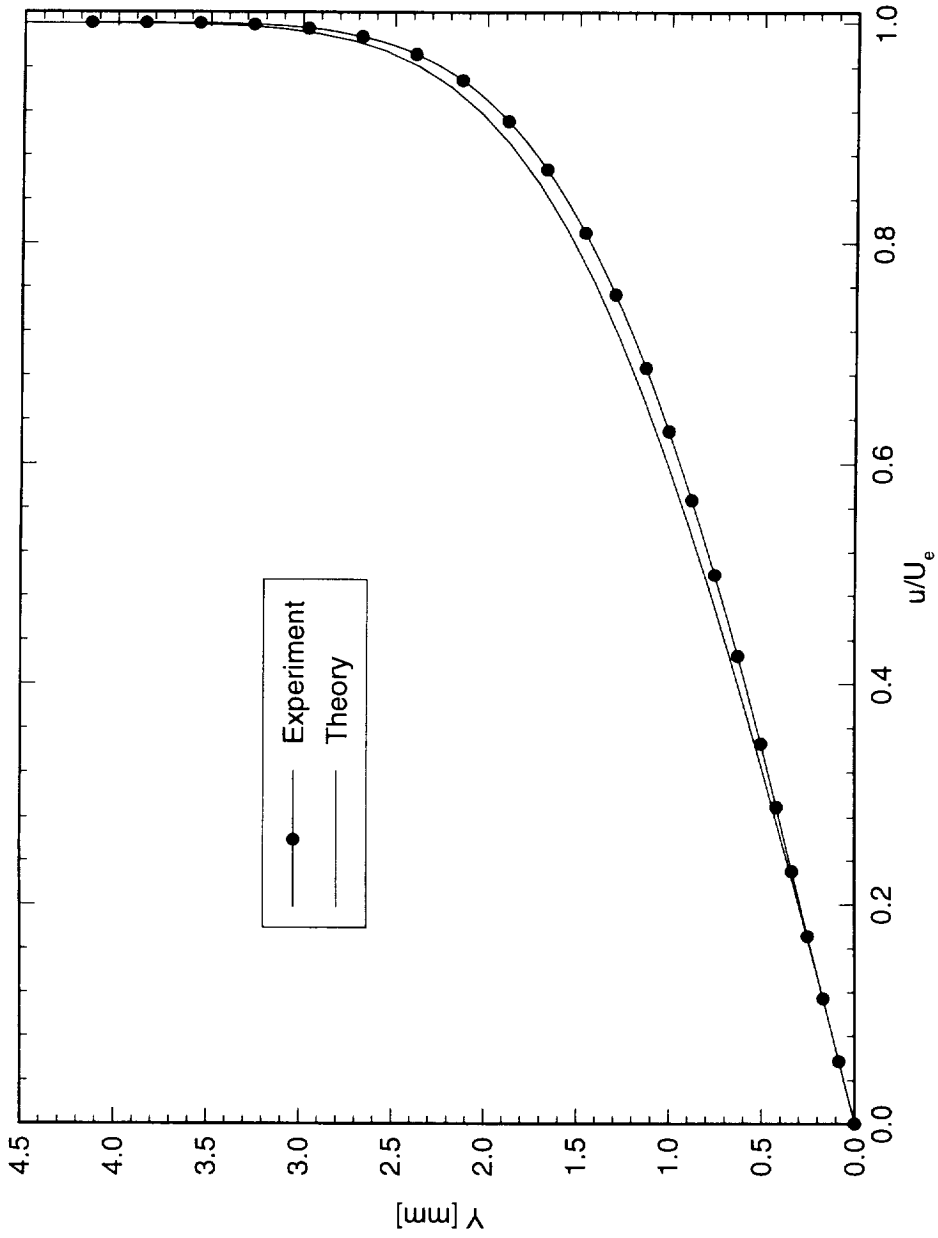

Figure 5.17: Comparison of experimental and theoretical basic-state boundary-layer profile at $x/c = 0.25$. $Re_c = 1.6 \times 10^6$. The dots are simply identifiers and do not represent measurement points.

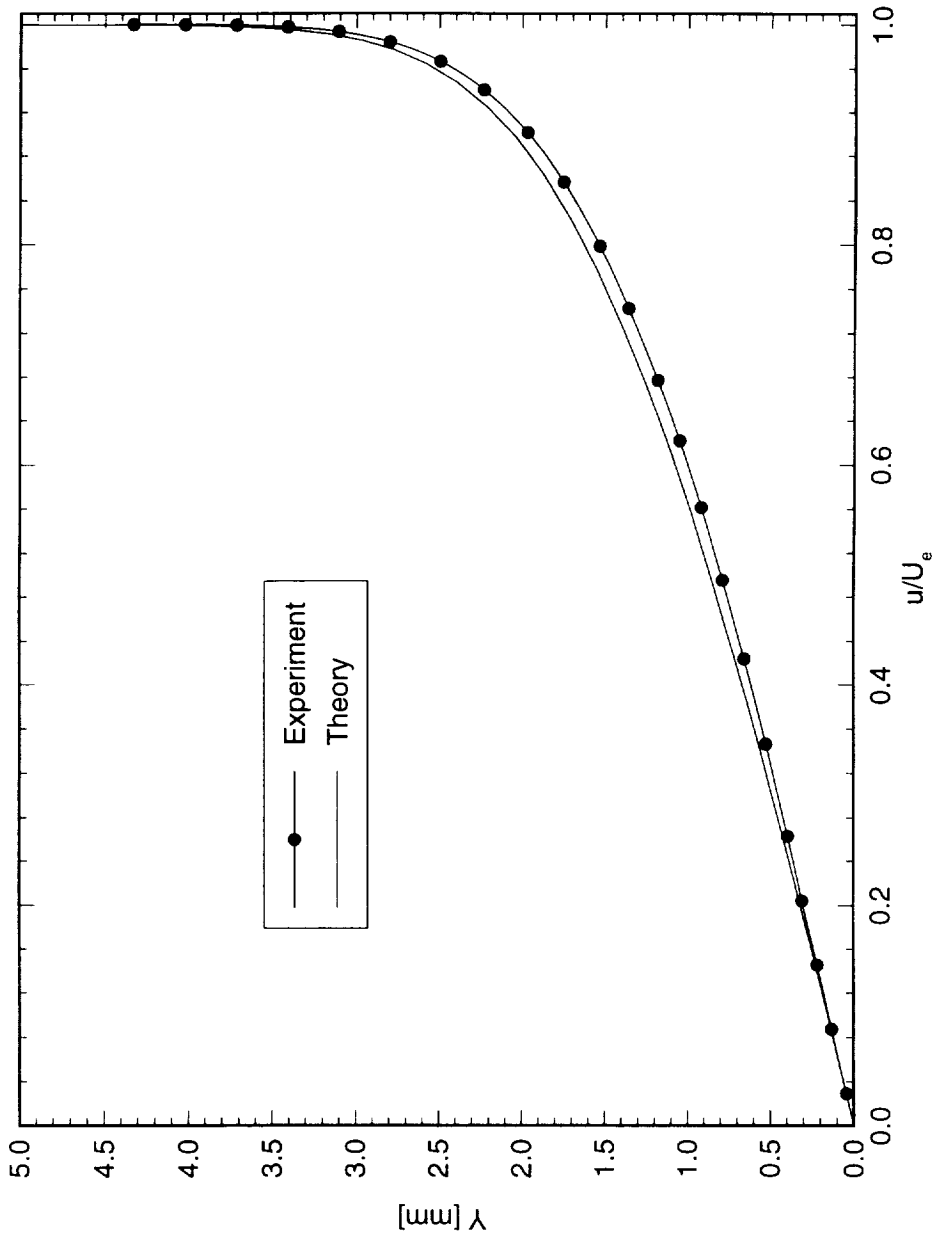

Figure 5.18: Comparison of experimental and theoretical basic-state boundary-layer profile at $x/c = 0.30$. $Re_c = 1.6 \times 10^6$. The dots are simply identifiers and do not represent measurement points.

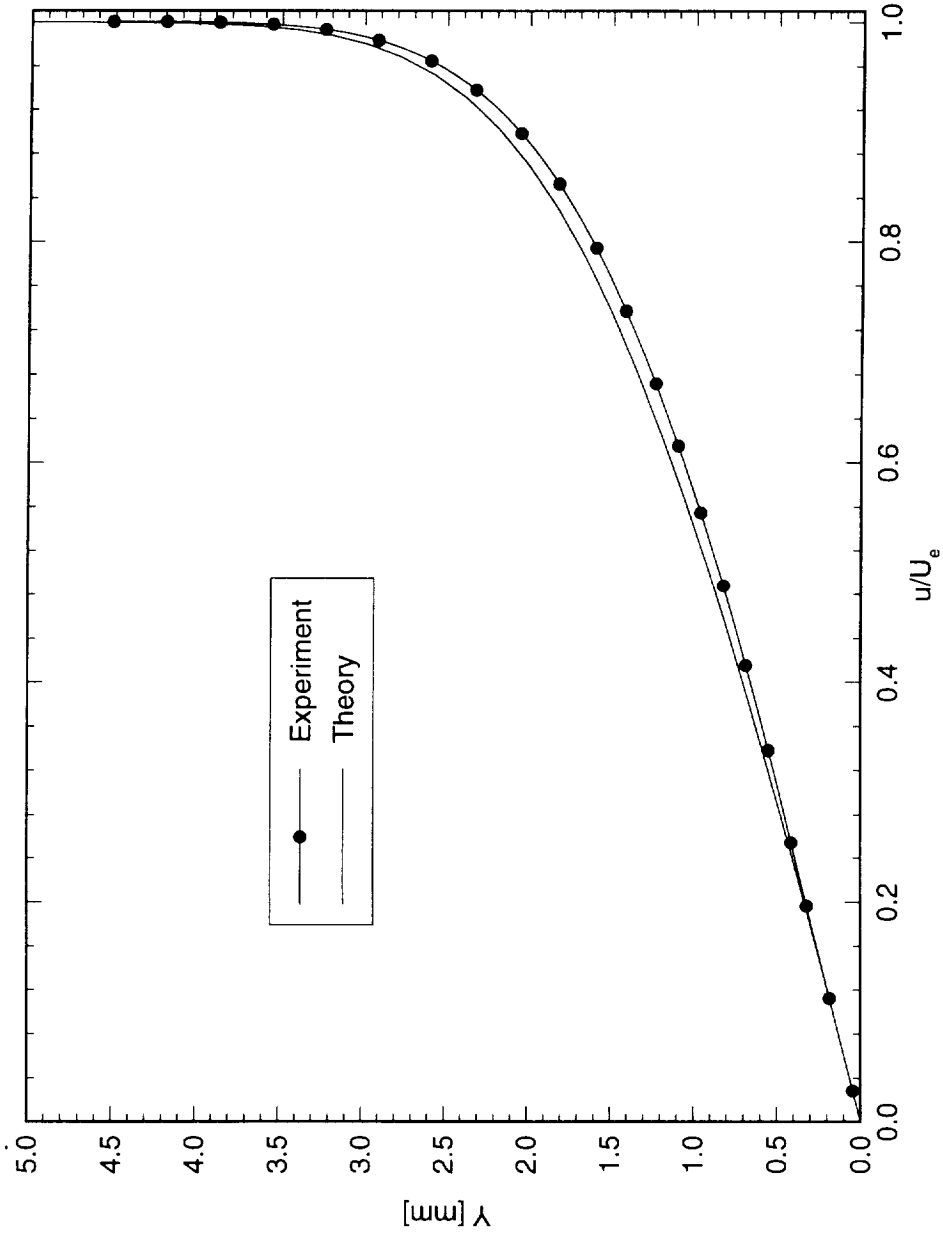

Figure 5.19: Comparison of experimental and theoretical basic-state boundary-layer profile at $x/c = 0.35$. $Re_c = 1.6 \times 10^6$. The dots are simply identifiers and do not represent measurement points.

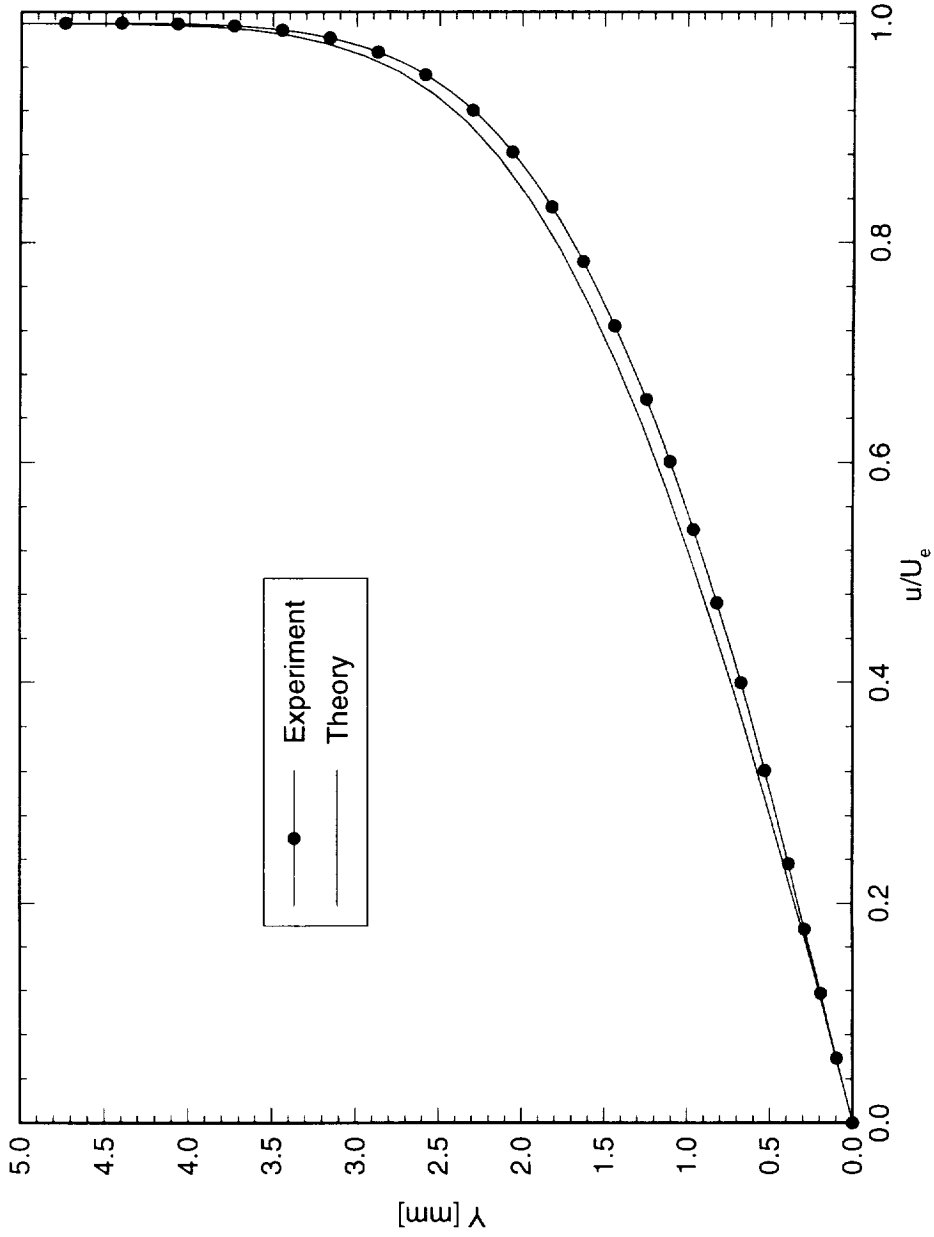

Figure 5.20: Comparison of experimental and theoretical basic-state boundary-layer profile at $x/c = 0.40$. $Re_c = 1.6 \times 10^6$. The dots are simply identifiers and do not represent measurement points.

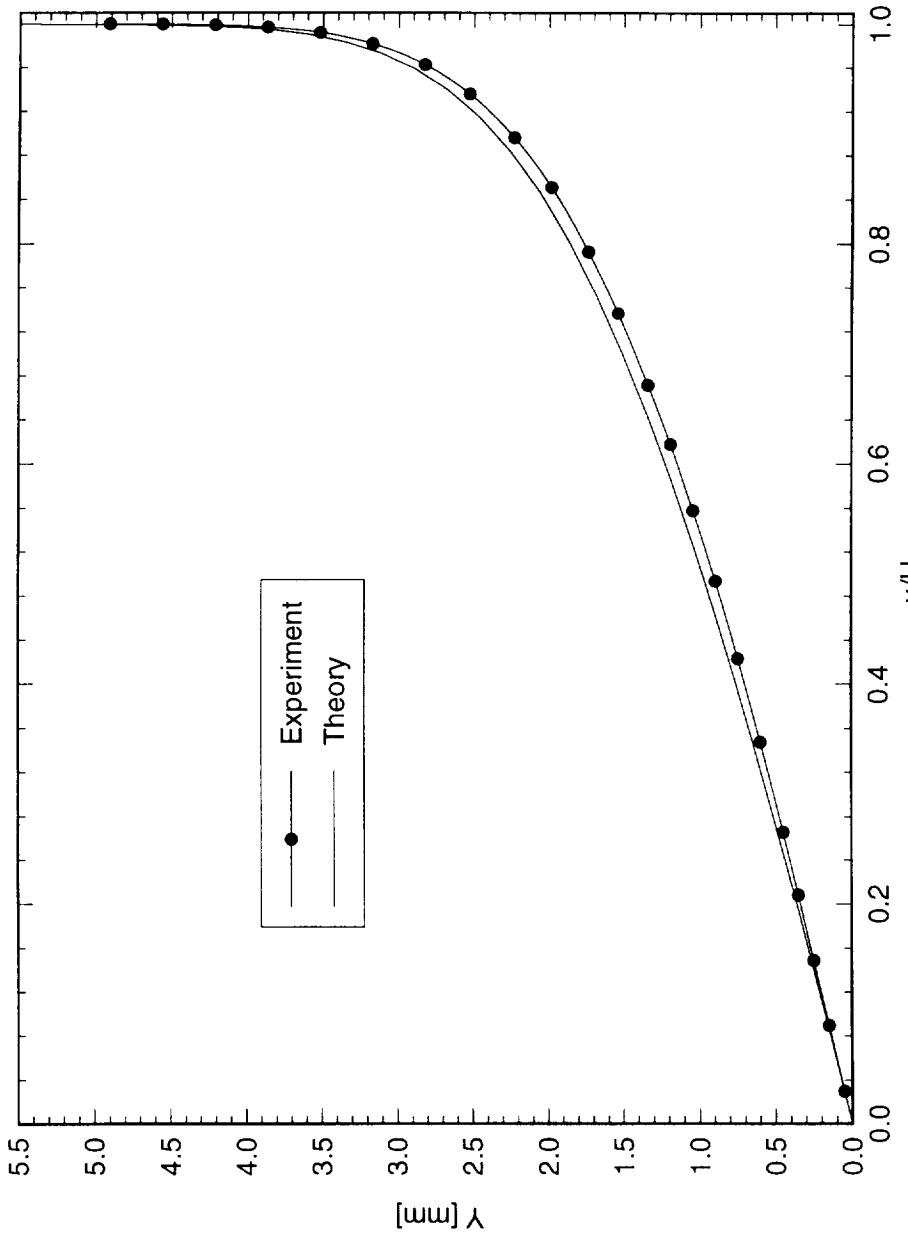

Figure 5.21: Comparison of experimental and theoretical basic-state boundary-layer profile at $x/c = 0.45$. $Re_c = 1.6 \times 10^6$. The dots are simply identifiers and do not represent measurement points.

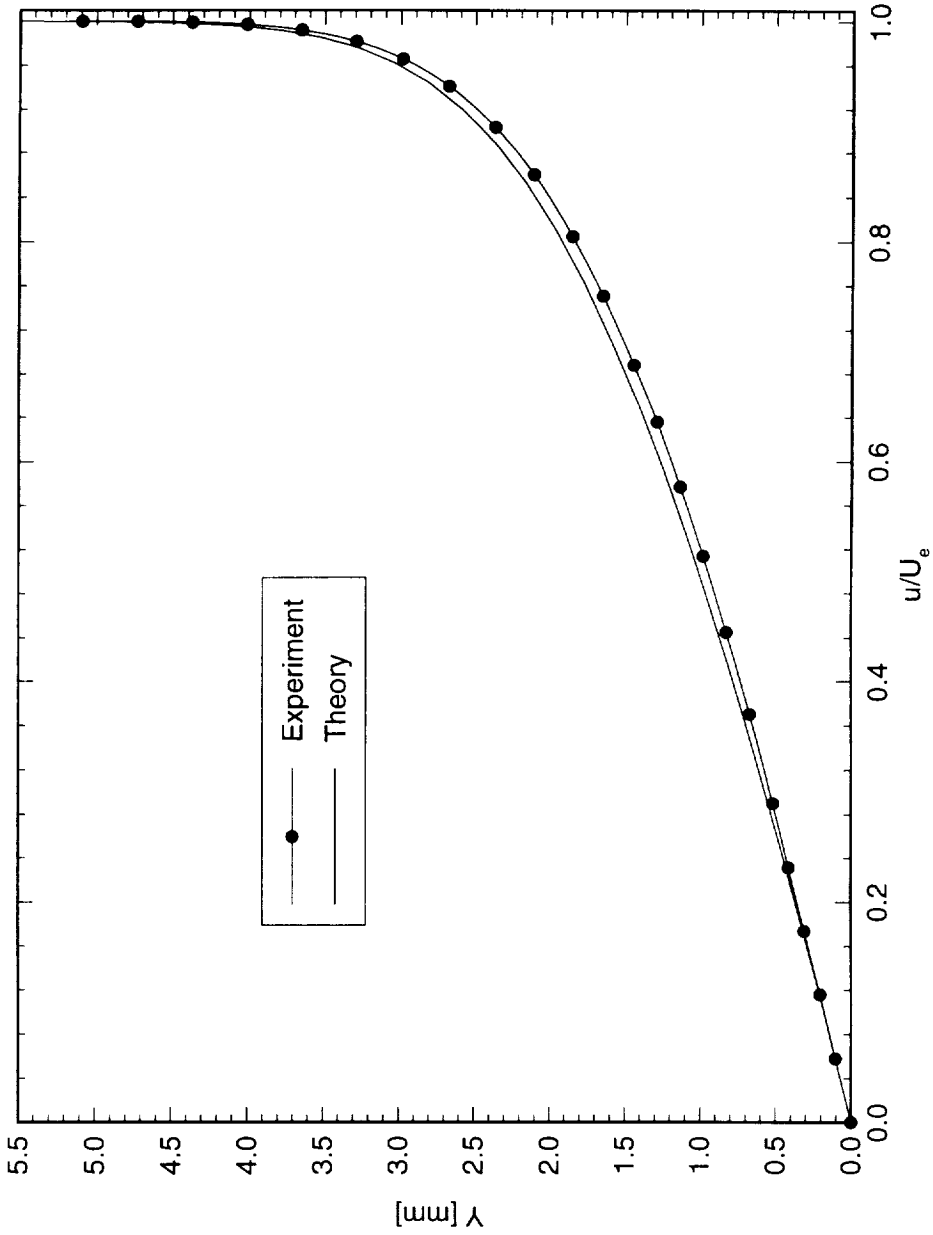

Figure 5.22: Comparison of experimental and theoretical basic-state boundary-layer profile at $x/c = 0.50$. $Re_c = 1.6 \times 10^6$. The dots are simply identifiers and do not represent measurement points.

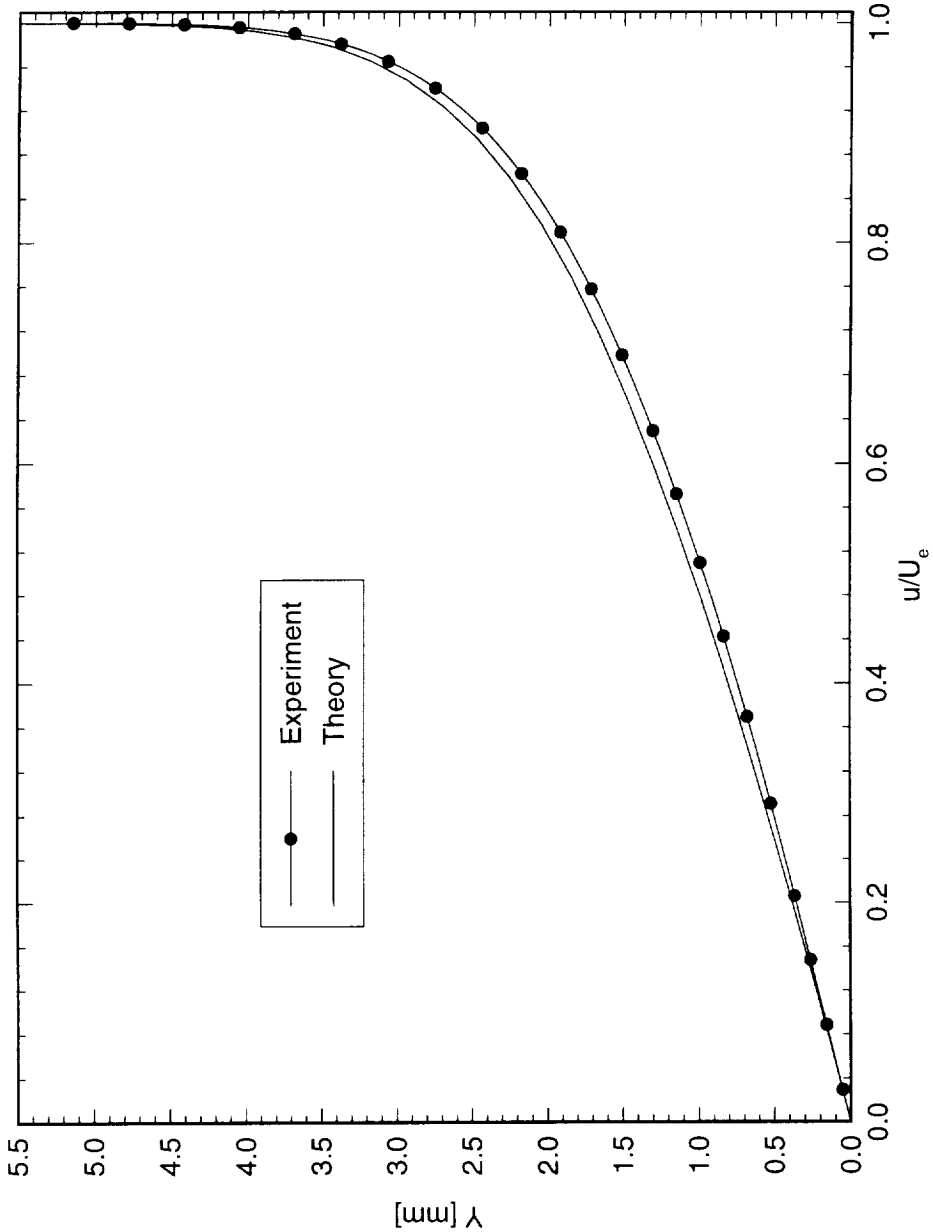

Figure 5.23: Comparison of experimental and theoretical basic-state boundary-layer profile at $x/c = 0.55$. $Re_c = 1.6 \times 10^6$. The dots are simply identifiers and do not represent measurement points.

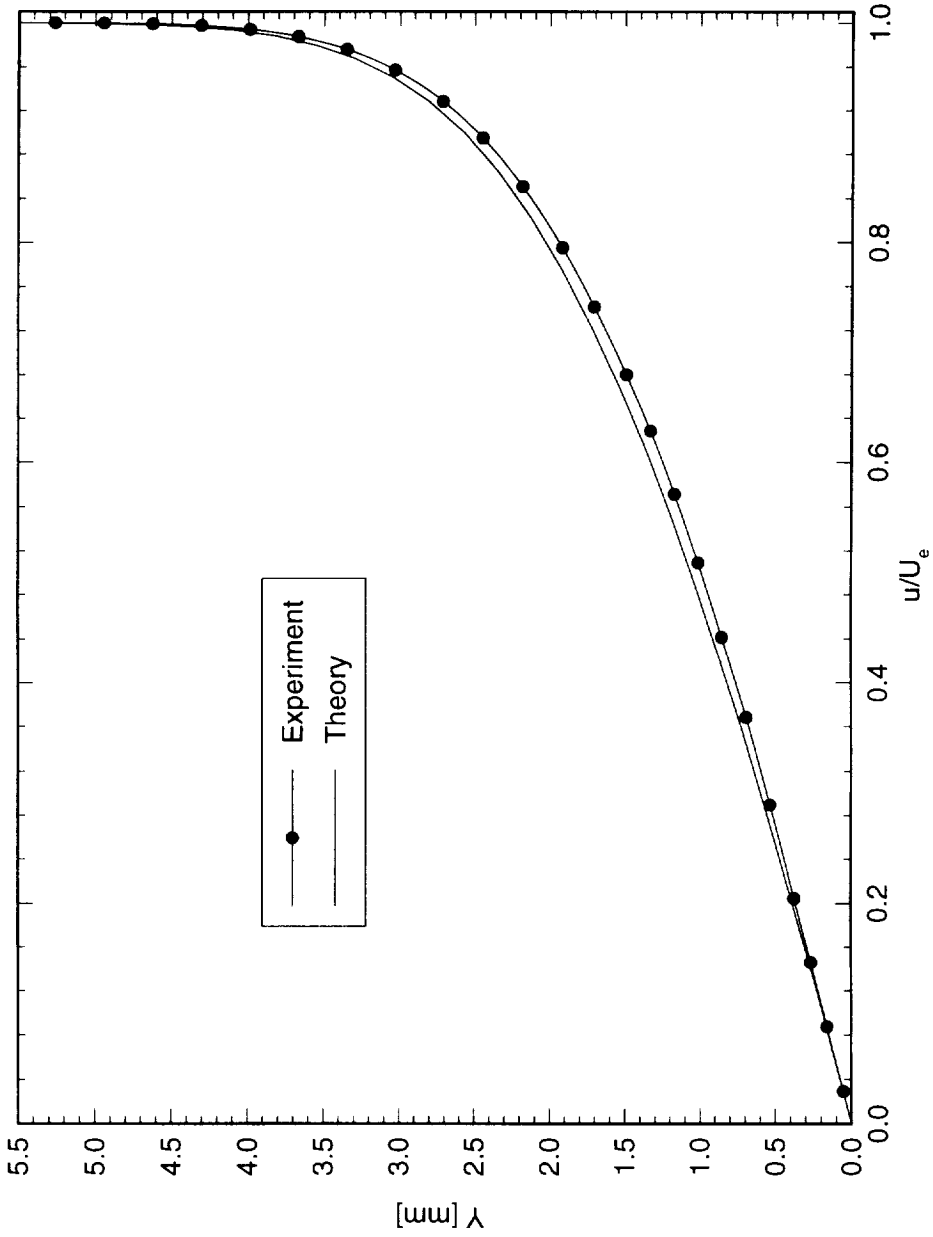

Figure 5.24: Comparison of experimental and theoretical basic-state boundary-layer profile at $x/c = 0.60$. $Re_c = 1.6 \times 10^6$. The dots are simply identifiers and do not represent measurement points.

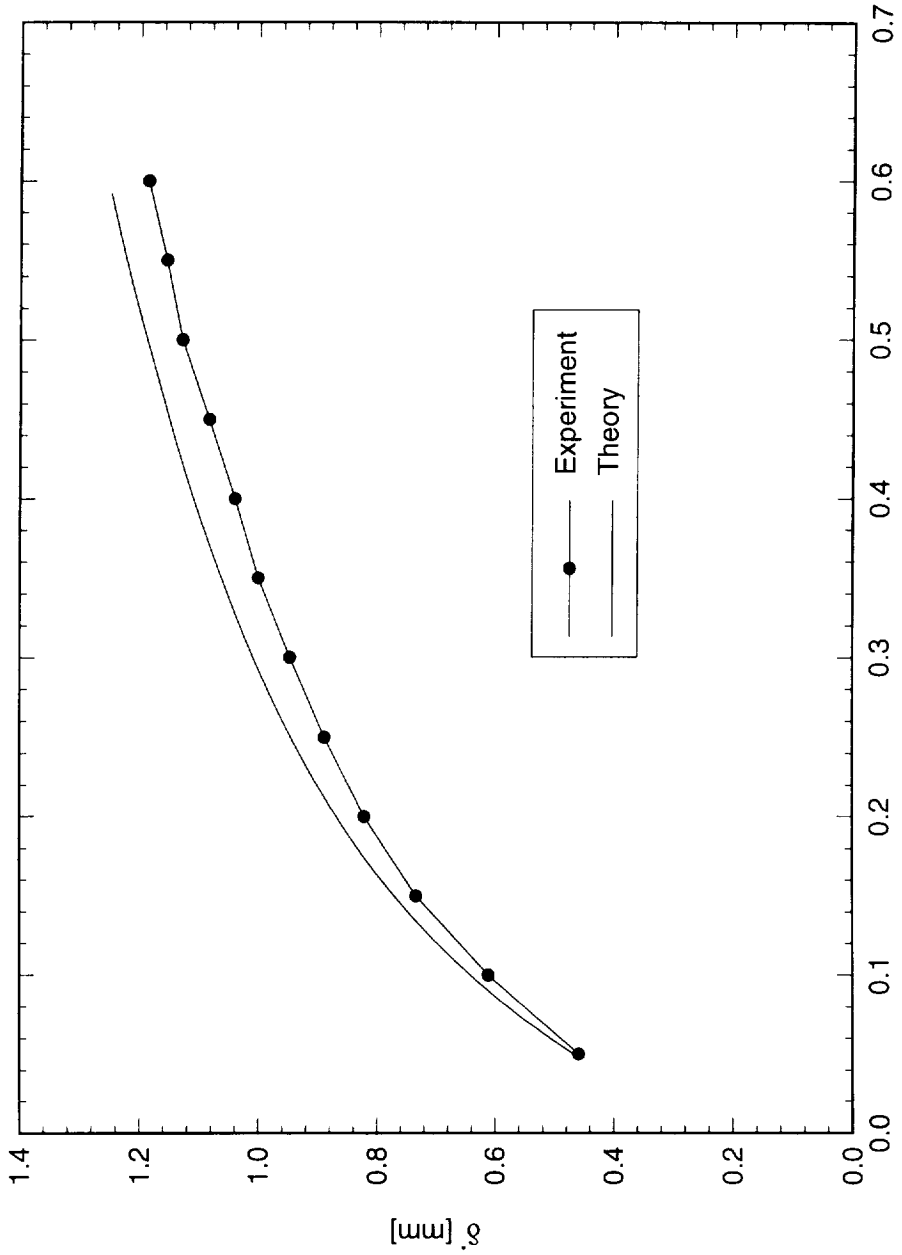

Figure 5.25: Comparison of experimental and theoretical displacement thickness for basic-state boundary layers. $Re_c = 1.6 \times 10^6$.

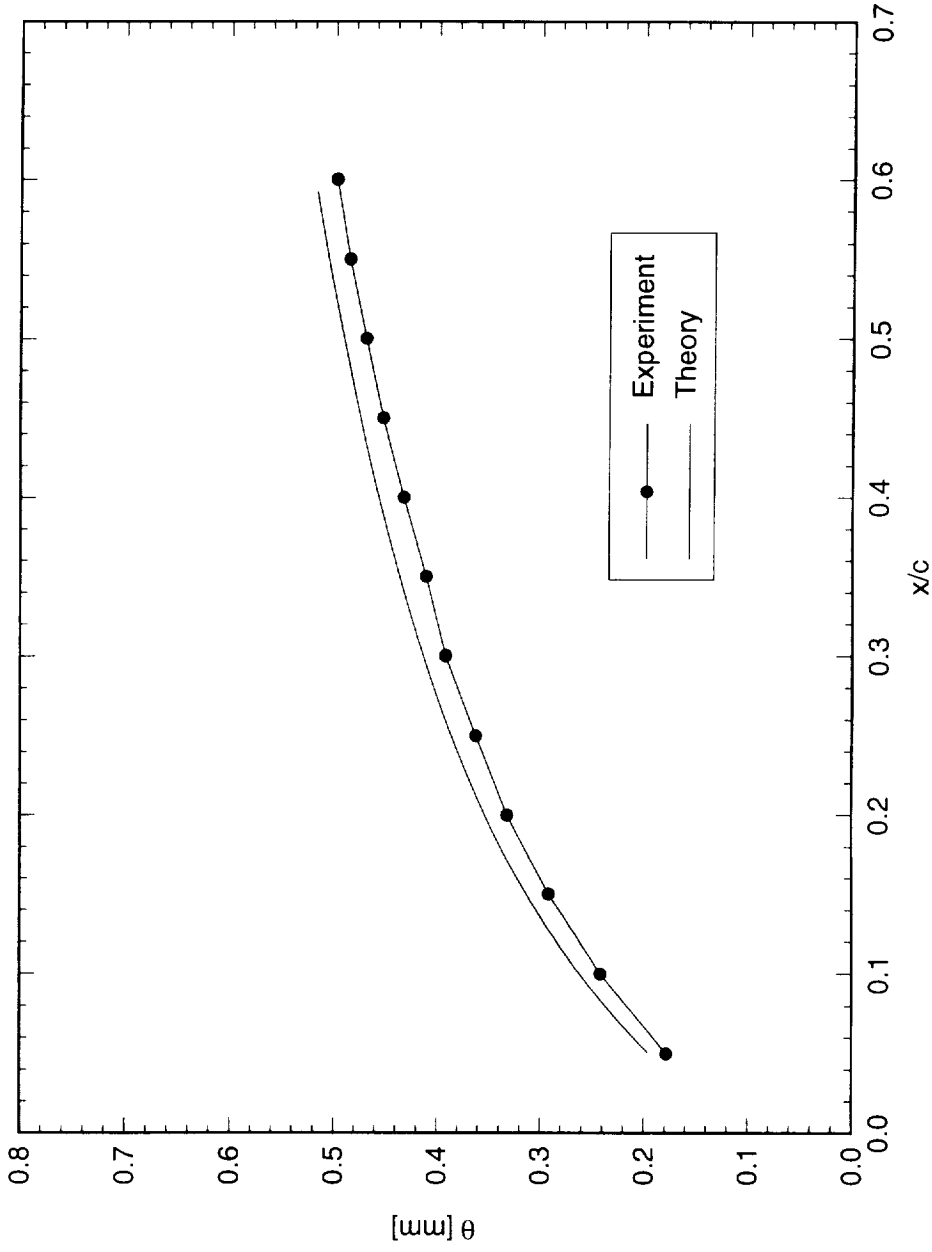

Figure 5.26: Comparison of experimental and theoretical momentum thickness for basic-state boundary layers. $Re_c = 1.6 \times 10^6$.

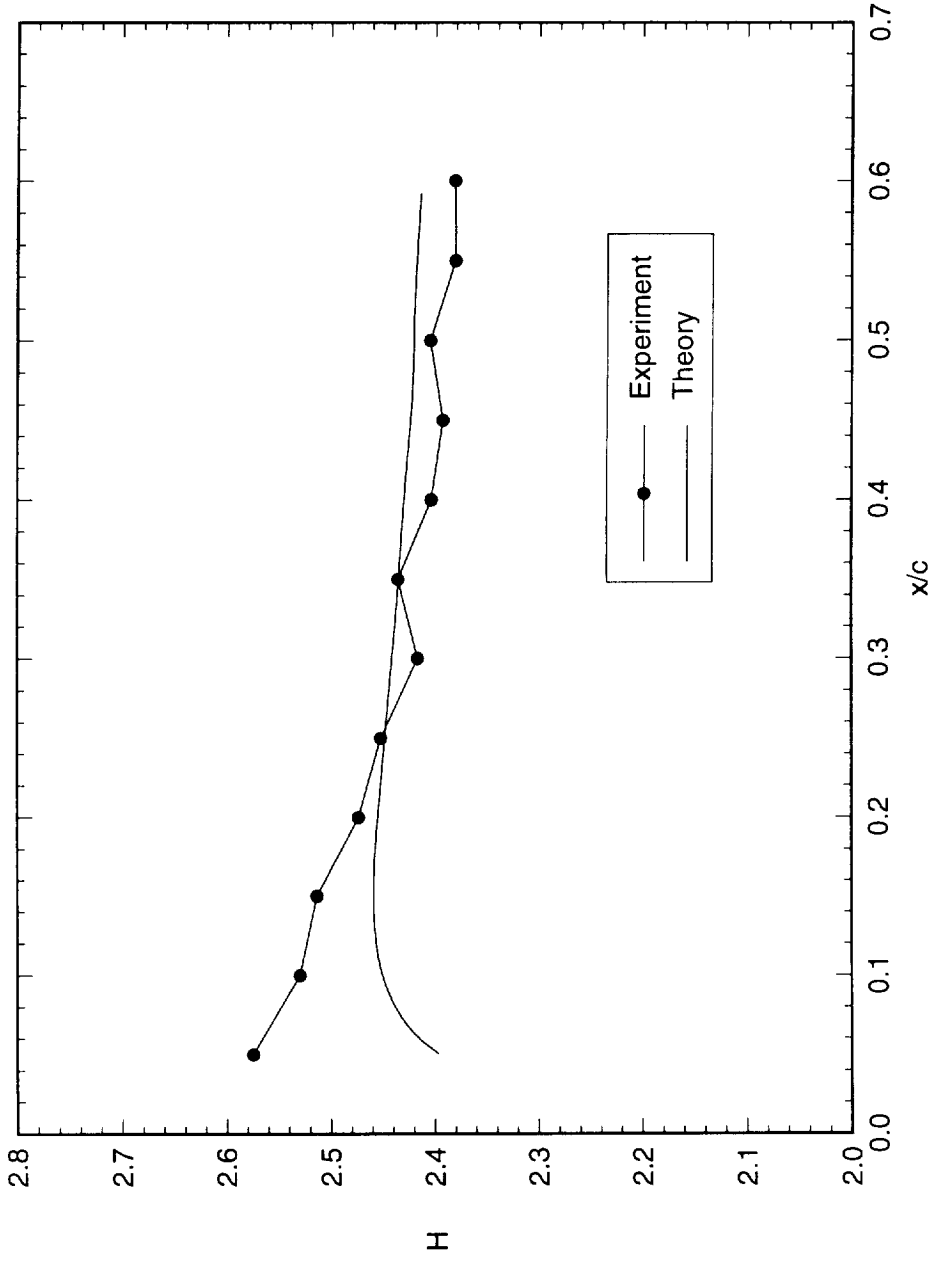

Figure 5.27: Comparison of experimental and theoretical shape factor for basic-state boundary layers. $Re_c = 1.6 \times 10^6$.

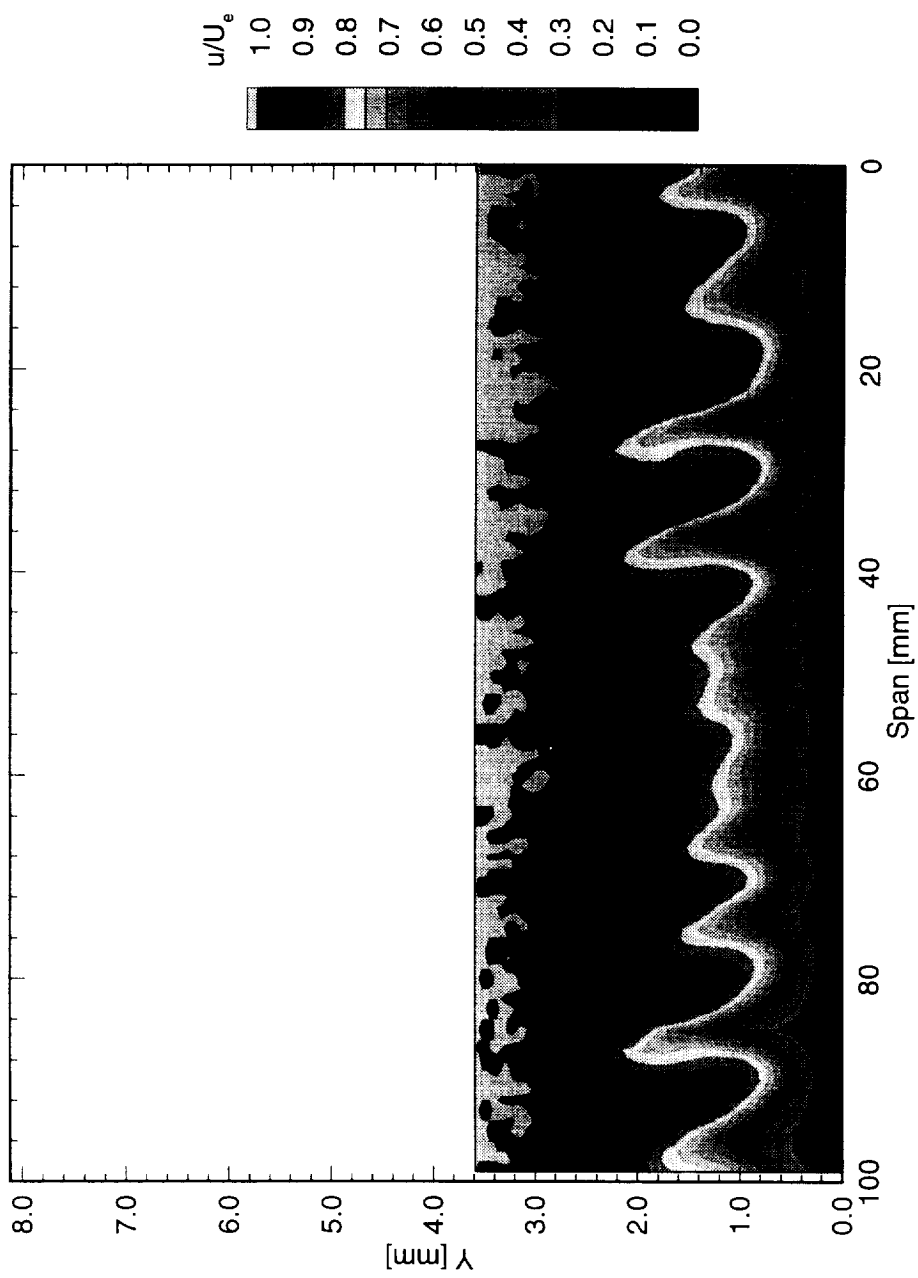

Figure 5.28: Streamwise velocity contours at $x/c = 0.45$. $Re_c = 3.0 \times 10^6$, no artificial roughness.

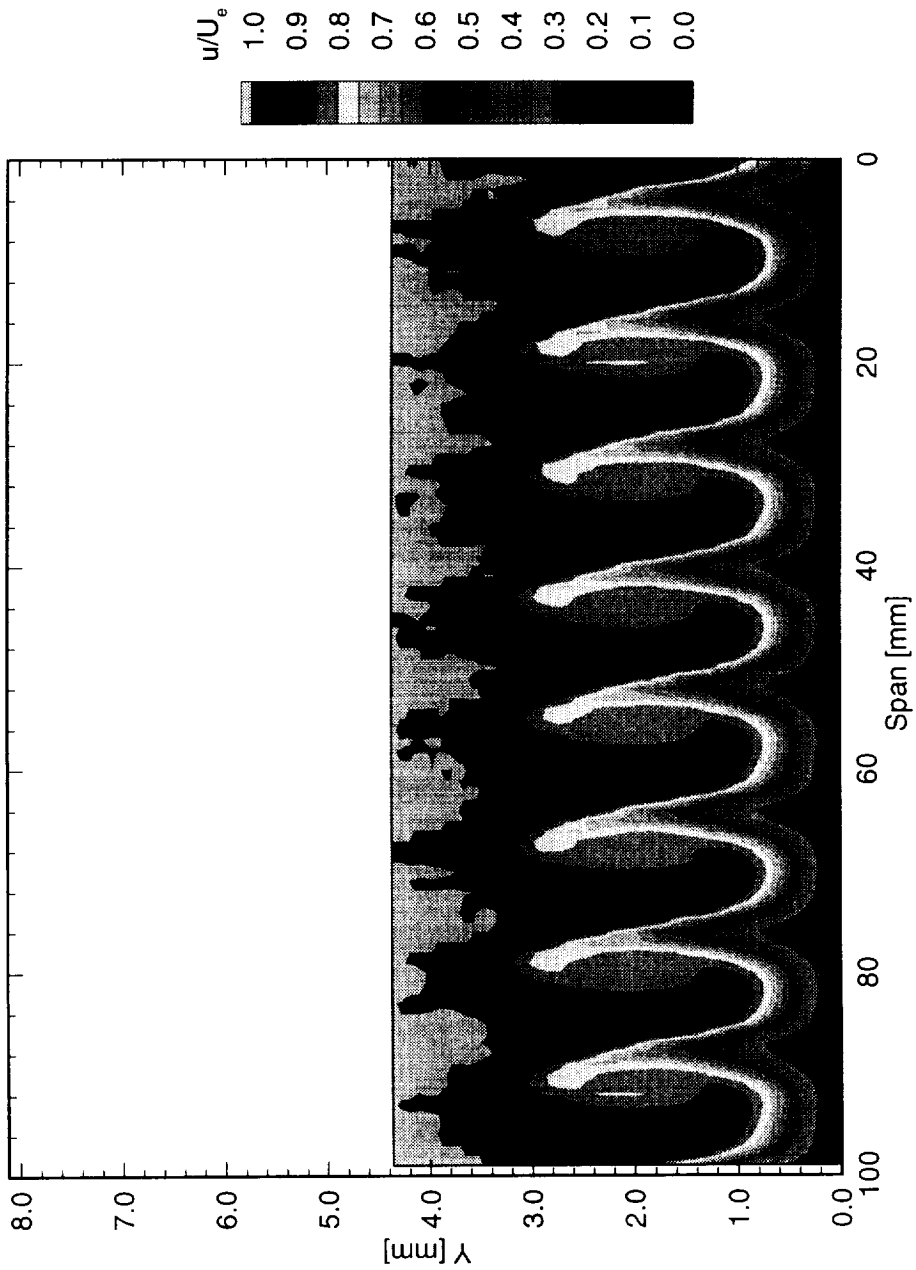

Figure 5.29: Streamwise velocity contours at $x/c = 0.45$. $Re_c = 2.4 \times 10^6$, [6|12] roughness.

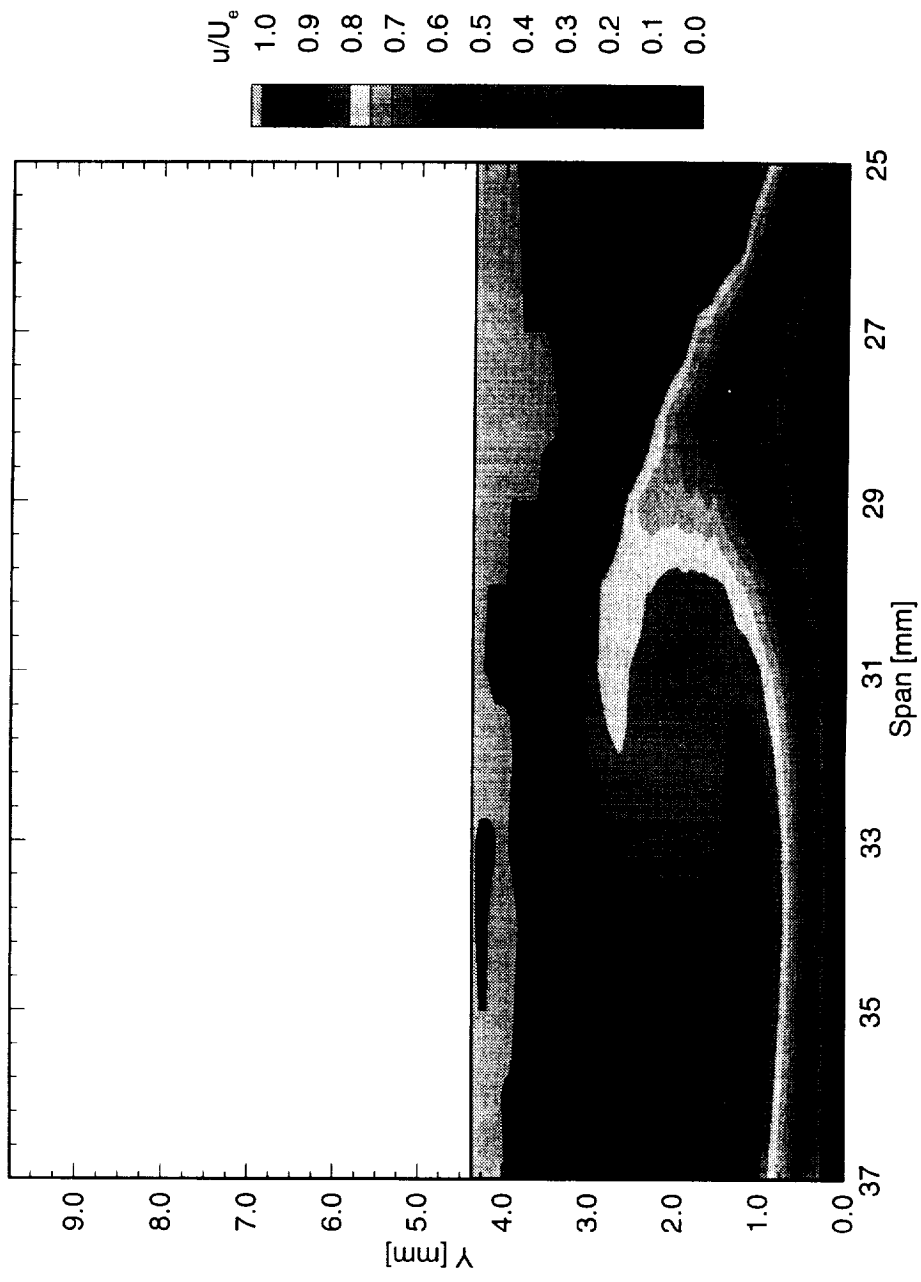

Figure 5.30: Single stationary crossflow vortex isolated from figure 5.29 and plotted on a 1:1 scale.

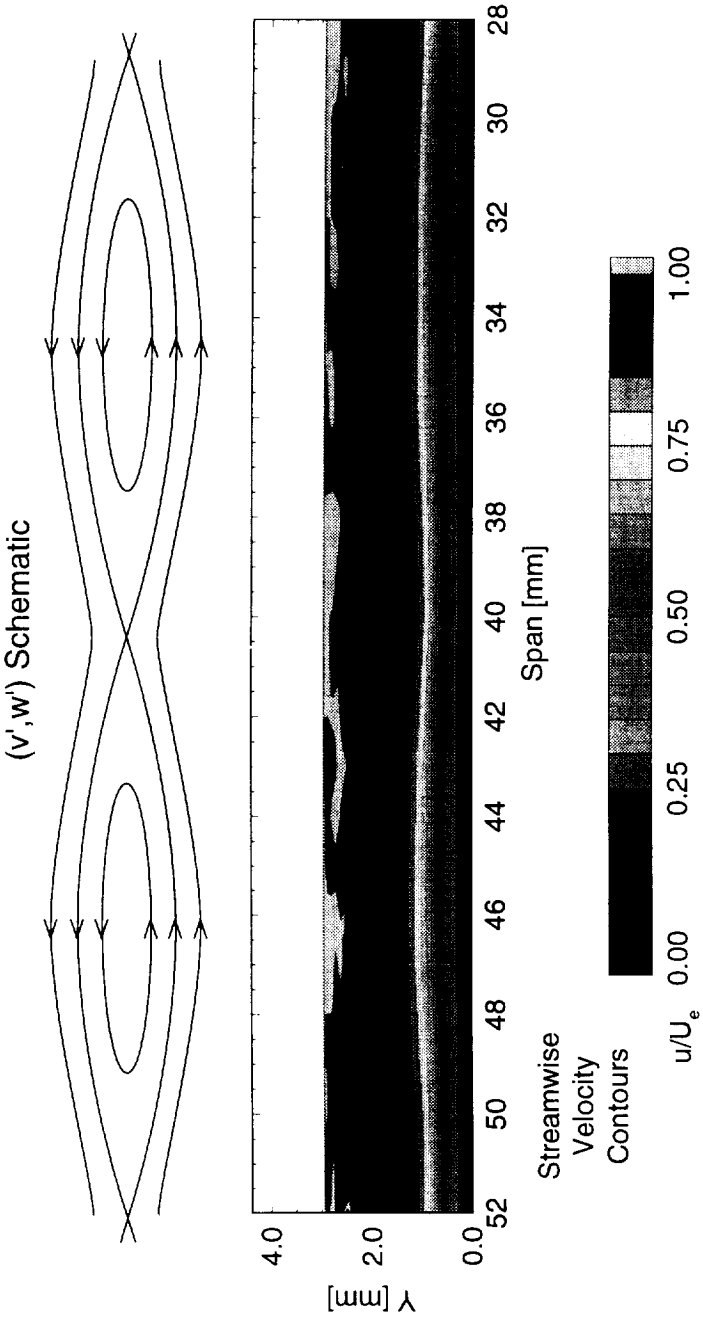

Figure 5.31: Effect of combined (v', w') disturbance motion on the streamwise boundary layer velocity at $x/c = 0.20$. $Re_c = 2.4 \times 10^6$, [6|12] roughness.

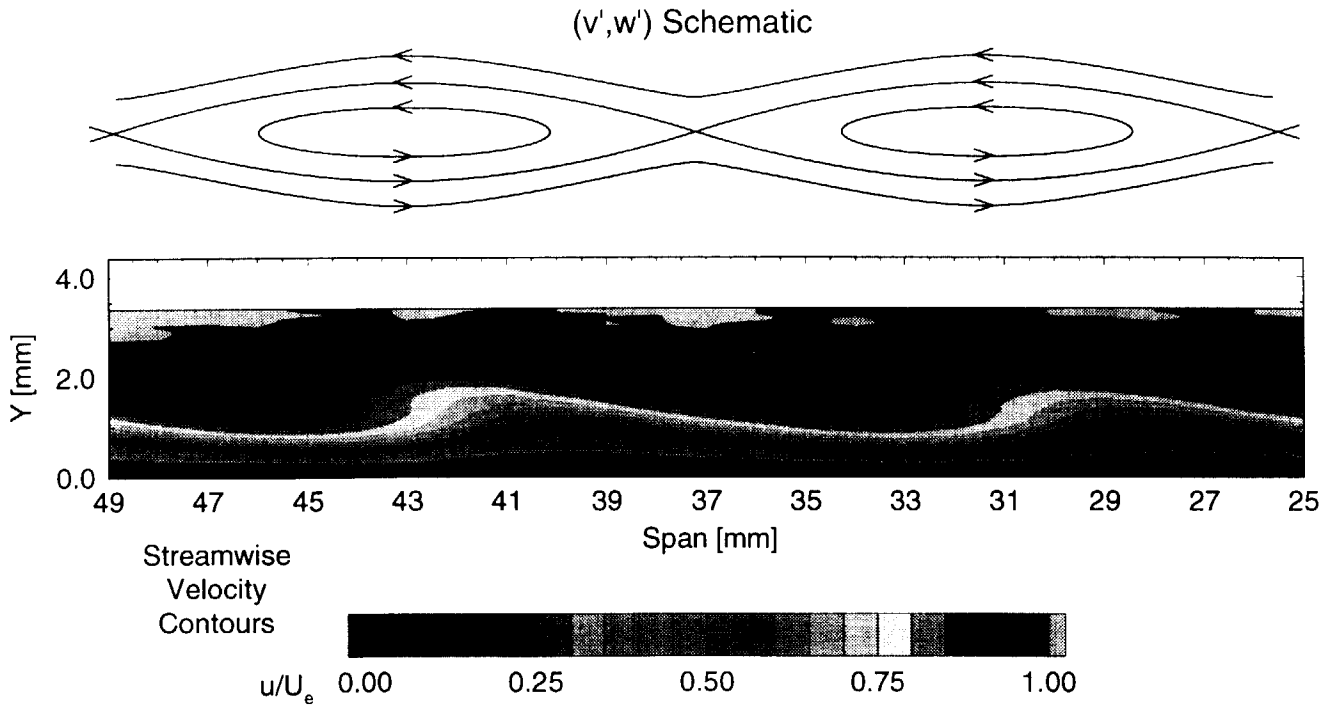

Figure 5.32: Effect of combined (v', w') disturbance motion on the streamwise boundary layer velocity at $x/c = 0.30$. $Re_c = 2.4 \times 10^6$, [6|12] roughness.

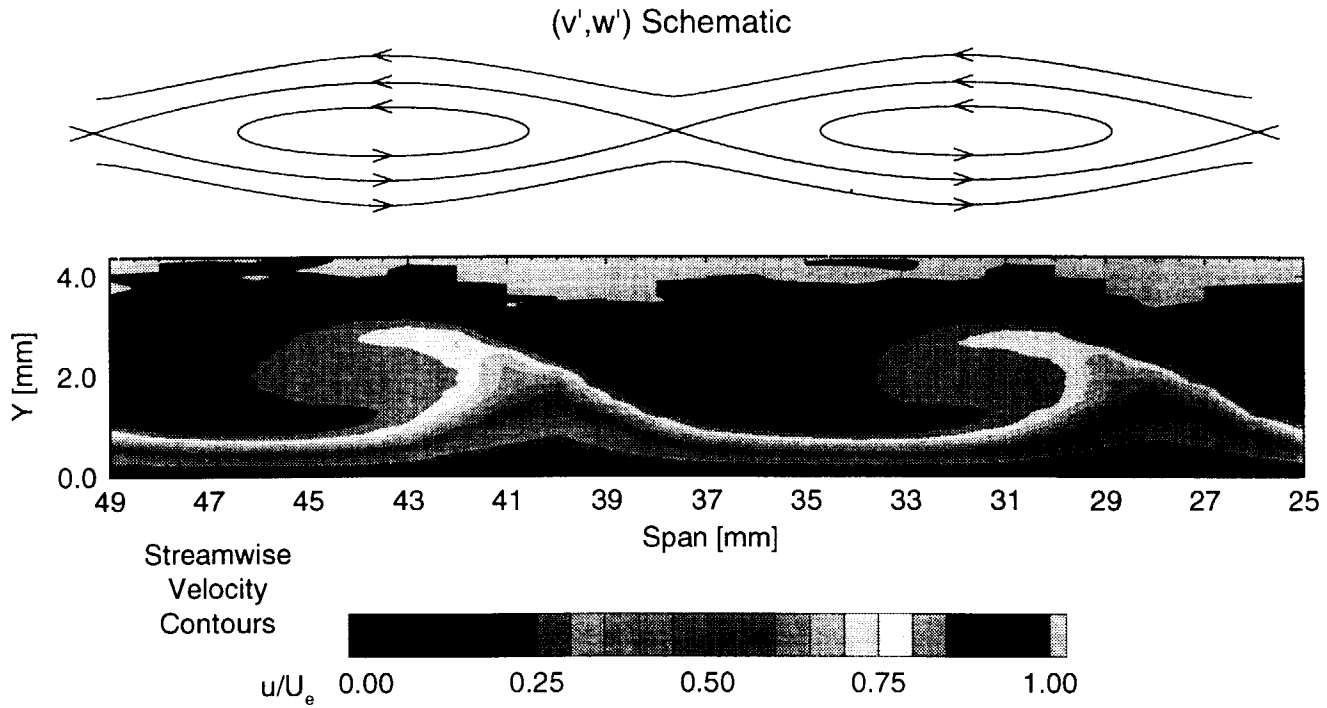

Figure 5.33: Effect of combined (v', w') disturbance motion on the streamwise boundary layer velocity at $x/c = 0.45$. $Re_c = 2.4 \times 10^6$, [6|12] roughness.

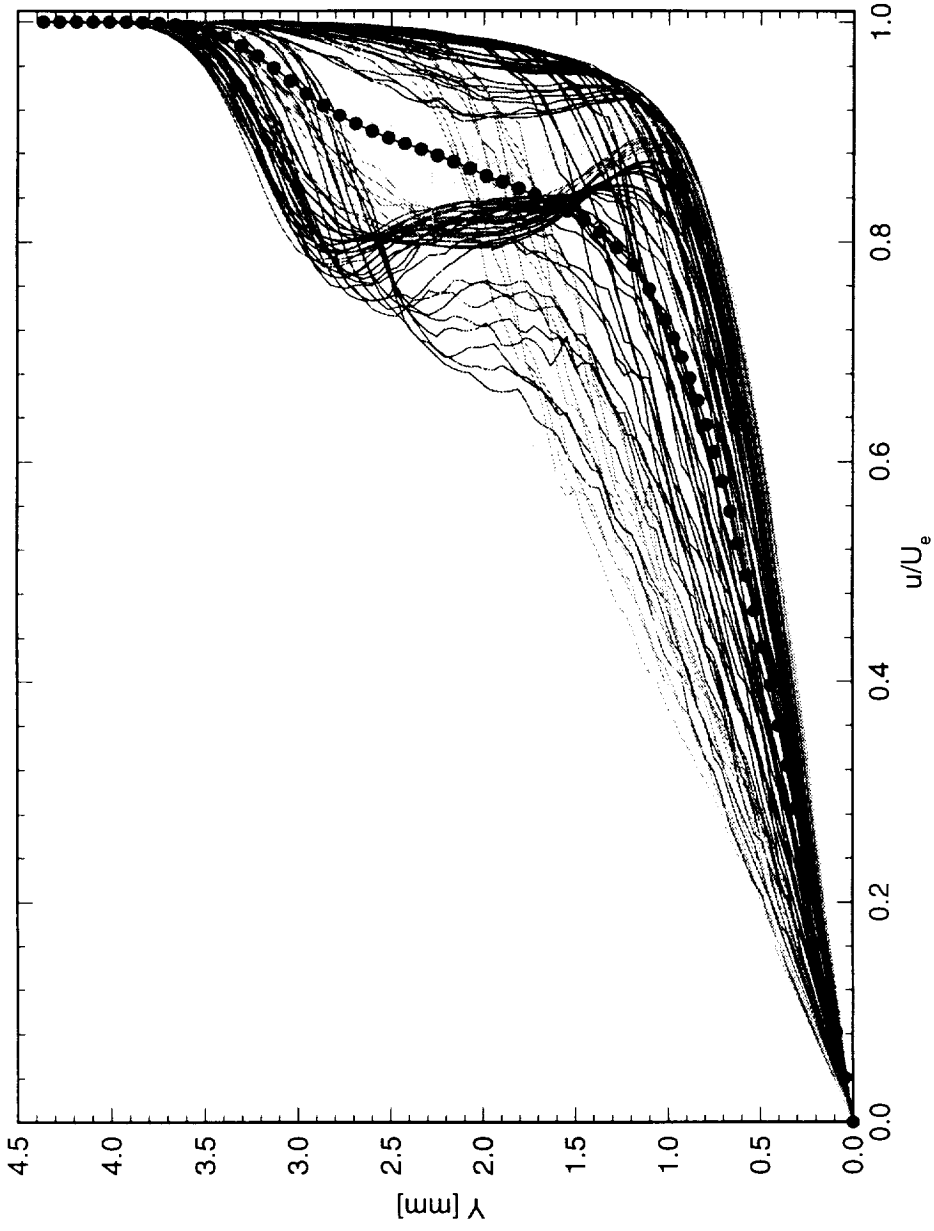

Figure 5.34: Spanwise array of 100 mean-flow boundary-layer profiles covering a span of 99 mm at $x/c = 0.45$. $Re_c = 2.4 \times 10^6$, [6|12] roughness. The dots indicate the mean of the profiles.

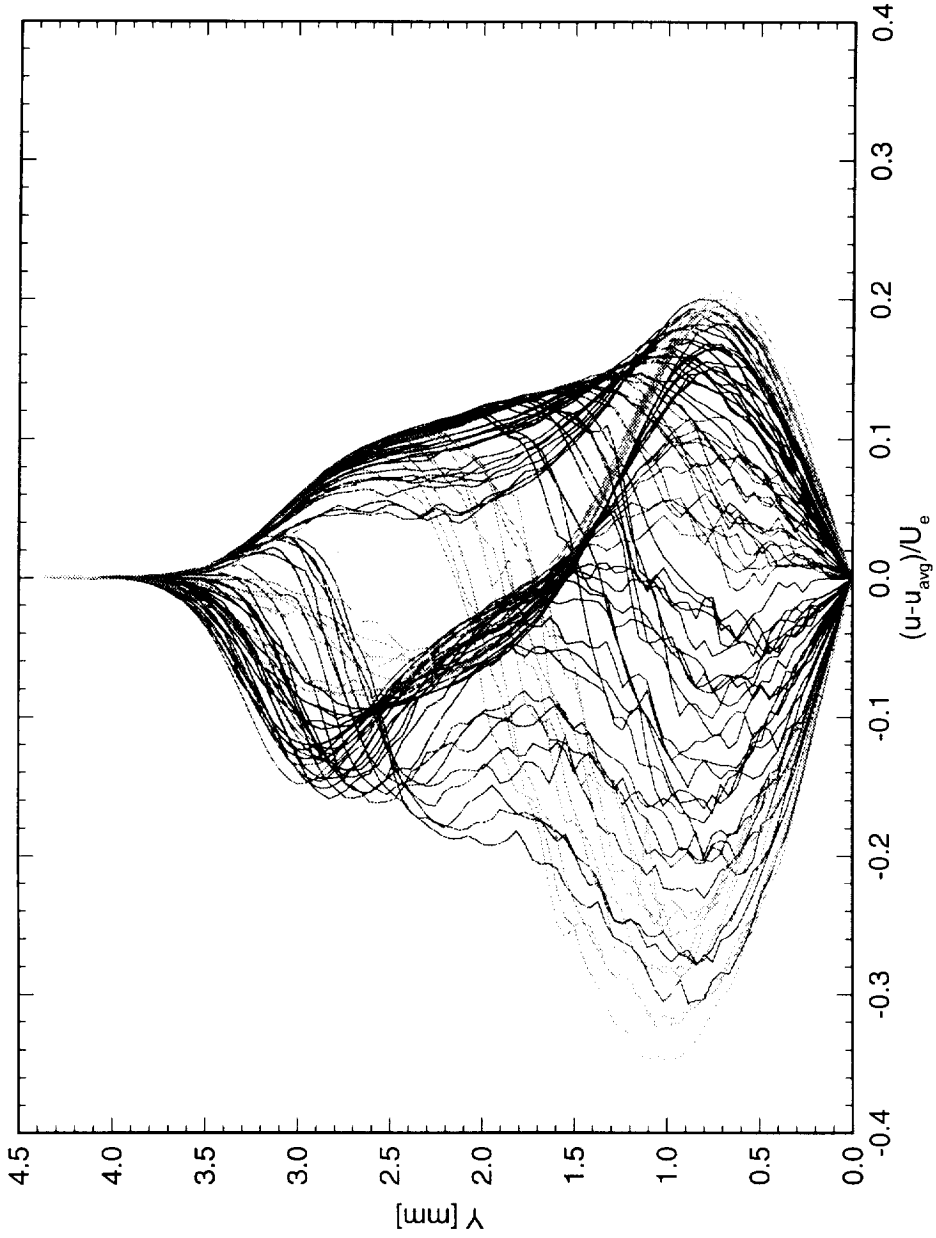

Figure 5.35: Spanwise array of 100 disturbance profiles covering a span of 99 mm at $x/c = 0.45$. $Re_c = 2.4 \times 10^6$, [6|12] roughness.

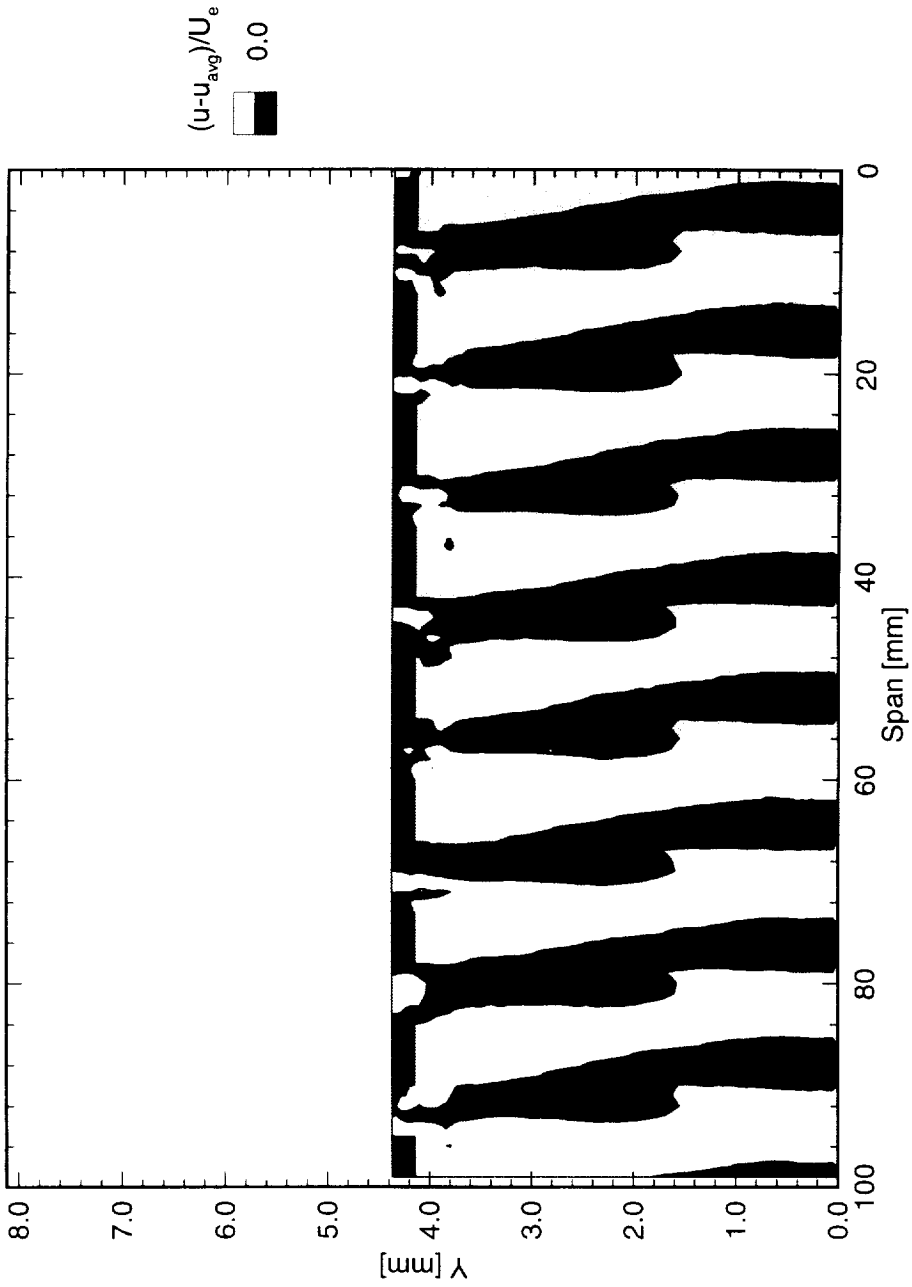

Figure 5.36: Disturbance velocity contours at $x/c = 0.45$. $Re_c = 2.4 \times 10^6$, [6|12] roughness.

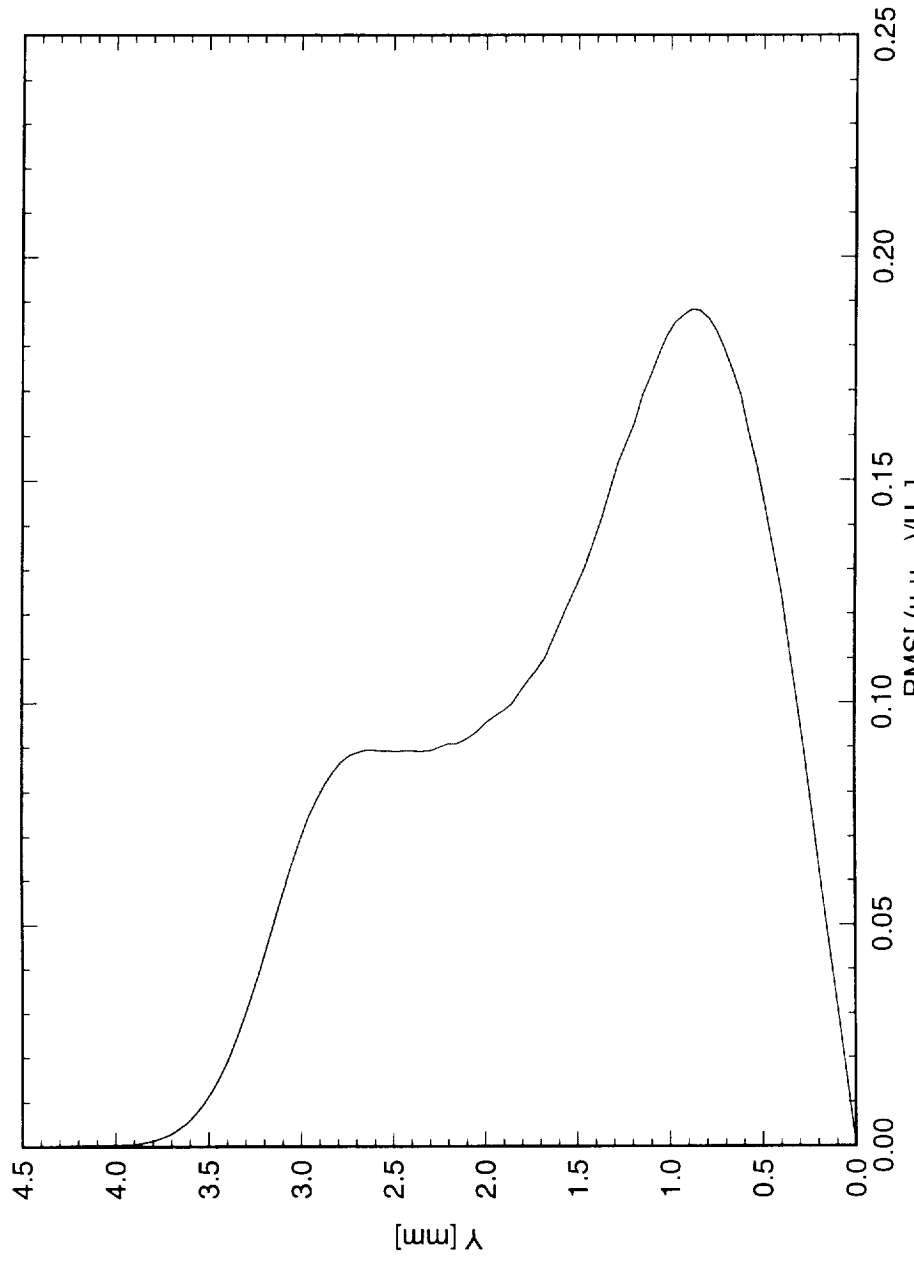

Figure 5.37: Stationary crossflow mode shape at $x/c = 0.45$. $Re_c = 2.4 \times 10^6$, [6|12] roughness.

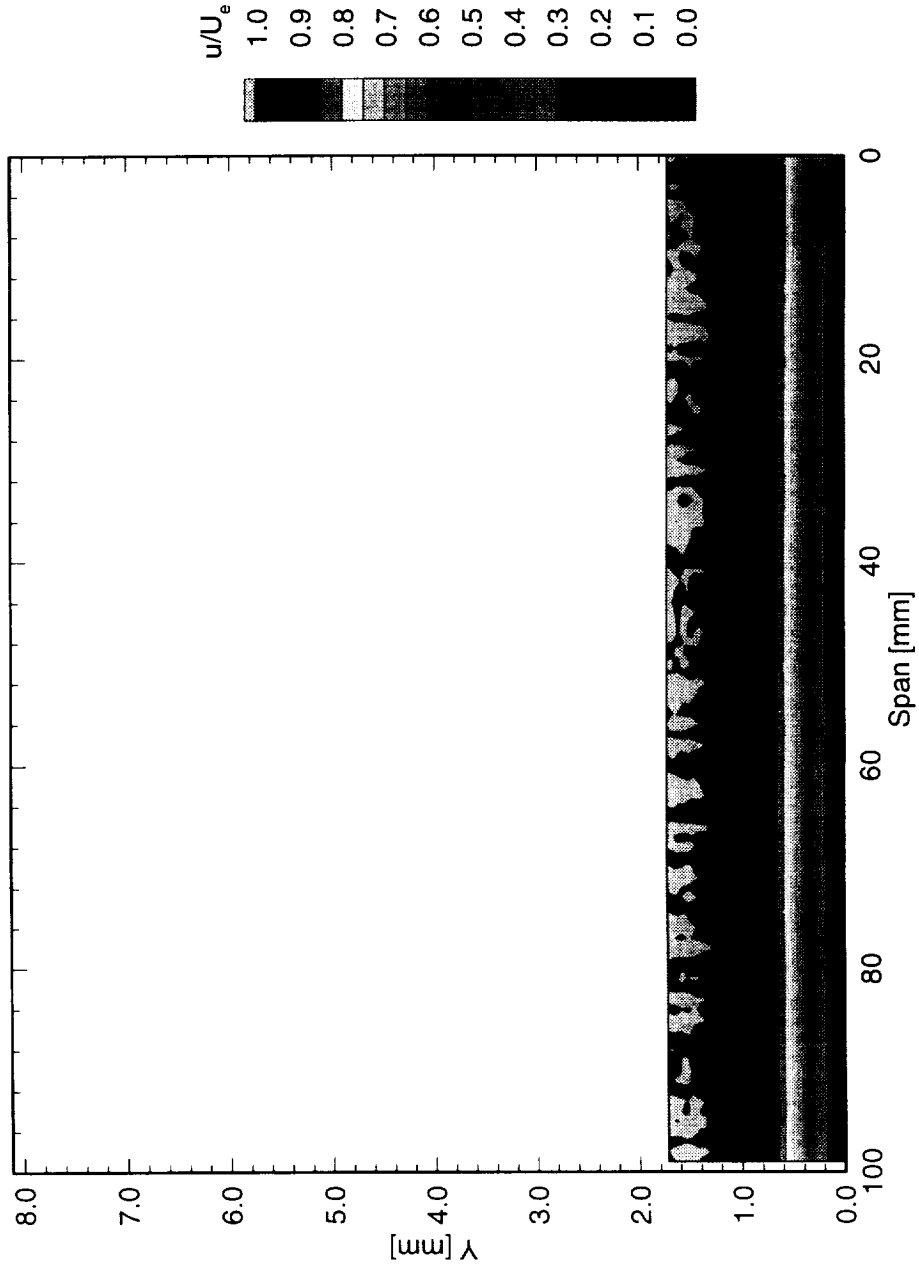

Figure 5.38: Streamwise velocity contours at $x/c = 0.05$. $Re_c = 2.4 \times 10^6$, [6|12] roughness.

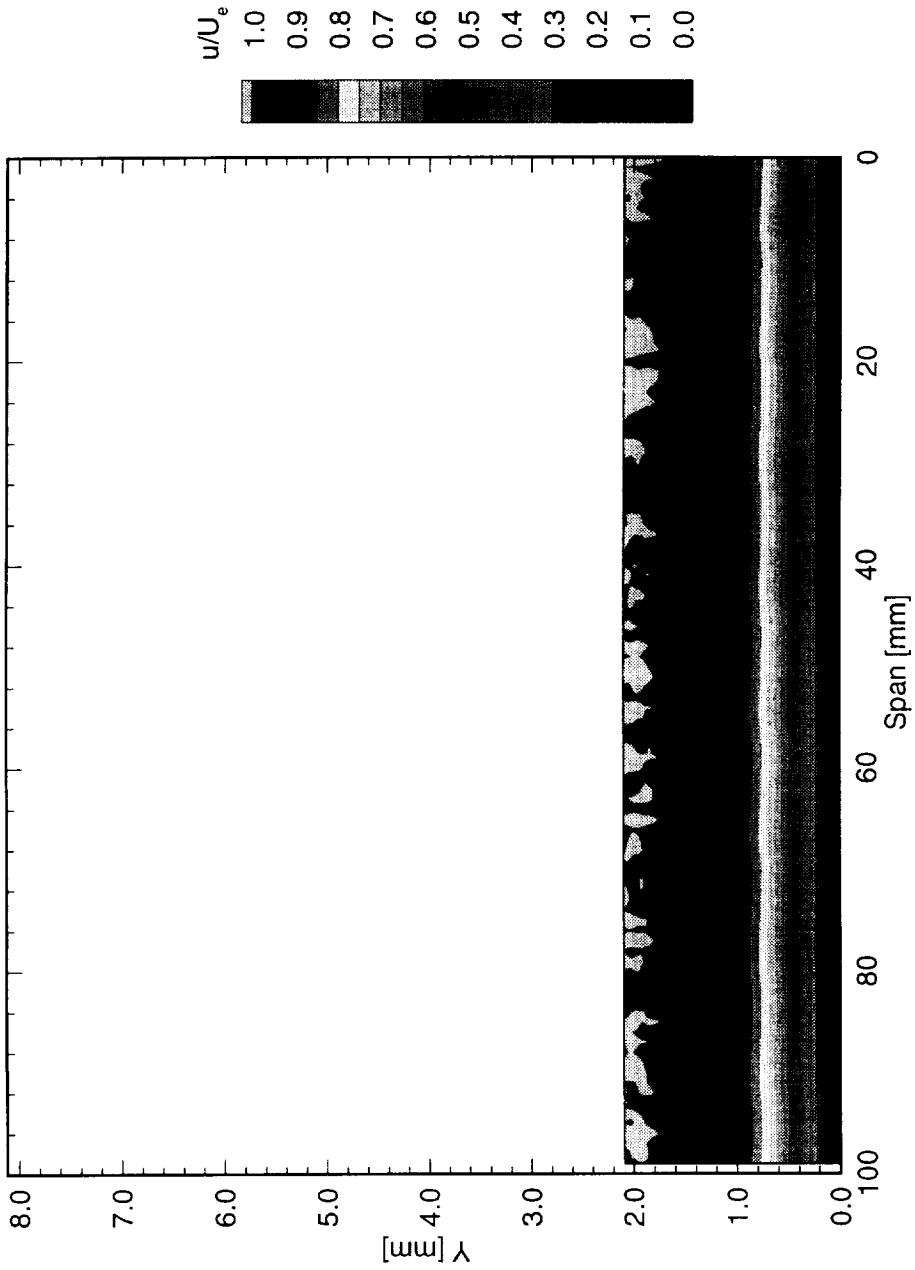

Figure 5.39: Streamwise velocity contours at $x/c = 0.10$. $Re_c = 2.4 \times 10^6$, [6|12] roughness.

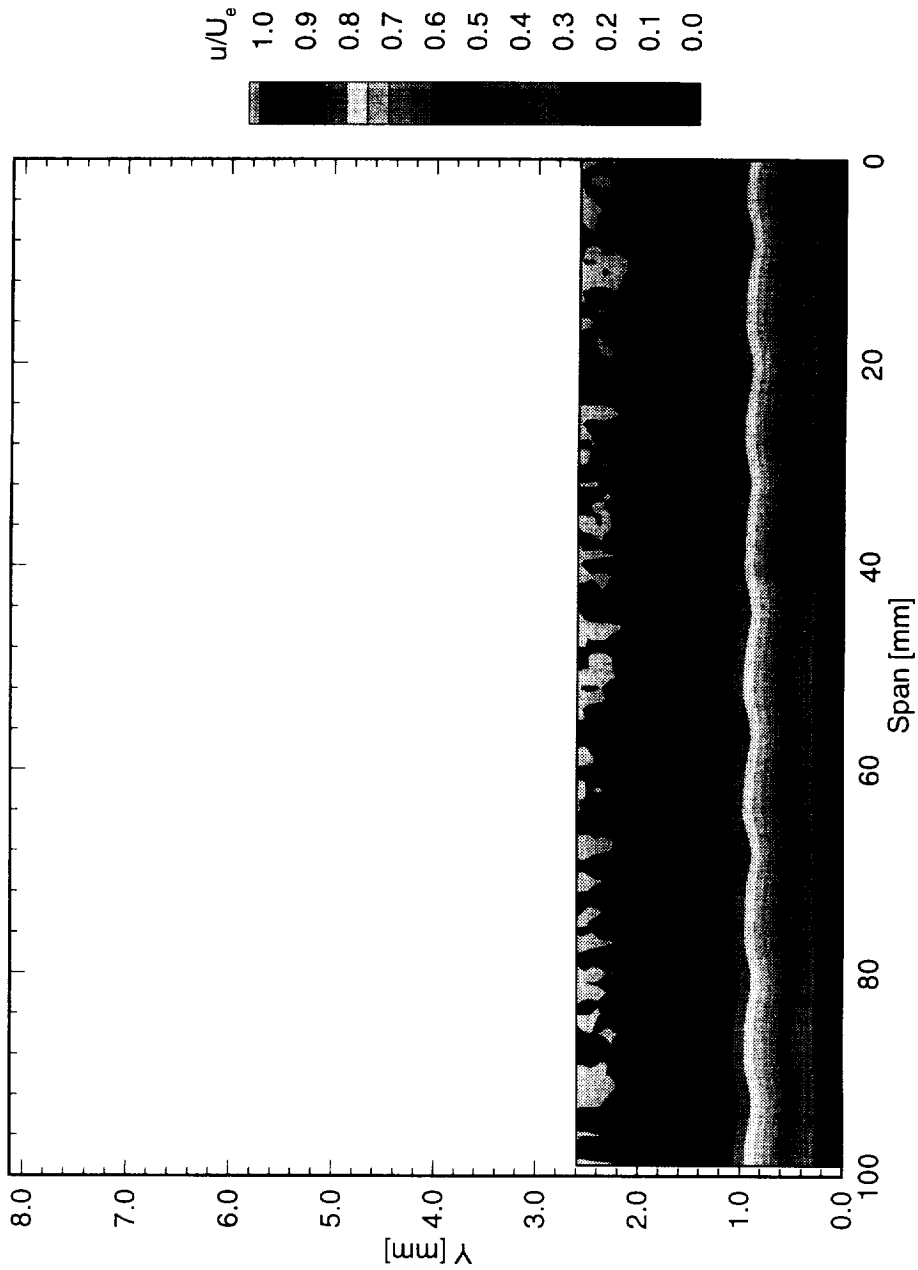

Figure 5.40: Streamwise velocity contours at $x/c = 0.15$. $Re_c = 2.4 \times 10^6$, [6|12] roughness.

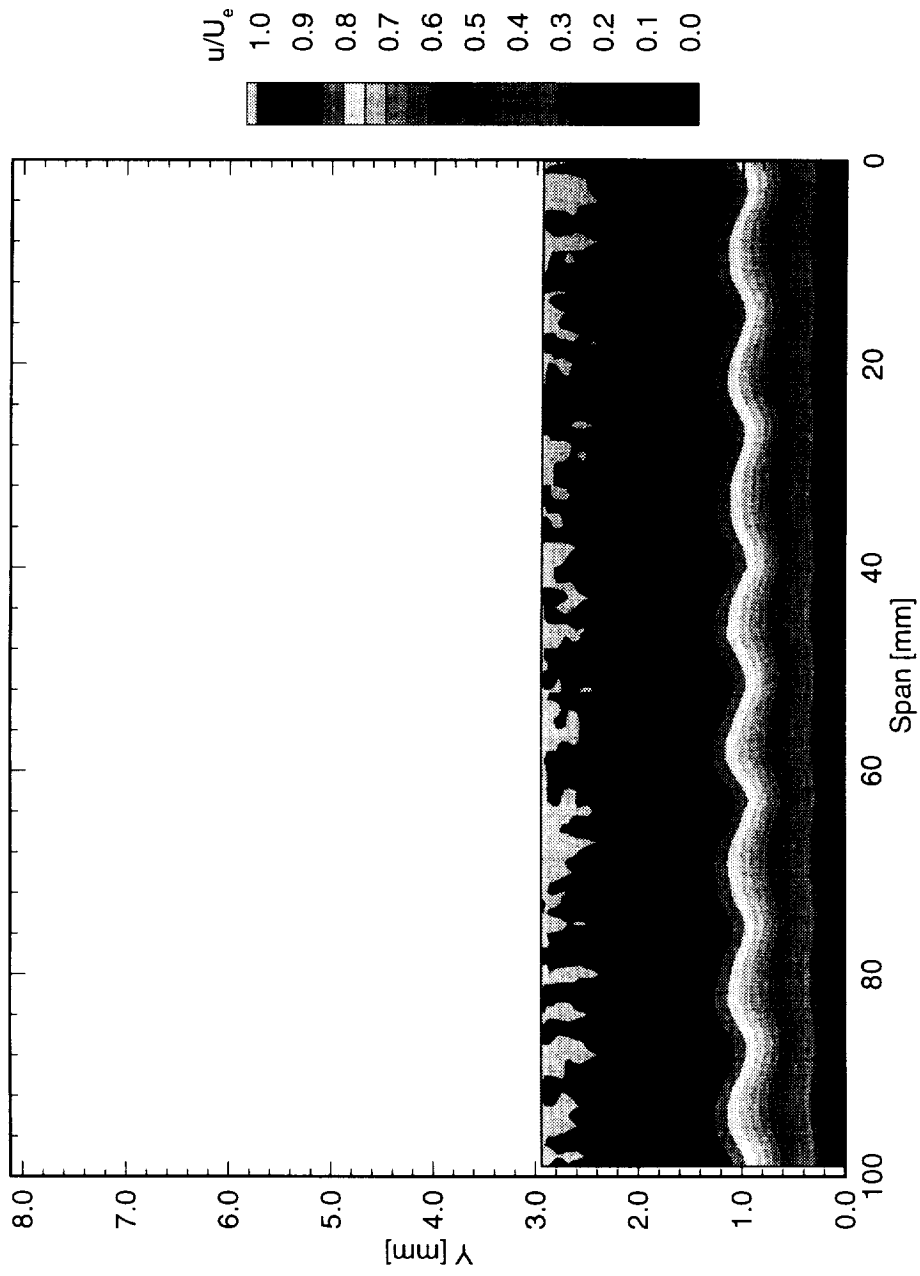

Figure 5.41: Streamwise velocity contours at $x/c = 0.20$. $Re_c = 2.4 \times 10^6$, [6|12] roughness.

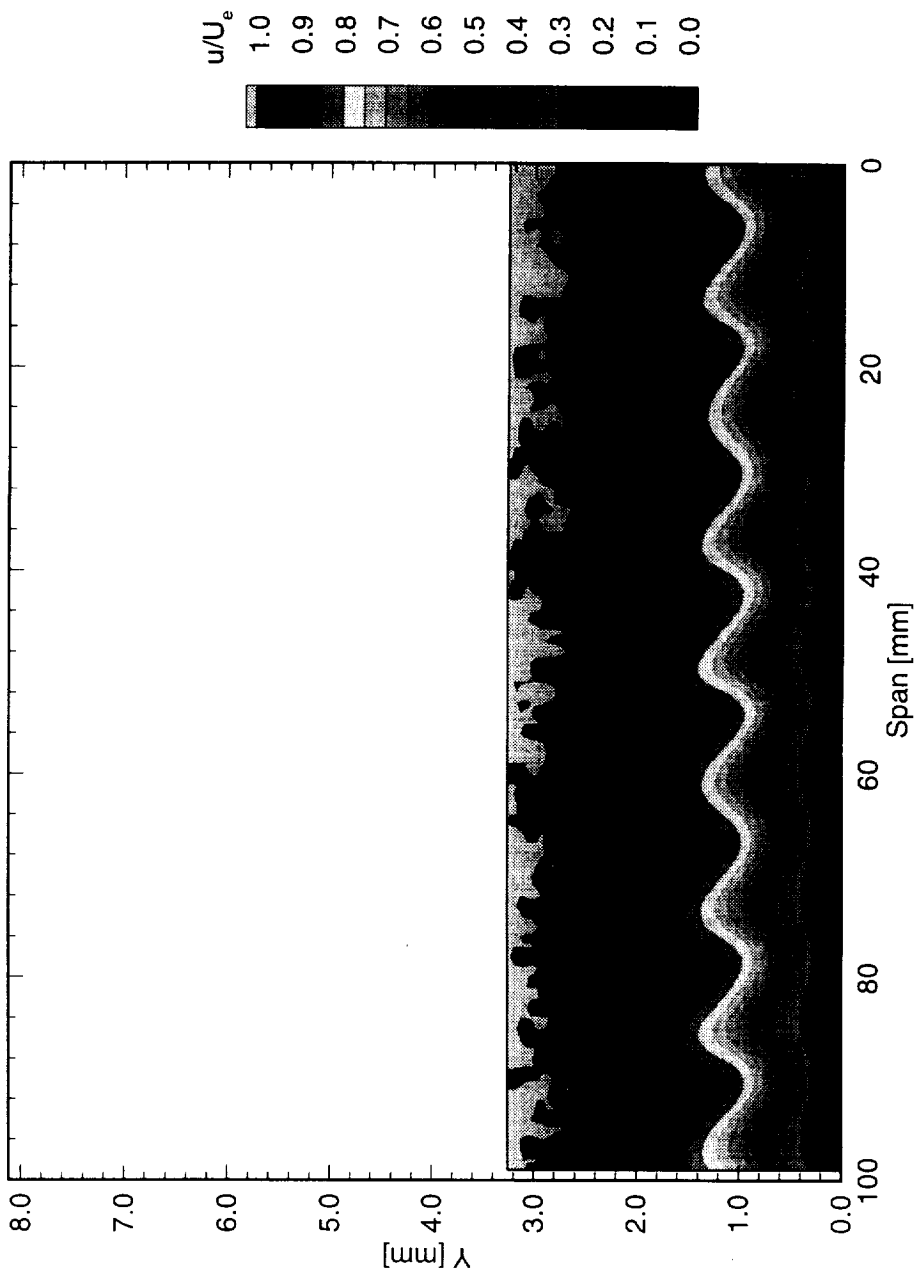

Figure 5.42: Streamwise velocity contours at $x/c = 0.25$. $Re_c = 2.4 \times 10^6$, [6|12] roughness.

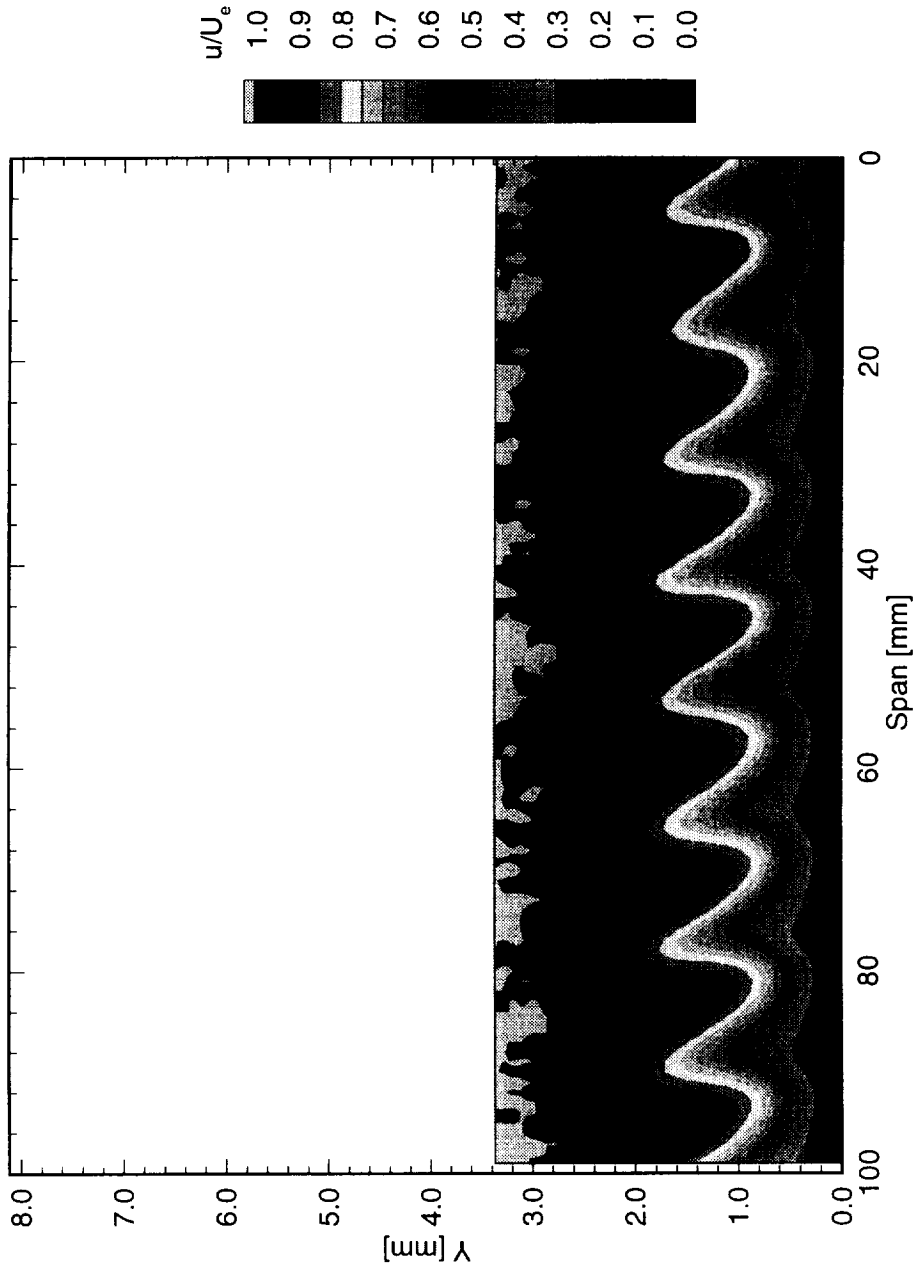

Figure 5.43: Streamwise velocity contours at $x/c = 0.30$. $Re_c = 2.4 \times 10^6$, [6|12] roughness.

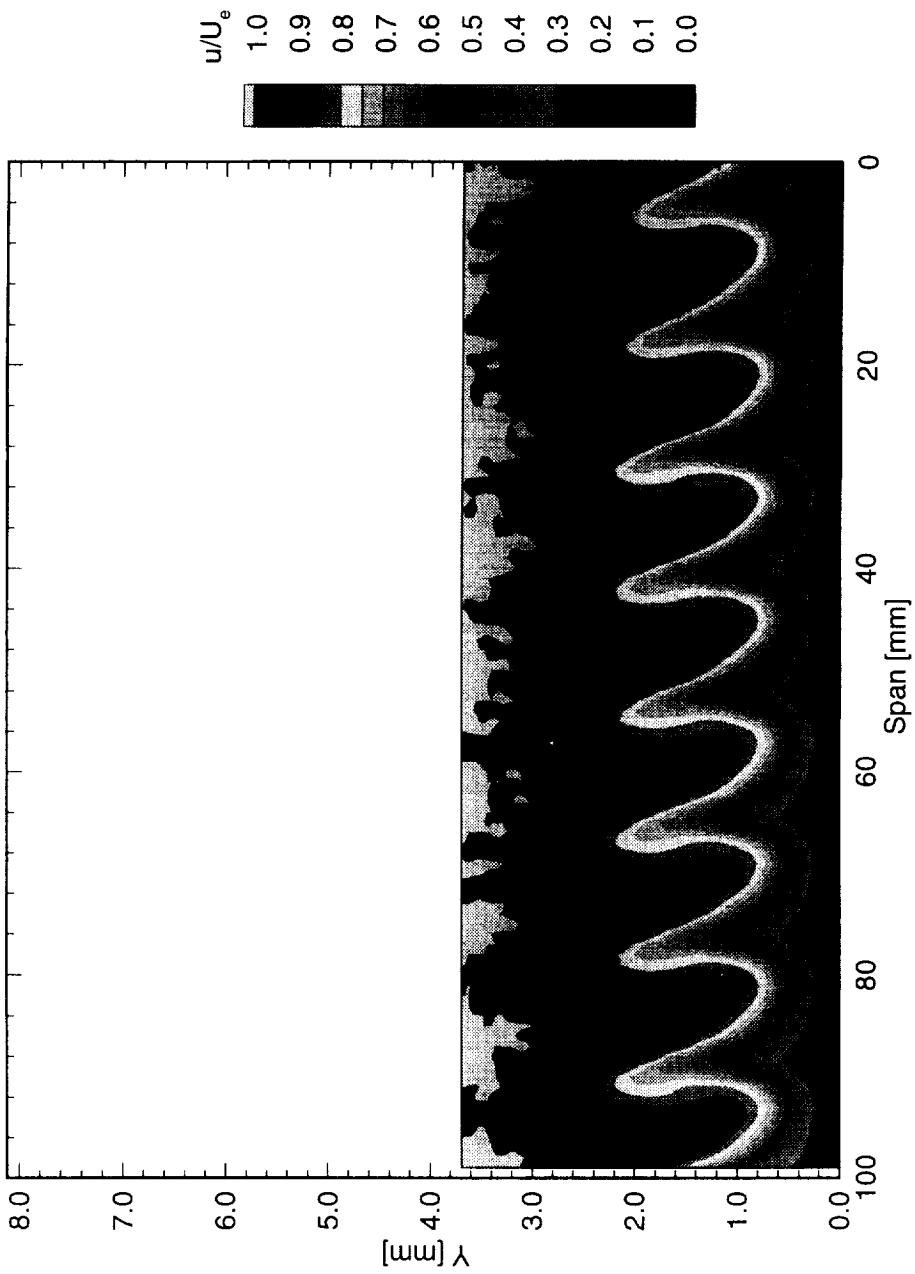

Figure 5.44: Streamwise velocity contours at $x/c = 0.35$. $Re_c = 2.4 \times 10^6$, [6|12] roughness.

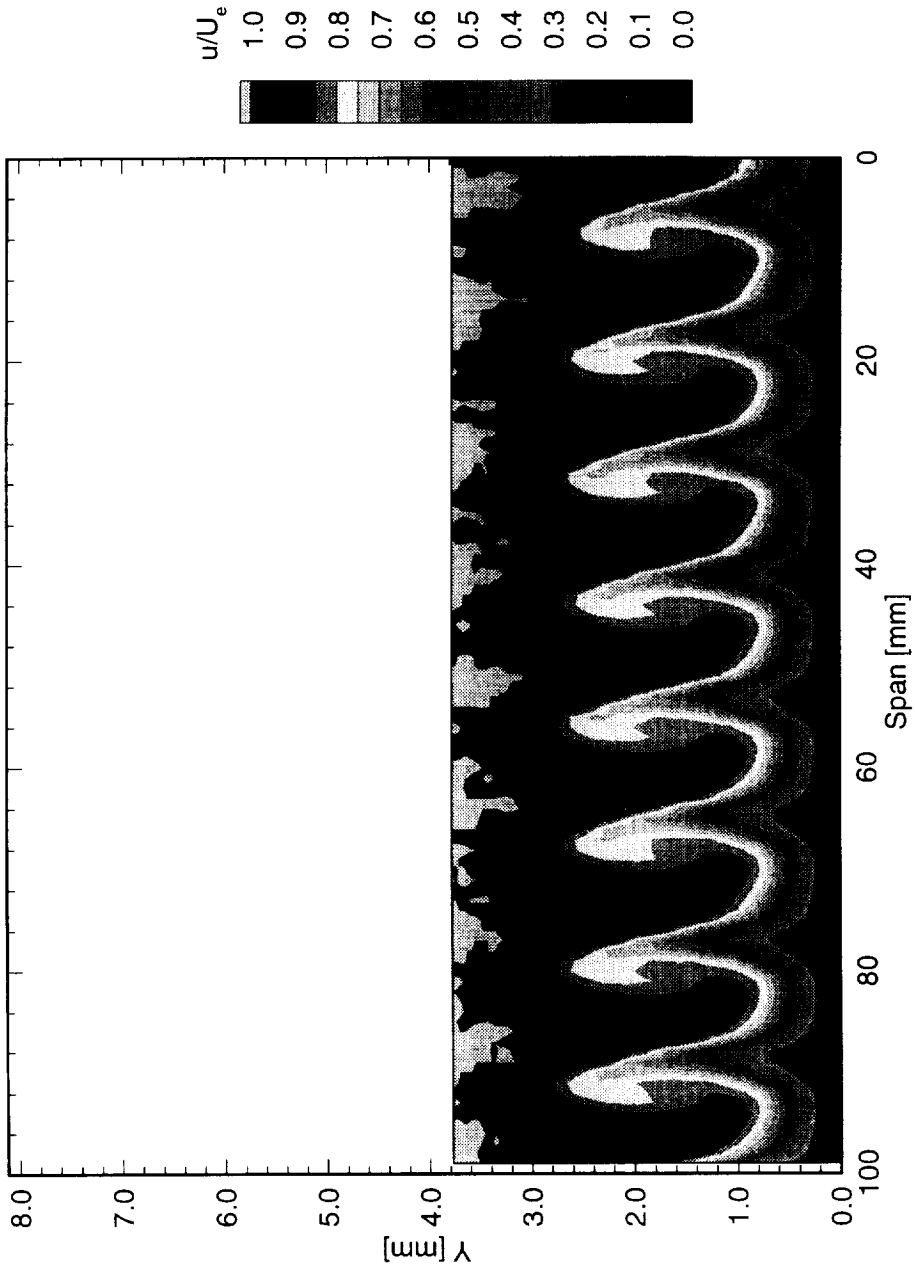

Figure 5.45: Streamwise velocity contours at $x/c = 0.40$. $Re_c = 2.4 \times 10^6$, [6|12] roughness.

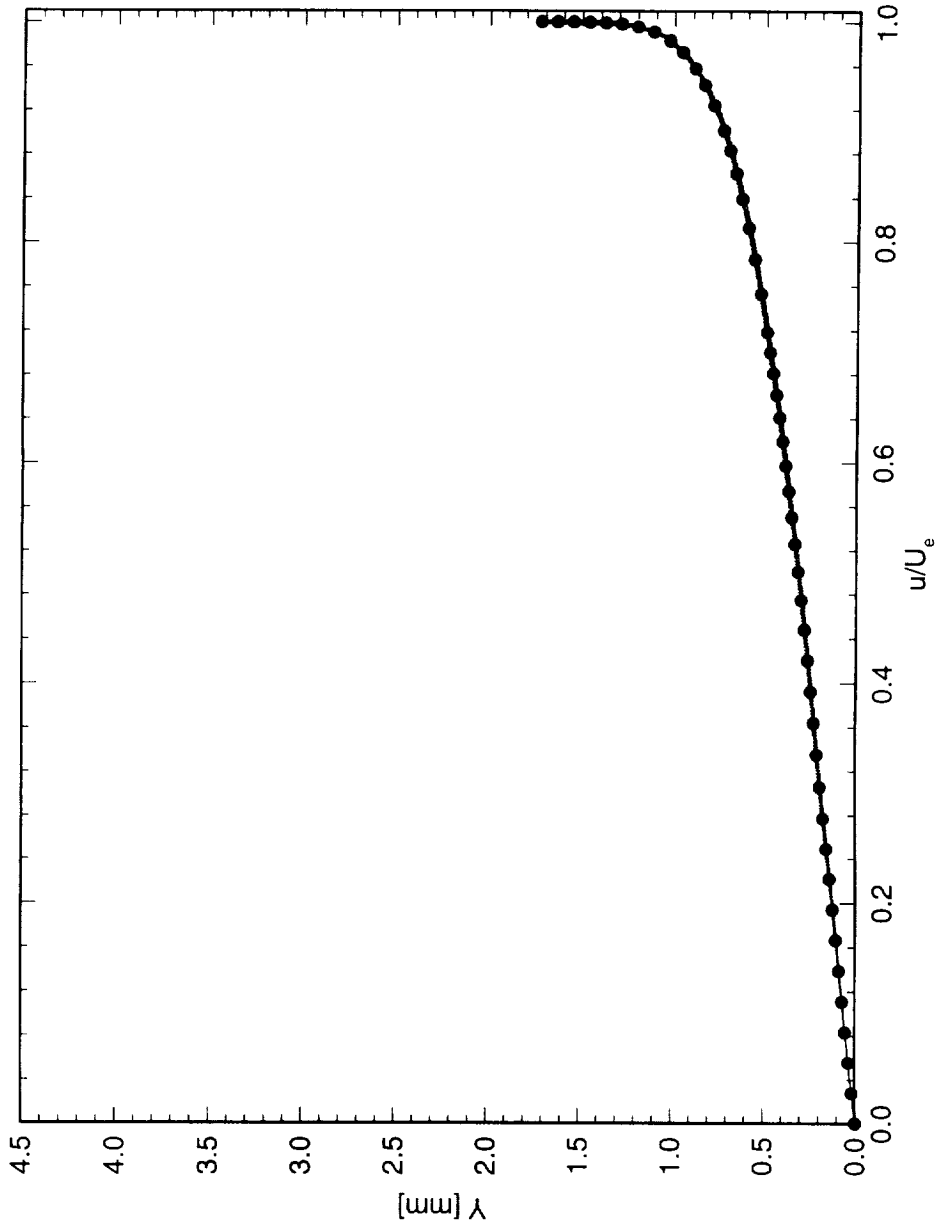

Figure 5.46: Spanwise array of 100 mean-flow boundary-layer profiles covering a span of 99 mm at $x/c = 0.05$. $Re_c = 2.4 \times 10^6$, [6|12] roughness. The dots indicate the mean of the profiles.

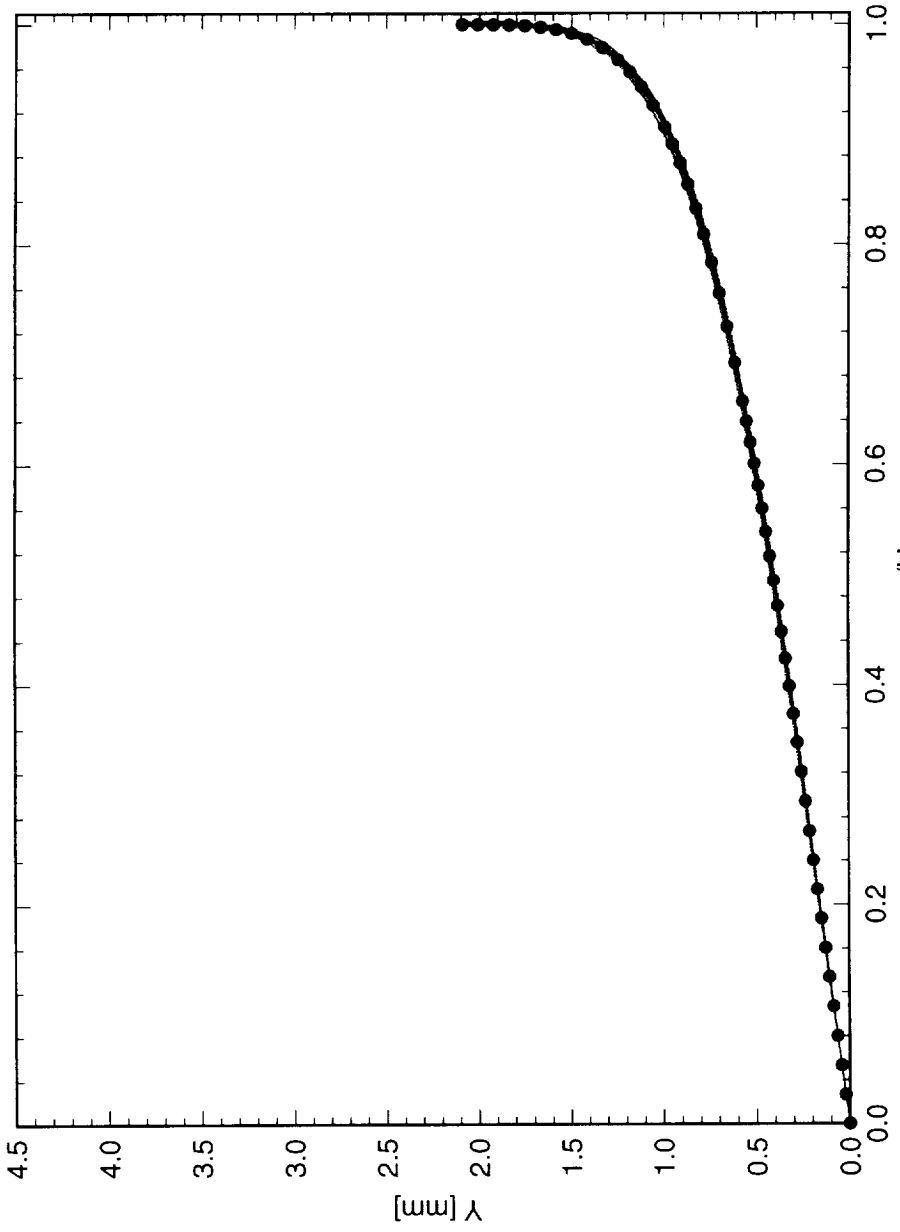

Figure 5.47: Spanwise array of 100 mean-flow boundary-layer profiles covering a span of 99 mm at $x/c = 0.10$. $Re_c = 2.4 \times 10^6$, [6|12] roughness. The dots indicate the mean of the profiles.

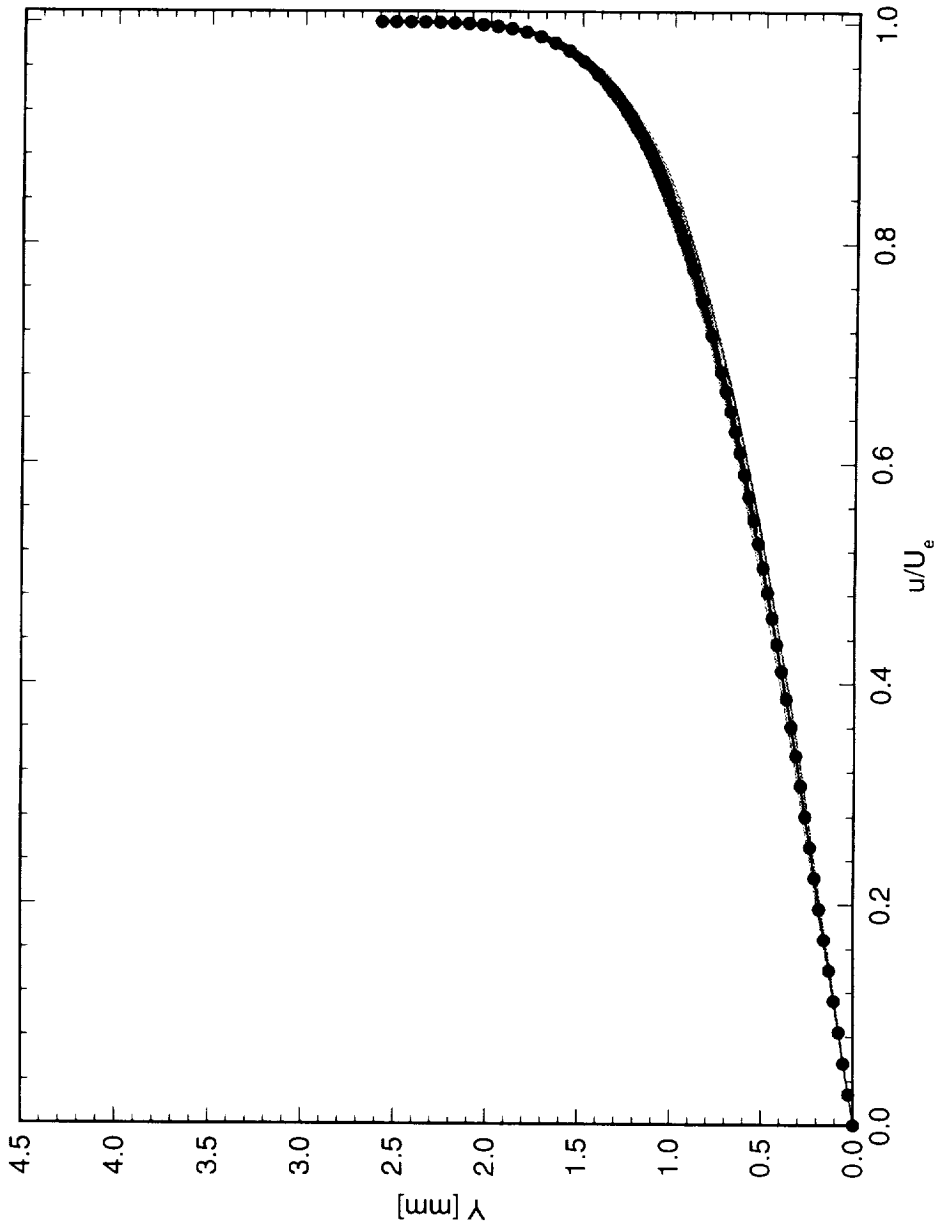

Figure 5.48: Spanwise array of 100 mean-flow boundary-layer profiles covering a span of 99 mm at $x/c = 0.15$. $Re_c = 2.4 \times 10^6$. [6|12] roughness. The dots indicate the mean of the profiles.

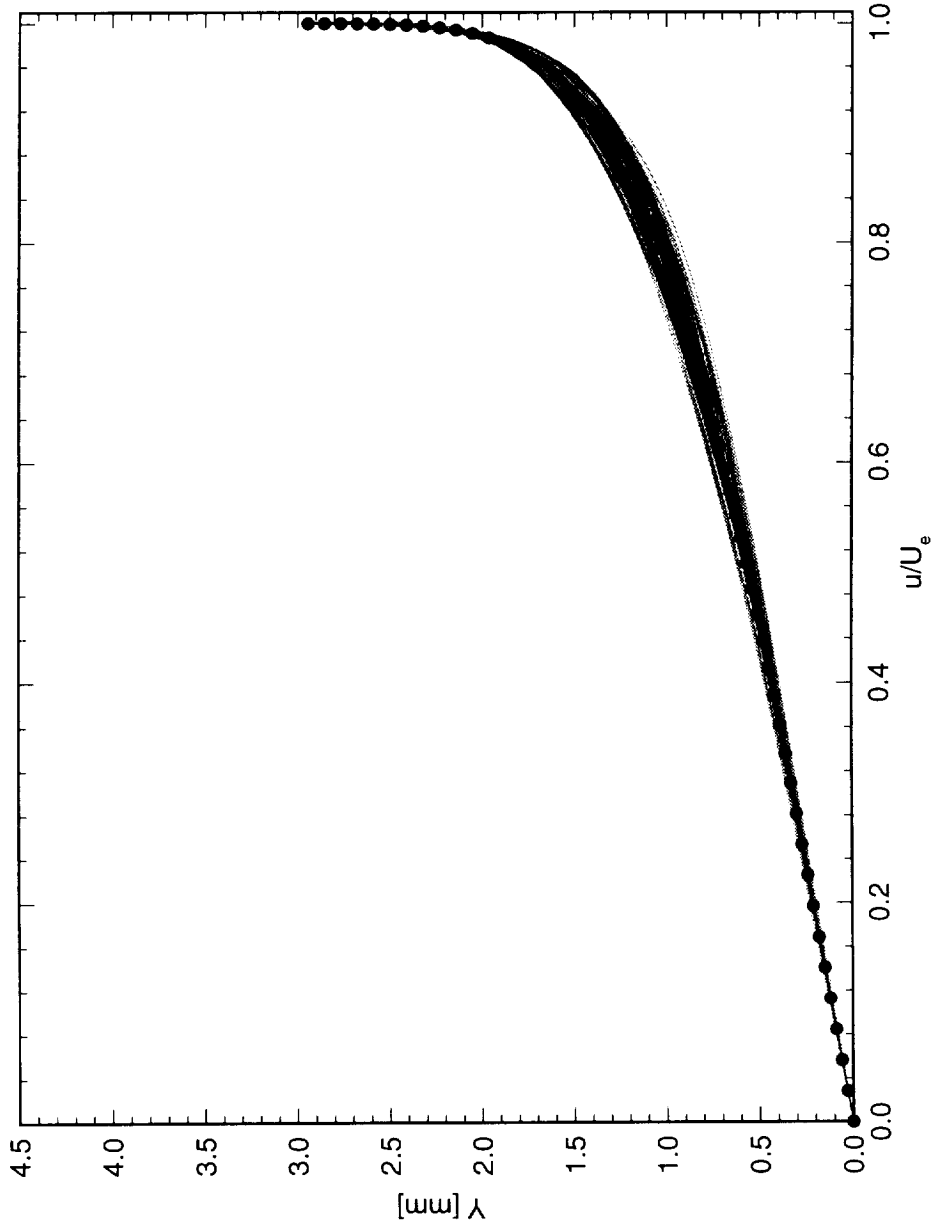

Figure 5.49: Spanwise array of 100 mean-flow boundary-layer profiles covering a span of 99 mm at $x/c = 0.20$. $Re_c = 2.4 \times 10^6$, [6|12] roughness. The dots indicate the mean of the profiles.

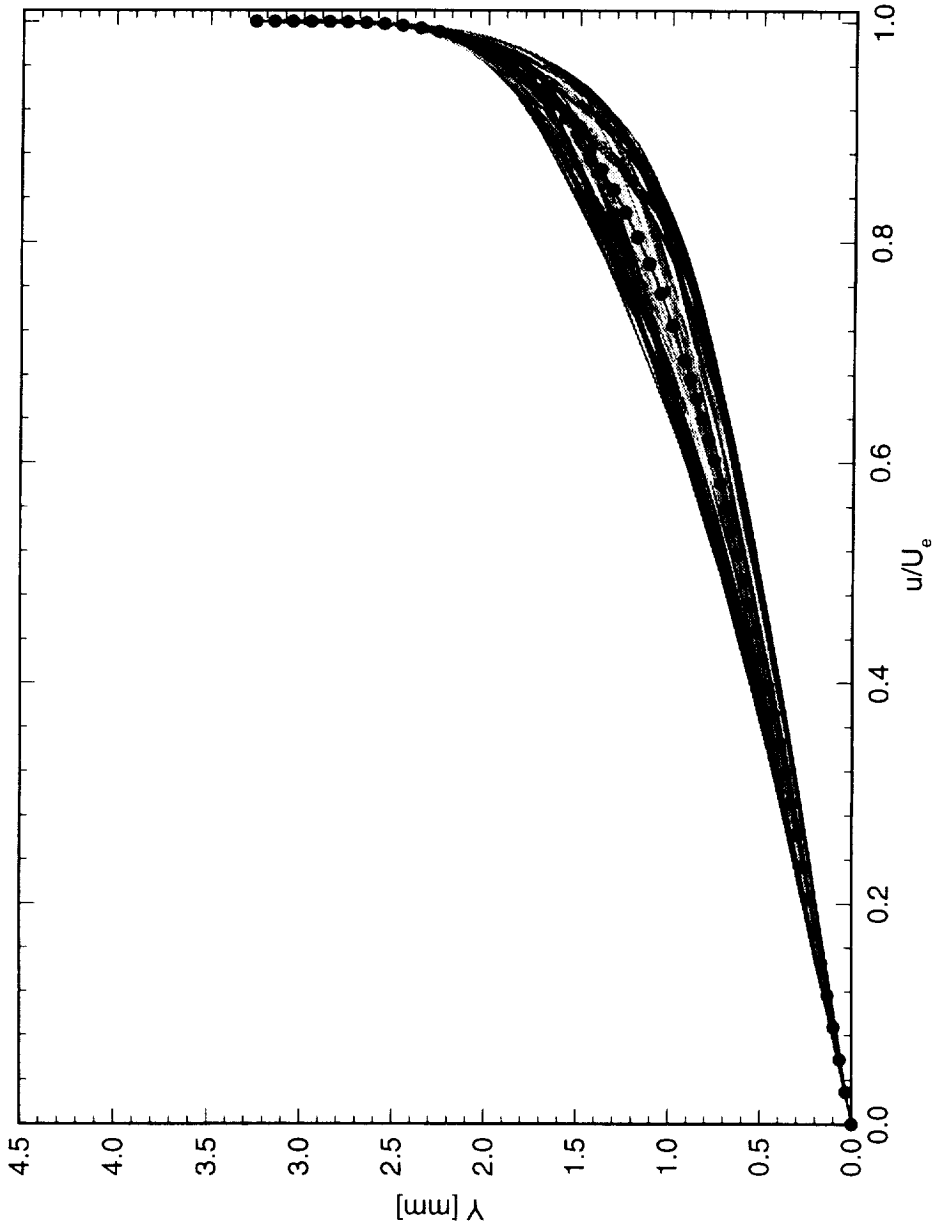

Figure 5.50: Spanwise array of 100 mean-flow boundary-layer profiles covering a span of 99 mm at $x/c = 0.25$. $Re_c = 2.4 \times 10^6$, [6|12] roughness. The dots indicate the mean of the profiles.

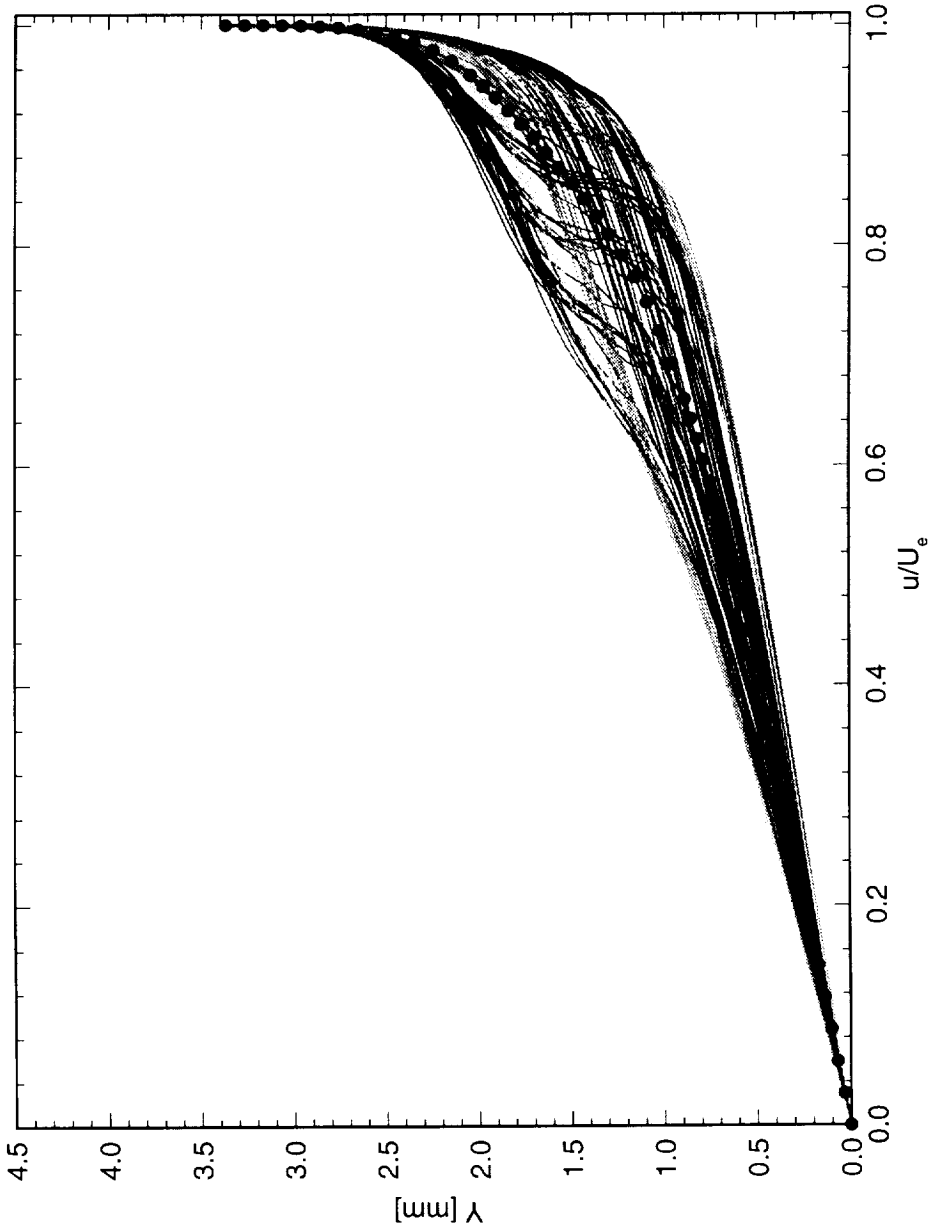

Figure 5.51: Spanwise array of 100 mean-flow boundary-layer profiles covering a span of 99 mm at $x/c = 0.30$. $Re_c = 2.4 \times 10^6$, [6|12] roughness. The dots indicate the mean of the profiles.

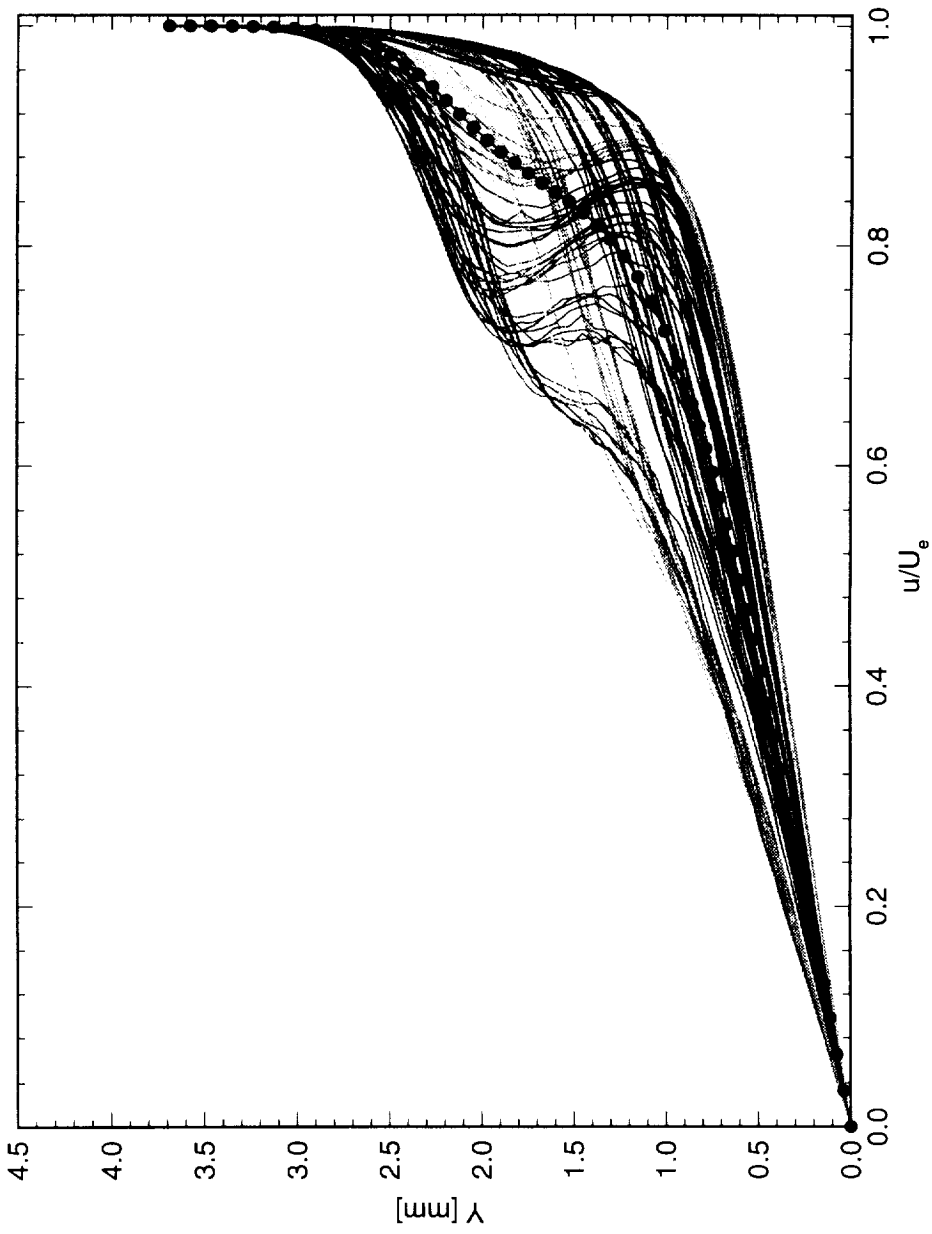

Figure 5.52: Spanwise array of 100 mean-flow boundary-layer profiles covering a span of 99 mm at $x/c = 0.35$. $Re_c = 2.4 \times 10^6$, [6|12] roughness. The dots indicate the mean of the profiles.

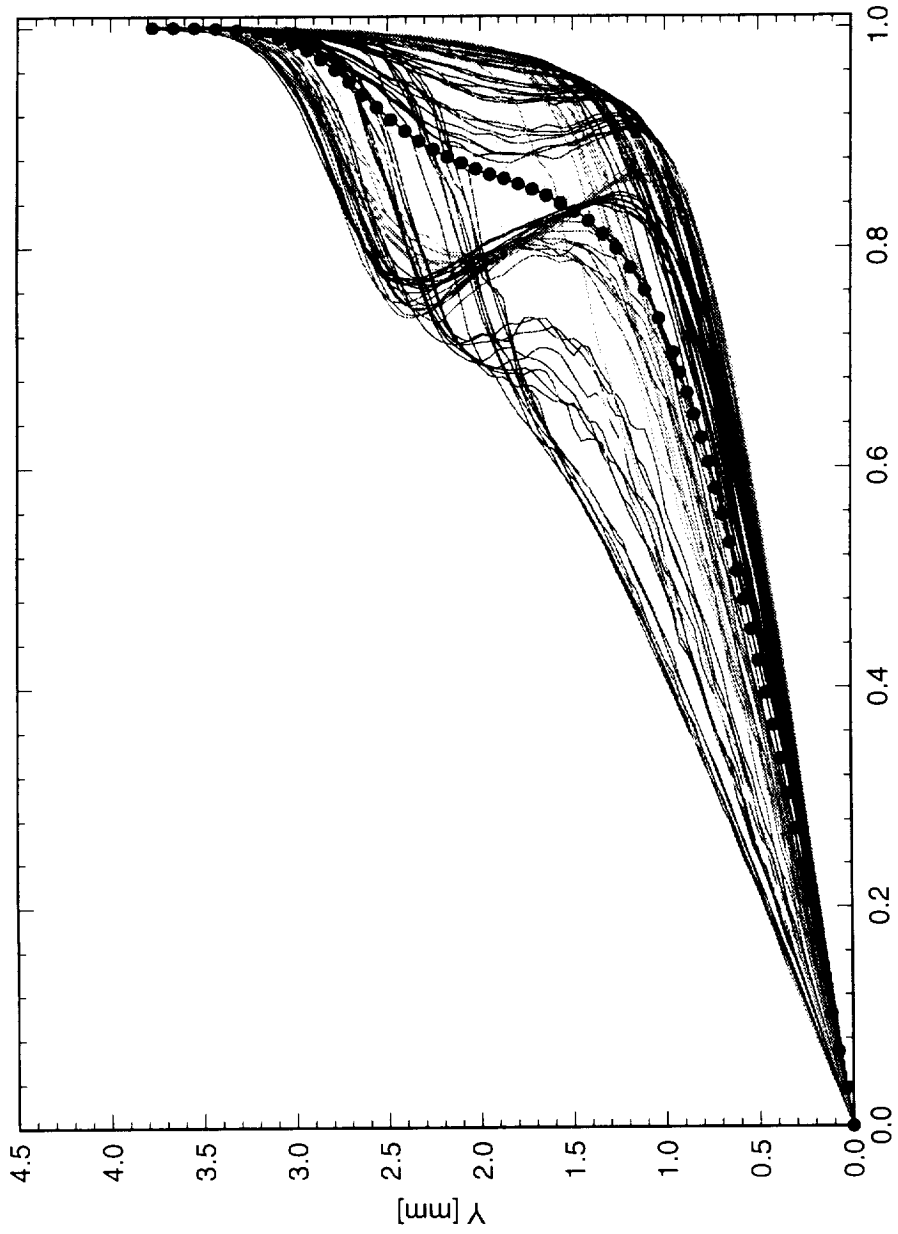

Figure 5.53: Spanwise array of 100 mean-flow boundary-layer profiles covering a span of 99 mm at $x/c = 0.40$. $Re_c = 2.4 \times 10^6$, [6|12] roughness. The dots indicate the mean of the profiles.

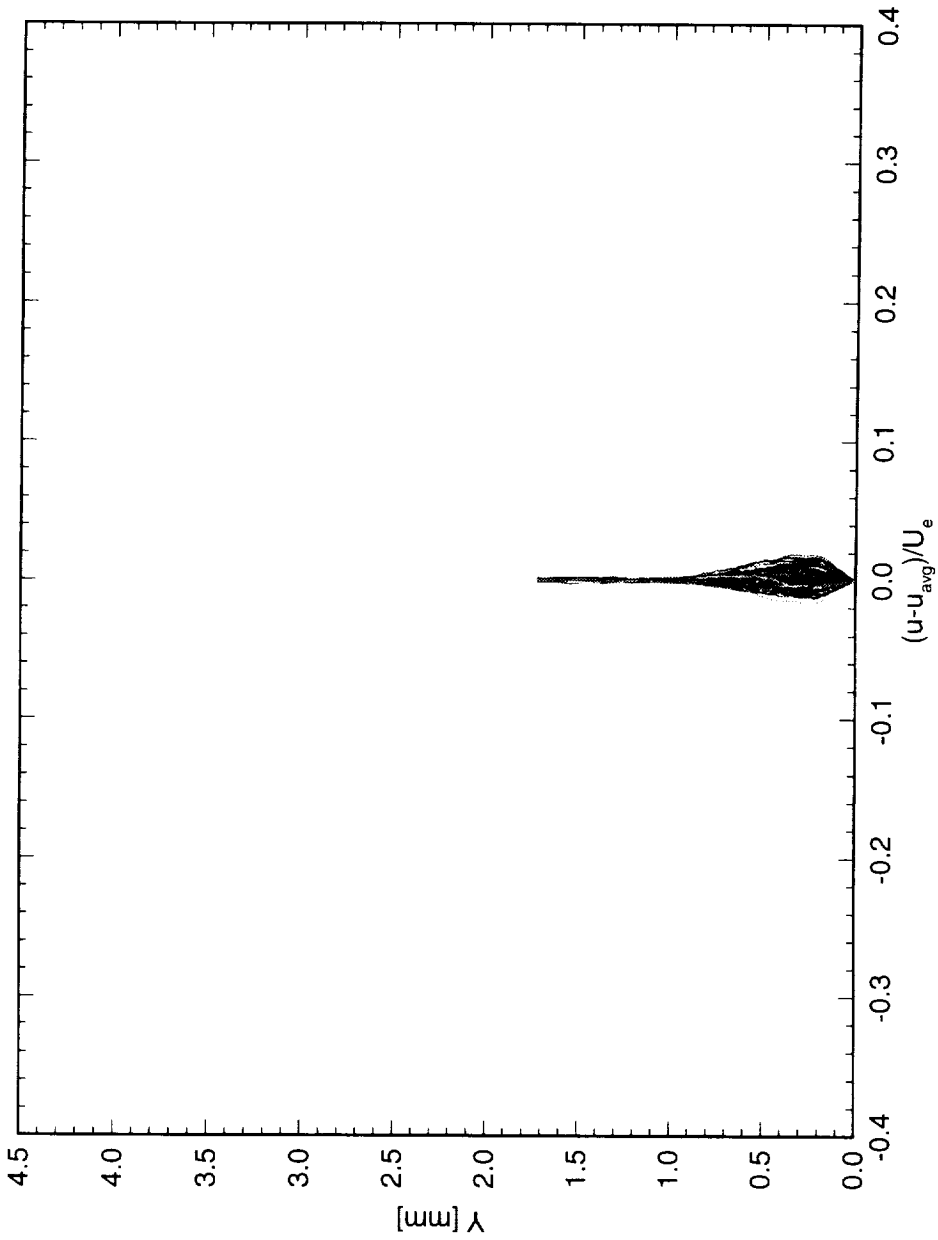

Figure 5.54: Spanwise array of 100 disturbance profiles covering a span of 99 mm at $x/c = 0.05$. $Re_c = 2.4 \times 10^6$, [6|12] roughness.

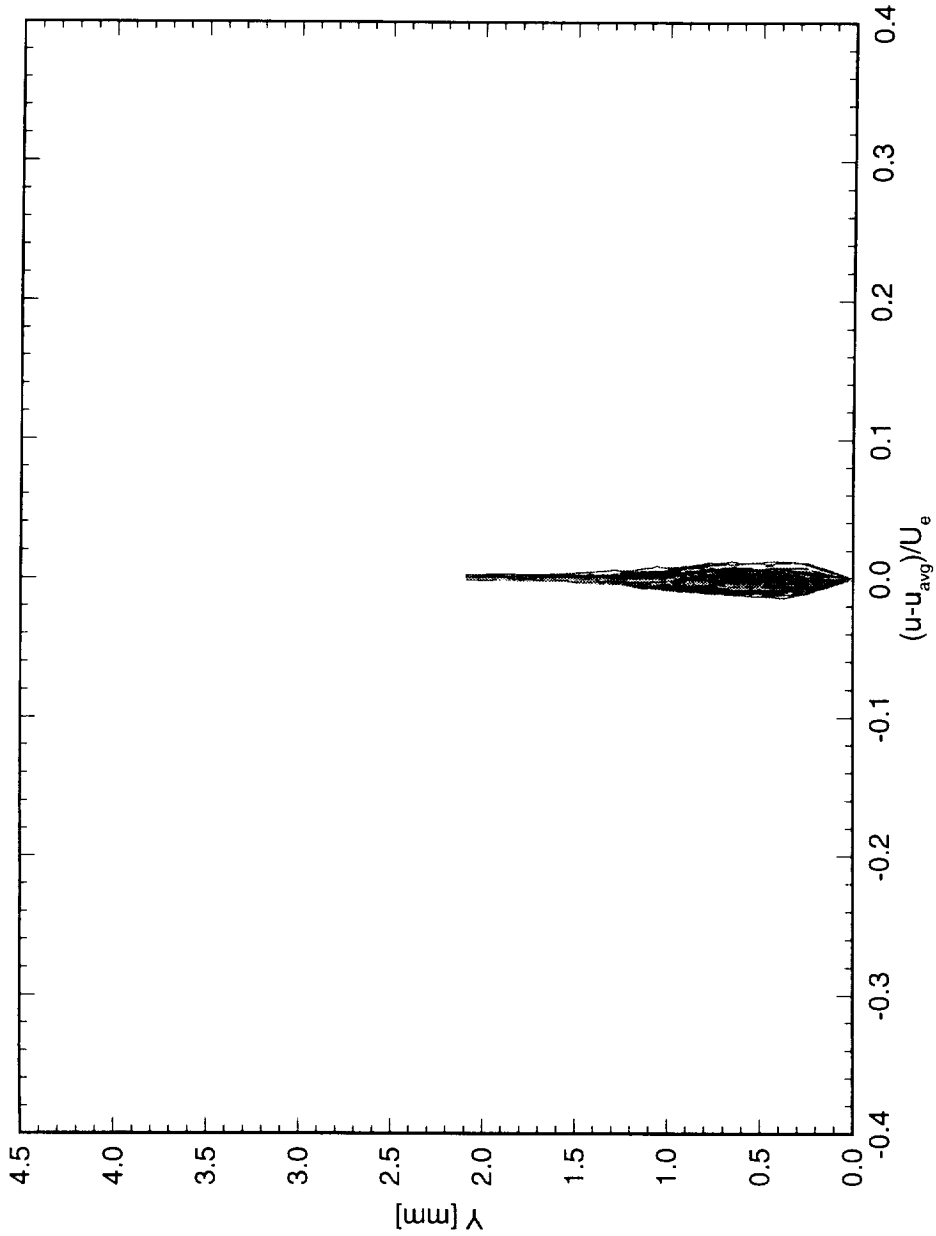

Figure 5.55: Spanwise array of 100 disturbance profiles covering a span of 99 mm at $x/c = 0.10$. $Re_c = 2.4 \times 10^6$, [6|12] roughness.

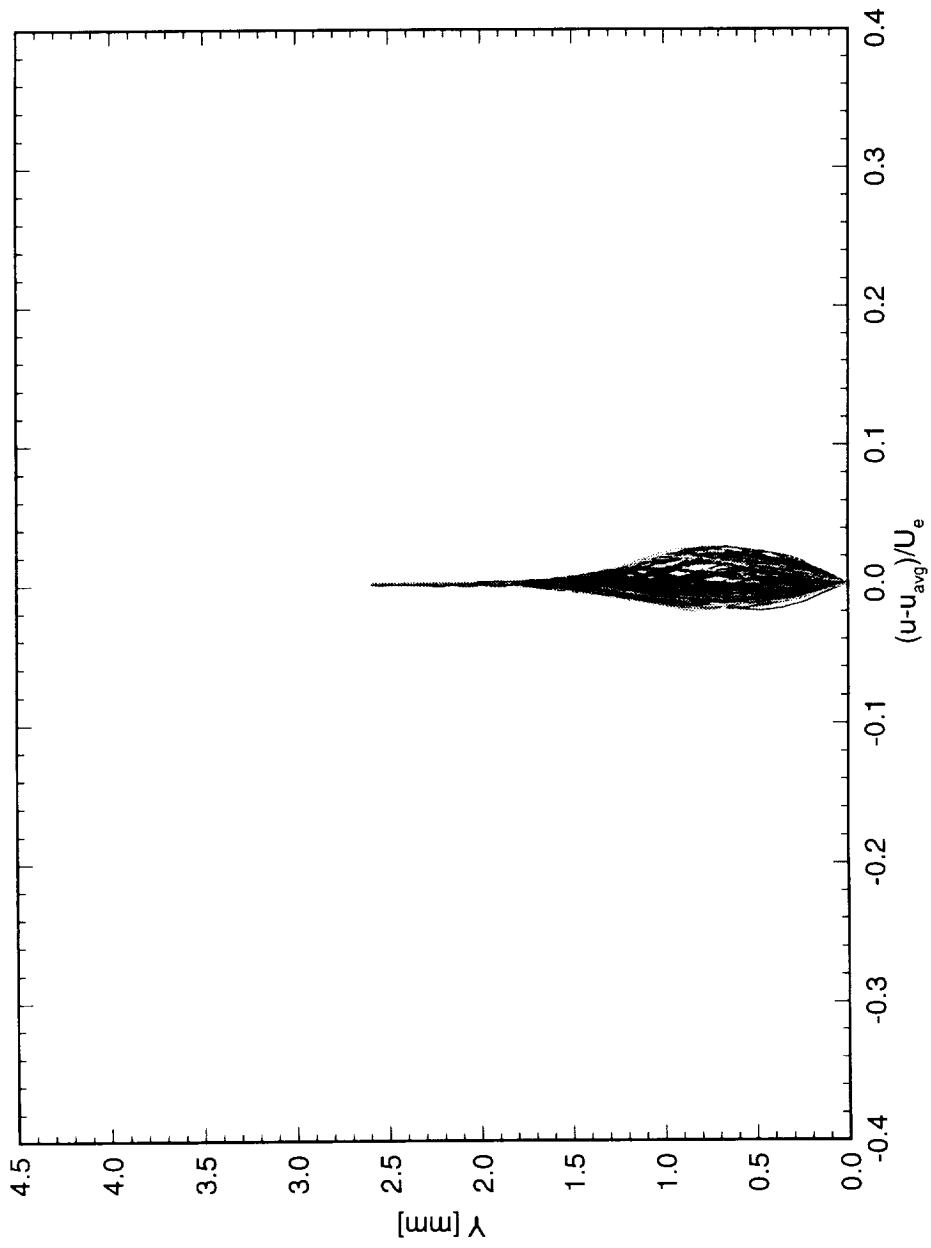

Figure 5.56: Spanwise array of 100 disturbance profiles covering a span of 99 mm at $x/c = 0.15$. $Re_c = 2.4 \times 10^6$, [6|12] roughness.

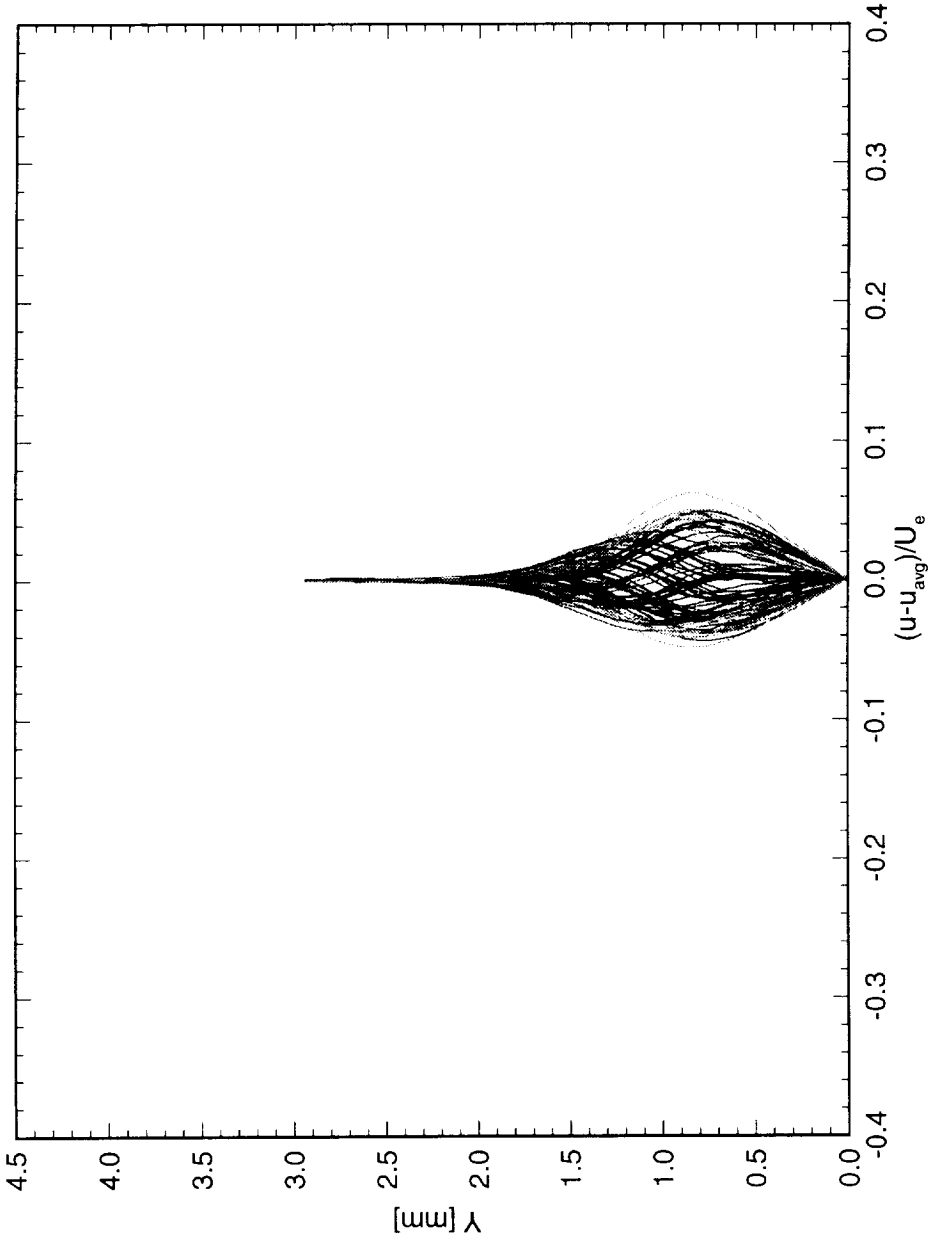

Figure 5.57: Spanwise array of 100 disturbance profiles covering a span of 99 mm at $x/c = 0.20$. $Re_c = 2.4 \times 10^6$, [6|12] roughness.

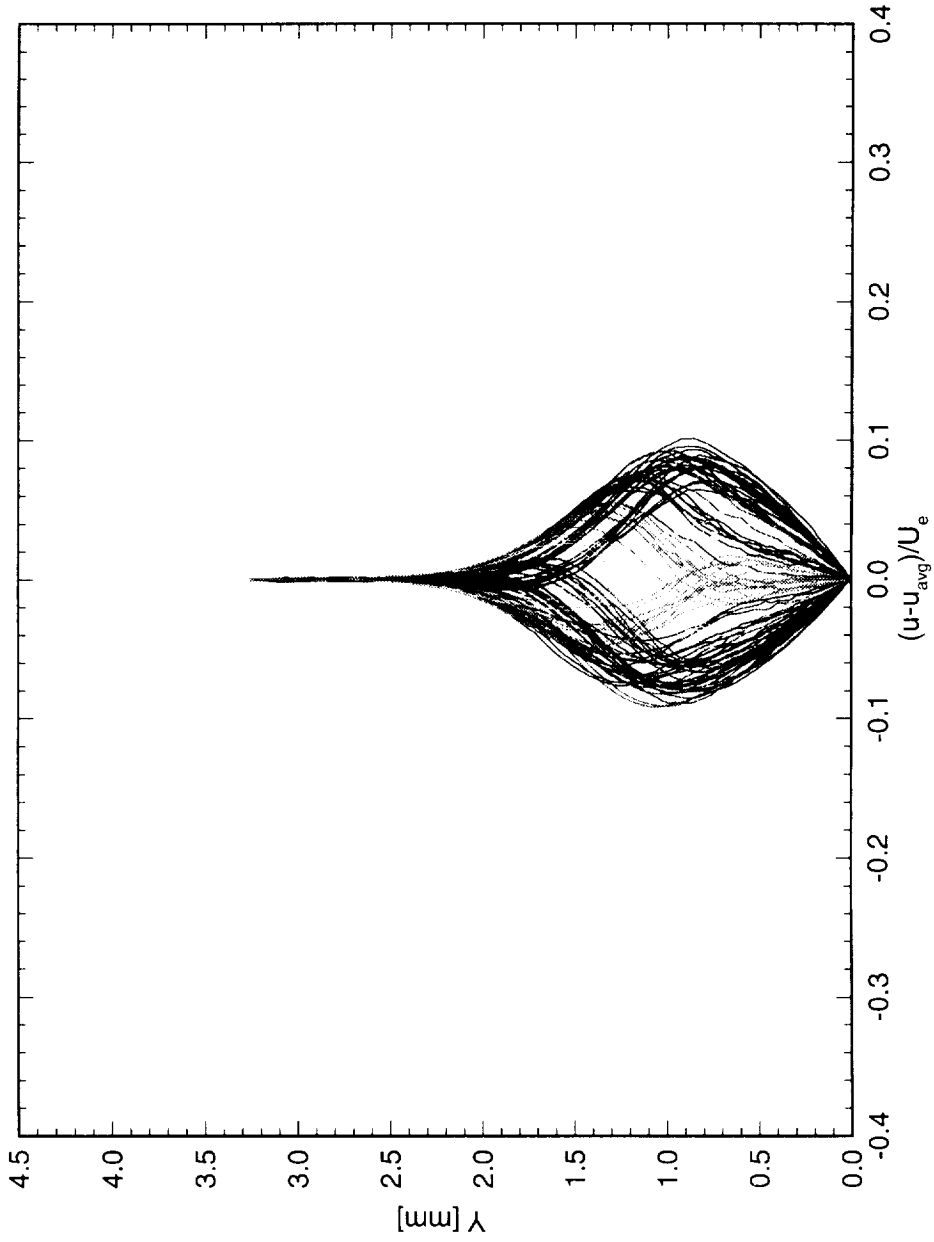

Figure 5.58: Spanwise array of 100 disturbance profiles covering a span of 99 mm at $x/c = 0.25$. $Re_c = 2.4 \times 10^6$, [6|12] roughness.

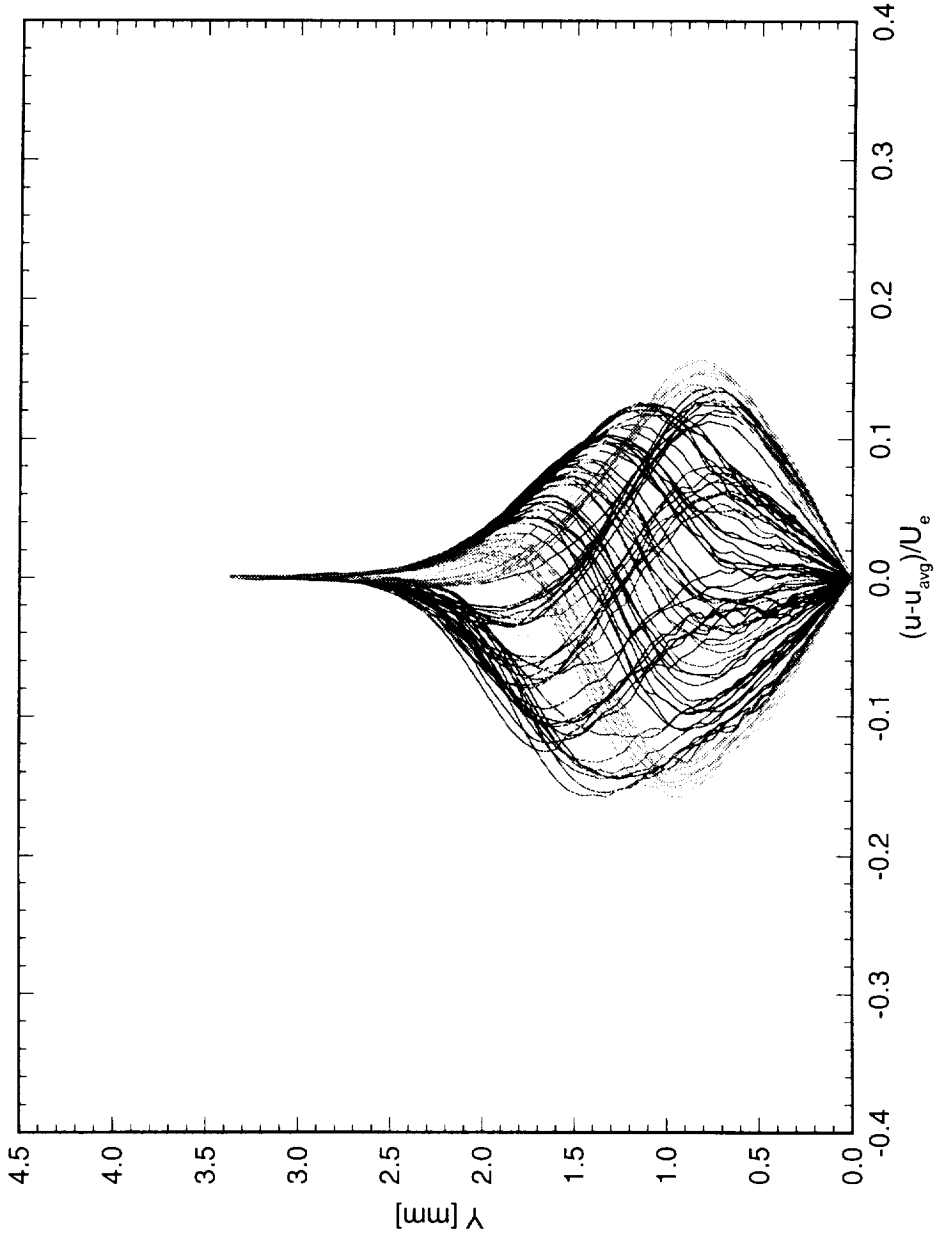

Figure 5.59: Spanwise array of 100 disturbance profiles covering a span of 99 mm at $x/c = 0.30$. $Re_c = 2.4 \times 10^6$. [6|12] roughness.

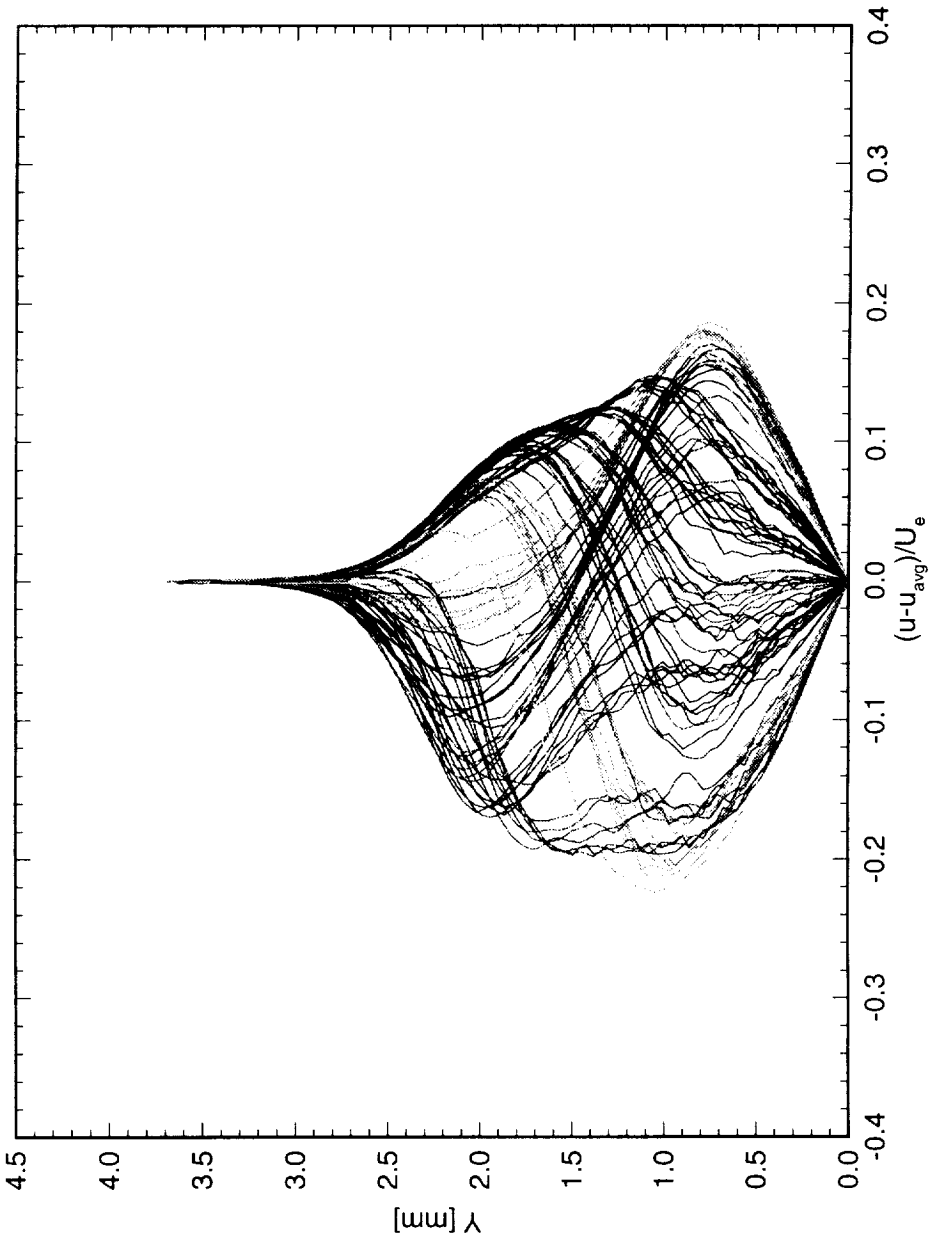

Figure 5.60: Spanwise array of 100 disturbance profiles covering a span of 99 mm at $x/c = 0.35$. $Re_c = 2.4 \times 10^6$, [6|12] roughness.

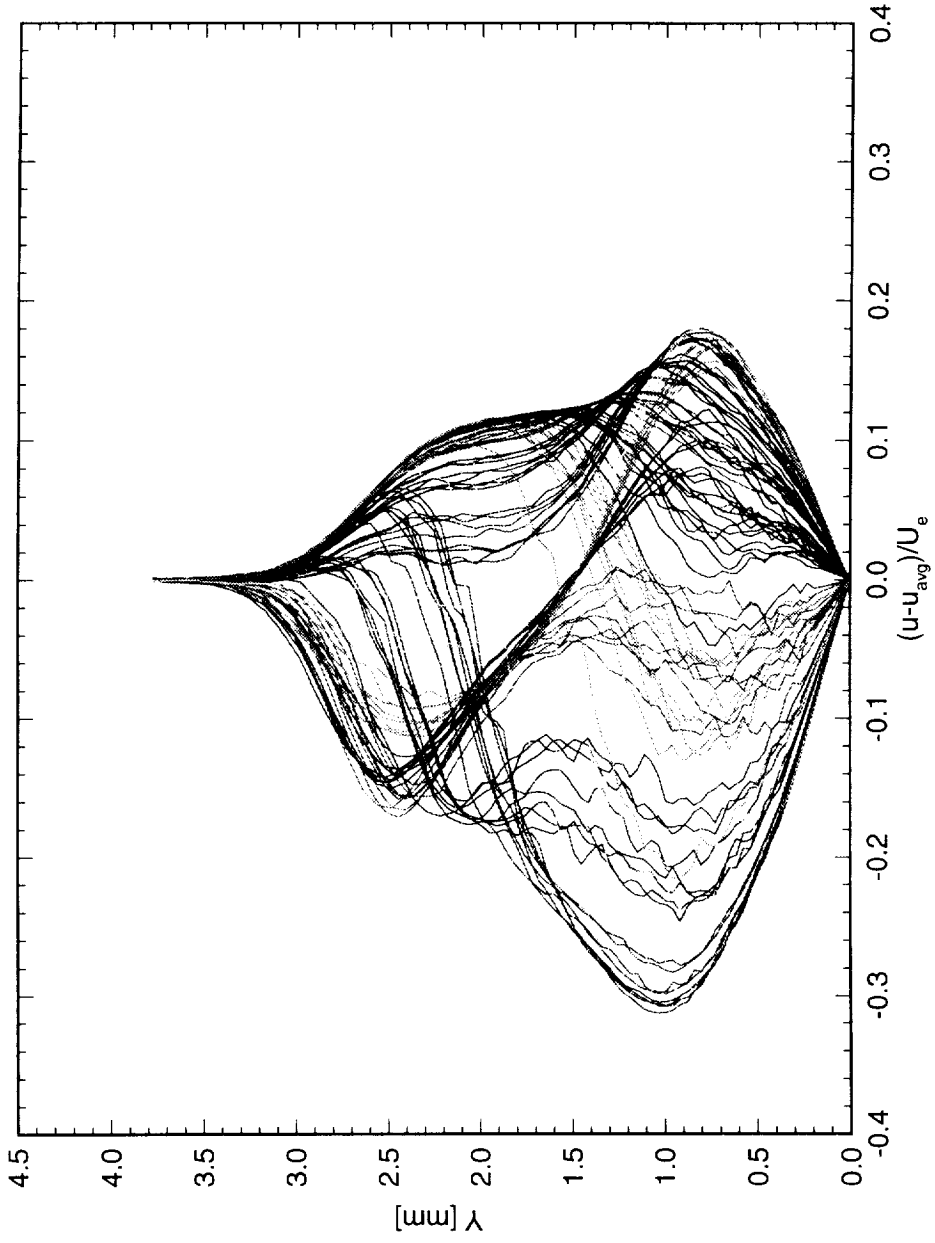

Figure 5.61: Spanwise array of 100 disturbance profiles covering a span of 99 mm at $x/c = 0.40$. $Re_c = 2.4 \times 10^6$, [6|12] roughness.

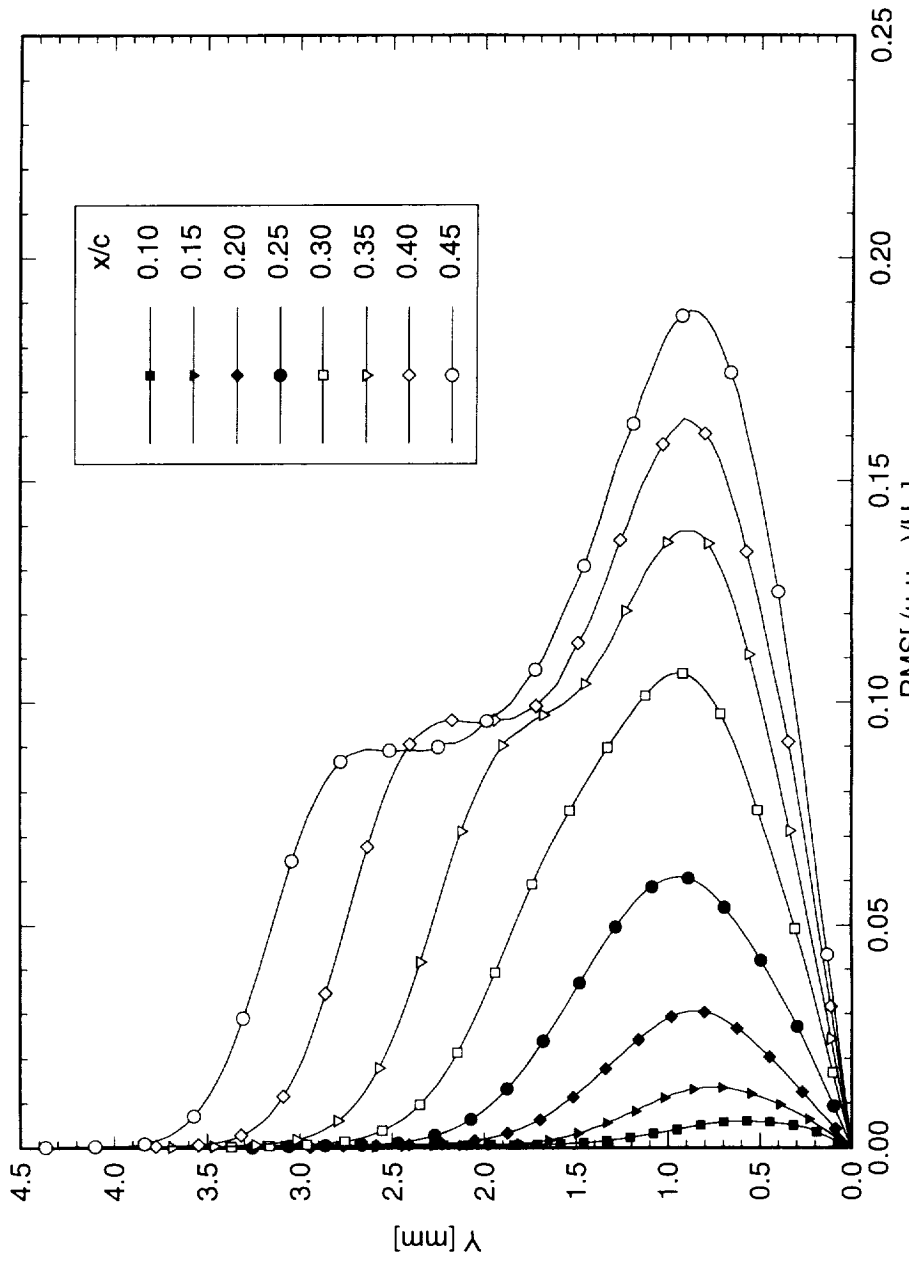

Figure 5.62: Stationary crossflow mode shapes for $Re_c = 2.4 \times 10^6$ and [6|12] roughness. The symbols are simply identifiers and do not represent measurement points.

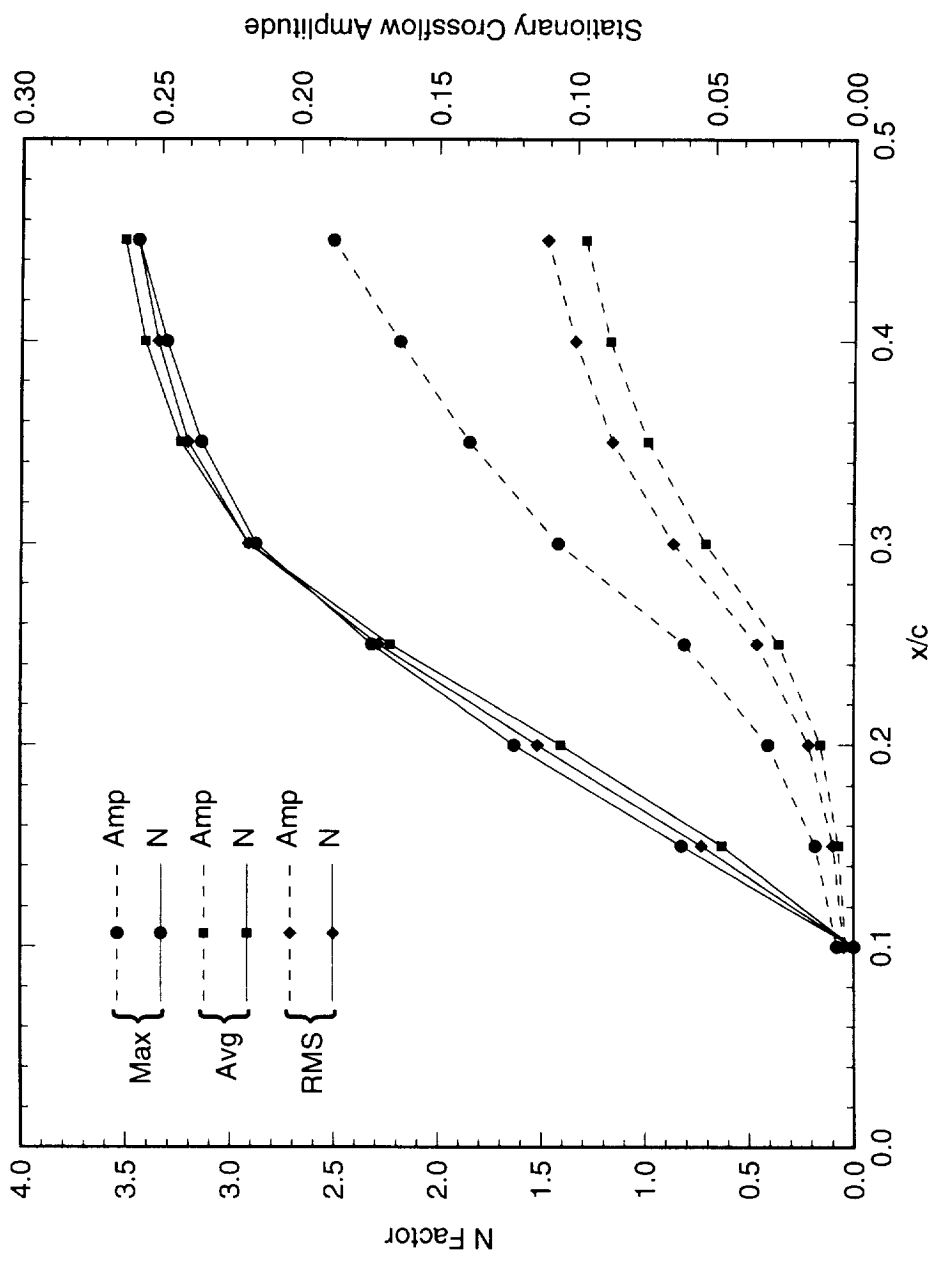

Figure 5.63: Total disturbance amplitude and amplification factor N for $Re_c = 2.4 \times 10^6$ and [6|12] roughness. The reference point for the N-factor calculations is $x/c = 0.10$.

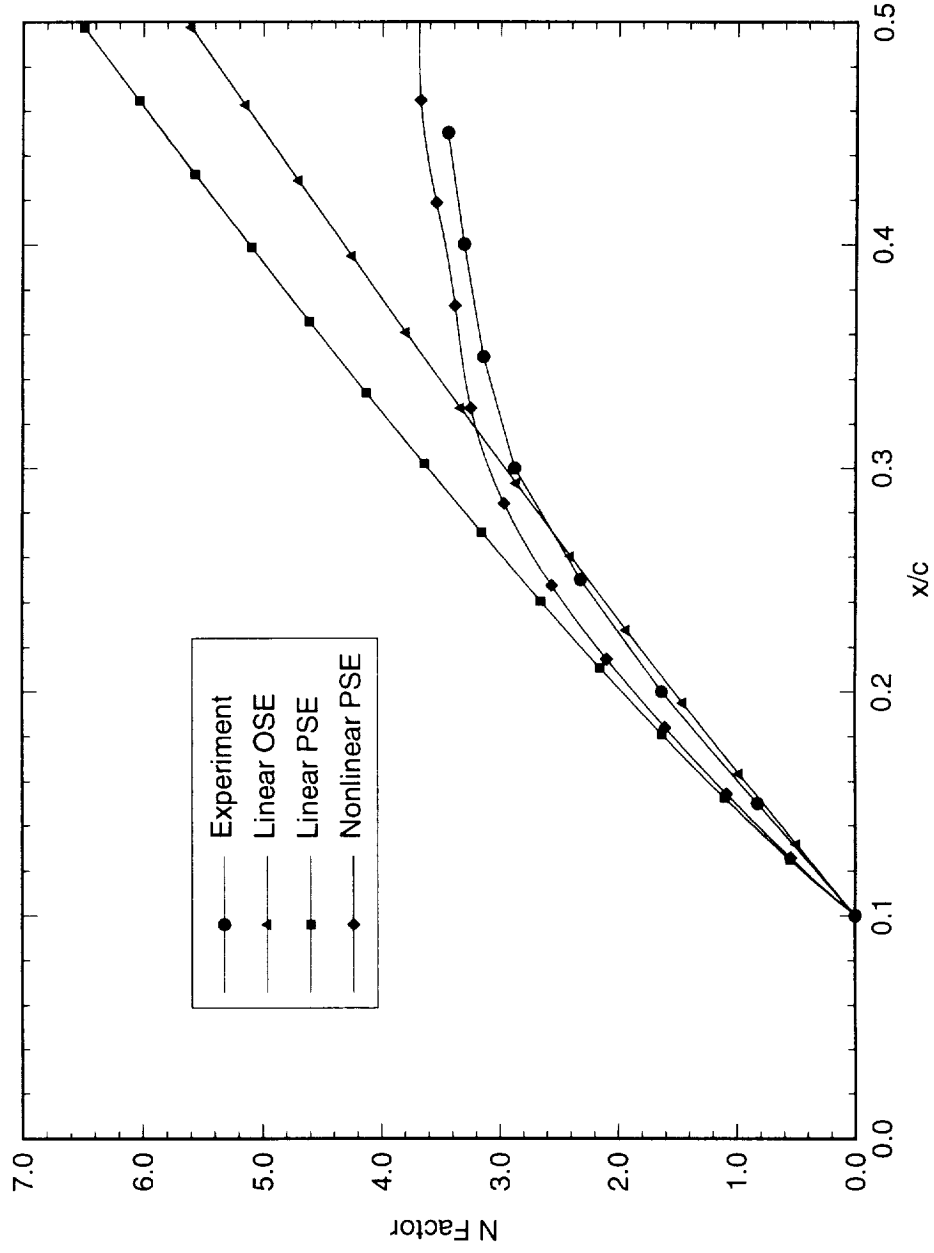

Figure 3.64: Comparison of experimental and theoretical total disturbance amplification factor N for $Re_c = 2.4 \times 10^6$ and [6|12] roughness. The reference point for the N-factor calculations is $x/c = 0.10$.

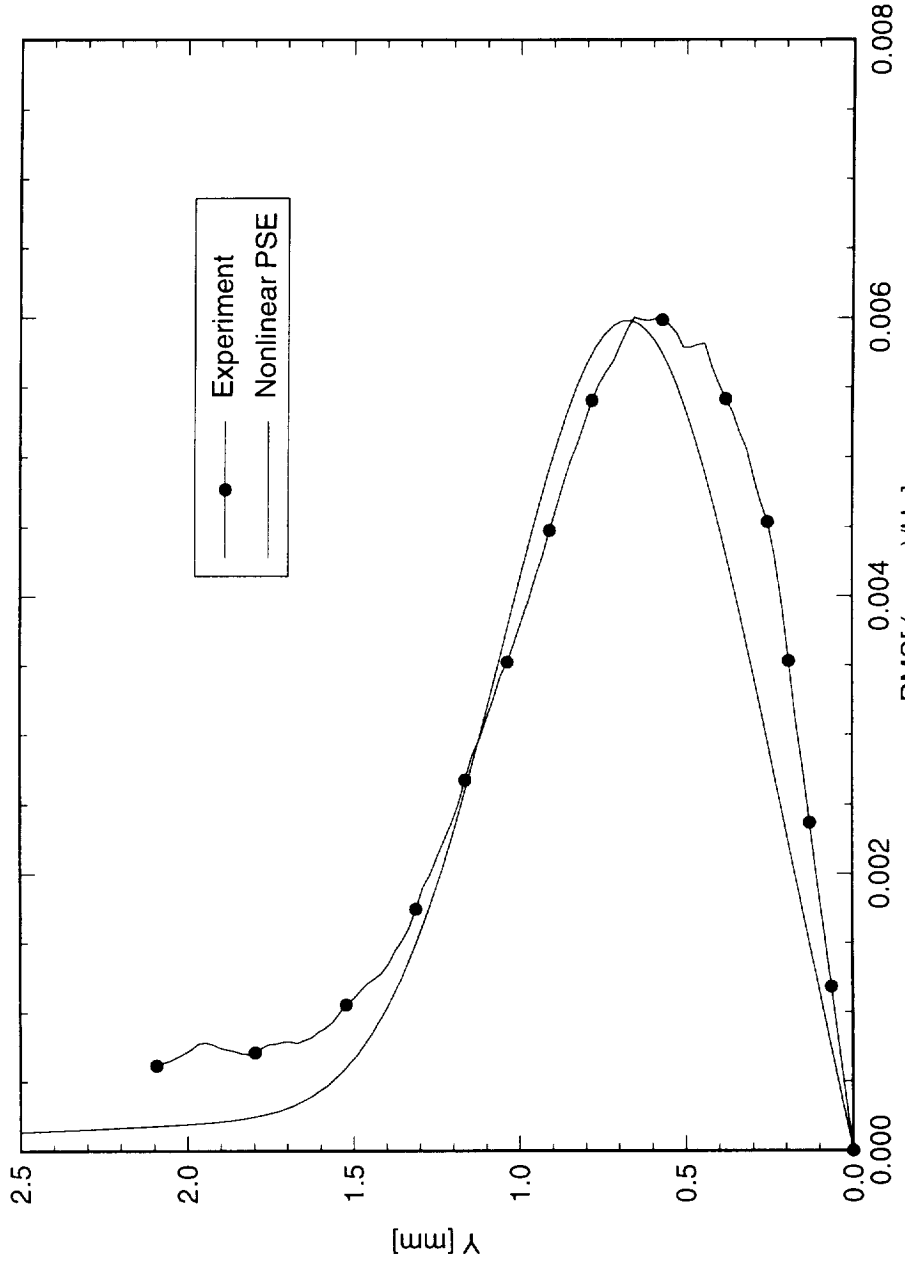

Figure 5.65: Comparison of experimental and theoretical crossflow mode shape at $x/c = 0.10$. $Re_c = 2.4 \times 10^6$, [6|12] roughness. The dots are simply identifiers and do not represent measurement points.

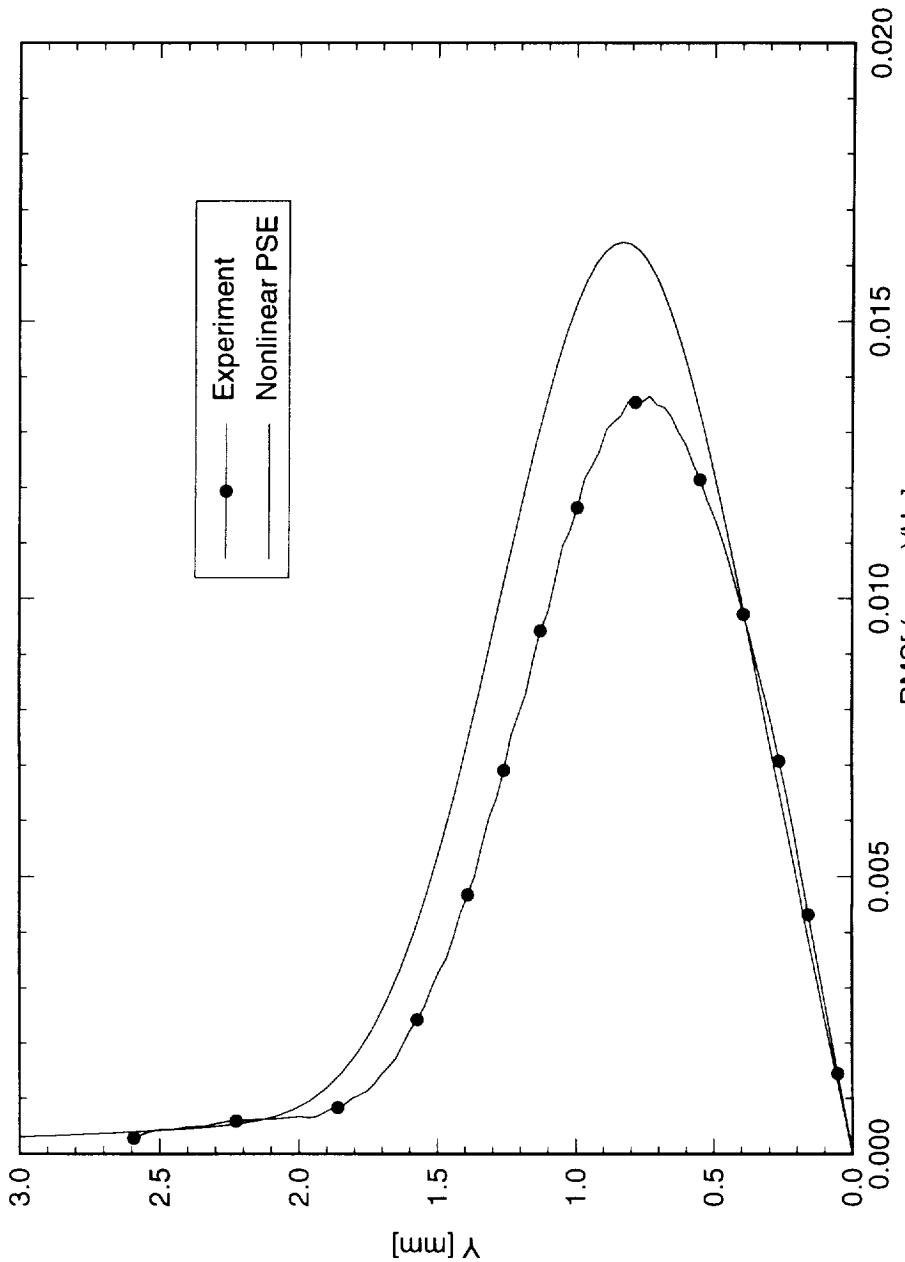

Figure 5.66: Comparison of experimental and theoretical crossflow mode shape at $x/c = 0.15$. $Re_c = 2.4 \times 10^6$. [6|12] roughness. The dots are simply identifiers and do not represent measurement points.

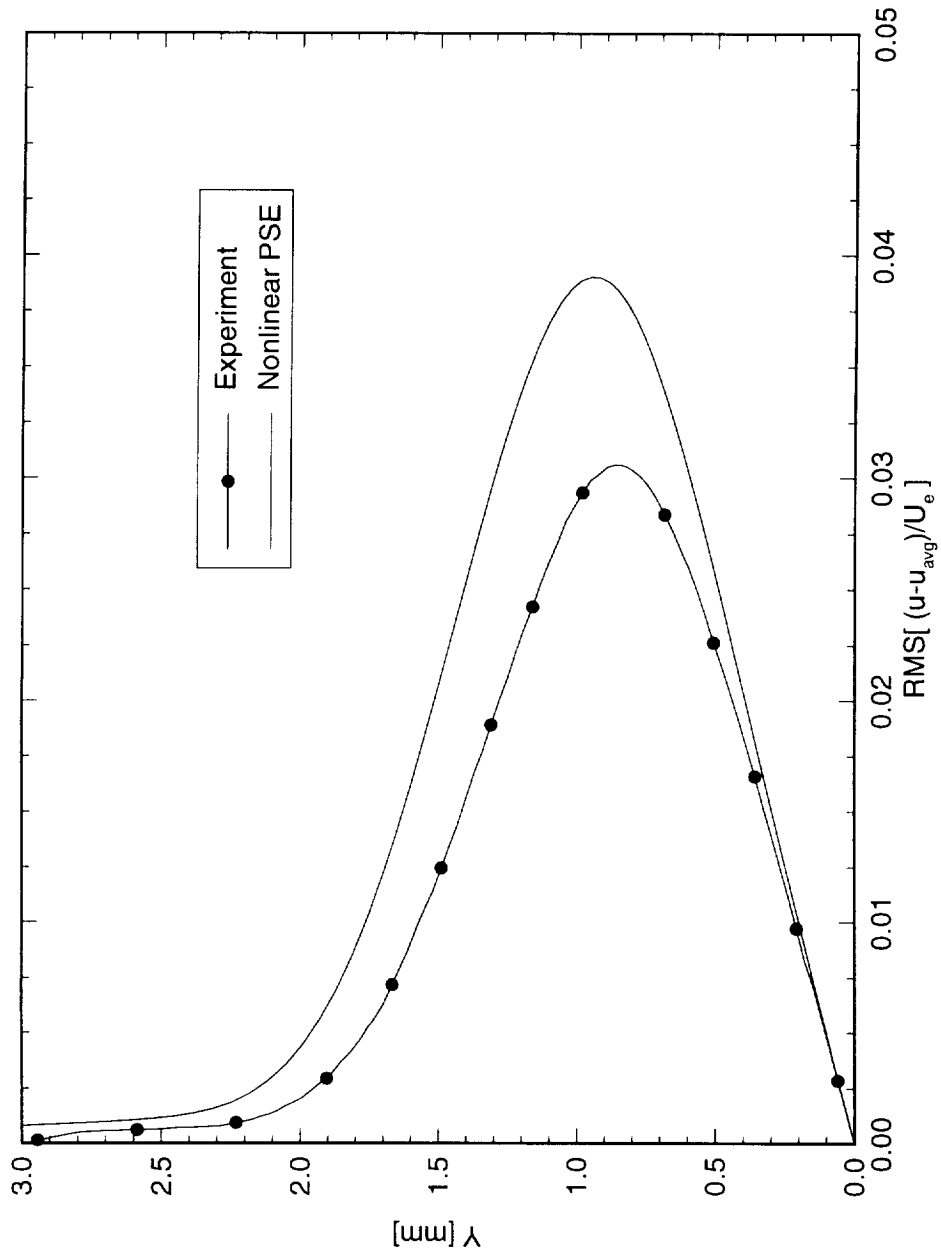

Figure 5.67: Comparison of experimental and theoretical crossflow mode shape at $x/c = 0.20$. $Re_c = 2.4 \times 10^6$, [6|12] roughness. The dots are simply identifiers and do not represent measurement points.

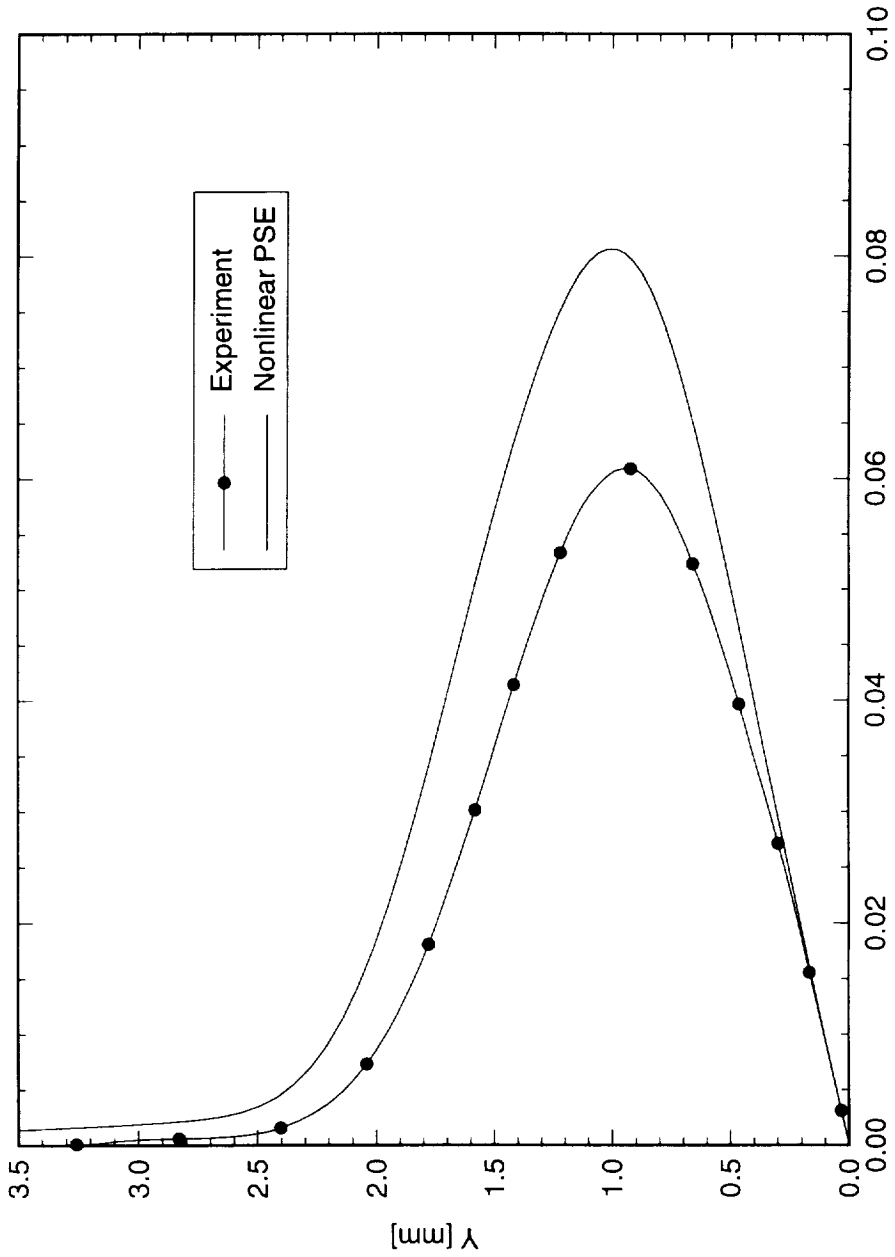

Figure 5.68: Comparison of experimental and theoretical crossflow mode shape at $x/c = 0.25$. $Re_c = 2.4 \times 10^6$, [6|12] roughness. The dots are simply identifiers and do not represent measurement points.

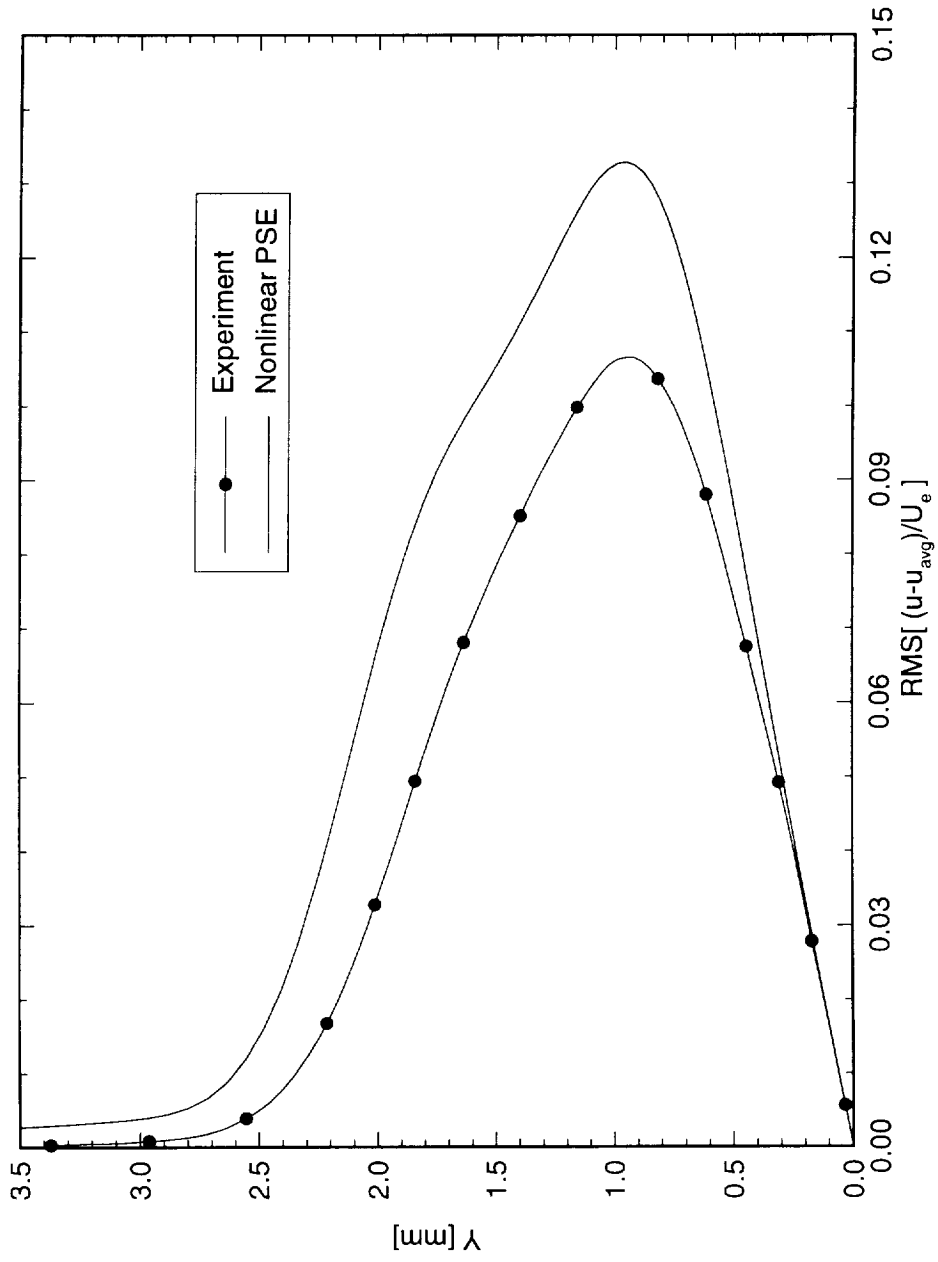

Figure 5.69: Comparison of experimental and theoretical crossflow mode shape at $x/c = 0.30$. $Re_c = 2.4 \times 10^6$, [6|12] roughness. The dots are simply identifiers and do not represent measurement points.

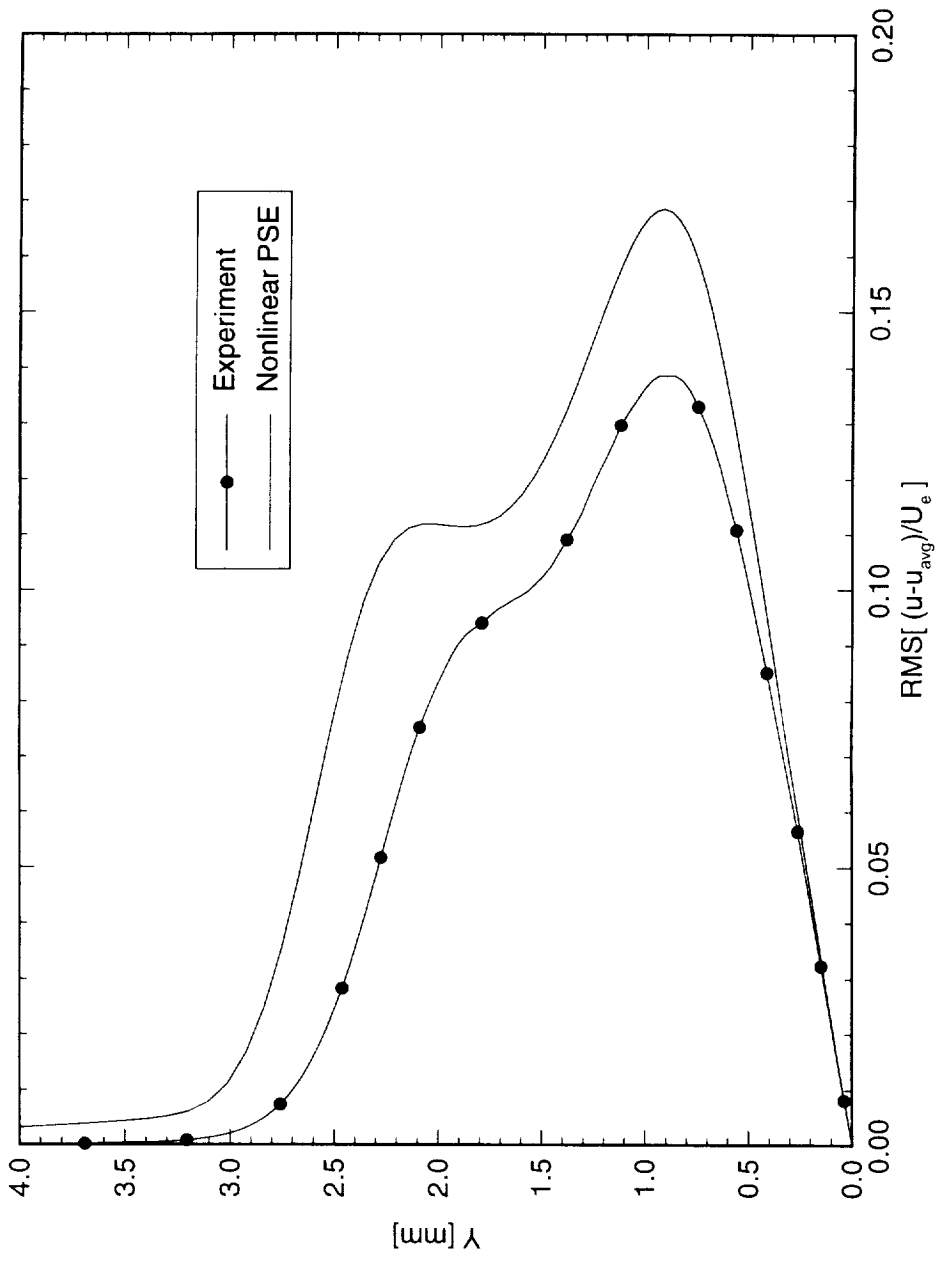

Figure 5.70: Comparison of experimental and theoretical crossflow mode shape at $x/c = 0.35$. $Re_c = 2.4 \times 10^6$, [6|12] roughness. The dots are simply identifiers and do not represent measurement points.

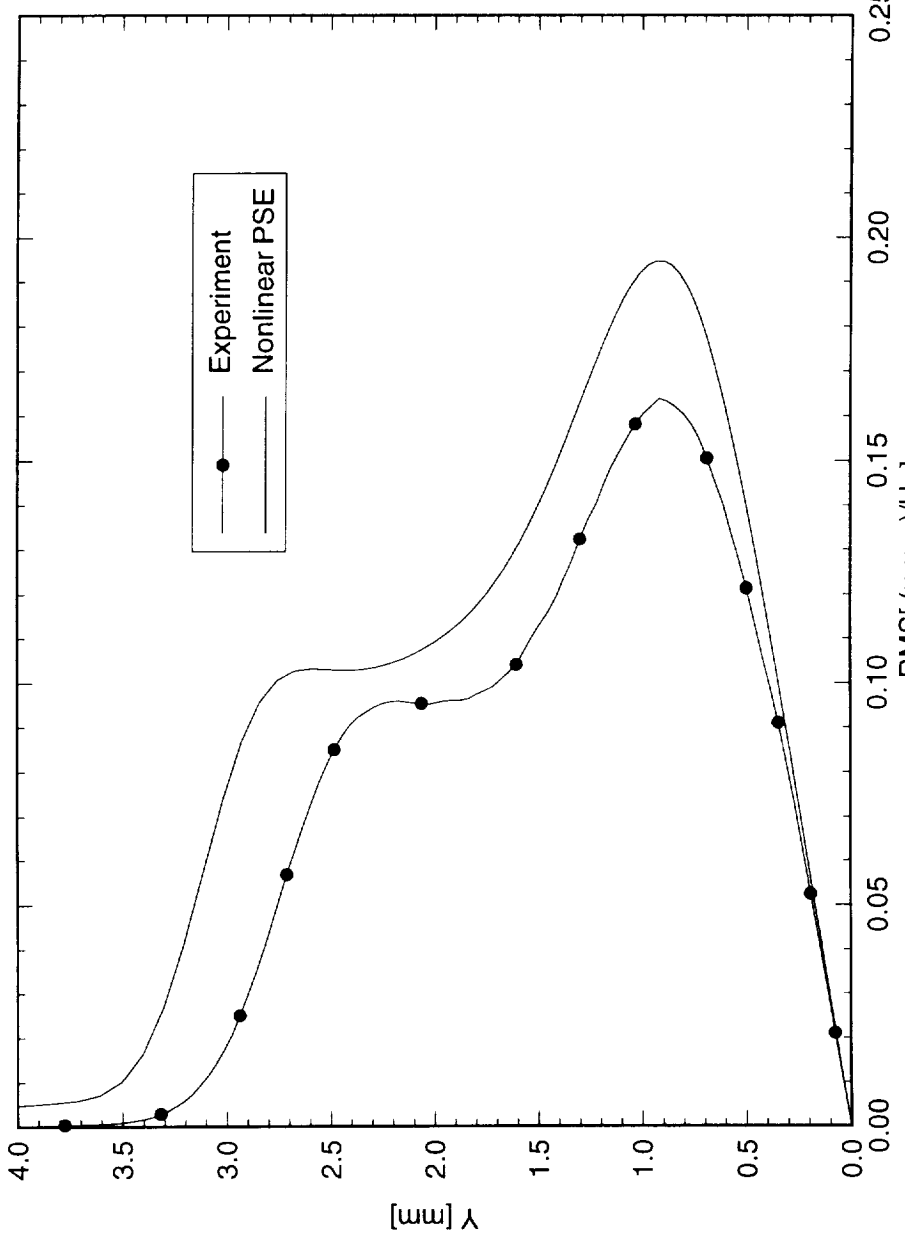

Figure 5.71: Comparison of experimental and theoretical crossflow mode shape at $x/c = 0.40$. $Re_c = 2.4 \times 10^6$, [6|12] roughness. The dots are simply identifiers and do not represent measurement points.

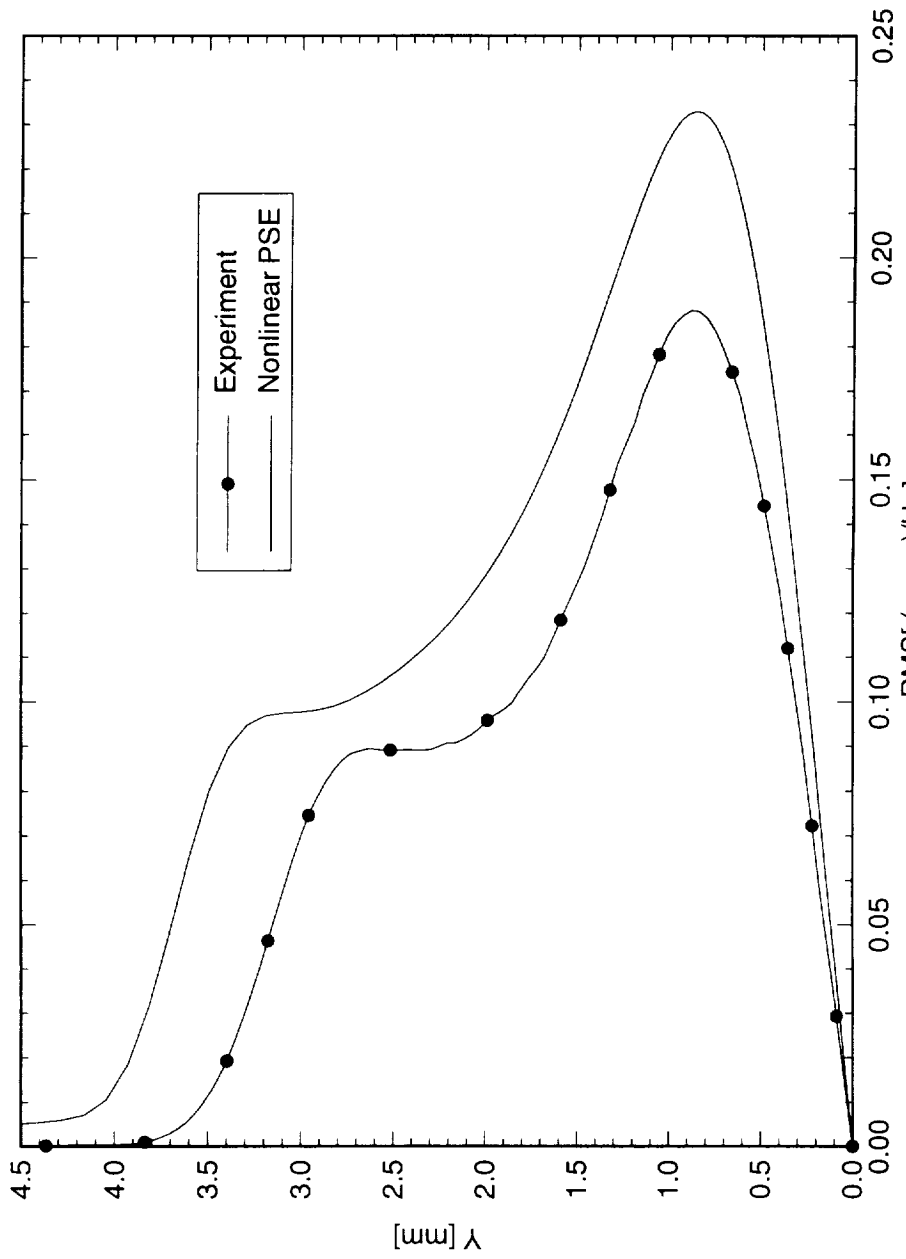

Figure 5.72: Comparison of experimental and theoretical crossflow mode shape at $x/c = 0.45$. $Re_c = 2.4 \times 10^6$, [6|12] roughness. The dots are simply identifiers and do not represent measurement points.

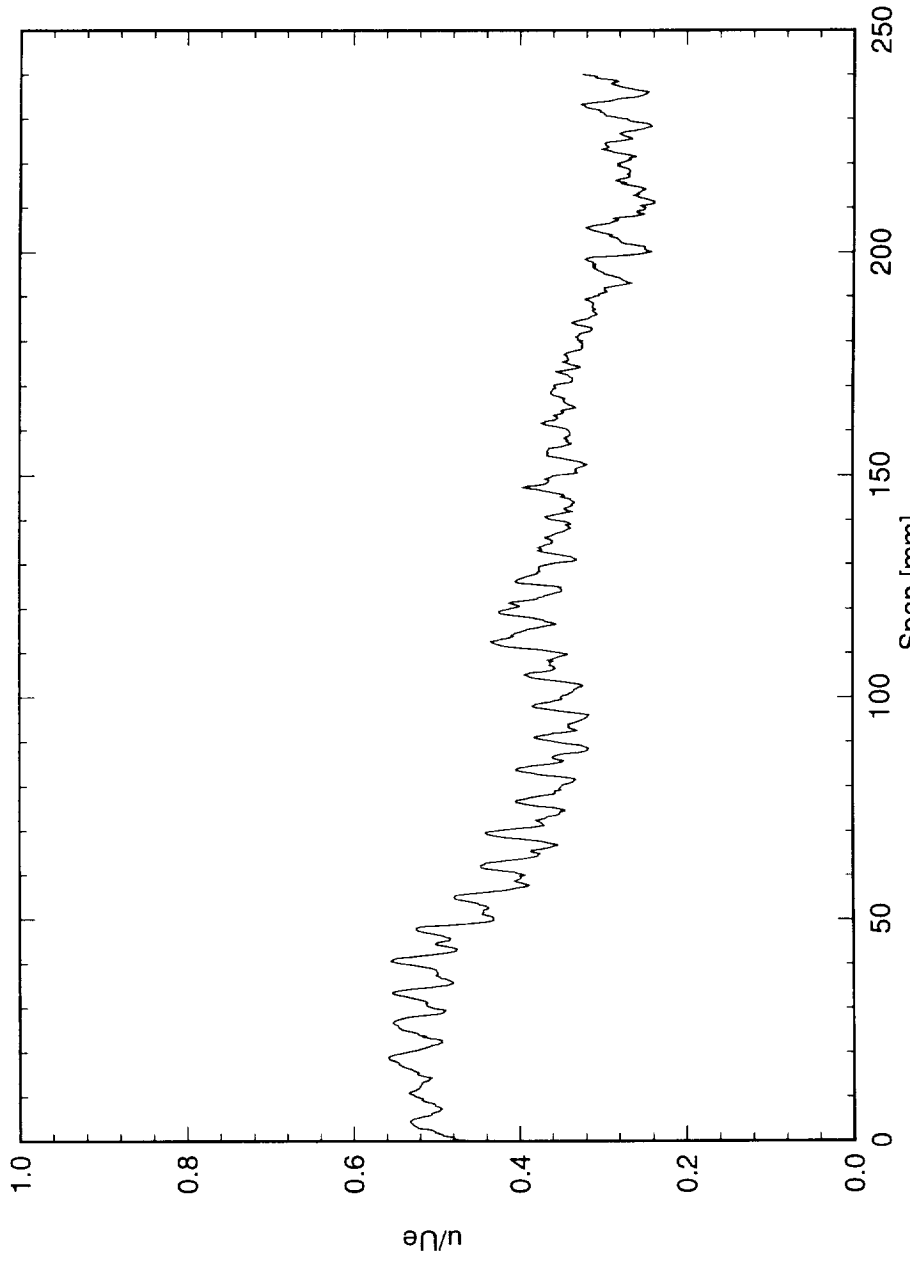

Figure 5.73: Spanwise hot-wire scan at $x/c = 0.05$, $Y = 0.3$ mm. $Re_c = 2.4 \times 10^6$, [6|12] roughness.

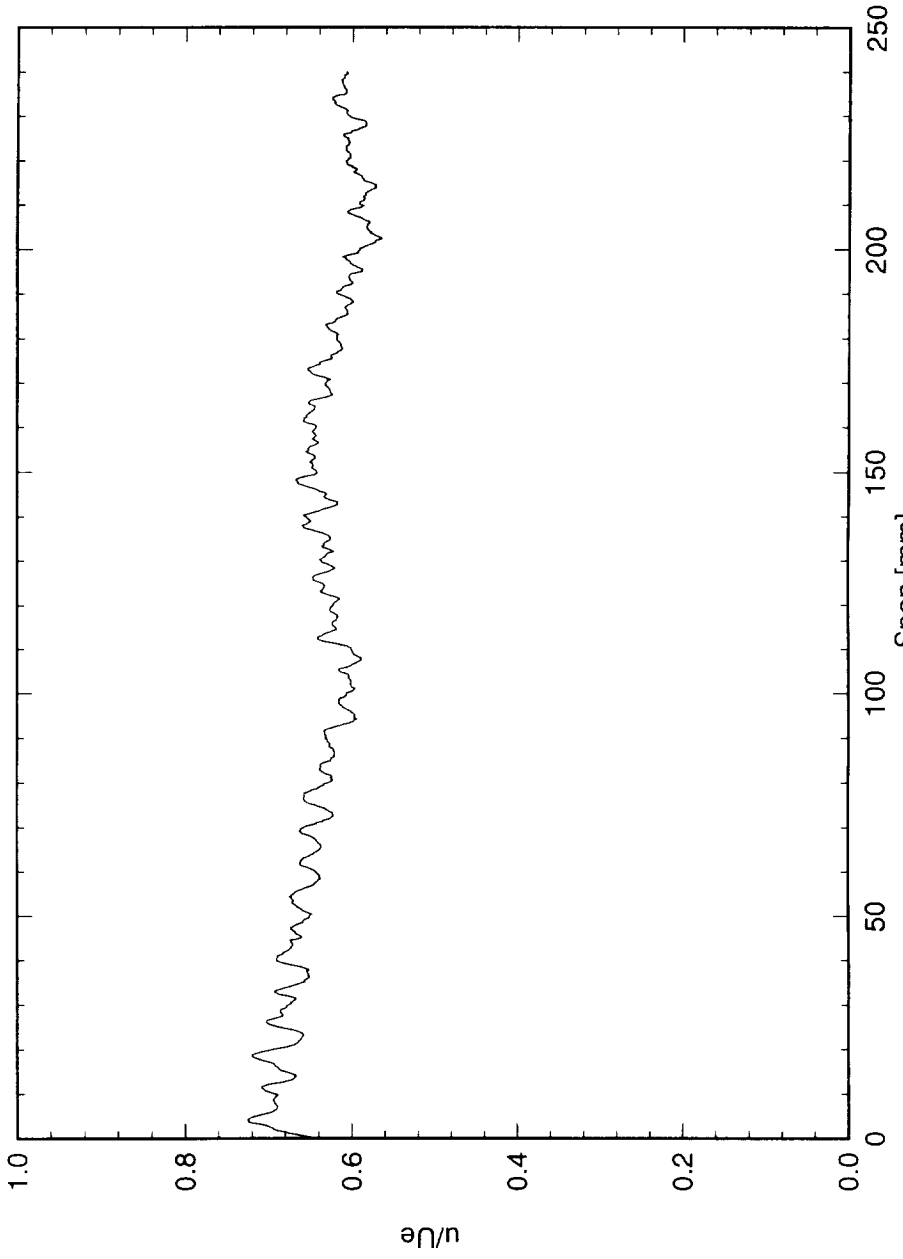

Figure 5.74: Spanwise hot-wire scan at $x/c = 0.10$, $Y = 0.6$ mm. $Re_c = 2.4 \times 10^6$, [6|12] roughness.

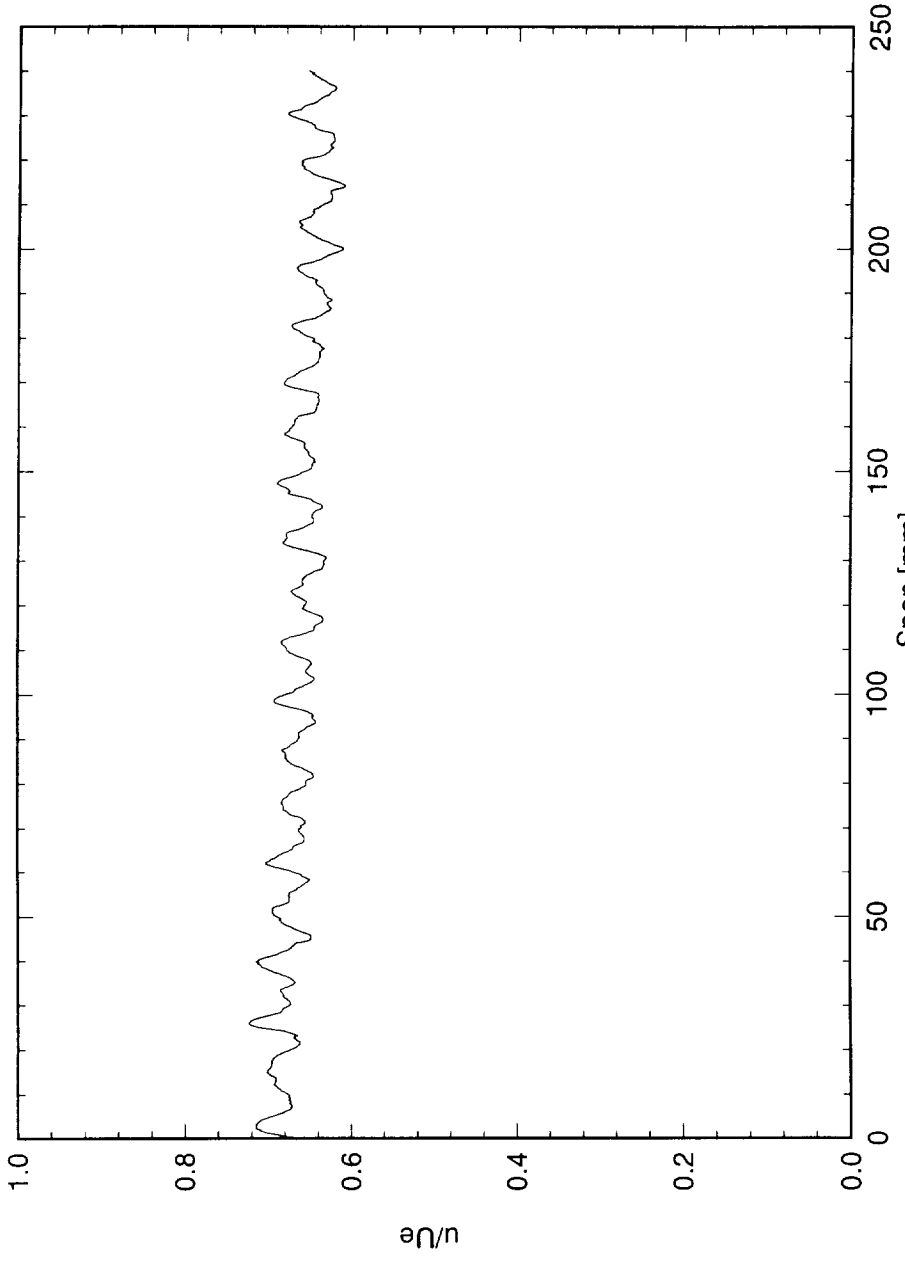

Figure 5.75: Spanwise hot-wire scan at $x/c = 0.15$, $Y = 0.75$ mm. $Re_c = 2.4 \times 10^6$, [6|12] roughness.

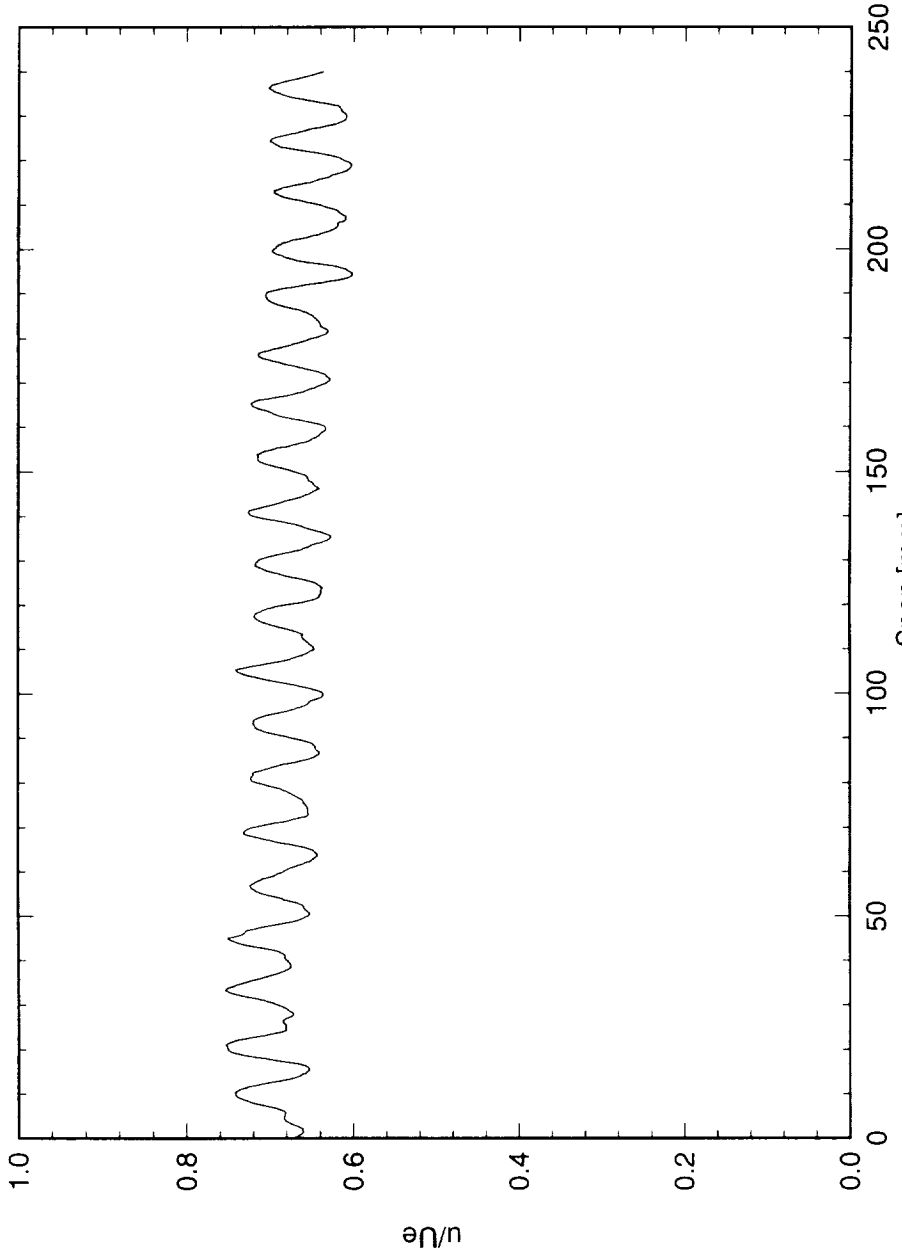

Figure 5.76: Spanwise hot-wire scan at $x/c = 0.20$, Y $= 0.85$ mm. $Re_c = 2.4 \times 10^6$, [6|12] roughness.

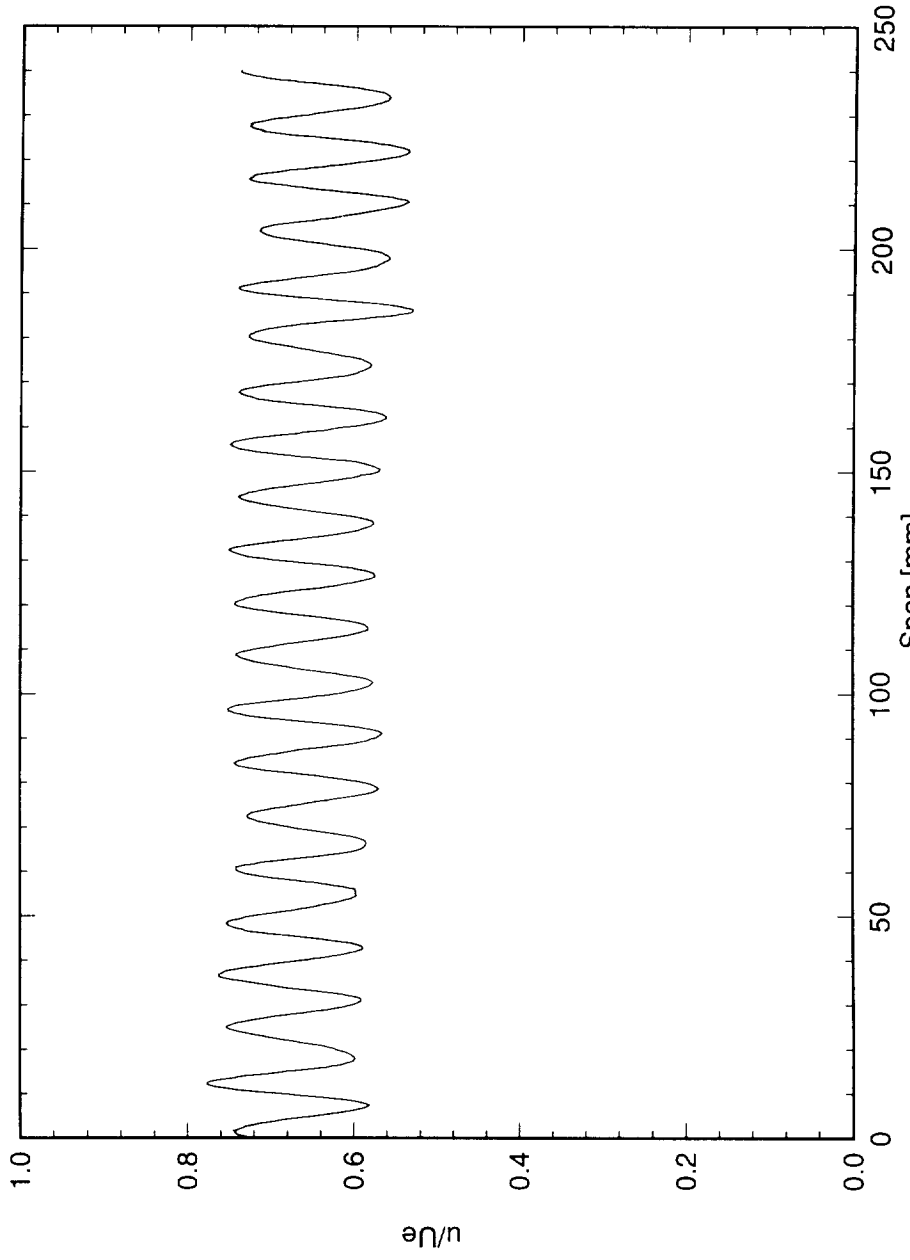

Figure 5.77: Spanwise hot-wire scan at $x/c = 0.25$, $Y = 0.9$ mm. $Re_c = 2.4 \times 10^6$, [6|12] roughness.

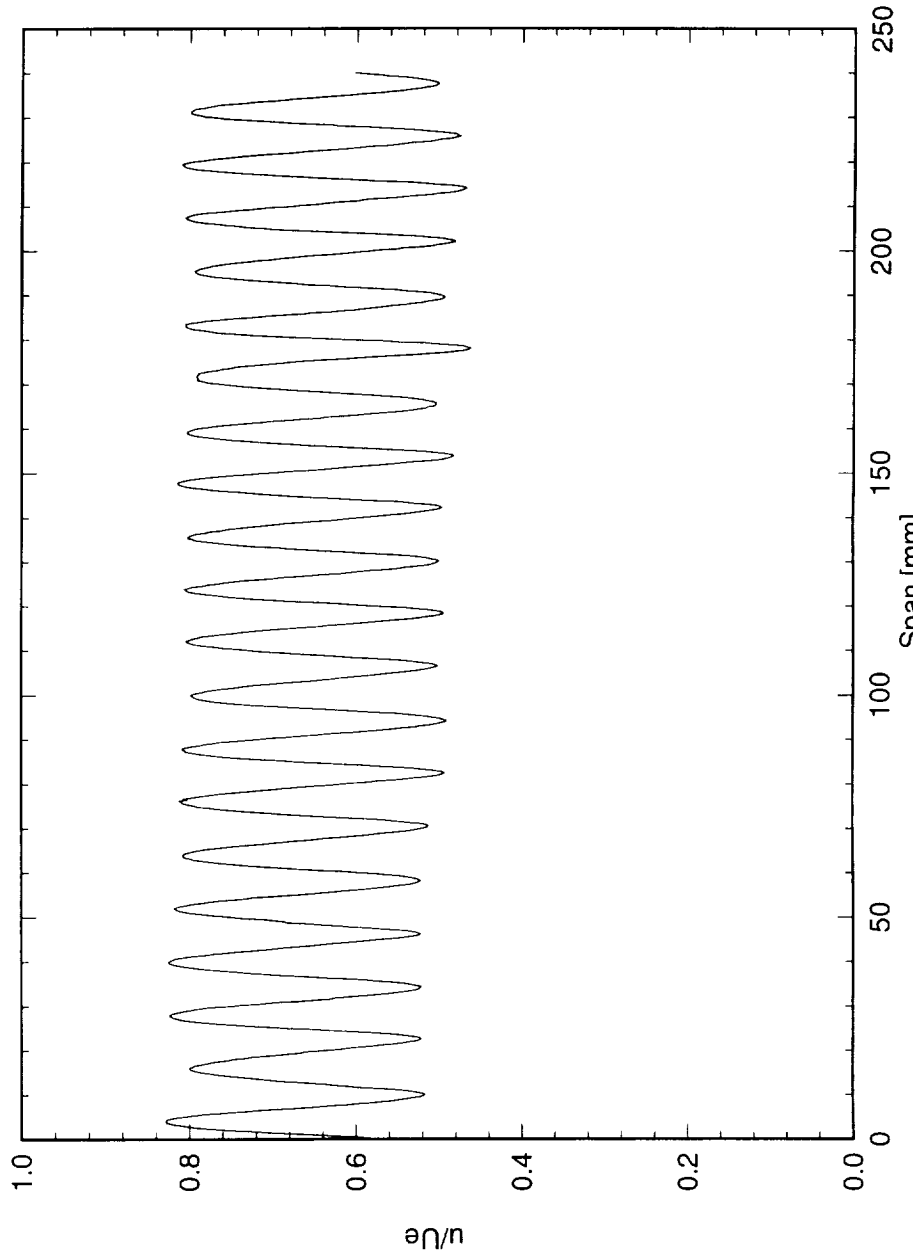

Figure 5.78: Spanwise hot-wire scan at $x/c = 0.30$, $Y = 0.9$ mm. $Re_c = 2.4 \times 10^6$, [6|12] roughness.

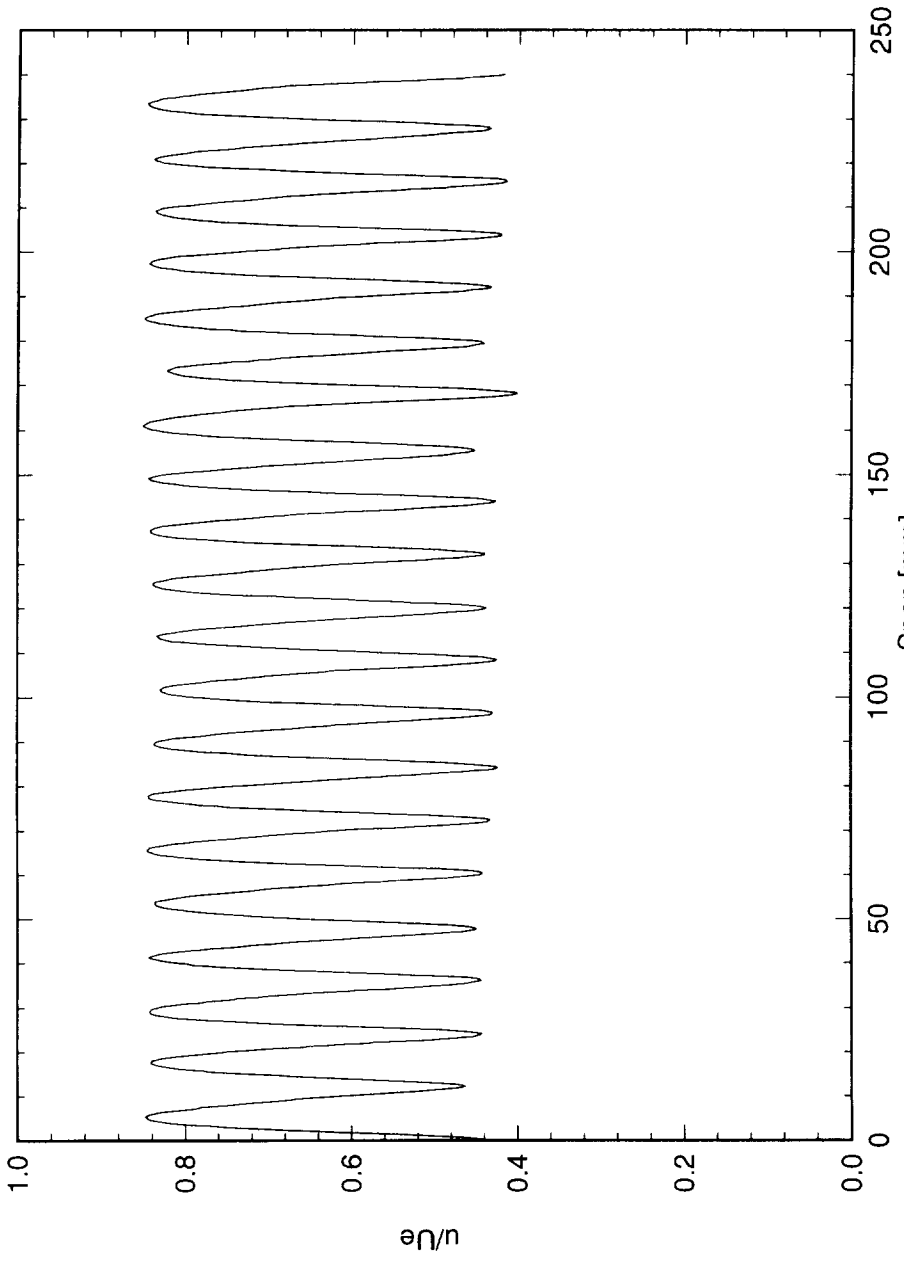

Figure 5.79: Spanwise hot-wire scan at $x/c = 0.35$, $Y = 0.9$ mm. $Re_c = 2.4 \times 10^6$, [6|12] roughness.

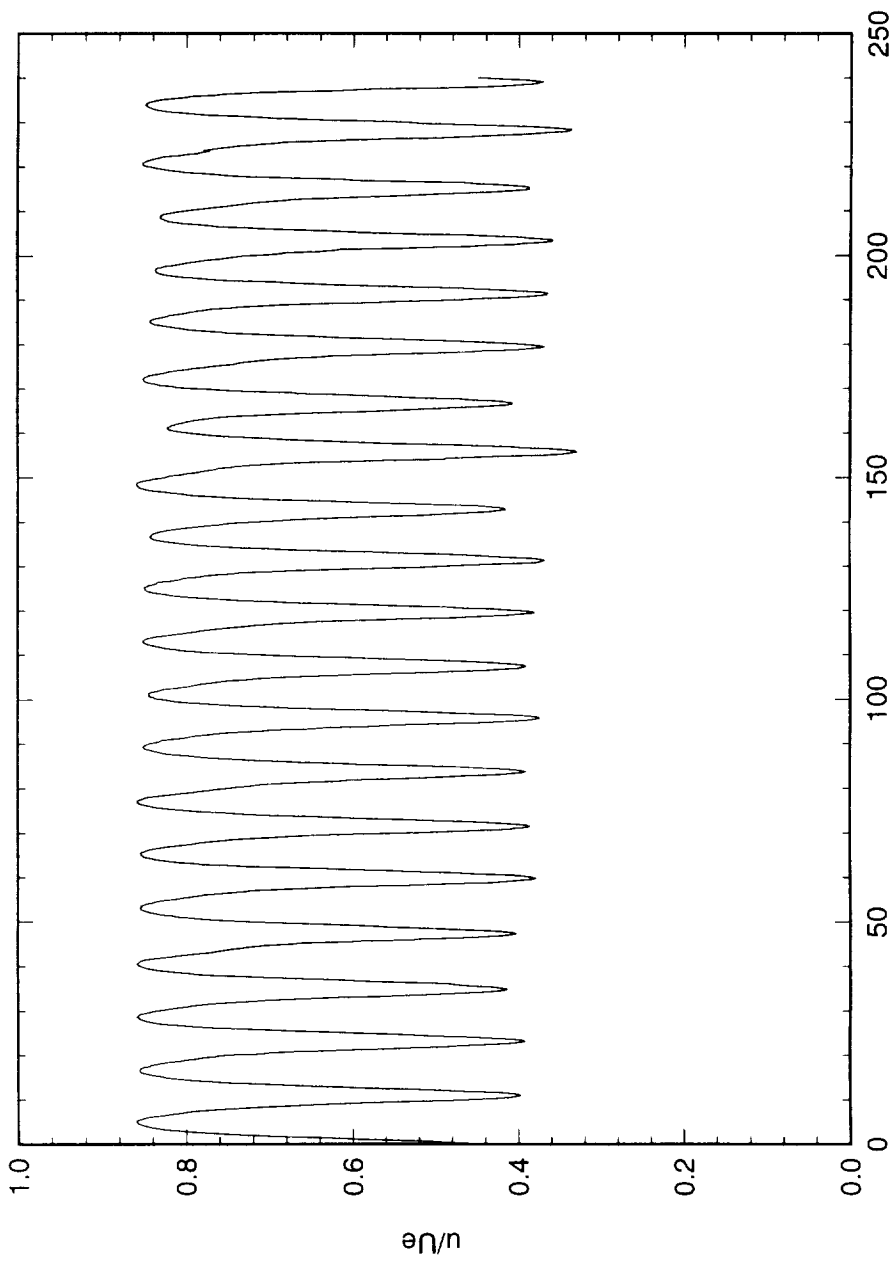

Figure 5.80: Spanwise hot-wire scan at $x/c = 0.40$, $Y = 0.9$ mm. $Re_c = 2.4 \times 10^6$, [6|12] roughness.

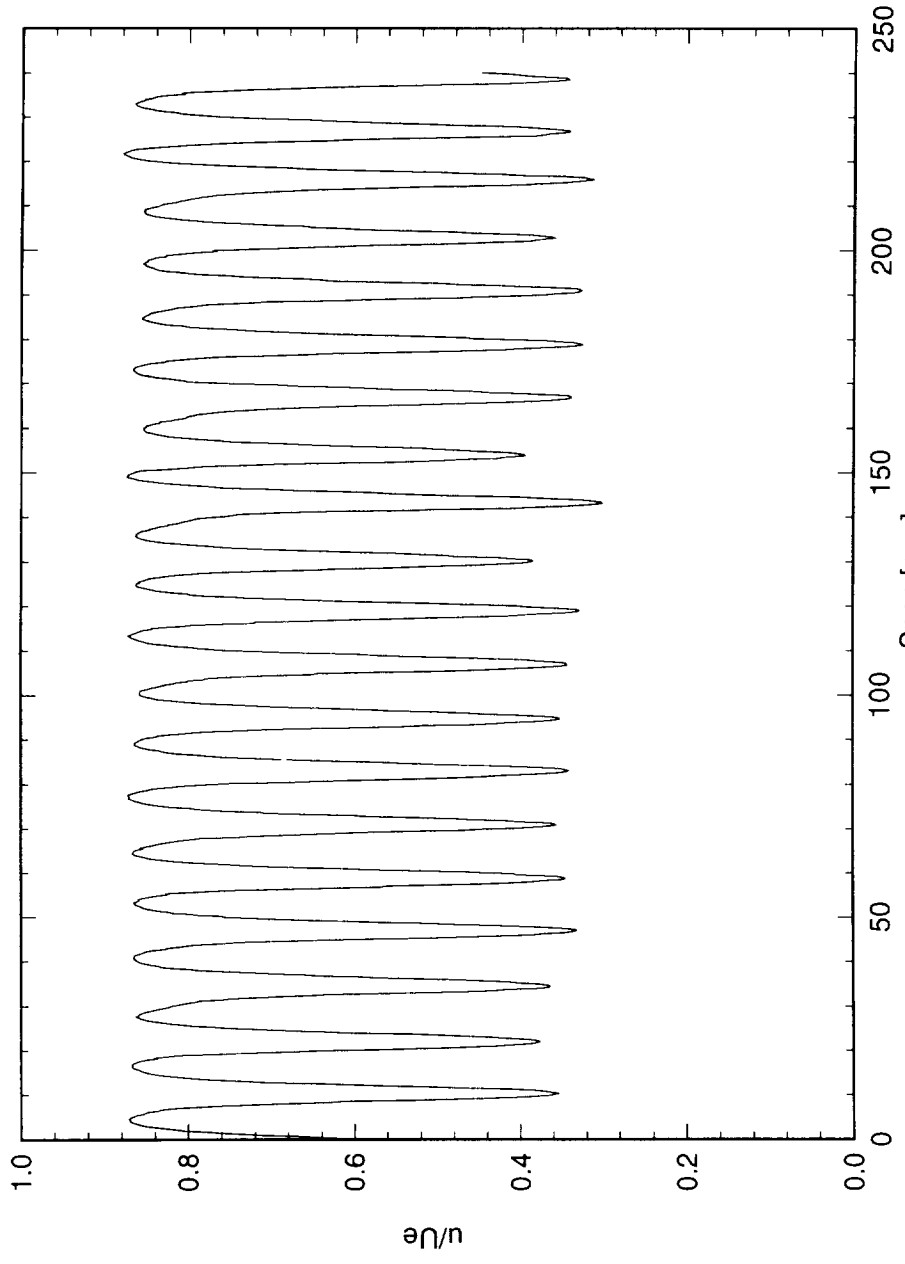

Figure 5.81: Spanwise hot-wire scan at $x/c = 0.45$, $Y = 0.9$ mm. $Re_c = 2.4 \times 10^6$, [6|12] roughness.

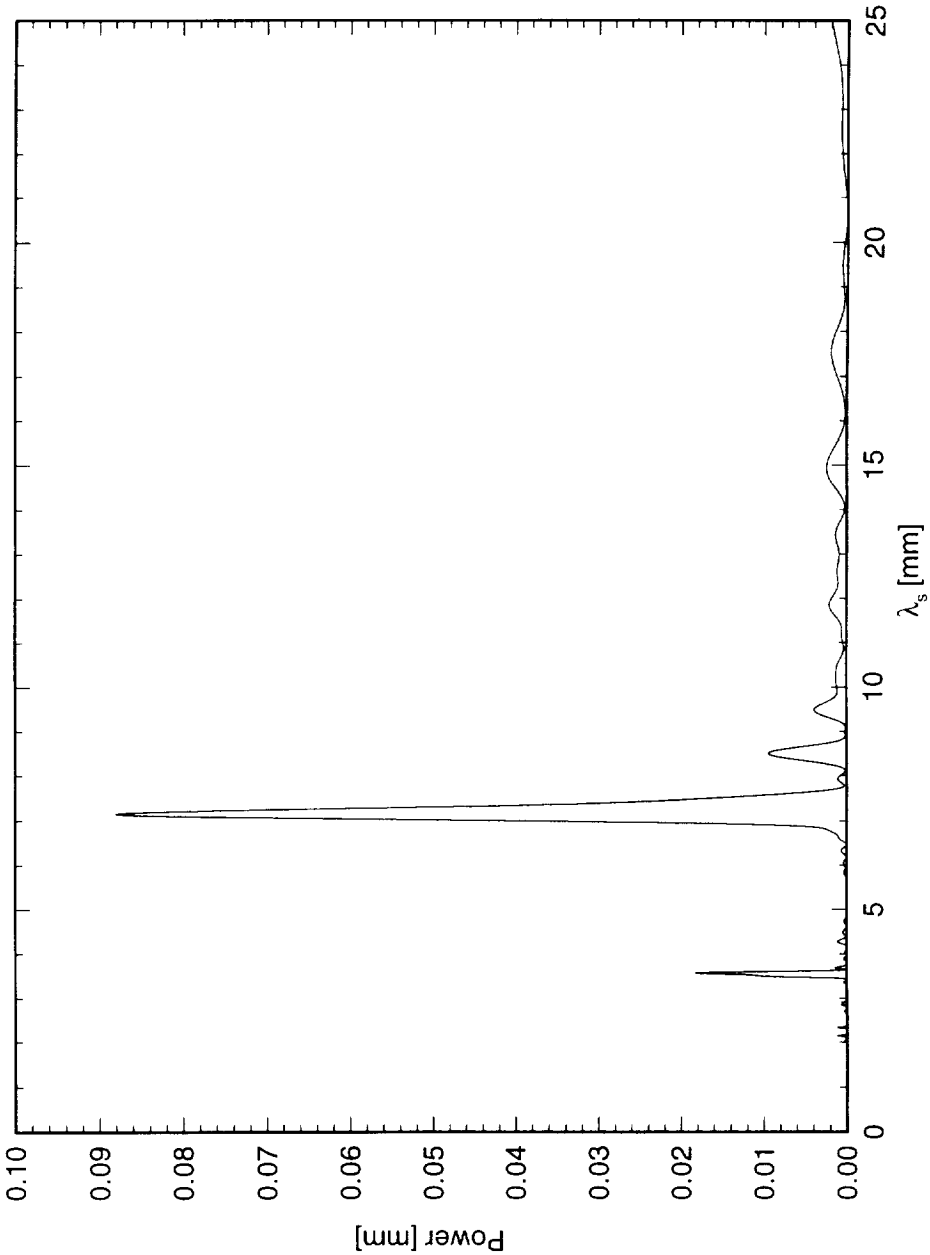

Figure 5.82: Power spectral density of spanwise hot-wire scan at $x/c = 0.05$, $Y = 0.3$ mm. $Re_c = 2.4 \times 10^6$, [6|12] roughness.

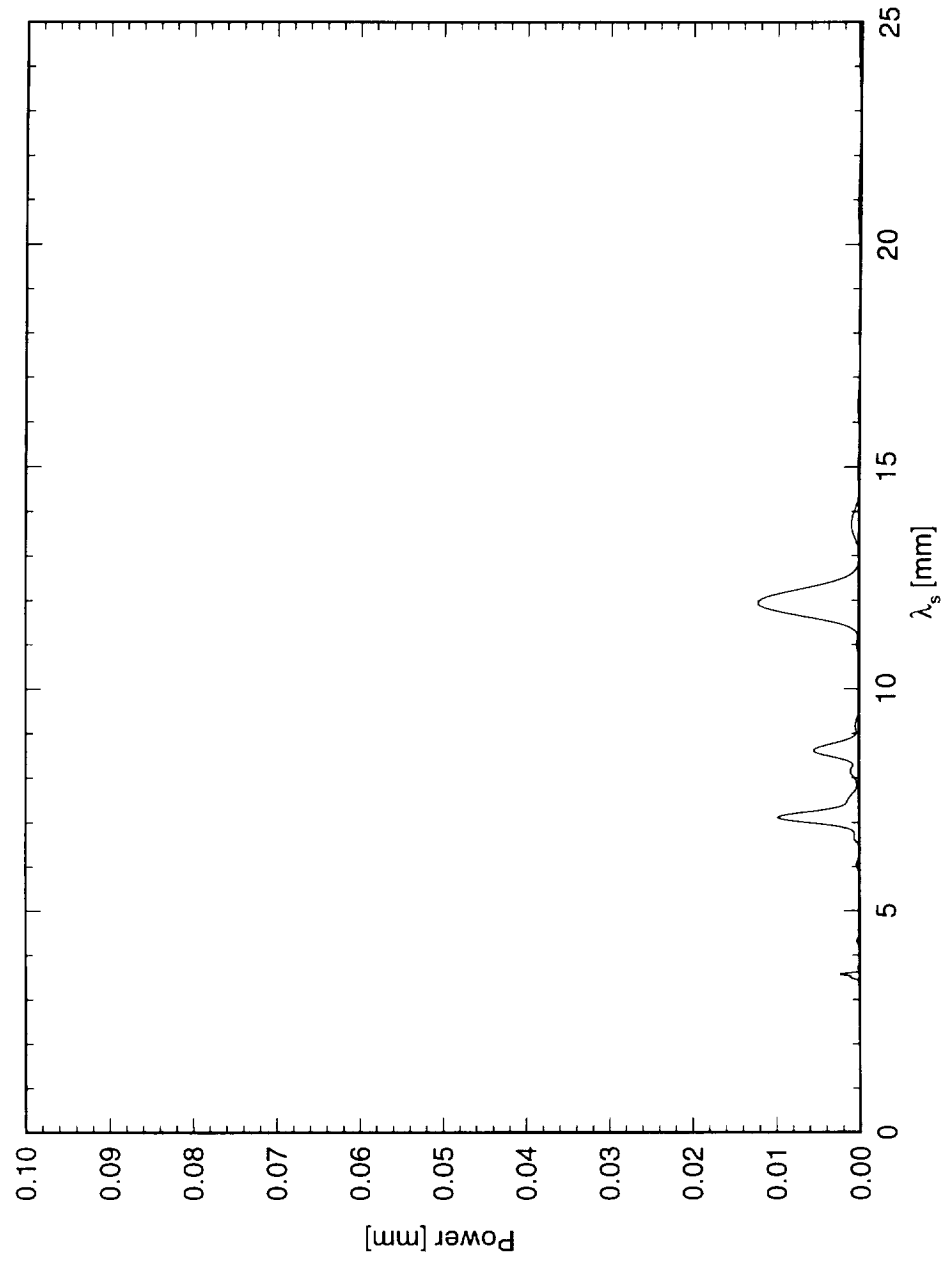

Figure 5.83: Power spectral density of spanwise hot-wire scan at $x/c = 0.10$, $Y = 0.6$ mm. $Re_c = 2.4 \times 10^6$, [6|12] roughness.

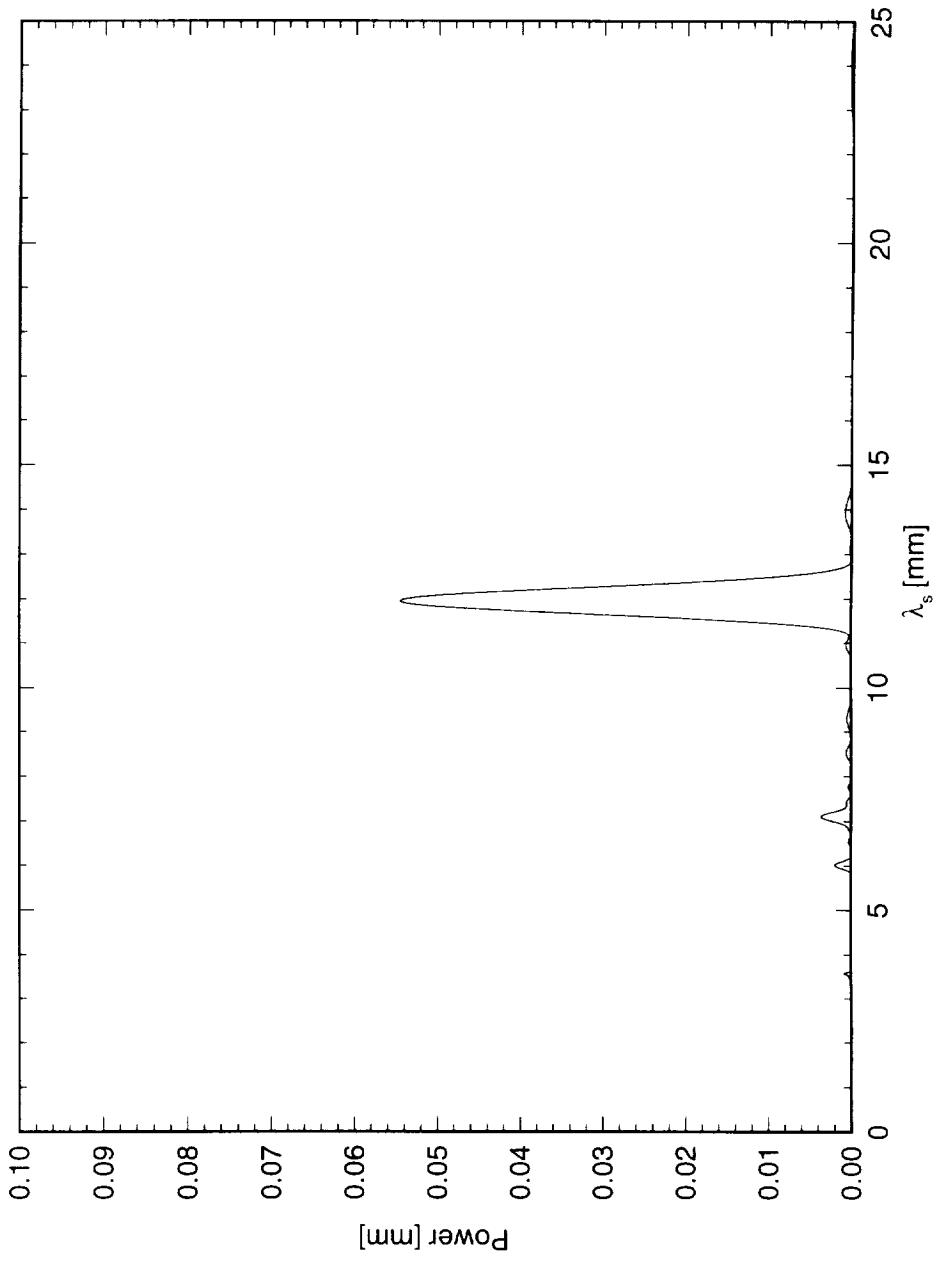

Figure 5.84: Power spectral density of spanwise hot-wire scan at $x/c = 0.15$, $Y = 0.75$ mm. $Re_c = 2.4 \times 10^6$, [6|12] roughness.

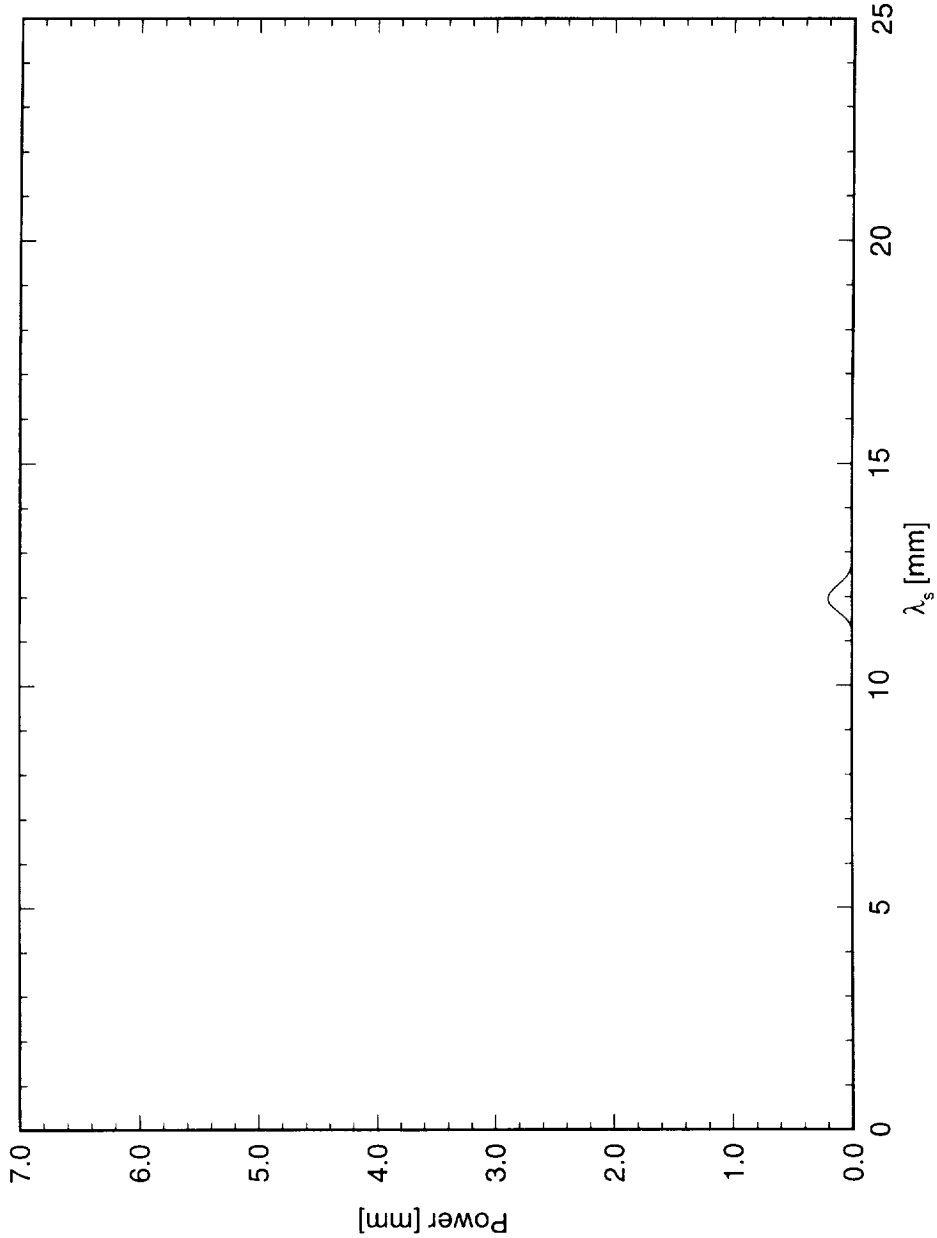

Figure 5.85: Power spectral density of spanwise hot-wire scan at $x/c = 0.20$, $Y = 0.85$ mm. $Re_c = 2.4 \times 10^6$, [6|12] roughness.

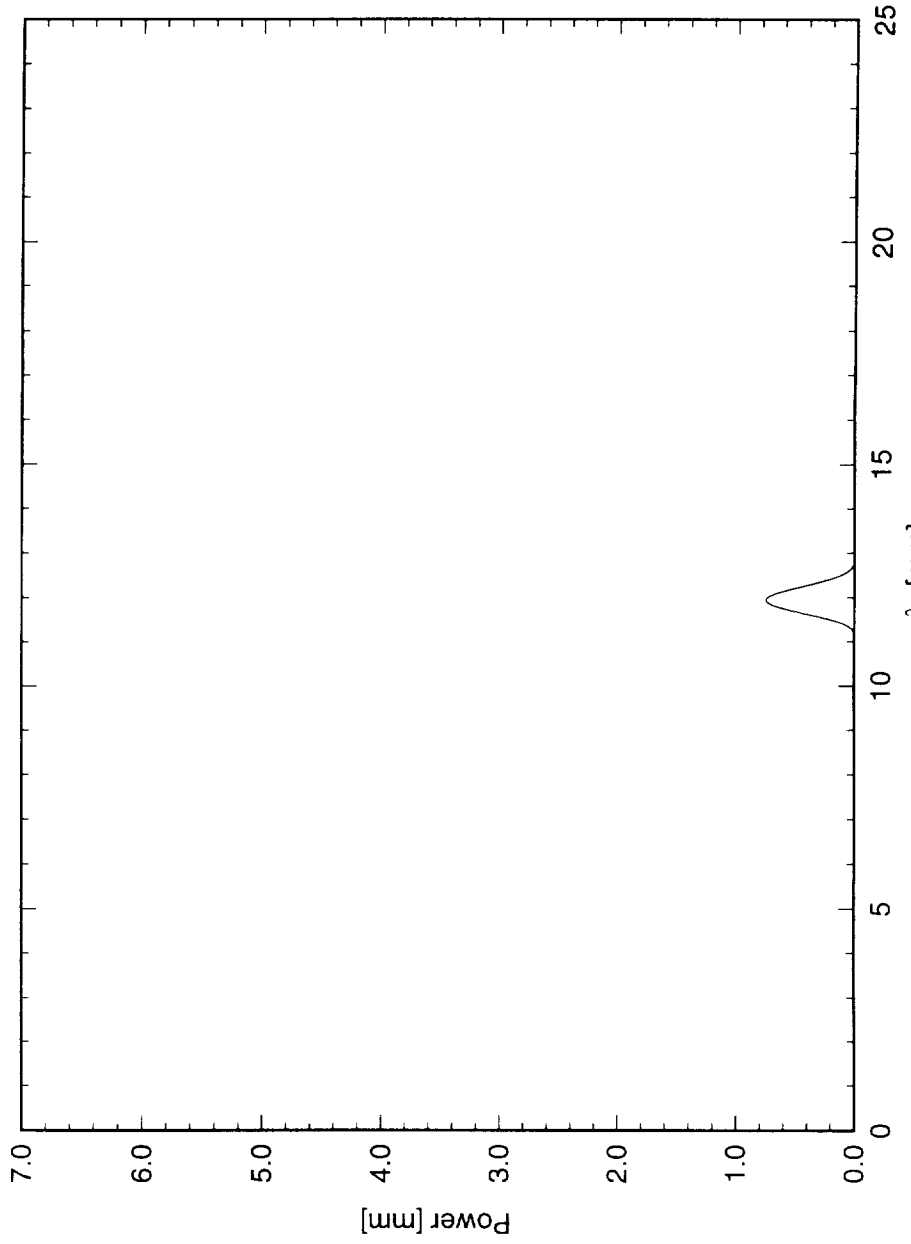

Figure 5.86: Power spectral density of spanwise hot-wire scan at $x/c = 0.25$, $Y = 0.9$ mm. $Re_c = 2.4 \times 10^6$, [6|12] roughness.

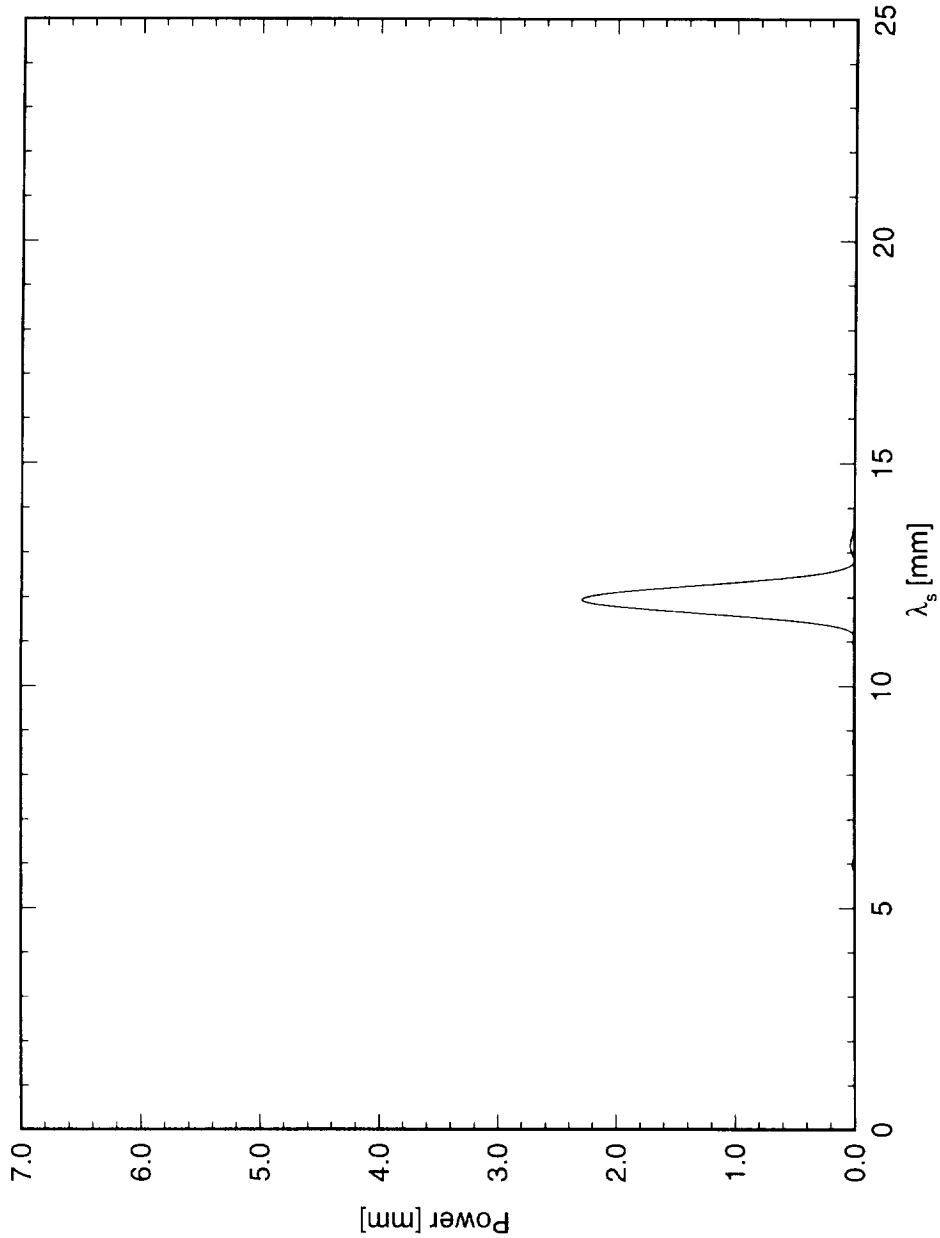

Figure 5.87: Power spectral density of spanwise hot-wire scan at $x/c = 0.30$, $Y = 0.9$ mm. $Re_c = 2.4 \times 10^6$, [6|12] roughness.

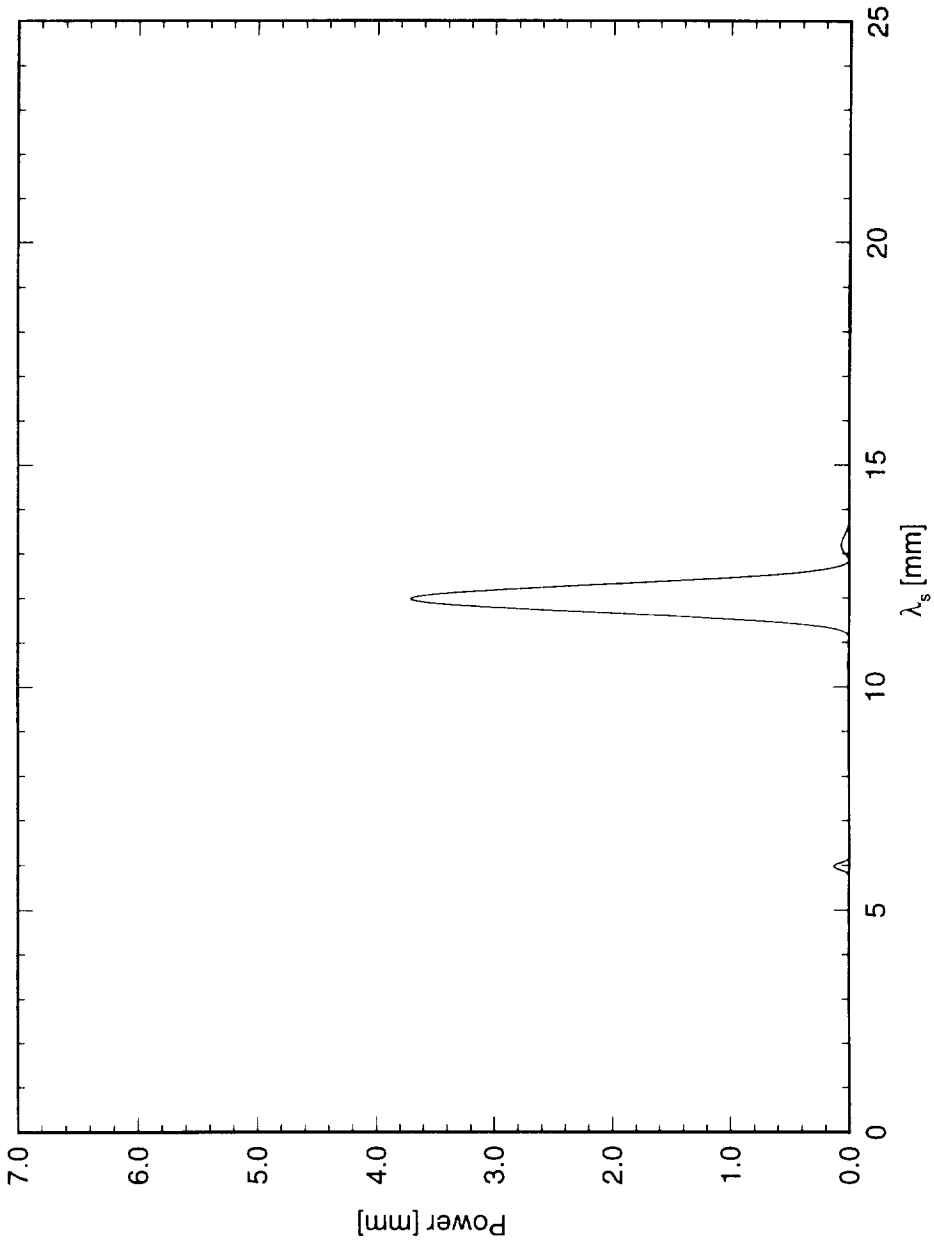

Figure 5.88: Power spectral density of spanwise hot-wire scan at $x/c = 0.35$, $Y = 0.9$ mm. $Re_c = 2.4 \times 10^6$, [6|12] roughness.

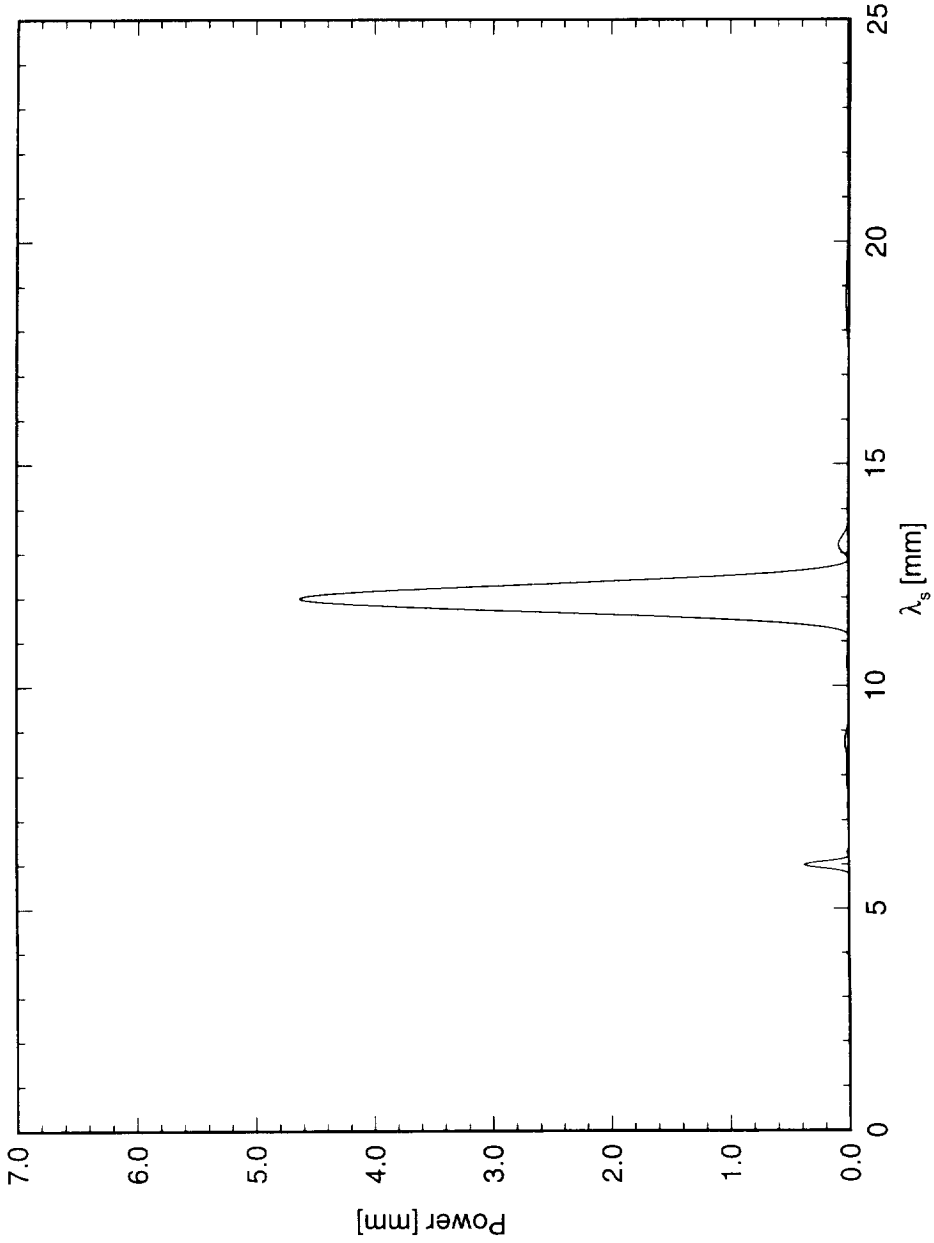

Figure 5.89: Power spectral density of spanwise hot-wire scan at $x/c = 0.40$, $Y = 0.9$ mm. $Re_c = 2.4 \times 10^6$, [6|12] roughness.

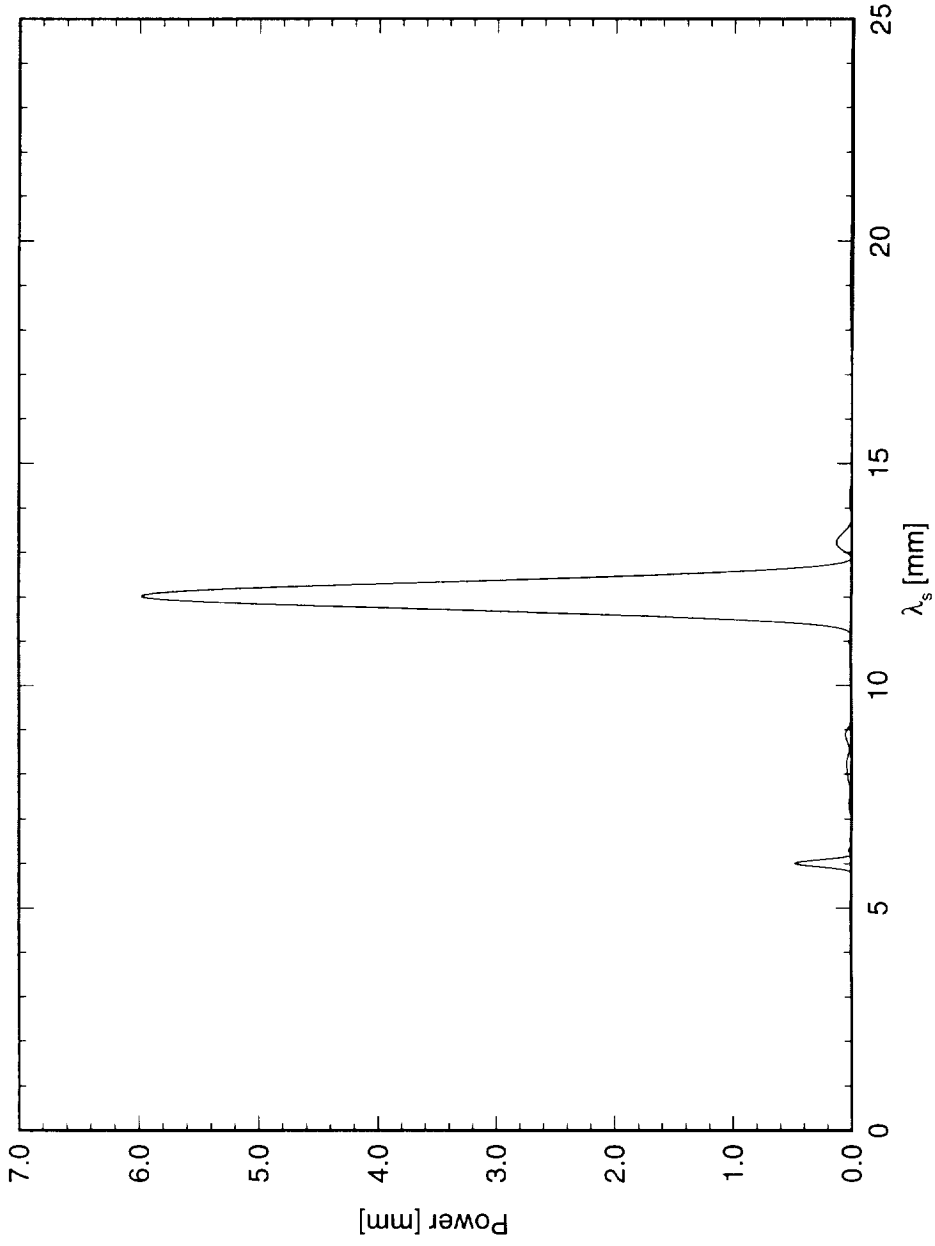

Figure 5.90: Power spectral density of spanwise hot-wire scan at $x/c = 0.45$, $Y = 0.9$ mm. $Re_c = 2.4 \times 10^6$, [6|12] roughness.

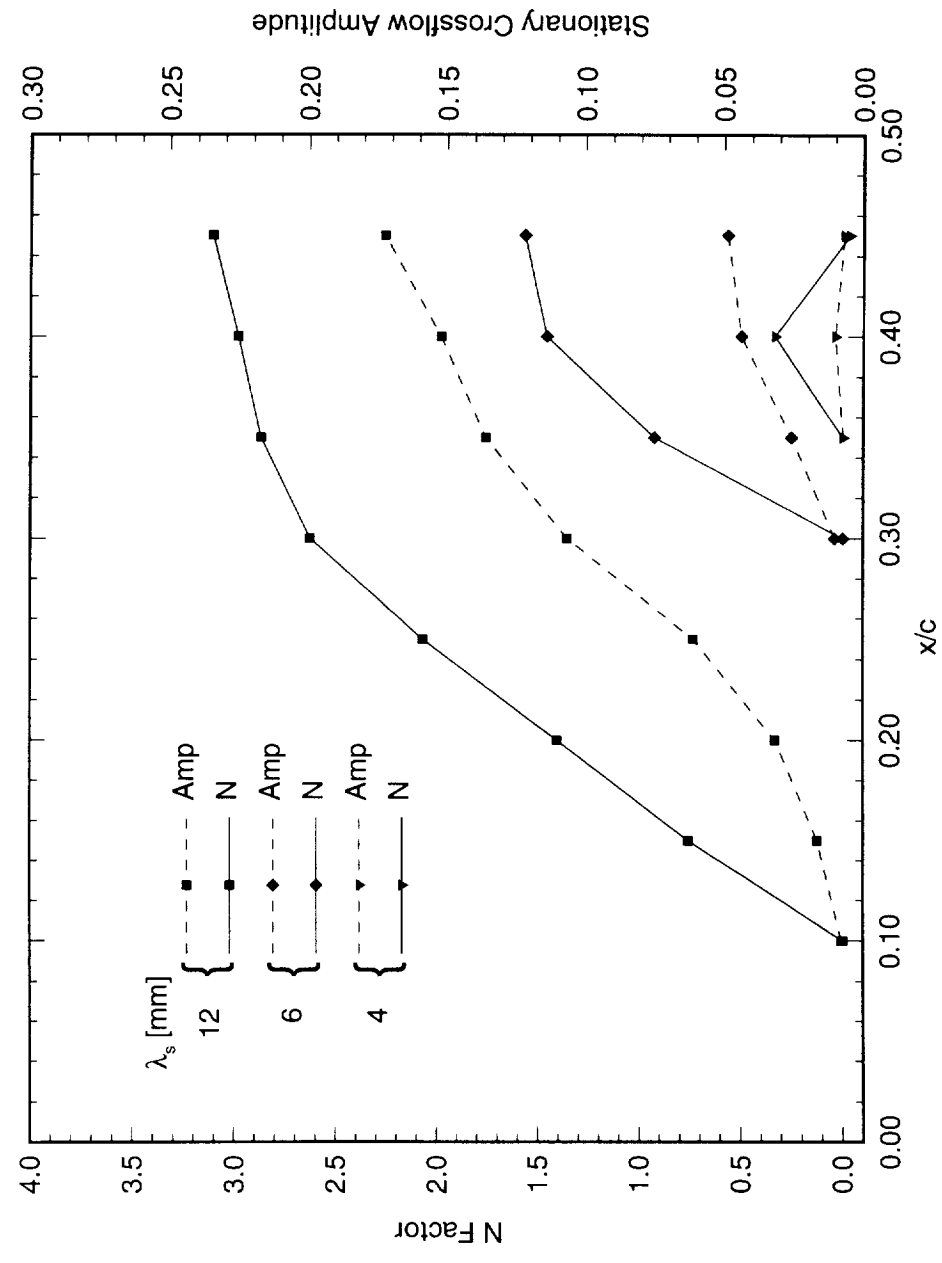

Figure 5.91: Individual-mode disturbance amplitude and amplification factor N for $Re_c = 2.4 \times 10^6$ and [6|12] roughness. N-factors are relative to the point at which the mode is first detected.

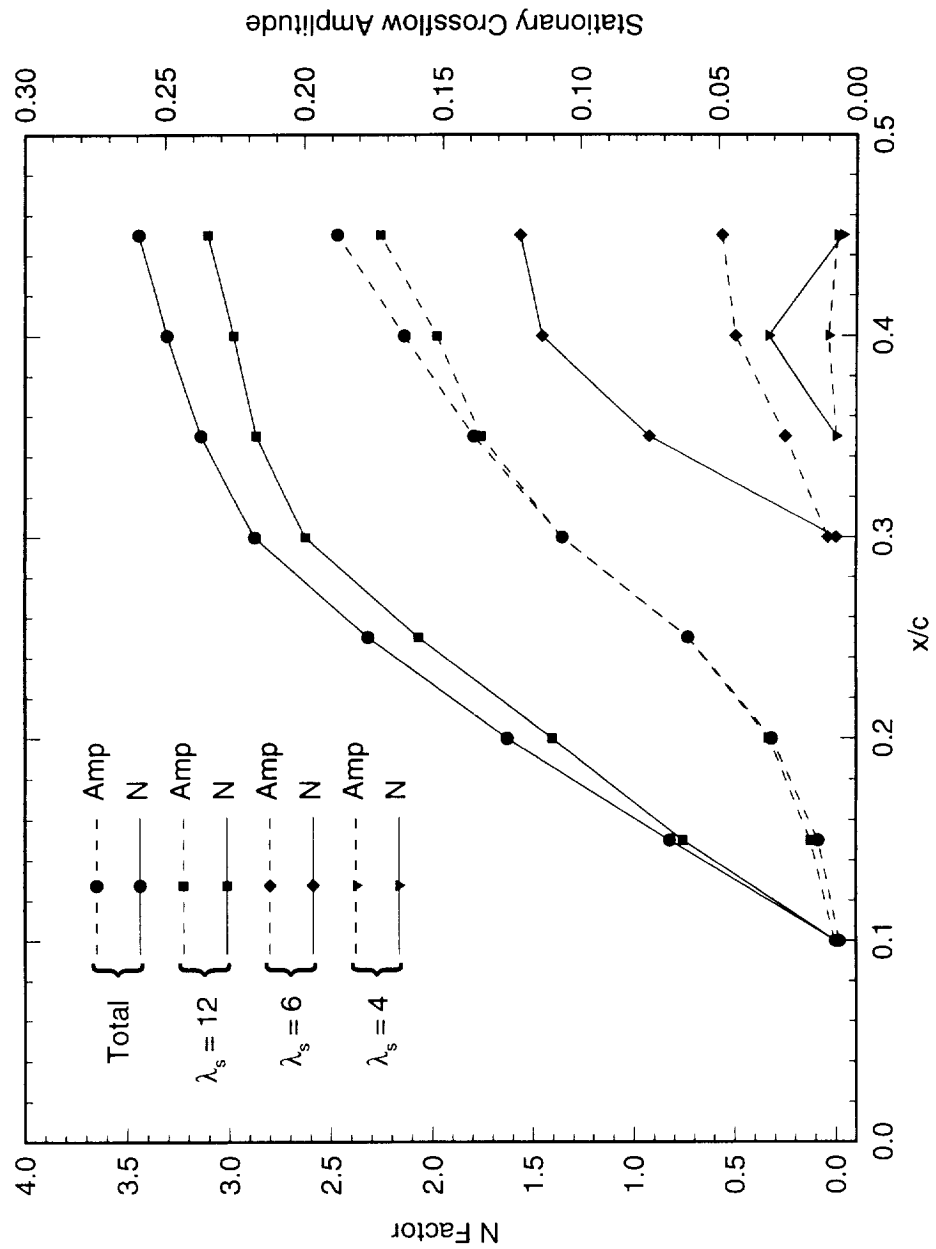

Figure 5.92: Total and individual-mode disturbance amplitude and amplification factor N for $Re_c = 2.4 \times 10^6$ and [6|12] roughness. N-factors are relative to the point at which the disturbance is first detected.

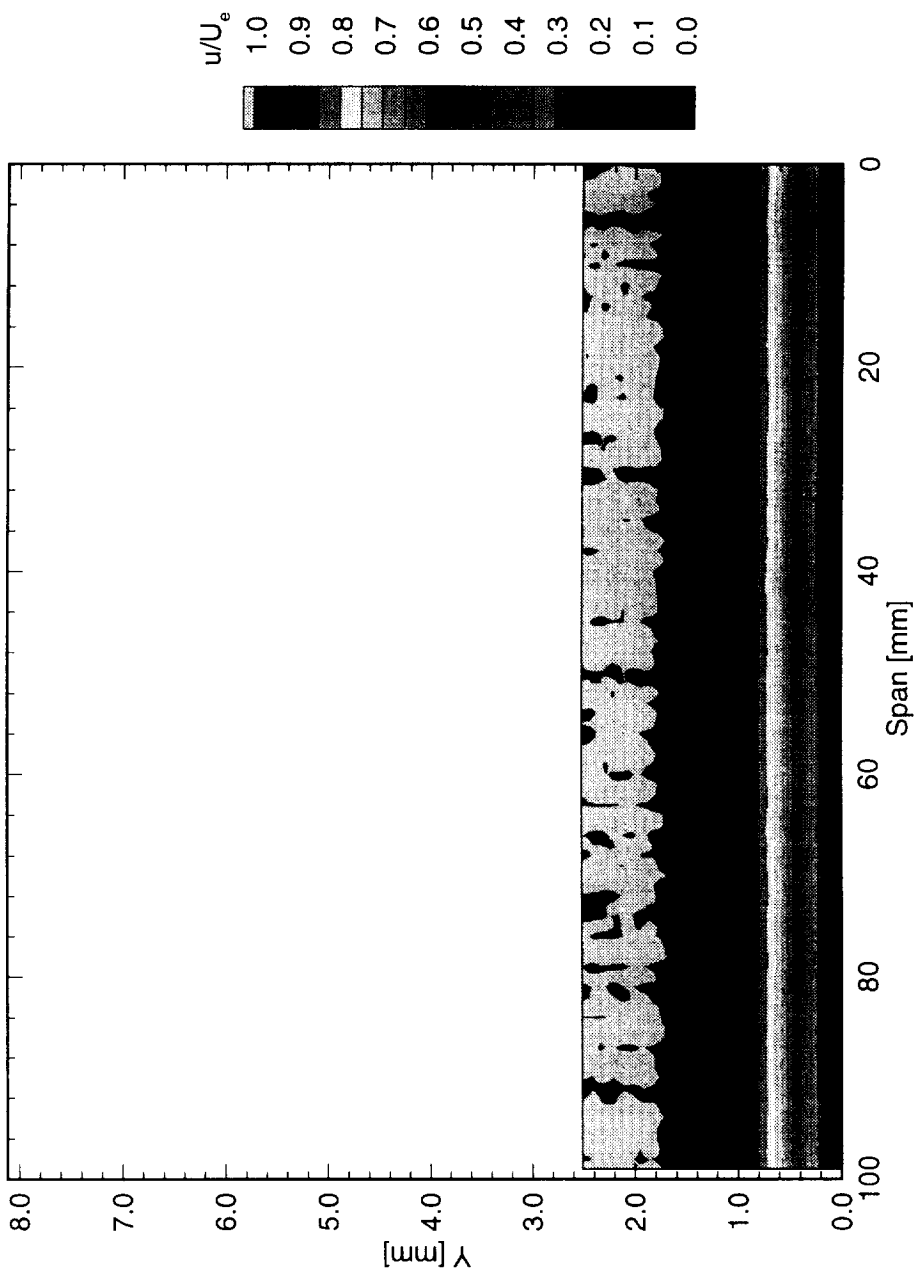

Figure 6.1: Streamwise velocity contours at $x/c = 0.05$. $Re_c = 1.6 \times 10^6$, [6|12] roughness.

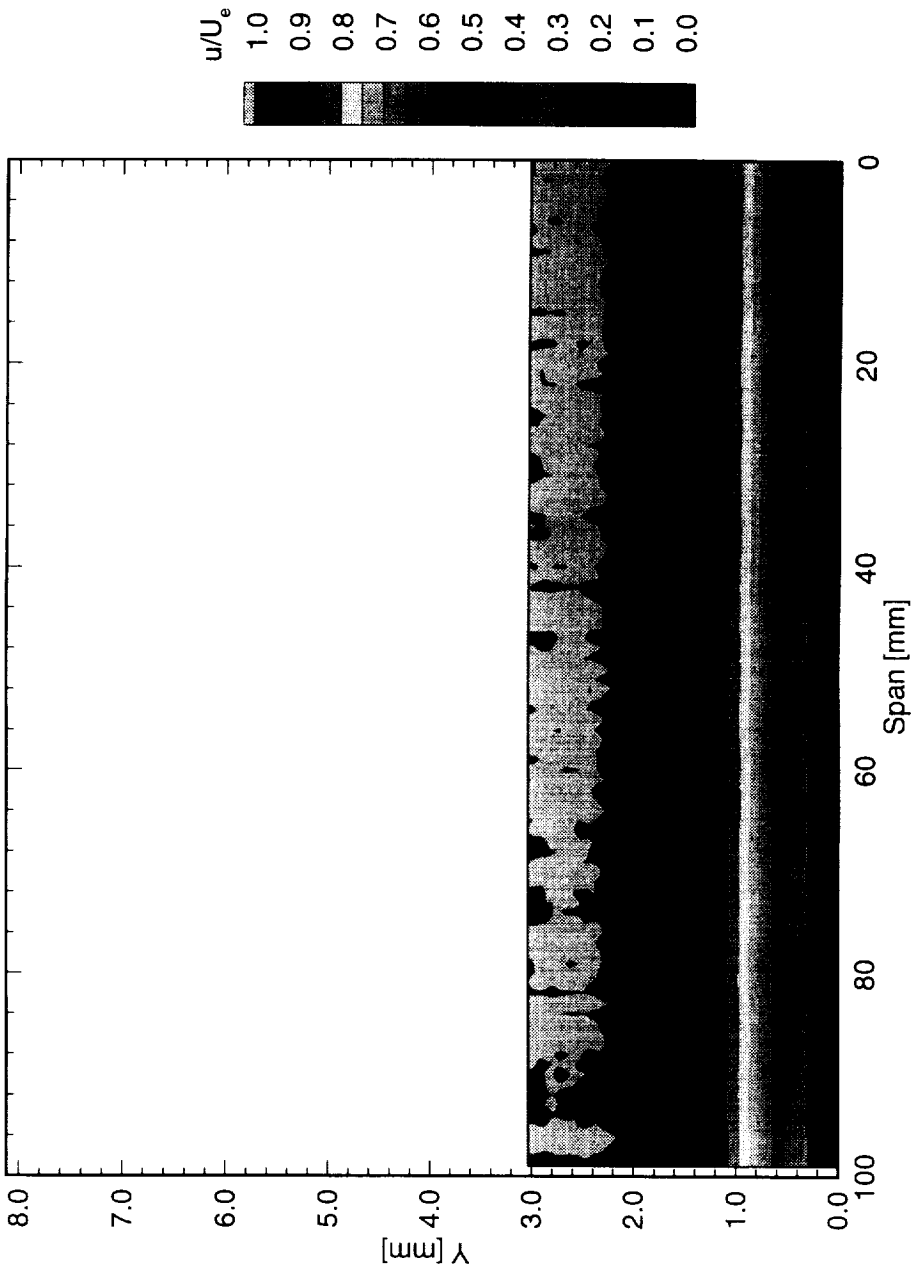

Figure 6.2: Streamwise velocity contours at $x/c = 0.10$. $Re_c = 1.6 \times 10^6$, [6|12] roughness.

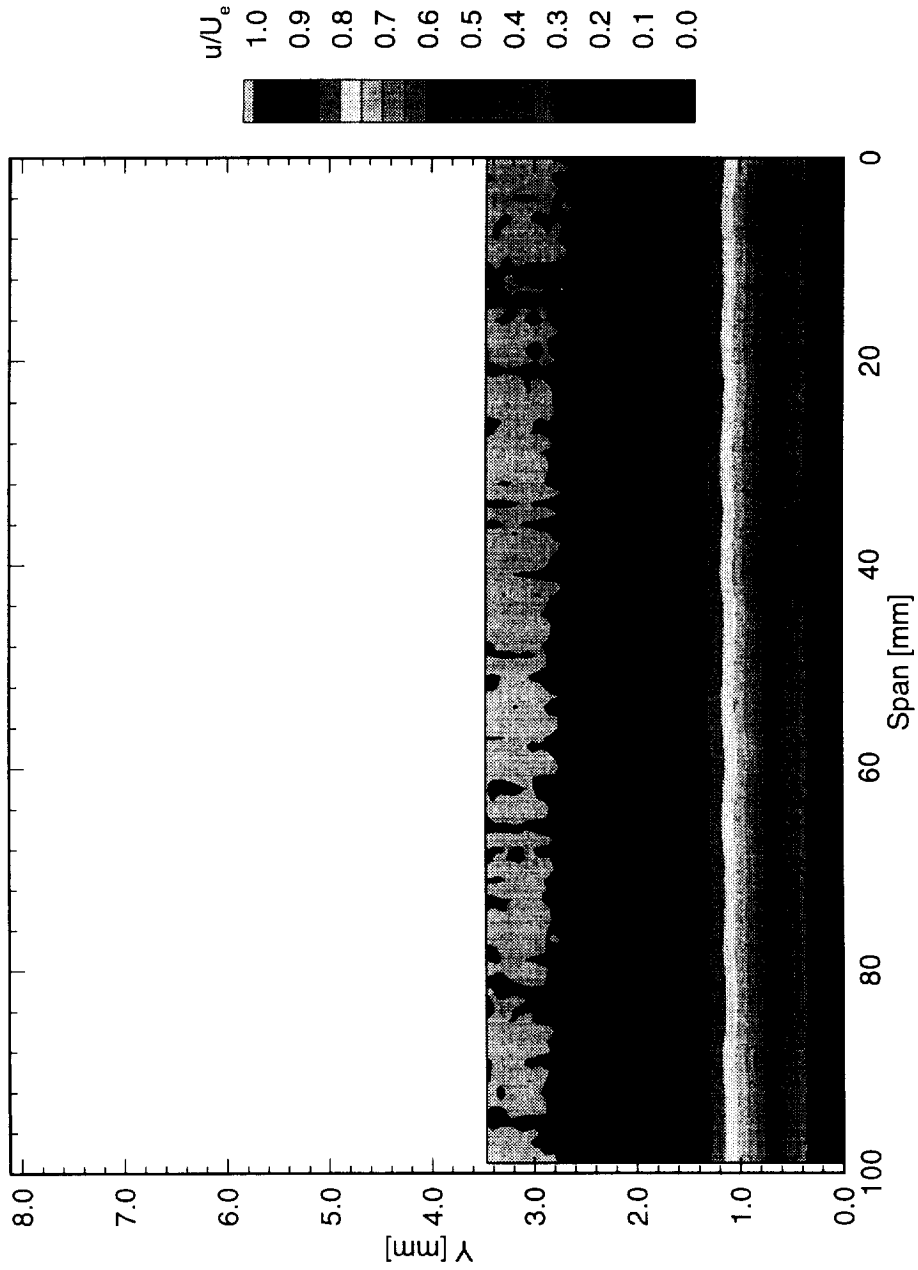

Figure 6.3: Streamwise velocity contours at $x/c = 0.15$. $Re_c = 1.6 \times 10^6$, [6|12] roughness.

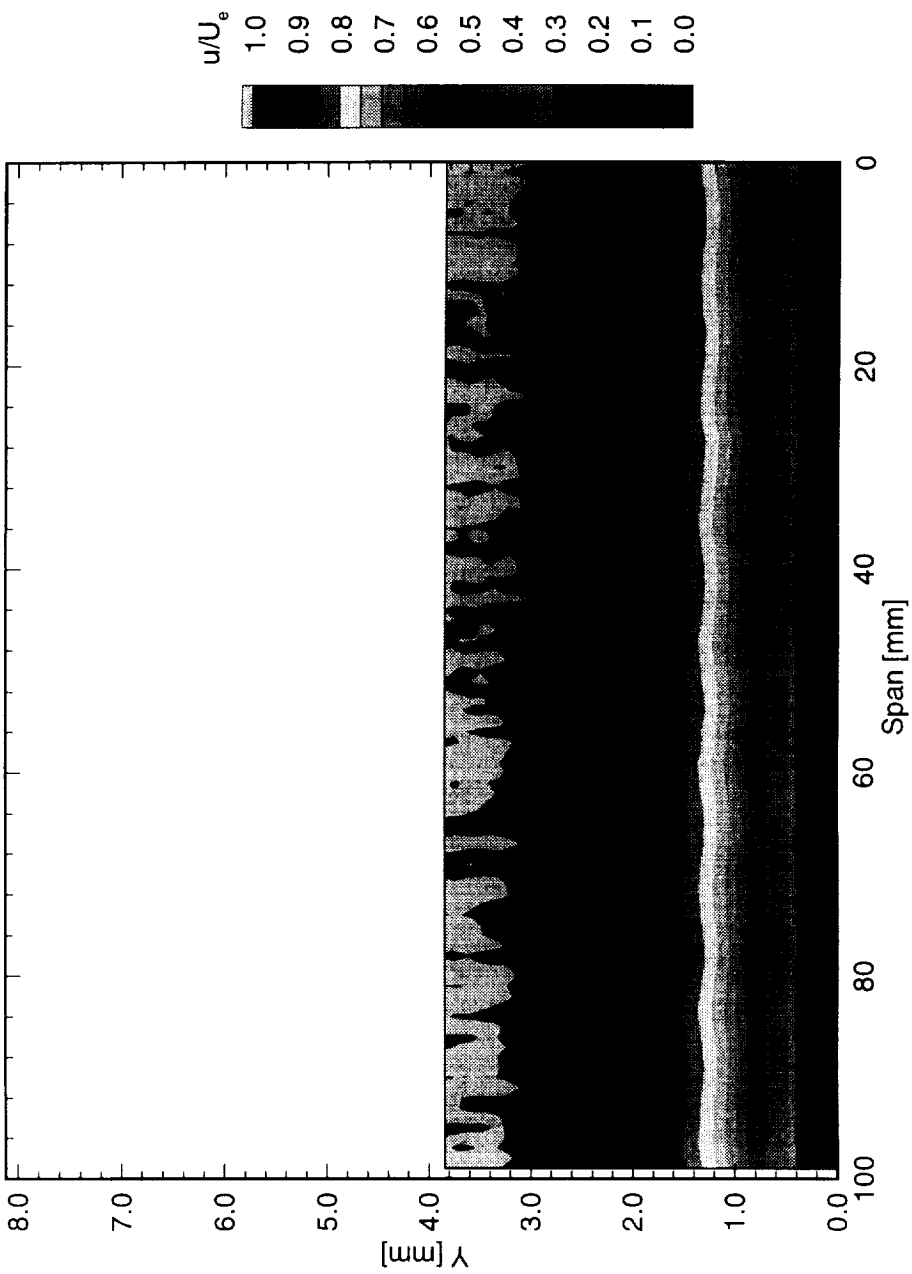

Figure 6.4: Streamwise velocity contours at $x/c = 0.20$. $Re_c = 1.6 \times 10^6$, [6|12] roughness.

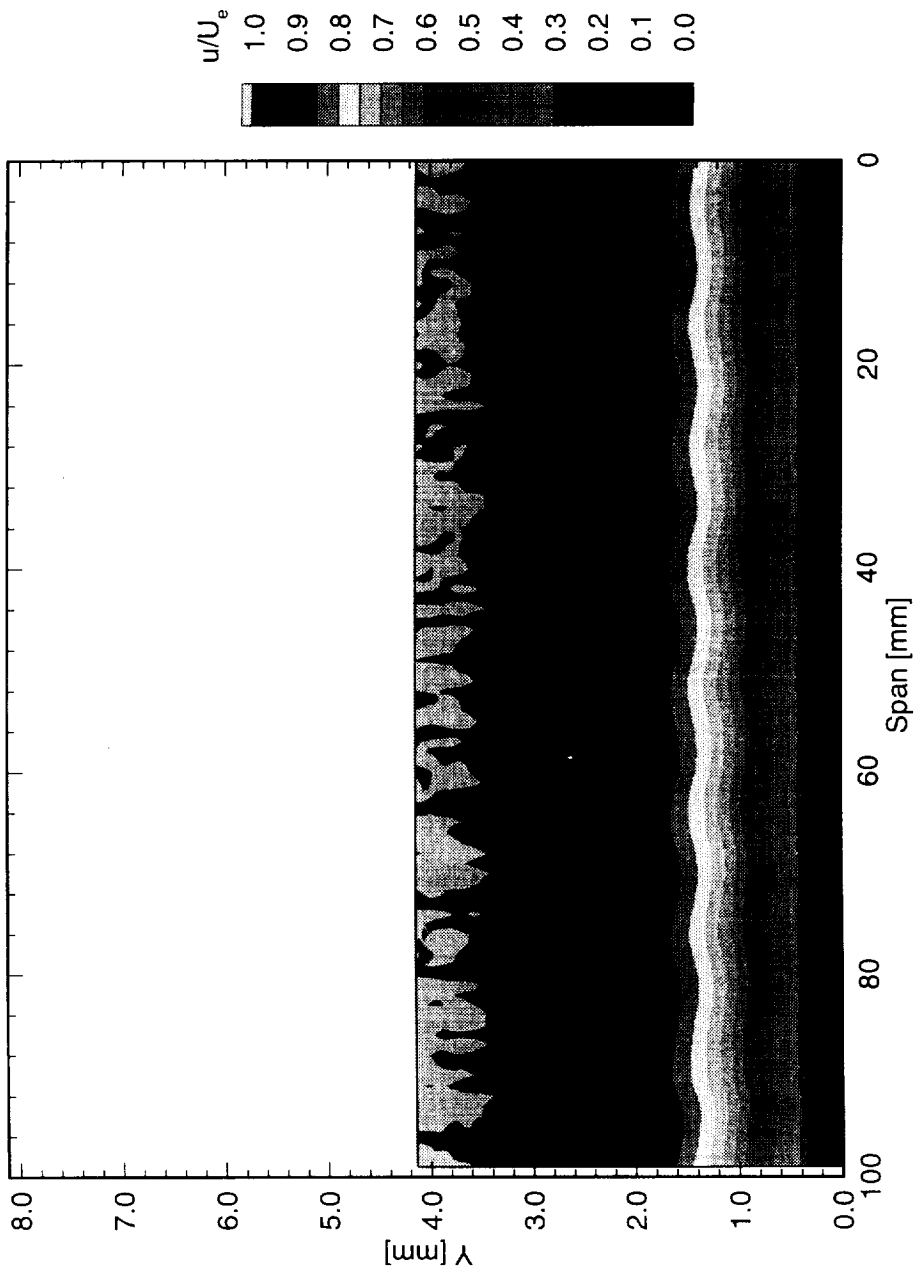

Figure 6.5: Streamwise velocity contours at $x/c = 0.25$. $Re_c = 1.6 \times 10^6$, [6|12] roughness.

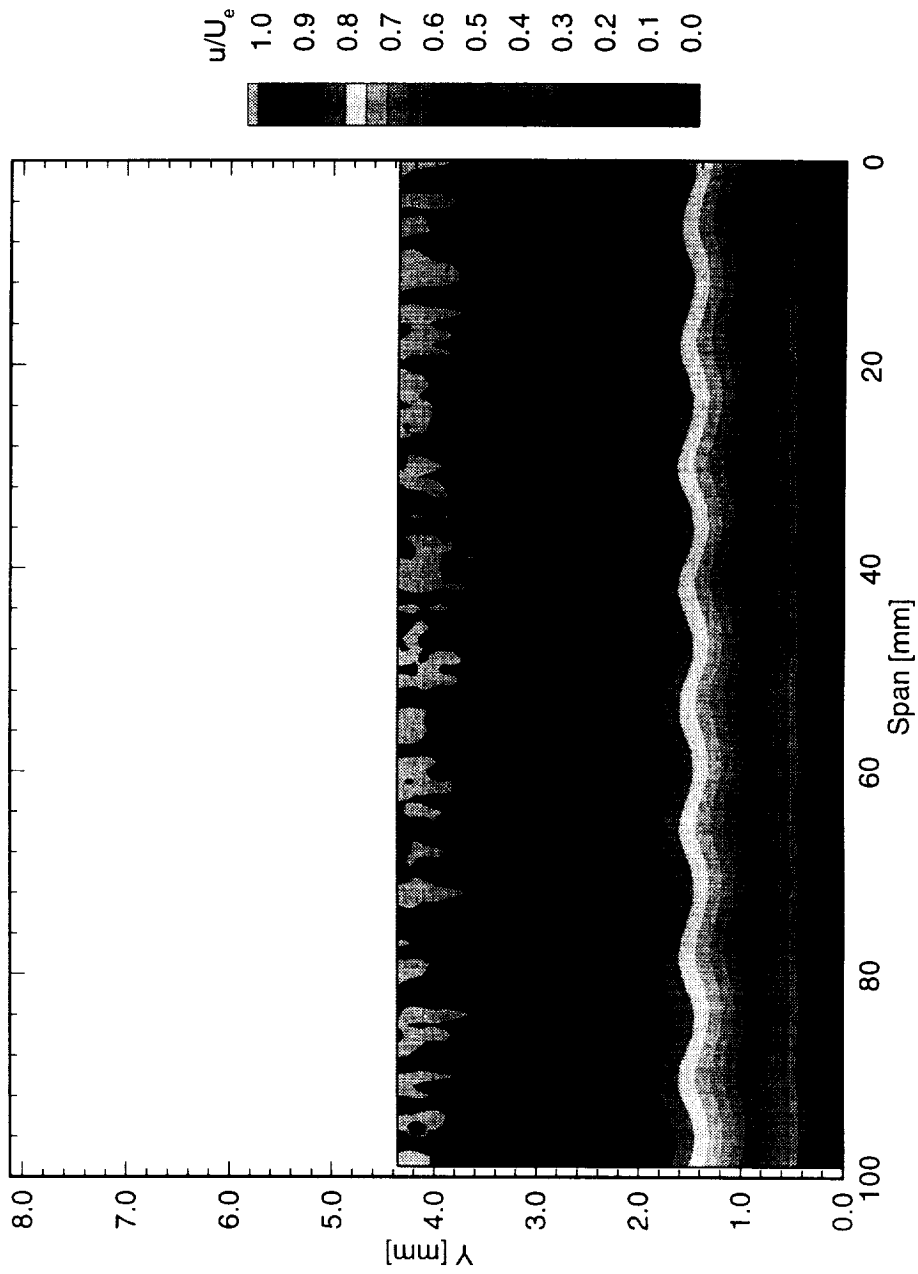

Figure 6.6: Streamwise velocity contours at $x/c = 0.30$. $Re_c = 1.6 \times 10^6$, [6|12] roughness.

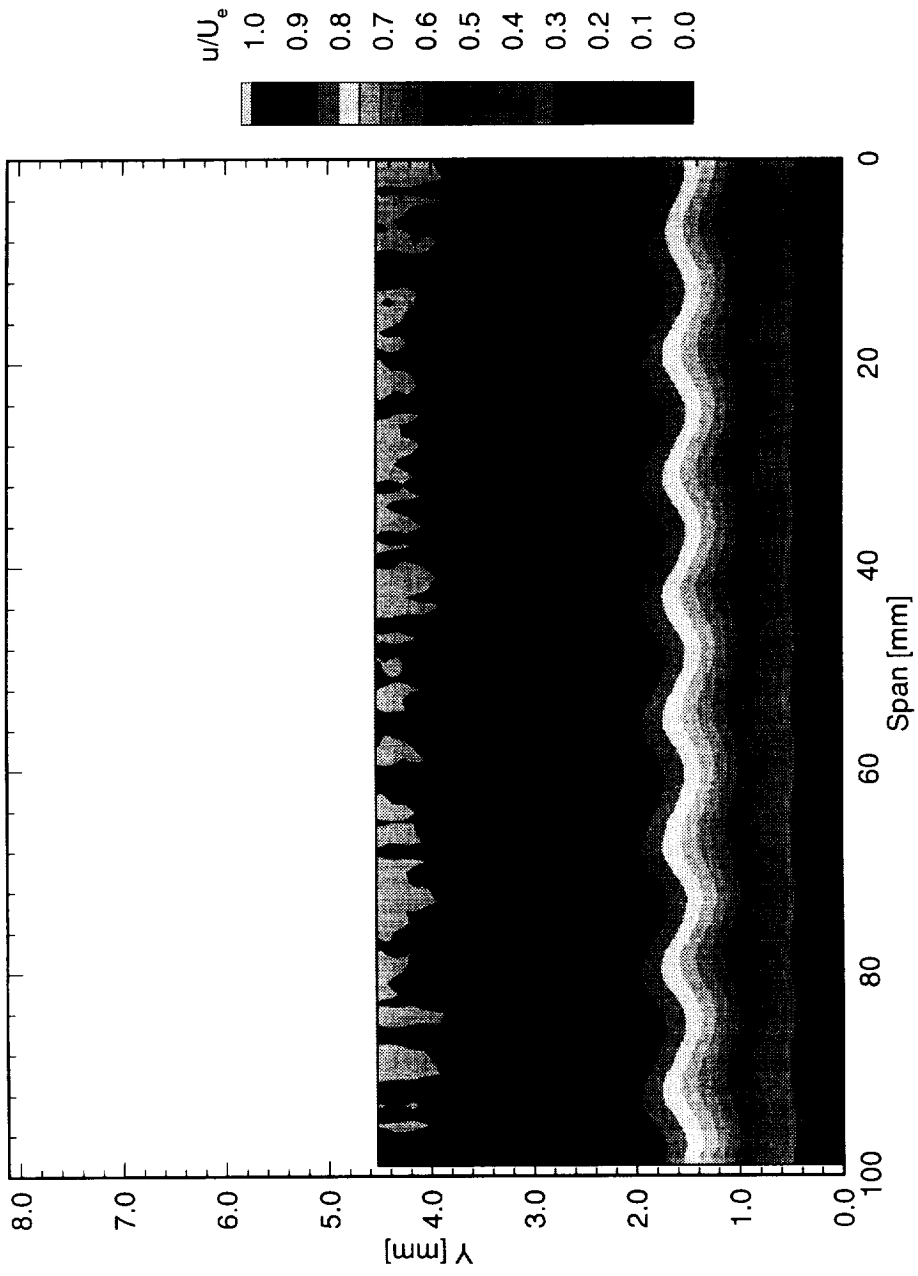

Figure 6.7: Streamwise velocity contours at $x/c = 0.35$. $Re_c = 1.6 \times 10^6$, [6|12] roughness.

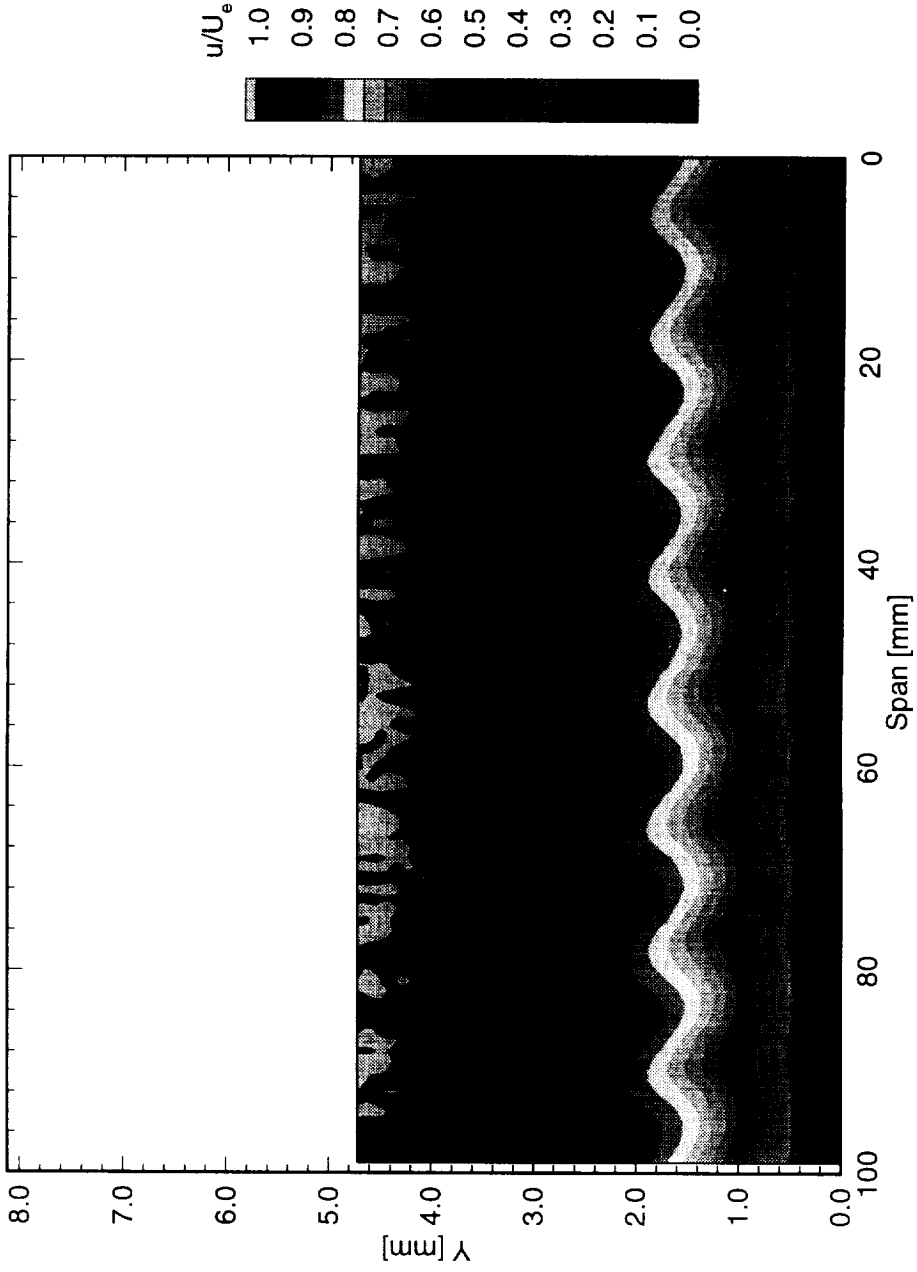

Figure 6.8: Streamwise velocity contours at $x/c = 0.40$. $Re_c = 1.6 \times 10^6$, [6|12] roughness.

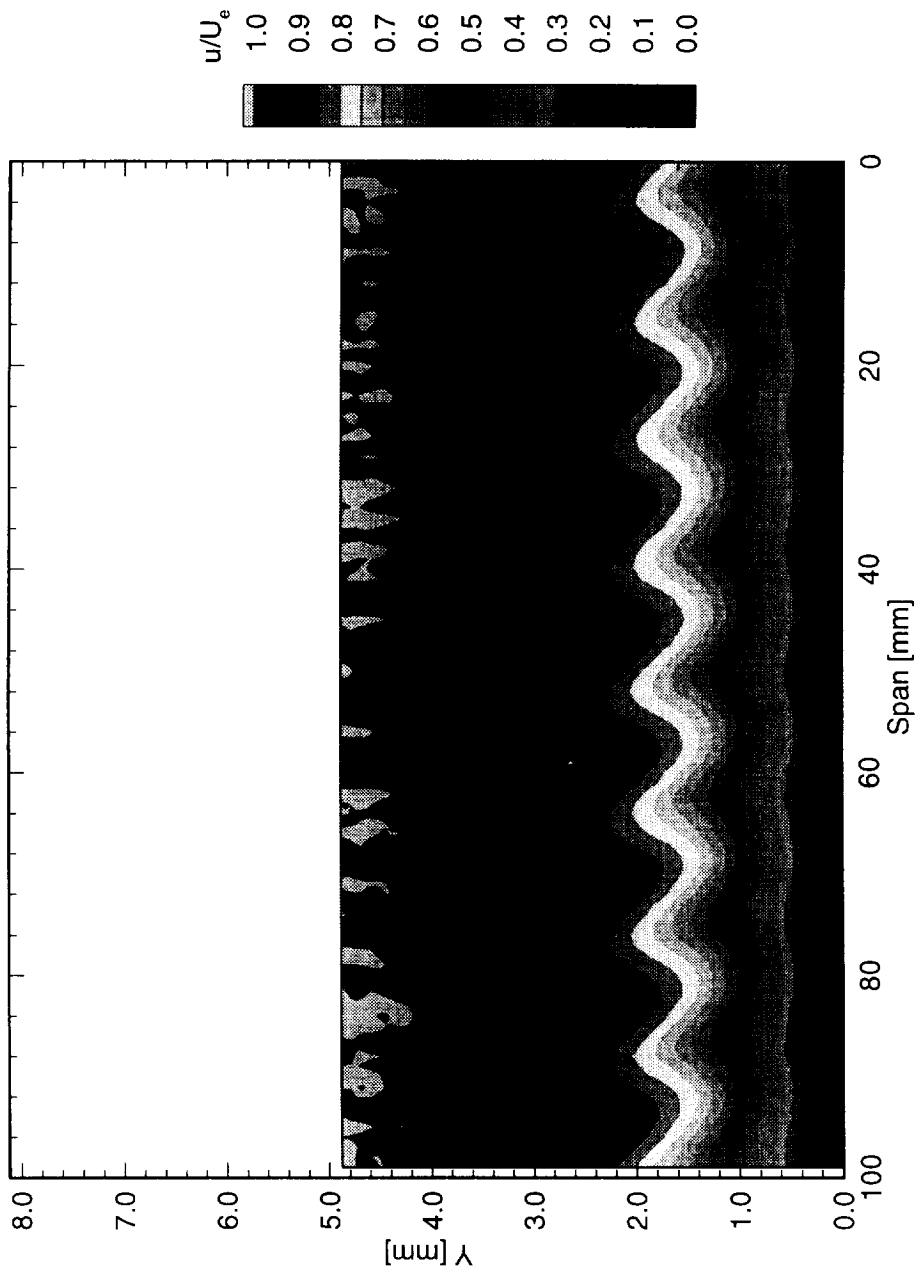

Figure 6.9: Streamwise velocity contours at $x/c = 0.45$. $Re_c = 1.6 \times 10^6$, [6|12] roughness.

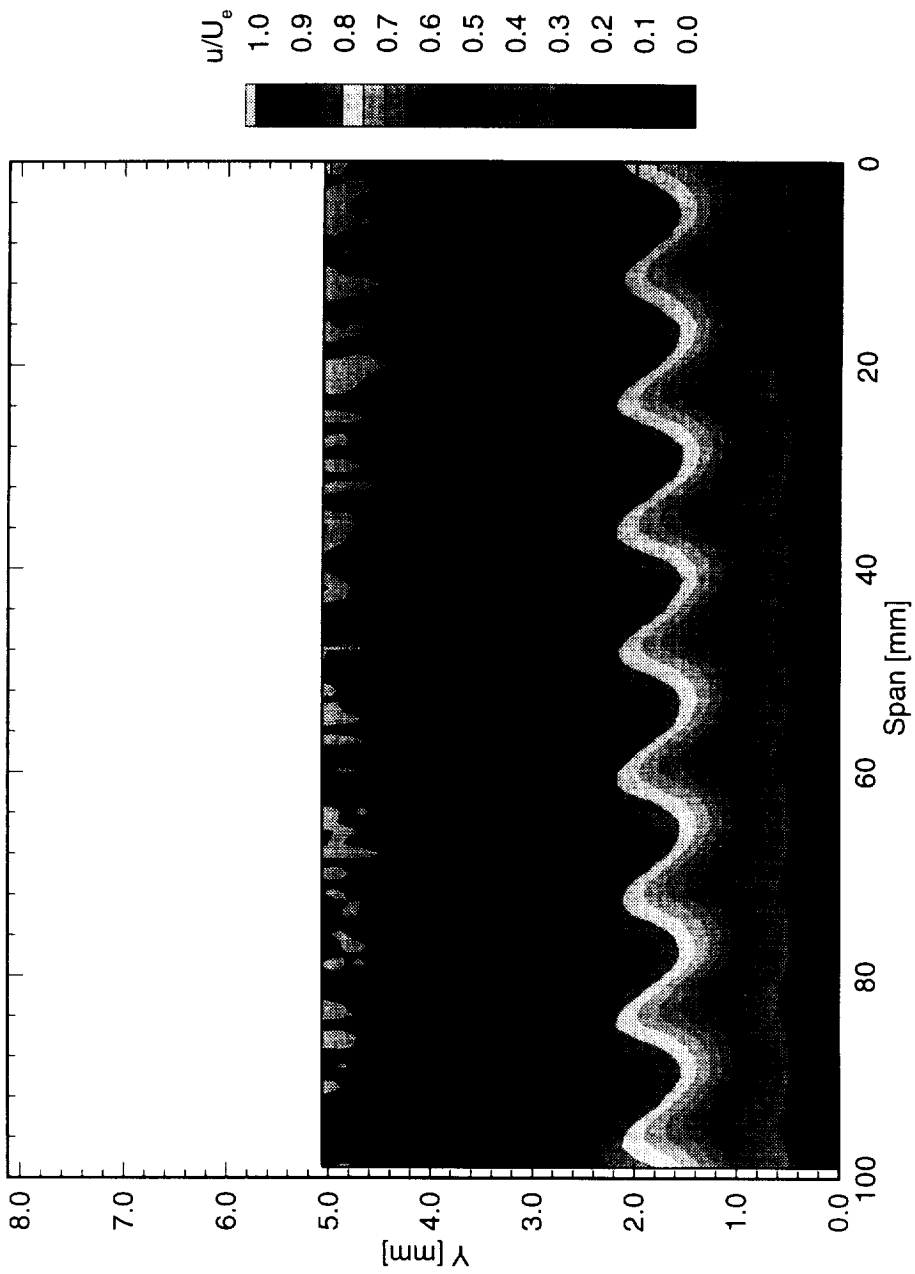

Figure 6.10: Streamwise velocity contours at $x/c = 0.50$. $Re_c = 1.6 \times 10^6$, [6|12] roughness.

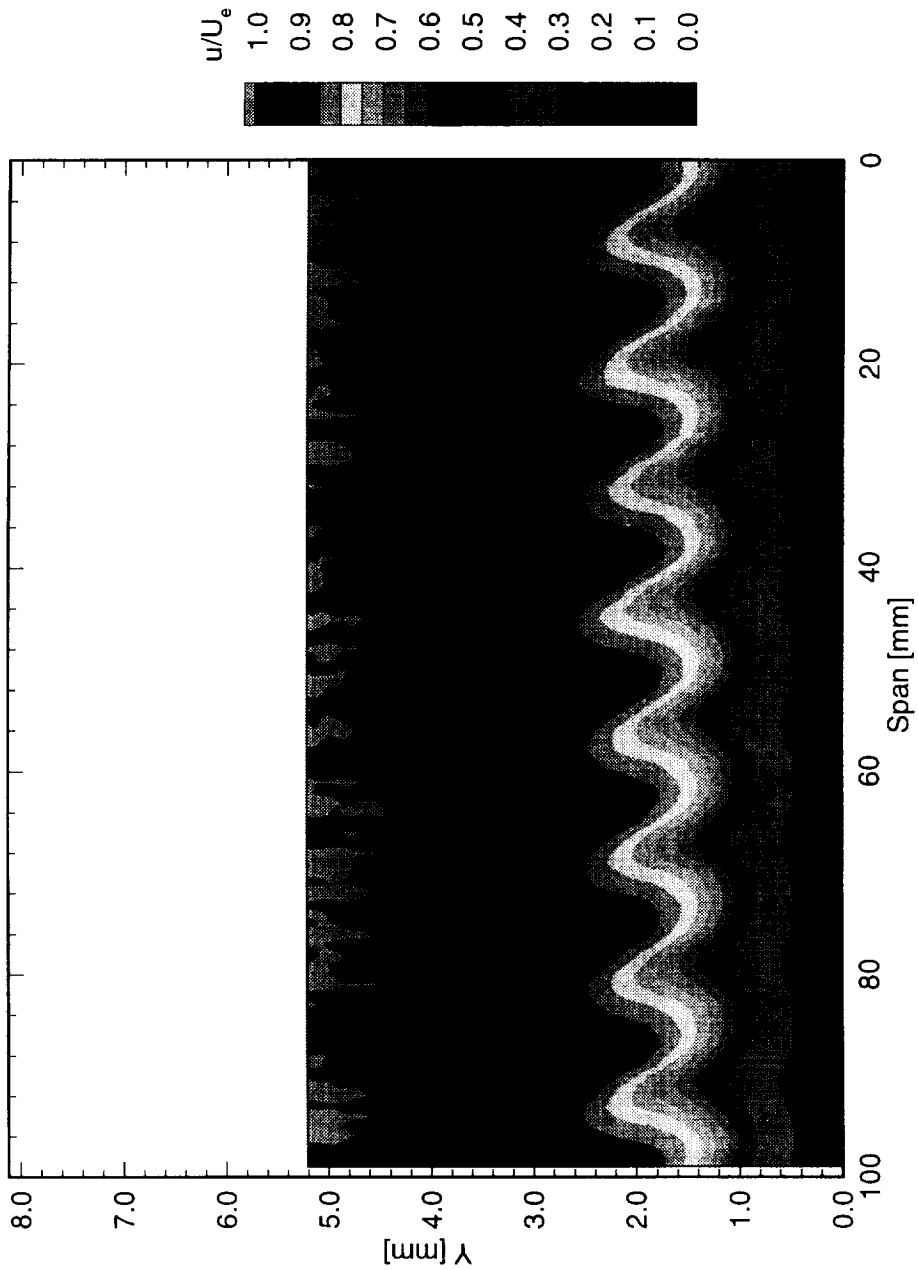

Figure 6.11: Streamwise velocity contours at $x/c = 0.55$. $Re_c = 1.6 \times 10^6$, [6|12] roughness.

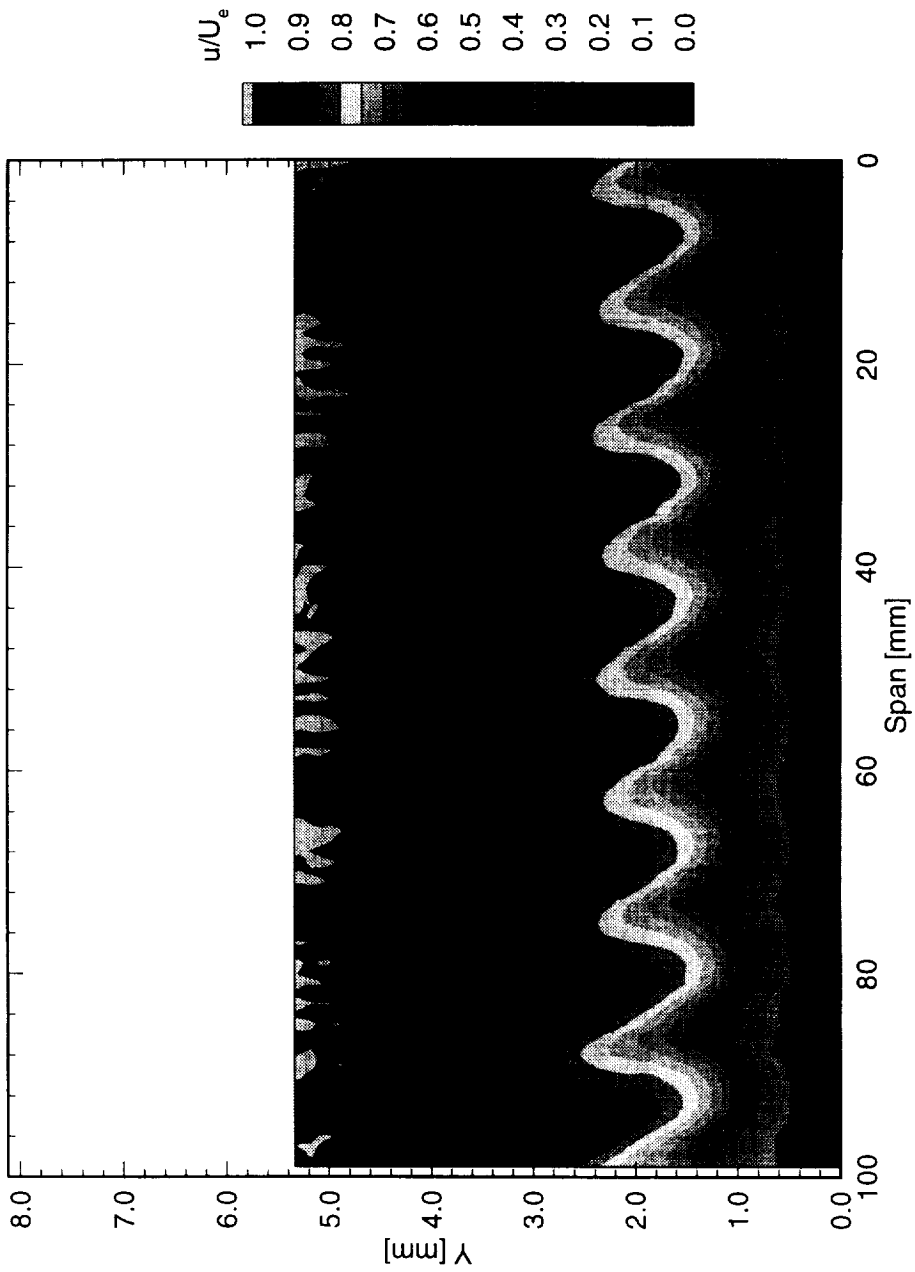

Figure 6.12: Streamwise velocity contours at $x/c = 0.60$. $Re_c = 1.6 \times 10^6$, [6|12] roughness.

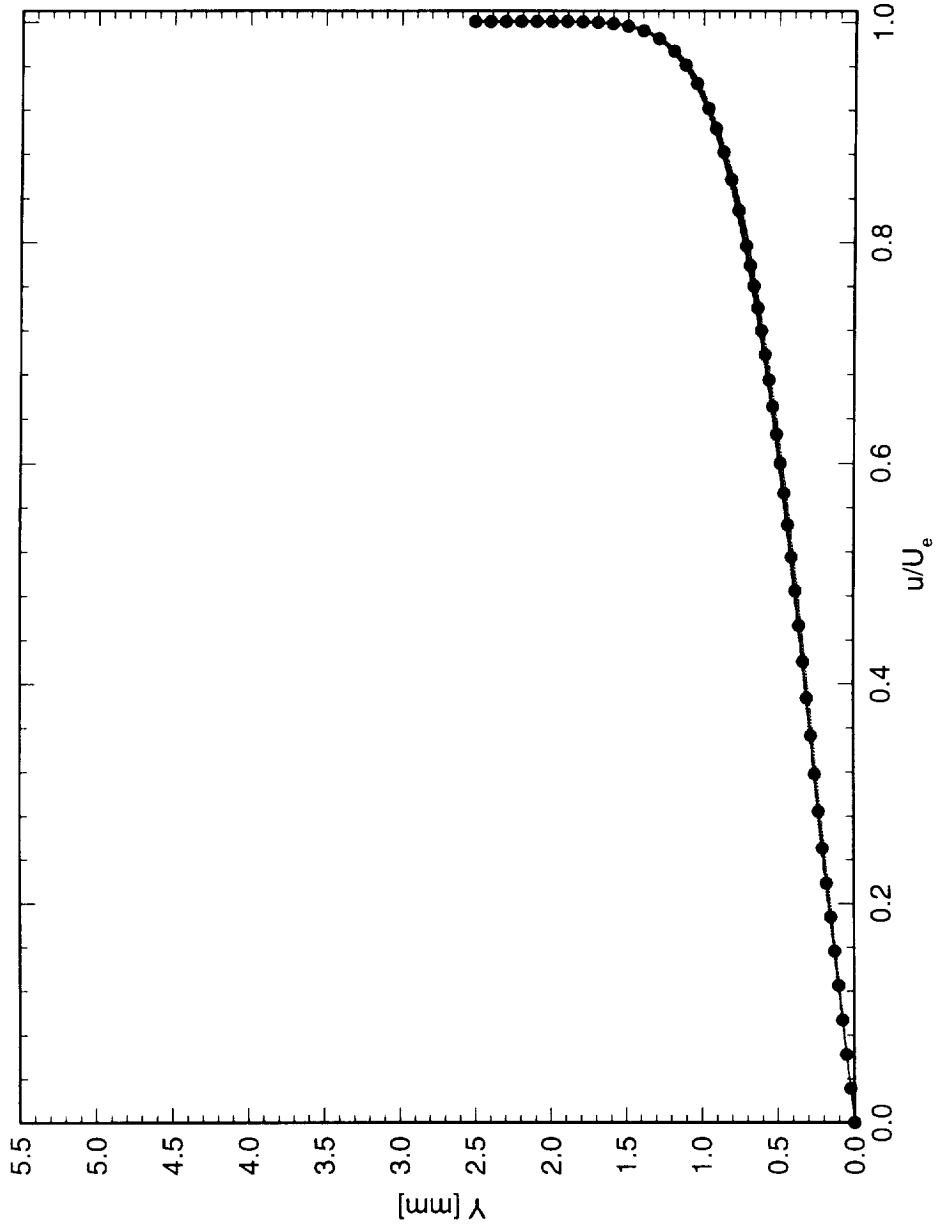

Figure 6.13: Spanwise array of 100 mean-flow boundary-layer profiles covering a span of 99 mm at $x/c = 0.05$. $Re_c = 1.6 \times 10^6$, [6|12] roughness. The dots indicate the mean of the profiles.

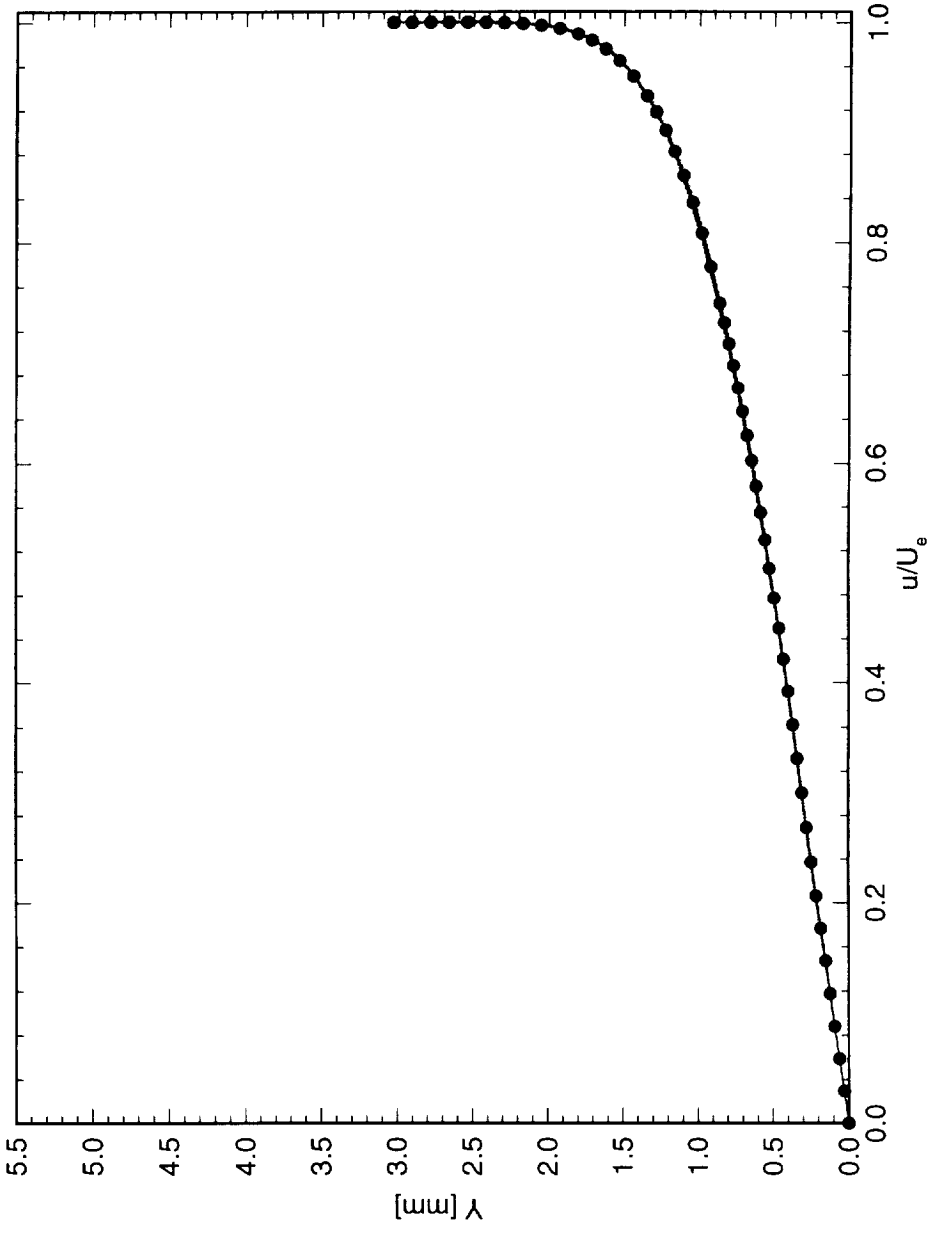

Figure 6.14: Spanwise array of 100 mean-flow boundary-layer profiles covering a span of 99 mm at $x/c = 0.10$. $Re_c = 1.6 \times 10^6$, [6|12] roughness. The dots indicate the mean of the profiles.

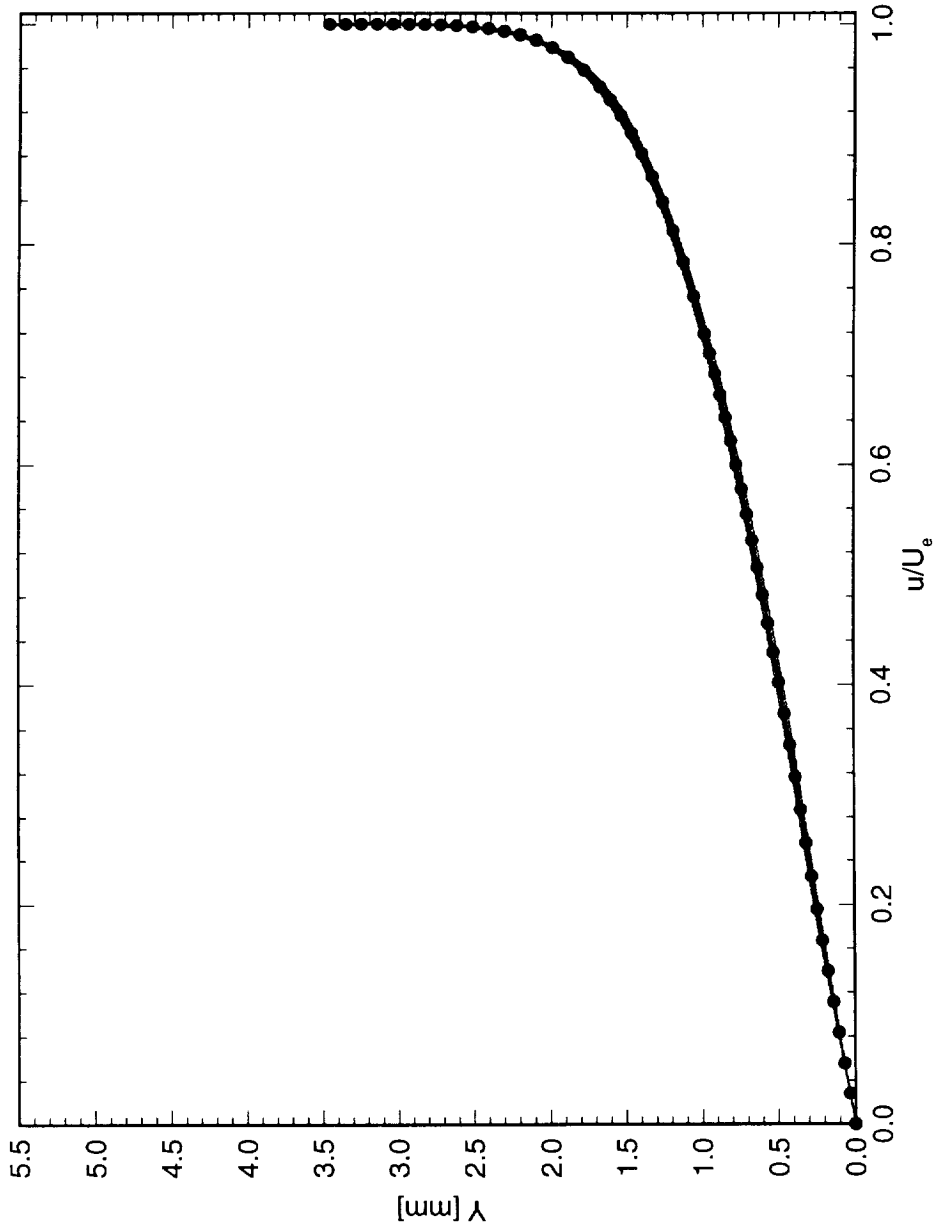

Figure 6.15: Spanwise array of 100 mean-flow boundary-layer profiles covering a span of 99 mm at $x/c = 0.15$. $Re_c = 1.6 \times 10^6$, [6|12] roughness. The dots indicate the mean of the profiles.

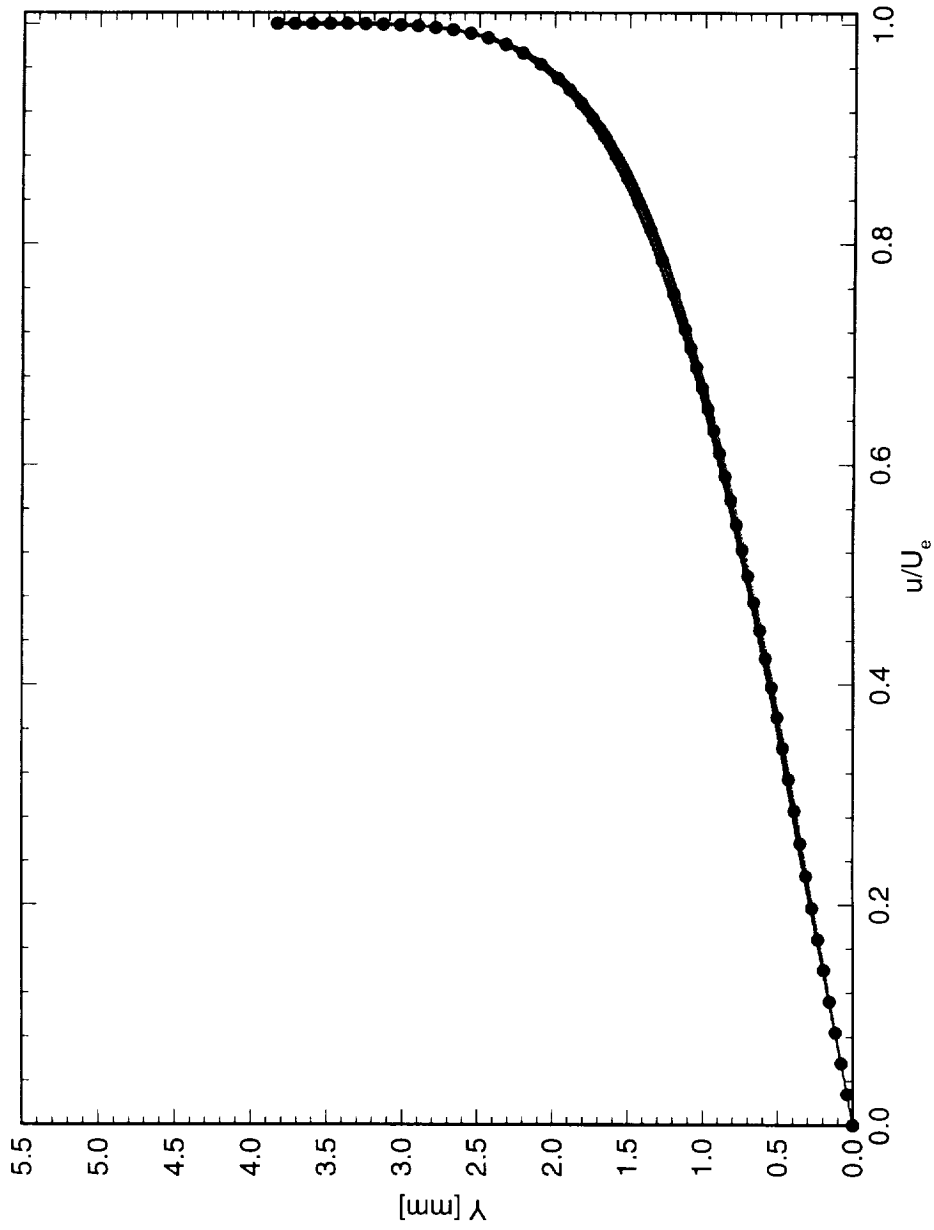

Figure 6.16: Spanwise array of 100 mean-flow boundary-layer profiles covering a span of 99 mm at $x/c = 0.20$. $Re_c = 1.6 \times 10^6$, [6|12] roughness. The dots indicate the mean of the profiles.

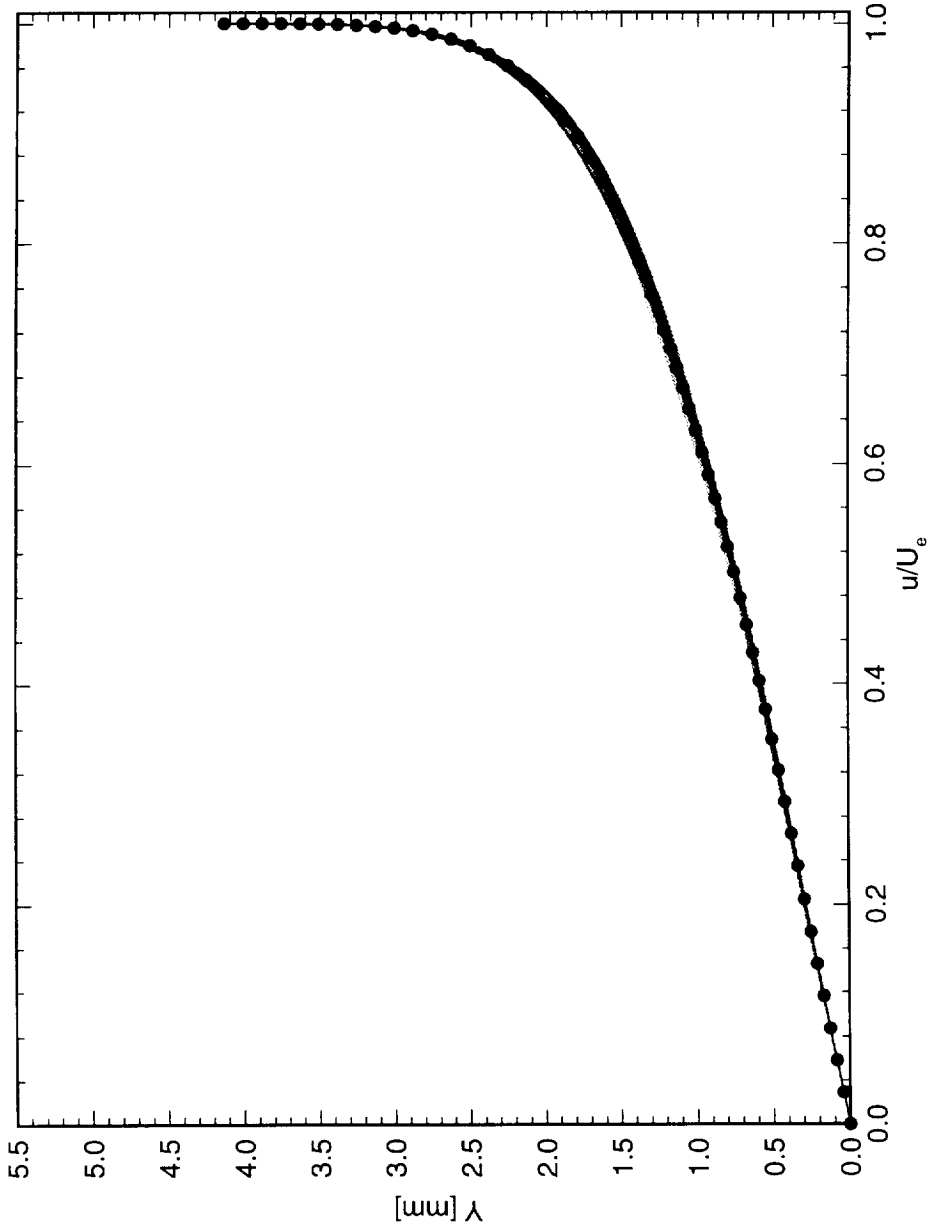

Figure 6.17: Spanwise array of 100 mean-flow boundary-layer profiles covering a span of 99 mm at $x/c = 0.25$. $Re_c = 1.6 \times 10^6$, [6|12] roughness. The dots indicate the mean of the profiles.

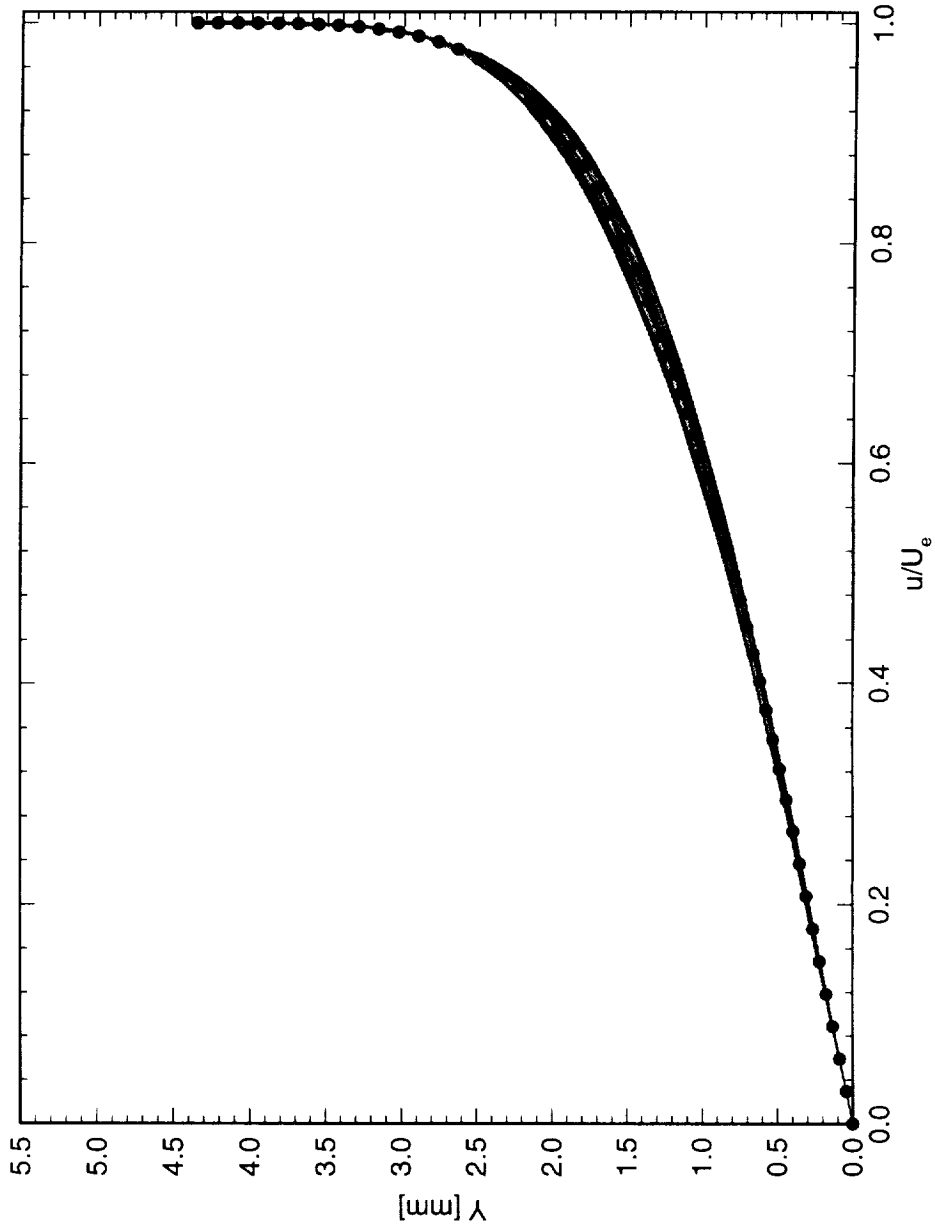

Figure 6.18: Spanwise array of 100 mean-flow boundary-layer profiles covering a span of 99 mm at $x/c = 0.30$. $Re_c = 1.6 \times 10^6$, [6|12] roughness. The dots indicate the mean of the profiles.

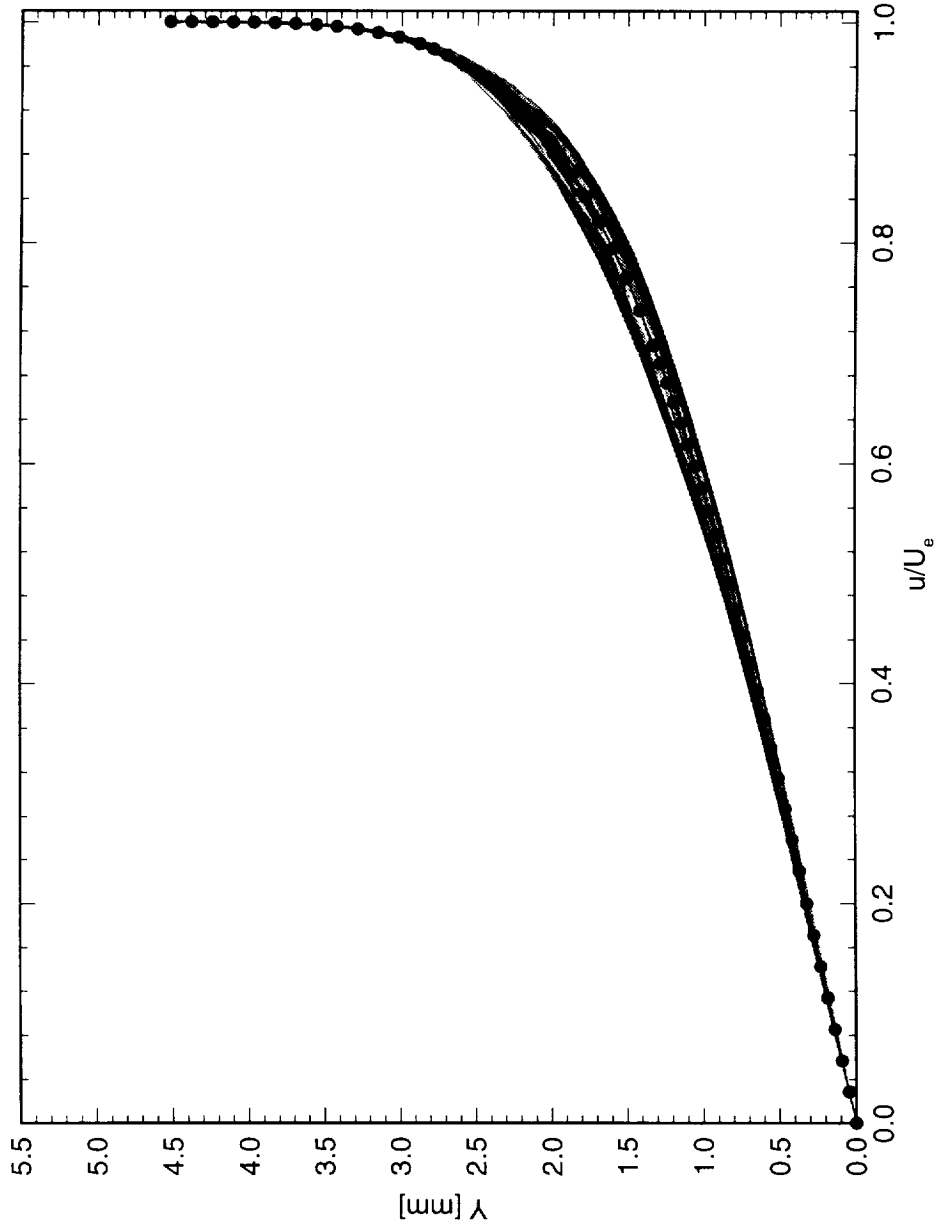

Figure 6.19: Spanwise array of 100 mean-flow boundary-layer profiles covering a span of 99 mm at $x/c = 0.35$. $Re_c = 1.6 \times 10^6$, [6|12] roughness. The dots indicate the mean of the profiles.

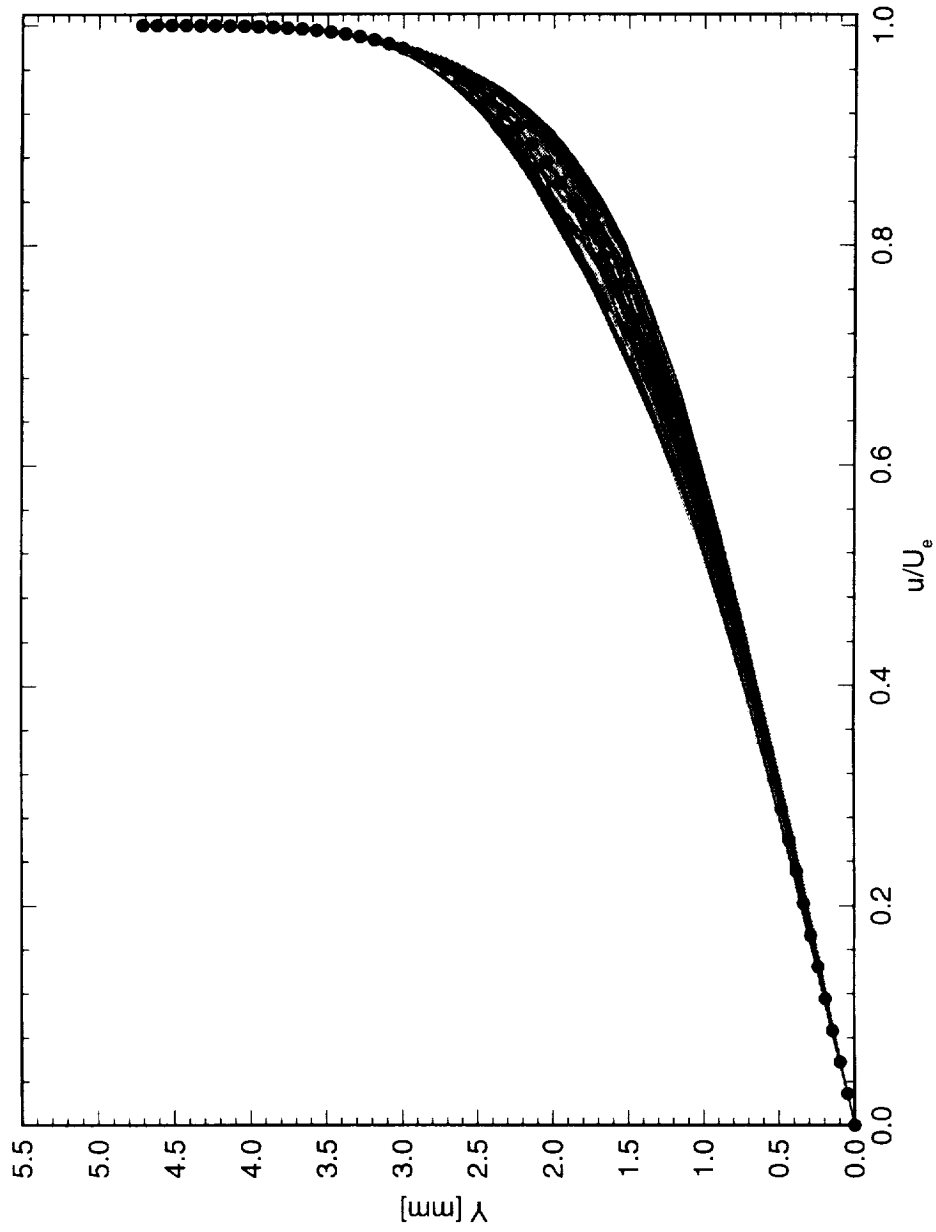

Figure 6.20: Spanwise array of 100 mean-flow boundary-layer profiles covering a span of 99 mm at $x/c = 0.40$. $Re_c = 1.6 \times 10^6$, [6|12] roughness. The dots indicate the mean of the profiles.

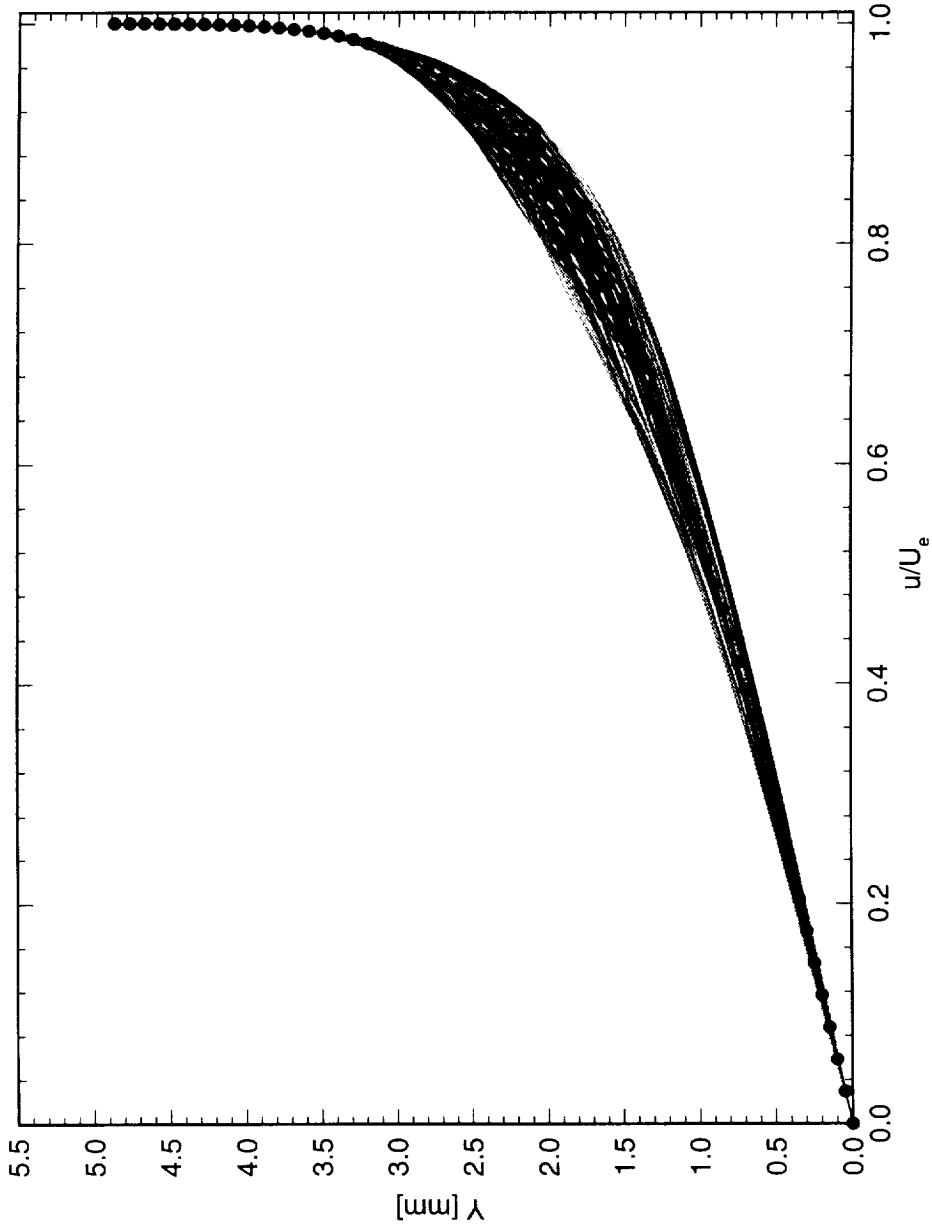

Figure 6.21: Spanwise array of 100 mean-flow boundary-layer profiles covering a span of 99 mm at $x/c = 0.45$. $Re_c = 1.6 \times 10^6$, [6|12] roughness. The dots indicate the mean of the profiles.

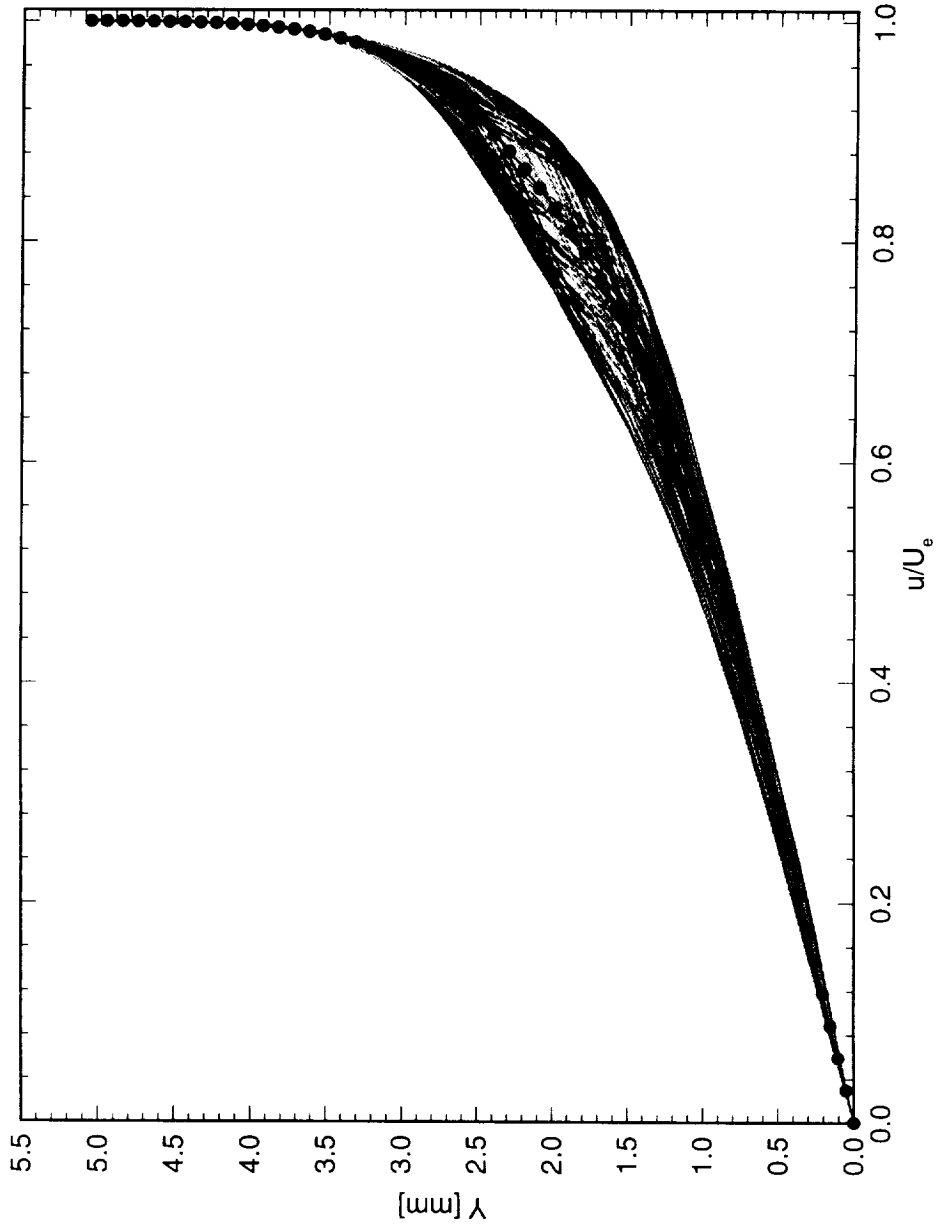

Figure 6.22: Spanwise array of 100 mean-flow boundary-layer profiles covering a span of 99 mm at $x/c = 0.50$. $Re_c = 1.6 \times 10^6$, [6|12] roughness. The dots indicate the mean of the profiles.

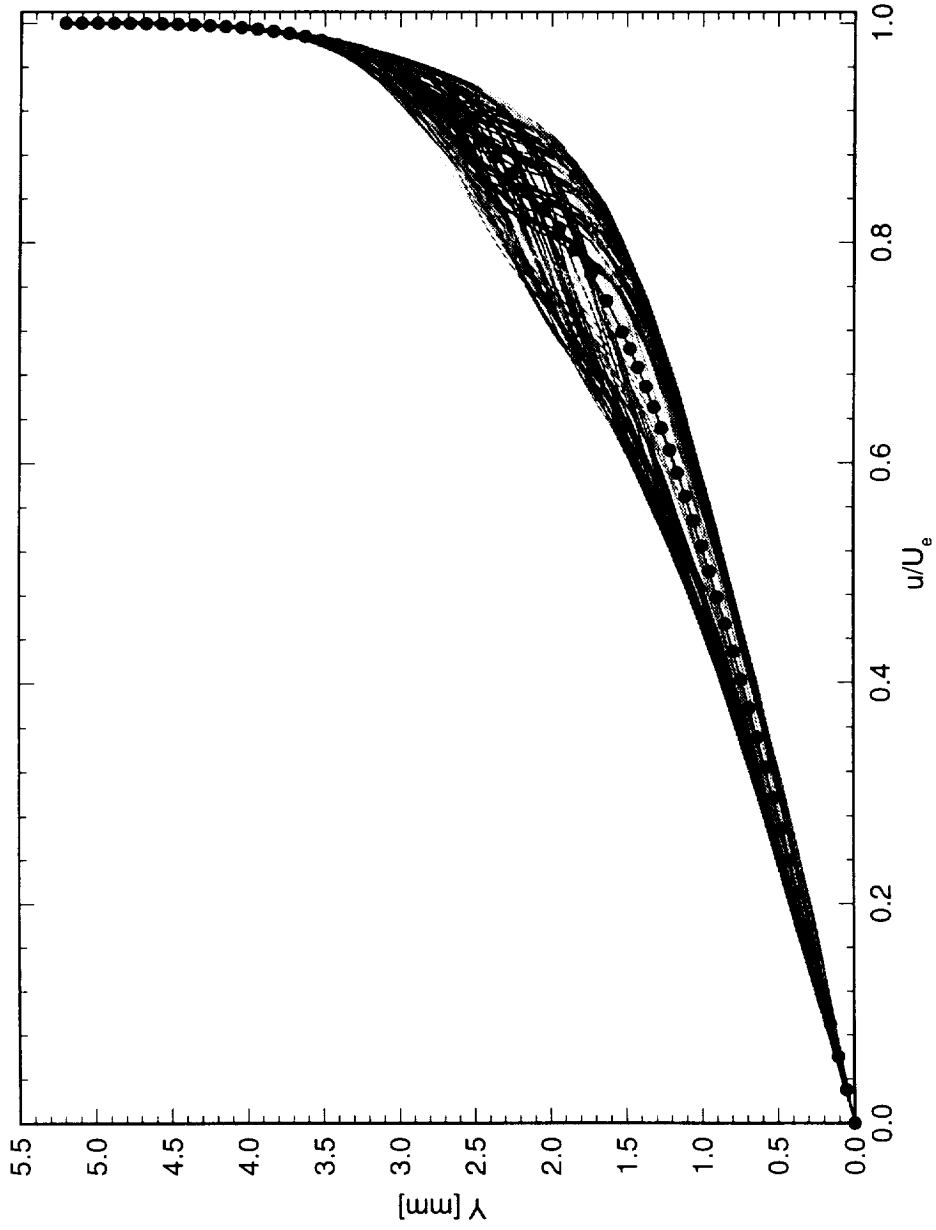

Figure 6.23: Spanwise array of 100 mean-flow boundary-layer profiles covering a span of 99 mm at $x/c = 0.55$. $Re_c = 1.6 \times 10^6$, [6|12] roughness. The dots indicate the mean of the profiles.

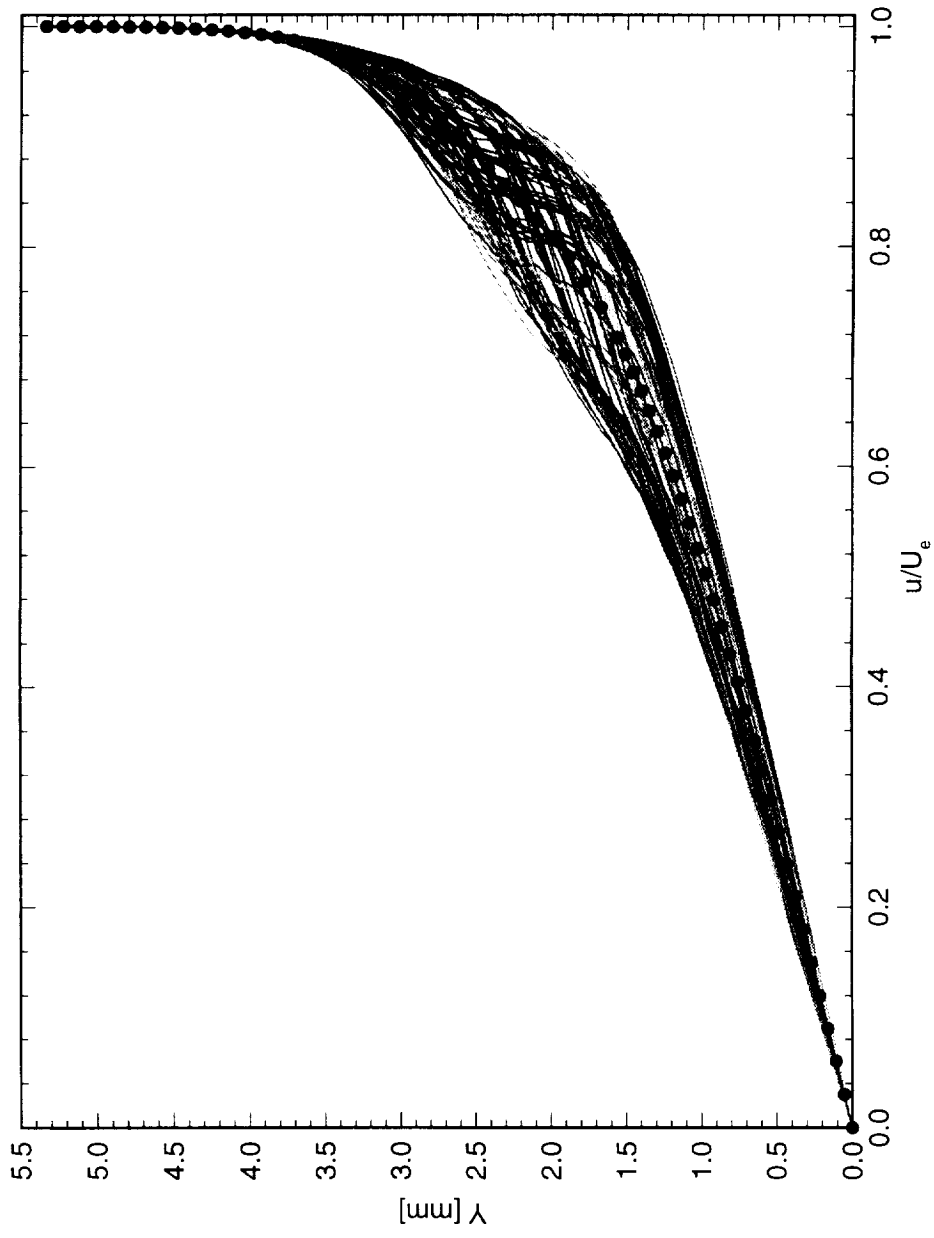

Figure 6.24: Spanwise array of 100 mean-flow boundary-layer profiles covering a span of 99 mm at $x/c = 0.60$. $Re_c = 1.6 \times 10^6$. [6|12] roughness. The dots indicate the mean of the profiles.

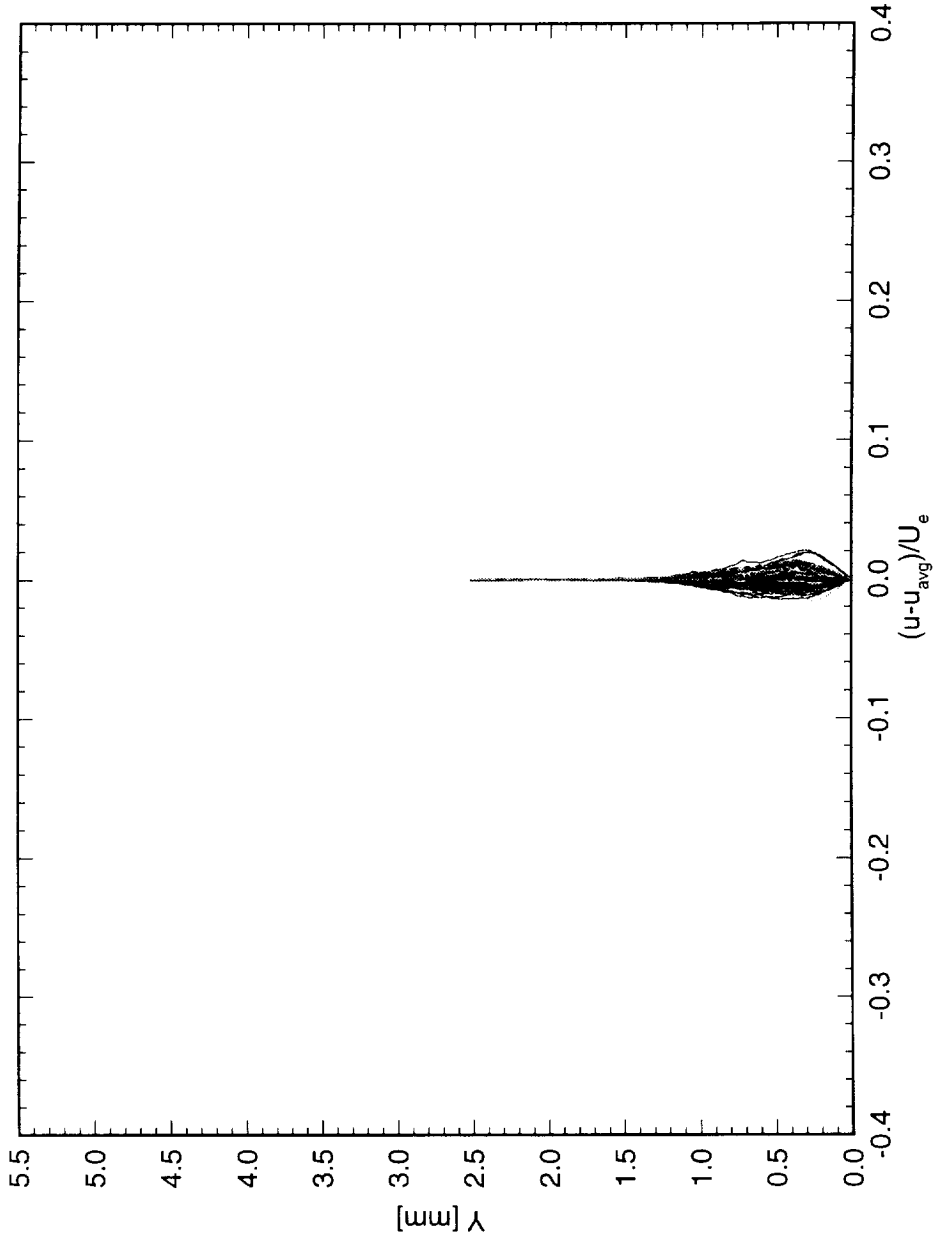

Figure 6.25: Spanwise array of 100 disturbance profiles covering a span of 99 mm at $x/c = 0.05$. $Re_c = 1.6 \times 10^6$, [6|12] roughness.

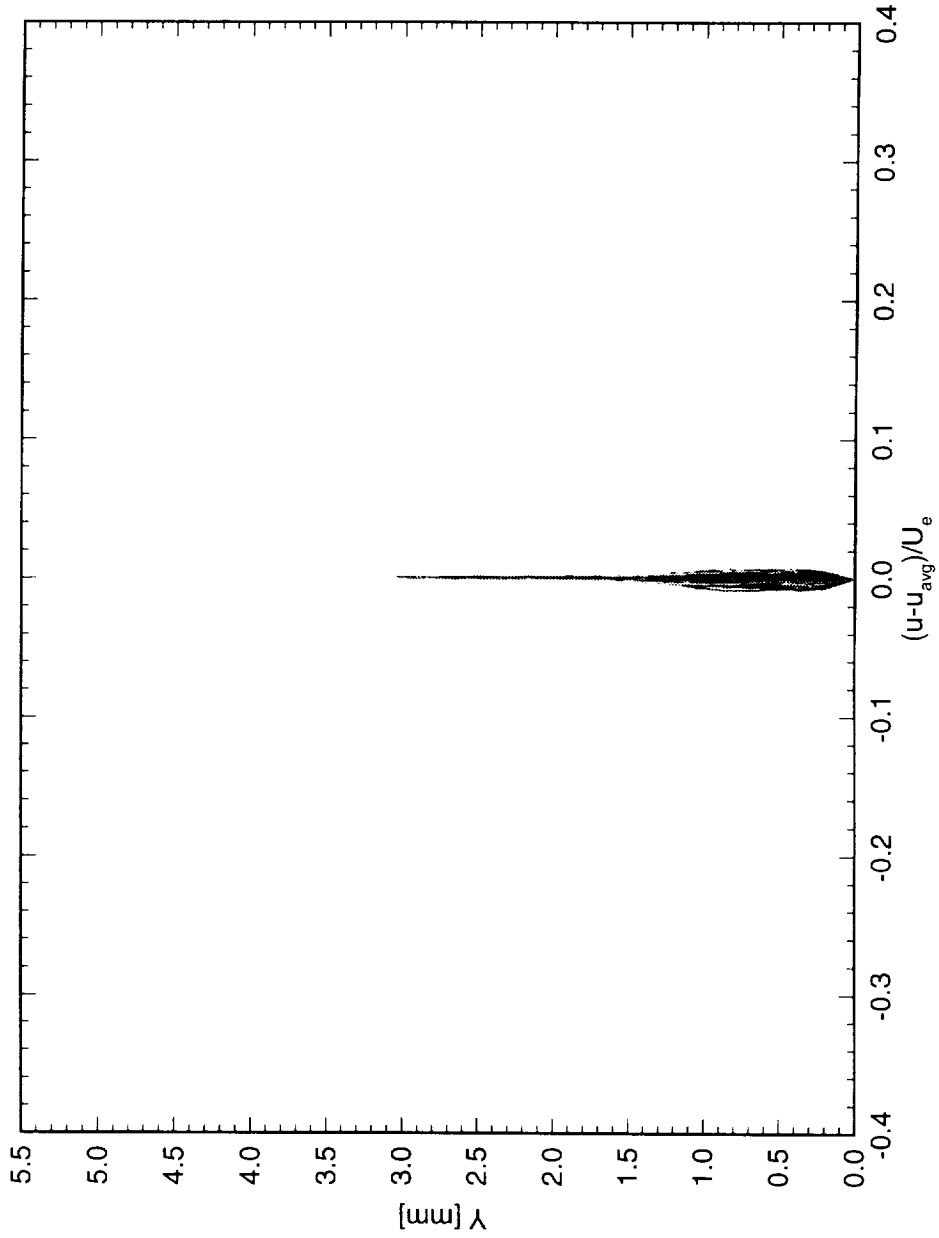

Figure 6.26: Spanwise array of 100 disturbance profiles covering a span of 99 mm at $x/c = 0.10$. $Re_c = 1.6 \times 10^6$, [6|12] roughness.

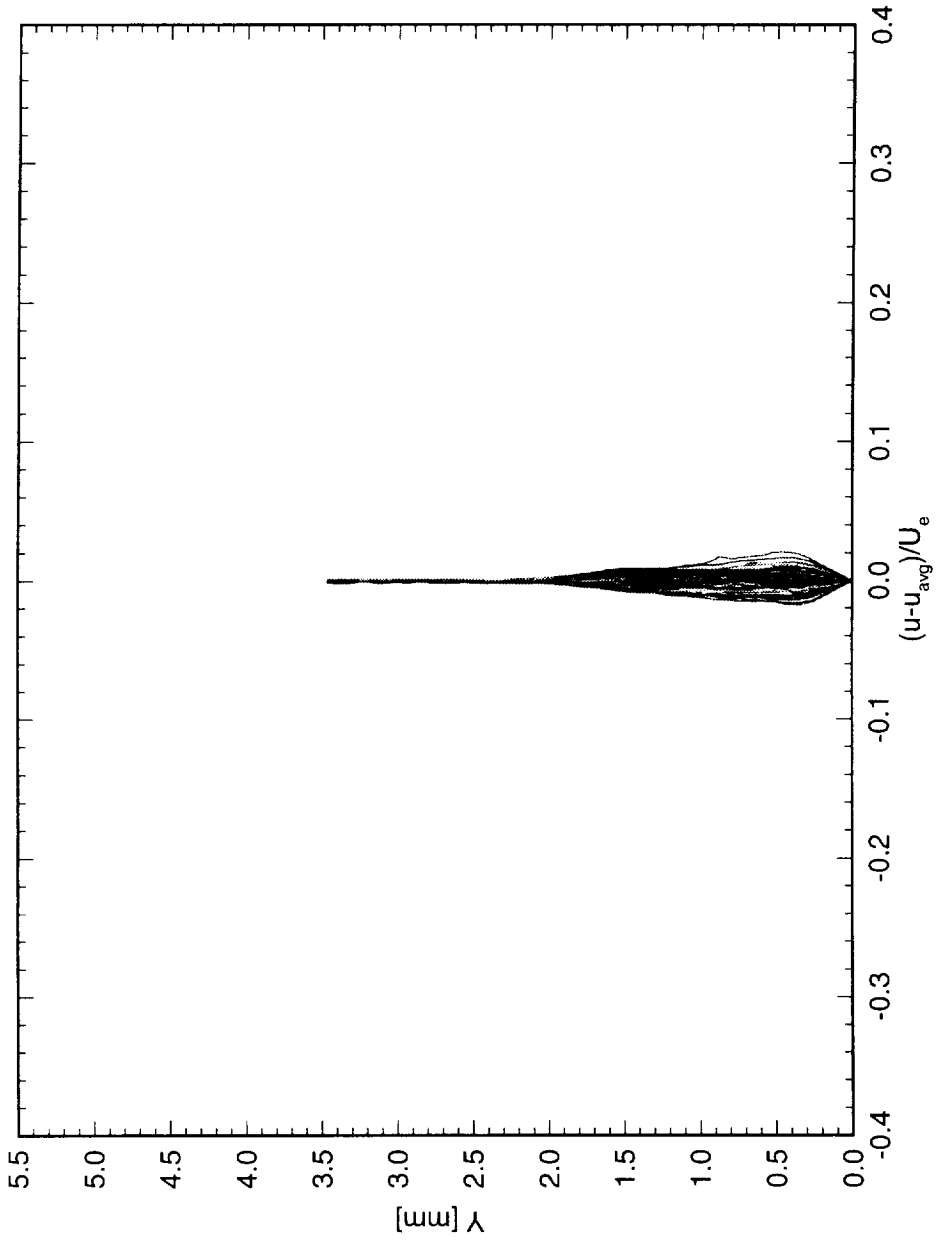

Figure 6.27: Spanwise array of 100 disturbance profiles covering a span of 99 mm at $x/c = 0.15$. $Re_c = 1.6 \times 10^6$, [6|12] roughness.

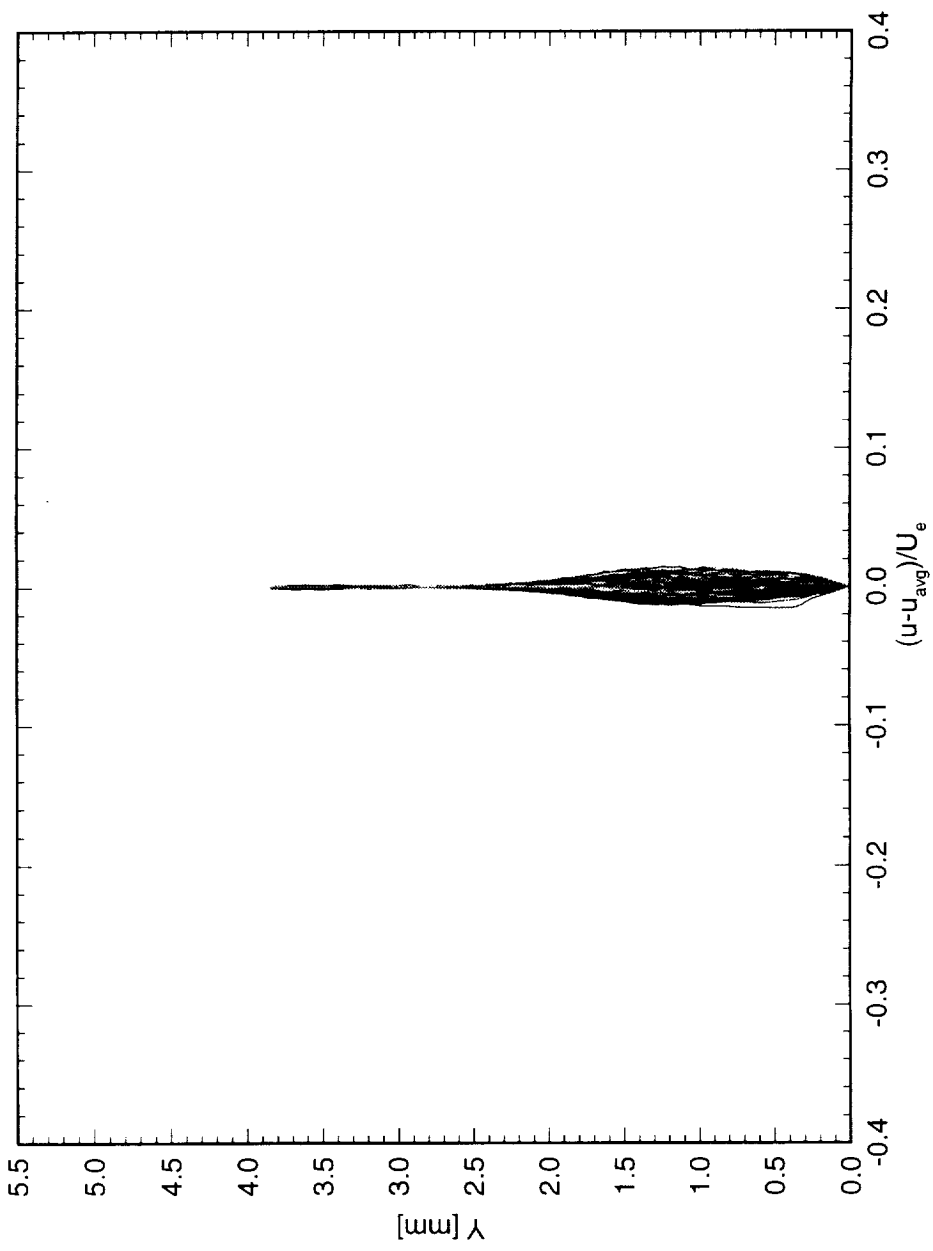

Figure 6.28: Spanwise array of 100 disturbance profiles covering a span of 99 mm at $x/c = 0.20$. $Re_c = 1.6 \times 10^6$, [6|12] roughness.

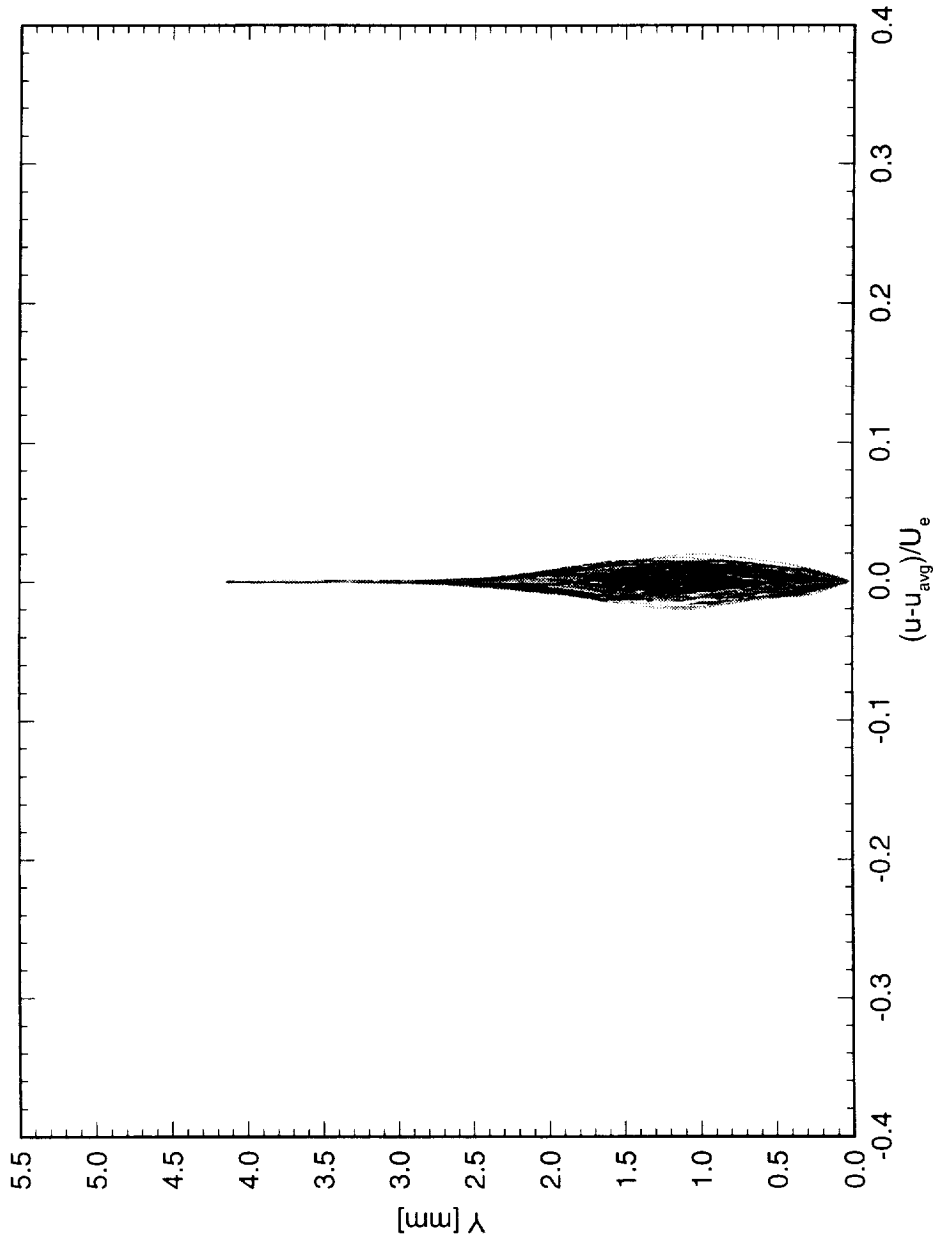

Figure 6.29: Spanwise array of 100 disturbance profiles covering a span of 99 mm at $x/c = 0.25$. $Re_c = 1.6 \times 10^6$, [6|12] roughness.

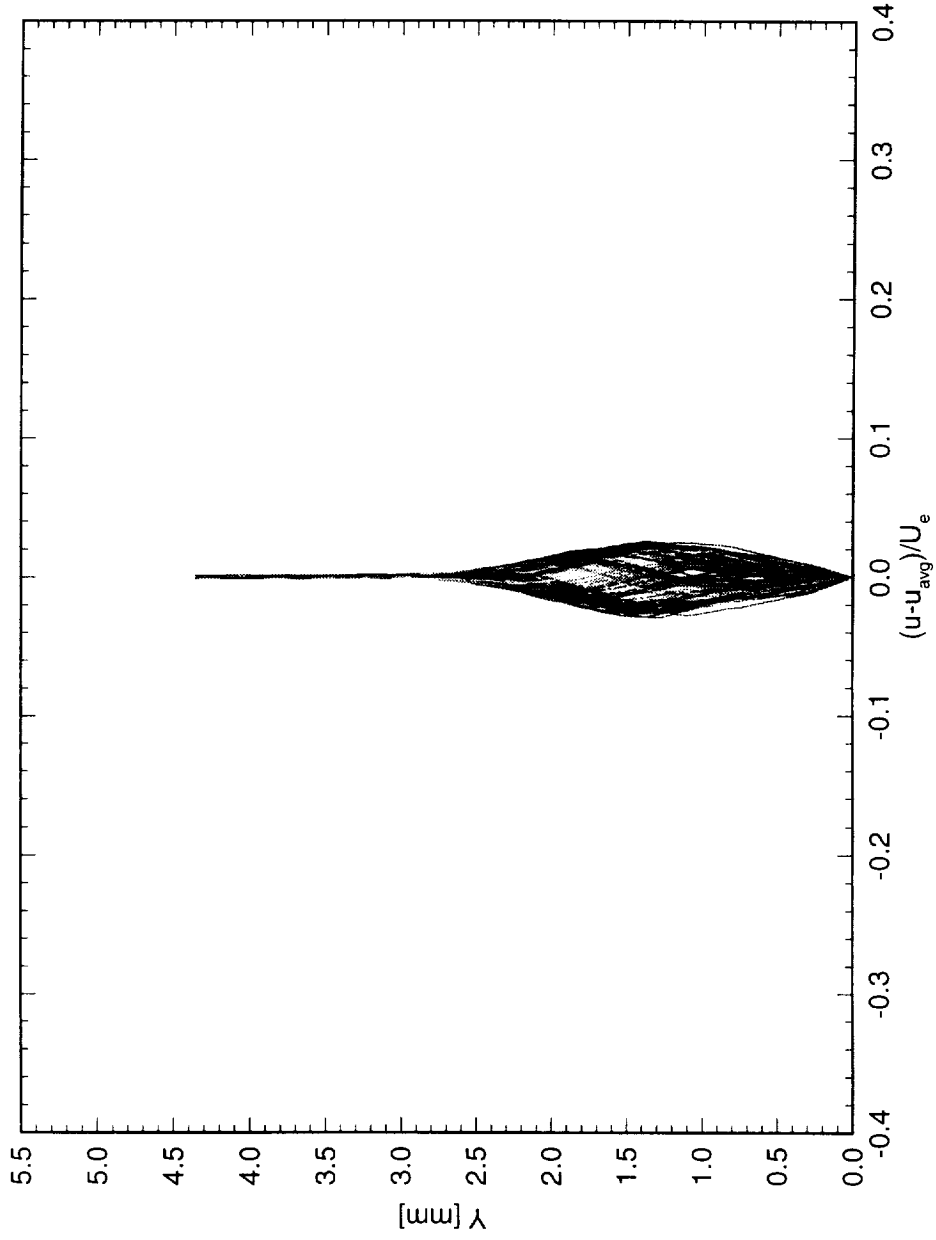

Figure 6.30: Spanwise array of 100 disturbance profiles covering a span of 99 mm at $x/c = 0.30$. $Re_c = 1.6 \times 10^6$, [6|12] roughness.

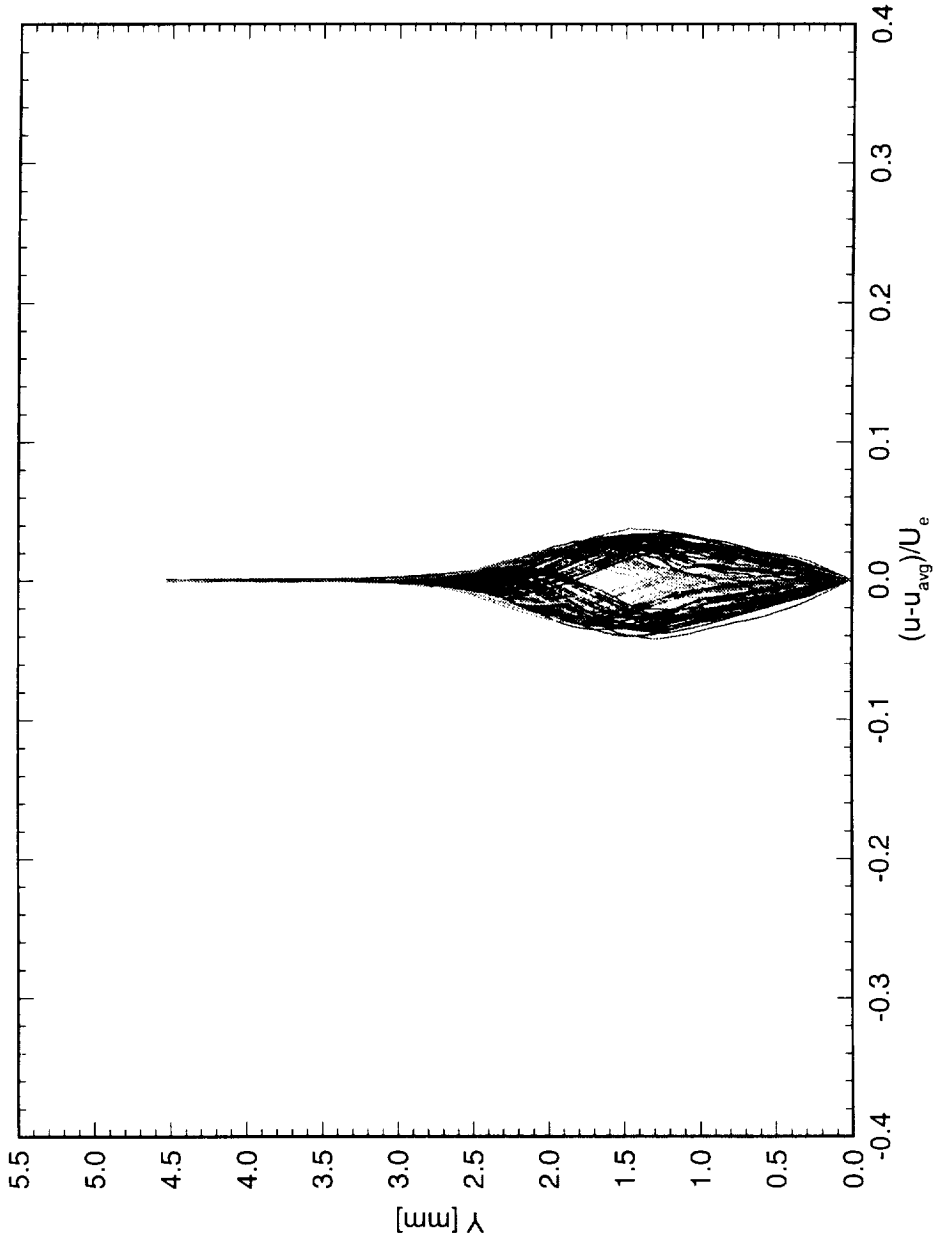

Figure 6.31: Spanwise array of 100 disturbance profiles covering a span of 99 mm at $x/c = 0.35$. $Re_c = 1.6 \times 10^6$, [6|12] roughness.

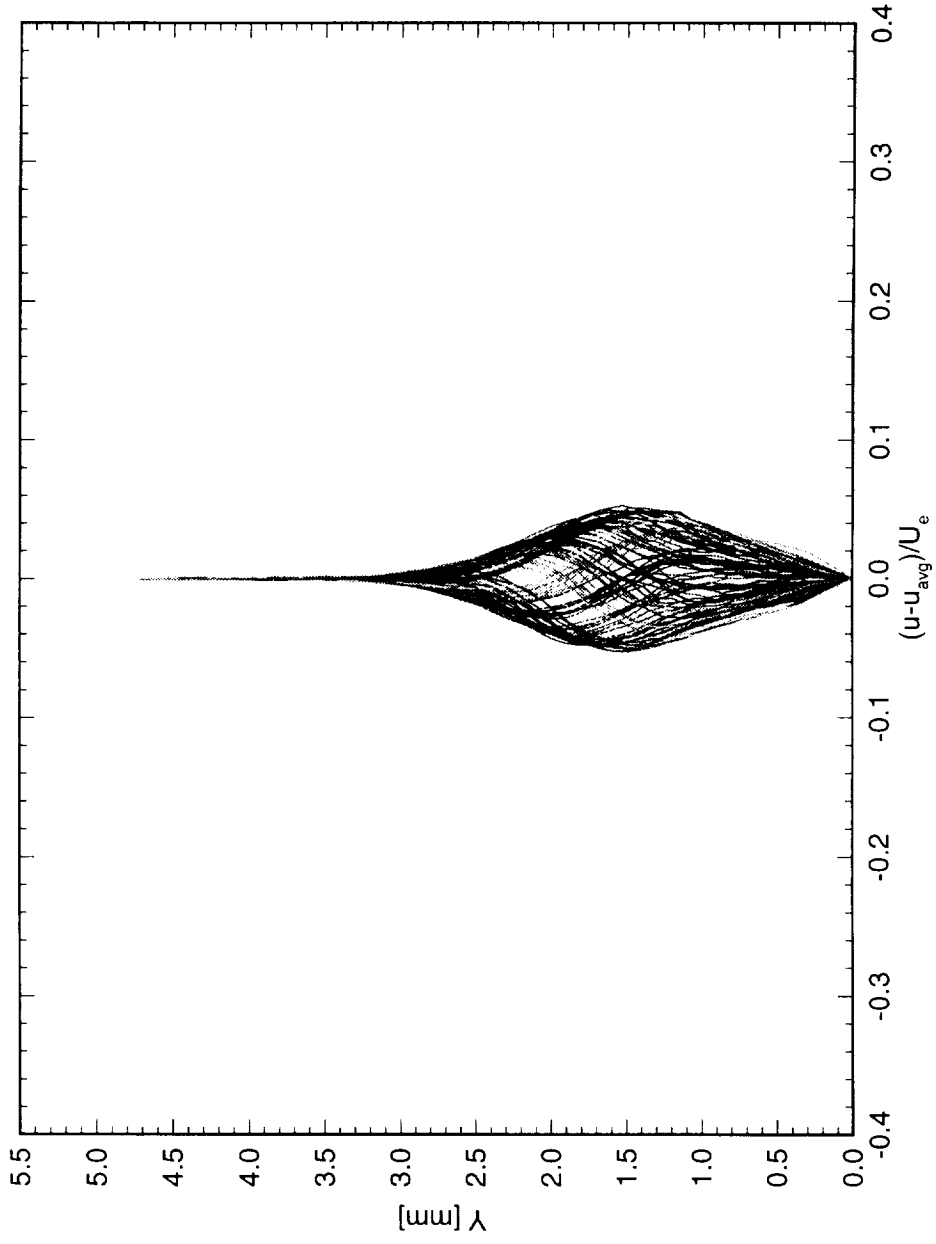

Figure 6.32: Spanwise array of 100 disturbance profiles covering a span of 99 mm at $x/c = 0.40$. $Re_c = 1.6 \times 10^6$, [6|12] roughness.

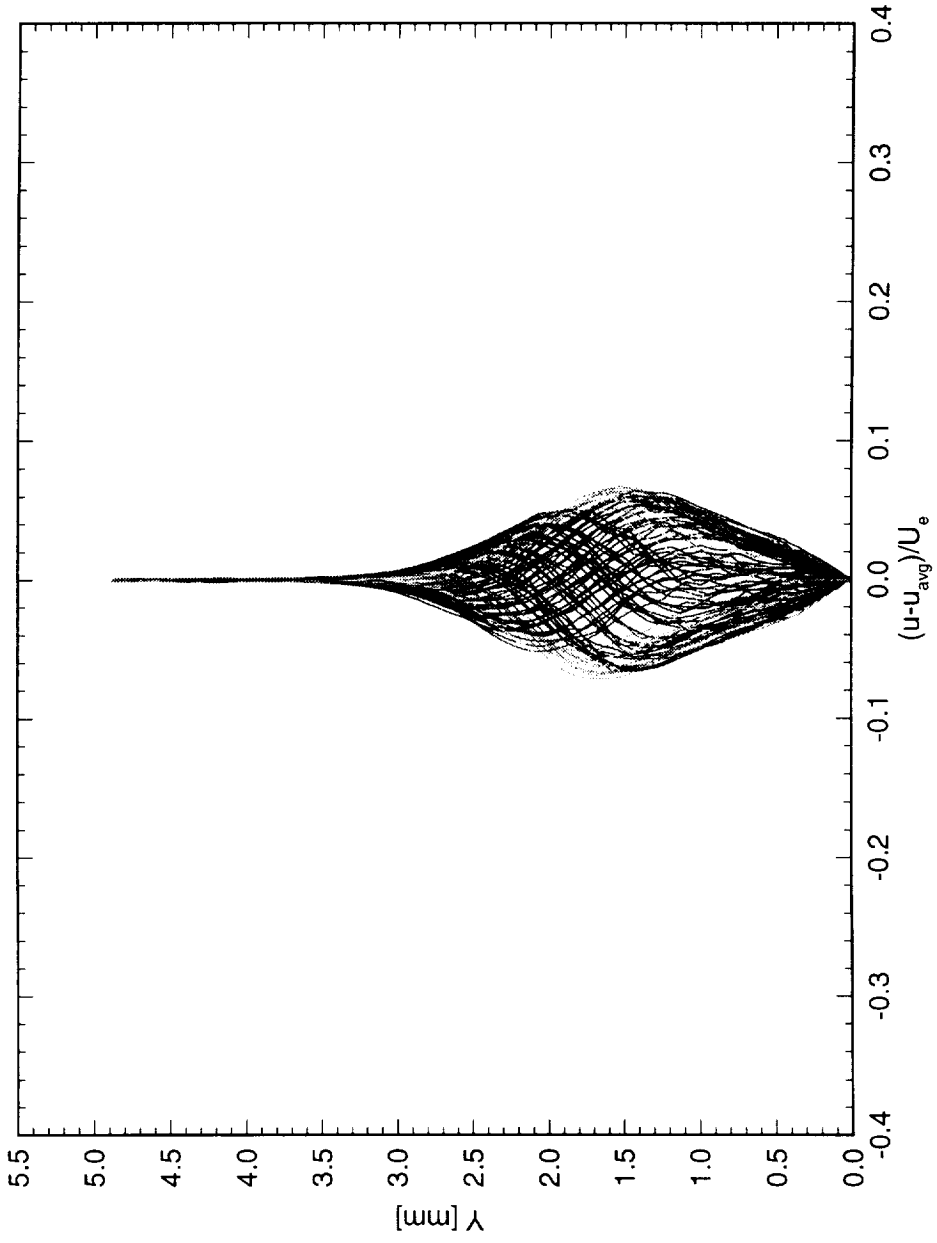

Figure 6.33: Spanwise array of 100 disturbance profiles covering a span of 99 mm at $x/c = 0.45$. $Re_c = 1.6 \times 10^6$, [6|12] roughness.

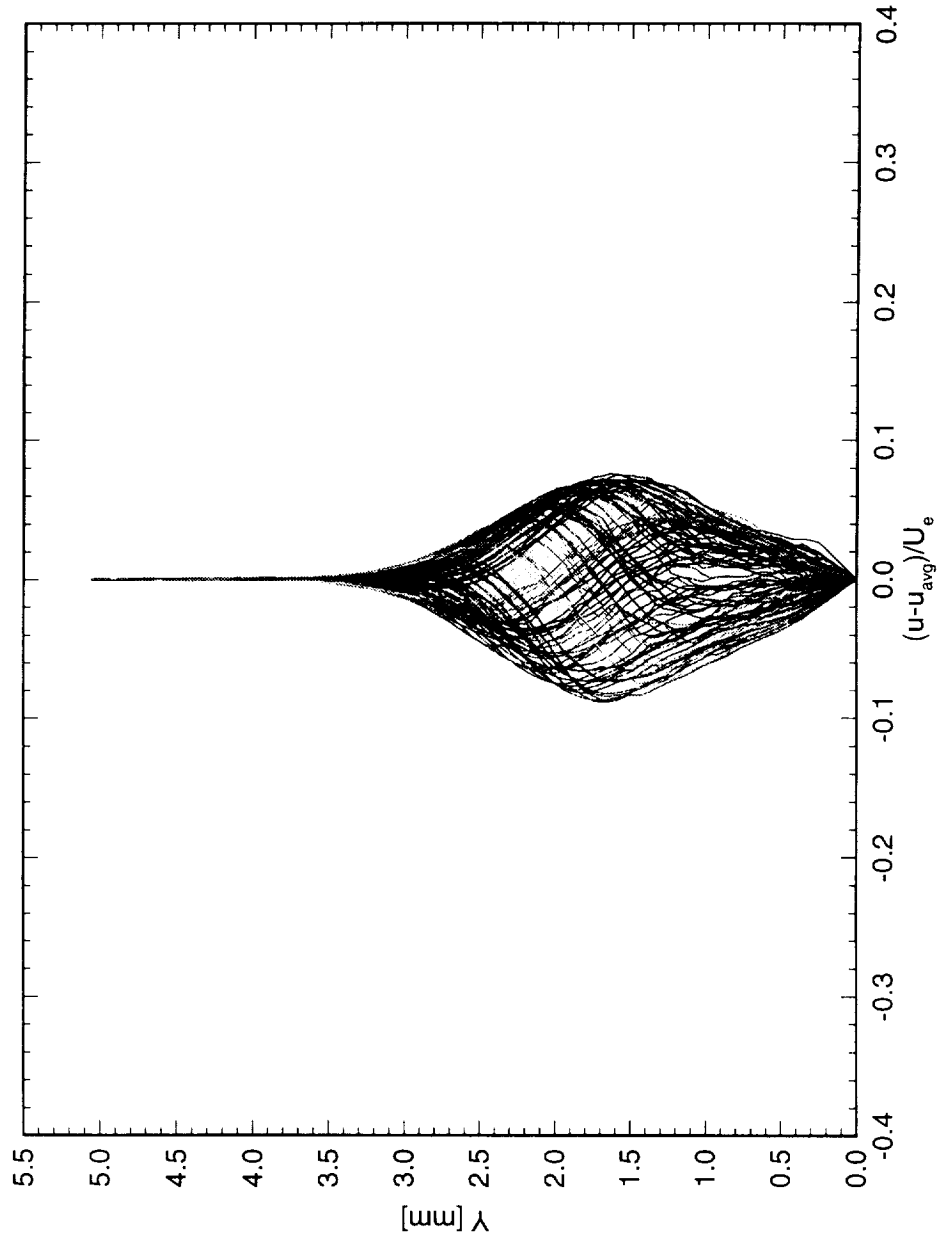

Figure 6.34: Spanwise array of 100 disturbance profiles covering a span of 99 mm at $x/c = 0.50$. $Re_c = 1.6 \times 10^6$, [6|12] roughness.

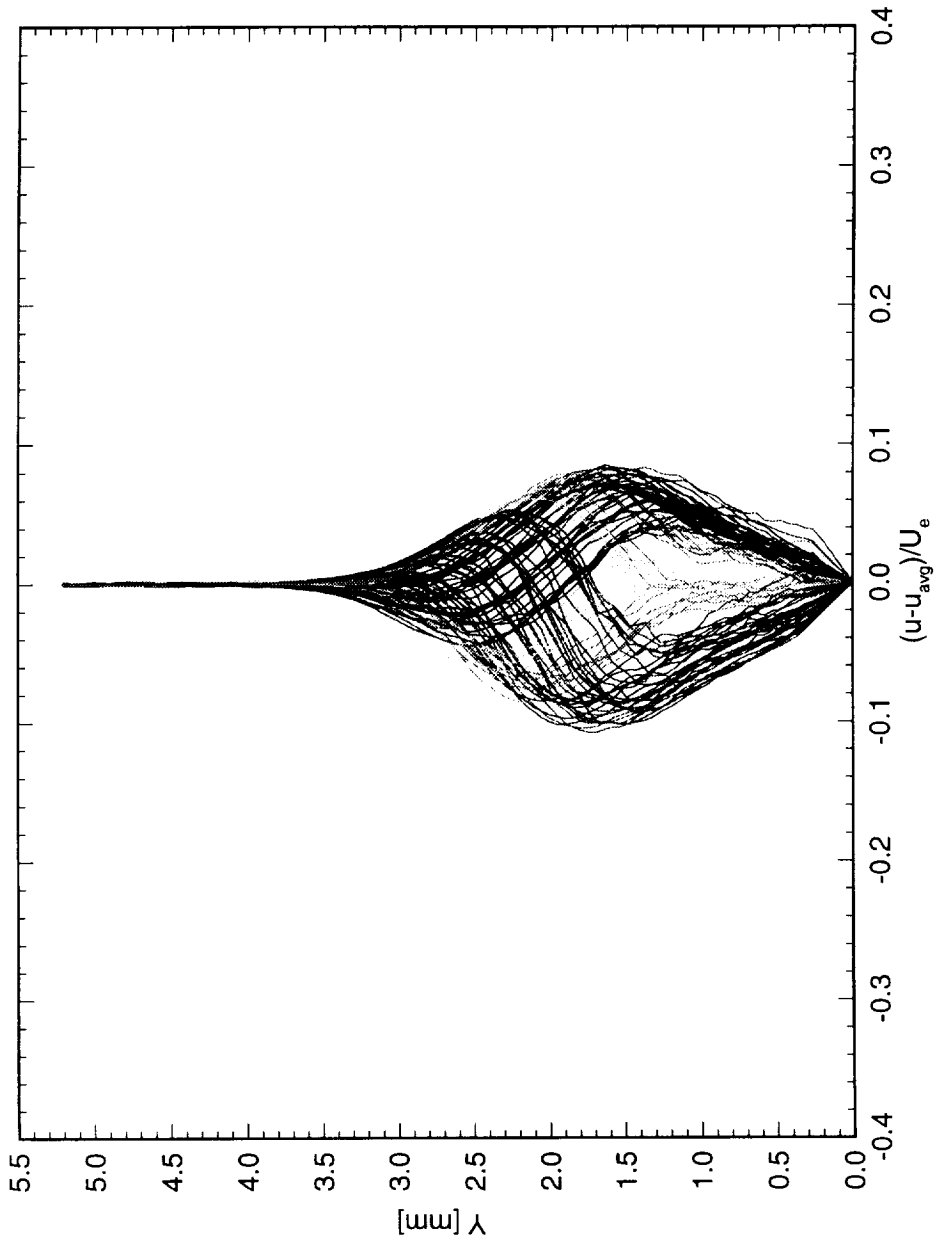

Figure 6.35: Spanwise array of 100 disturbance profiles covering a span of 99 mm at $x/c = 0.55$. $Re_c = 1.6 \times 10^6$, [6|12] roughness.

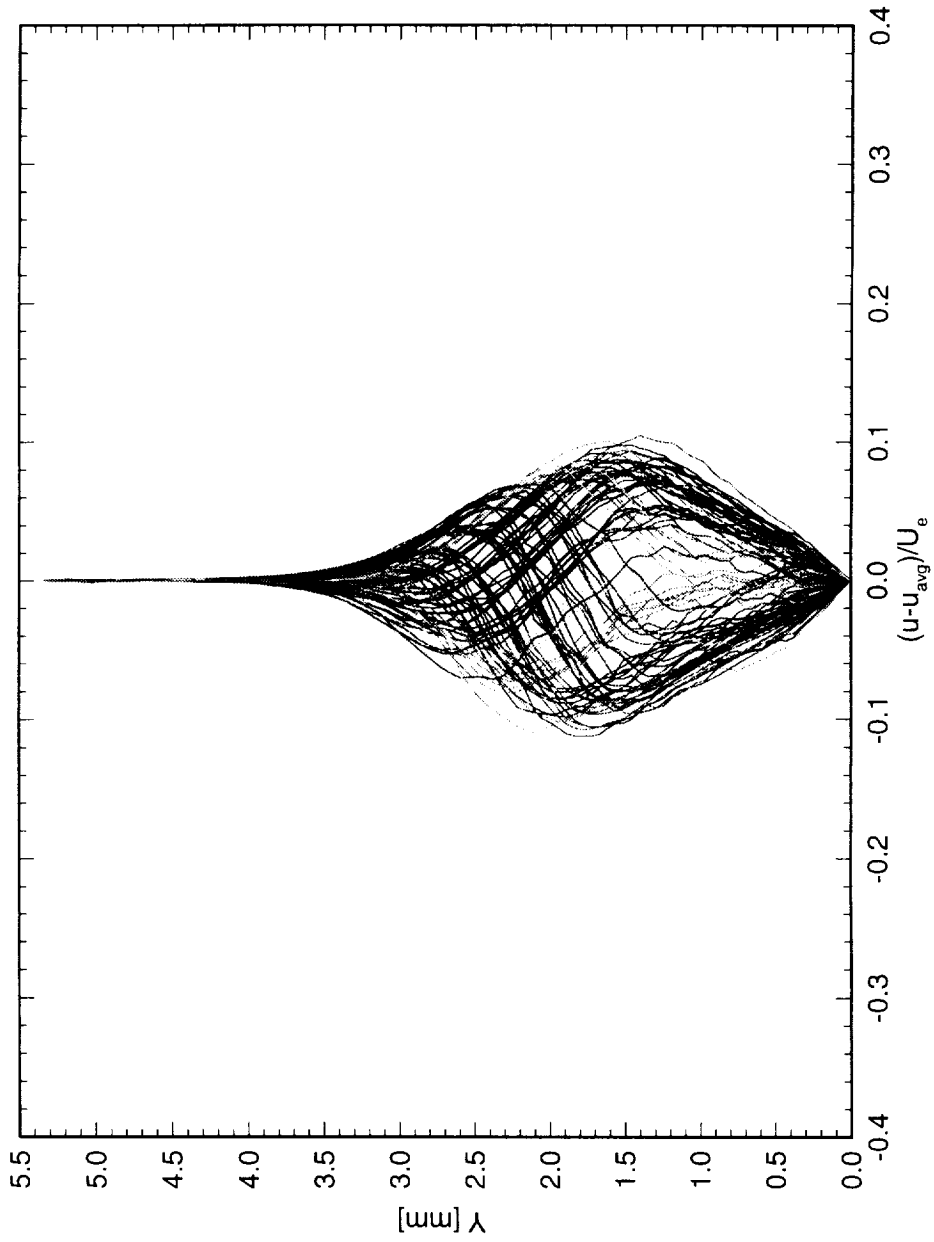

Figure 6.36: Spanwise array of 100 disturbance profiles covering a span of 99 mm at $x/c = 0.60$. $Re_c = 1.6 \times 10^6$, [6|12] roughness.

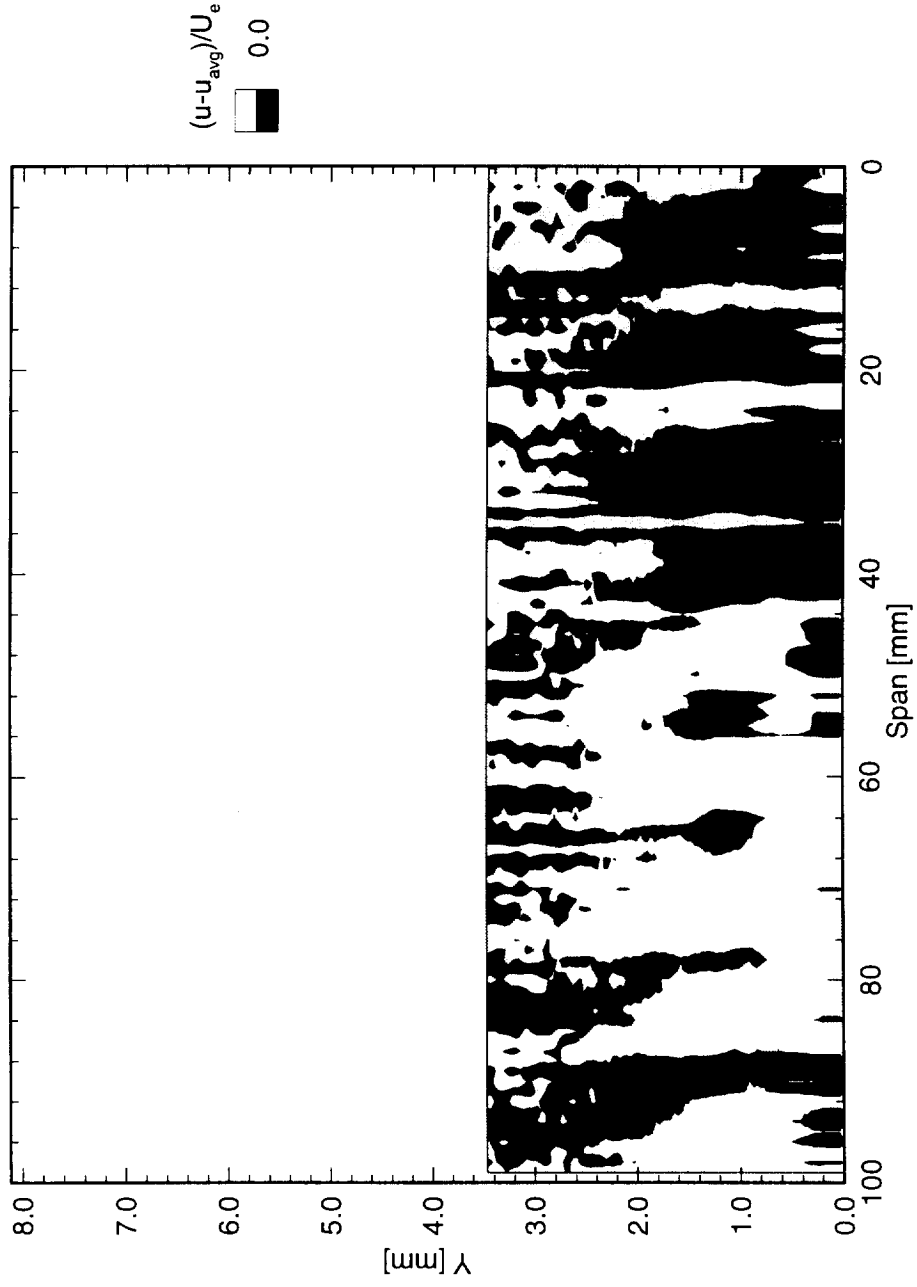

Figure 6.37: Disturbance velocity contours at $x/c = 0.15$. $Re_c = 1.6 \times 10^6$, [6|12] roughness.

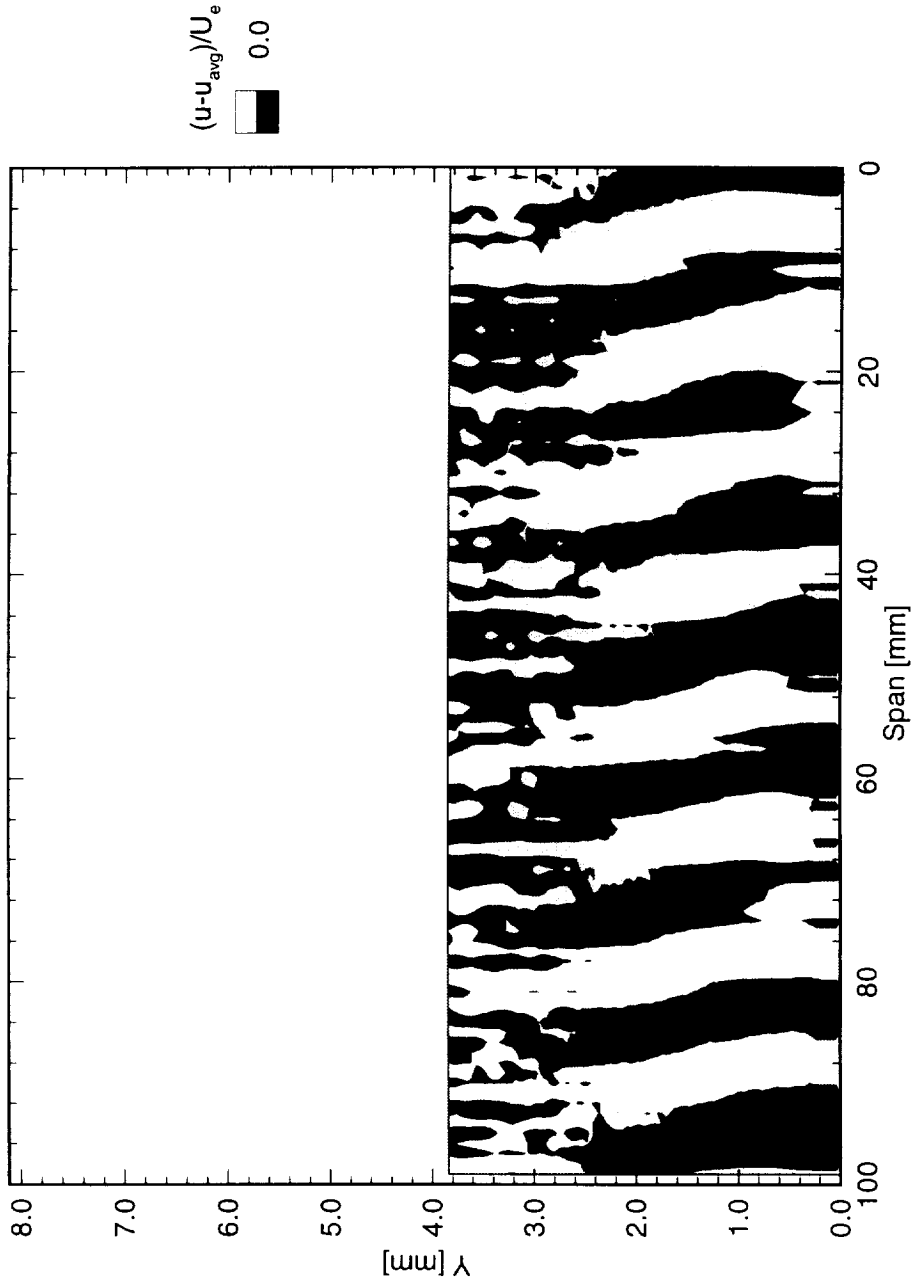

Figure 6.38: Disturbance velocity contours at $x/c = 0.20$. $Re_c = 1.6 \times 10^6$, [6|12] roughness.

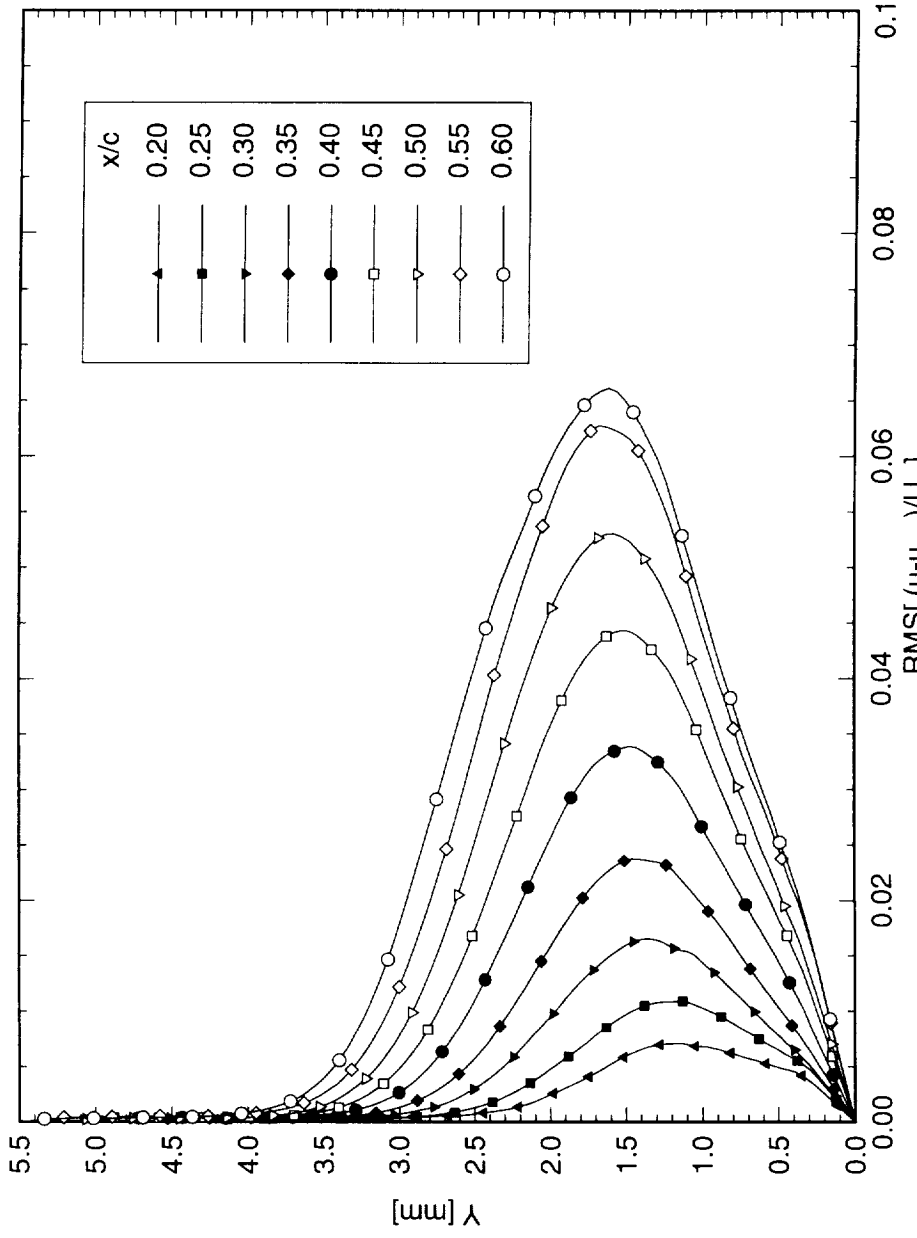

Figure 6.39: Stationary crossflow mode shapes for $Re_c = 1.6 \times 10^6$ and [6|12] roughness. The symbols are simply identifiers and do not represent measurement points.

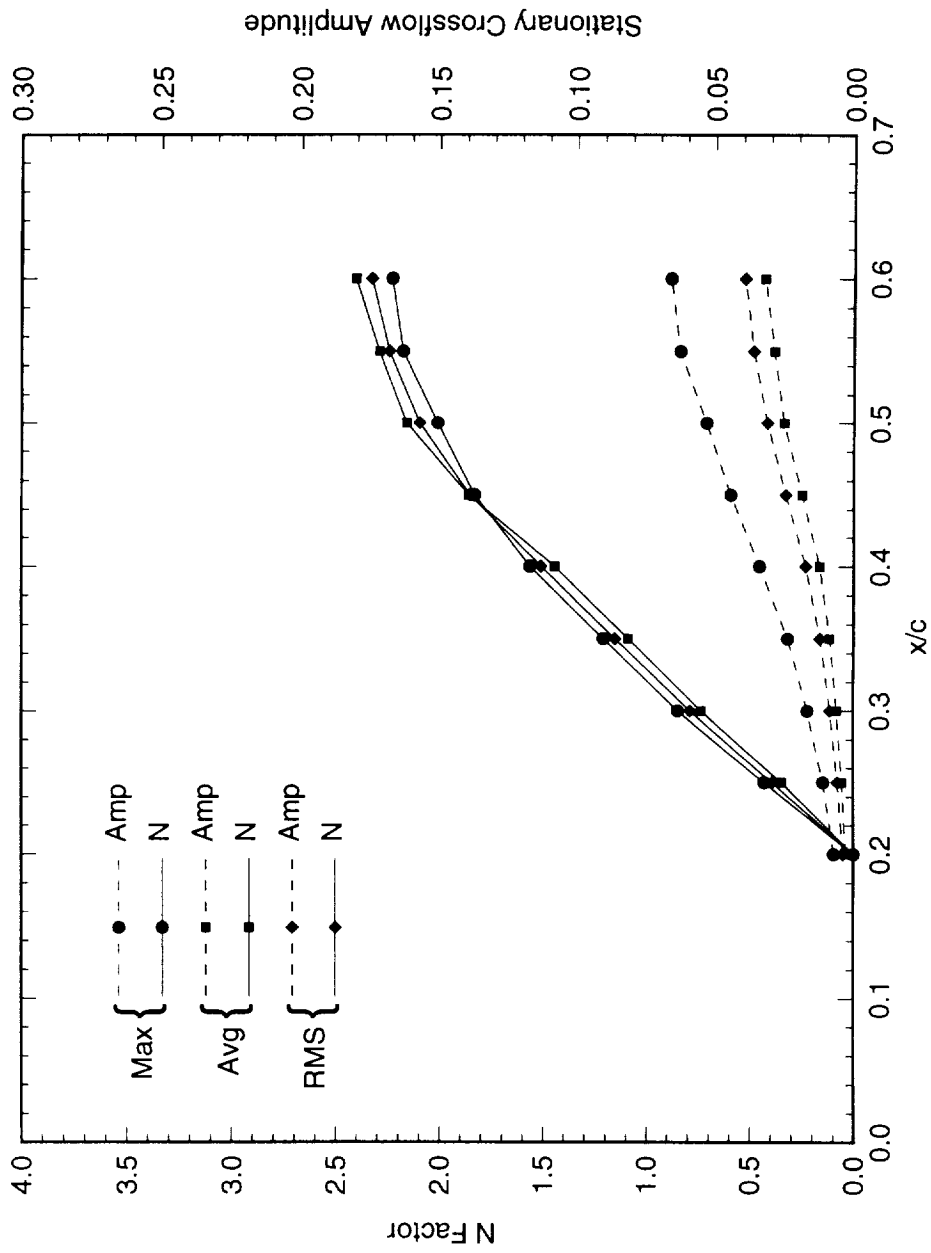

Figure 6.40: Total disturbance amplitude and amplification factor N for $Re_c = 1.6 \times 10^6$ and [6|12] roughness. The reference point for the N-factor calculations is $x/c = 0.20$.

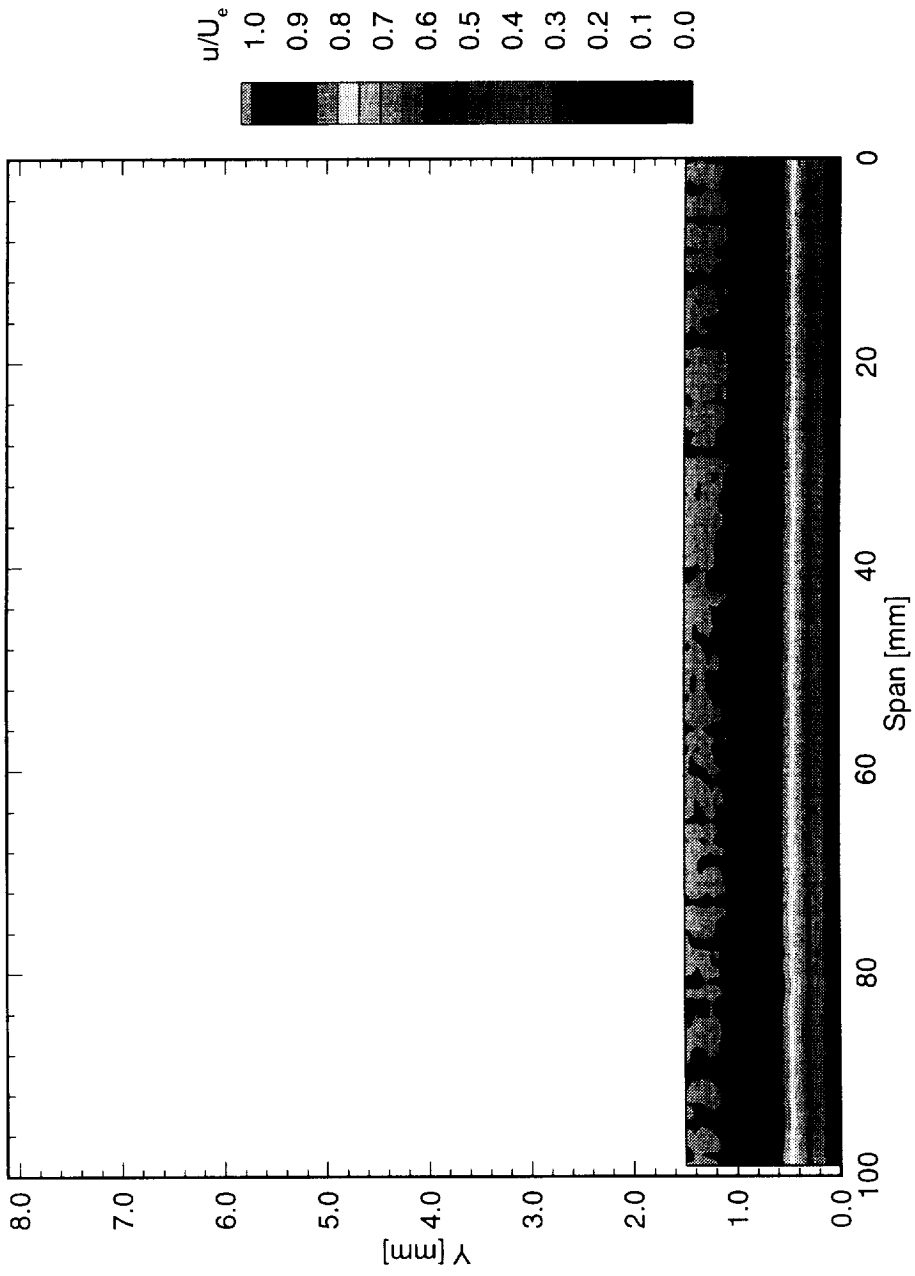

Figure 6.41: Streamwise velocity contours at $x/c = 0.05$. $Re_c = 3.2 \times 10^6$, [6|12] roughness.

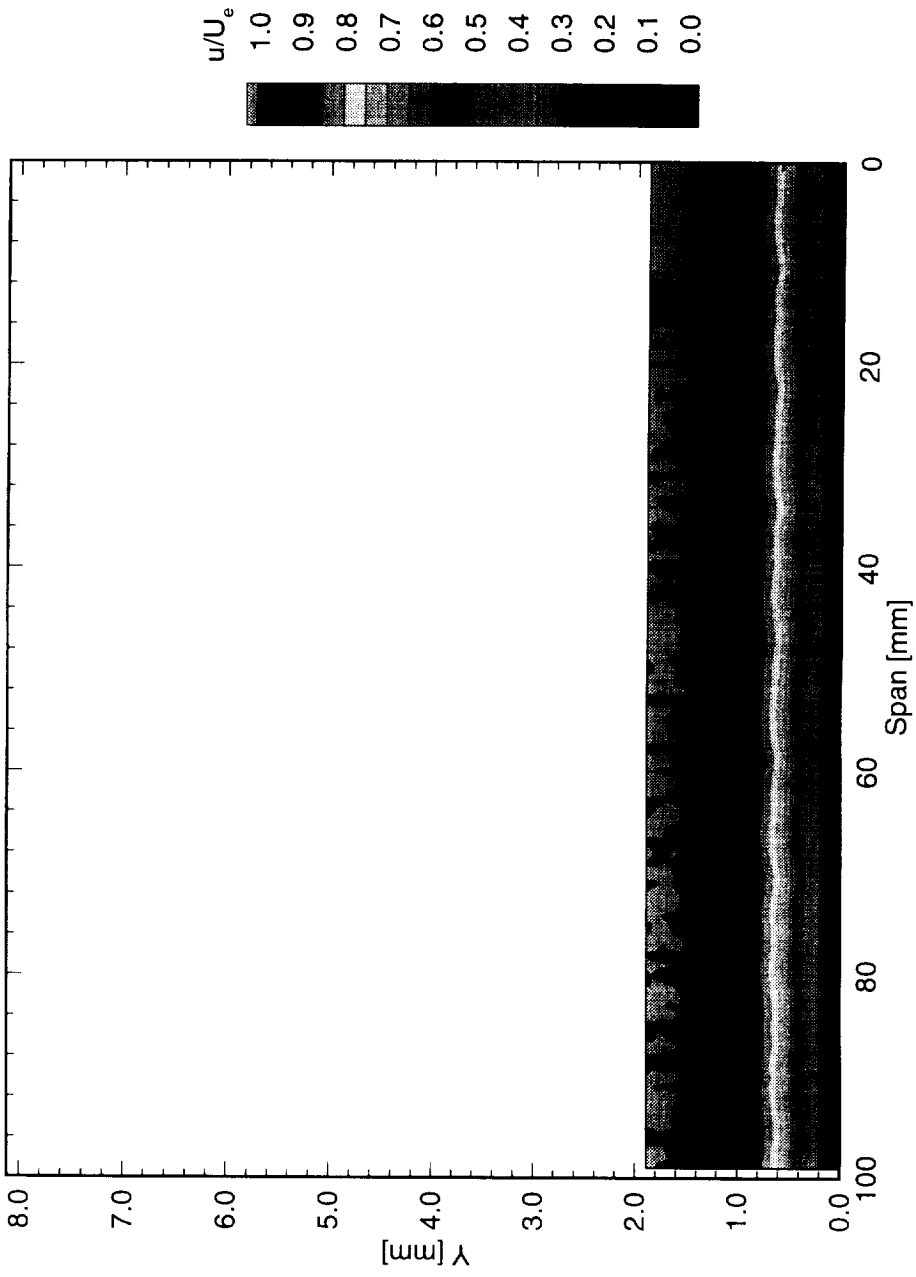

Figure 6.42: Streamwise velocity contours at $x/c = 0.10$. $Re_c = 3.2 \times 10^6$, [6|12] roughness.

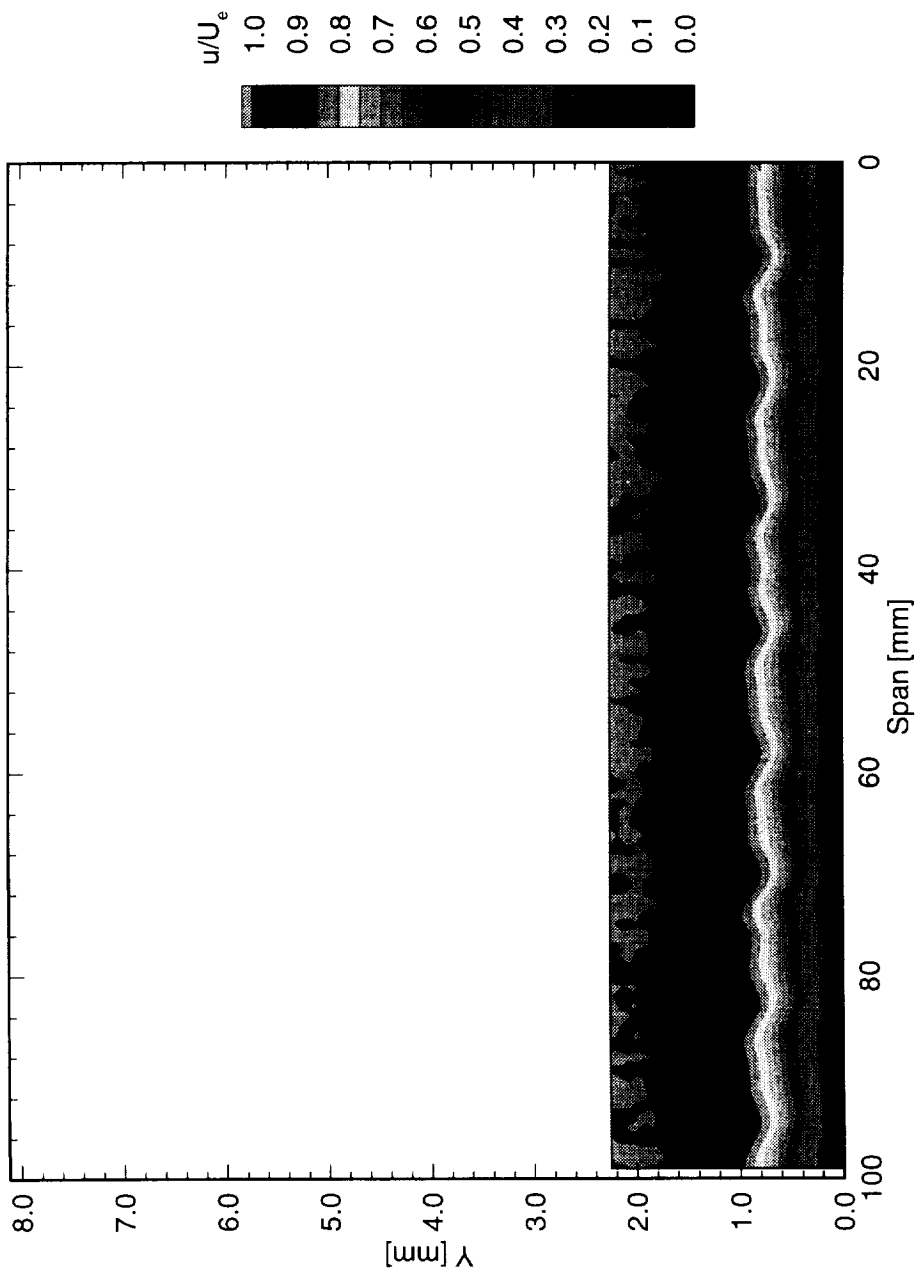

Figure 6.43: Streamwise velocity contours at $x/c = 0.15$. $Re_c = 3.2 \times 10^6$, [6|12] roughness.

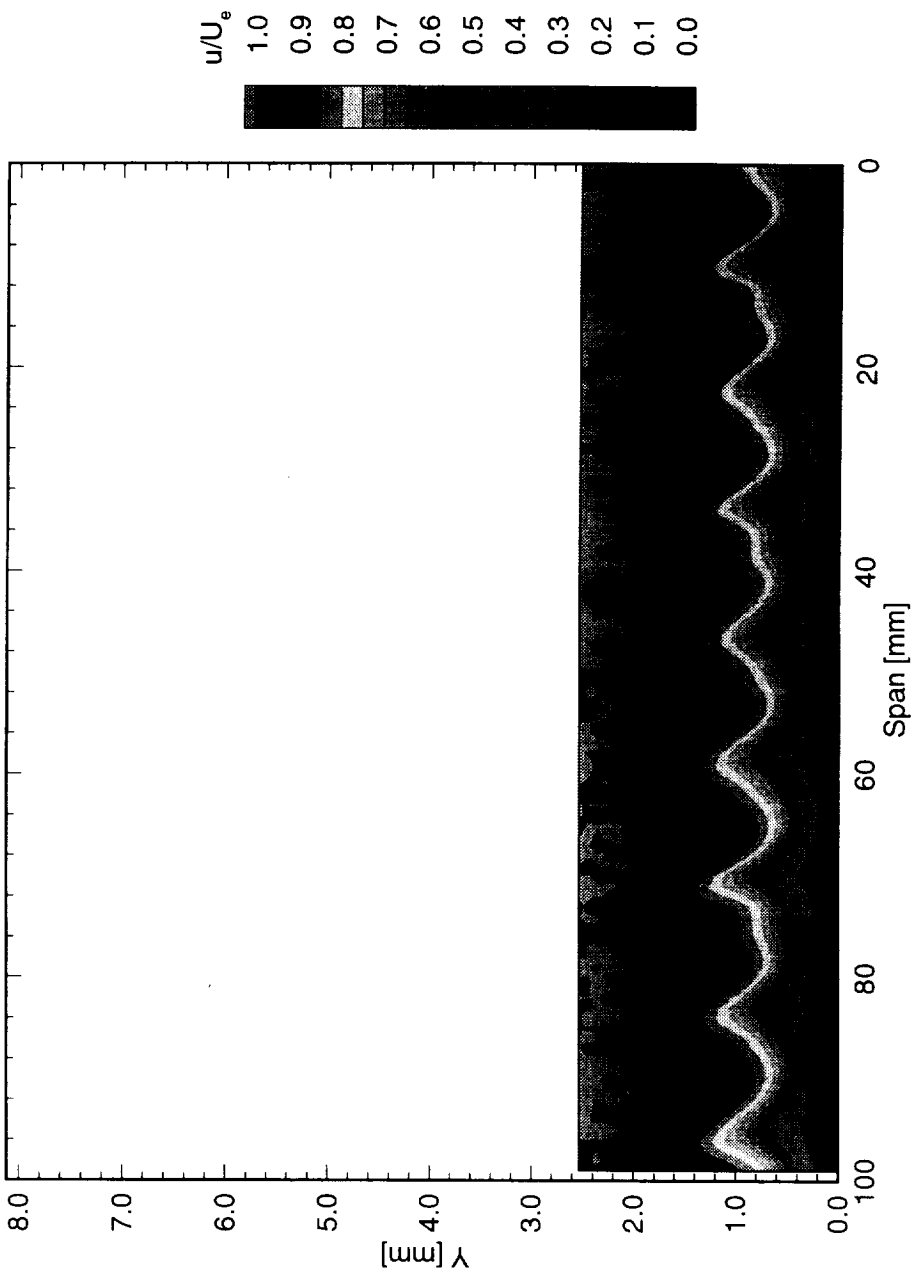

Figure 6.44: Streamwise velocity contours at $x/c = 0.20$. $Re_c = 3.2 \times 10^6$, [6|12] roughness.

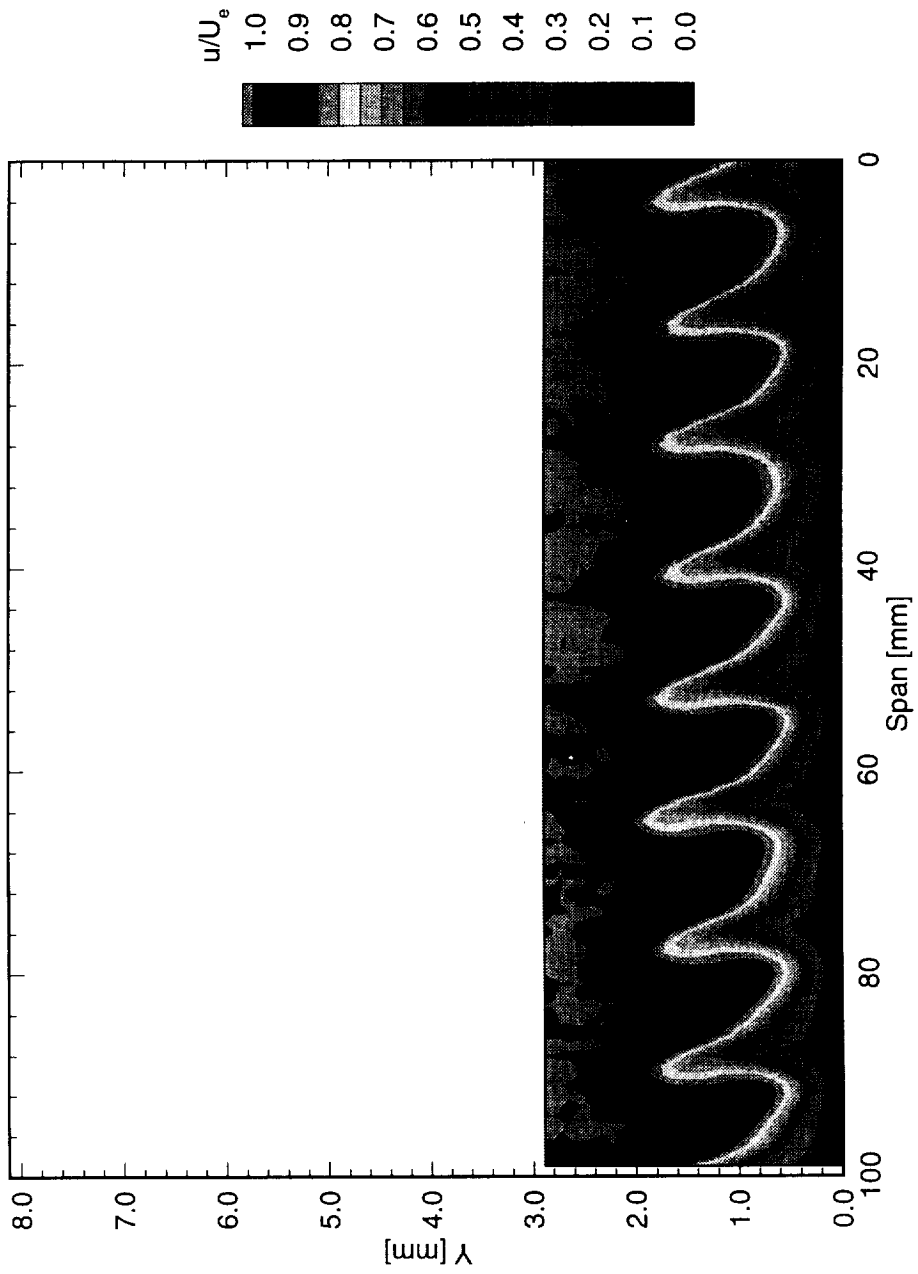

Figure 6.45: Streamwise velocity contours at $x/c = 0.25$. $Re_c = 3.2 \times 10^6$, [6|12] roughness.

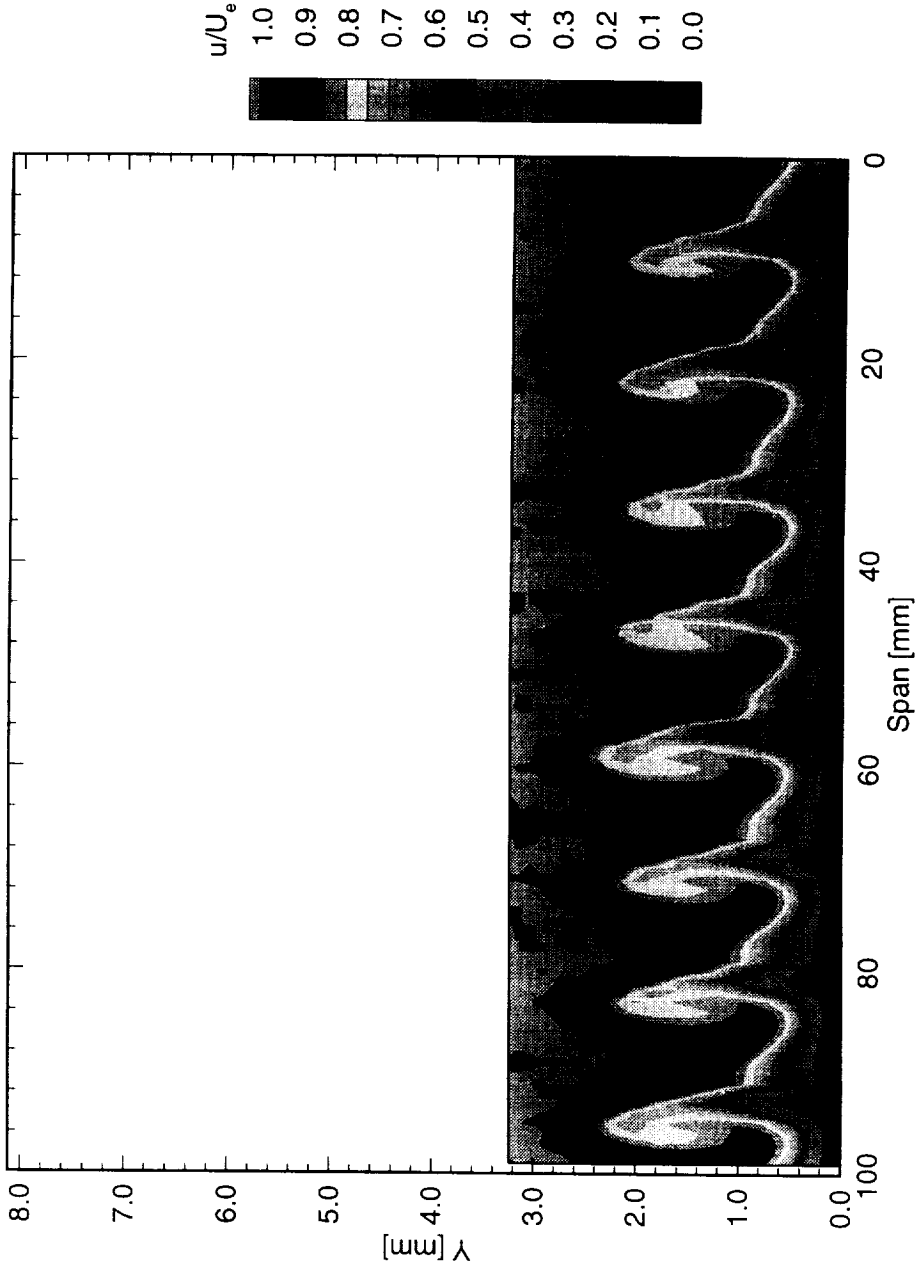

Figure 6.46: Streamwise velocity contours at $x/c = 0.29$. $Re_c = 3.2 \times 10^6$, [6|12] roughness.

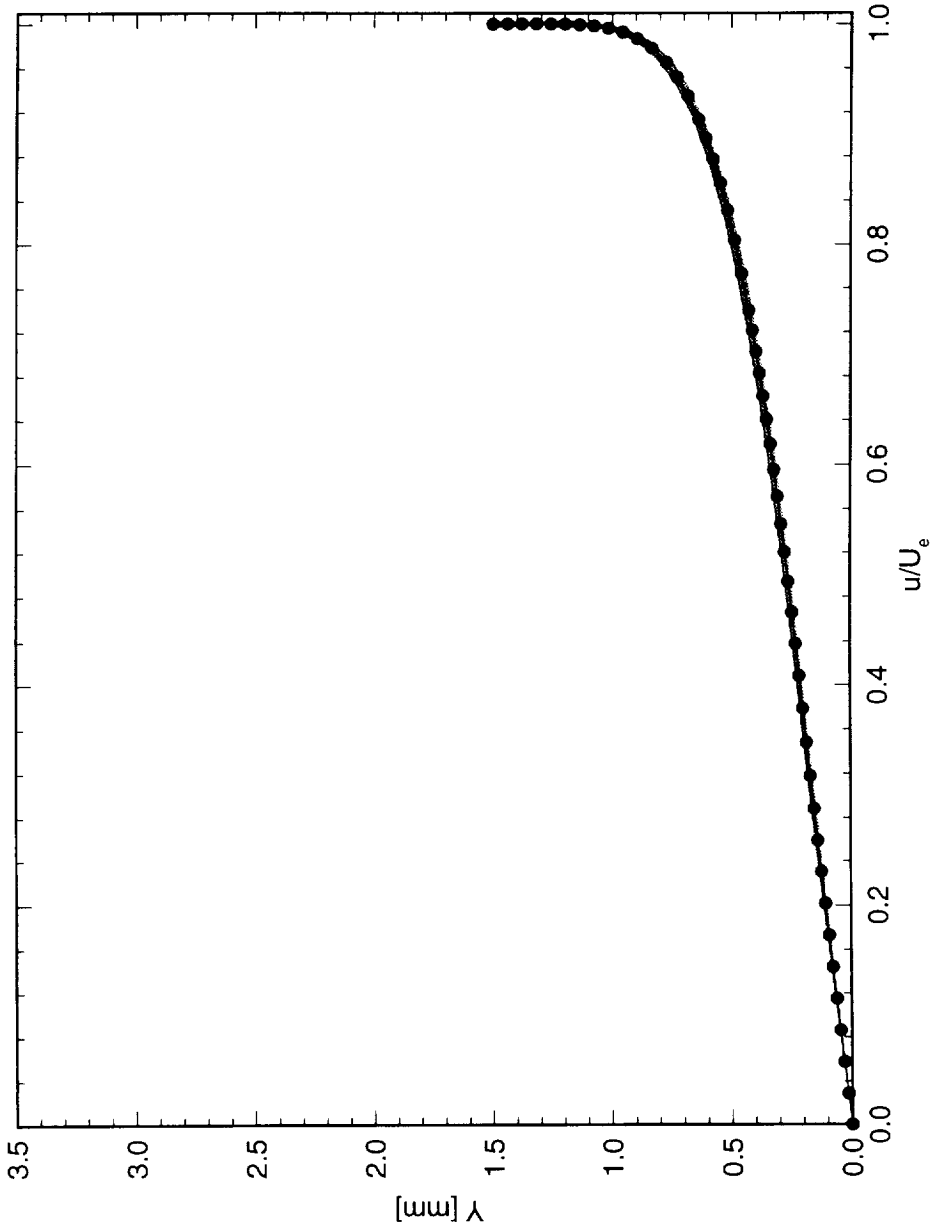

Figure 6.47: Spanwise array of 100 mean-flow boundary-layer profiles covering a span of 99 mm at $x/c = 0.05$. $Re_c = 3.2 \times 10^6$, [6|12] roughness. The dots indicate the mean of the profiles.

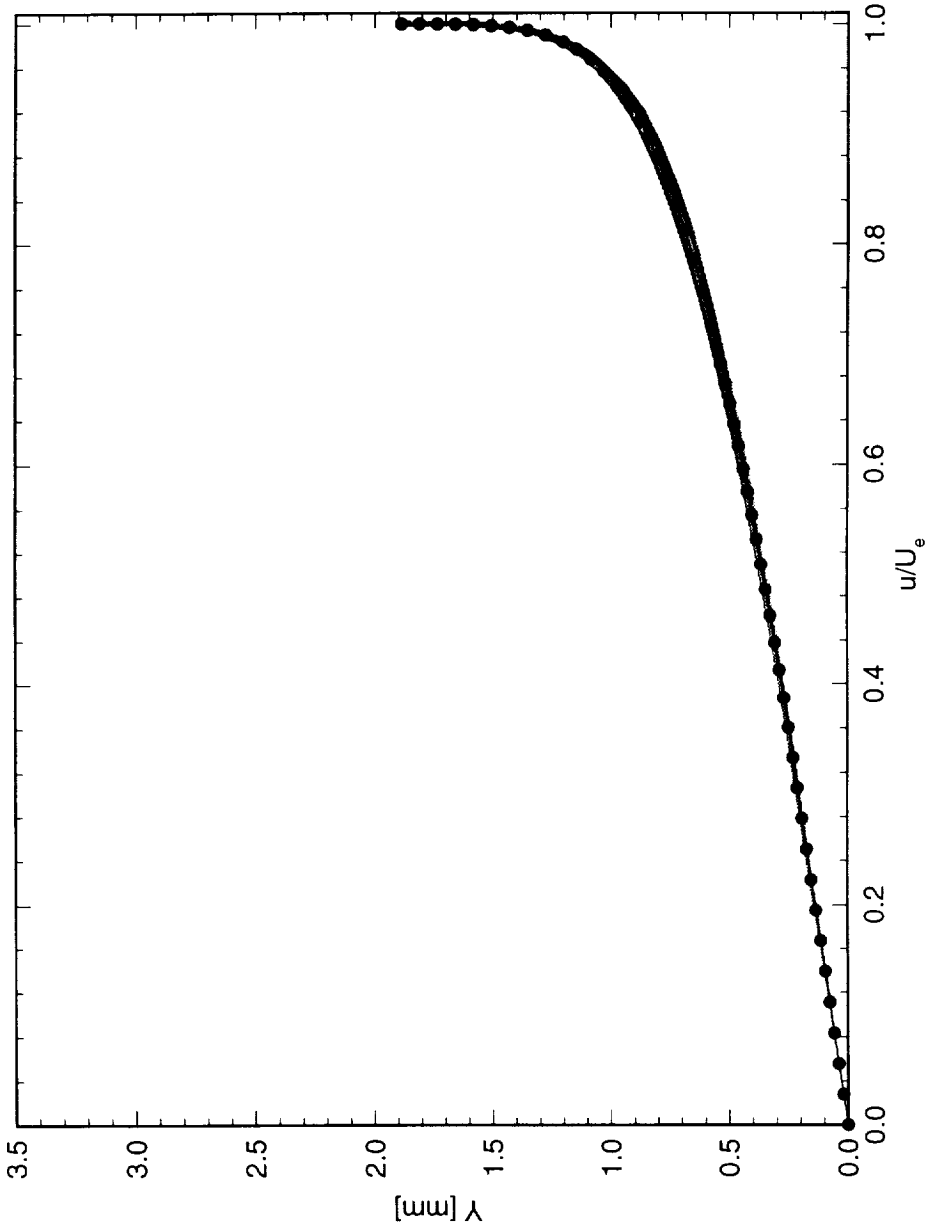

Figure 6.48: Spanwise array of 100 mean-flow boundary-layer profiles covering a span of 99 mm at $x/c = 0.10$. $Re_c = 3.2 \times 10^6$. [6|12] roughness. The dots indicate the mean of the profiles.

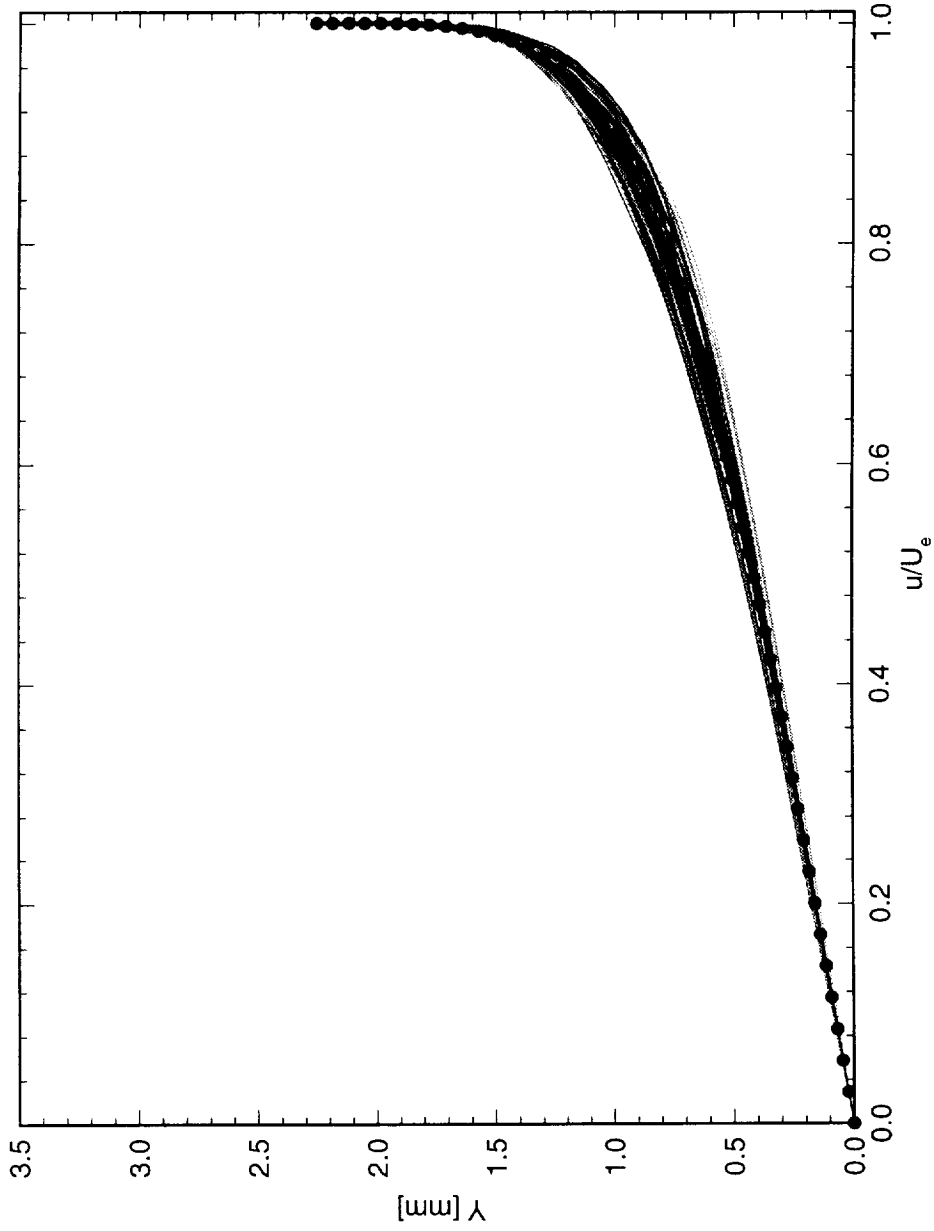

Figure 6.49: Spanwise array of 100 mean-flow boundary-layer profiles covering a span of 99 mm at $x/c = 0.15$. $Re_c = 3.2 \times 10^6$, [6|12] roughness. The dots indicate the mean of the profiles.

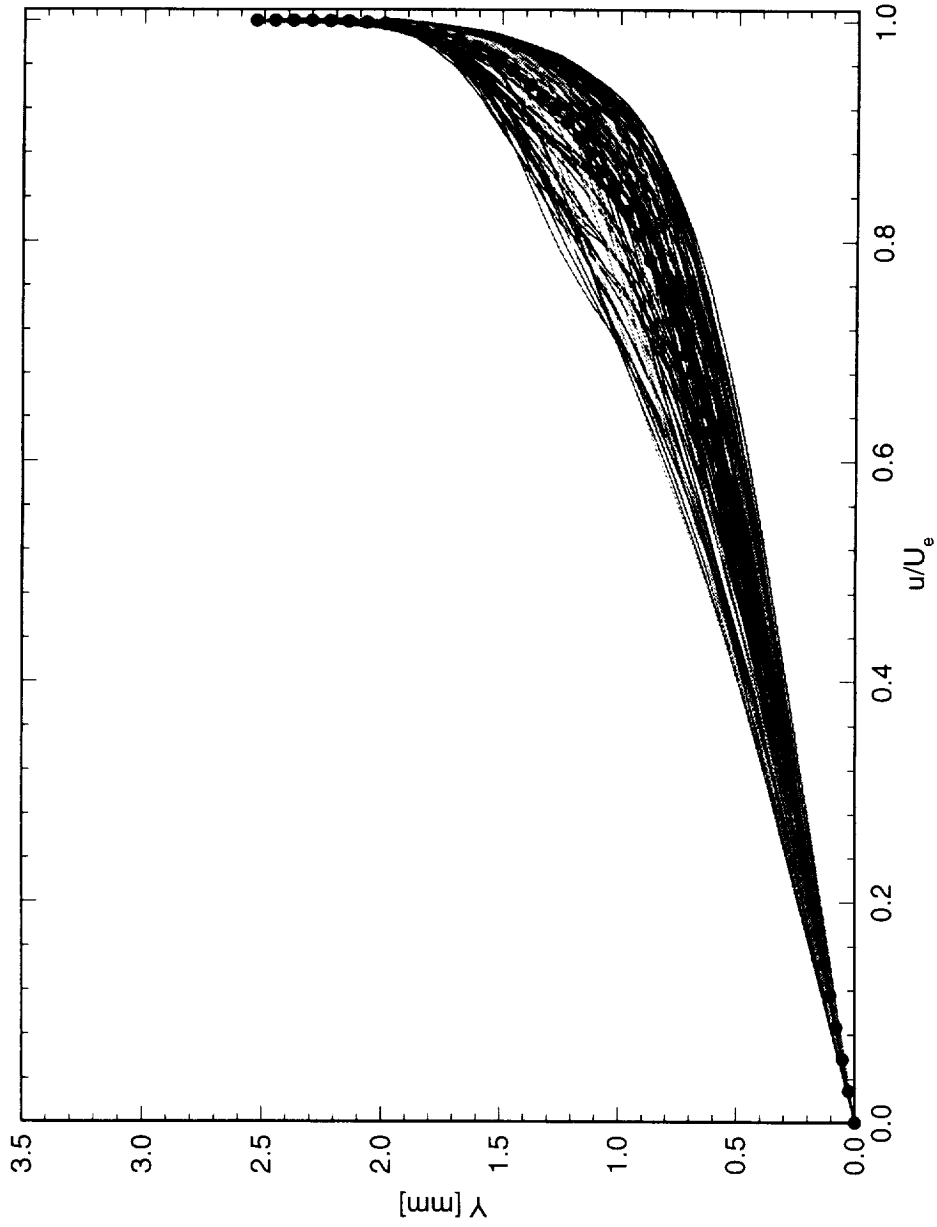

Figure 6.50: Spanwise array of 100 mean-flow boundary-layer profiles covering a span of 99 mm at $x/c = 0.20$. $Re_c = 3.2 \times 10^6$, [6|12] roughness. The dots indicate the mean of the profiles.

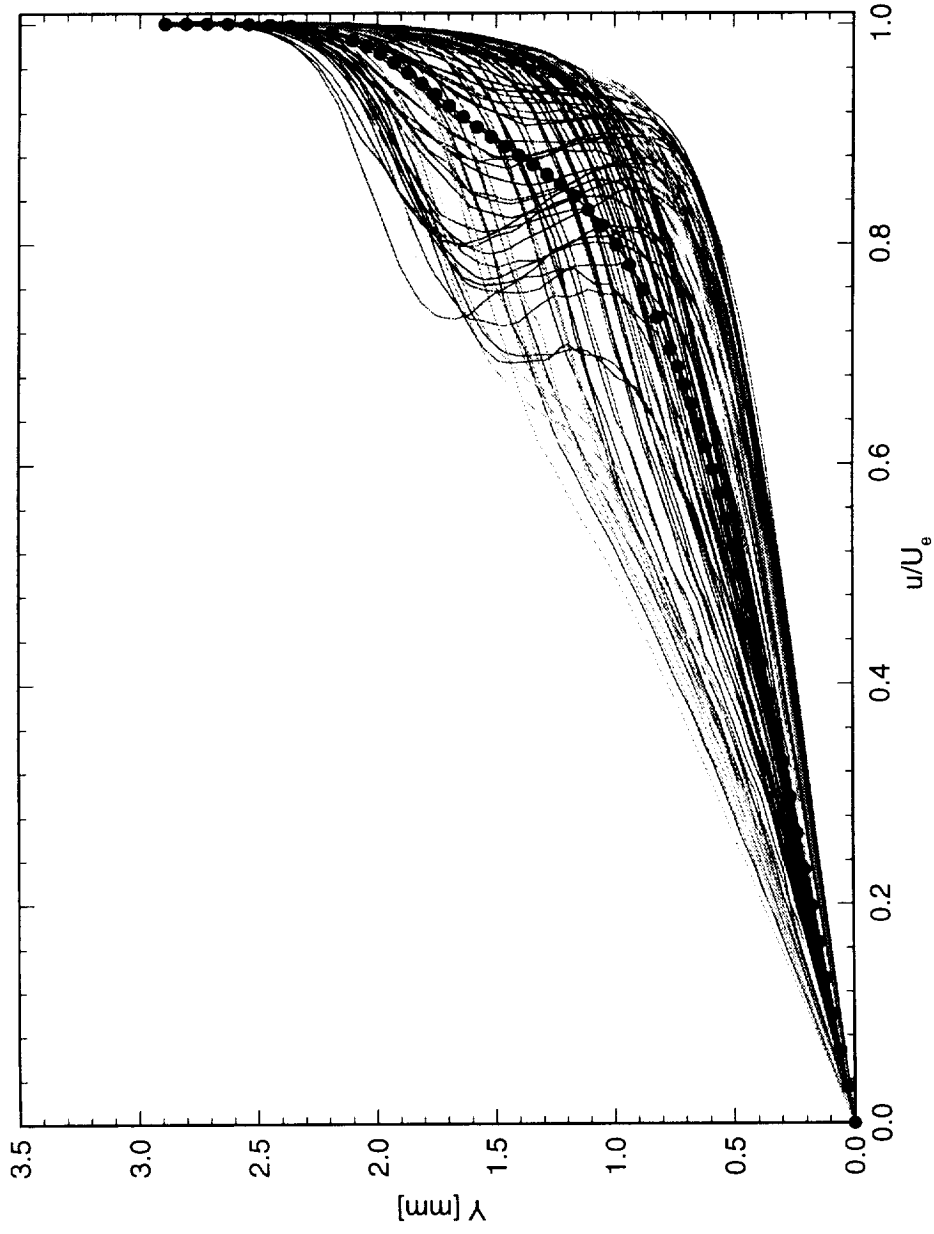

Figure 6.51: Spanwise array of 100 mean-flow boundary-layer profiles covering a span of 99 mm at $x/c = 0.25$. $Re_c = 3.2 \times 10^6$, [6|12] roughness. The dots indicate the mean of the profiles.

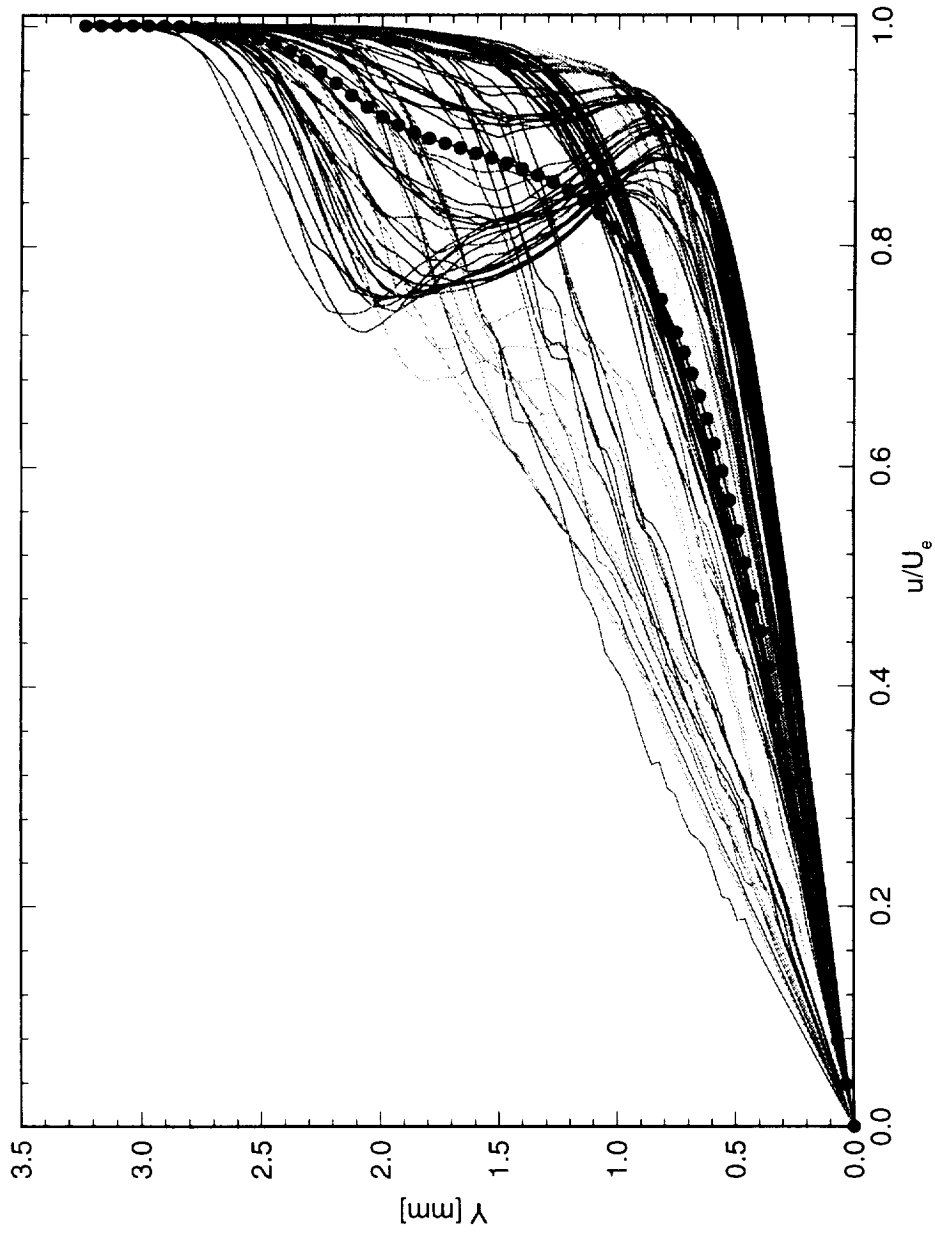

Figure 6.52: Spanwise array of 100 mean-flow boundary-layer profiles covering a span of 99 mm at $x/c = 0.29$. $Re_c = 3.2 \times 10^6$, [6|12] roughness. The dots indicate the mean of the profiles.

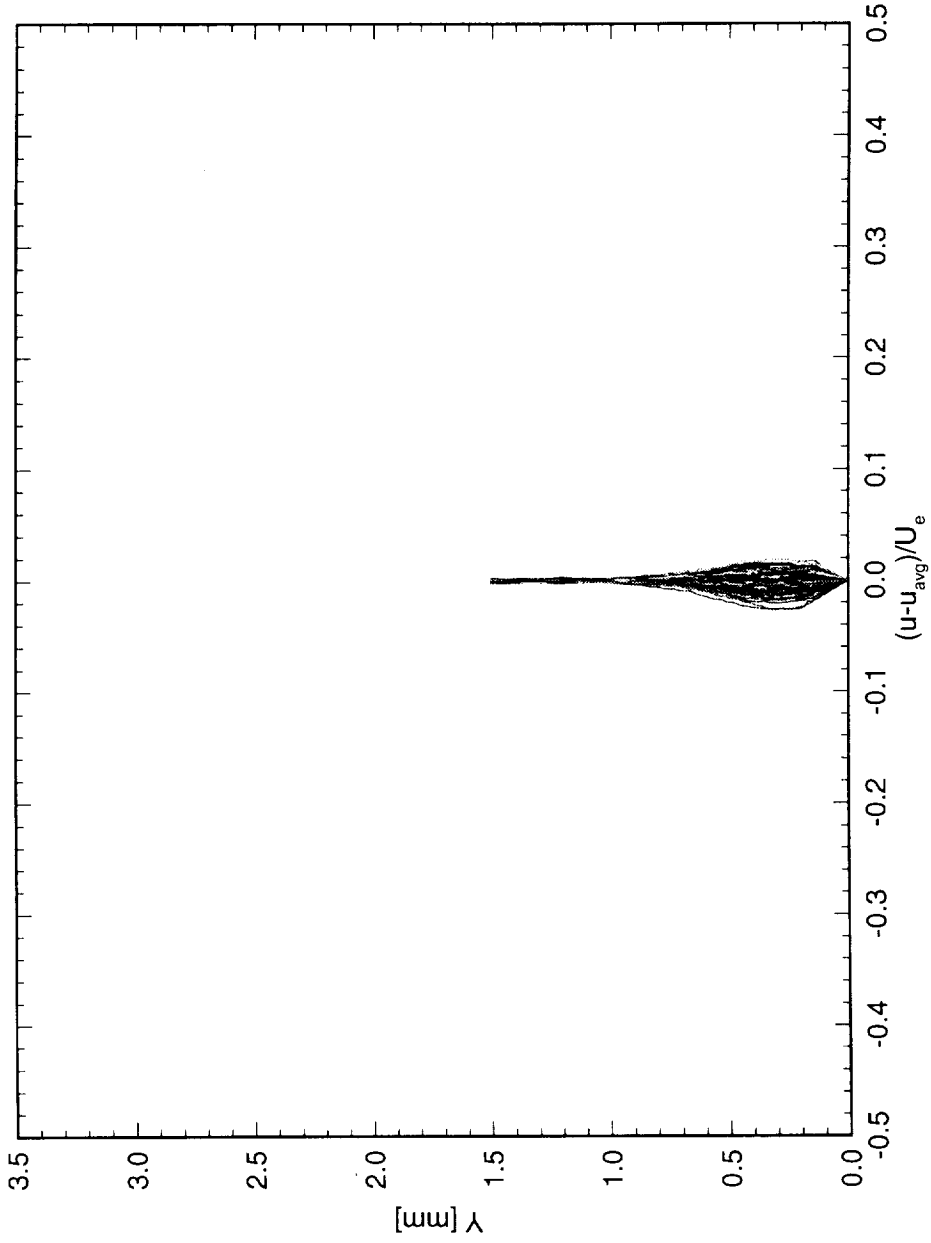

Figure 6.53: Spanwise array of 100 disturbance profiles covering a span of 99 mm at $x/c = 0.05$. $Re_c = 3.2 \times 10^6$, [6|12] roughness.

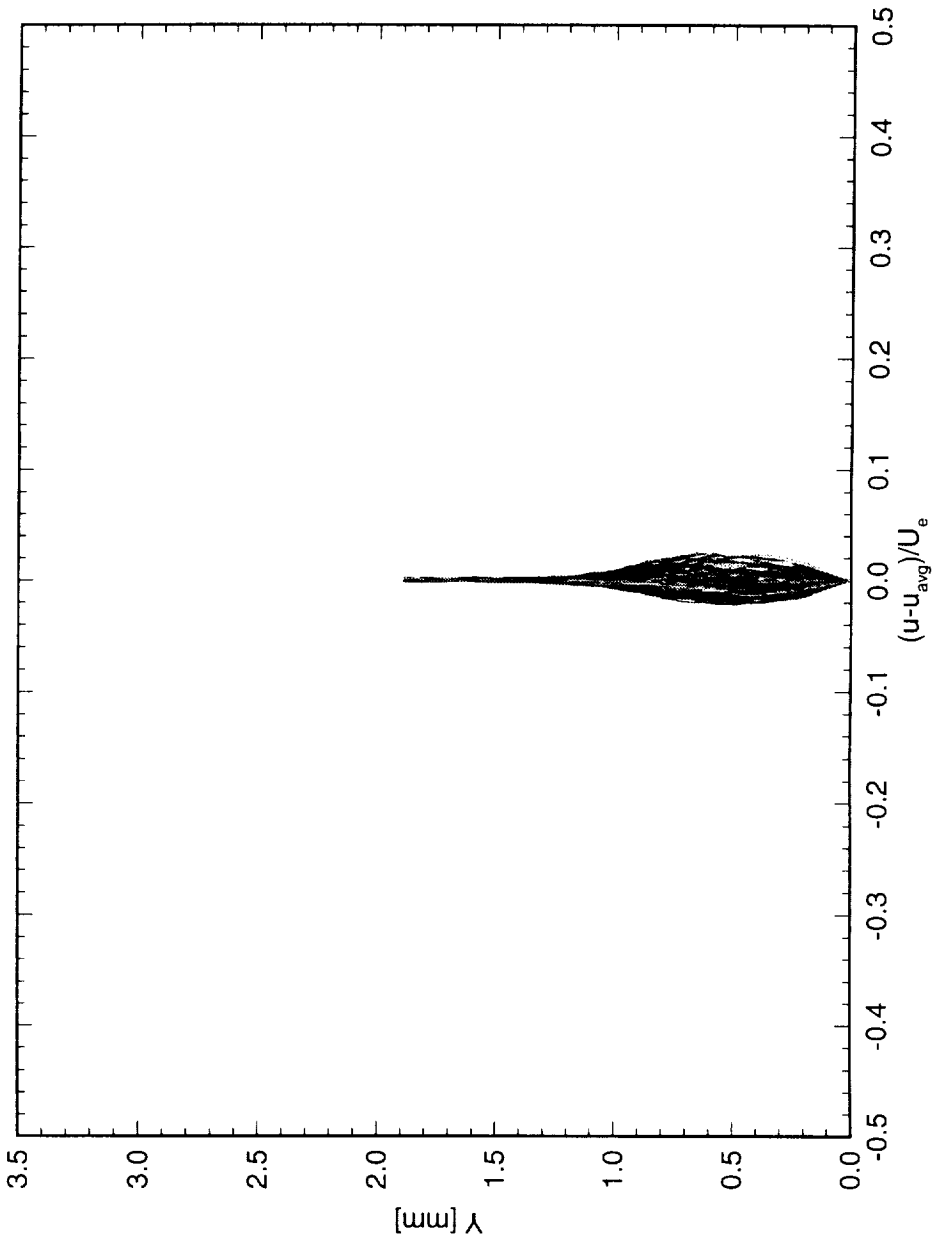

Figure 6.54: Spanwise array of 100 disturbance profiles covering a span of 99 mm at $x/c = 0.10$. $Re_c = 3.2 \times 10^6$, [6|12] roughness.

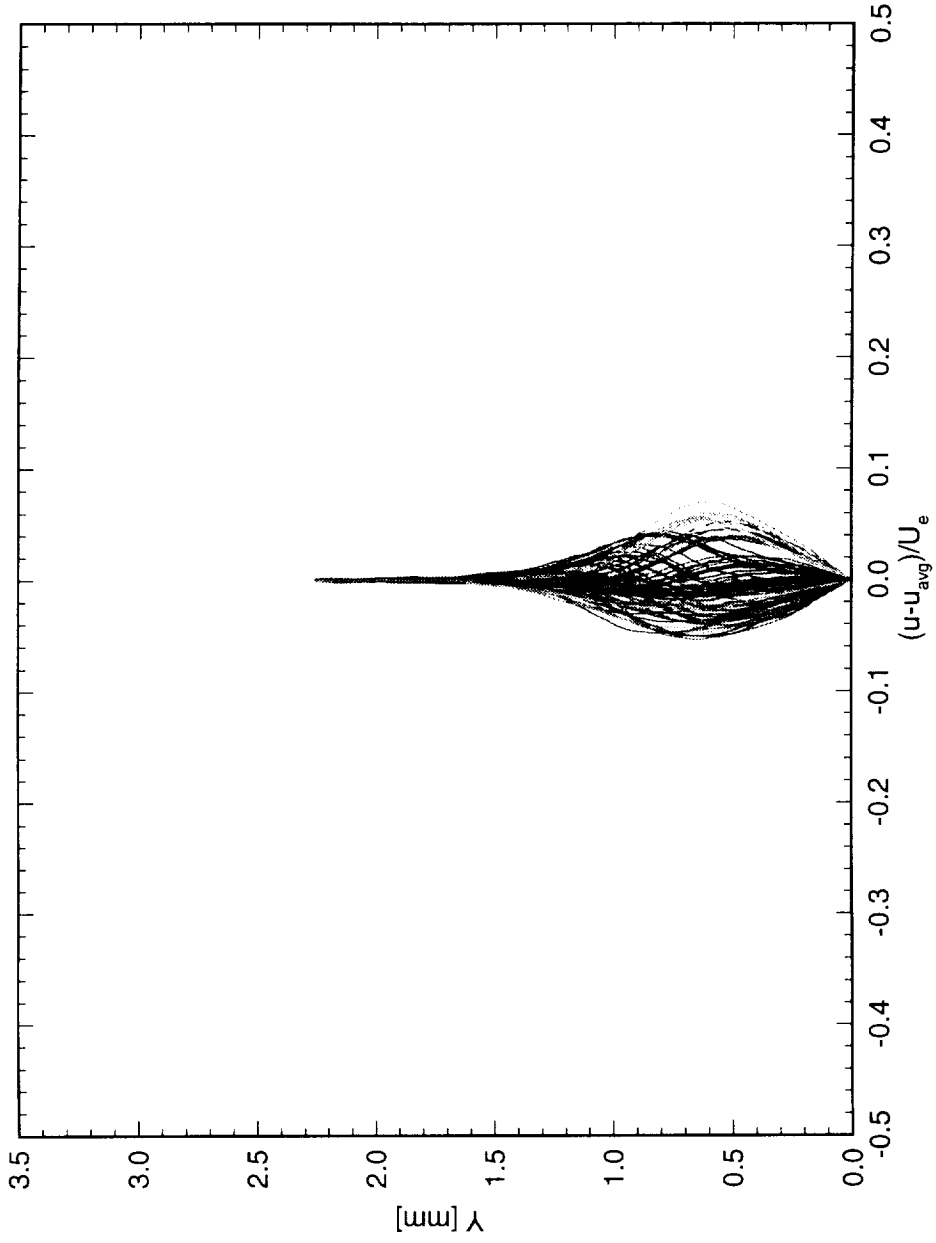

Figure 6.55: Spanwise array of 100 disturbance profiles covering a span of 99 mm at $x/c = 0.15$. $Re_c = 3.2 \times 10^6$, [6|12] roughness.

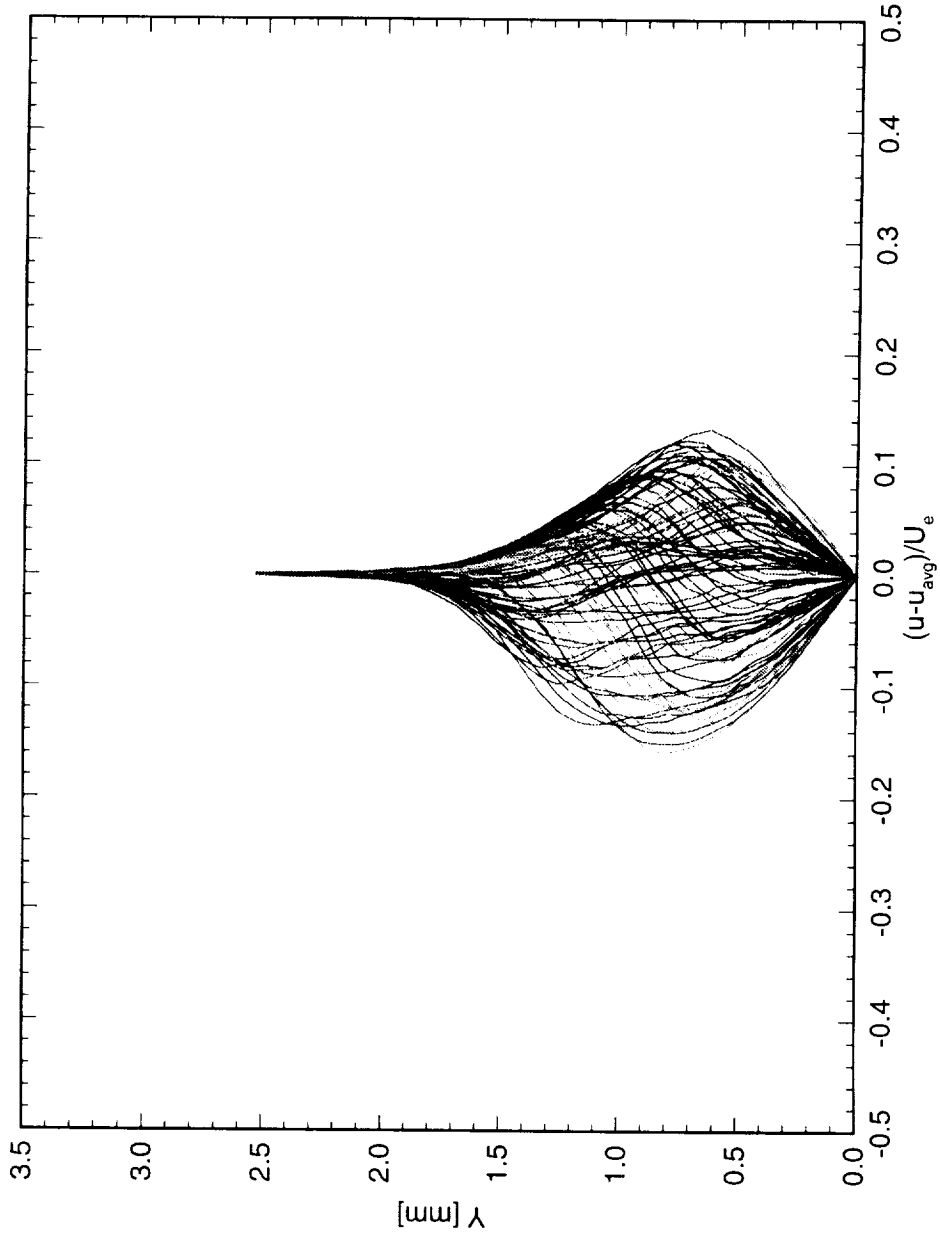

Figure 6.56: Spanwise array of 100 disturbance profiles covering a span of 99 mm at $x/c = 0.20$. $Re_c = 3.2 \times 10^6$, [6|12] roughness.

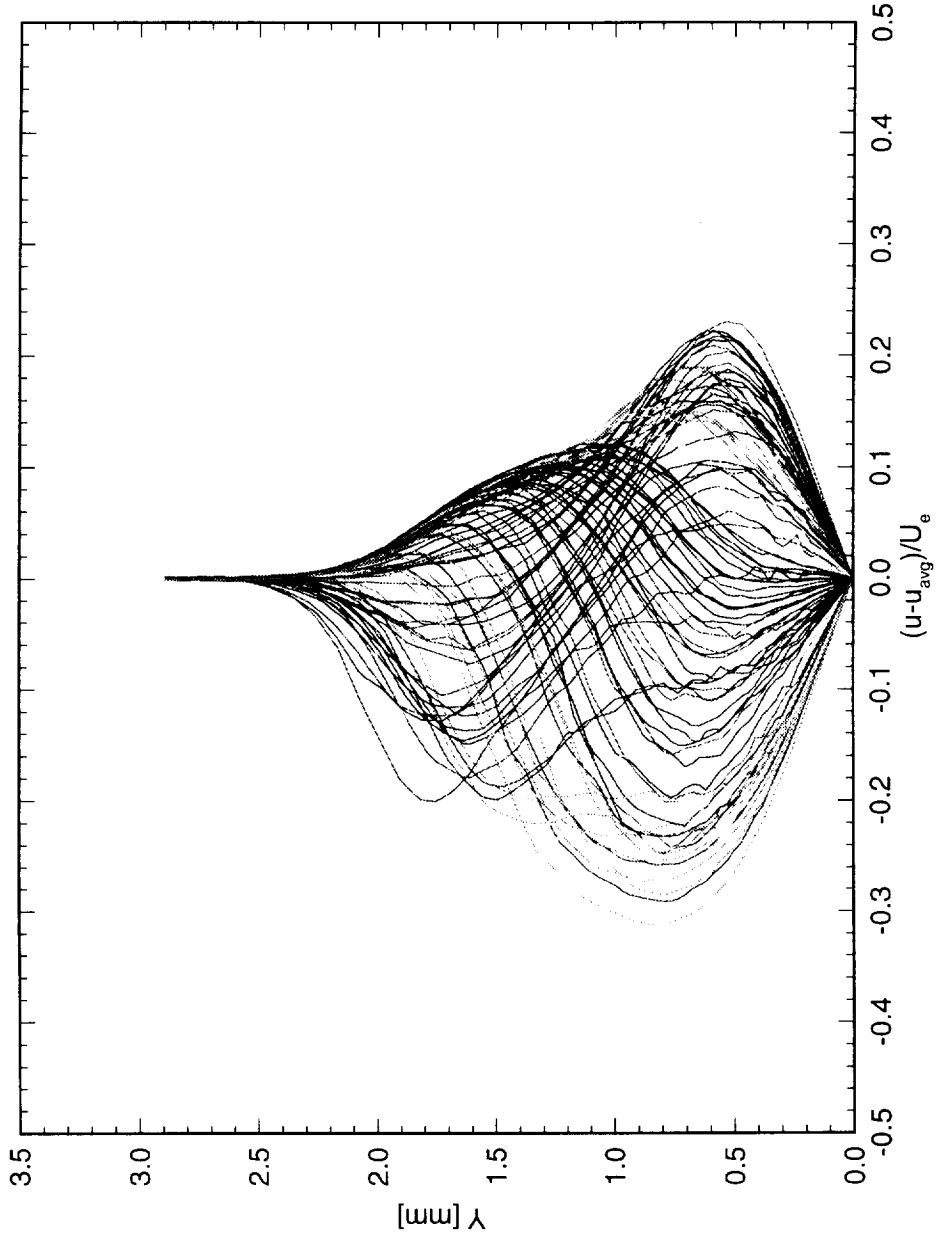

Figure 6.57: Spanwise array of 100 disturbance profiles covering a span of 99 mm at $x/c = 0.25$. $Re_c = 3.2 \times 10^6$, [6|12] roughness.

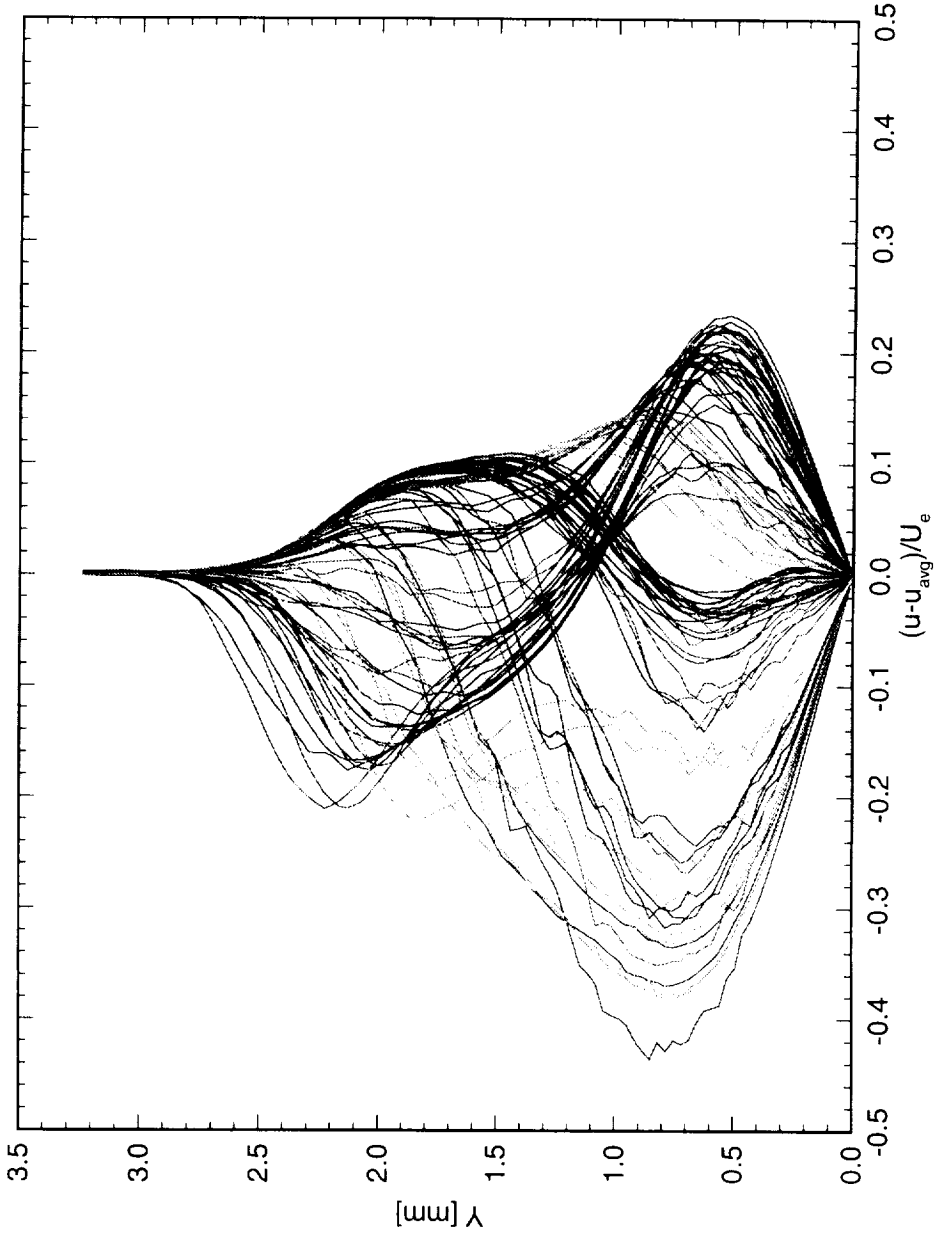

Figure 6.58: Spanwise array of 100 disturbance profiles covering a span of 99 mm at $x/c = 0.29$. $Re_c = 3.2 \times 10^6$, [6|12] roughness.

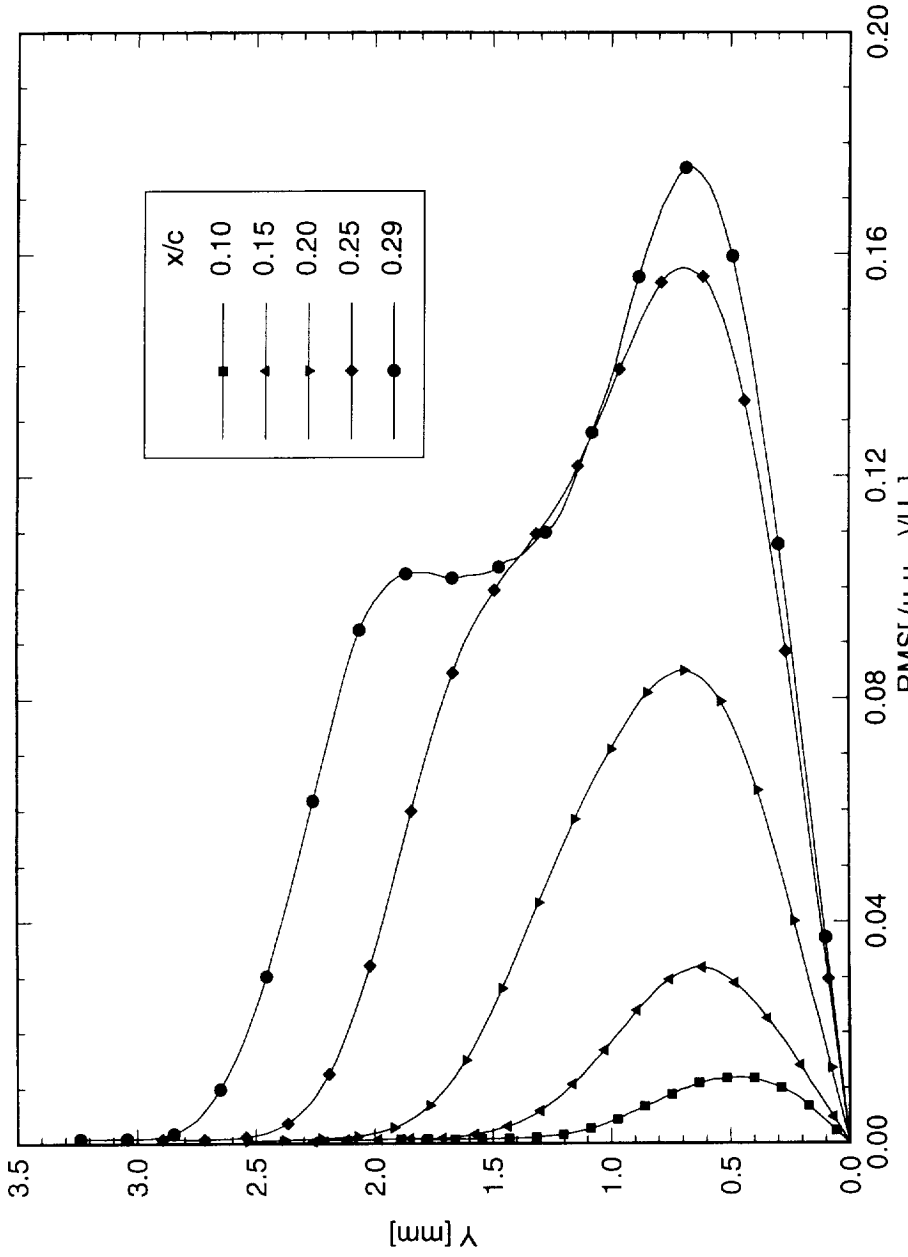

Figure 6.59: Stationary crossflow mode shapes for $Re_c = 3.2 \times 10^6$ and [6|12] roughness. The symbols are simply identifiers and do not represent measurement points.

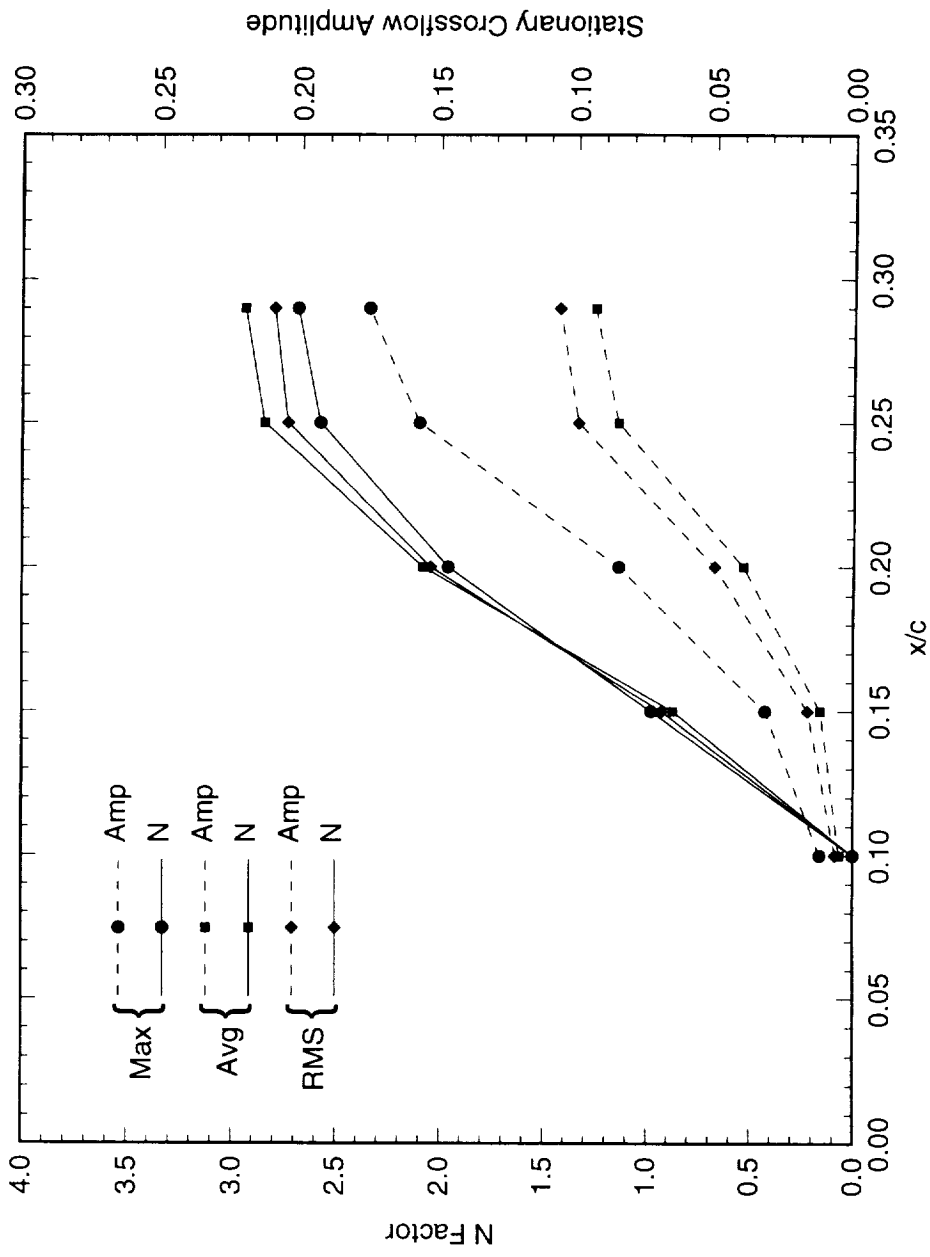

Figure 6.60: Total disturbance amplitude and amplification factor N for $Re_c = 3.2 \times 10^6$ and [6|12] roughness. The reference point for the N-factor calculations is $x/c = 0.10$.

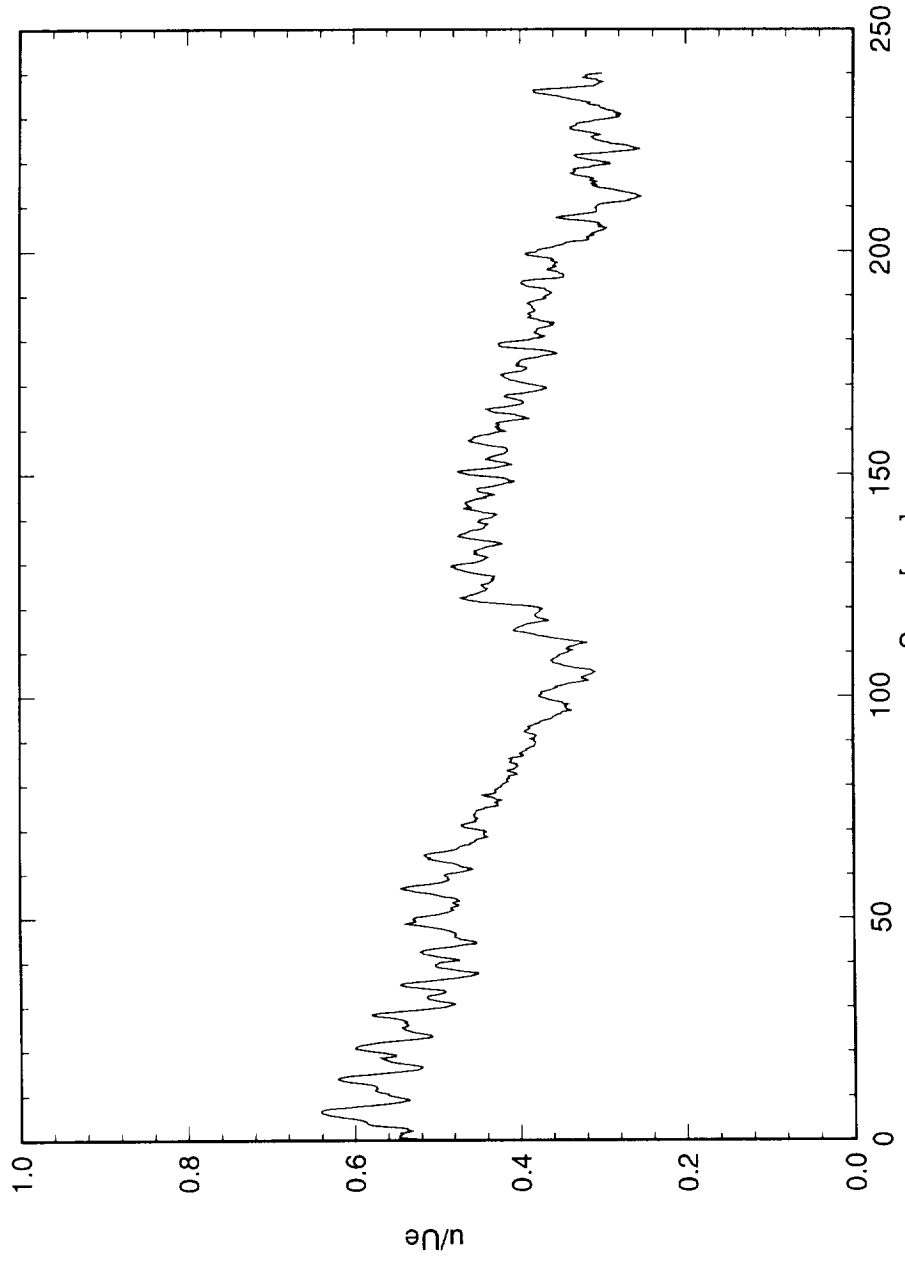

Figure 6.61: Spanwise hot-wire scan at $x/c = 0.05$, $Y = 0.3$ mm. $Re_c = 3.2 \times 10^6$, [6|12] roughness.

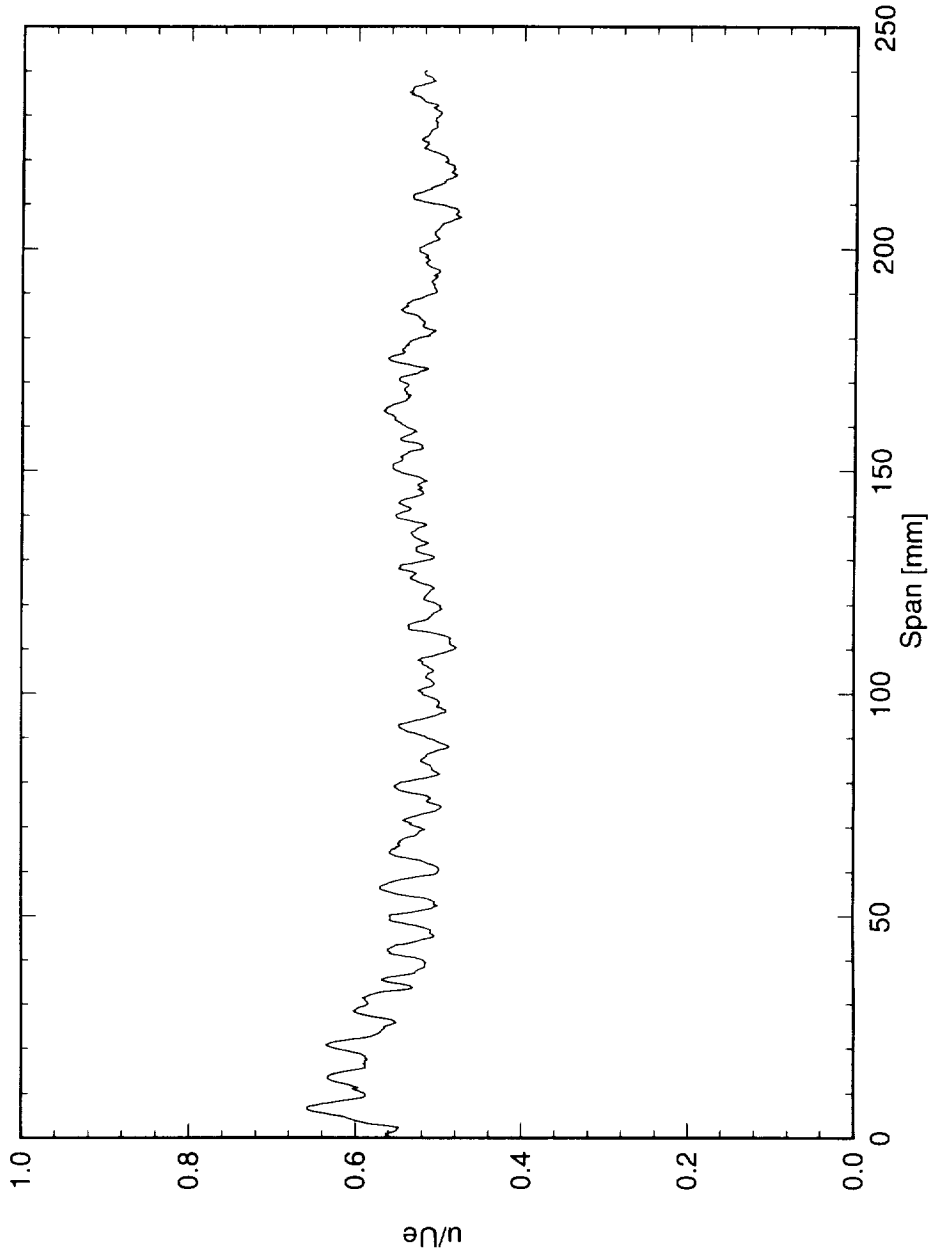

Figure 6.62: Spanwise hot-wire scan at $x/c = 0.10$, $Y = 0.45$ mm. $Re_c = 3.2 \times 10^6$, [6|12] roughness.

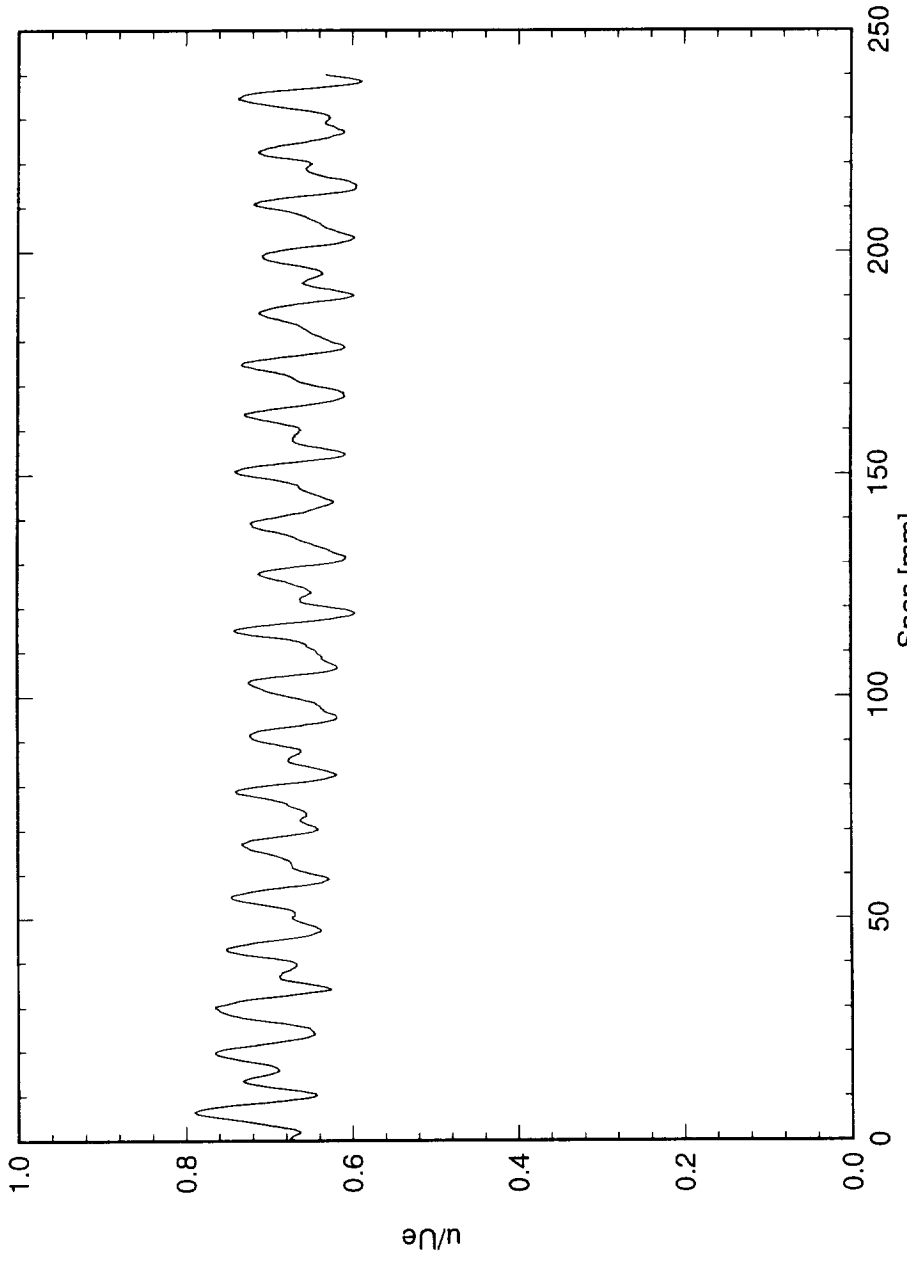

Figure 6.63: Spanwise hot-wire scan at $x/c = 0.15$, $Y = 0.65$ mm. $Re_c = 3.2 \times 10^6$, [6|12] roughness.

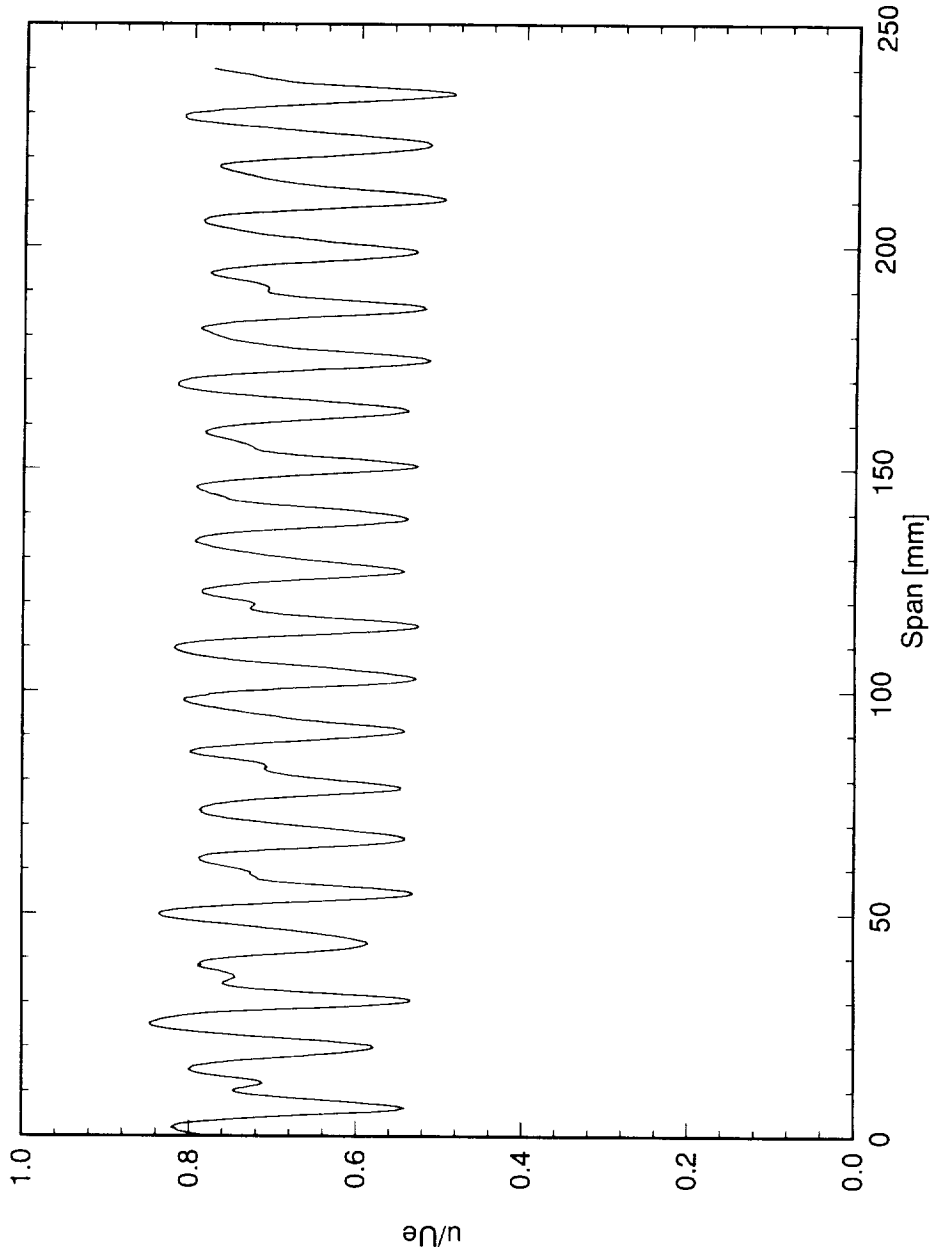

Figure 6.64: Spanwise hot-wire scan at $x/c = 0.20$, $Y = 0.7$ mm. $Re_c = 3.2 \times 10^6$, [6|12] roughness.

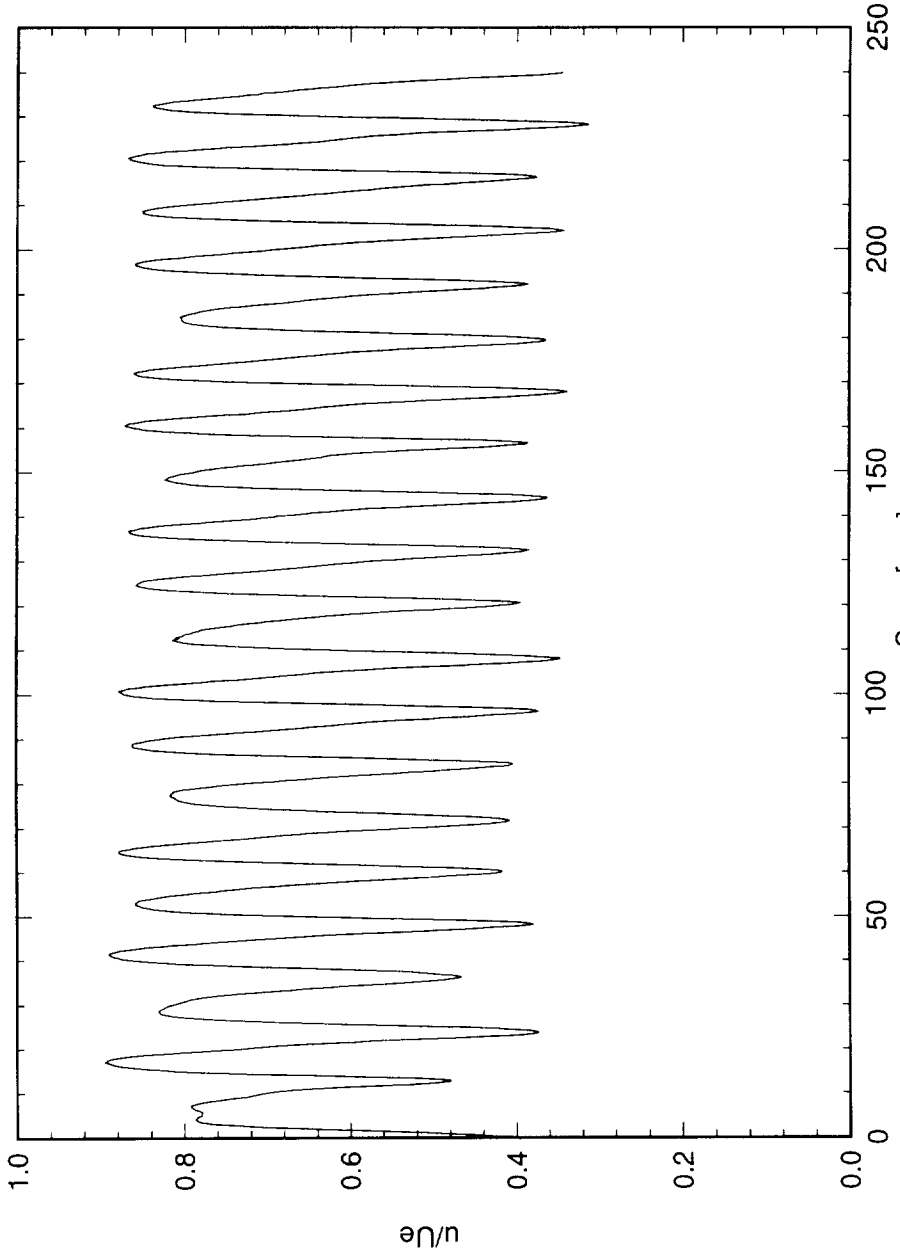

Figure 6.65: Spanwise hot-wire scan at $x/c = 0.25$, Y = 0.7 mm. $Re_c = 3.2 \times 10^6$, [6|12] roughness.

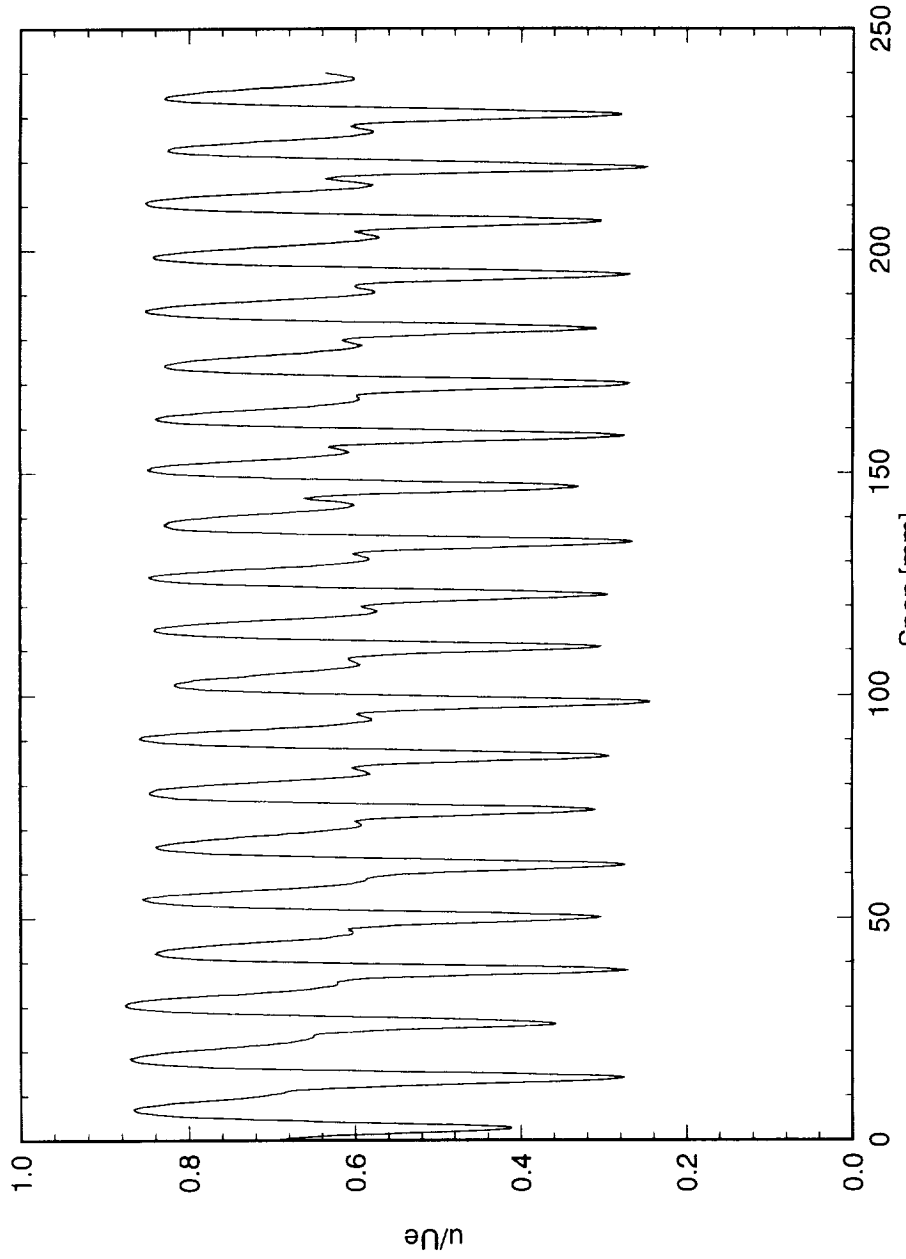

Figure 6.66: Spanwise hot-wire scan at $x/c = 0.29$, $\Upsilon = 0.65$ mm. $Re_c = 3.2 \times 10^6$, [6|12] roughness.

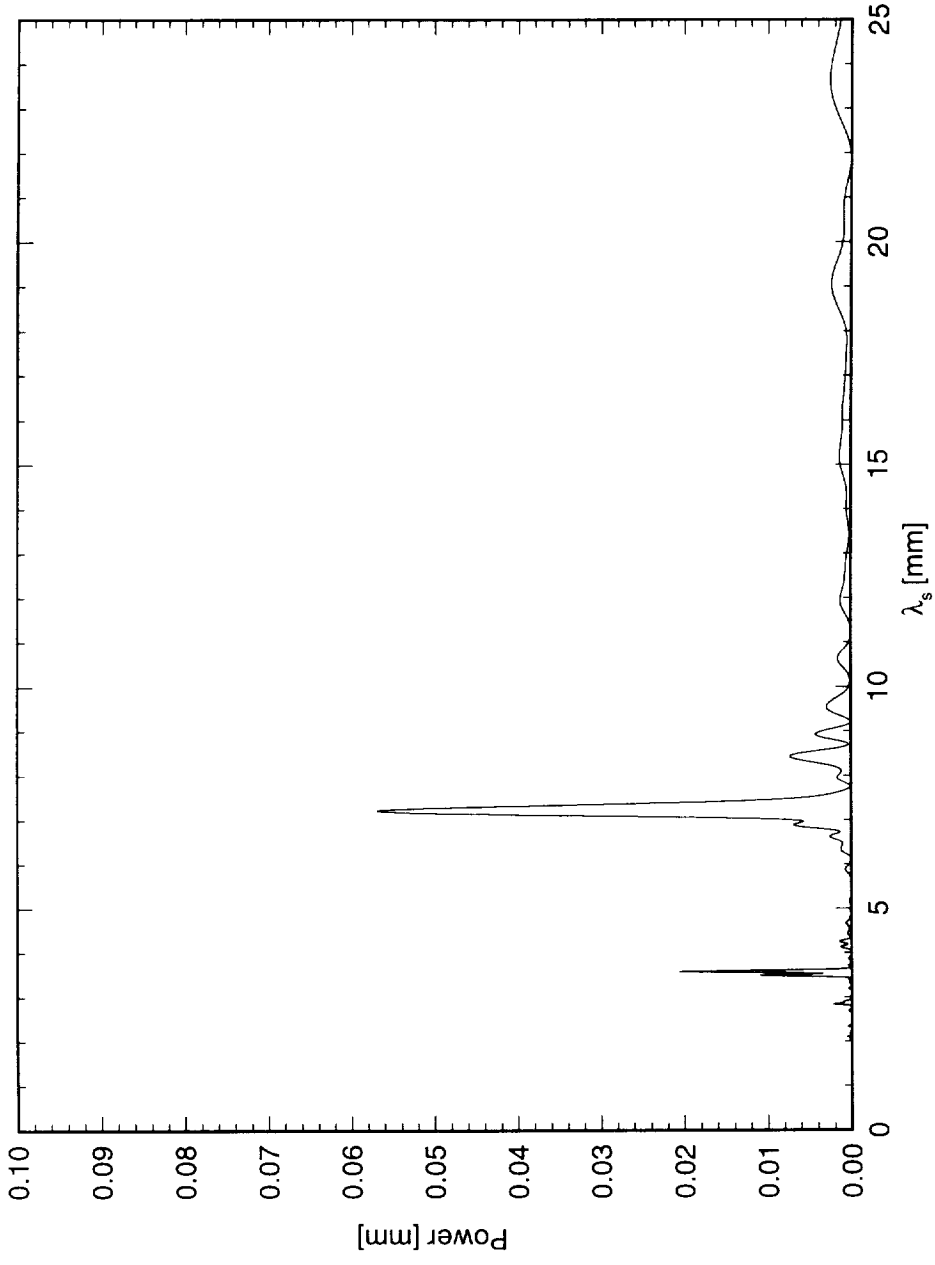

Figure 6.67: Power spectral density of spanwise hot-wire scan at $x/c = 0.05$, $Y = 0.3$ mm. $Re_c = 3.2 \times 10^6$, [6|12] roughness.

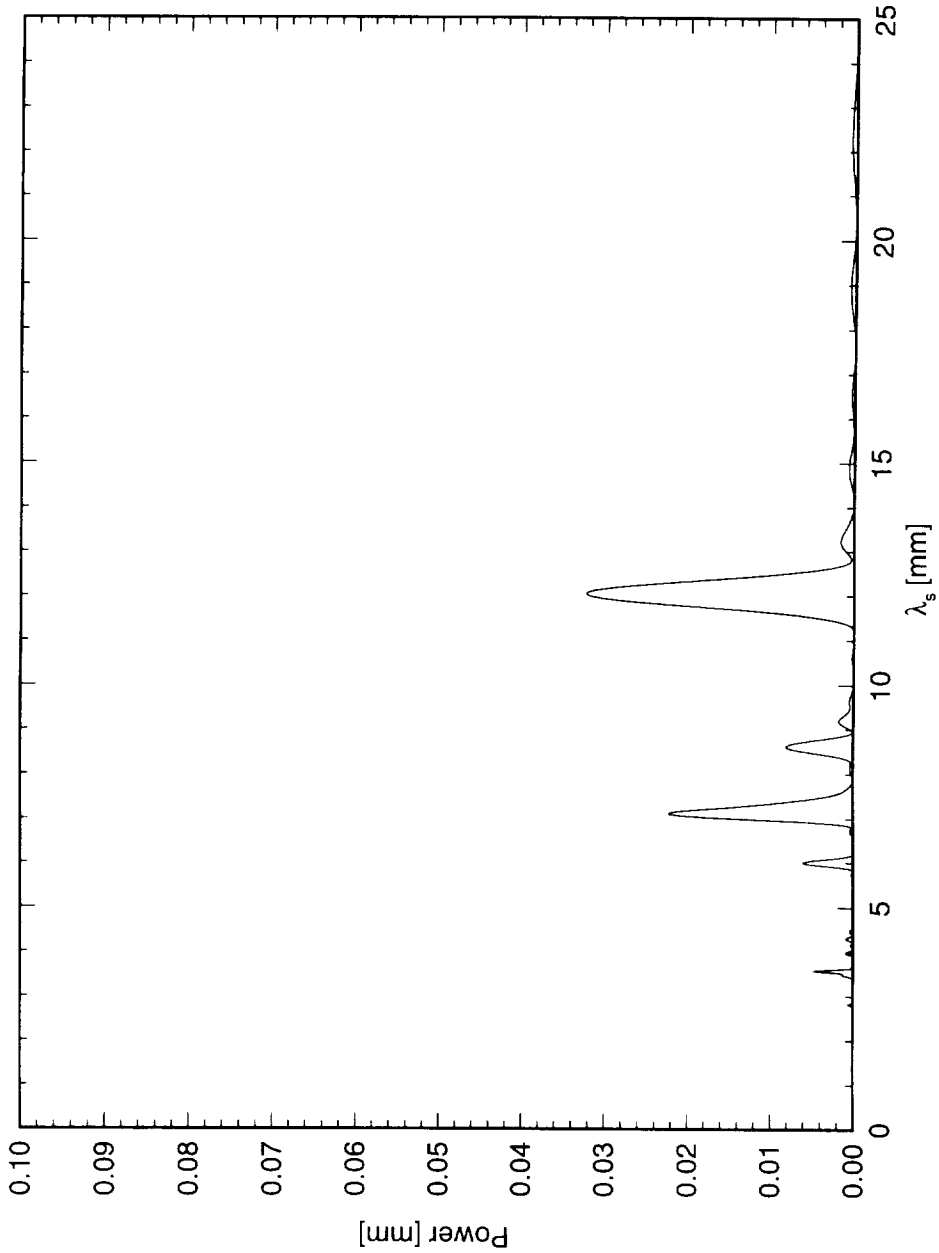

Figure 6.68: Power spectral density of spanwise hot-wire scan at $x/c = 0.10$, $Y = 0.45$ mm. $Re_c = 3.2 \times 10^6$. [6|12] roughness.

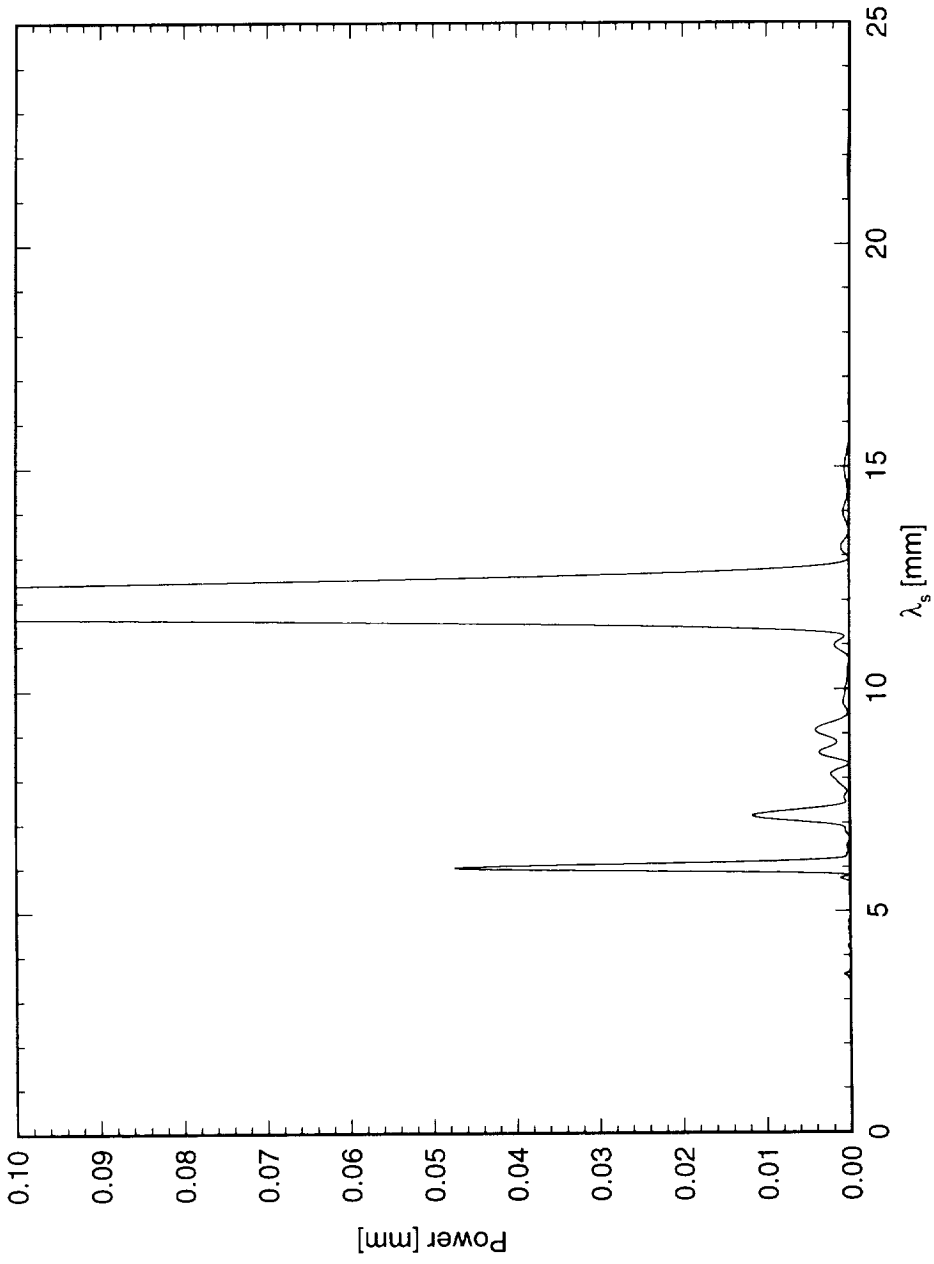

Figure 6.69: Power spectral density of spanwise hot-wire scan at $x/c = 0.15$, $Y = 0.65$ mm. $Re_c = 3.2 \times 10^6$, [6|12] roughness.

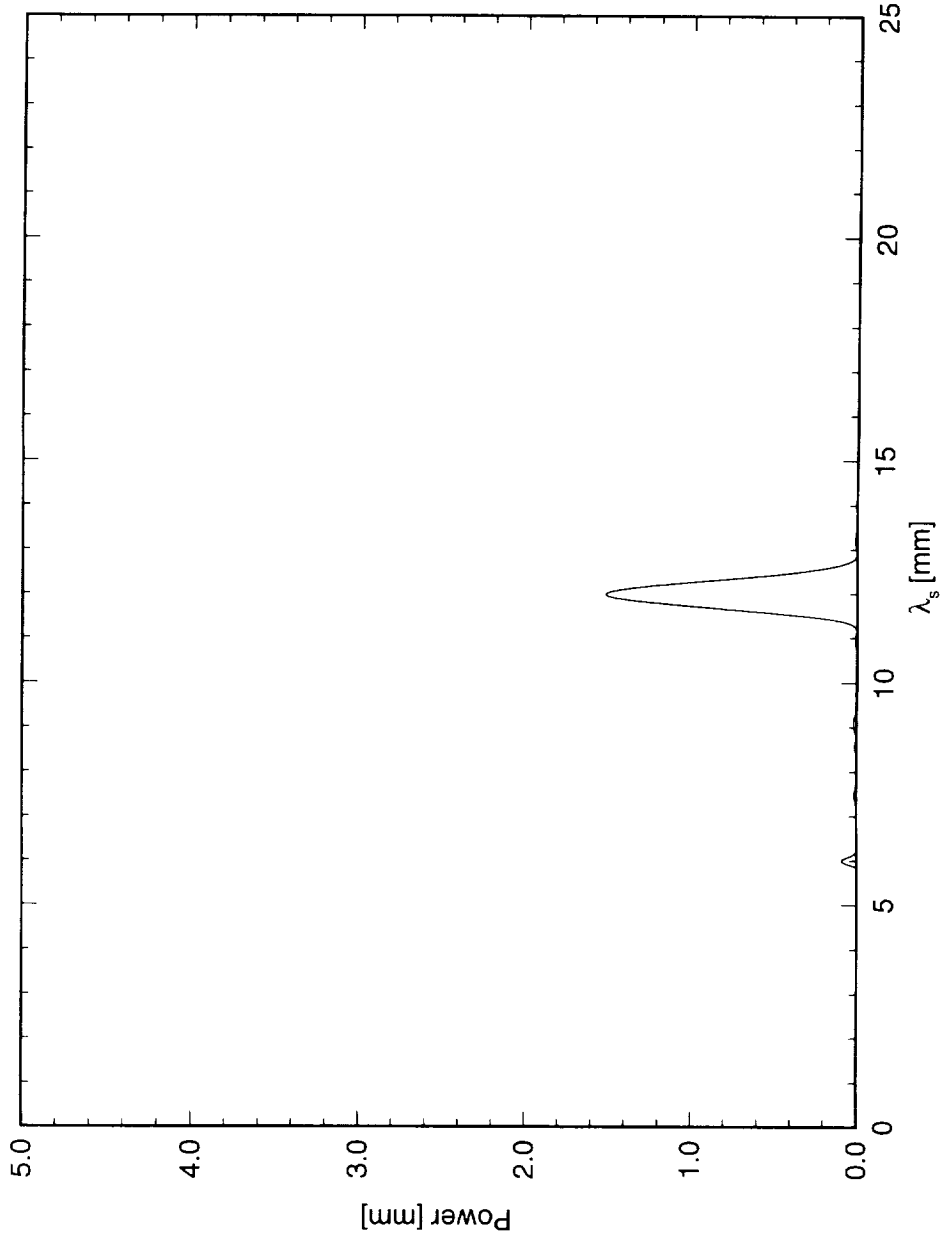

Figure 6.70: Power spectral density of spanwise hot-wire scan at $x/c = 0.20$, $Y = 0.7$ mm. $Re_c = 3.2 \times 10^6$, [6|12] roughness.

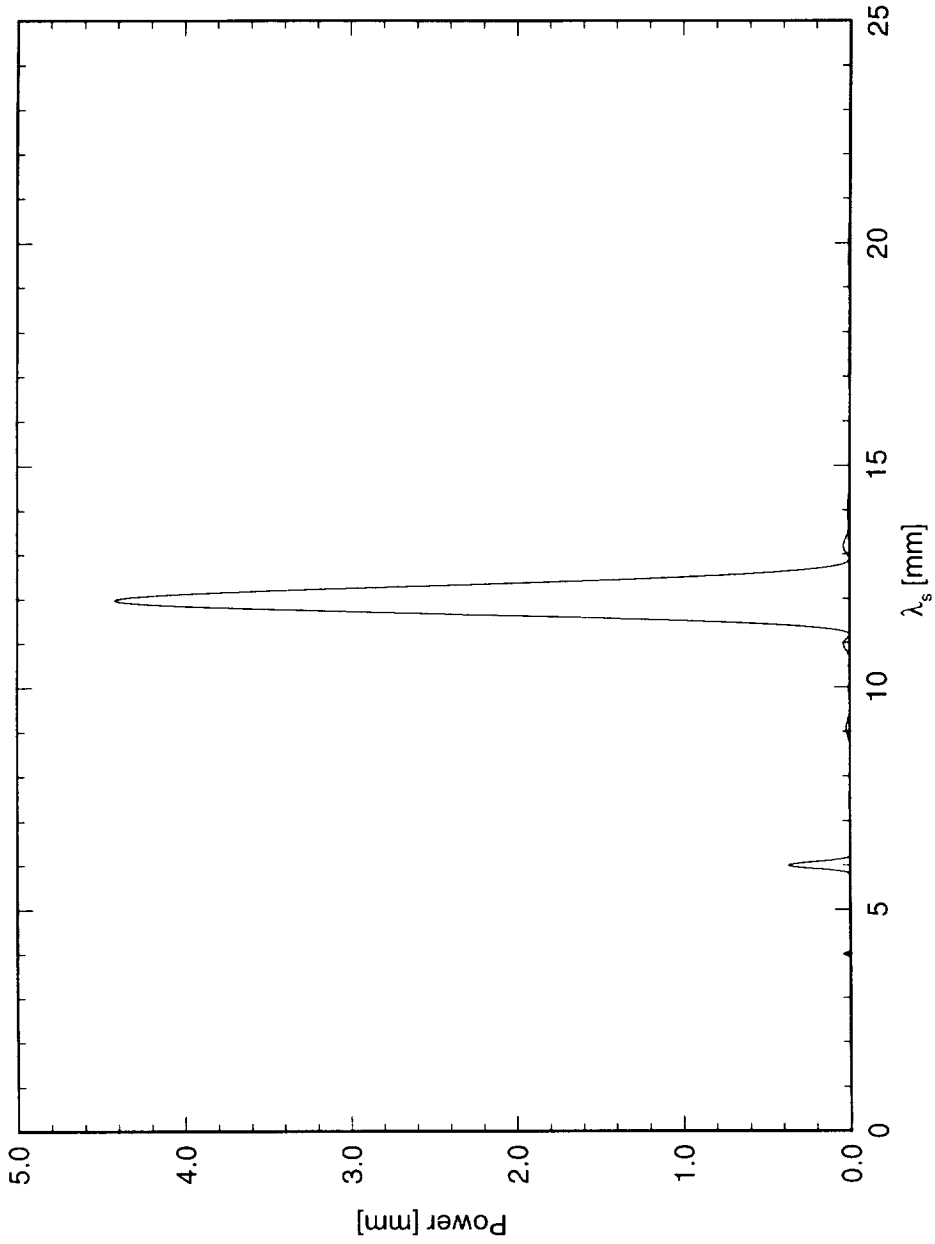

Figure 6.71: Power spectral density of spanwise hot-wire scan at $x/c = 0.25$, $Y = 0.7$ mm. $Re_c = 3.2 \times 10^6$, [6|12] roughness.

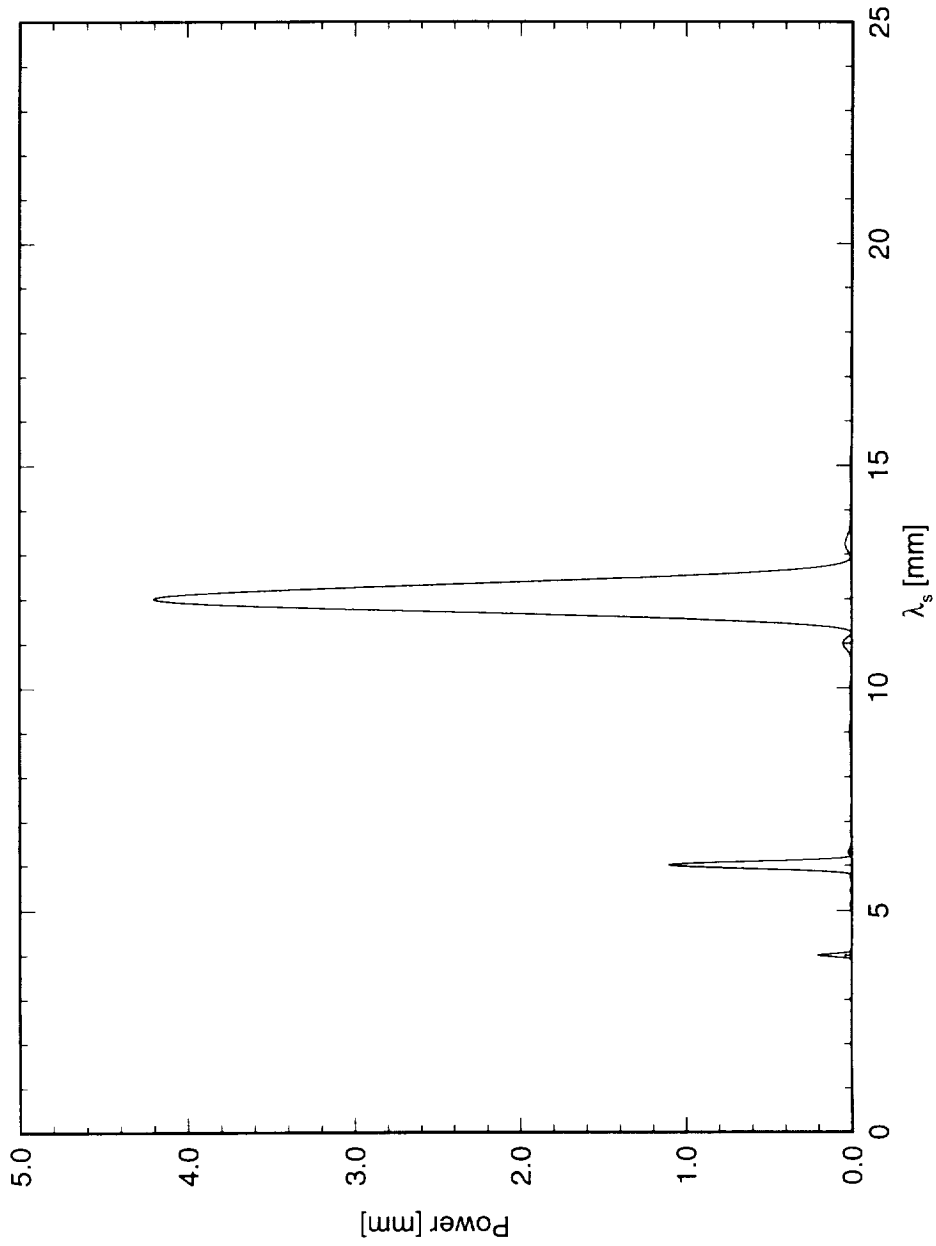

Figure 6.72: Power spectral density of spanwise hot-wire scan at $x/c = 0.29$, $Y = 0.65$ mm. $Re_c = 3.2 \times 10^6$, [6|12] roughness.

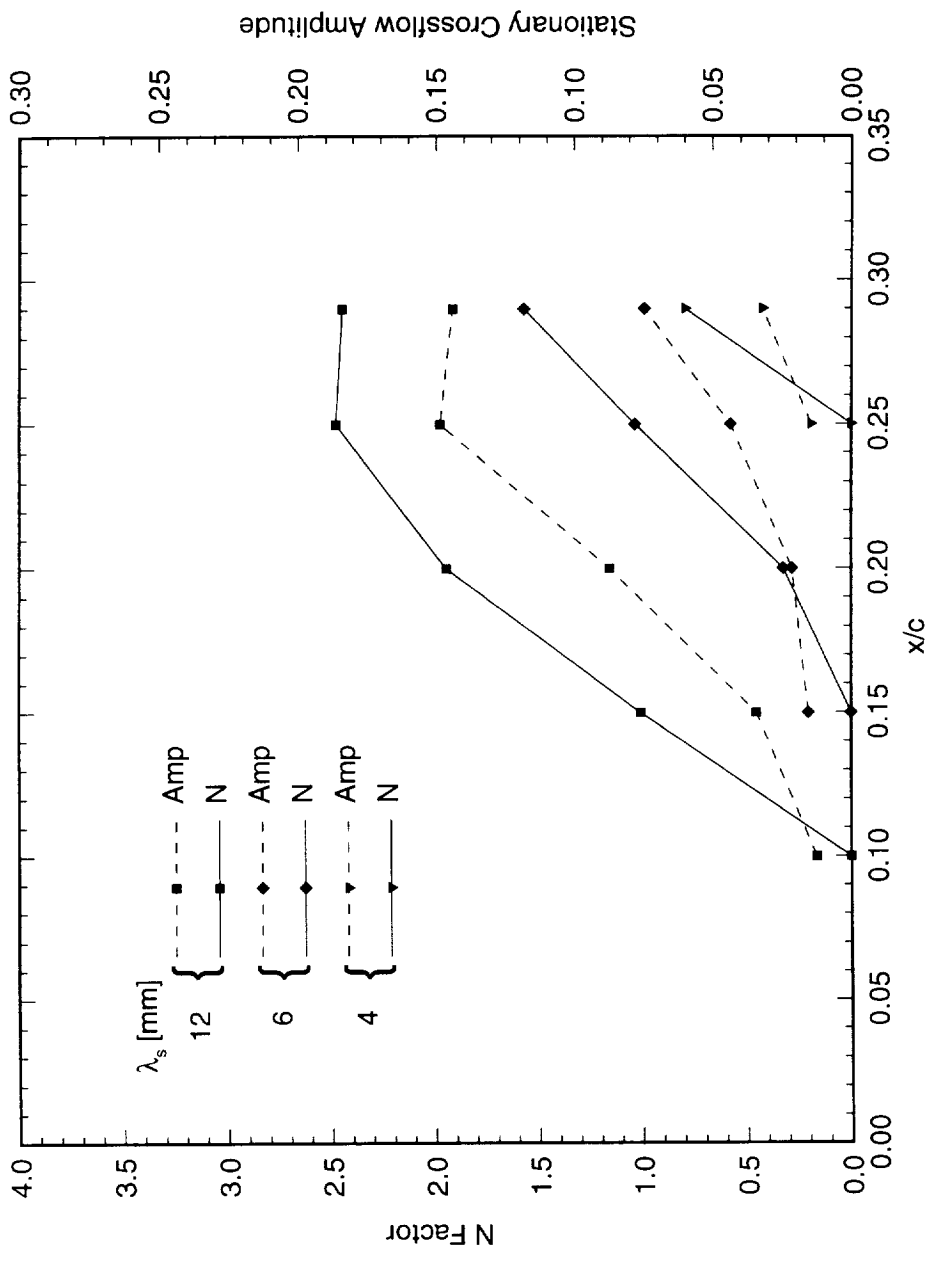

Figure 6.73: Individual-mode disturbance amplitude and amplification factor N for $Re_c = 3.2 \times 10^6$ and [6|12] roughness. N-factors are relative to the point at which the mode is first detected.

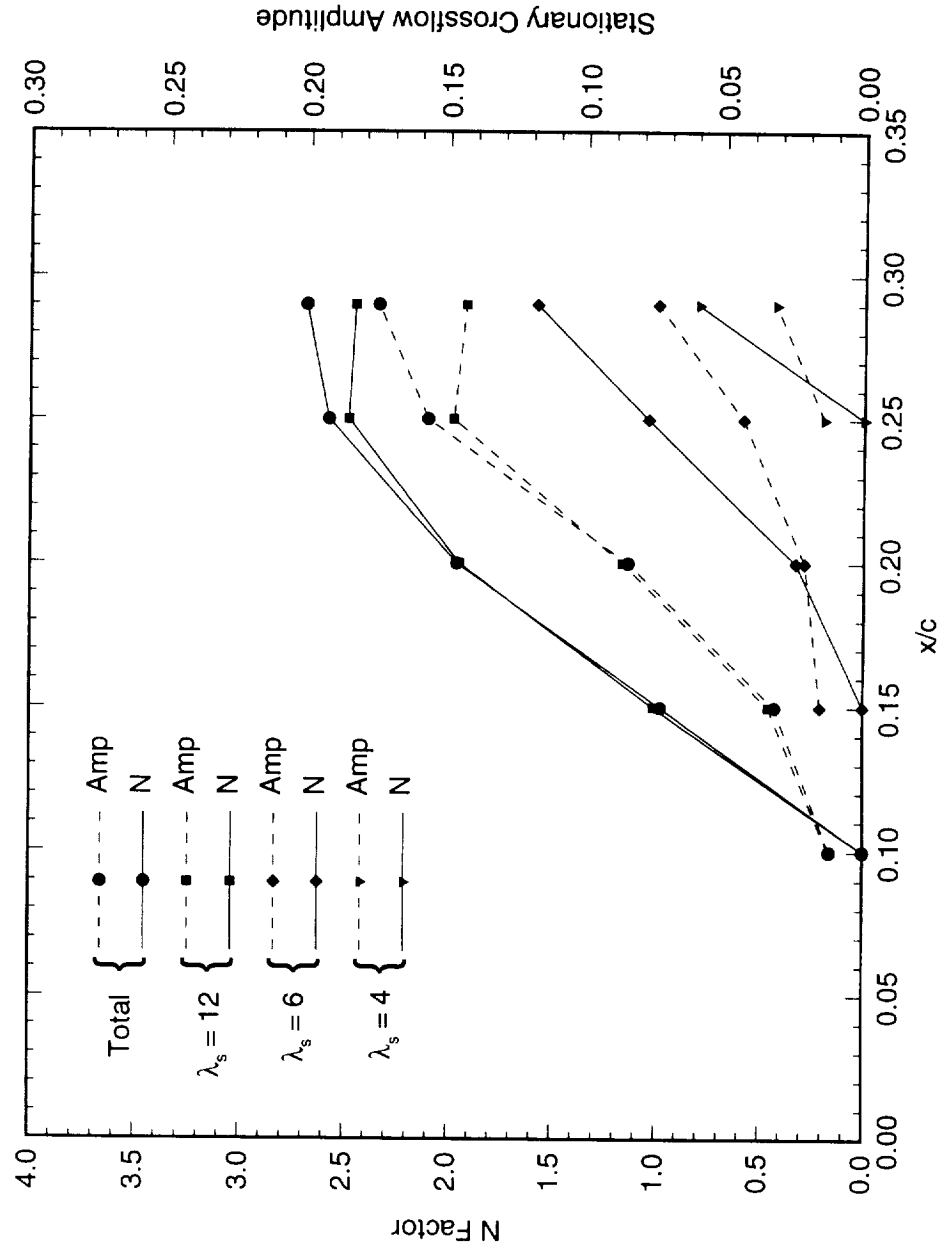

Figure 6.74: Total and individual-mode disturbance amplitude and amplification factor N for $Re_c = 3.2 \times 10^6$ and [6|12] roughness. N-factors are relative to the point at which the disturbance is first detected.

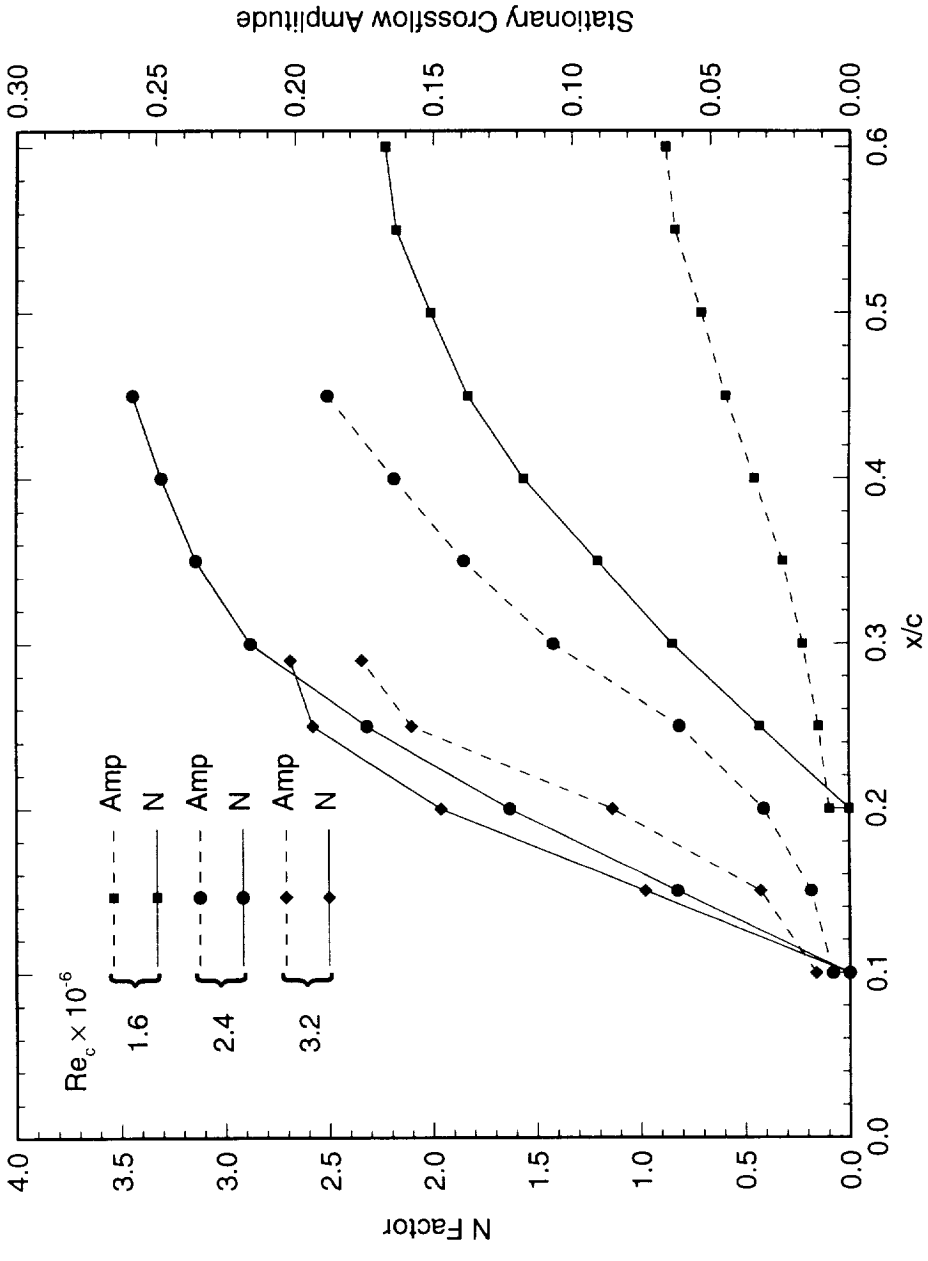

Figure 6.75: Reynolds number effect on the total disturbance amplitude and amplification factor N. [6|12] roughness. N-factors are relative to the point at which the disturbance is first detected.

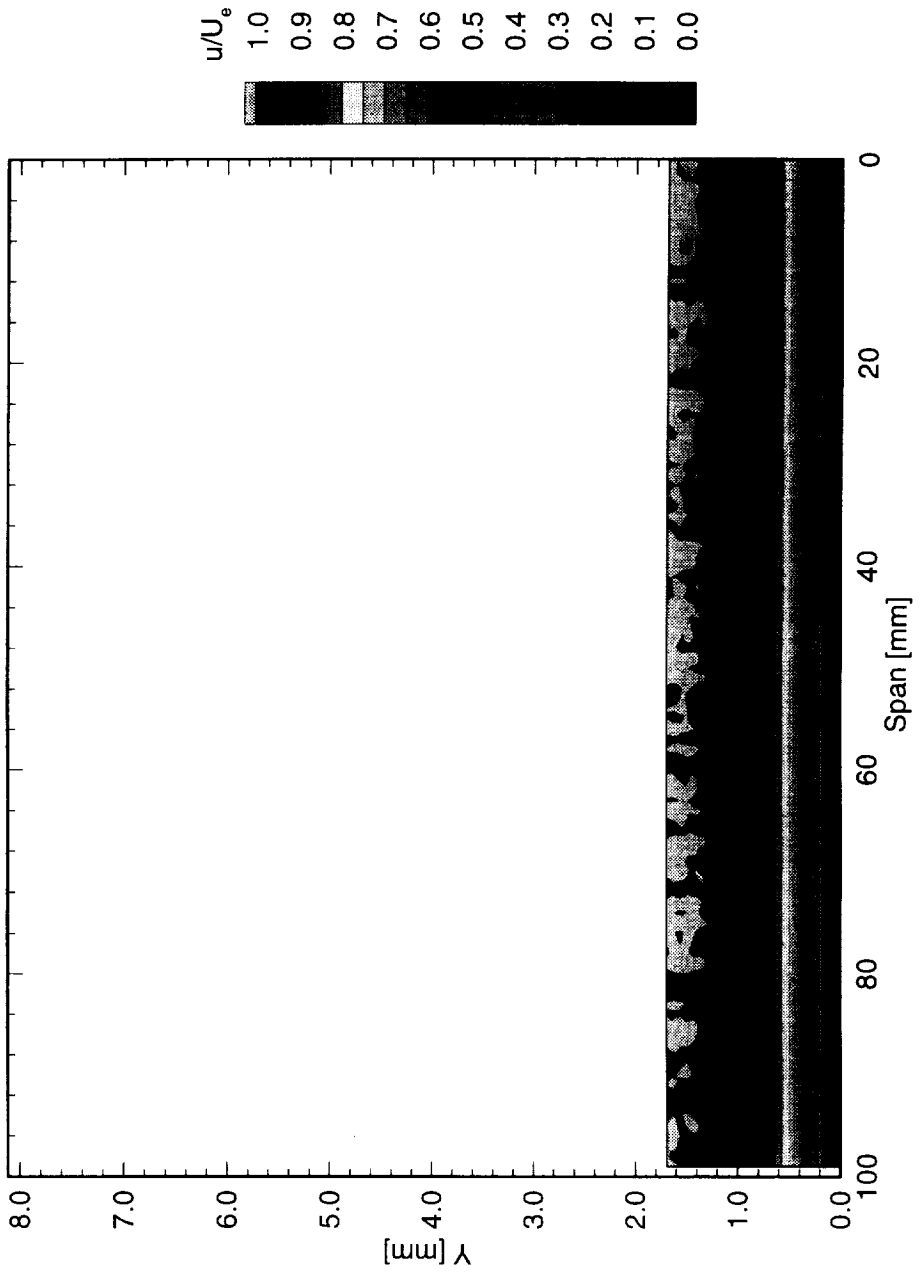

Figure 6.76: Streamwise velocity contours at $x/c = 0.05$. $Re_c = 2.4 \times 10^6$, [6|36] roughness.

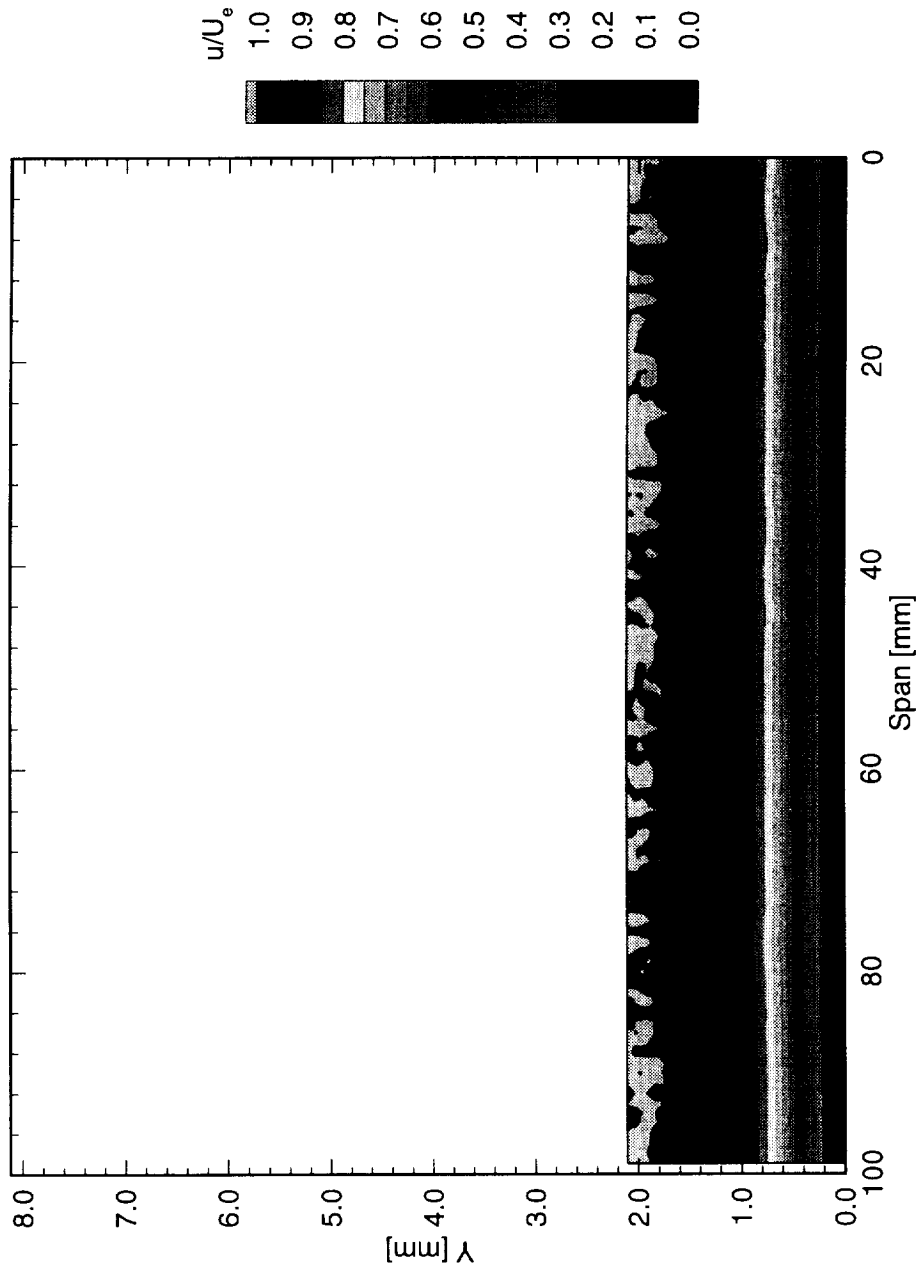

Figure 6.77: Streamwise velocity contours at $x/c = 0.10$. $Re_c = 2.4 \times 10^6$, [6|36] roughness.

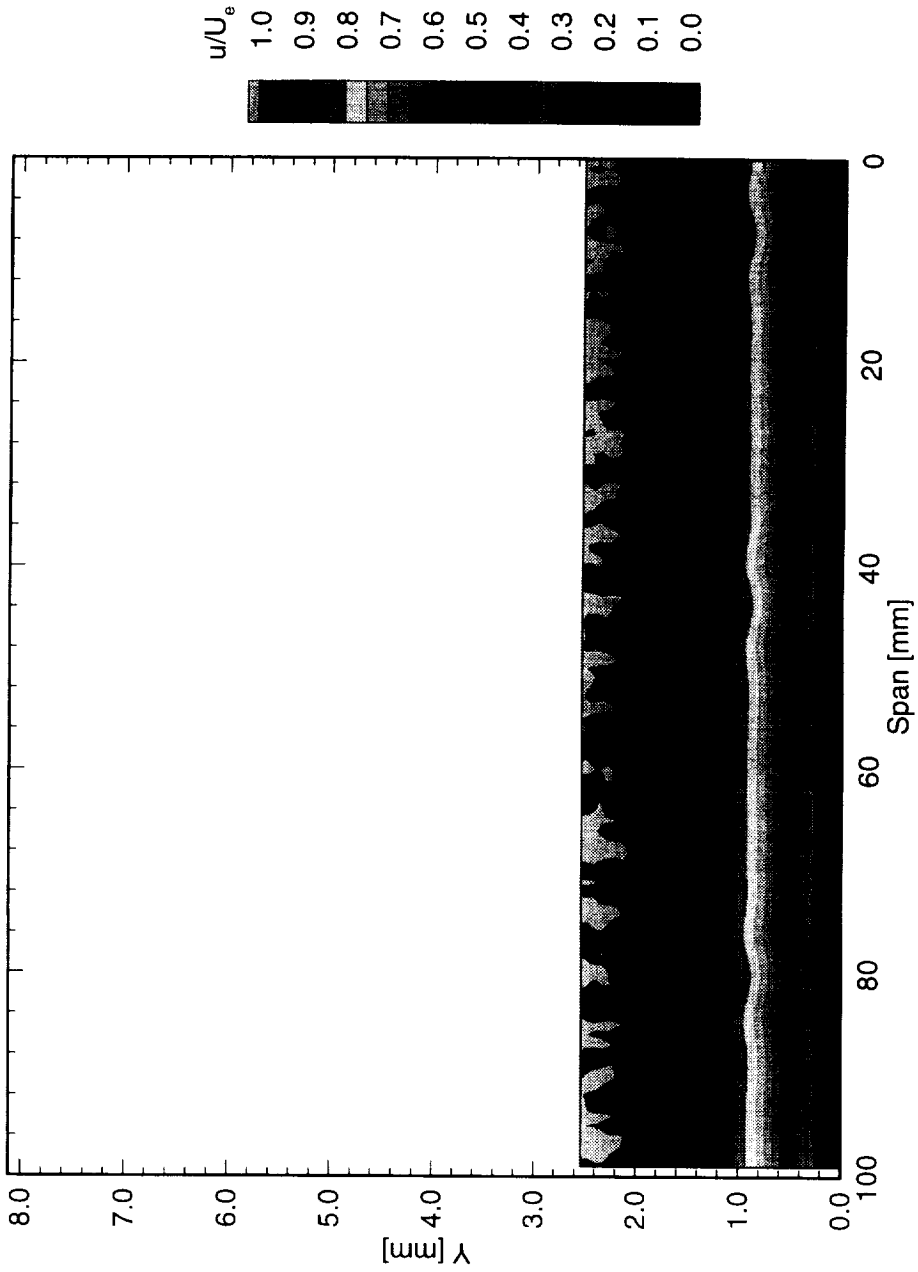

Figure 6.78: Streamwise velocity contours at $x/c = 0.15$. $Re_c = 2.4 \times 10^6$, [6|36] roughness.

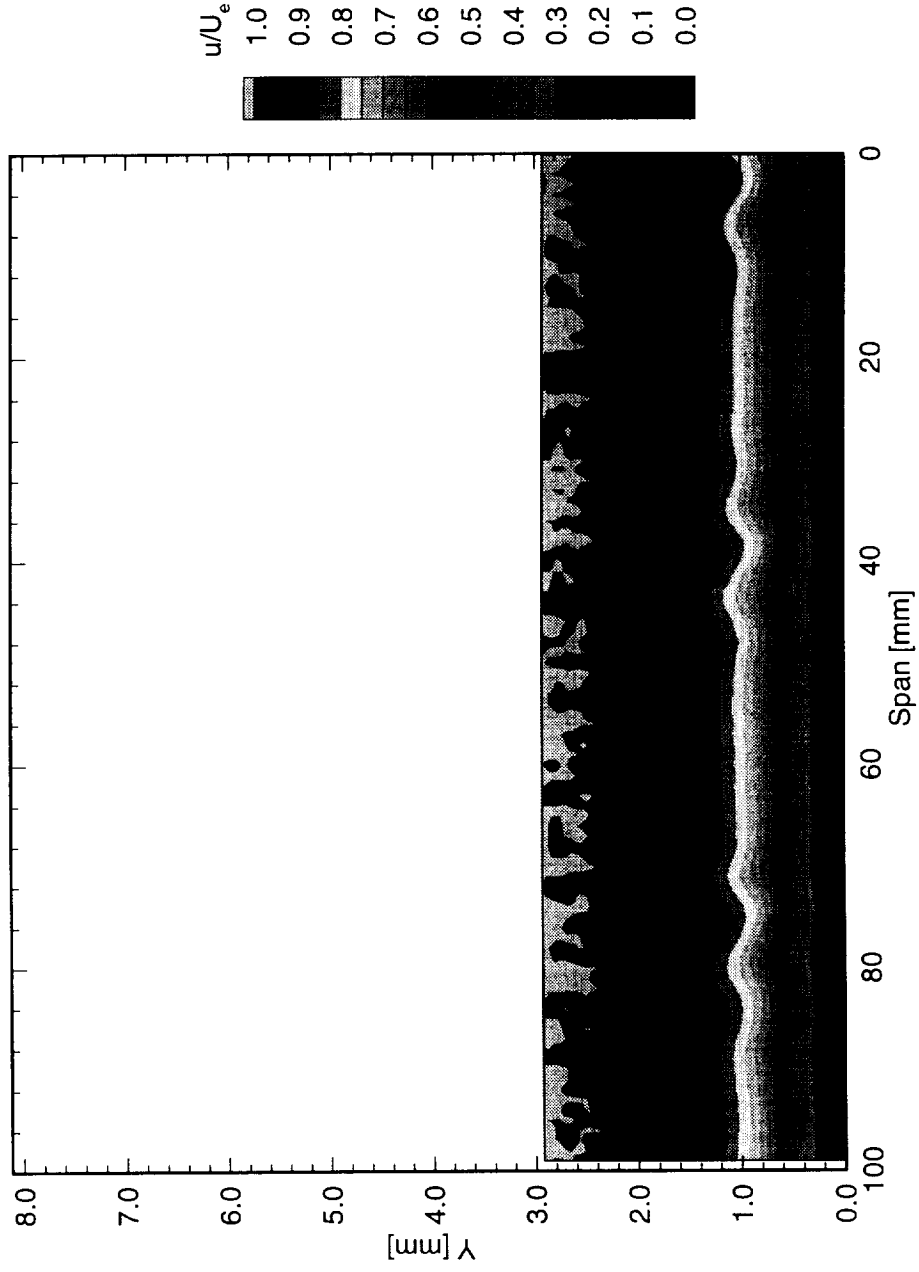

Figure 6.79: Streamwise velocity contours at $x/c = 0.20$. $Re_c = 2.4 \times 10^6$, [6|36] roughness.

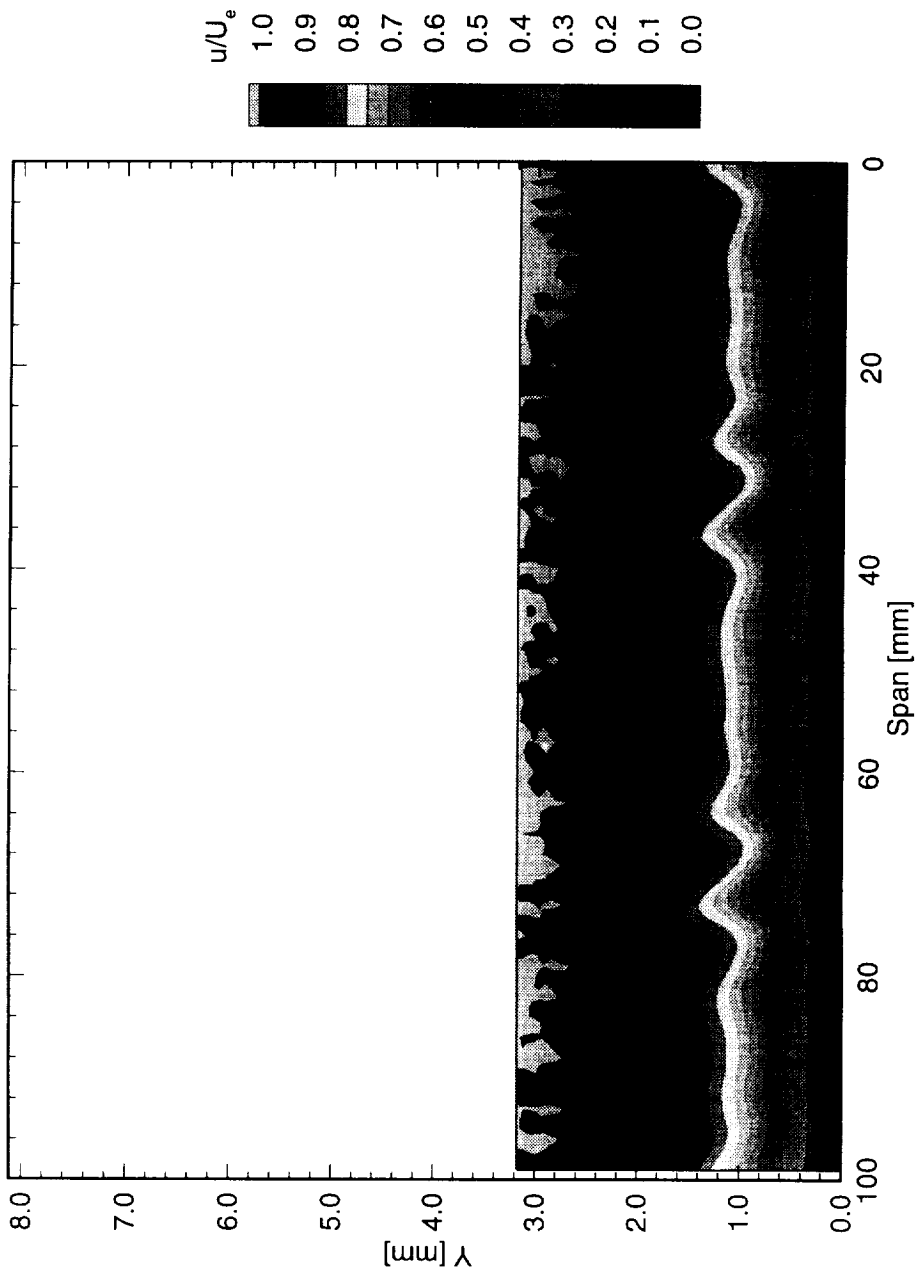

Figure 6.80: Streamwise velocity contours at $x/c = 0.25$. $Re_c = 2.4 \times 10^6$, [6|36] roughness.

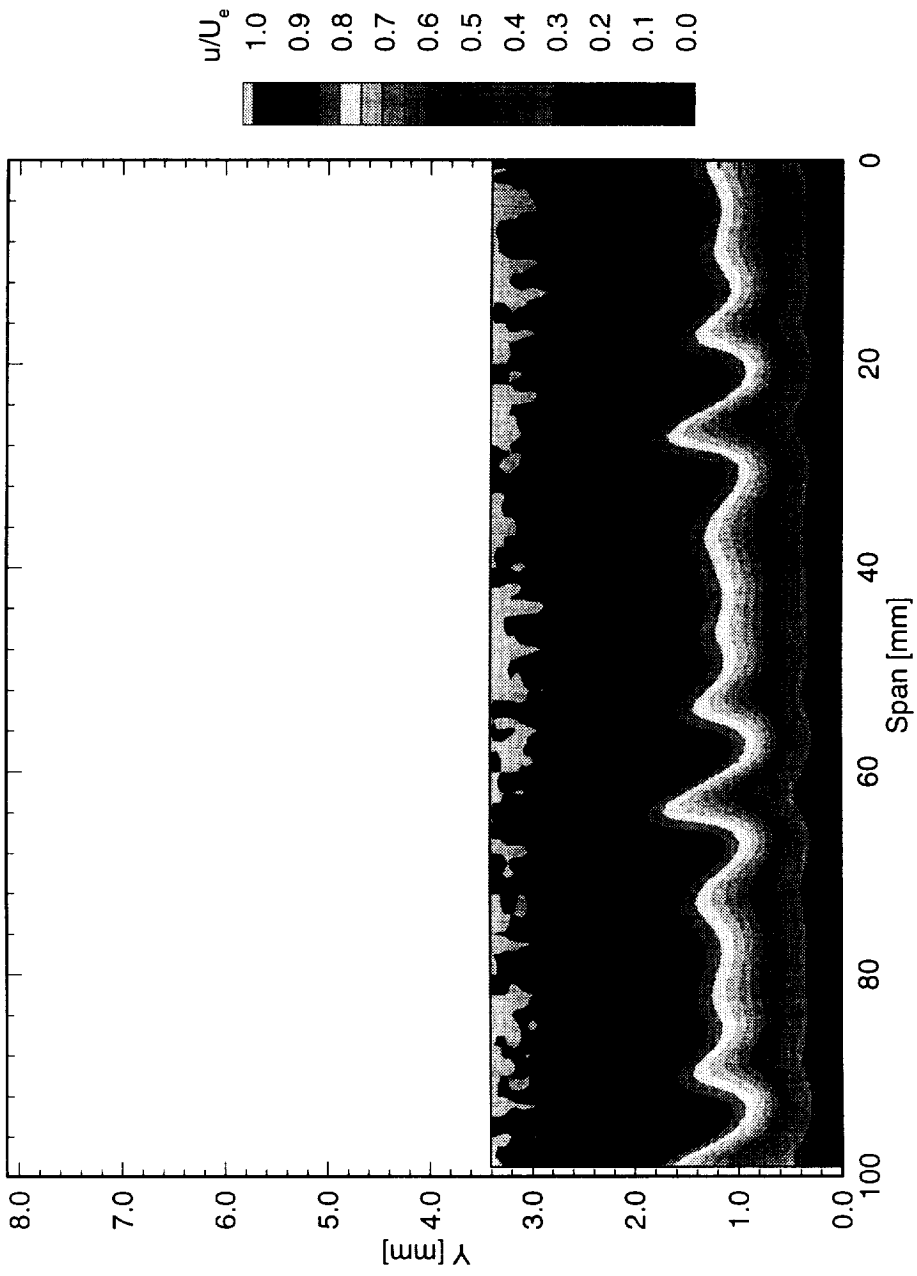

Figure 6.81: Streamwise velocity contours at $x/c = 0.30$. $Re_c = 2.4 \times 10^6$, [6|36] roughness.

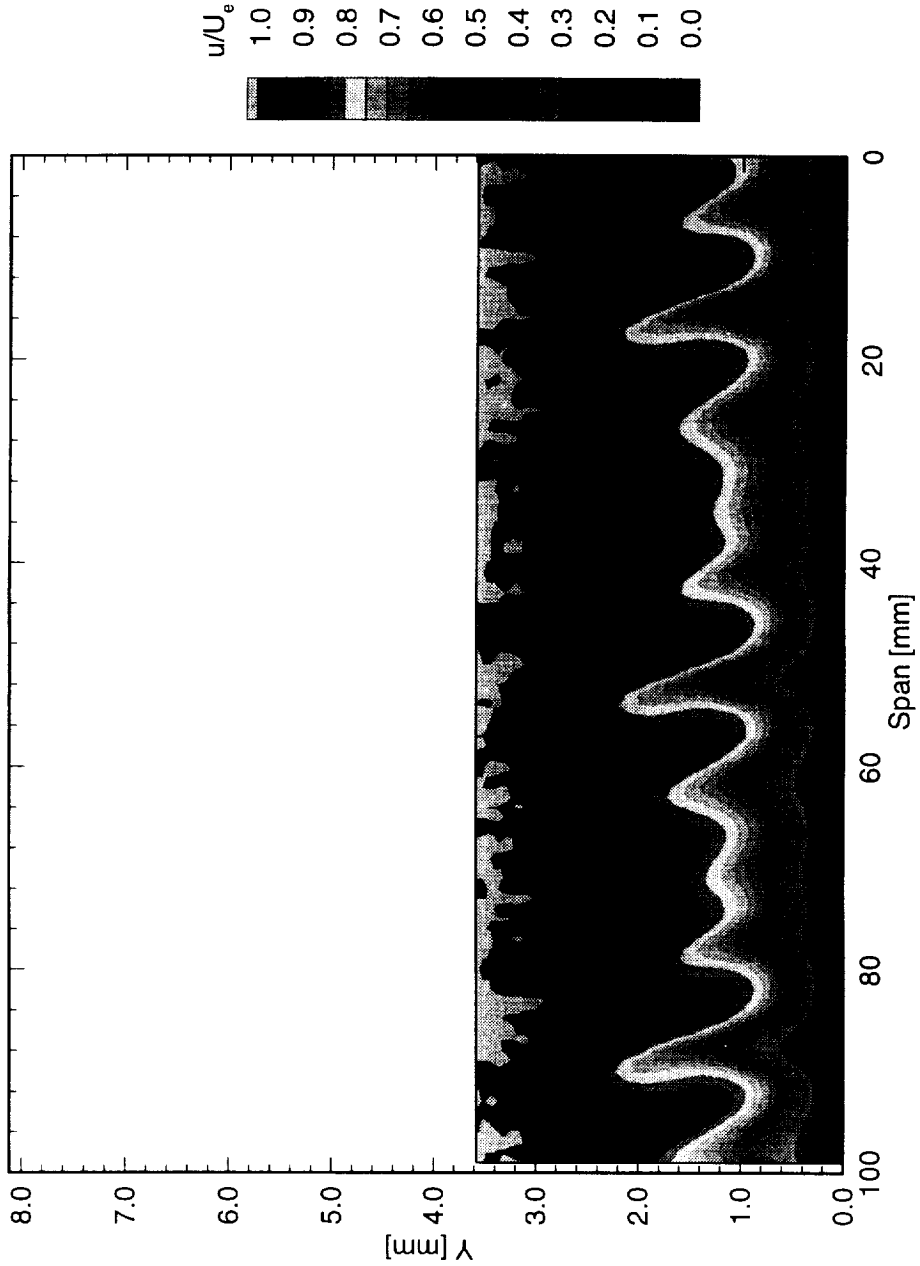

Figure 6.82: Streamwise velocity contours at $x/c = 0.35$. $Re_c = 2.4 \times 10^6$, [6|36] roughness.

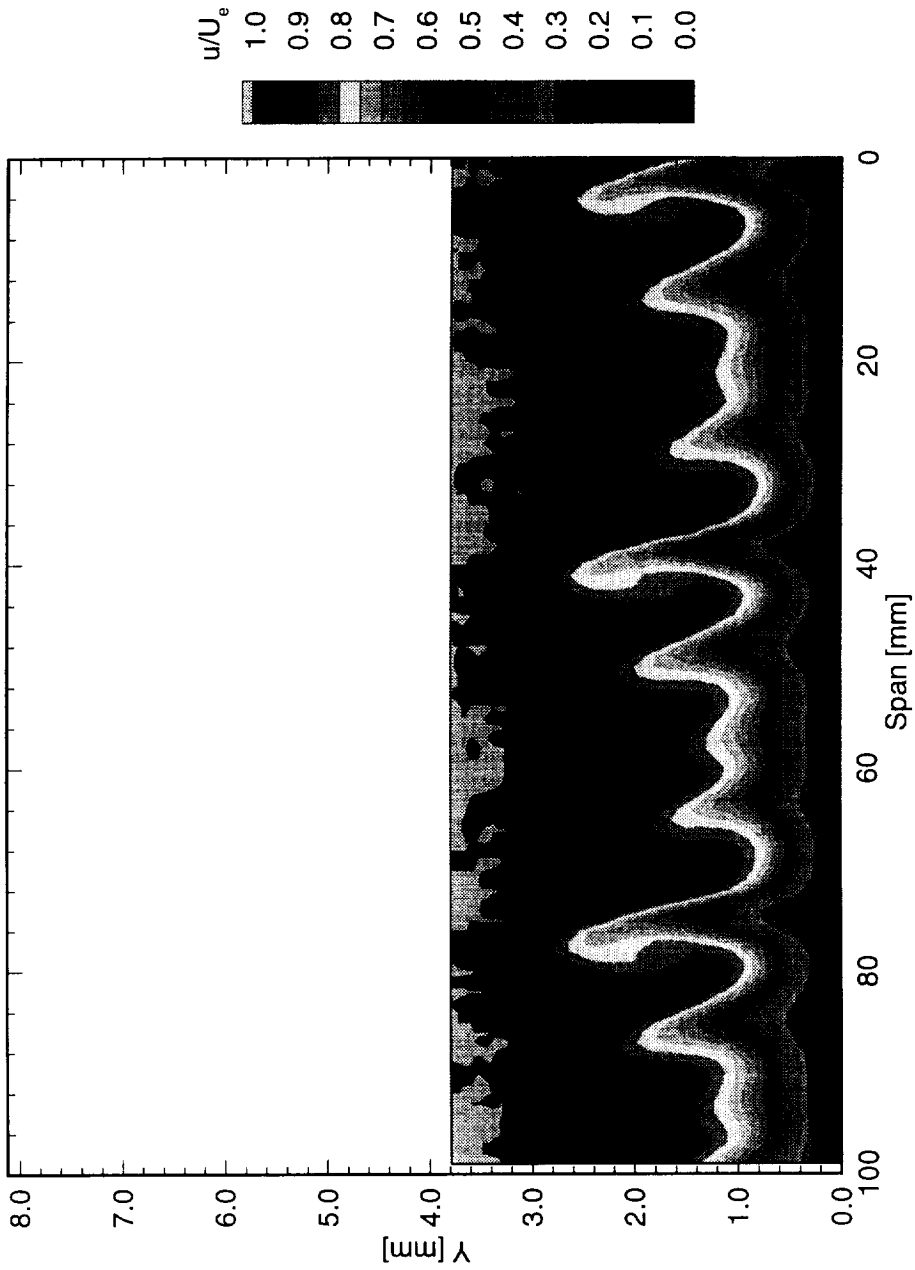

Figure 6.83: Streamwise velocity contours at $x/c = 0.40$. $Re_c = 2.4 \times 10^6$, [6|36] roughness.

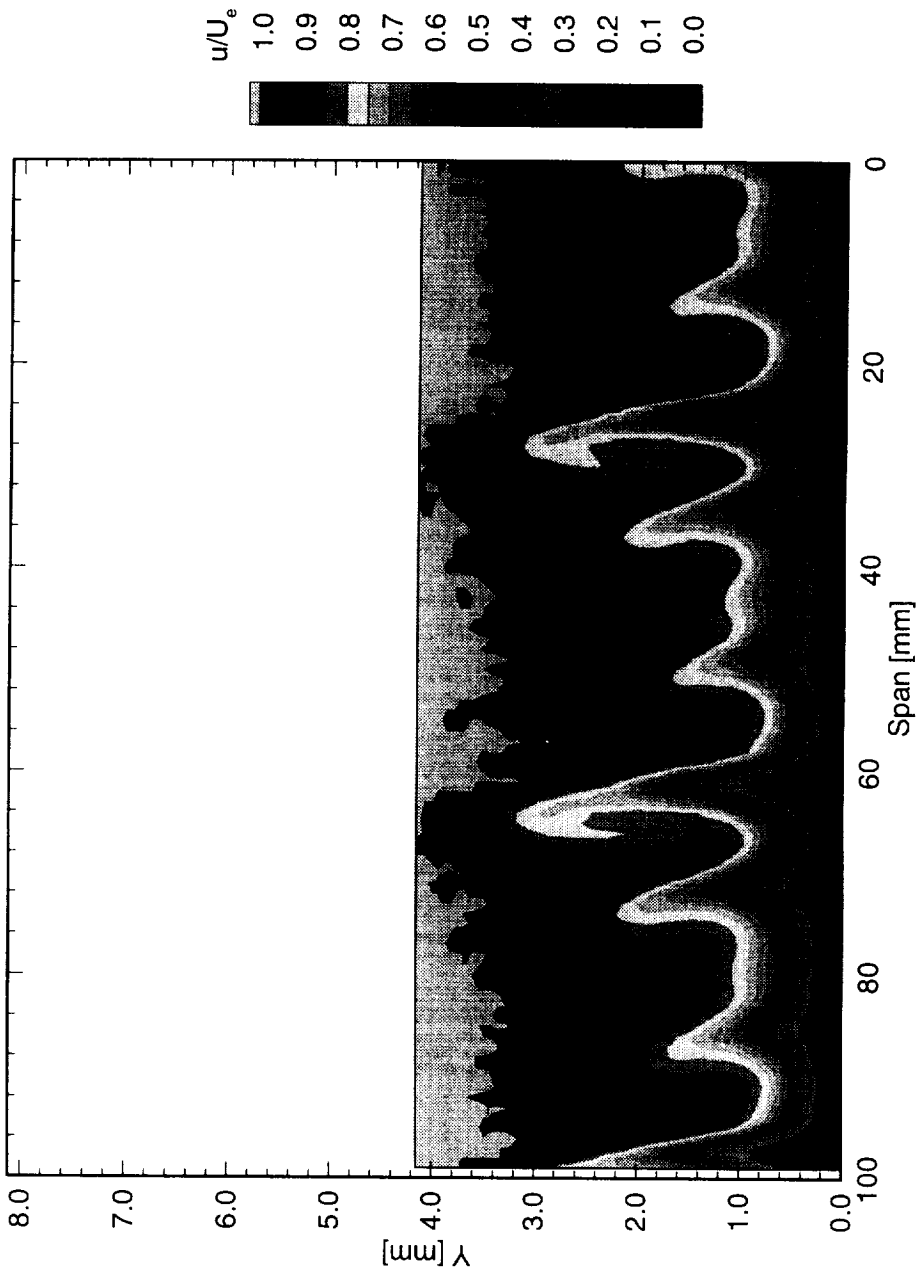

Figure 6.84: Streamwise velocity contours at $x/c = 0.45$. $Re_c = 2.4 \times 10^6$, [6|36] roughness.

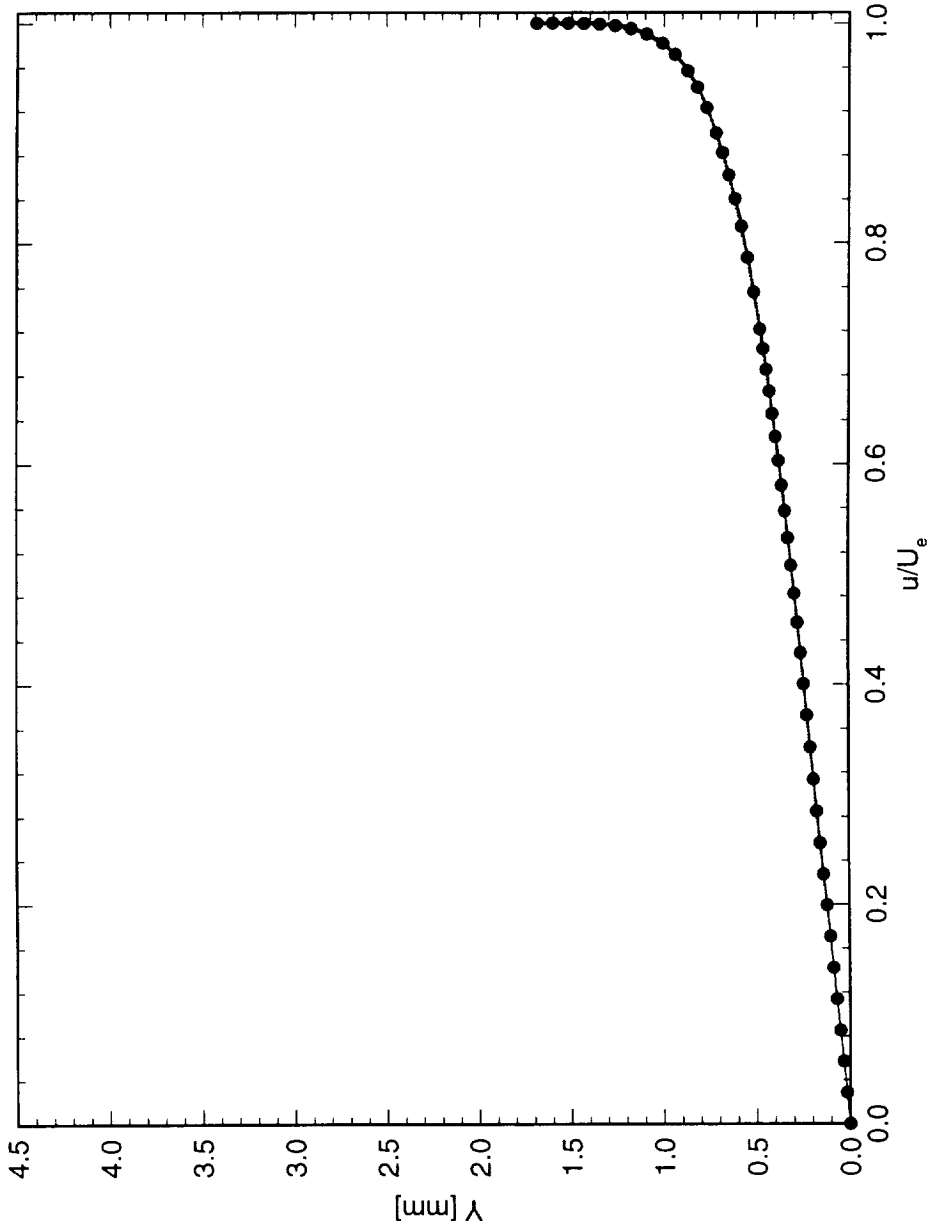

Figure 6.85: Spanwise array of 100 mean-flow boundary-layer profiles covering a span of 99 mm at $x/c = 0.05$. $Re_c = 2.4 \times 10^6$, [6|36] roughness. The dots indicate the mean of the profiles.

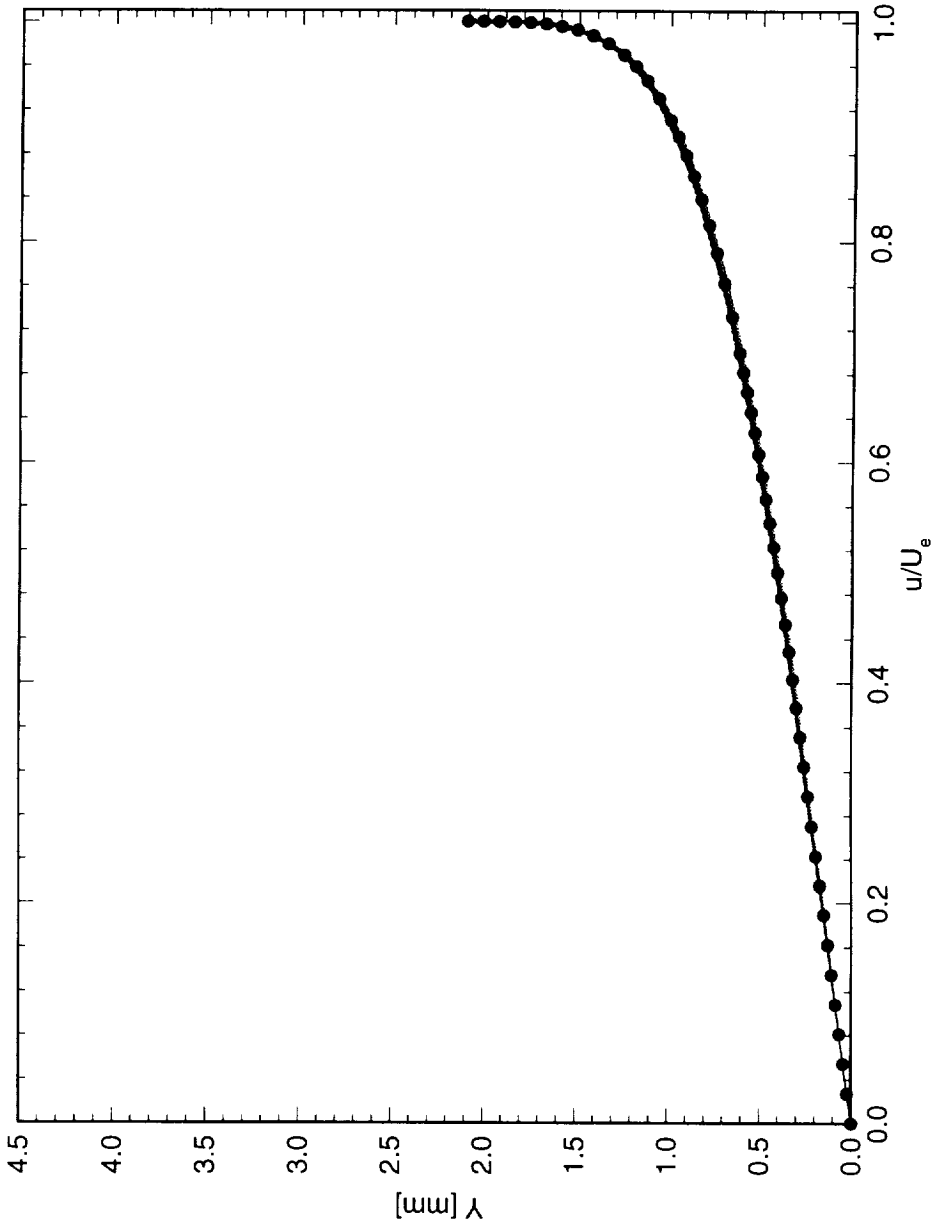

Figure 6.86: Spanwise array of 100 mean-flow boundary-layer profiles covering a span of 99 mm at $x/c = 0.10$. $Re_c = 2.4 \times 10^6$. [6|36] roughness. The dots indicate the mean of the profiles.

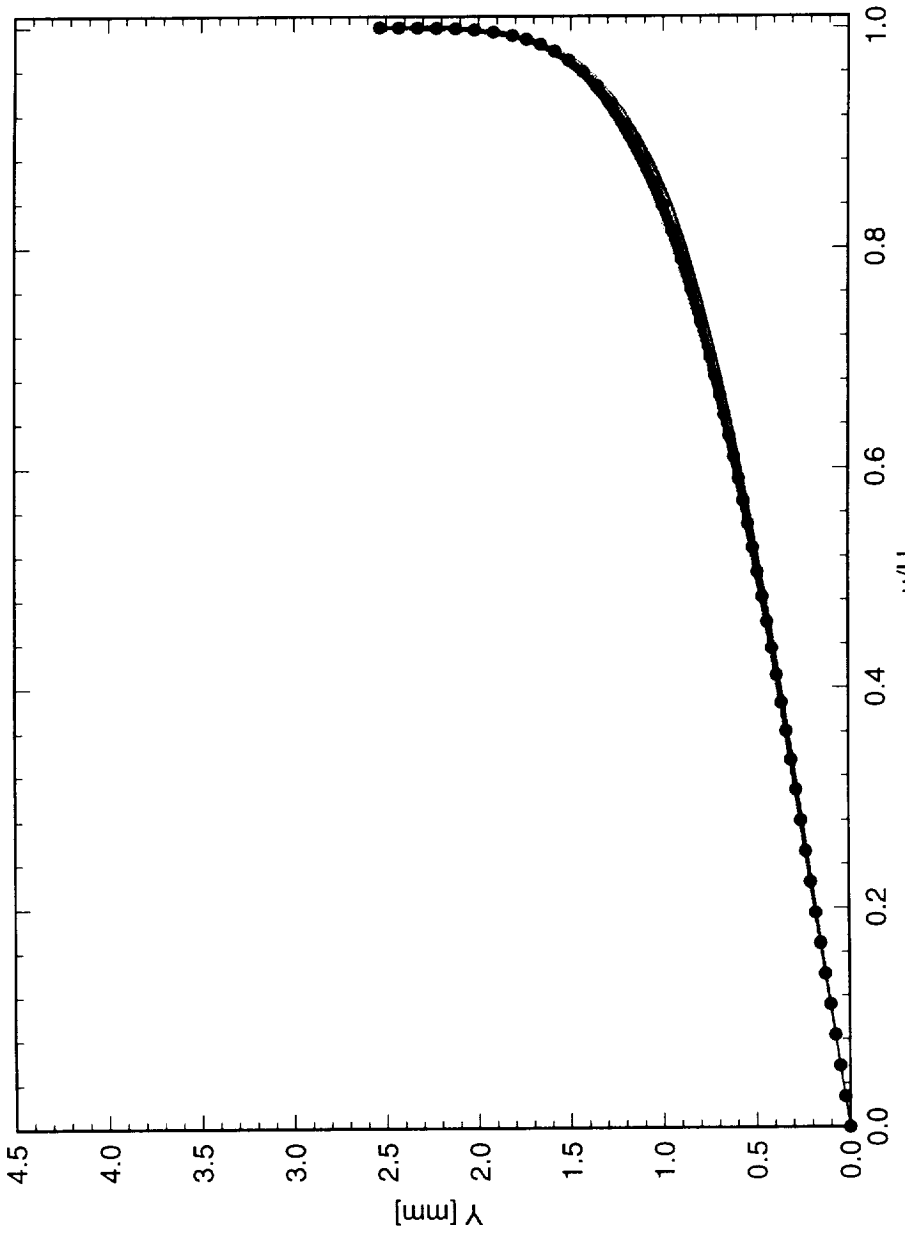

Figure 6.87: Spanwise array of 100 mean-flow boundary-layer profiles covering a span of 99 mm at $x/c = 0.15$. $Re_c = 2.4 \times 10^6$, [6|36] roughness. The dots indicate the mean of the profiles.

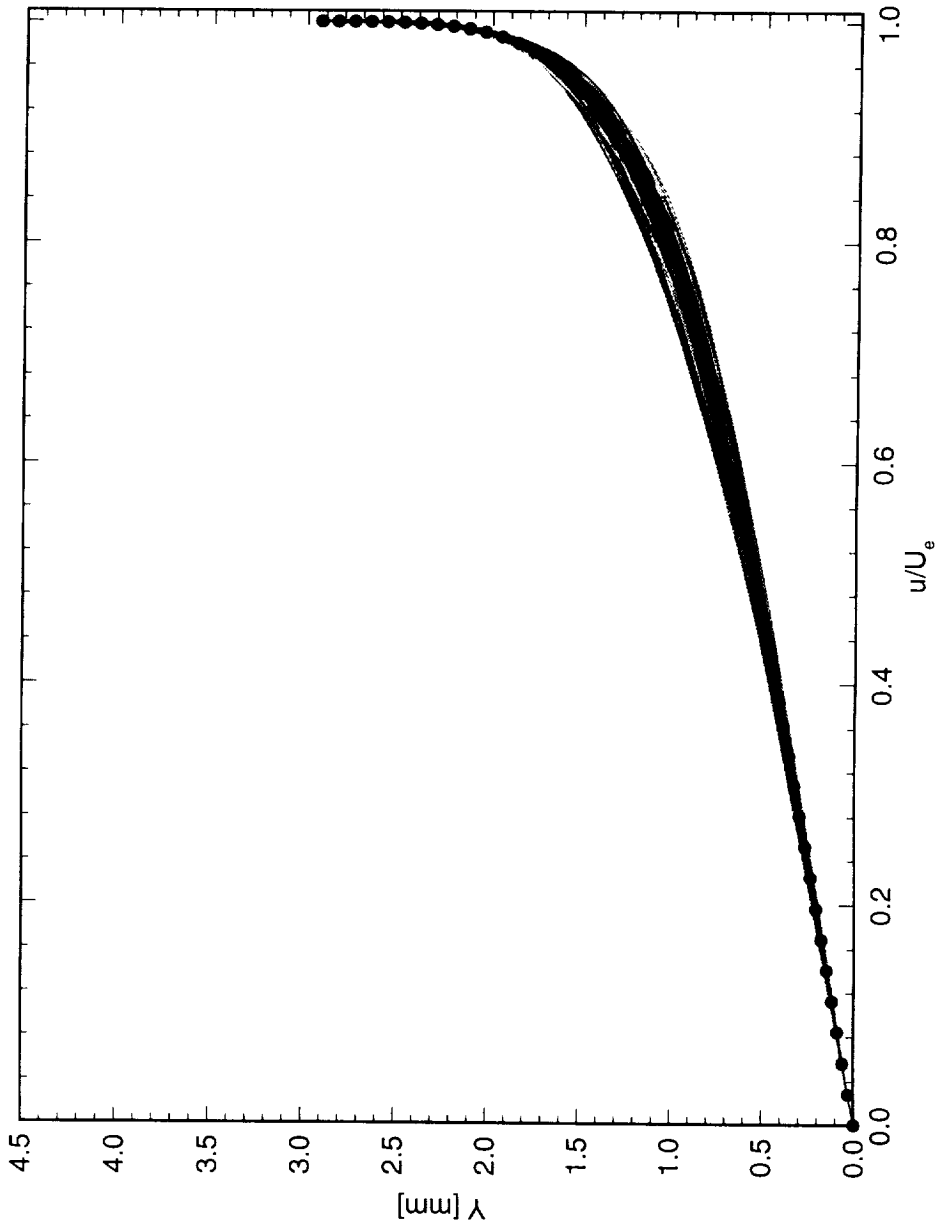

Figure 6.88: Spanwise array of 100 mean-flow boundary-layer profiles covering a span of 99 mm at $x/c = 0.20$. $Re_c = 2.4 \times 10^6$, [6|36] roughness. The dots indicate the mean of the profiles.

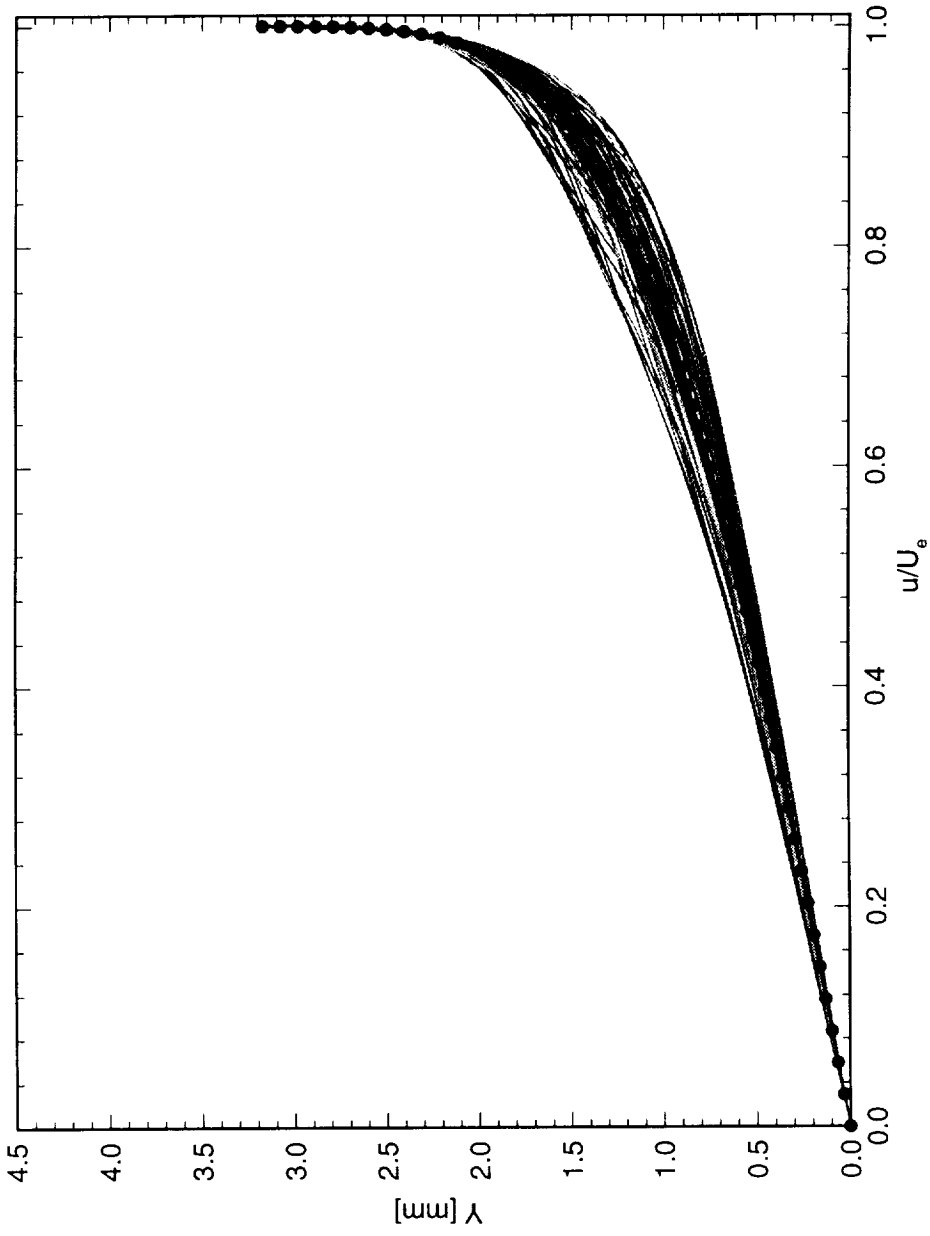

Figure 6.89: Spanwise array of 100 mean-flow boundary-layer profiles covering a span of 99 mm at $x/c = 0.25$. $Re_c = 2.4 \times 10^6$, [6|36] roughness. The dots indicate the mean of the profiles.

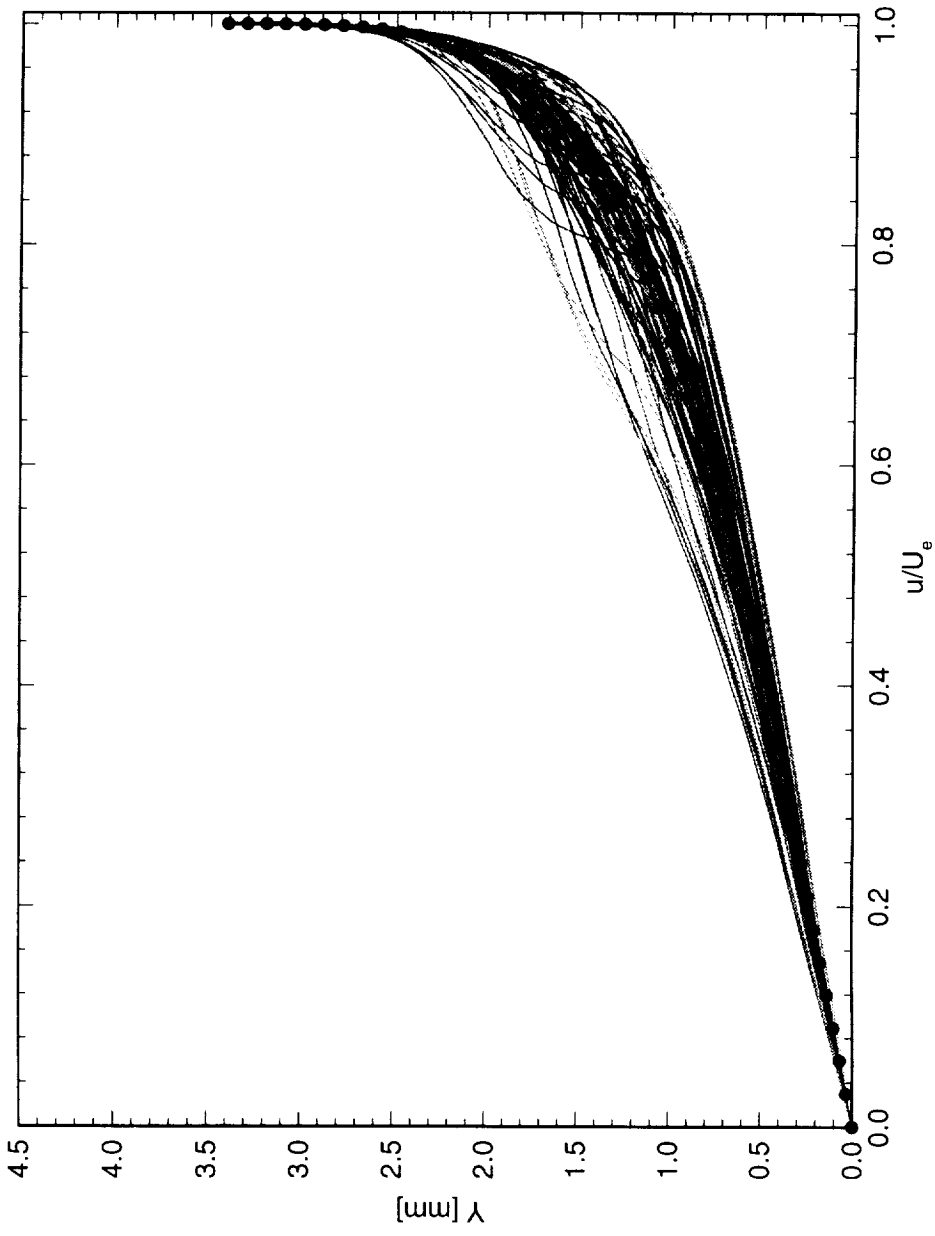

Figure 6.90: Spanwise array of 100 mean-flow boundary-layer profiles covering a span of 99 mm at $x/c = 0.30$. $Re_c = 2.4 \times 10^6$, [6|36] roughness. The dots indicate the mean of the profiles.

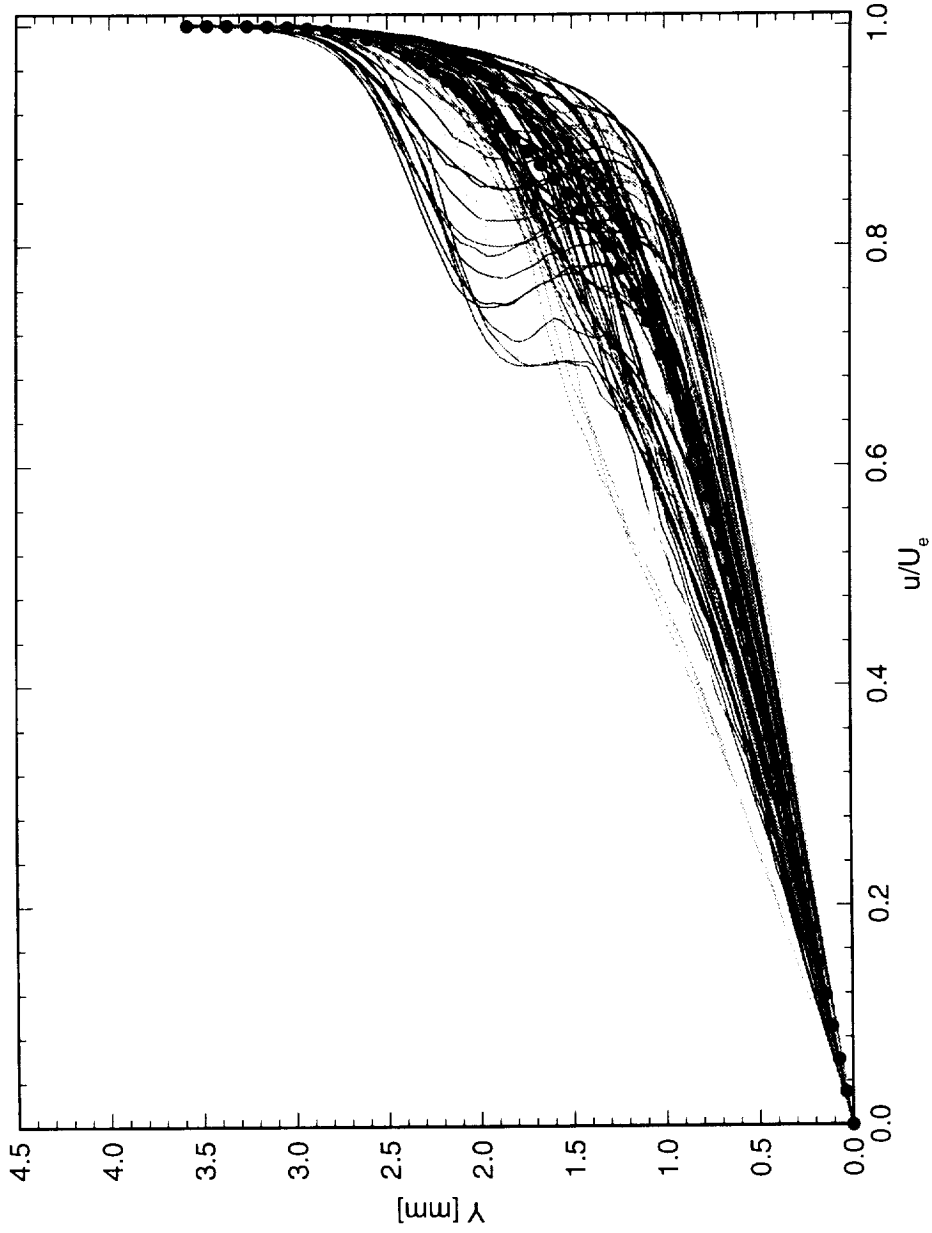

Figure 6.91: Spanwise array of 100 mean-flow boundary-layer profiles covering a span of 99 mm at $x/c = 0.35$. $Re_c = 2.4 \times 10^6$, [6|36] roughness. The dots indicate the mean of the profiles.

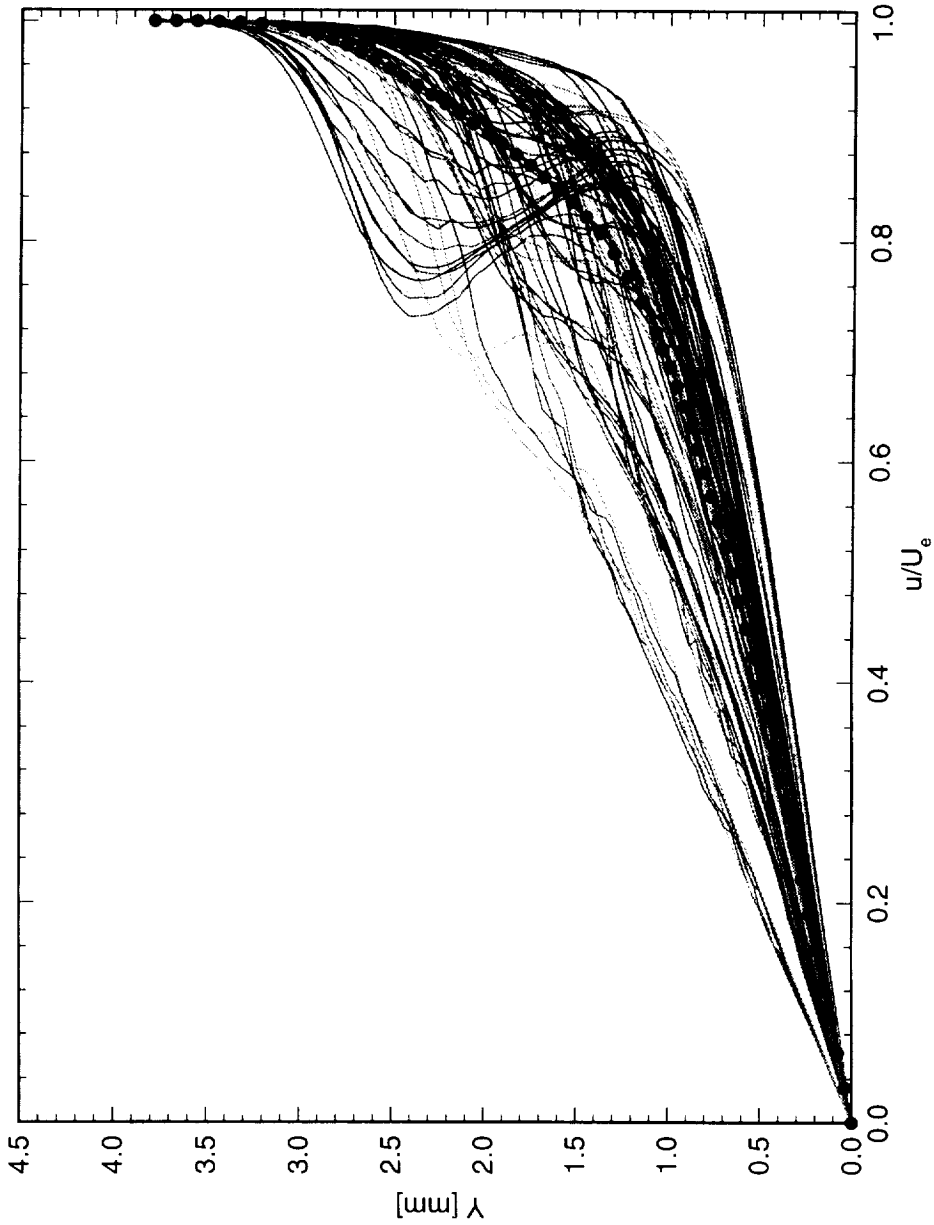

Figure 6.92: Spanwise array of 100 mean-flow boundary-layer profiles covering a span of 99 mm at $x/c = 0.40$. $Re_c = 2.4 \times 10^6$, [6|36] roughness. The dots indicate the mean of the profiles.

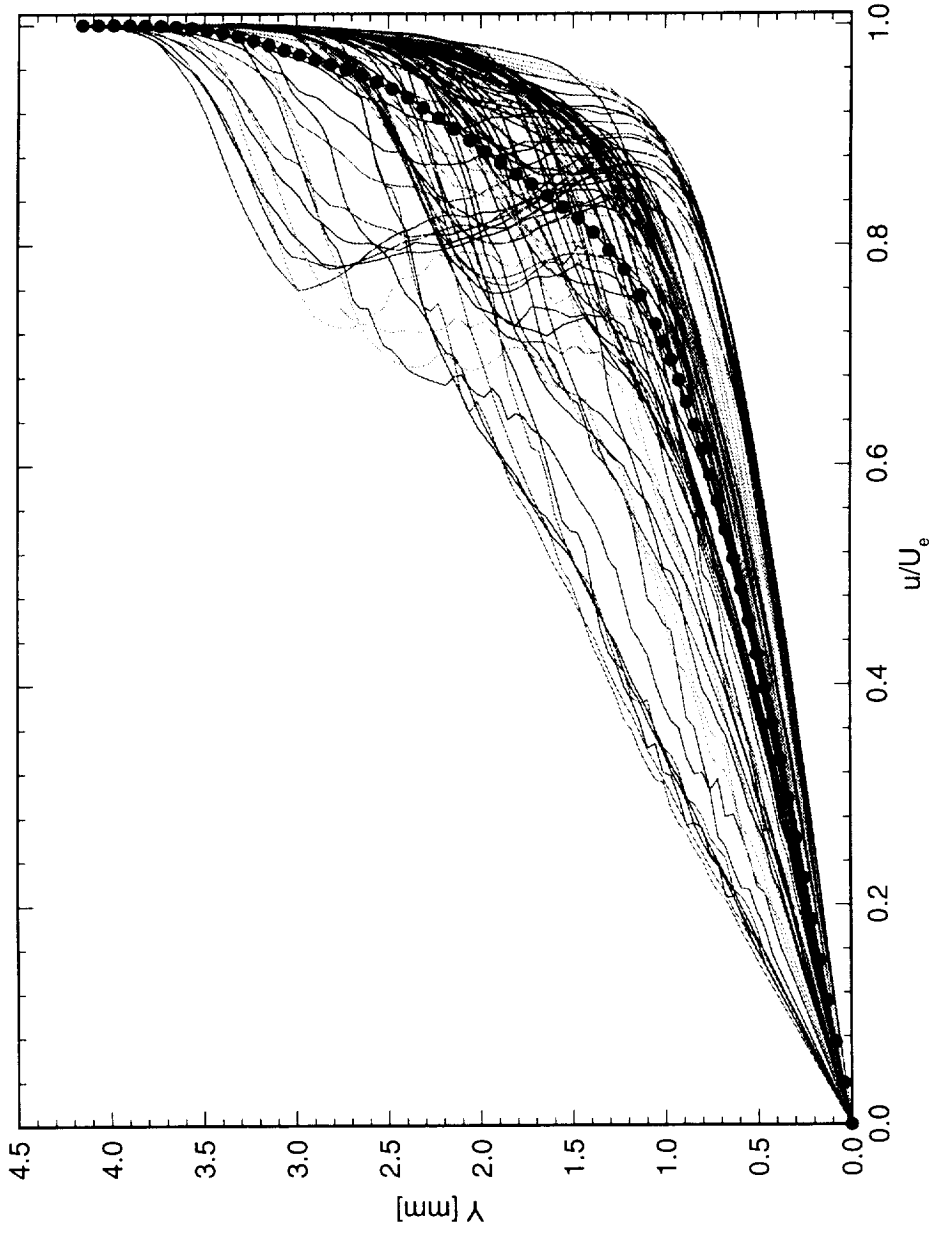

Figure 6.93: Spanwise array of 100 mean-flow boundary-layer profiles covering a span of 99 mm at $x/c = 0.45$. $Re_c = 2.4 \times 10^6$, [6|36] roughness. The dots indicate the mean of the profiles.

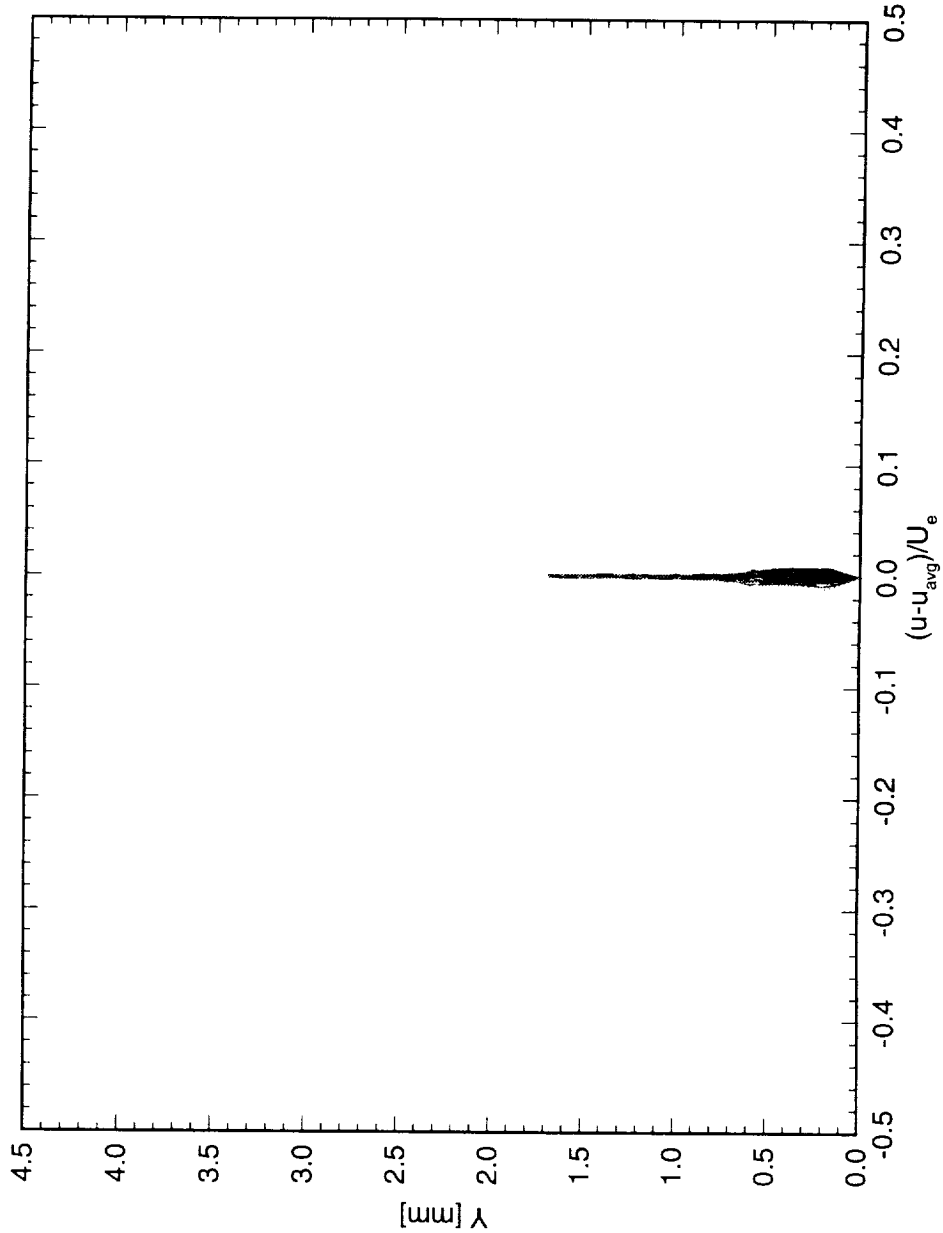

Figure 6.94: Spanwise array of 100 disturbance profiles covering a span of 99 mm at $x/c = 0.05$. $Re_c = 2.4 \times 10^6$, [6|36] roughness.

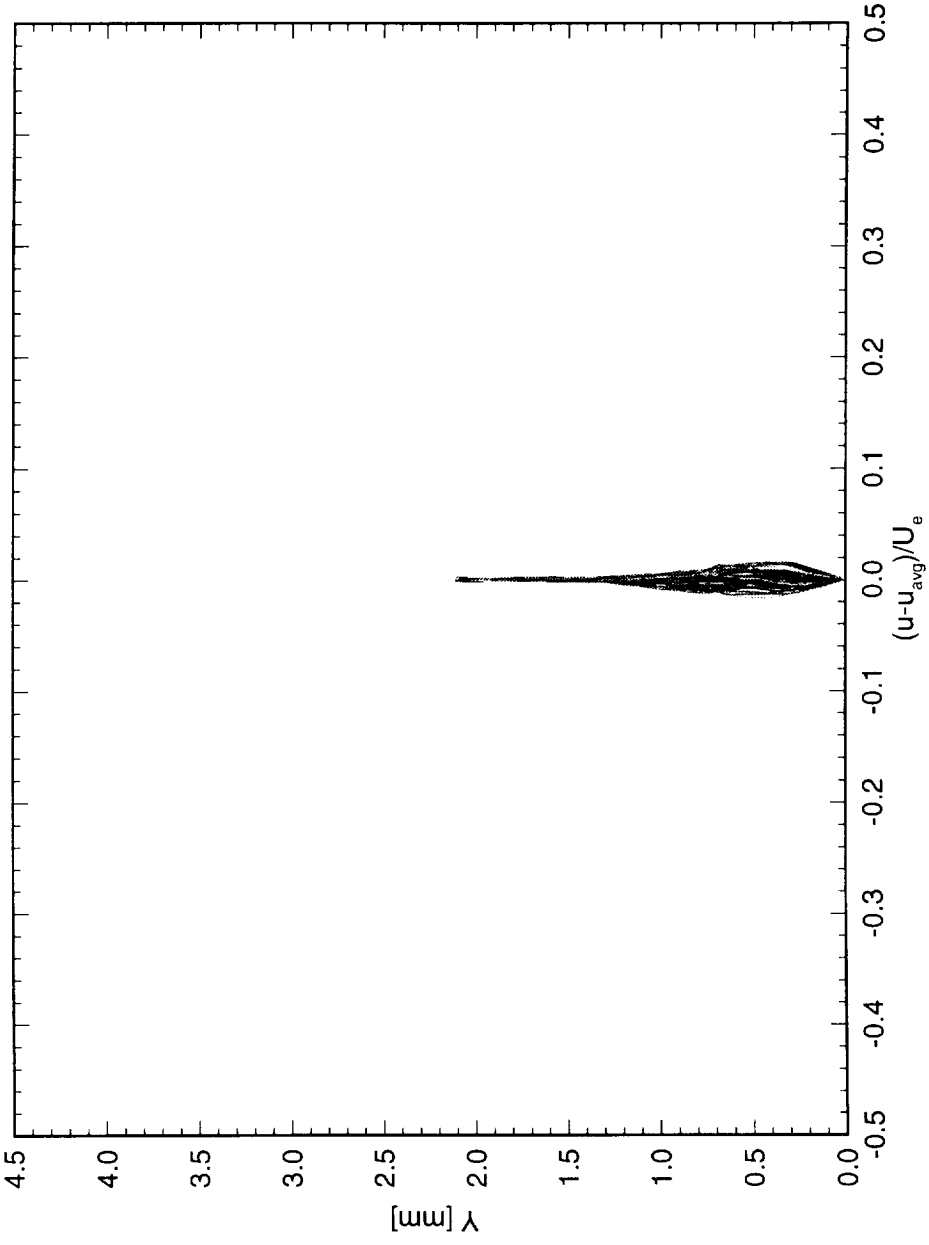

Figure 6.95: Spanwise array of 100 disturbance profiles covering a span of 99 mm at $x/c = 0.10$. $Re_c = 2.4 \times 10^6$, [6|36] roughness.

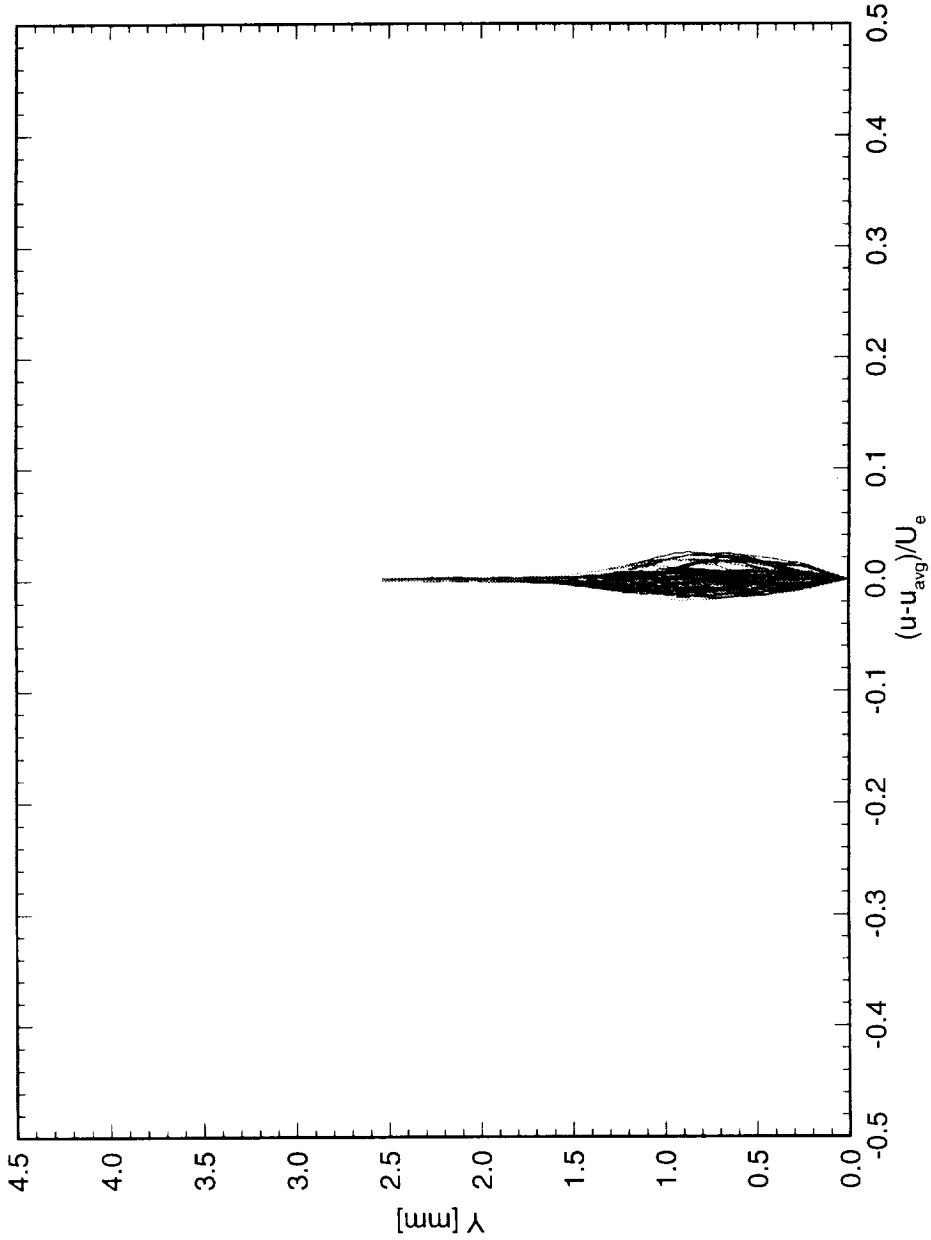

Figure 6.96: Spanwise array of 100 disturbance profiles covering a span of 99 mm at $x/c = 0.15$. $Re_c = 2.4 \times 10^6$, [6|36] roughness.

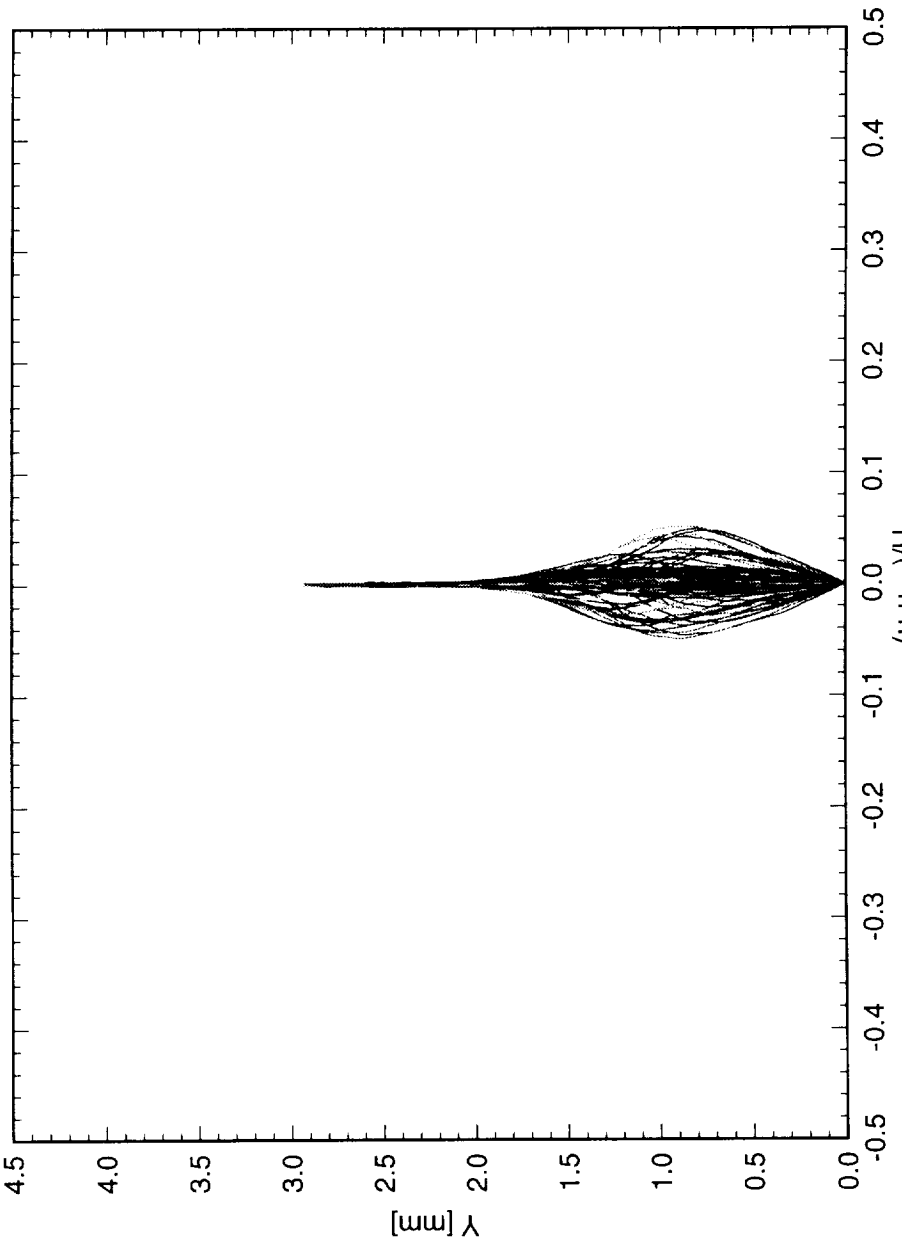

Figure 6.97: Spanwise array of 100 disturbance profiles covering a span of 99 mm at $x/c = 0.20$. $Re_c = 2.4 \times 10^6$, [6|36] roughness.

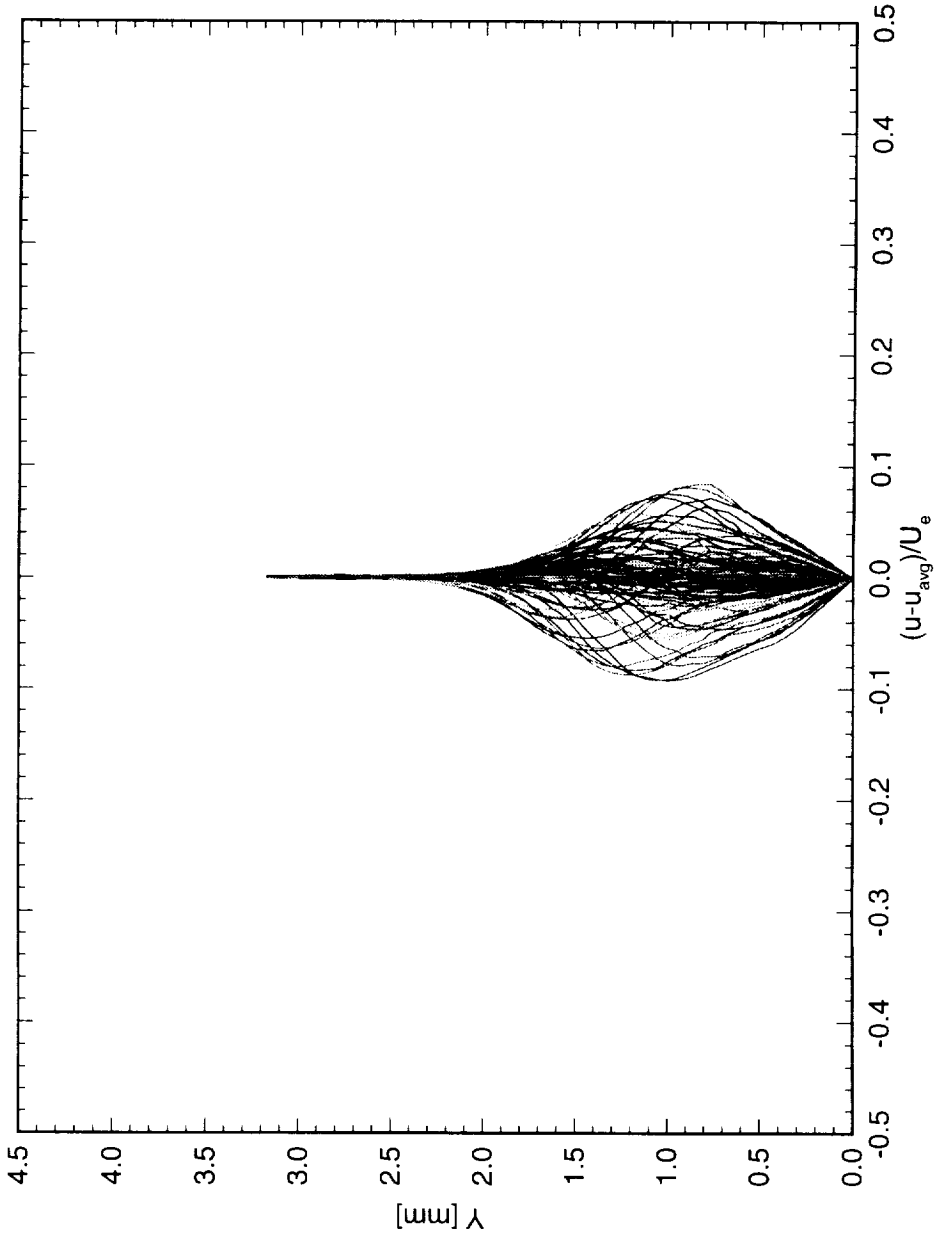

Figure 6.98: Spanwise array of 100 disturbance profiles covering a span of 99 mm at $x/c = 0.25$. $Re_c = 2.4 \times 10^6$, [6|36] roughness.

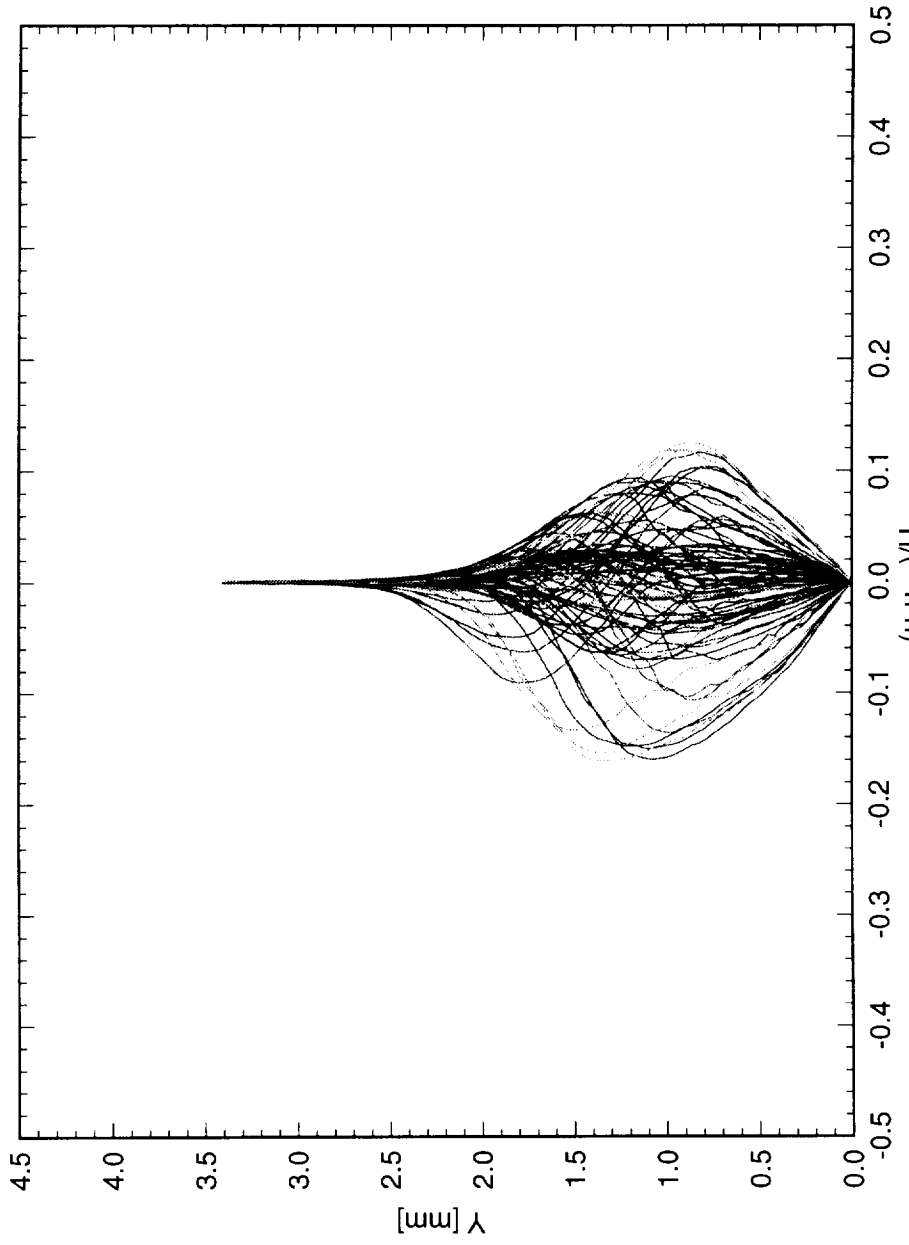

Figure 6.99: Spanwise array of 100 disturbance profiles covering a span of 99 mm at $x/c = 0.30$. $Re_c = 2.4 \times 10^6$, [6|36] roughness.

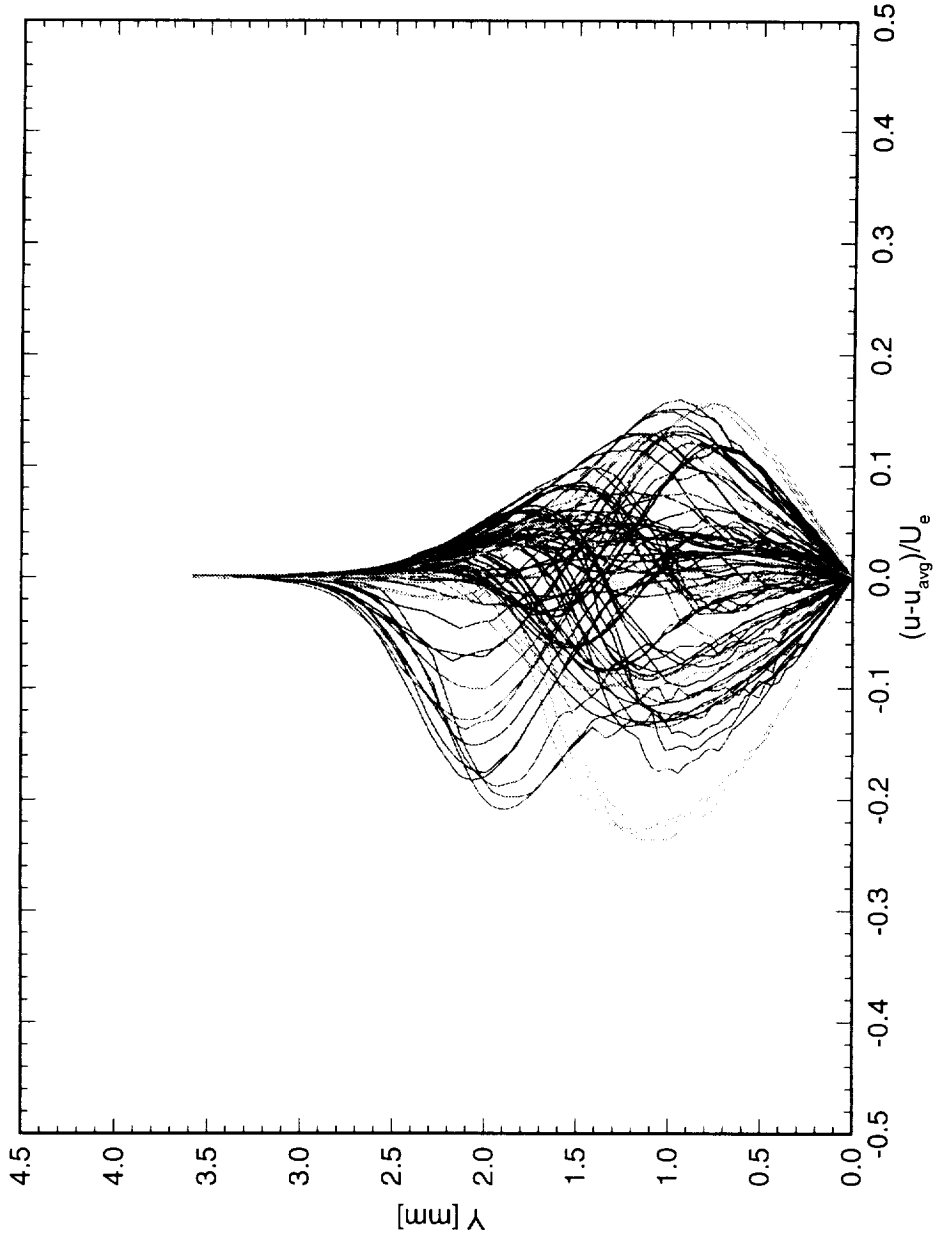

Figure 6.100: Spanwise array of 100 disturbance profiles covering a span of 99 mm at $x/c = 0.35$. $Re_c = 2.4 \times 10^6$, [6|36] roughness.

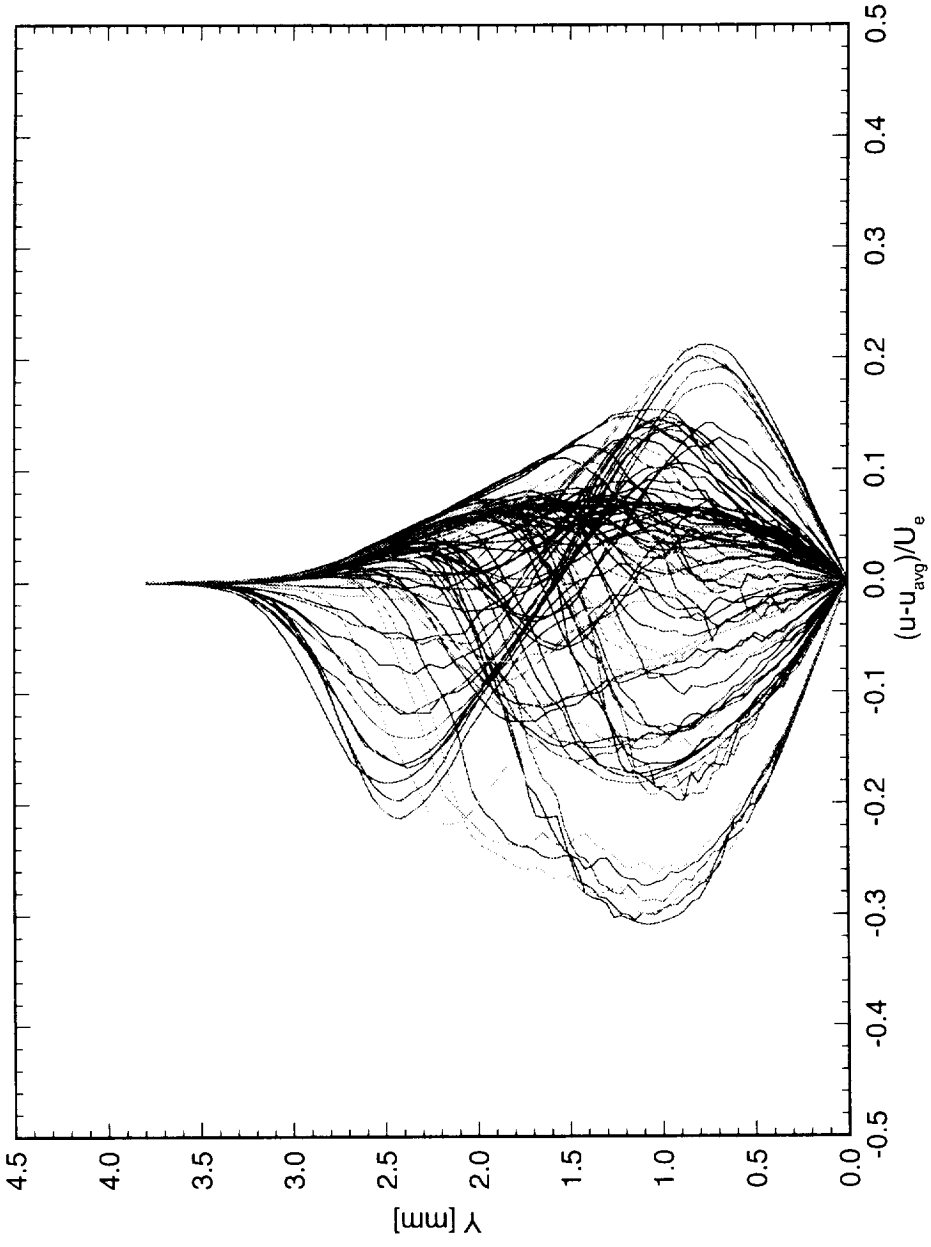

Figure 6.101: Spanwise array of 100 disturbance profiles covering a span of 99 mm at $x/c = 0.40$. $Re_c = 2.4 \times 10^6$, [6|36] roughness.

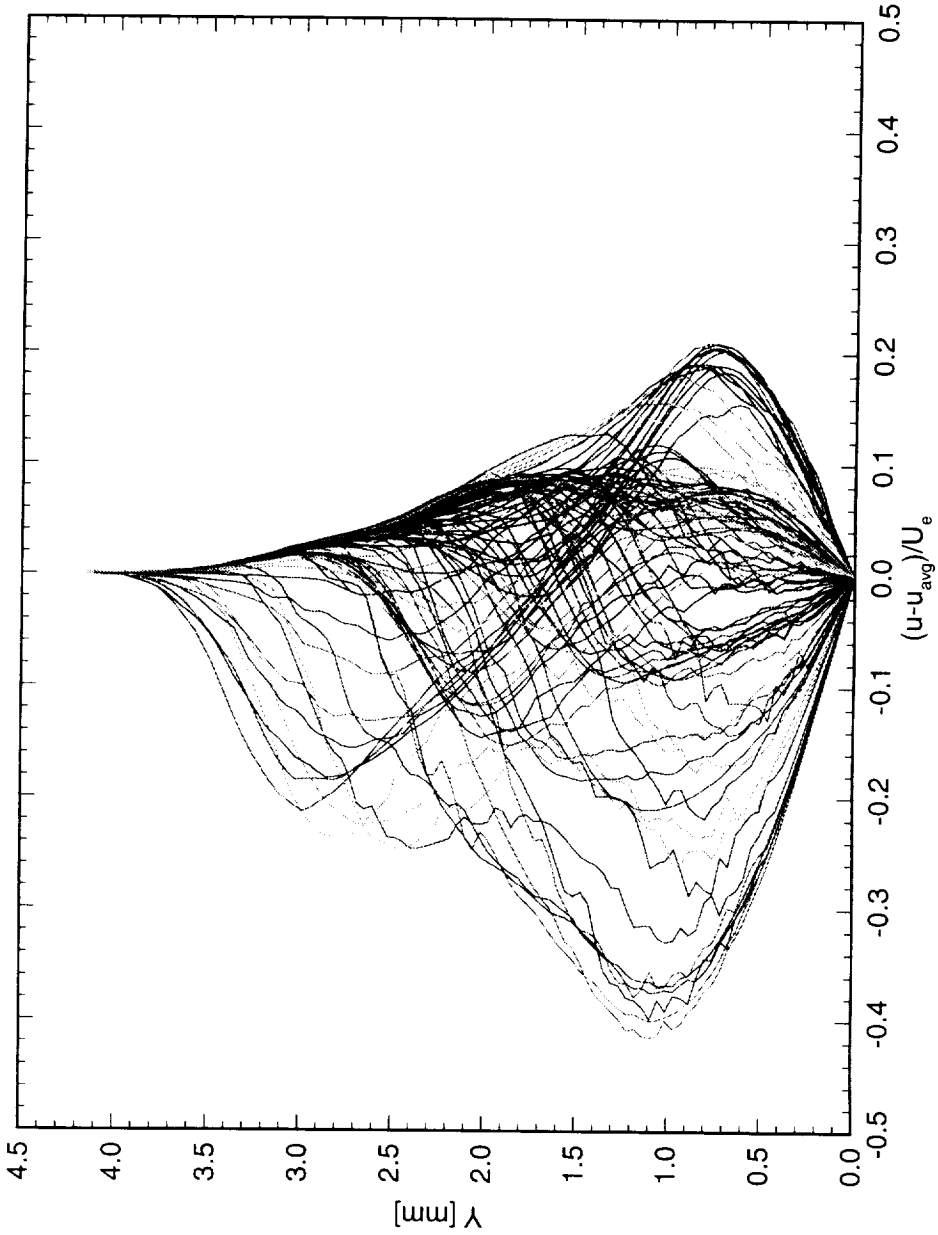

Figure 6.102: Spanwise array of 100 disturbance profiles covering a span of 99 mm at $x/c = 0.45$. $Re_c = 2.4 \times 10^6$, [6|36] roughness.

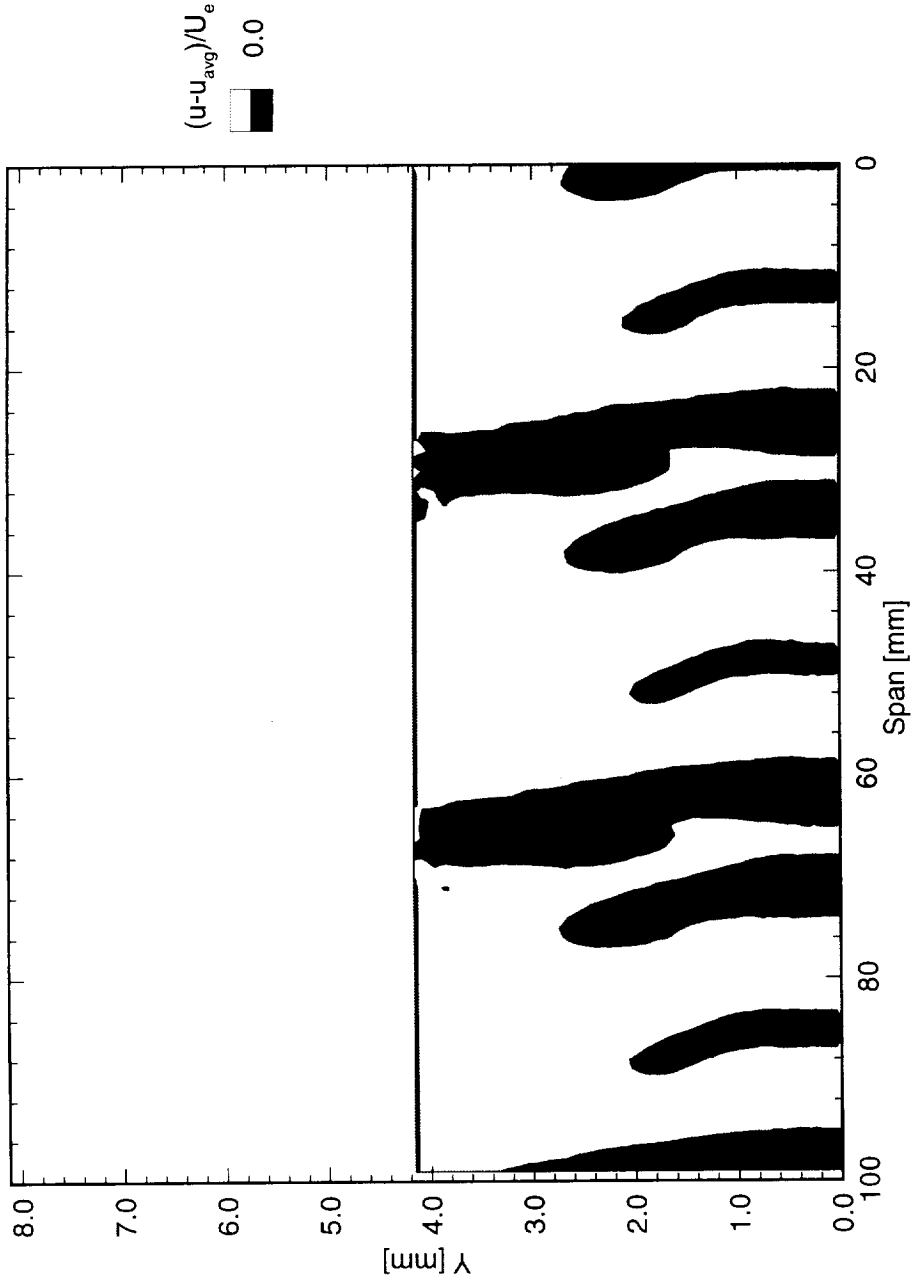

Figure 6.103: Disturbance velocity contours at $x/c = 0.45$. $Re_c = 2.4 \times 10^6$, [6|36] roughness.

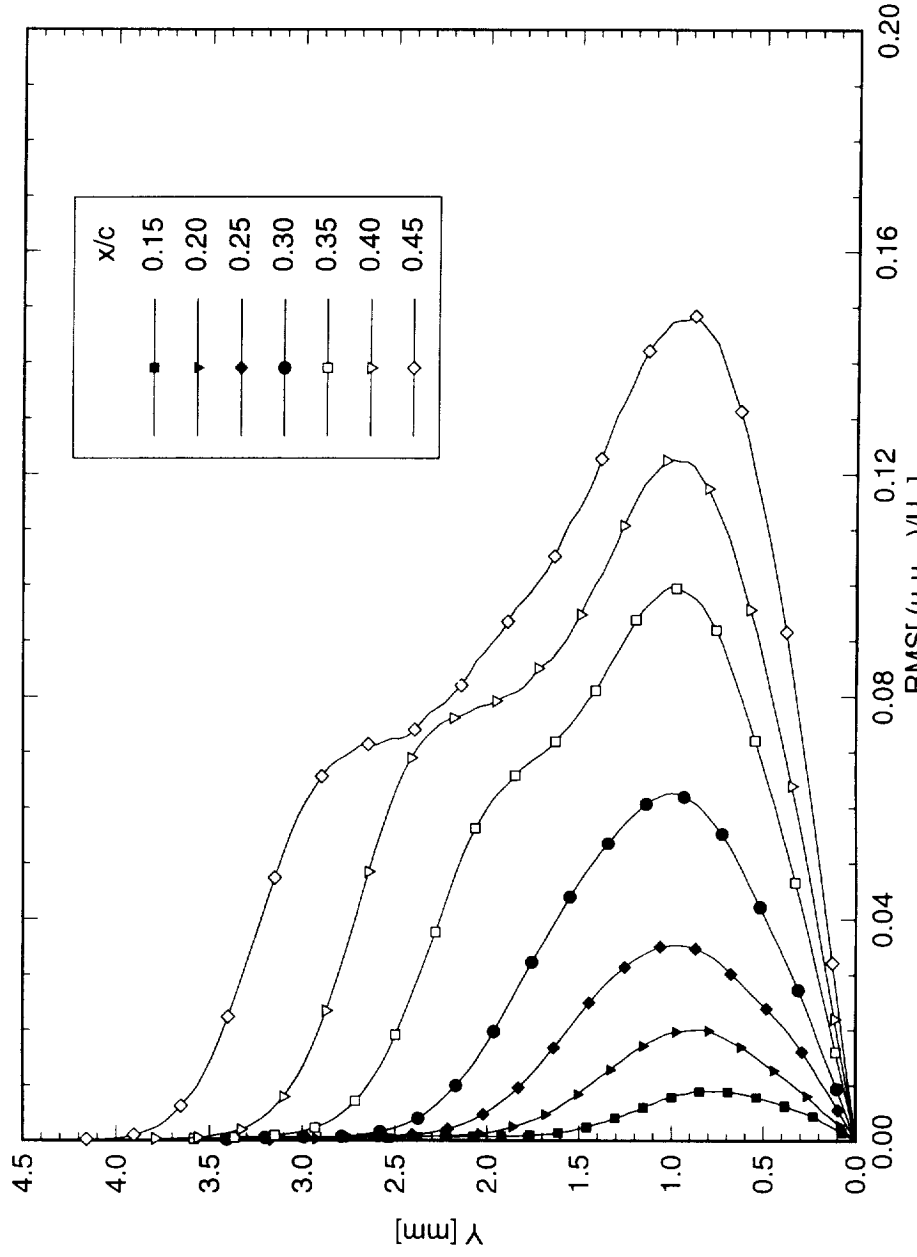

Figure 6.104: Stationary crossflow mode shapes for $Re_c = 2.4 \times 10^6$ and [6|36] roughness. The symbols are simply identifiers and do not represent measurement points.

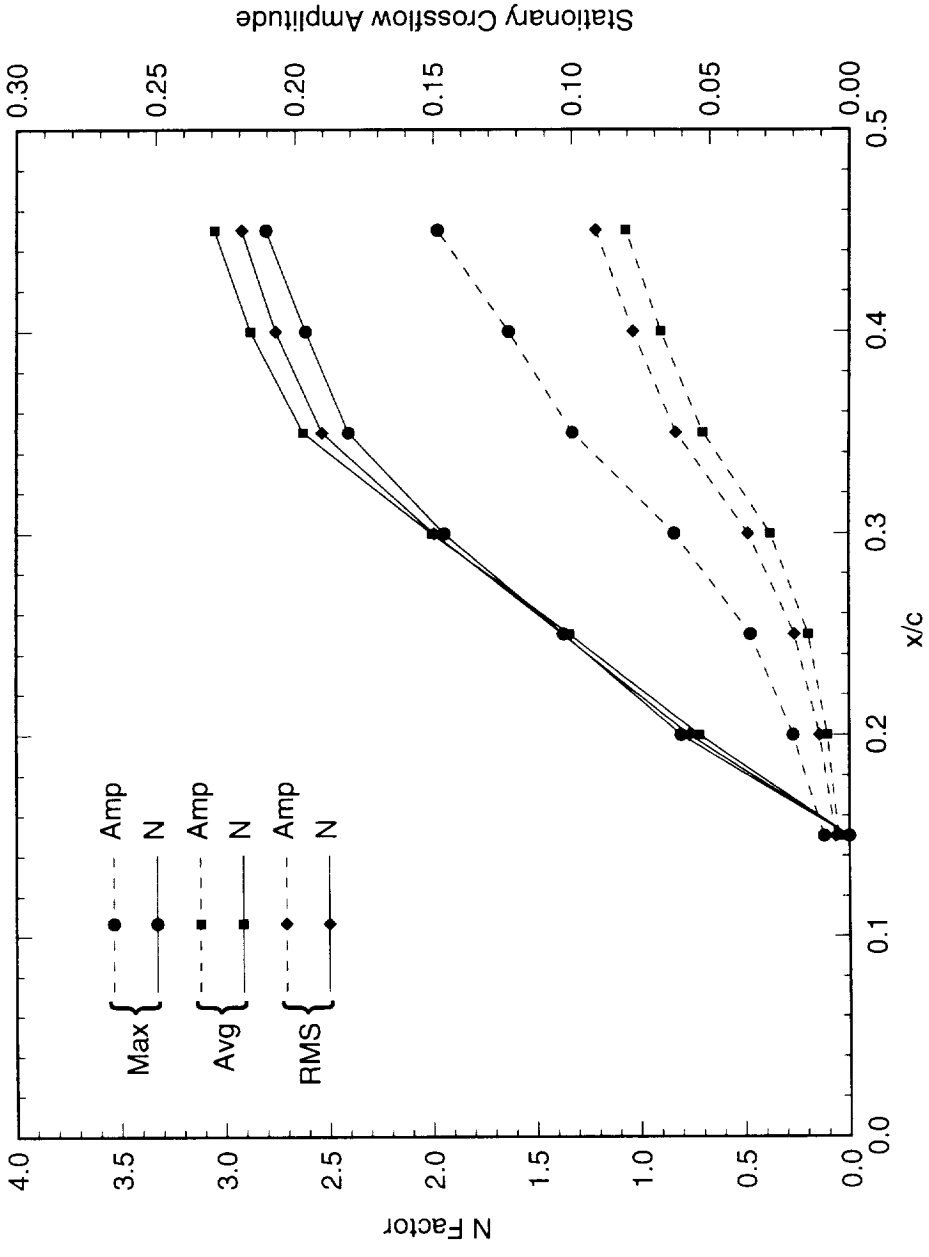

Figure 6.105: Total disturbance amplitude and amplification factor N for $Re_c = 2.4 \times 10^6$ and [6|36] roughness. The reference point for the N-factor calculations is $x/c = 0.15$.

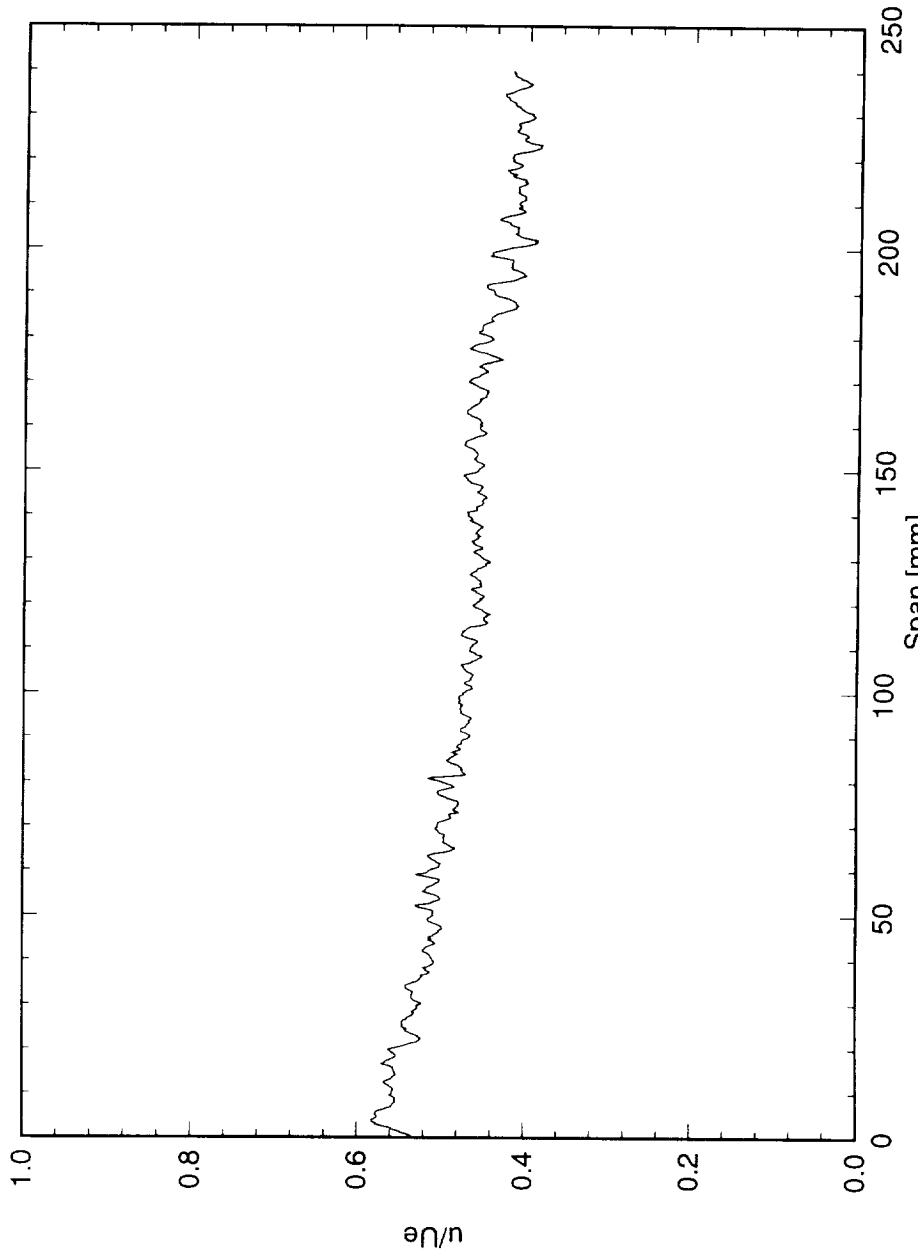

Figure 6.106: Spanwise hot-wire scan at $x/c = 0.10$, $Y = 0.4$ mm. $Re_c = 2.4 \times 10^6$, [6|36] roughness.

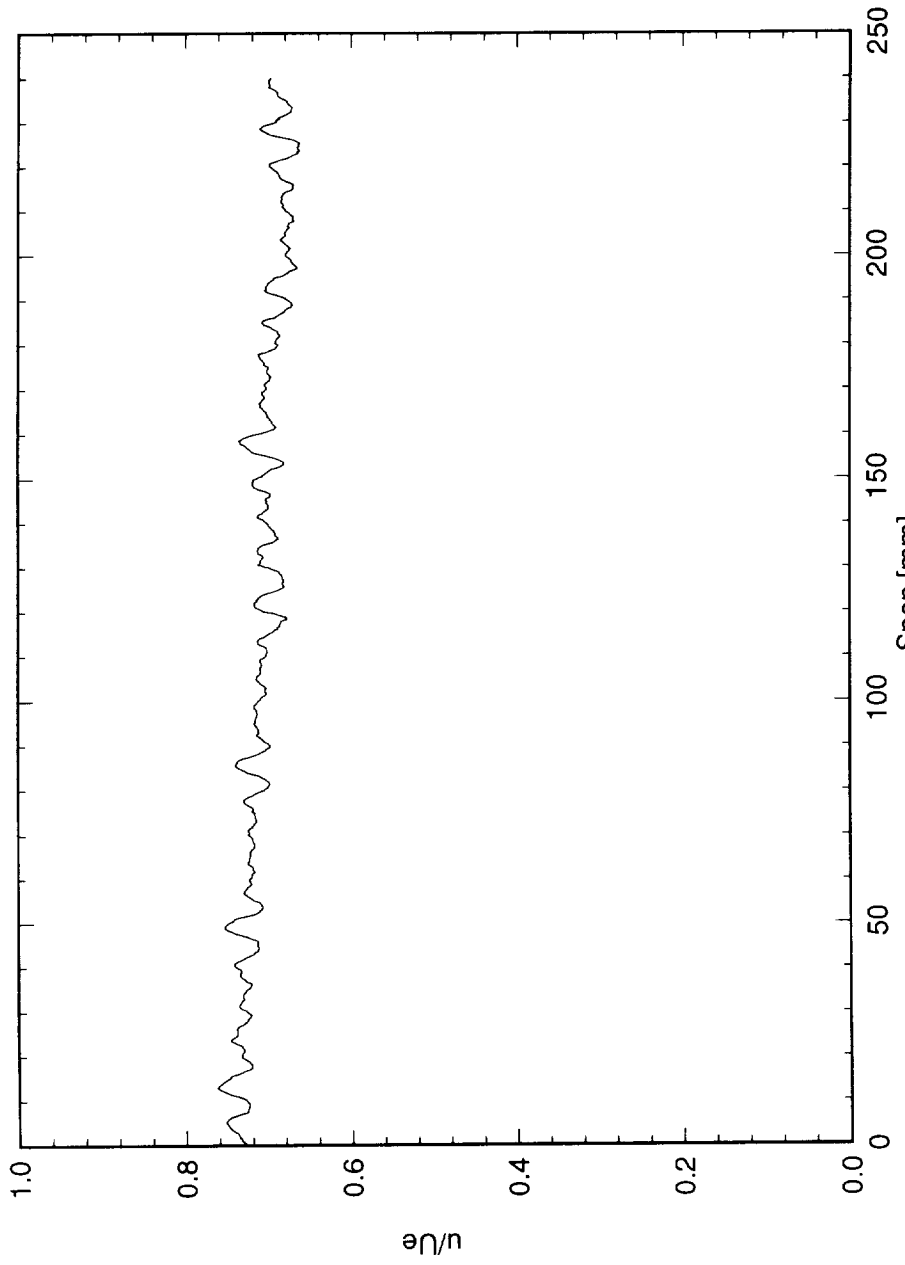

Figure 6.107: Spanwise hot-wire scan at $x/c = 0.15$, $Y = 0.8$ mm. $Re_c = 2.4 \times 10^6$, [6|36] roughness.

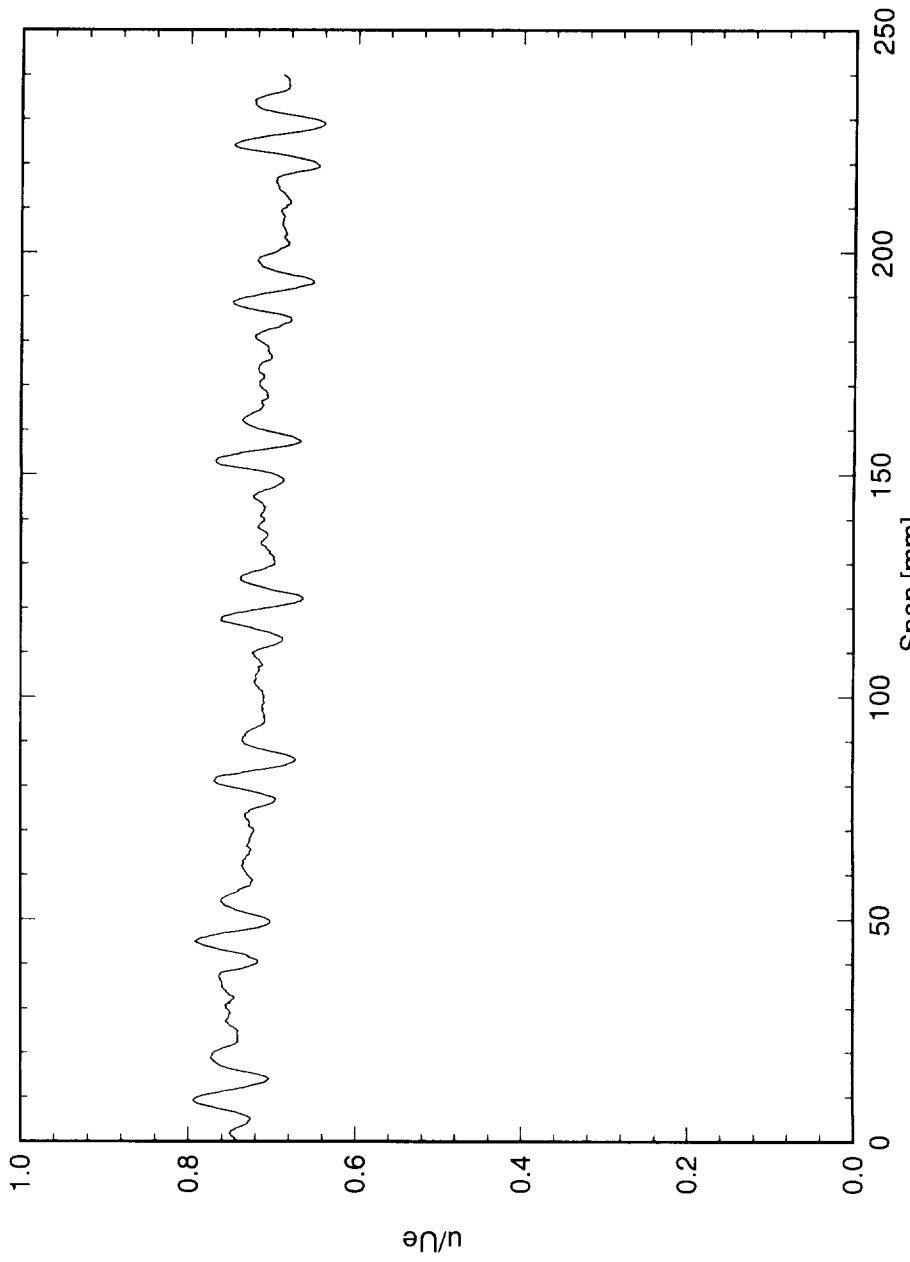

Figure 6.108: Spanwise hot-wire scan at $x/c = 0.20$, $Y = 0.9$ mm. $Re_c = 2.4 \times 10^6$, [6|36] roughness.

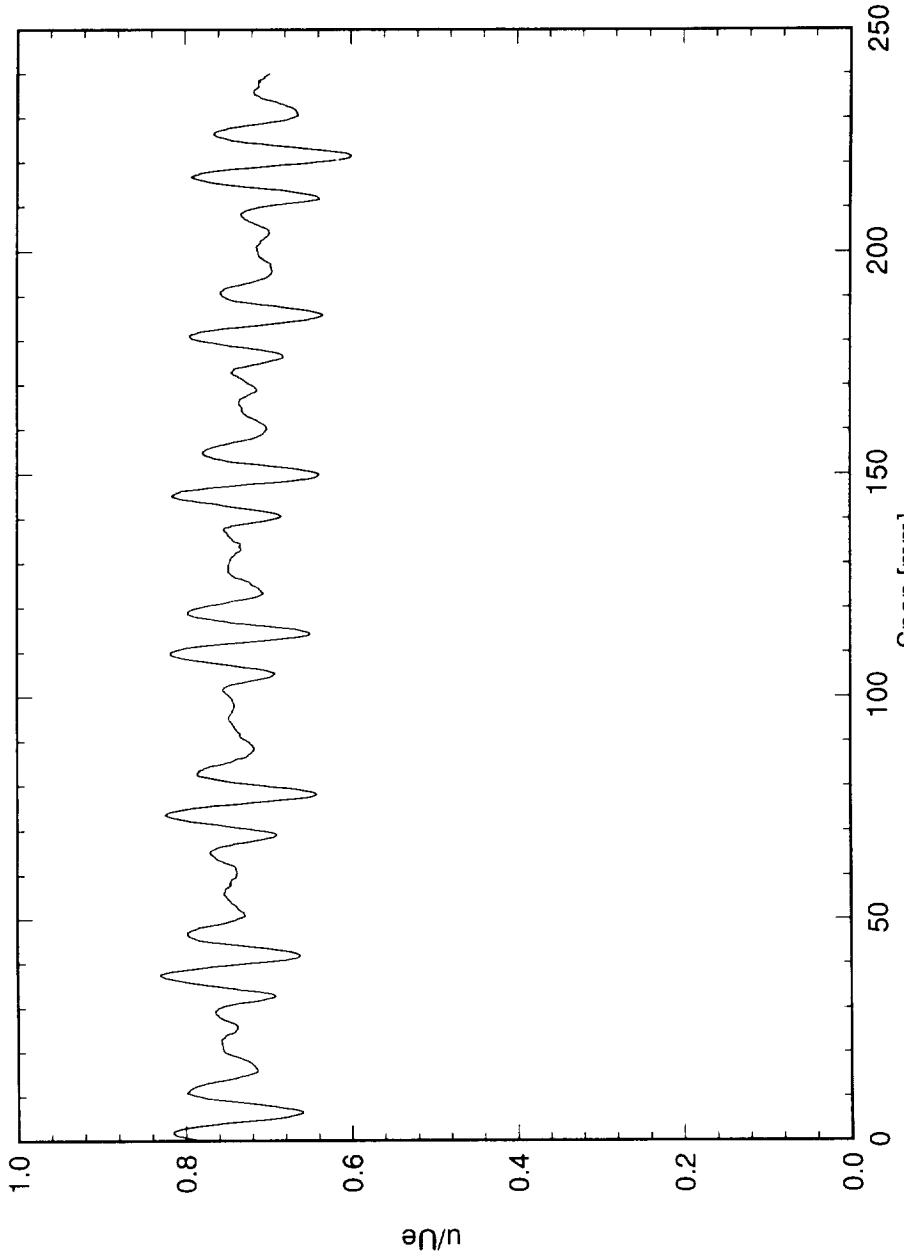

Figure 6.109: Spanwise hot-wire scan at $x/c = 0.25$, $Y = 1.0$ mm. $Re_c = 2.4 \times 10^6$, [6|36] roughness.

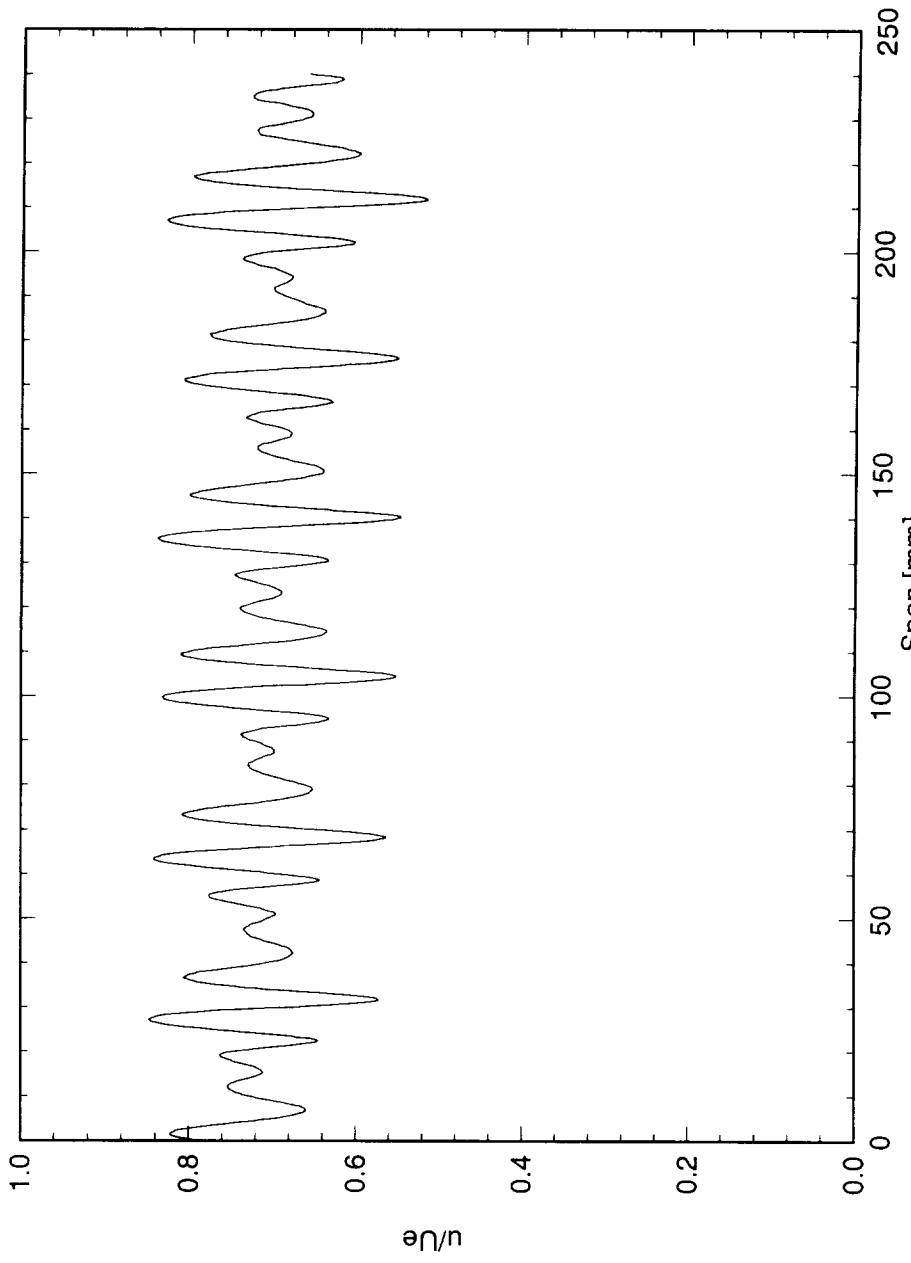

Figure 6.110: Spanwise hot-wire scan at $x/c = 0.30$, $Y = 1.0$ mm. $Re_c = 2.4 \times 10^6$, [6|36] roughness.

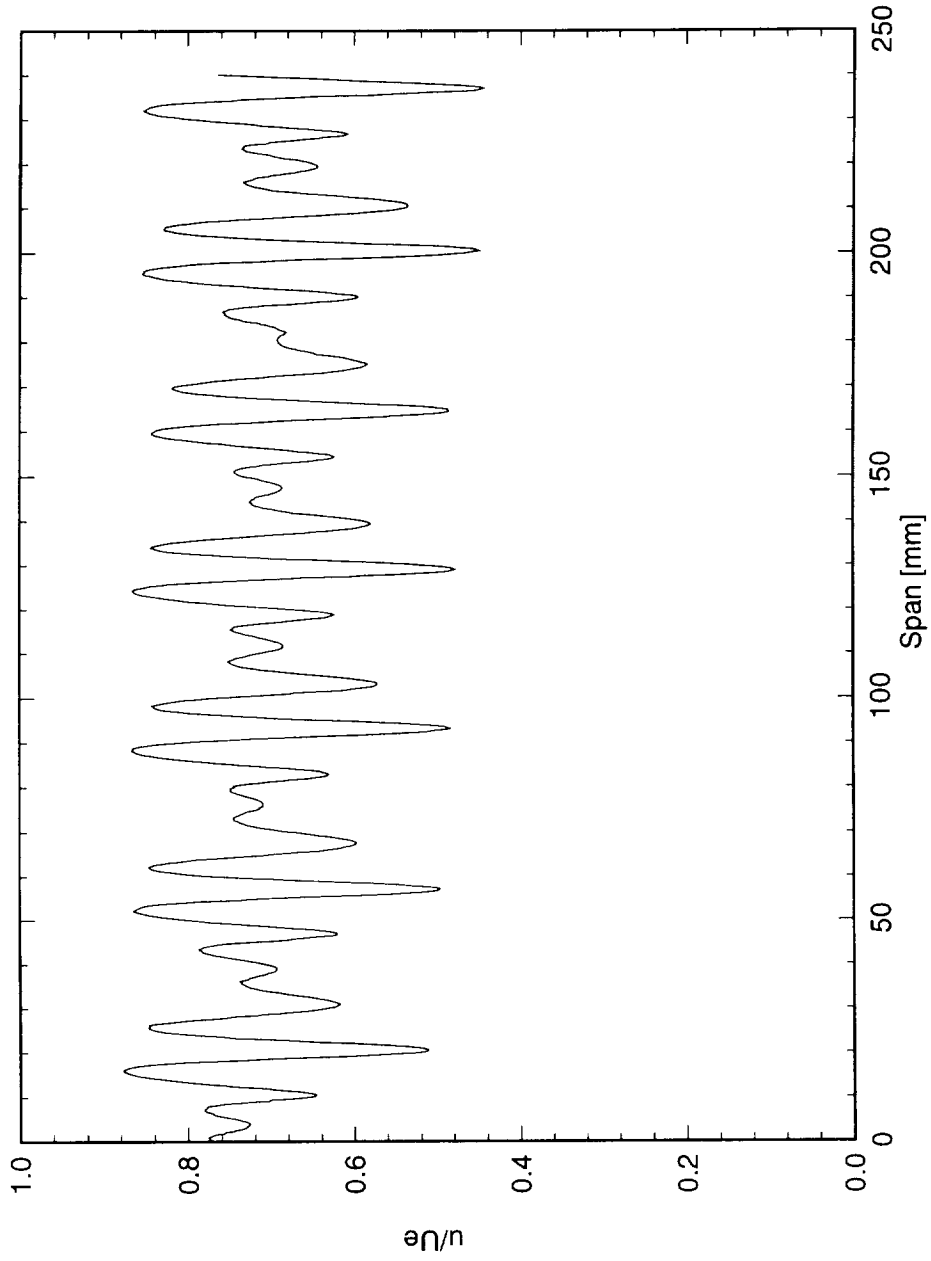

Figure 6.111: Spanwise hot-wire scan at $x/c = 0.35$, $Y = 1.0$ mm. $Re_c = 2.4 \times 10^6$, [6|36] roughness.

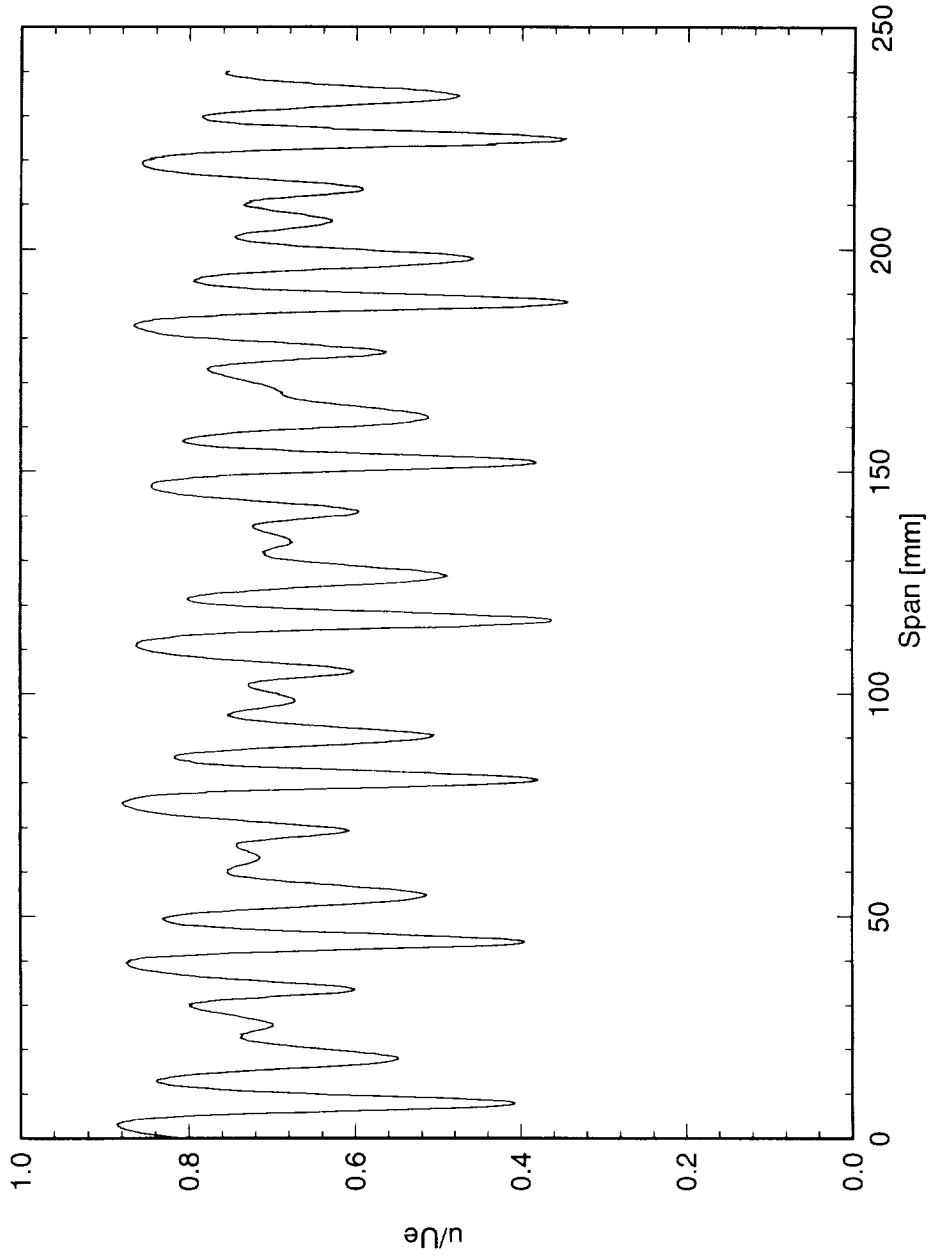

Figure 6.112: Spanwise hot-wire scan at $x/c = 0.40$, $\Upsilon = 0.95$ mm. $Re_c = 2.4 \times 10^6$, [6|36] roughness.

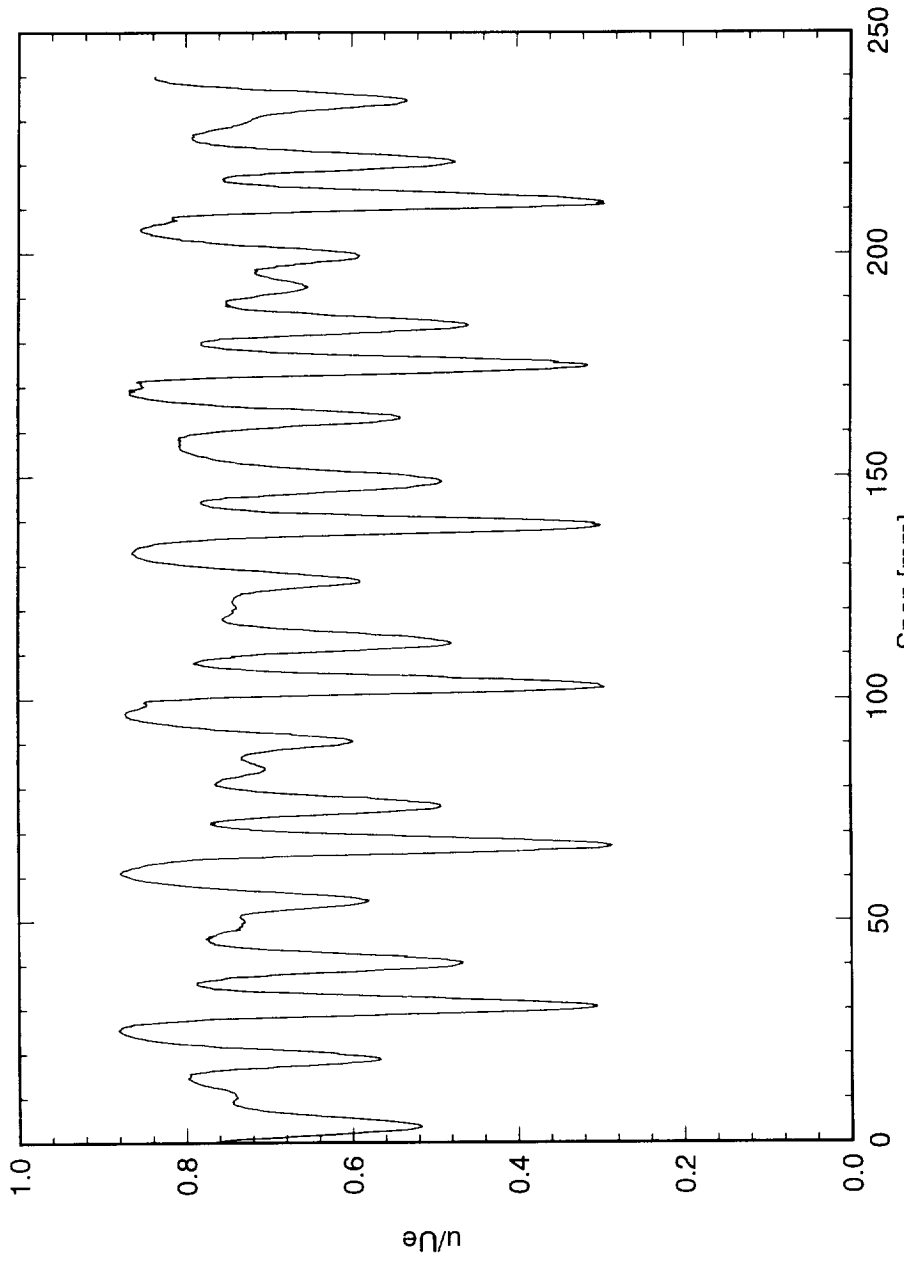

Figure 6.113: Spanwise hot-wire scan at $x/c = 0.45$, $Y = 0.9$ mm. $Re_c = 2.4 \times 10^6$, [6|36] roughness.

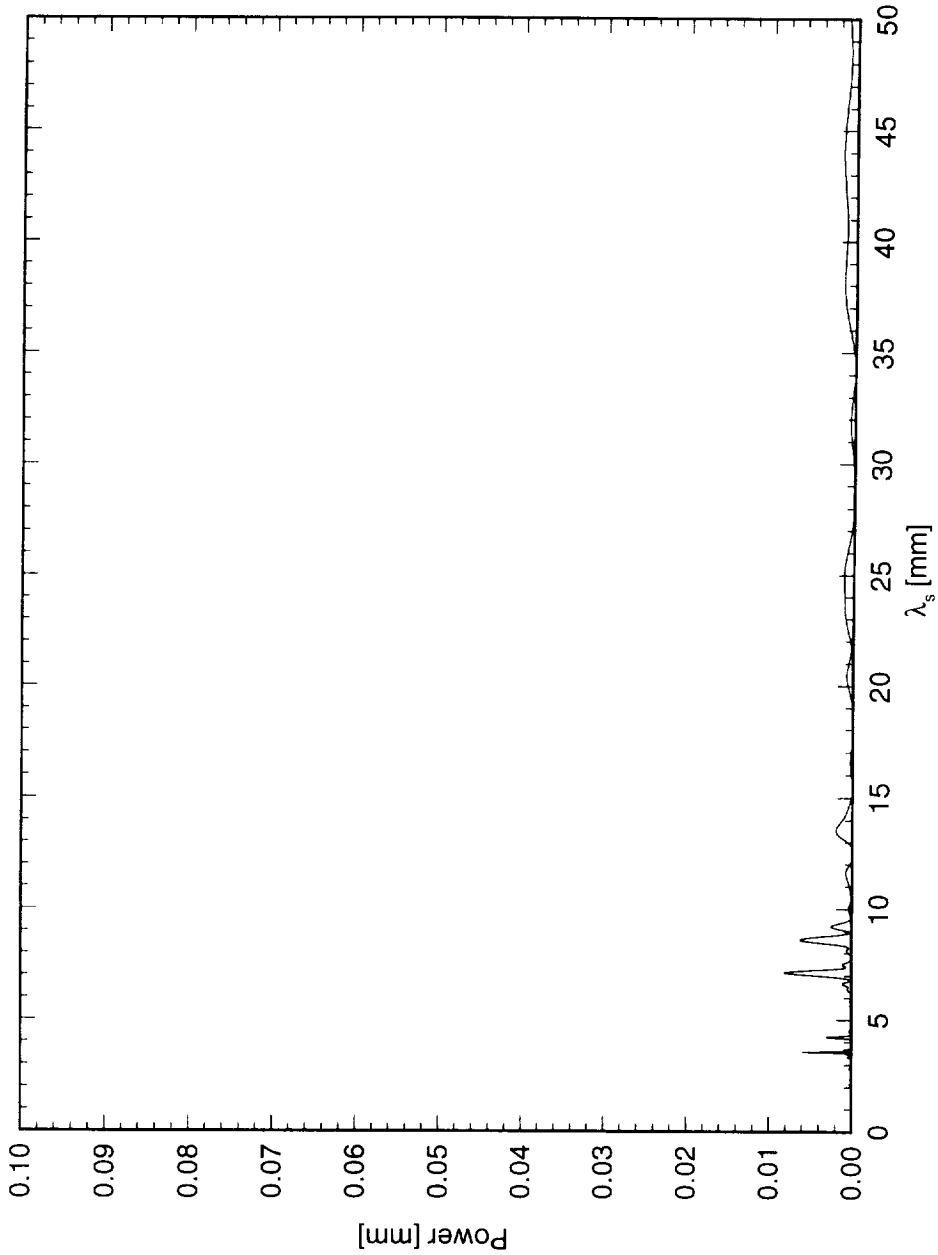

Figure 6.114: Power spectral density of spanwise hot-wire scan at $x/c = 0.10$, $Y = 0.4$ mm. $Re_c = 2.4 \times 10^6$, [6|36] roughness.

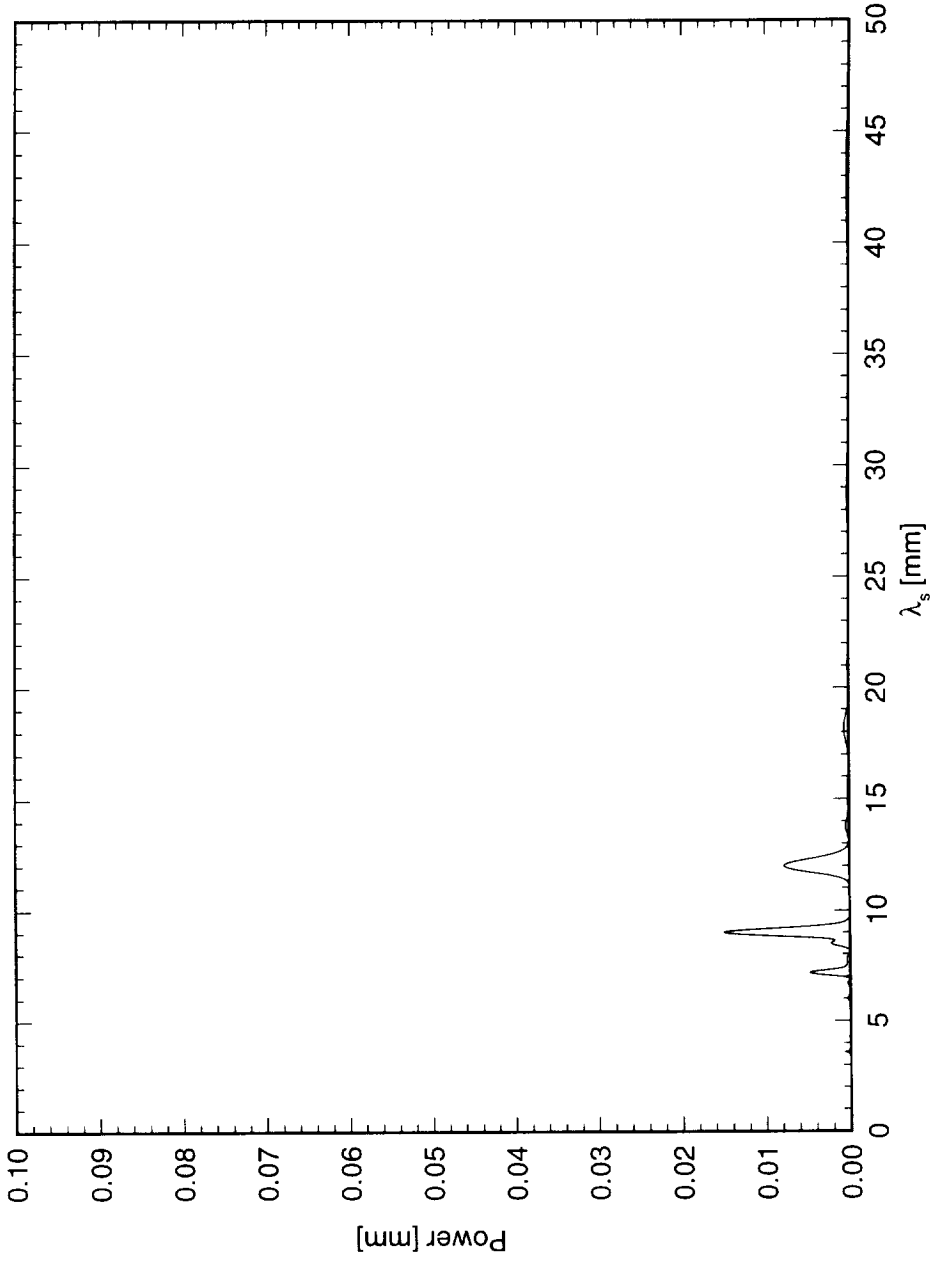

Figure 6.115: Power spectral density of spanwise hot-wire scan at $x/c = 0.15$, $Y = 0.8$ mm. $Re_c = 2.4 \times 10^6$, [6|36] roughness.

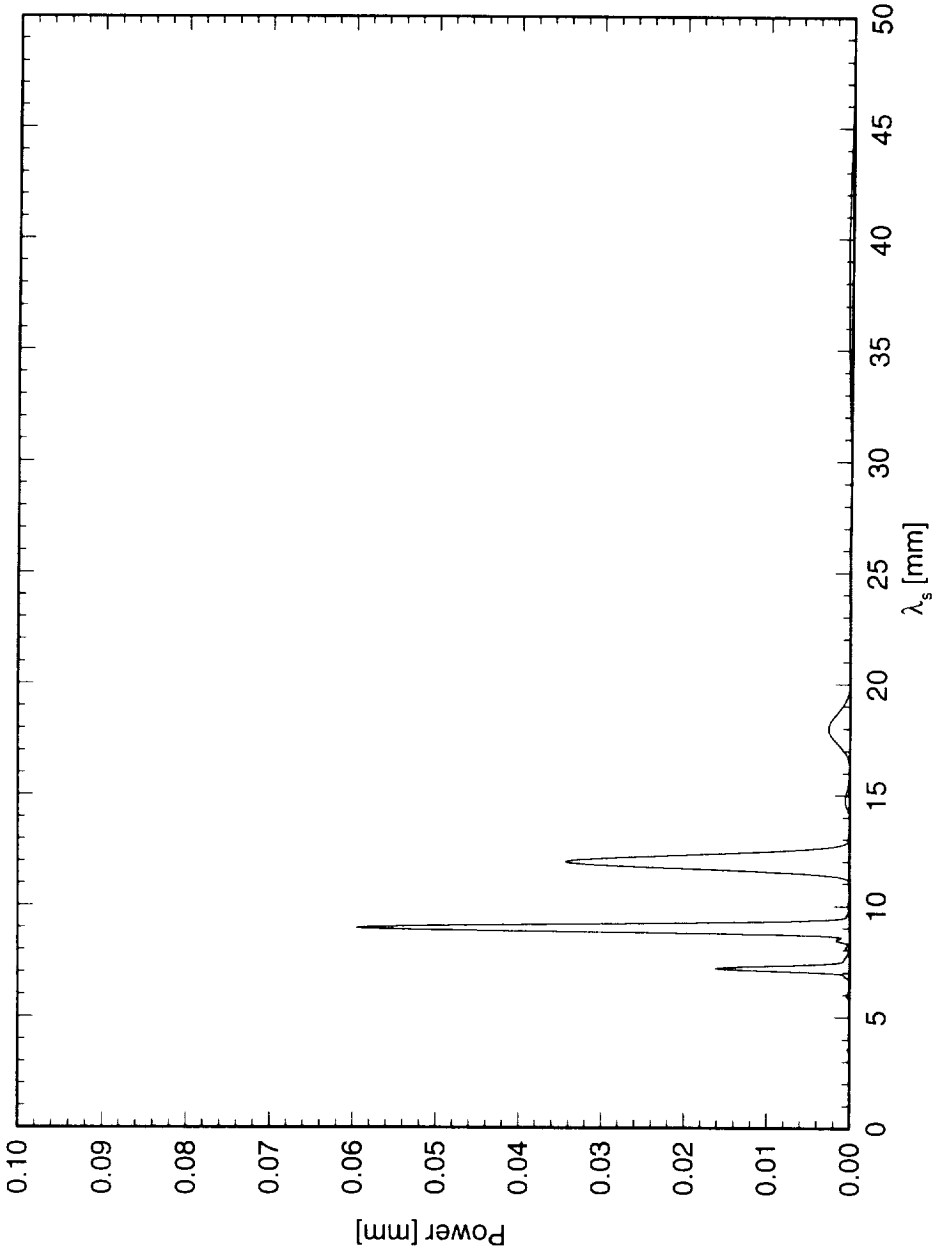

Figure 6.116: Power spectral density of spanwise hot-wire scan at $x/c = 0.20$, $Y = 0.9$ mm. $Re_c = 2.4 \times 10^6$, [6|36] roughness.

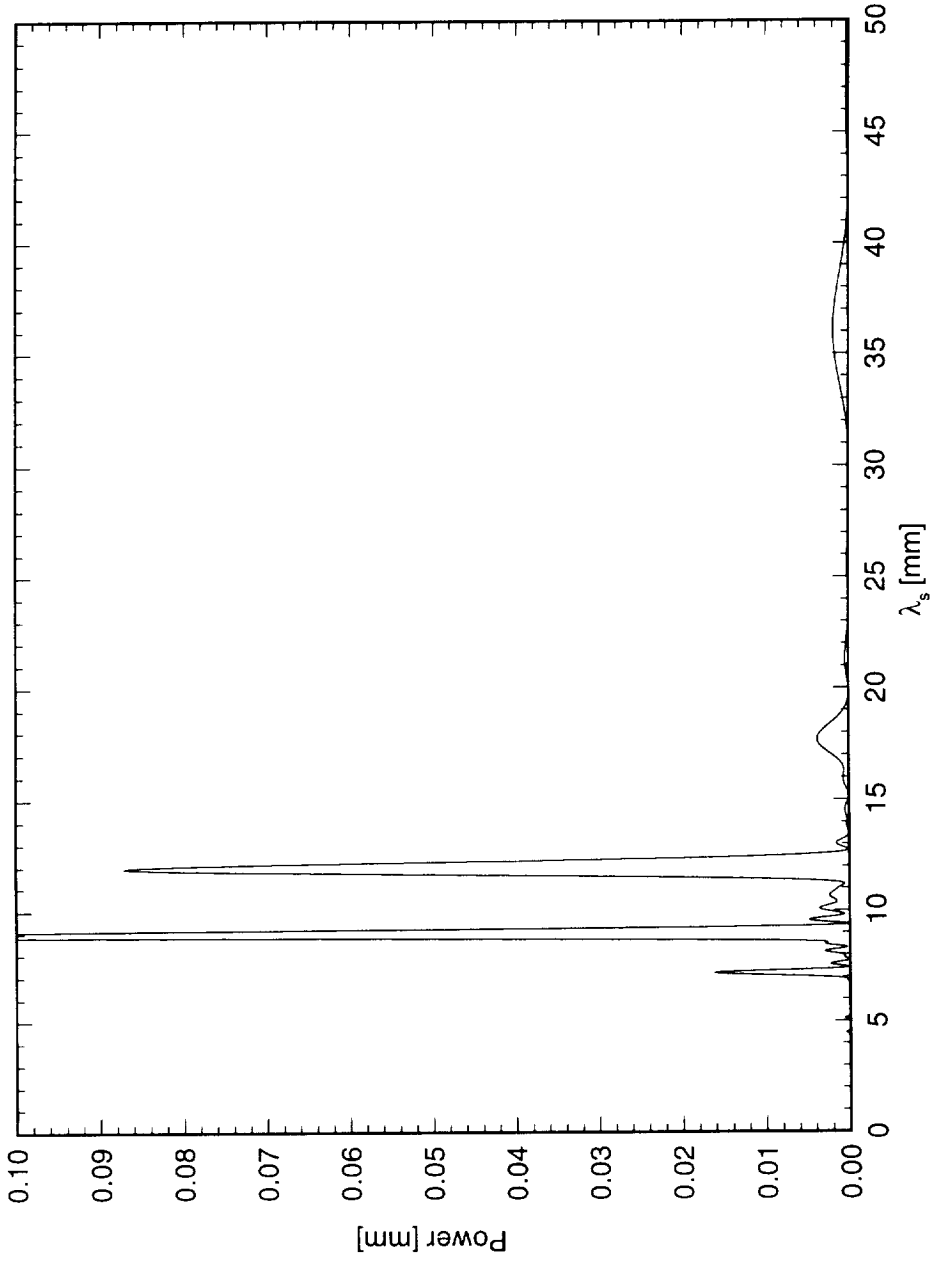

Figure 6.117: Power spectral density of spanwise hot-wire scan at $x/c = 0.25$, $Y = 1.0$ mm. $Re_c = 2.4 \times 10^6$, [6|36] roughness.

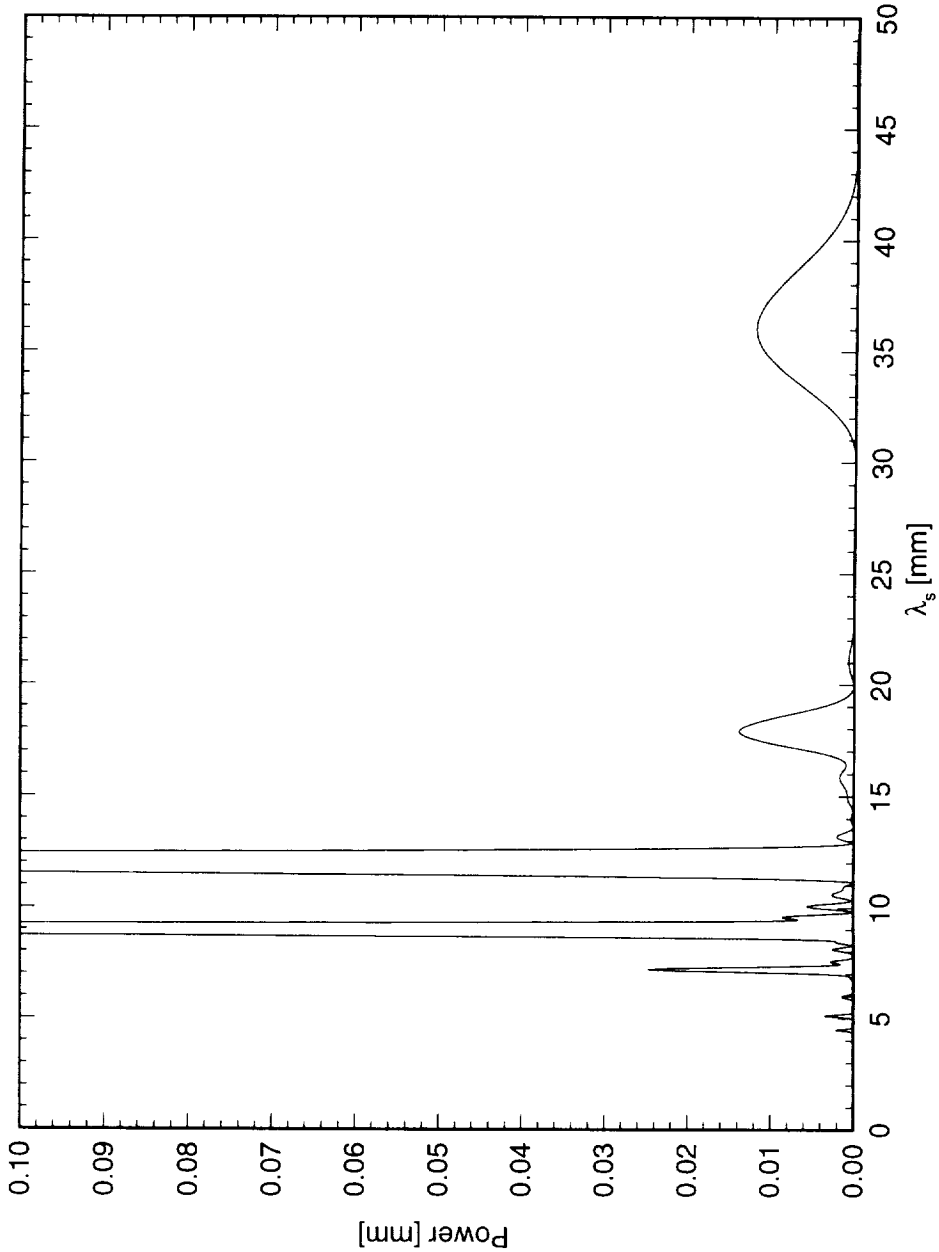

Figure 6.118: Power spectral density of spanwise hot-wire scan at $x/c = 0.30$, $Y = 1.0$ mm. $Re_c = 2.4 \times 10^6$, [6|36] roughness.

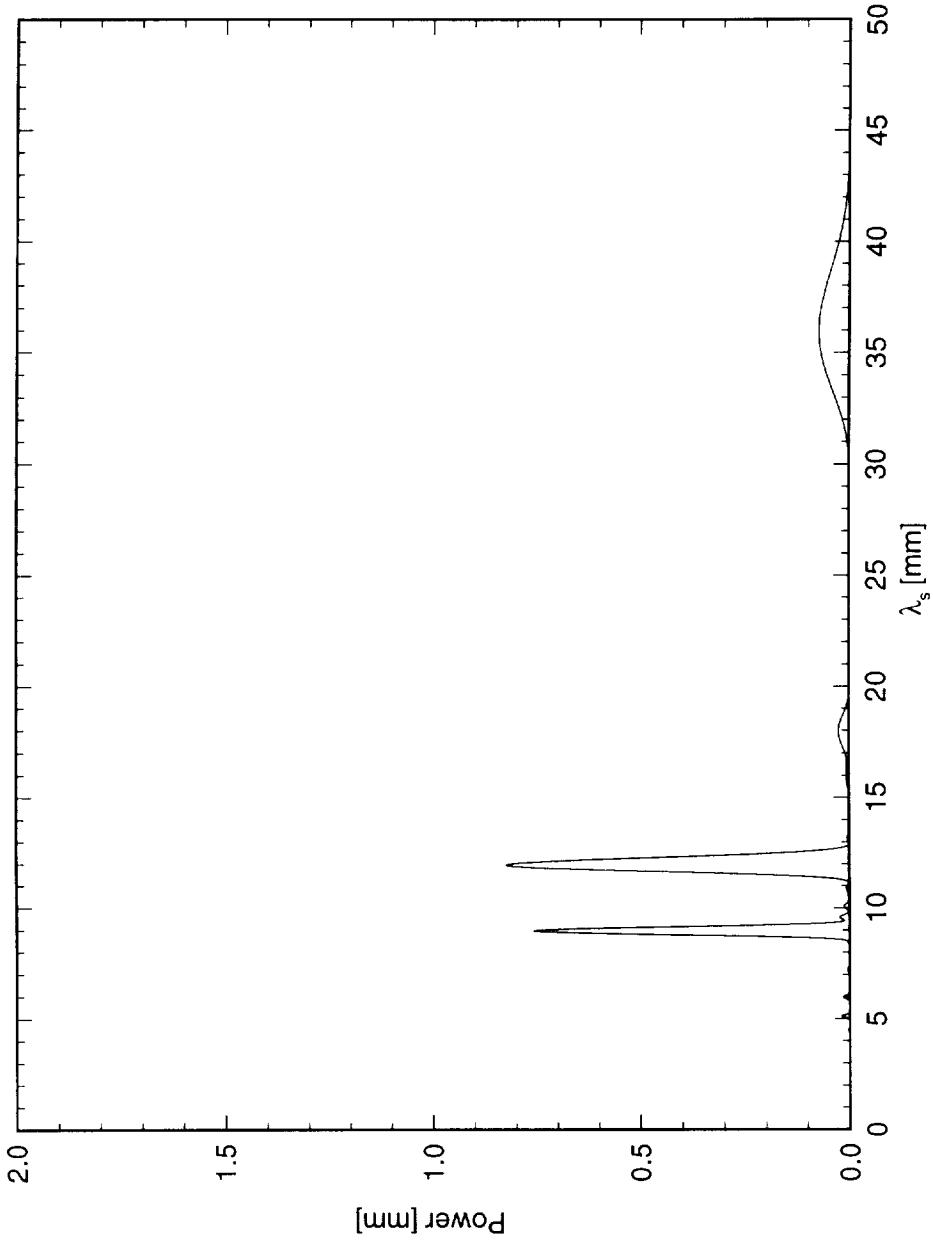

Figure 6.119: Power spectral density of spanwise hot-wire scan at $x/c = 0.35$, $Y = 1.0$ mm. $Re_c = 2.4 \times 10^6$, [6|36] roughness.

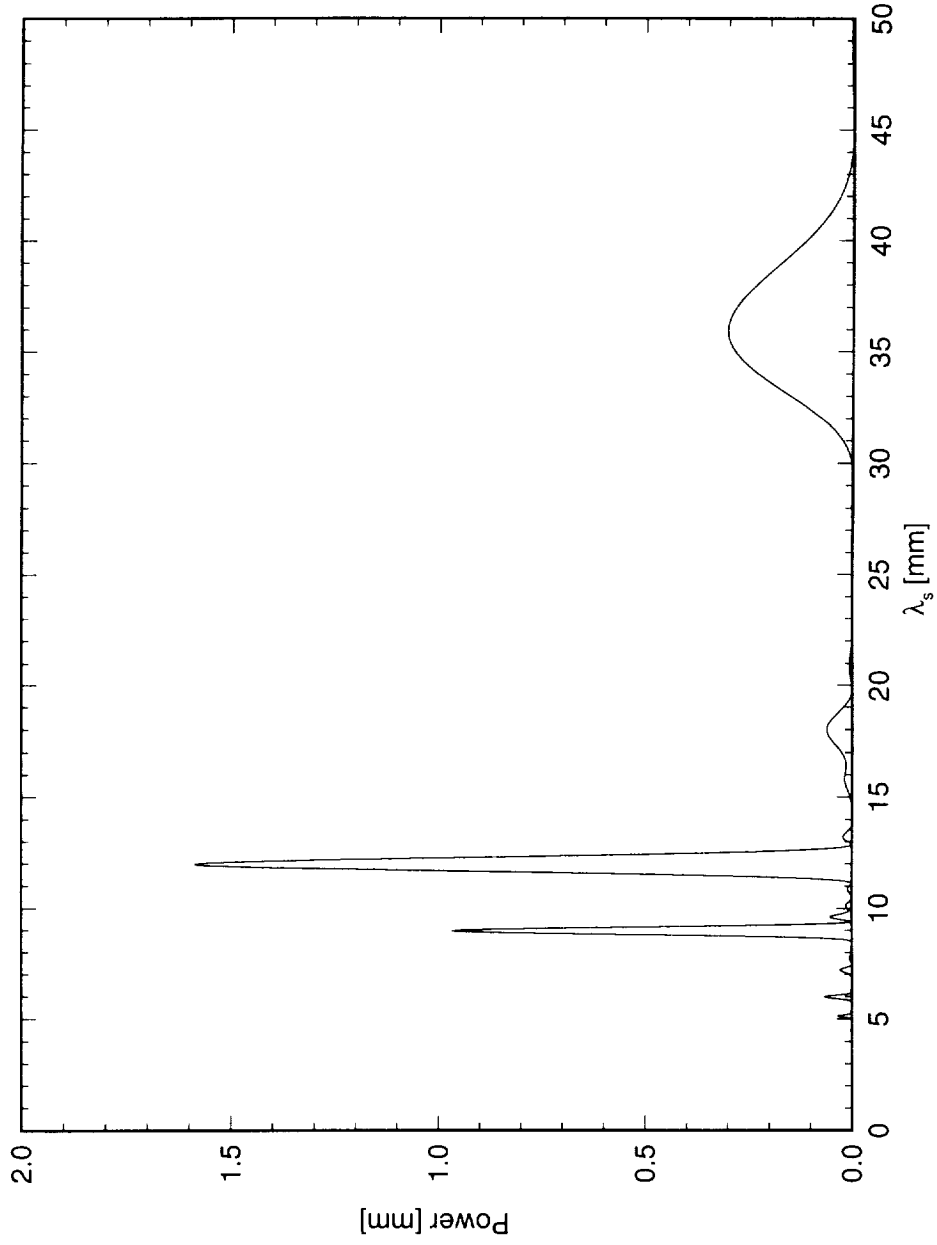

Figure 6.120: Power spectral density of spanwise hot-wire scan at $x/c = 0.40$, $Y = 0.95$ mm. $Re_c = 2.4 \times 10^6$, [6|36] roughness.

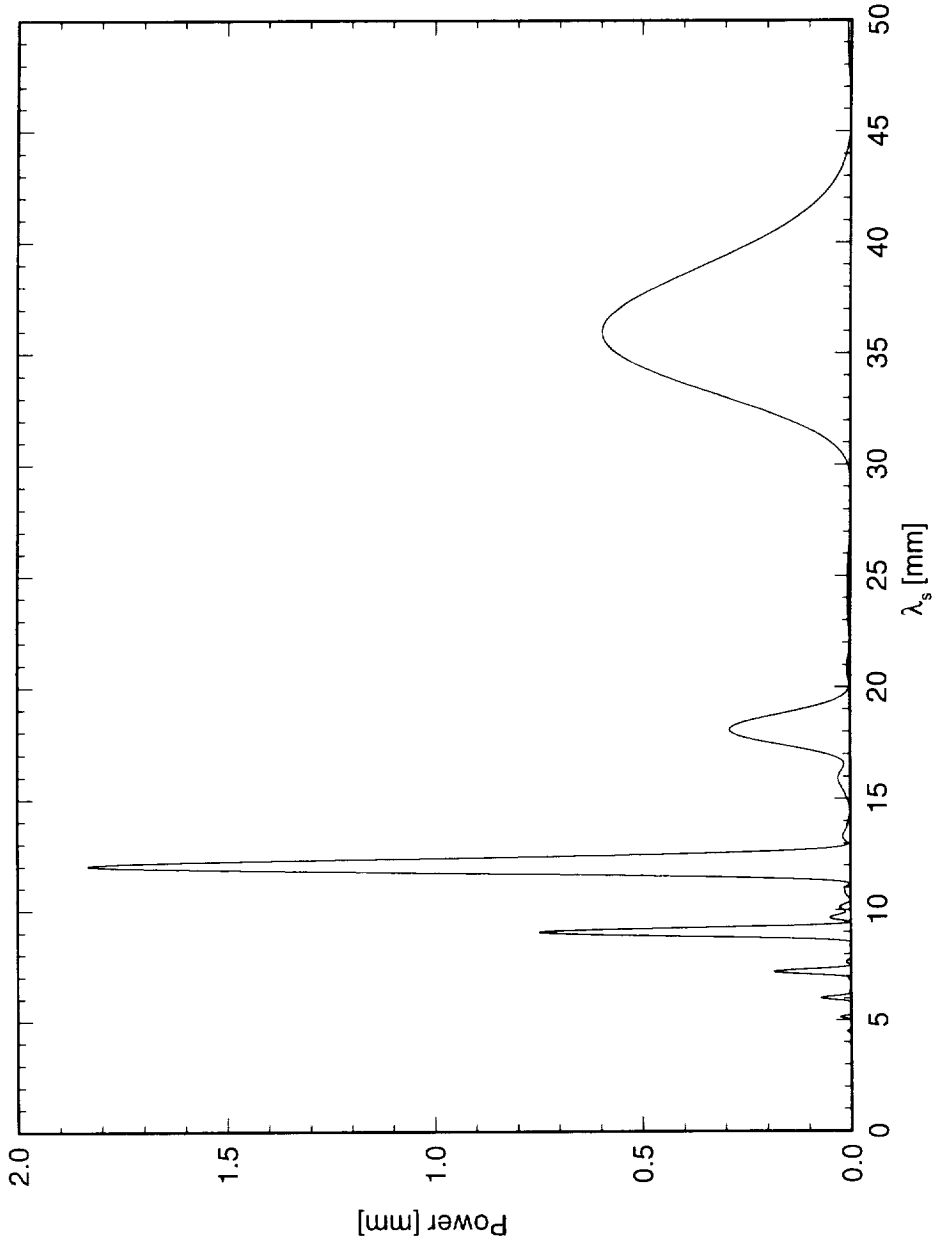

Figure 6.121: Power spectral density of spanwise hot-wire scan at $x/c = 0.45$, $Y = 0.9$ mm. $Re_c = 2.4 \times 10^6$, [6|36] roughness.

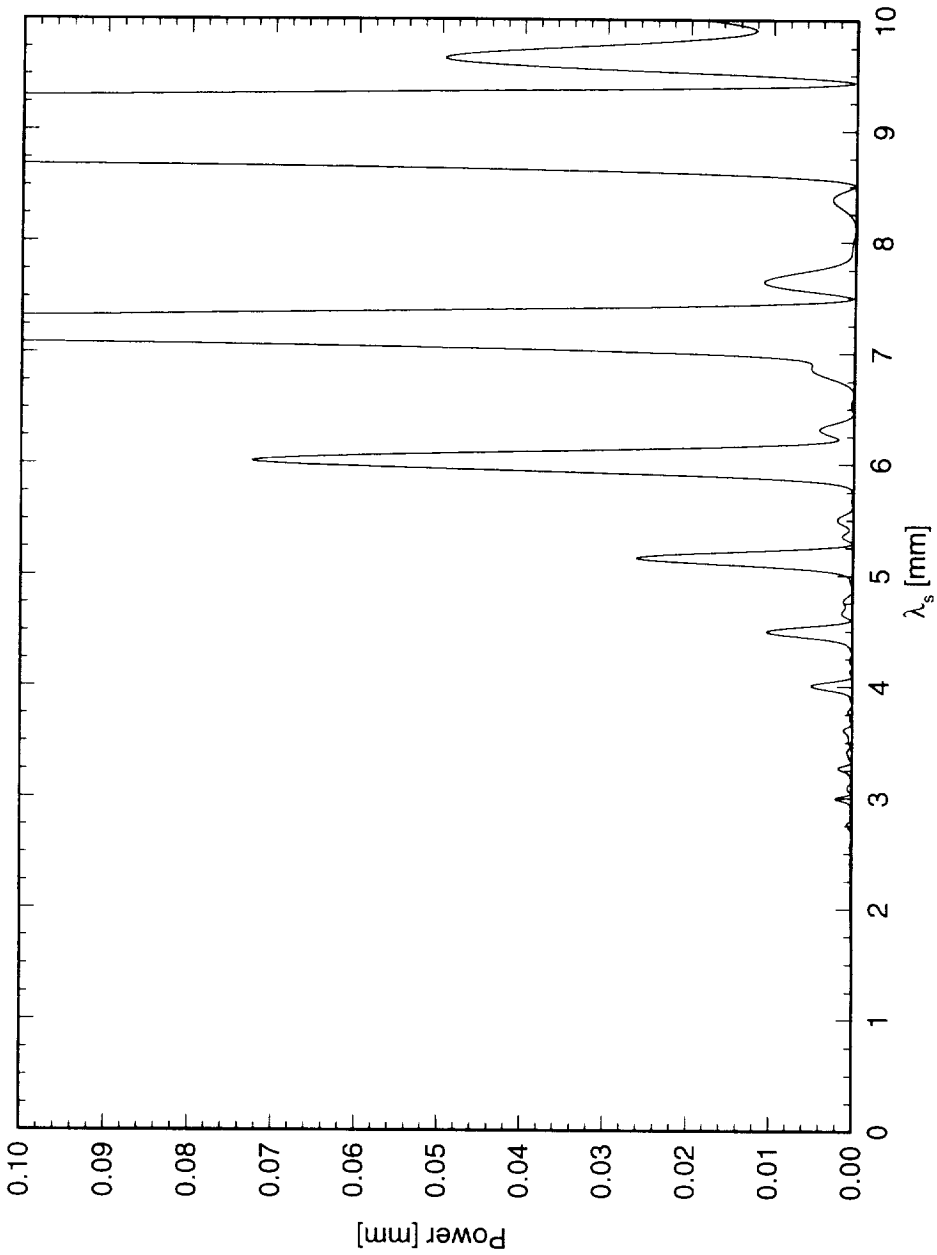

Figure 6.122: Power spectral density of spanwise hot-wire scan at $x/c = 0.45$, $Y = 0.9$ mm. $Re_c = 2.4 \times 10^6$. [6|36] roughness. Enhanced view showing amplitude of small-wavelength disturbances.

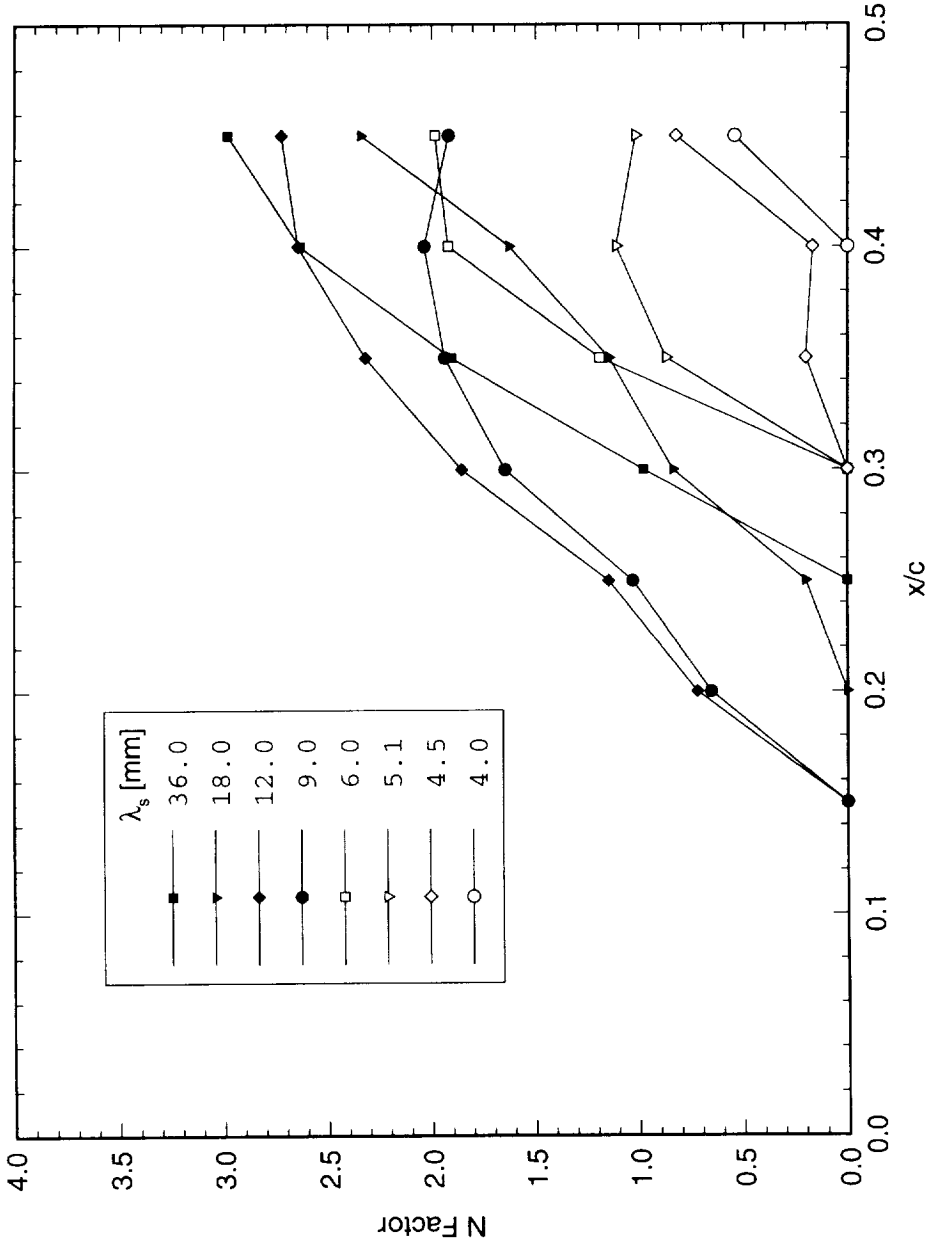

Figure 6.123: Individual-mode disturbance amplification factor N for $Re_c = 2.4 \times 10^6$ and [6|36] roughness. N-factors are relative to the point at which the mode is first detected.

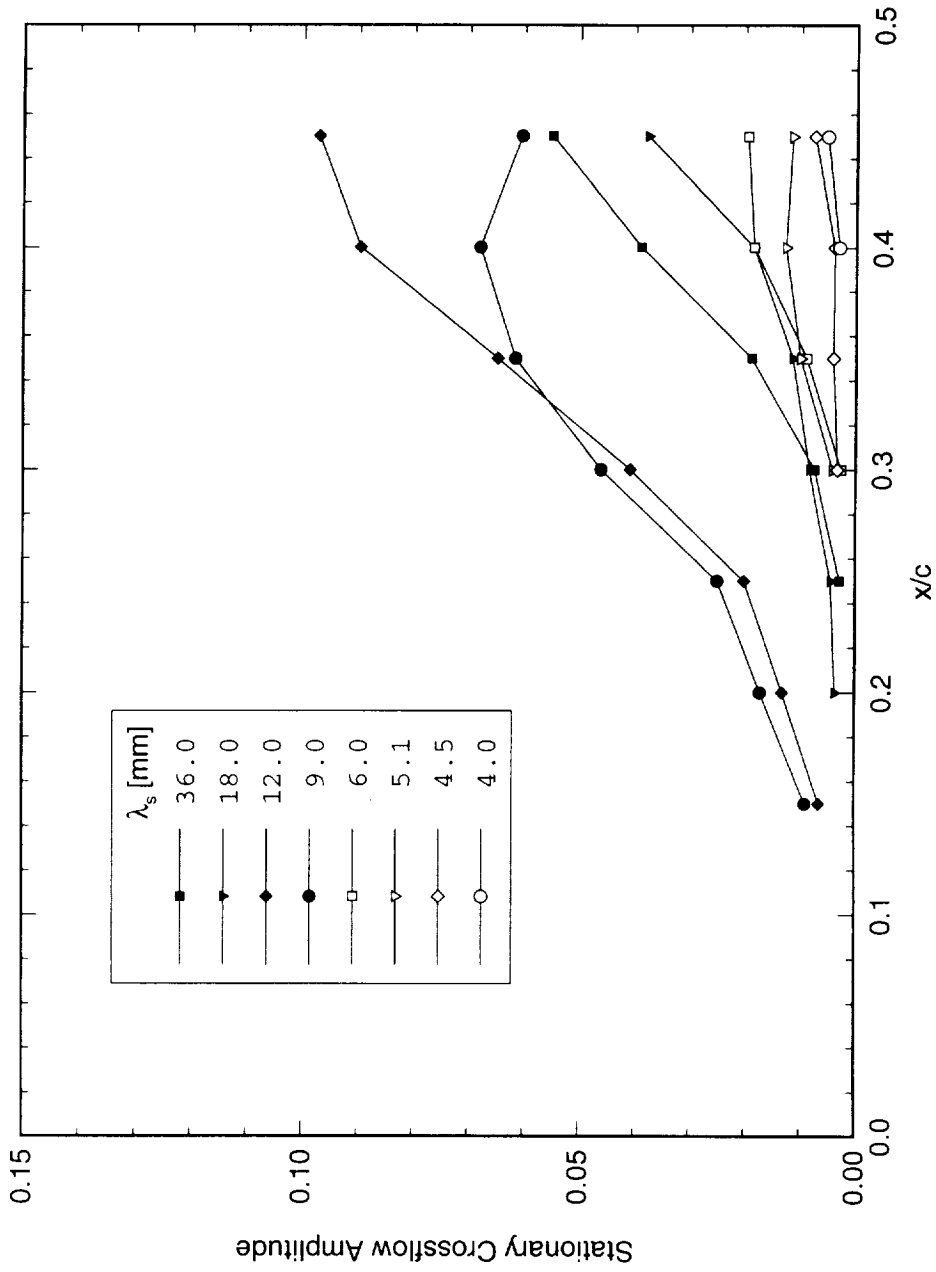

Figure 6.124: Individual-mode disturbance amplitude for $Re_c = 2.4 \times 10^6$ and [6|36] roughness.

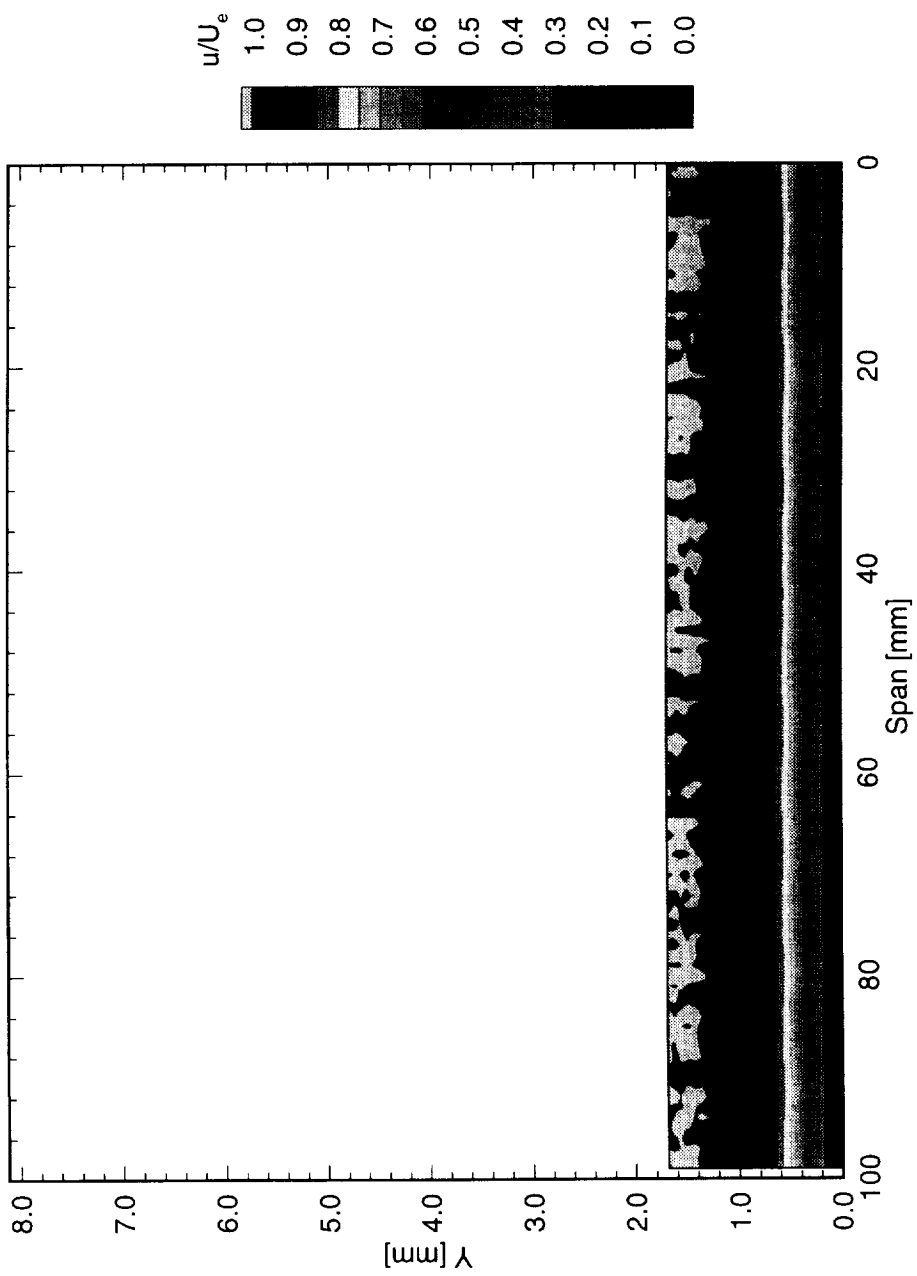

Figure 6.125: Streamwise velocity contours at $x/c = 0.05$. $Re_c = 2.4 \times 10^6$, [18|12] roughness.

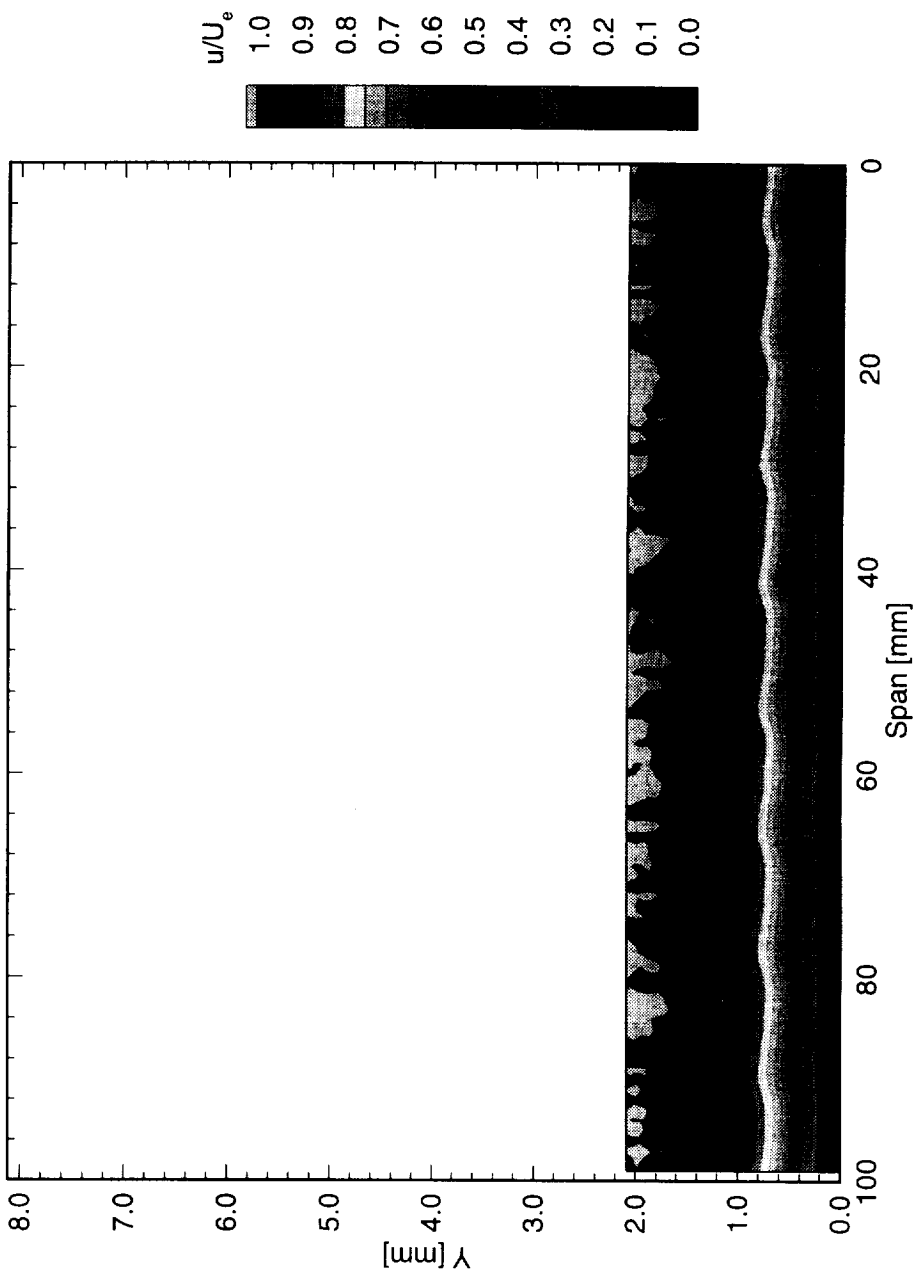

Figure 6.126: Streamwise velocity contours at $x/c = 0.10$. $Re_c = 2.4 \times 10^6$, [18|12] roughness.

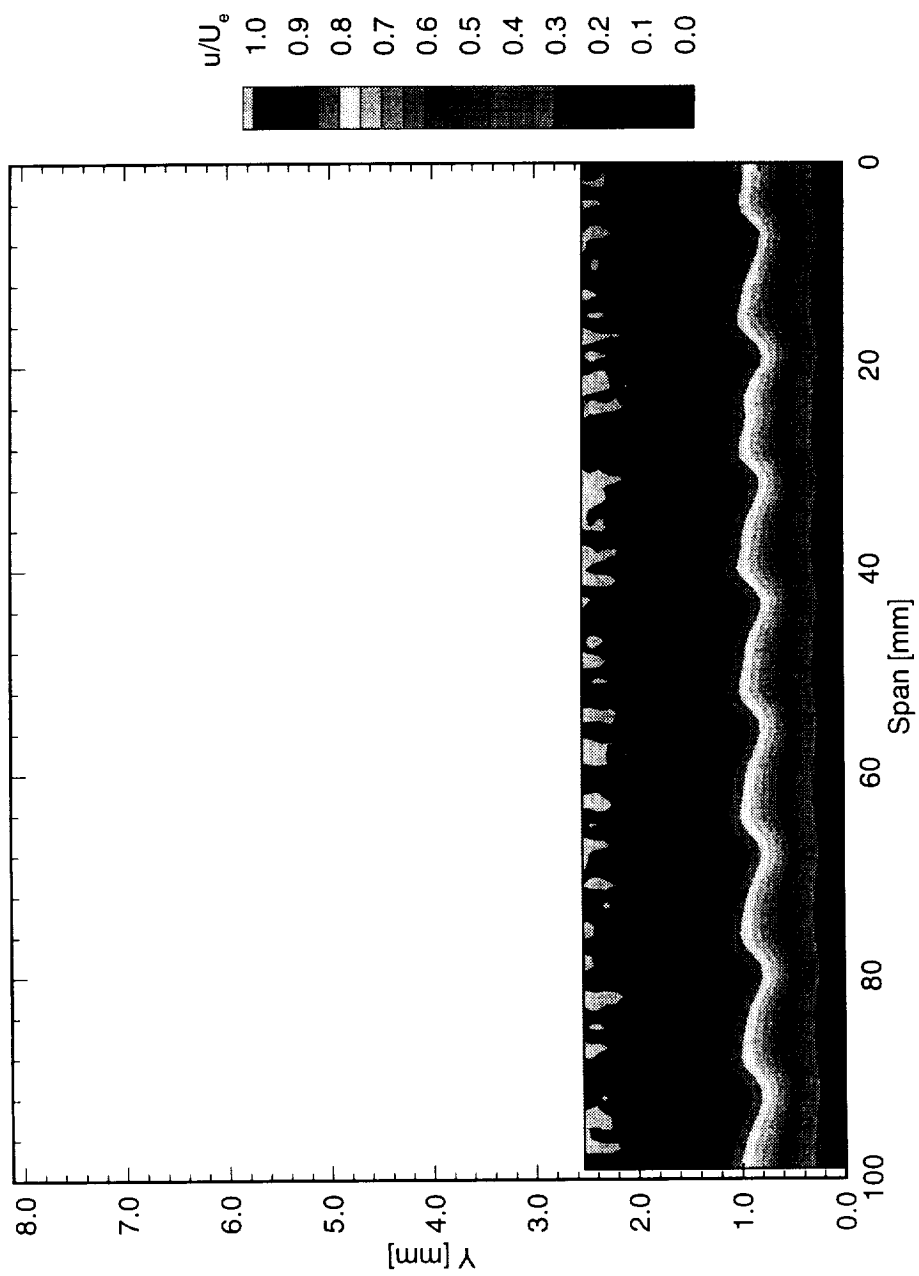

Figure 6.127: Streamwise velocity contours at $x/c = 0.15$. $Re_c = 2.4 \times 10^6$, [18|12] roughness.

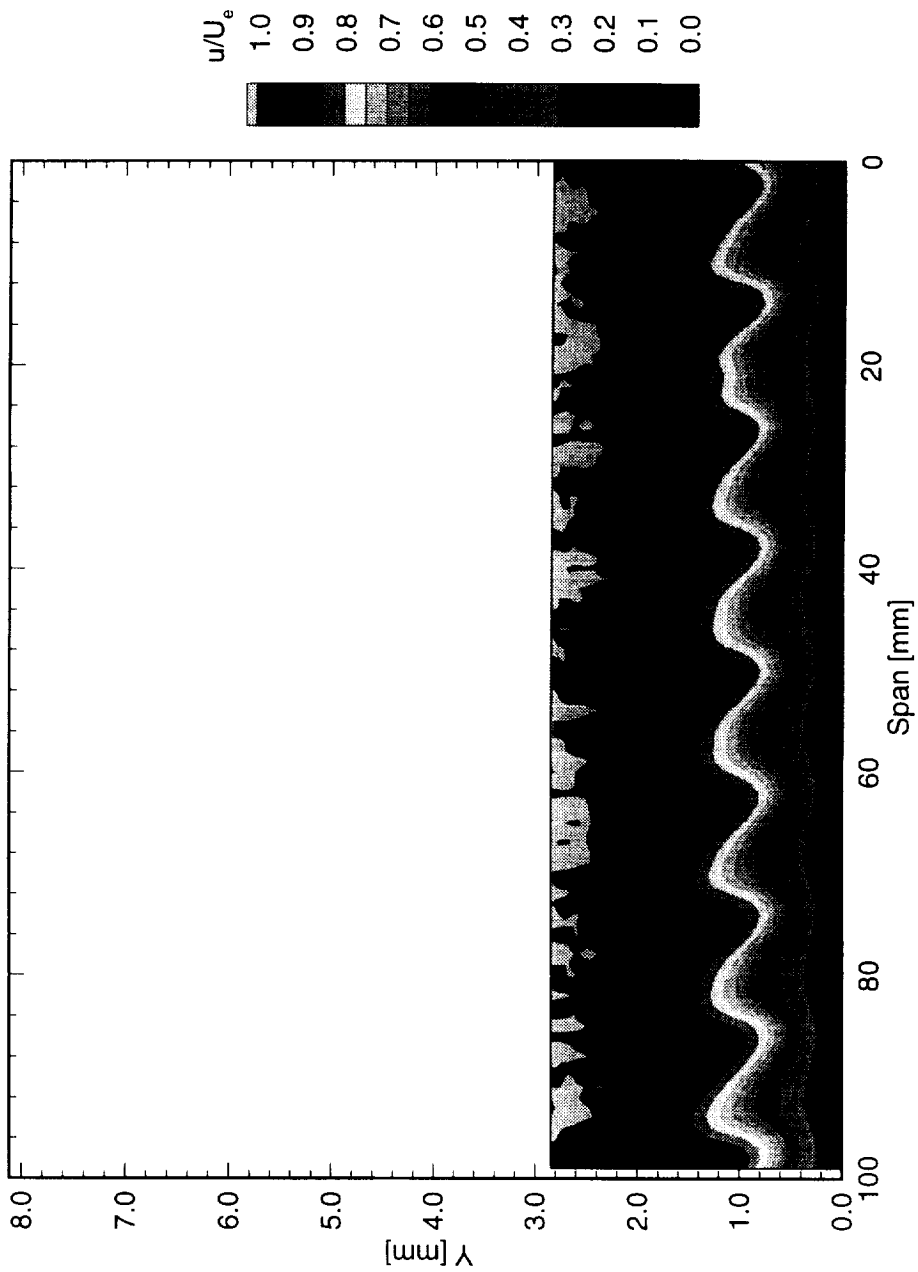

Figure 6.128: Streamwise velocity contours at $x/c = 0.20$. $Re_c = 2.4 \times 10^6$, [18|12] roughness.

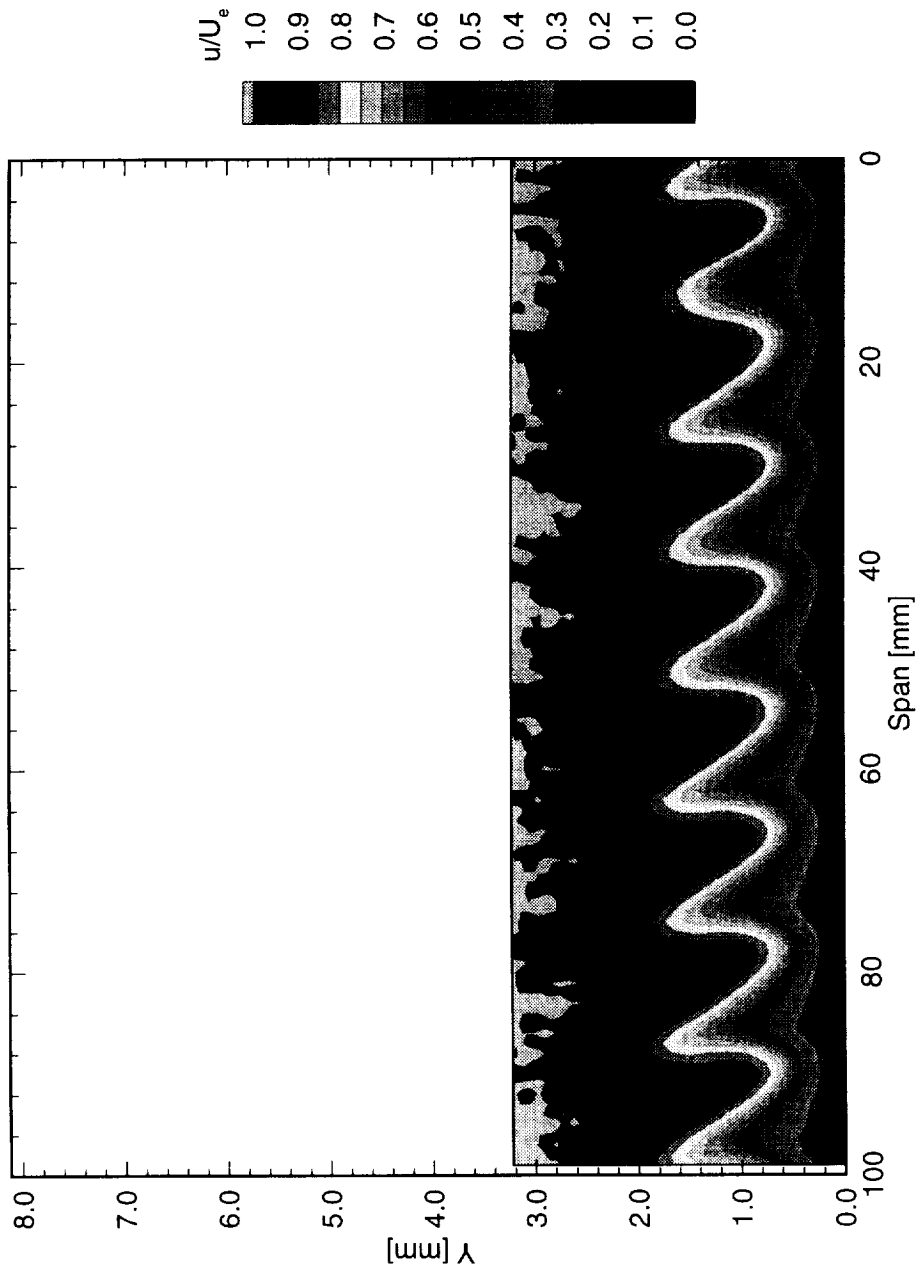

Figure 6.129: Streamwise velocity contours at $x/c = 0.25$. $Re_c = 2.4 \times 10^6$, [18|12] roughness.

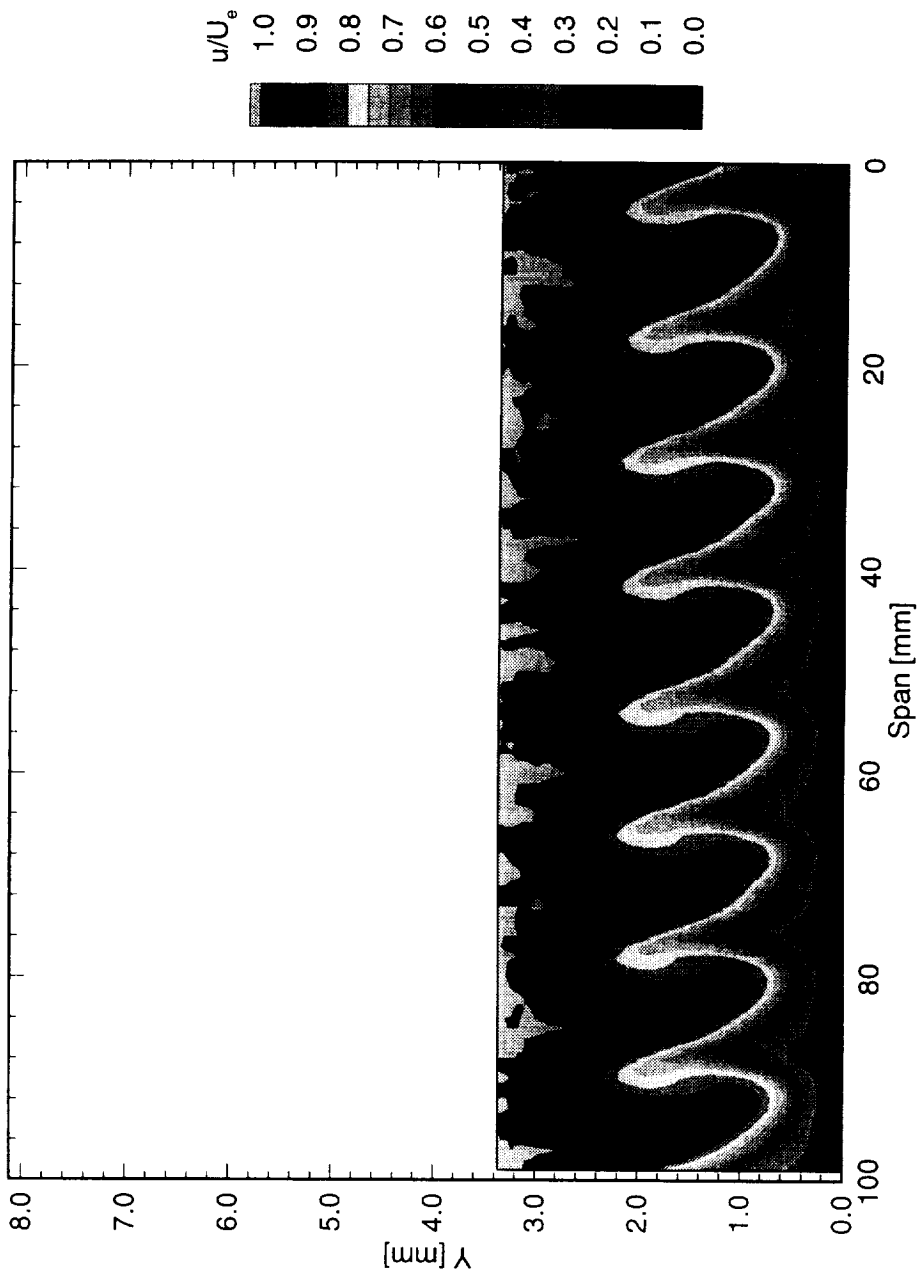

Figure 6.130: Streamwise velocity contours at $x/c = 0.30$. $Re_c = 2.4 \times 10^6$, [18|12] roughness.

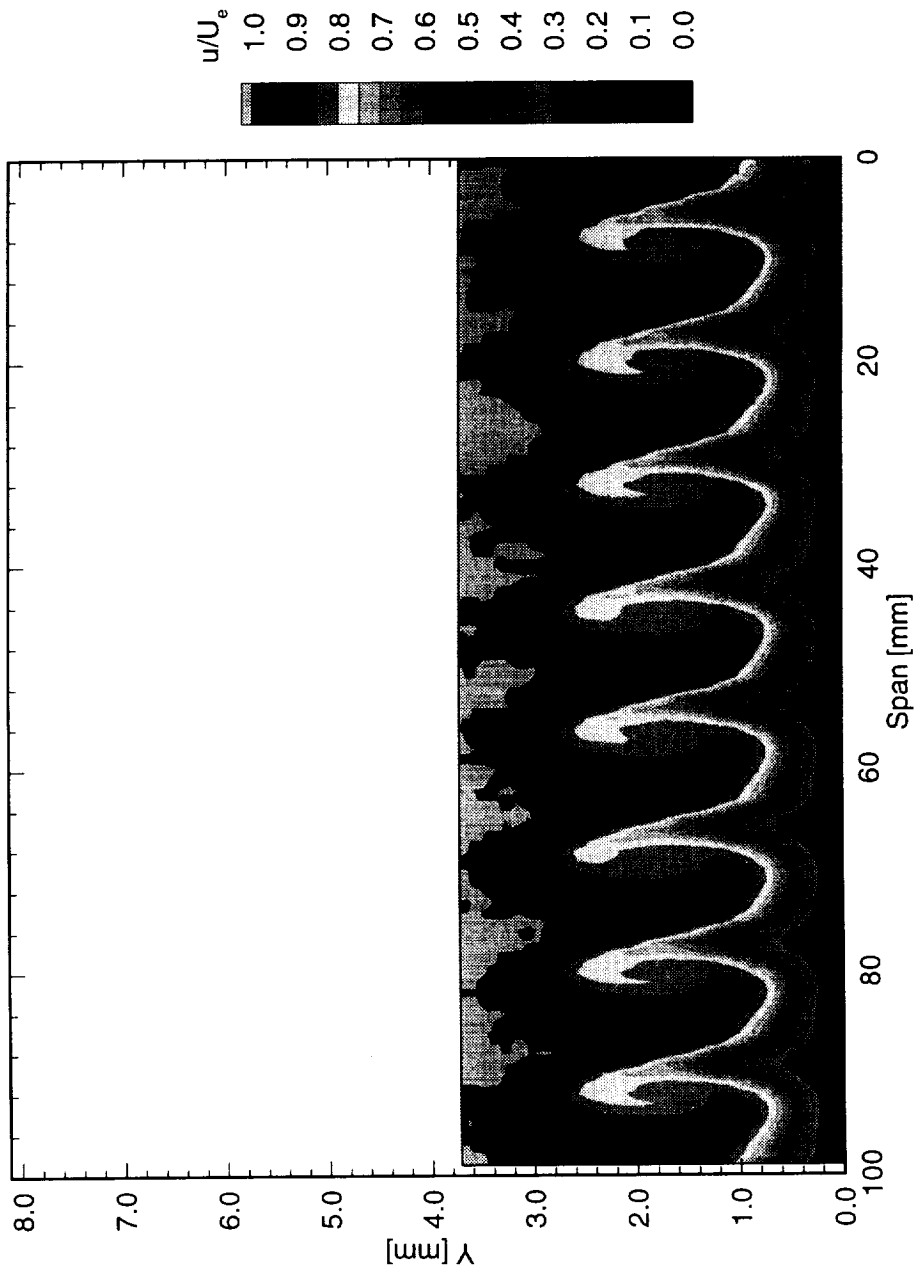

Figure 6.131: Streamwise velocity contours at $x/c = 0.35$. $Re_c = 2.4 \times 10^6$, [18|12] roughness.

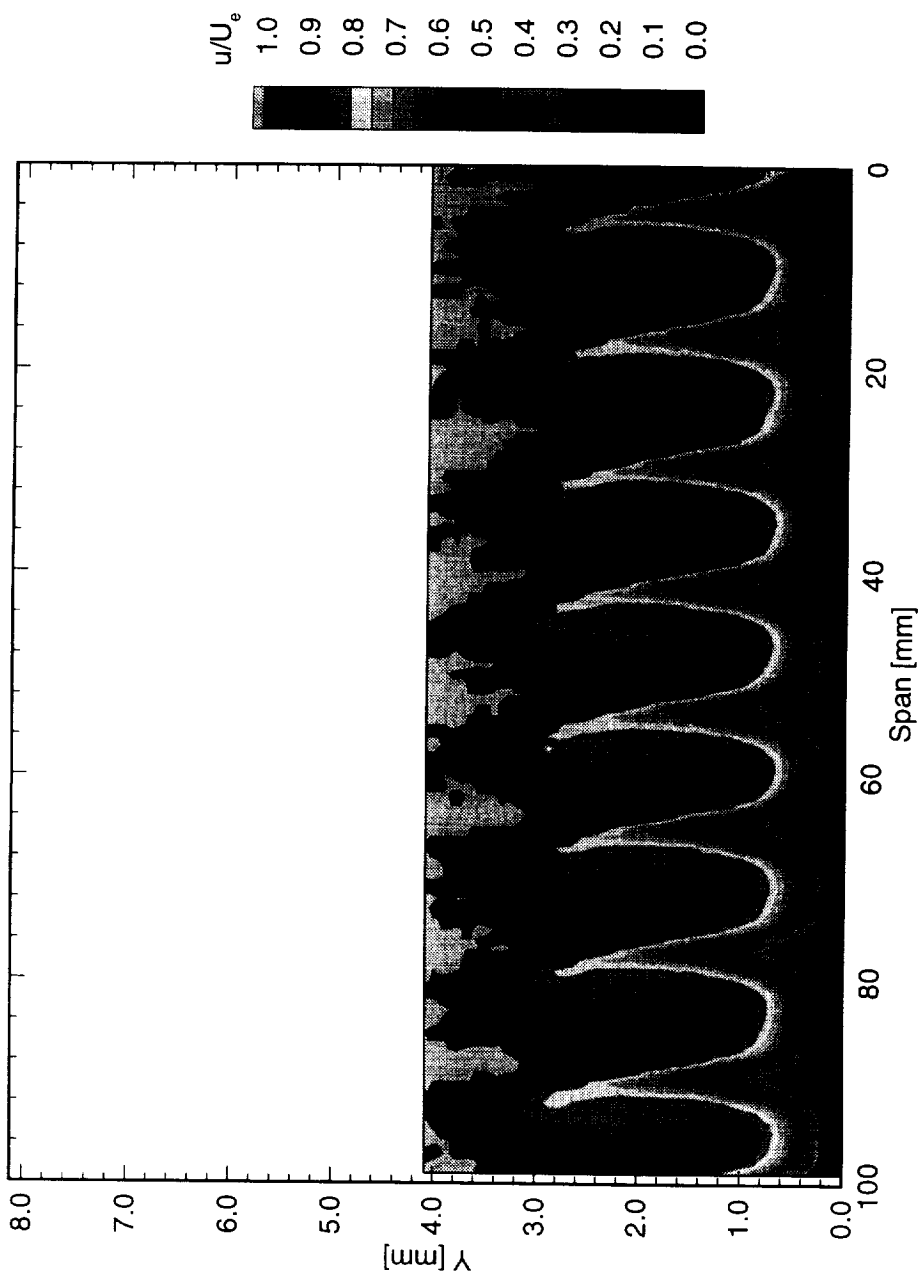

Figure 6.132: Streamwise velocity contours at $x/c = 0.40$. $Re_c = 2.4 \times 10^6$, [18|12] roughness.

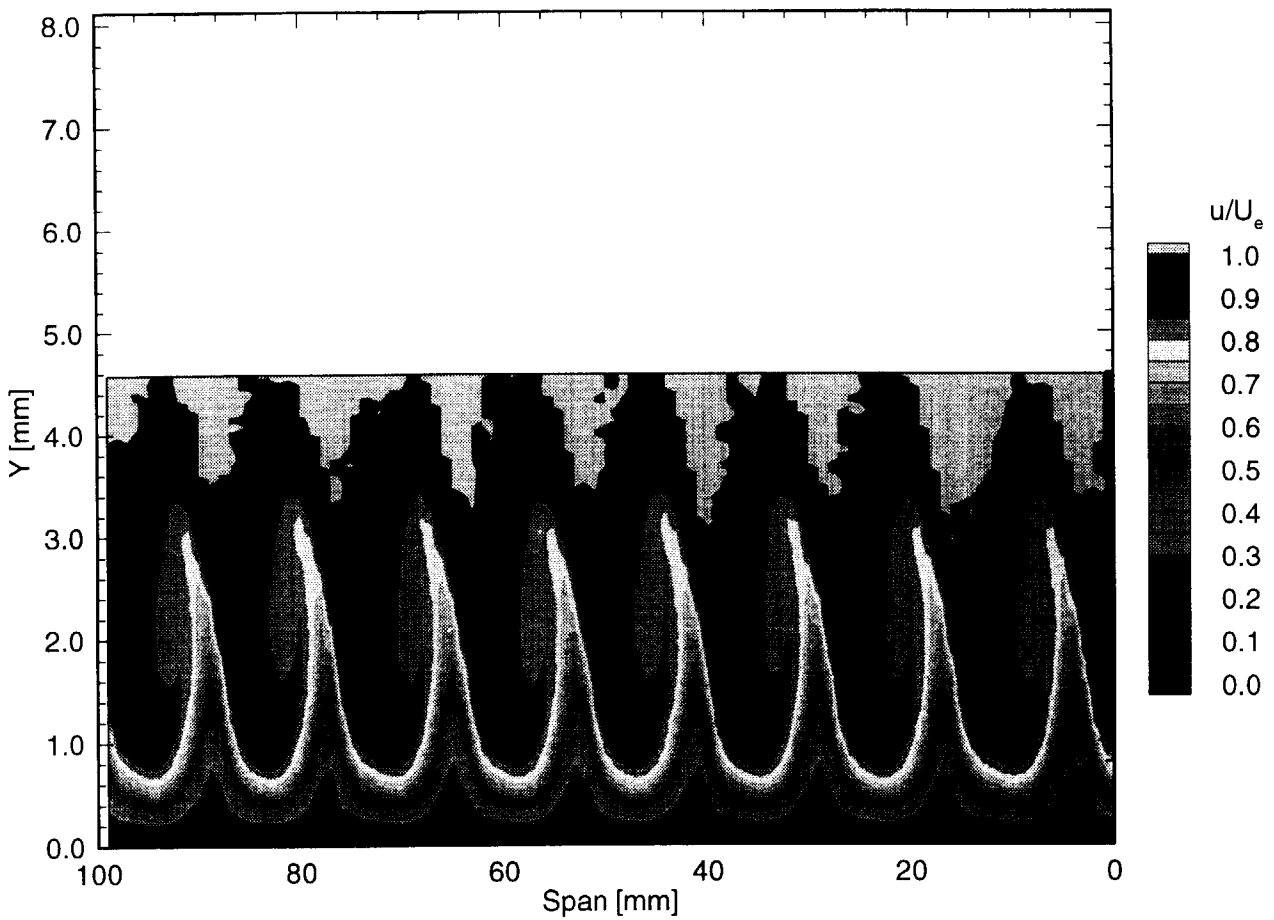

Figure 6.133: Streamwise velocity contours at $x/c = 0.45$. $Re_c = 2.4 \times 10^6$, [18|12] roughness.

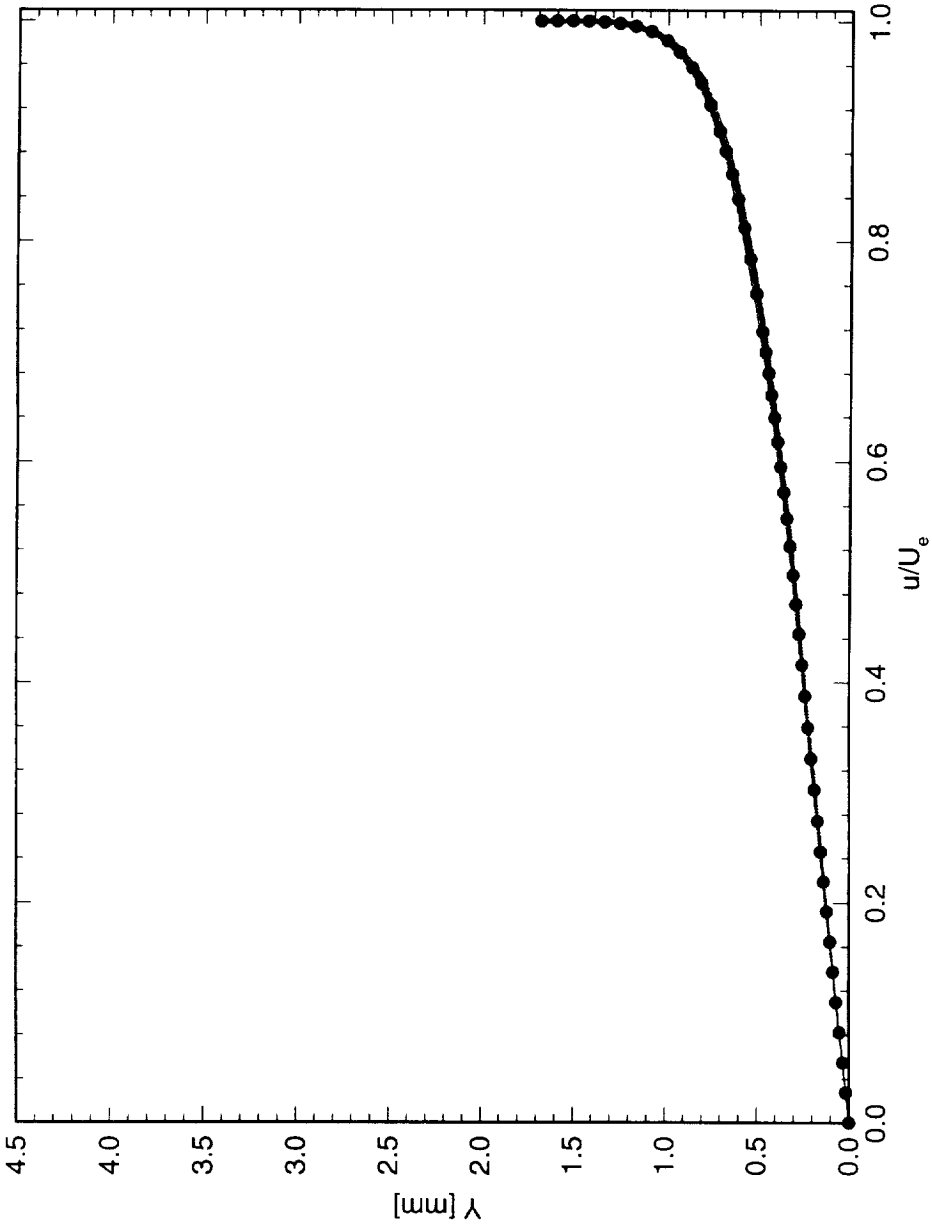

Figure 6.134: Spanwise array of 100 mean-flow boundary-layer profiles covering a span of 99 mm at $x/c = 0.05$. $Re_c = 2.4 \times 10^6$, [18|12] roughness. The dots indicate the mean of the profiles.

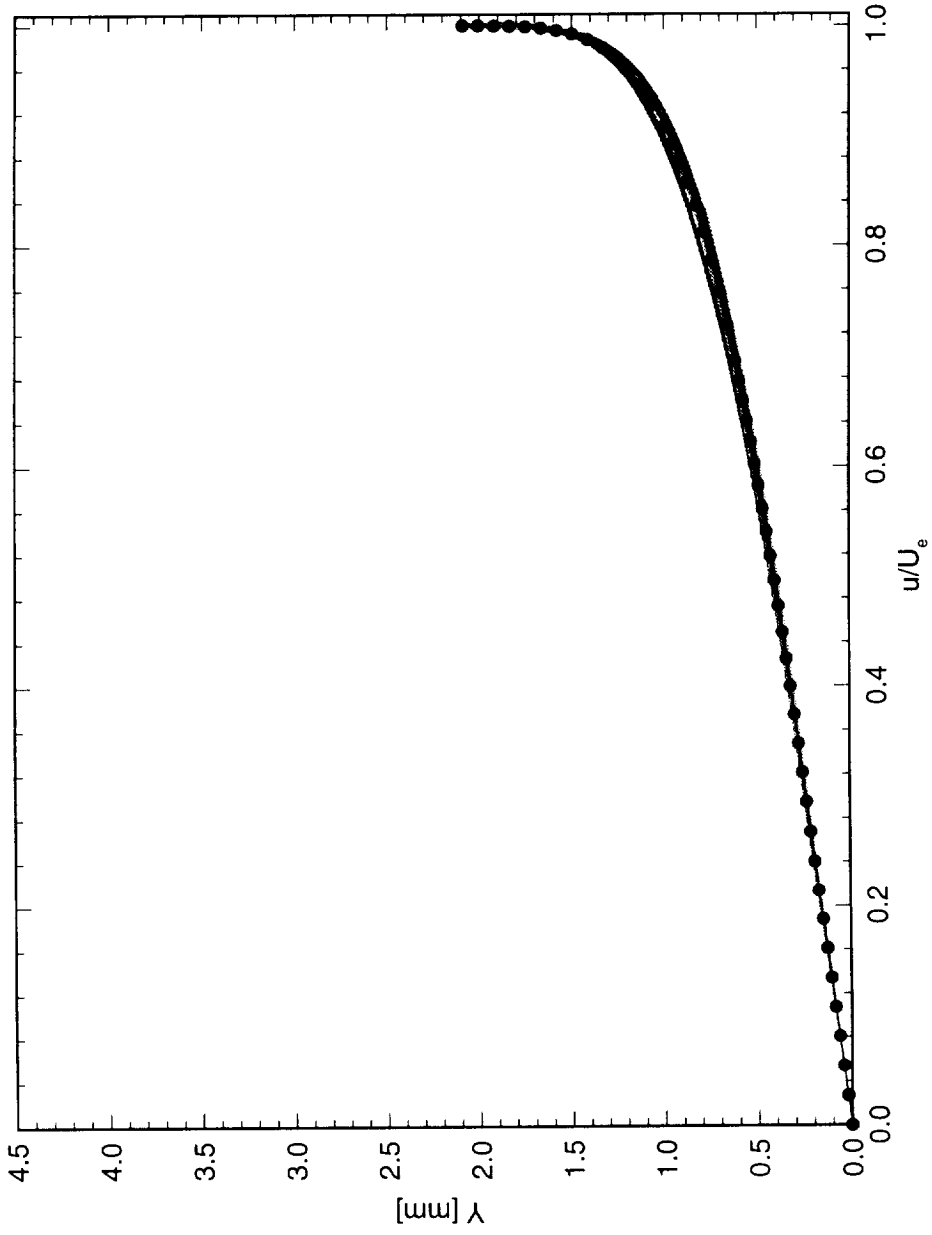

Figure 6.135: Spanwise array of 100 mean-flow boundary-layer profiles covering a span of 99 mm at $x/c = 0.10$. $Re_c = 2.4 \times 10^6$, [18|12] roughness. The dots indicate the mean of the profiles.

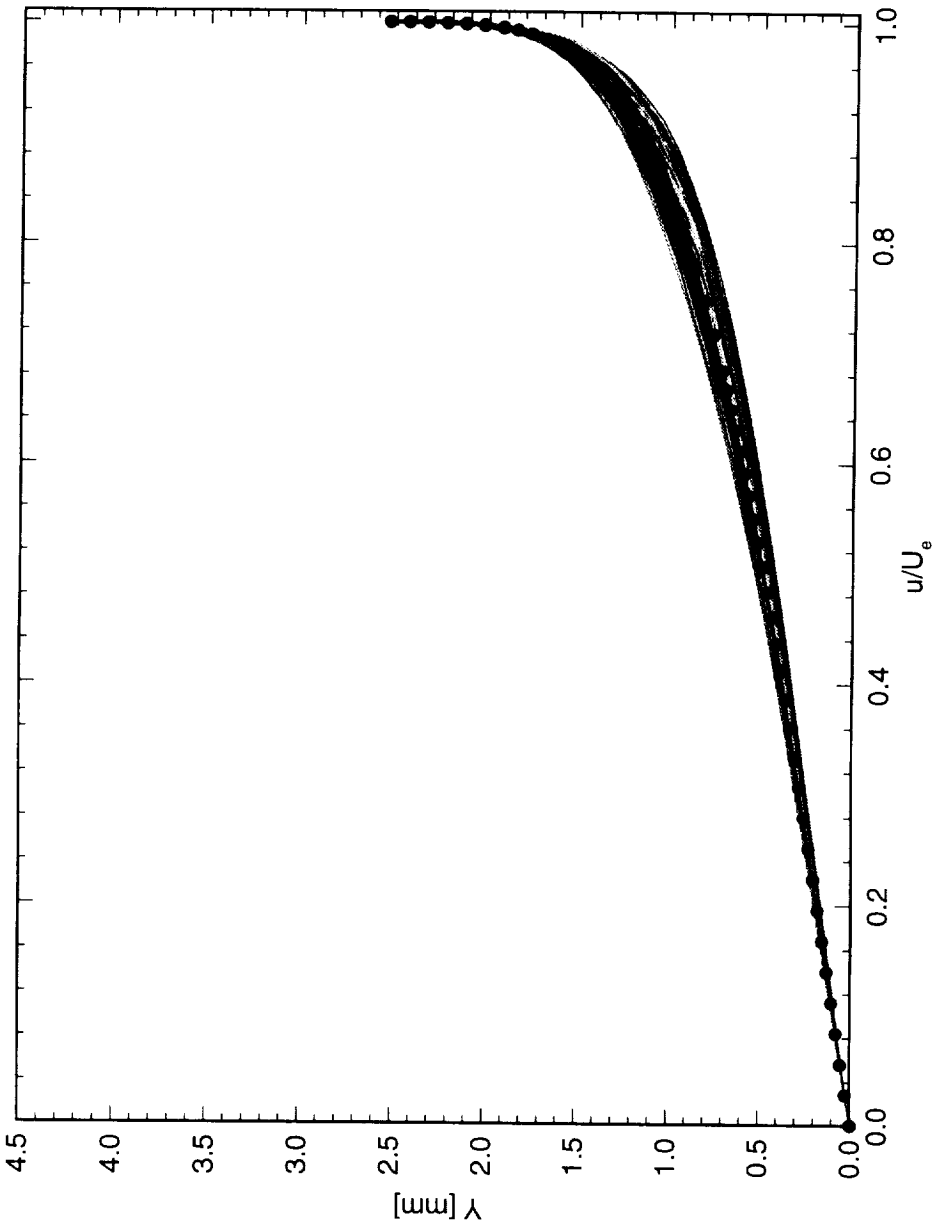

Figure 6.136: Spanwise array of 100 mean-flow boundary-layer profiles covering a span of 99 mm at $x/c = 0.15$. $Re_c = 2.4 \times 10^6$, [18|12] roughness. The dots indicate the mean of the profiles.

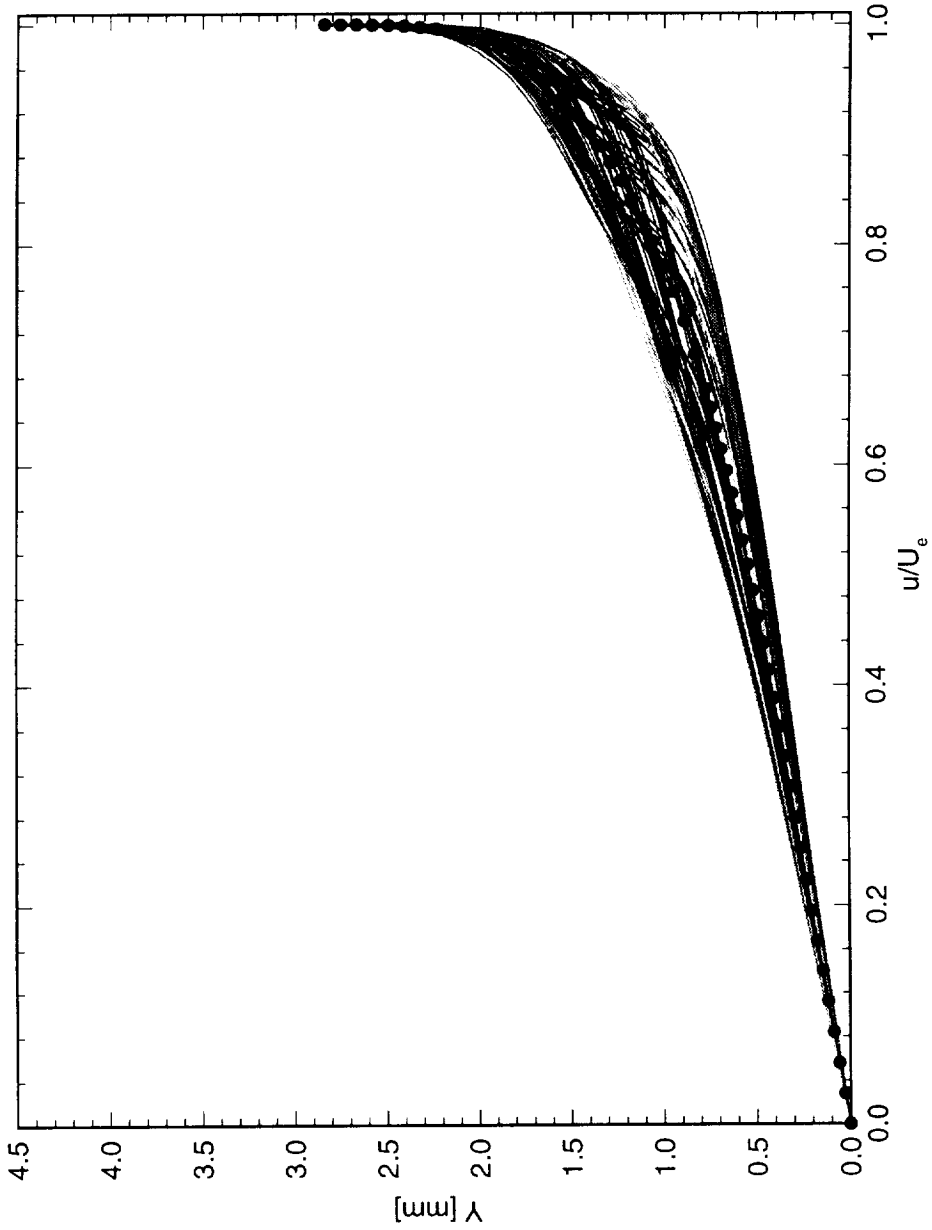

Figure 6.137: Spanwise array of 100 mean-flow boundary-layer profiles covering a span of 99 mm at $x/c = 0.20$. $Re_c = 2.4 \times 10^6$, [18|12] roughness. The dots indicate the mean of the profiles.

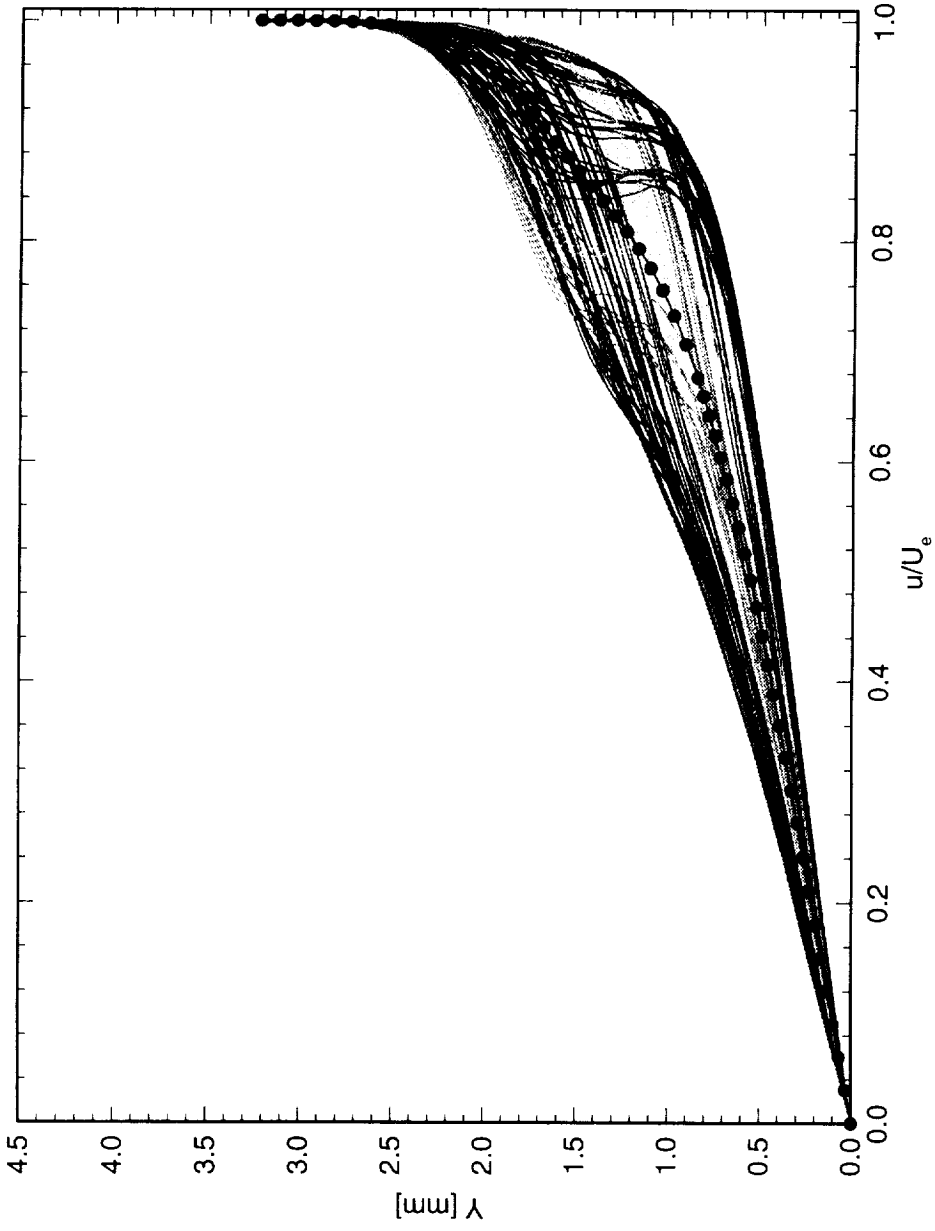

Figure 6.138: Spanwise array of 100 mean-flow boundary-layer profiles covering a span of 99 mm at $x/c = 0.25$. $Re_c = 2.4 \times 10^6$, [18|12] roughness. The dots indicate the mean of the profiles.

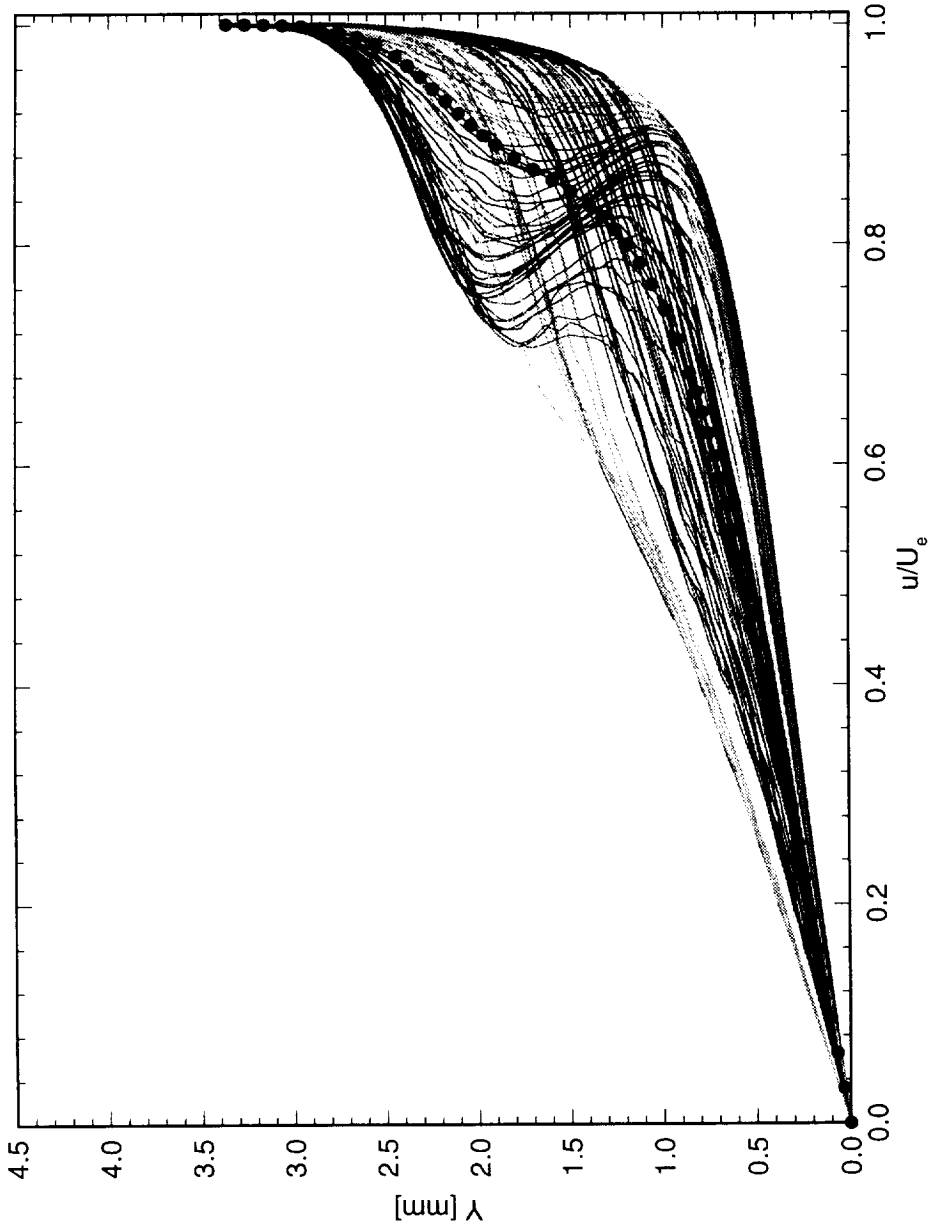

Figure 6.139: Spanwise array of 100 mean-flow boundary-layer profiles covering a span of 99 mm at $x/c = 0.30$. $Re_c = 2.4 \times 10^6$, [18|12] roughness. The dots indicate the mean of the profiles.

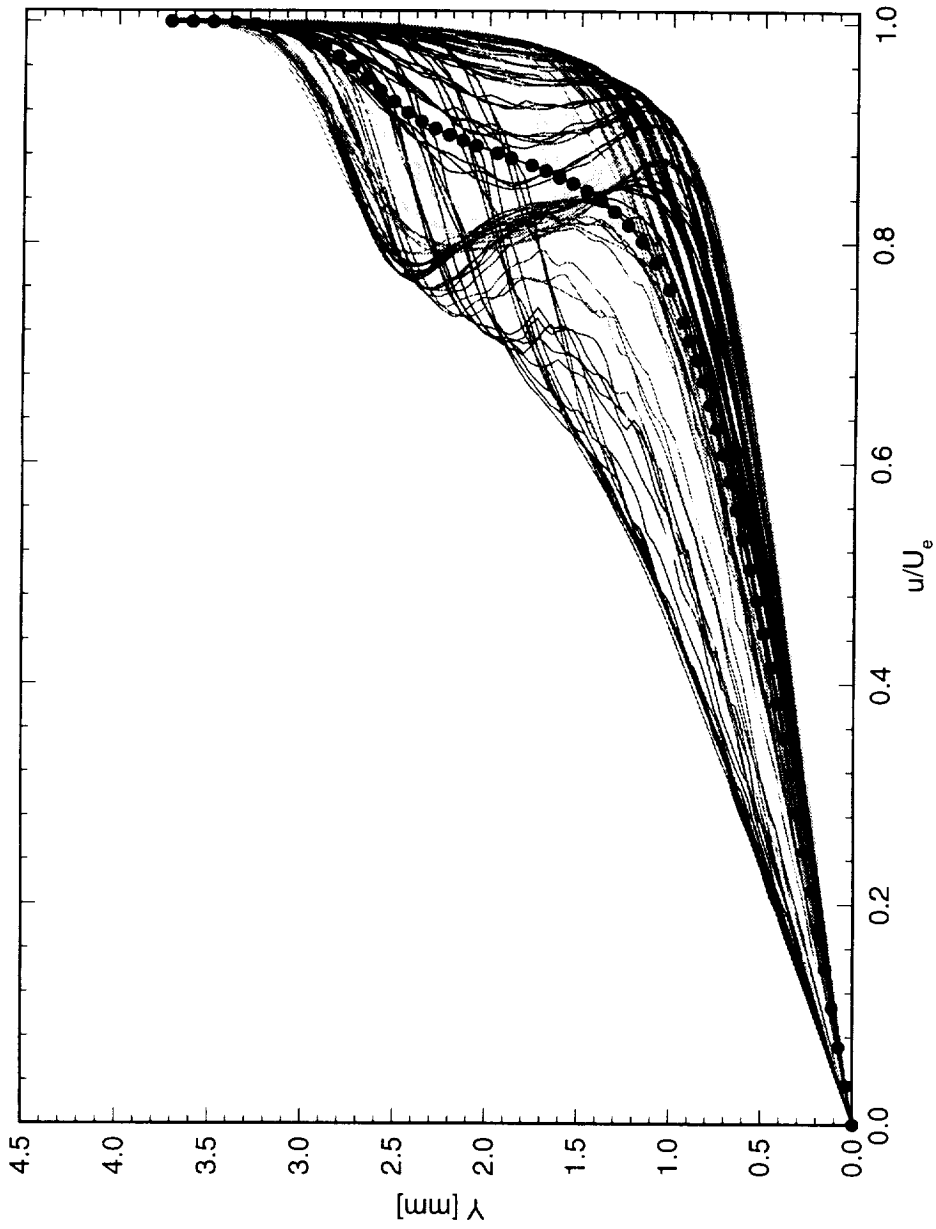

Figure 6.140: Spanwise array of 100 mean-flow boundary-layer profiles covering a span of 99 mm at $x/c = 0.35$. $Re_c = 2.4 \times 10^6$, [18|12] roughness. The dots indicate the mean of the profiles.

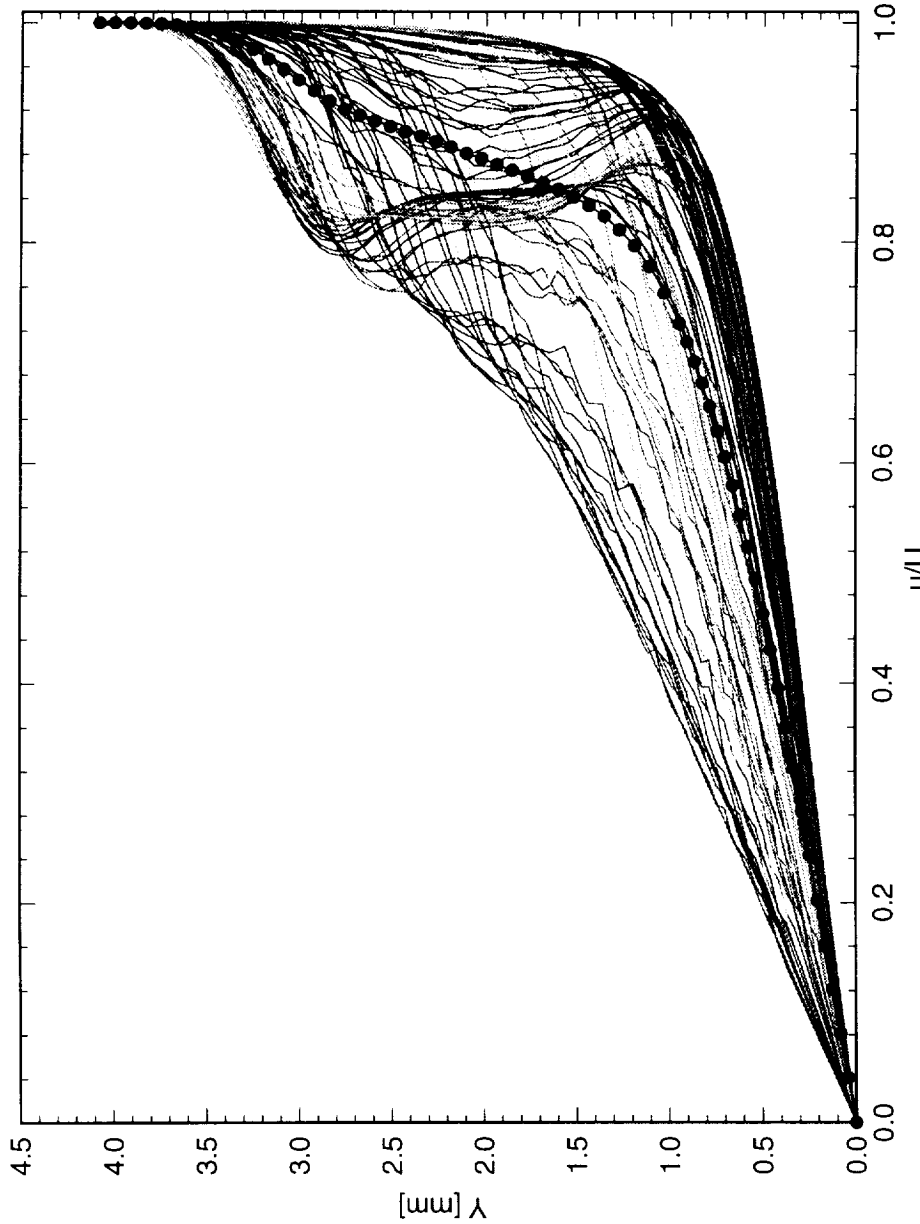

Figure 6.141: Spanwise array of 100 mean-flow boundary-layer profiles covering a span of 99 mm at $x/c = 0.40$. $Re_c = 2.4 \times 10^6$, [18|12] roughness. The dots indicate the mean of the profiles.

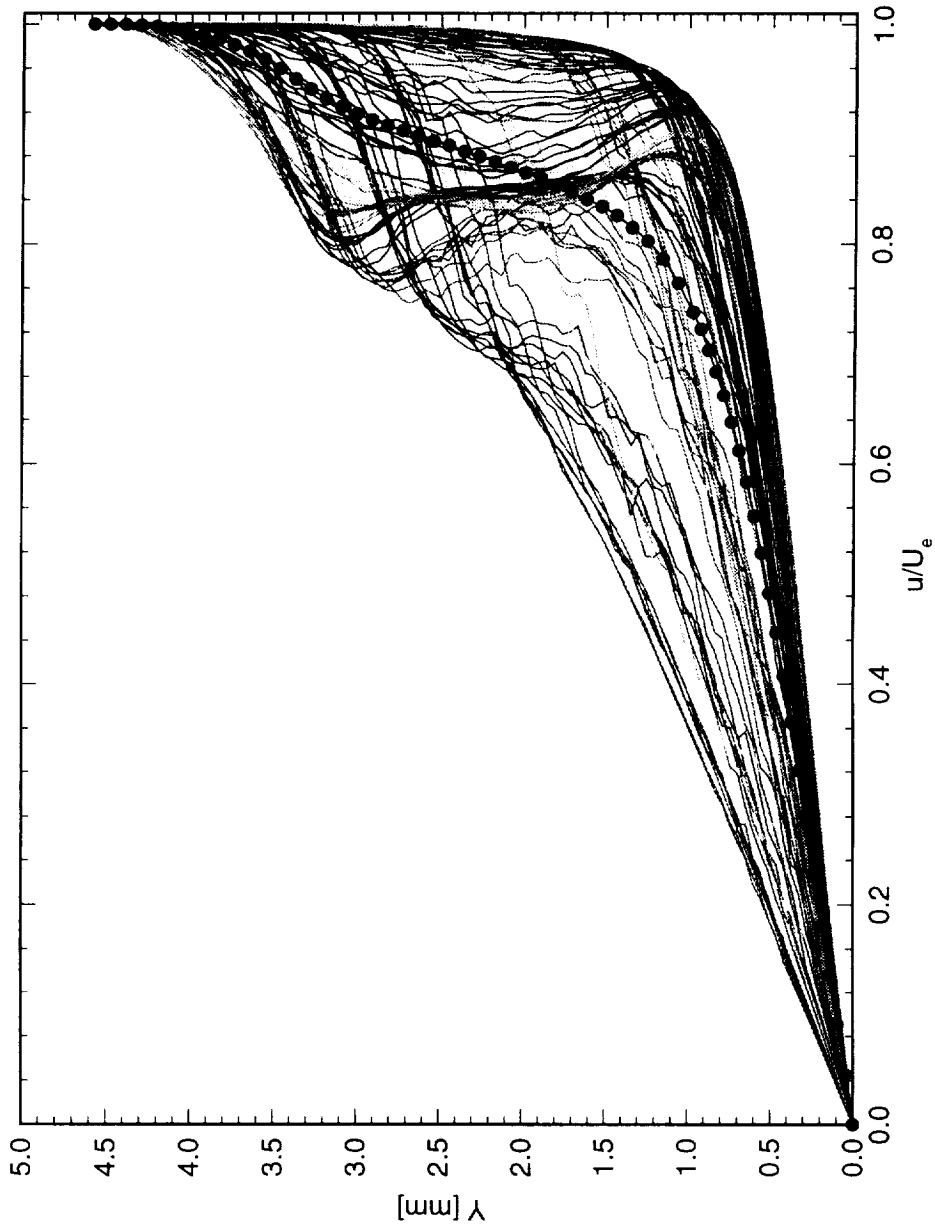

Figure 6.142: Spanwise array of 100 mean-flow boundary-layer profiles covering a span of 99 mm at $x/c = 0.45$. $Re_c = 2.4 \times 10^6$, [18|12] roughness. The dots indicate the mean of the profiles.

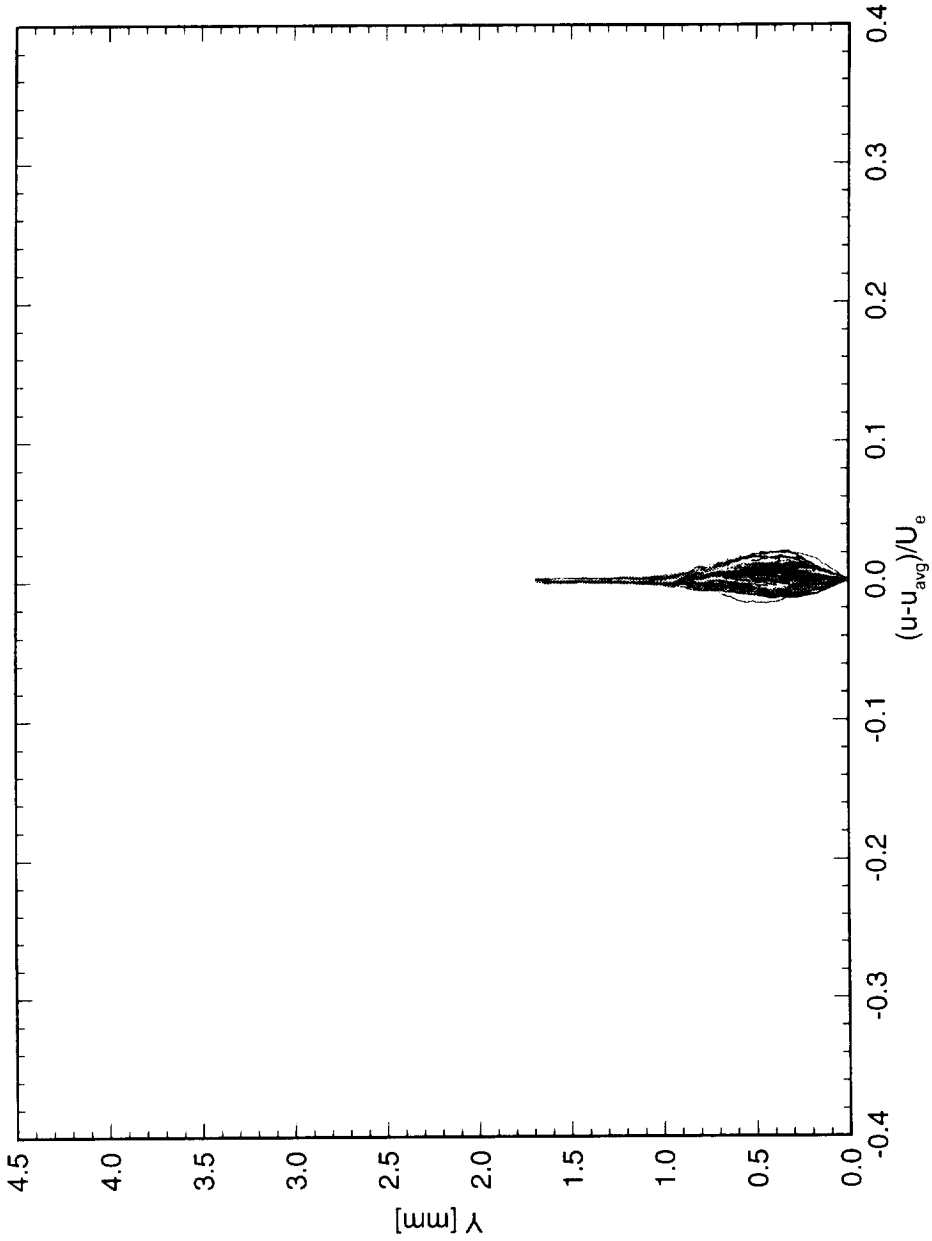

Figure 6.143: Spanwise array of 100 disturbance profiles covering a span of 99 mm at $x/c = 0.05$. $Re_c = 2.4 \times 10^6$, [18|12] roughness.

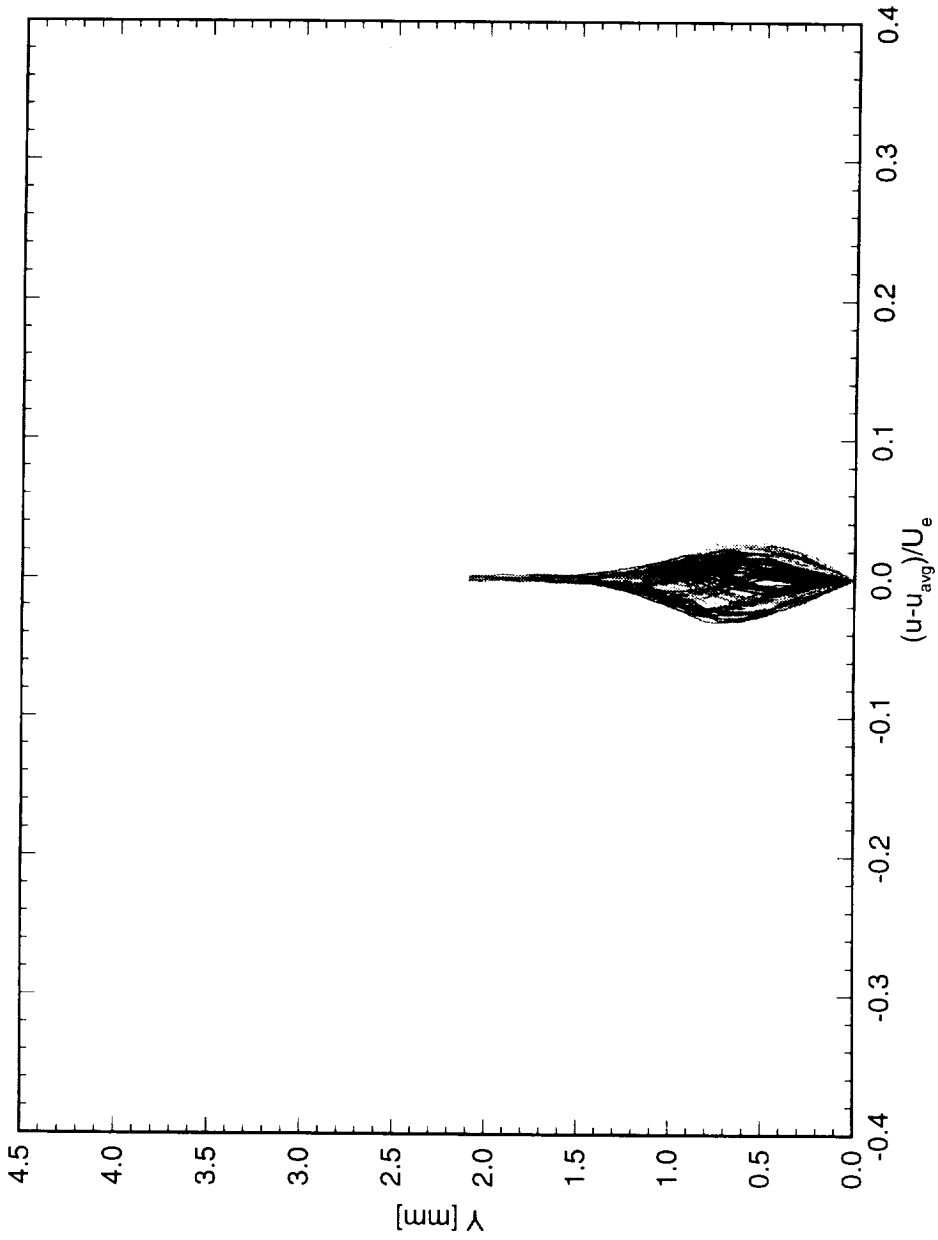

Figure 6.144: Spanwise array of 100 disturbance profiles covering a span of 99 mm at $x/c = 0.10$. $Re_c = 2.4 \times 10^6$, [18|12] roughness.

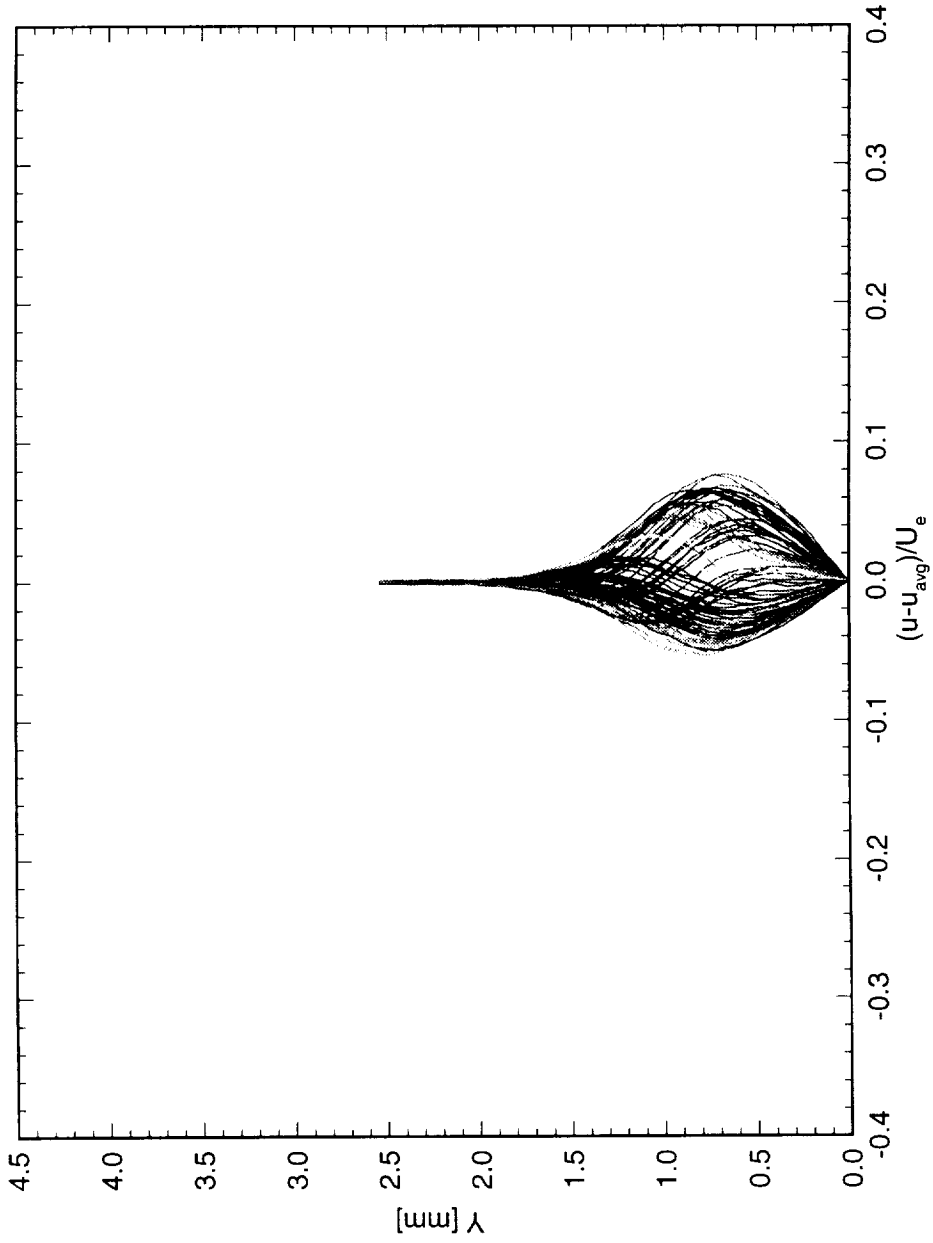

Figure 6.145: Spanwise array of 100 disturbance profiles covering a span of 99 mm at $x/c = 0.15$. $Re_c = 2.4 \times 10^6$, [18|12] roughness.

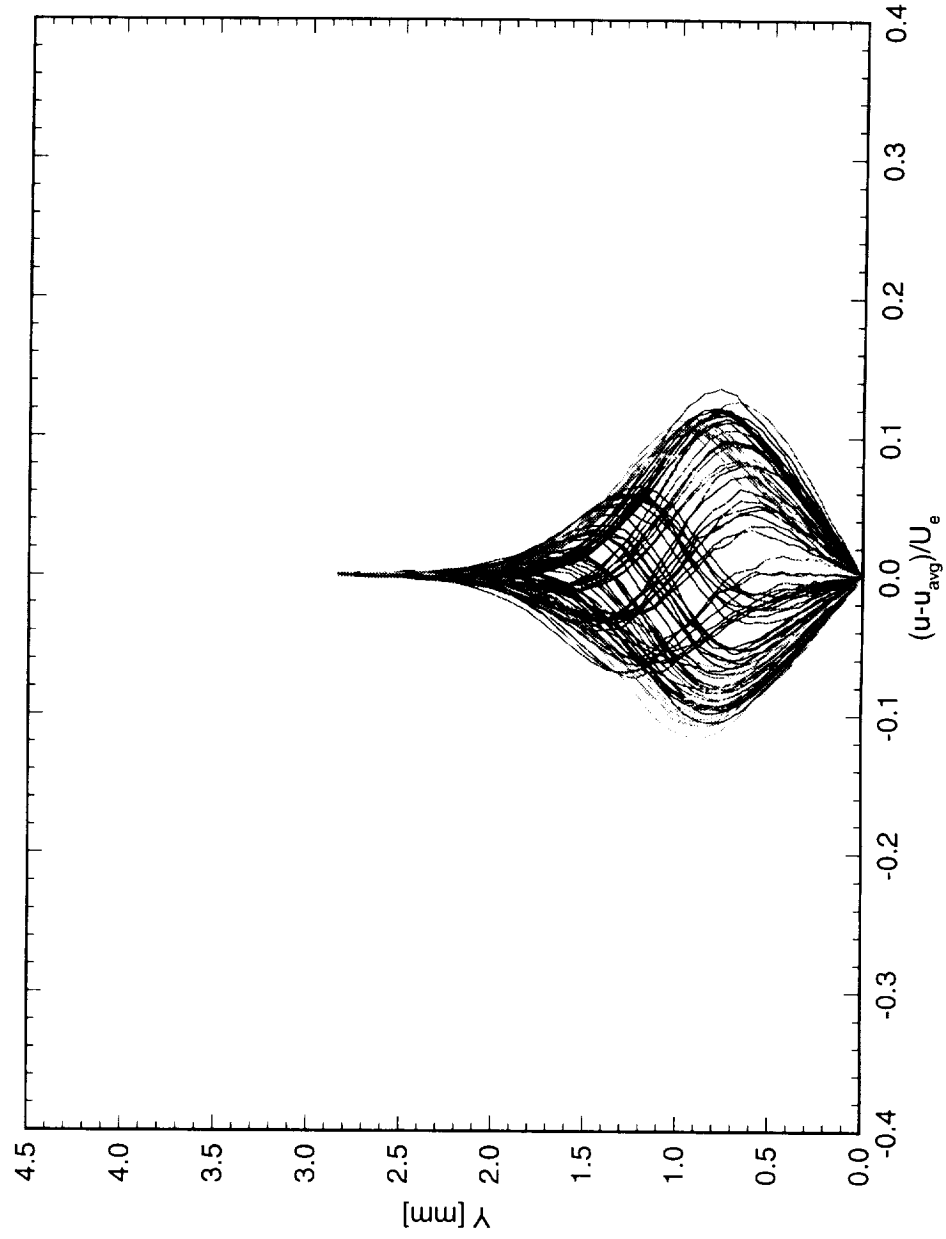

Figure 6.146: Spanwise array of 100 disturbance profiles covering a span of 99 mm at $x/c = 0.20$. $Re_c = 2.4 \times 10^6$, [18|12] roughness.

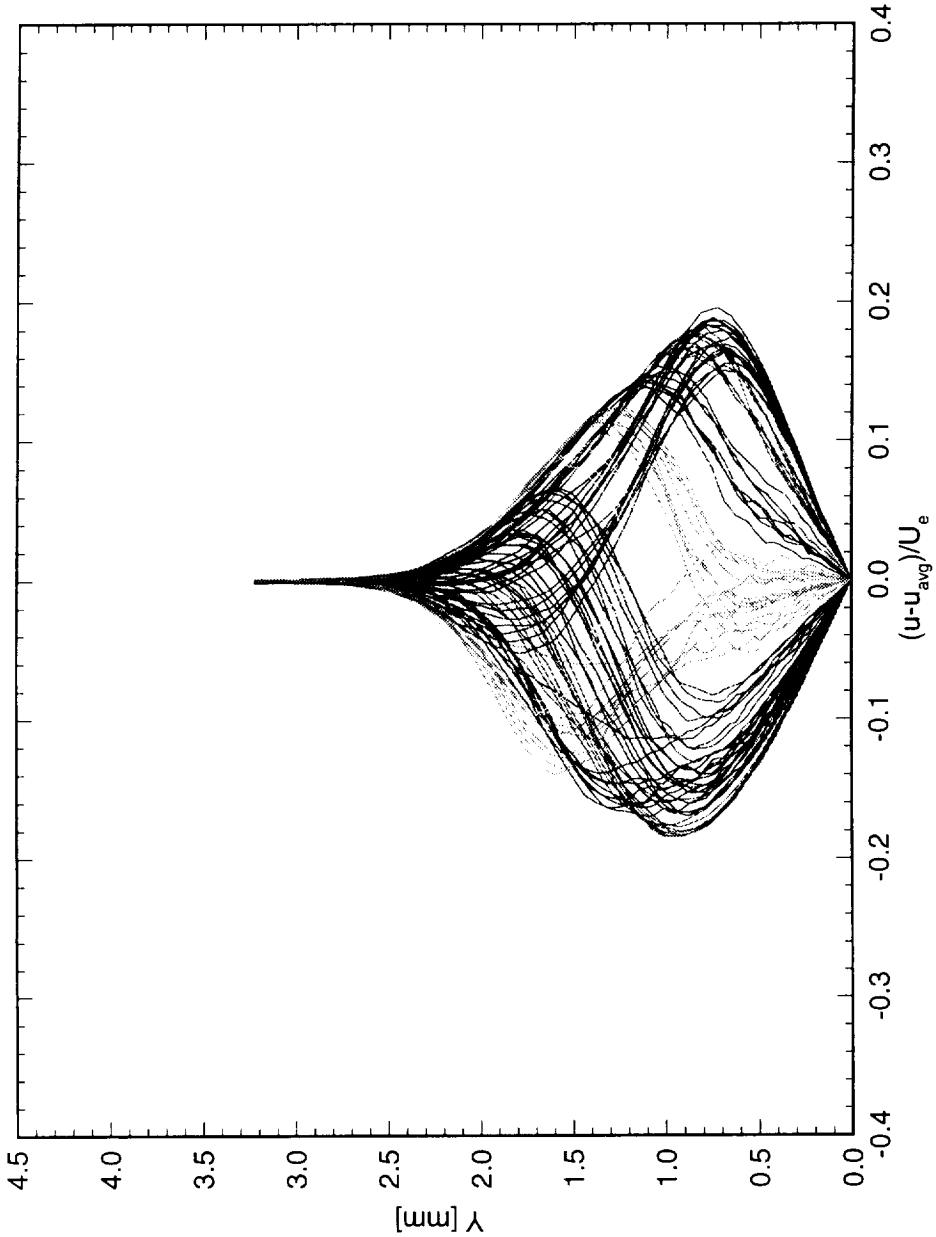

Figure 6.147: Spanwise array of 100 disturbance profiles covering a span of 99 mm at $x/c = 0.25$. $Re_c = 2.4 \times 10^6$, [18|12] roughness.

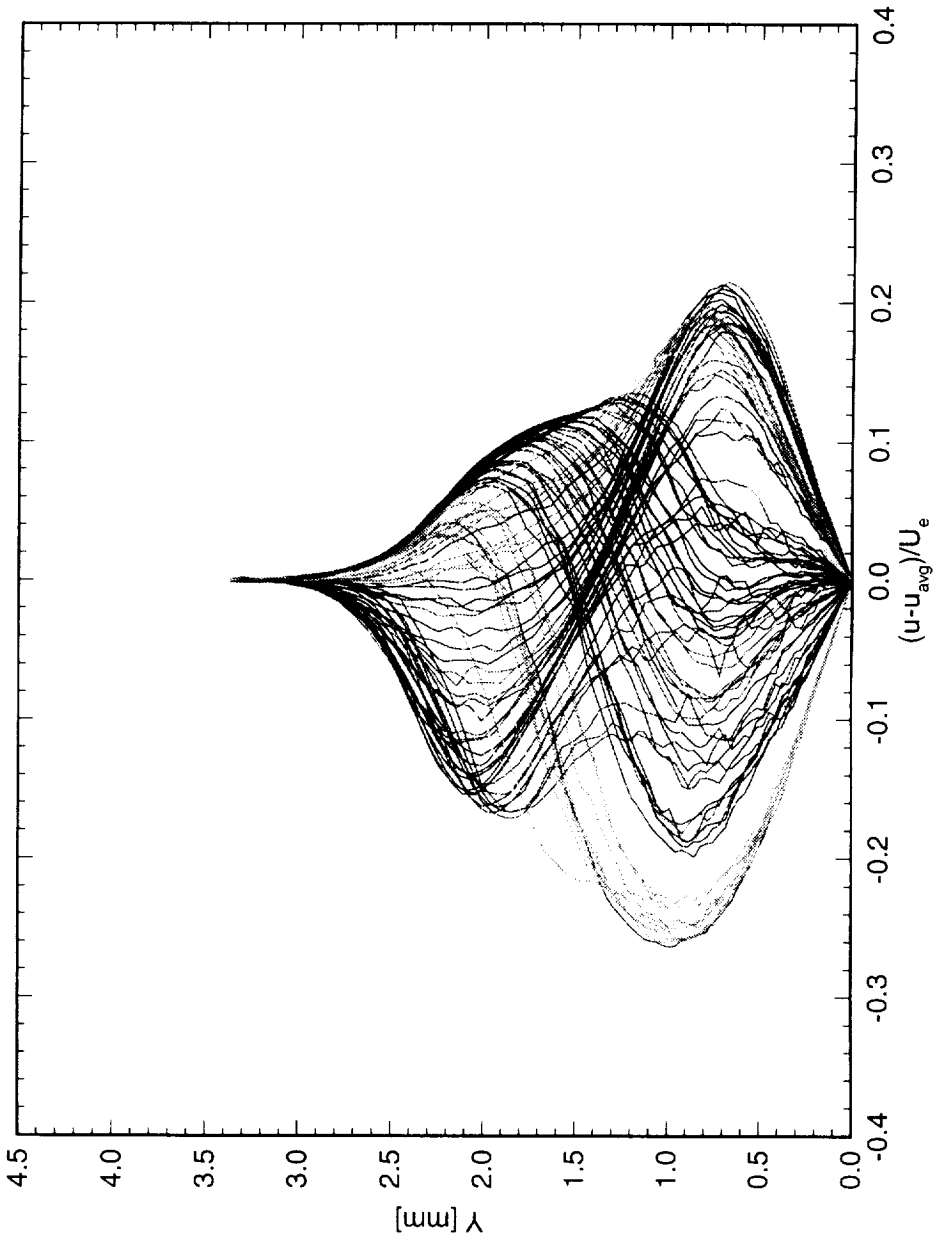

Figure 6.148: Spanwise array of 100 disturbance profiles covering a span of 99 mm at $x/c = 0.30$. $Re_c = 2.4 \times 10^6$, [18|12] roughness.

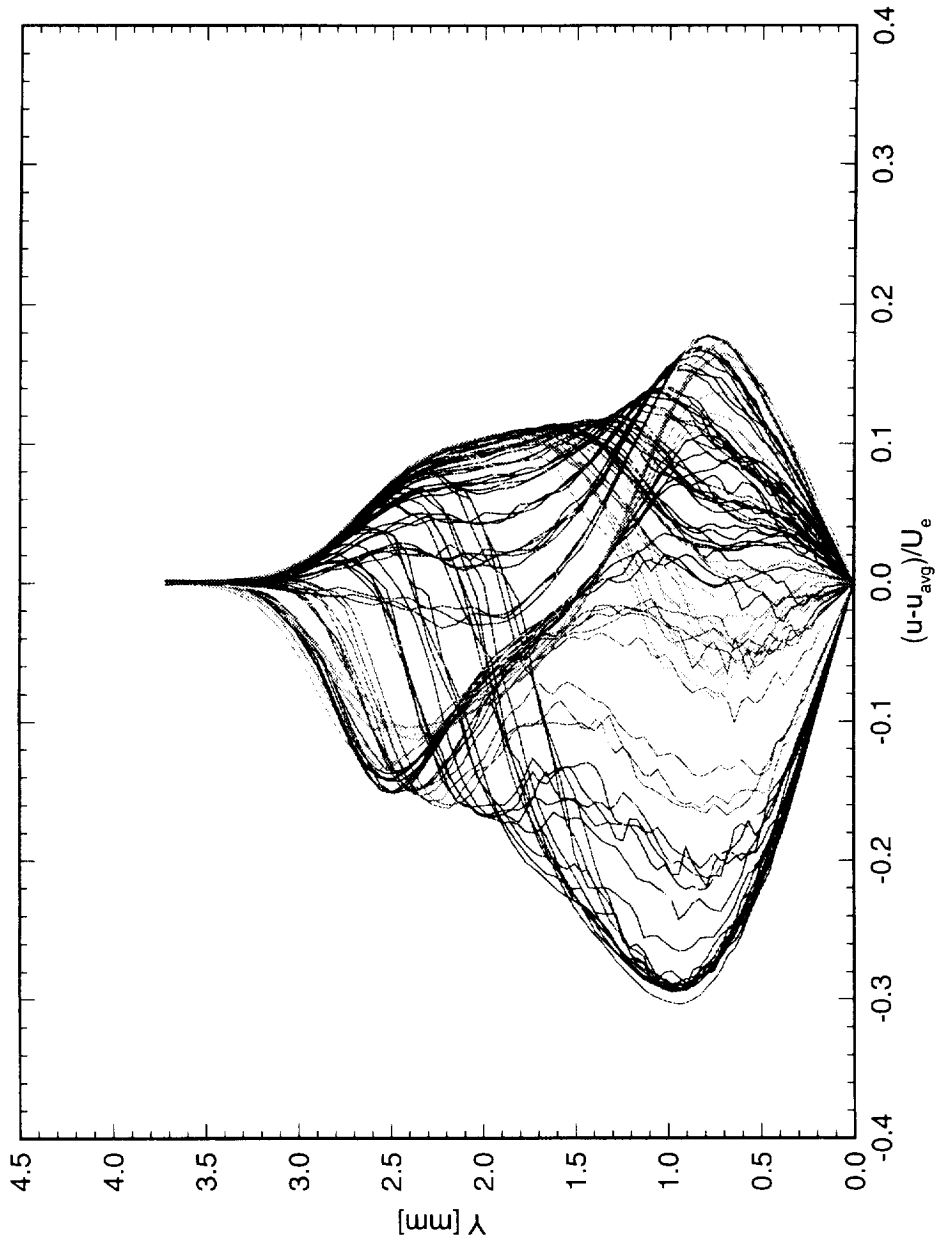

Figure 6.149: Spanwise array of 100 disturbance profiles covering a span of 99 mm at $x/c = 0.35$. $Re_c = 2.4 \times 10^6$, [18|12] roughness.

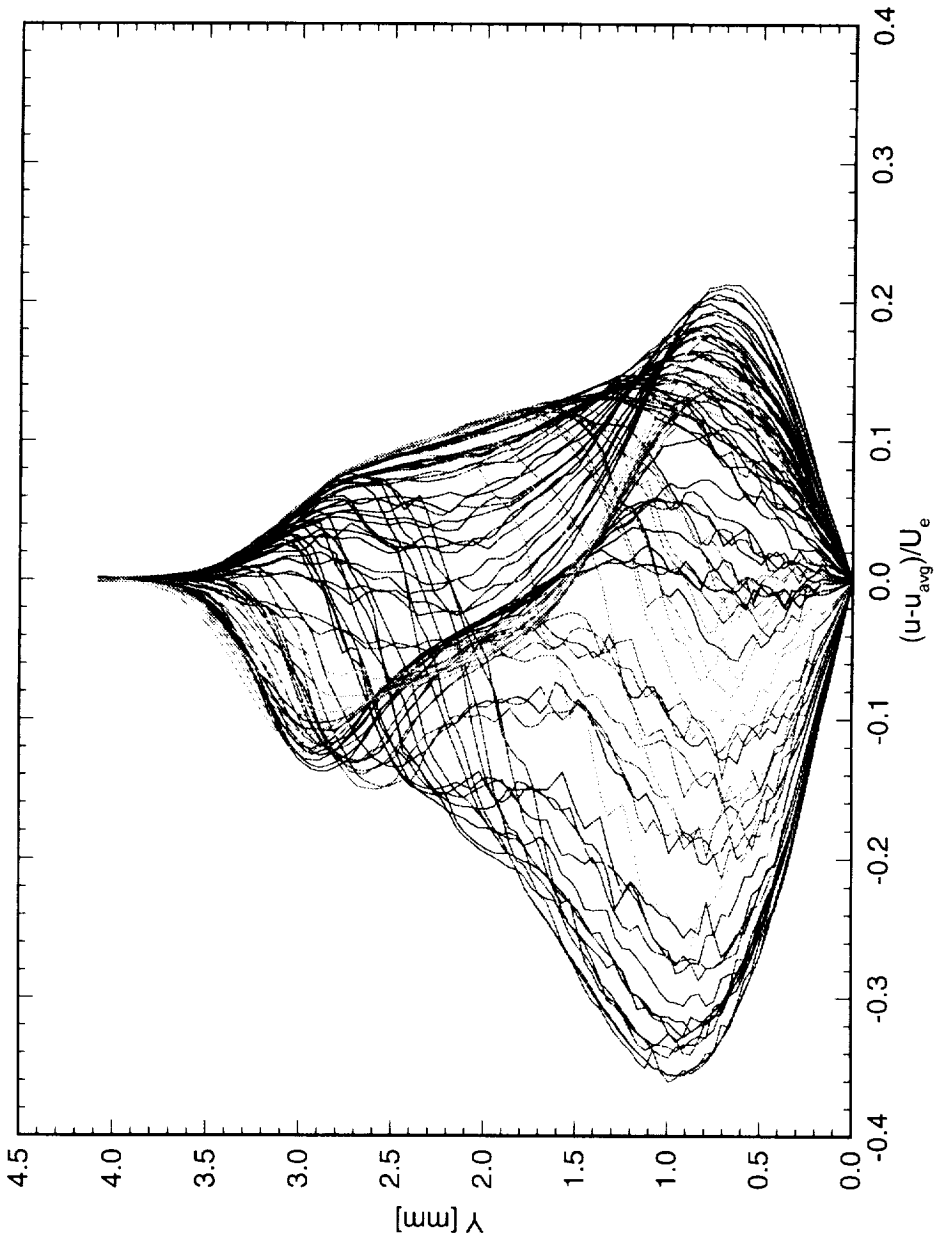

Figure 6.150: Spanwise array of 100 disturbance profiles covering a span of 99 mm at $x/c = 0.40$. $Re_c = 2.4 \times 10^6$, [18|12] roughness.

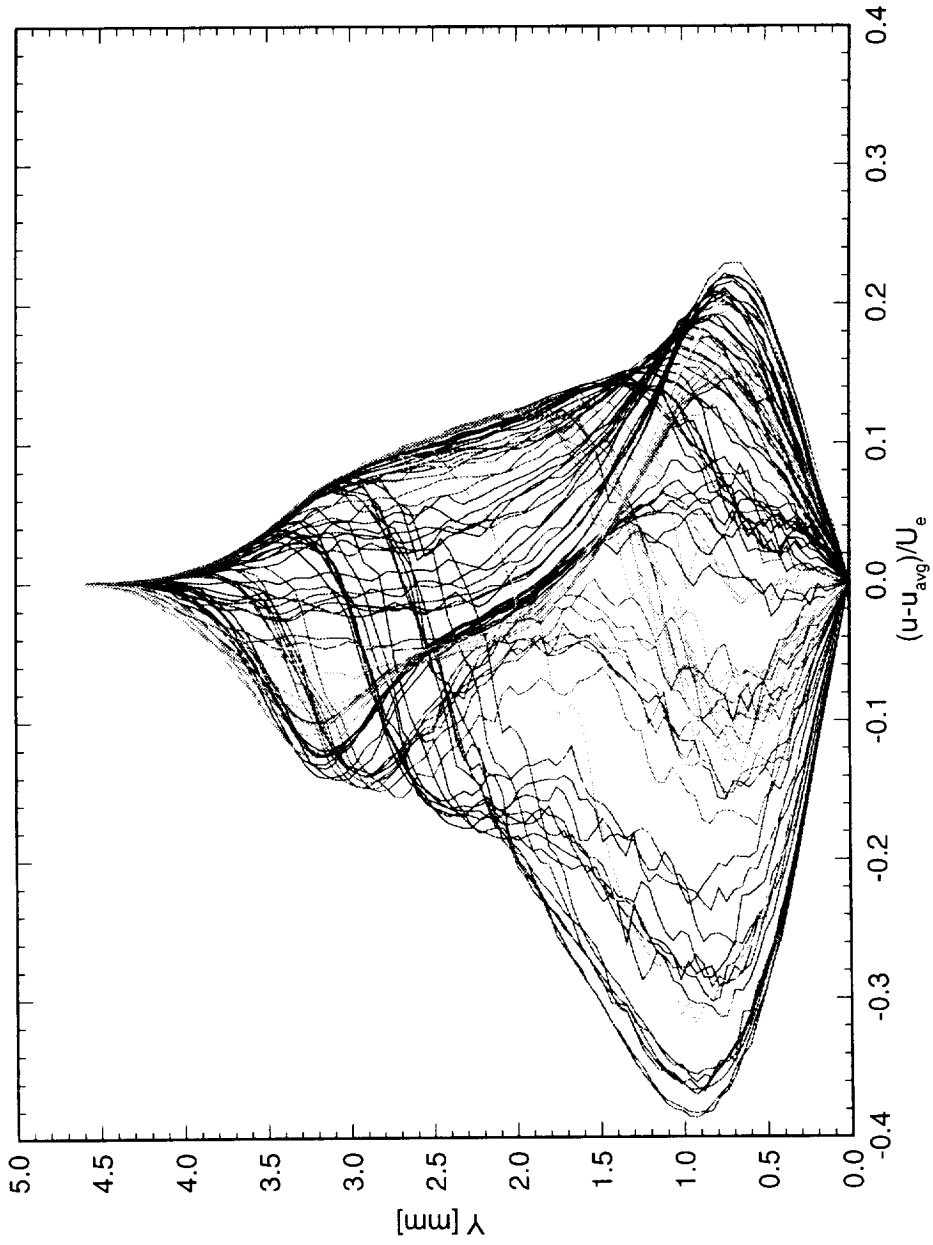

Figure 6.151: Spanwise array of 100 disturbance profiles covering a span of 99 mm at $x/c = 0.45$. $Re_c = 2.4 \times 10^6$, [18|12] roughness.

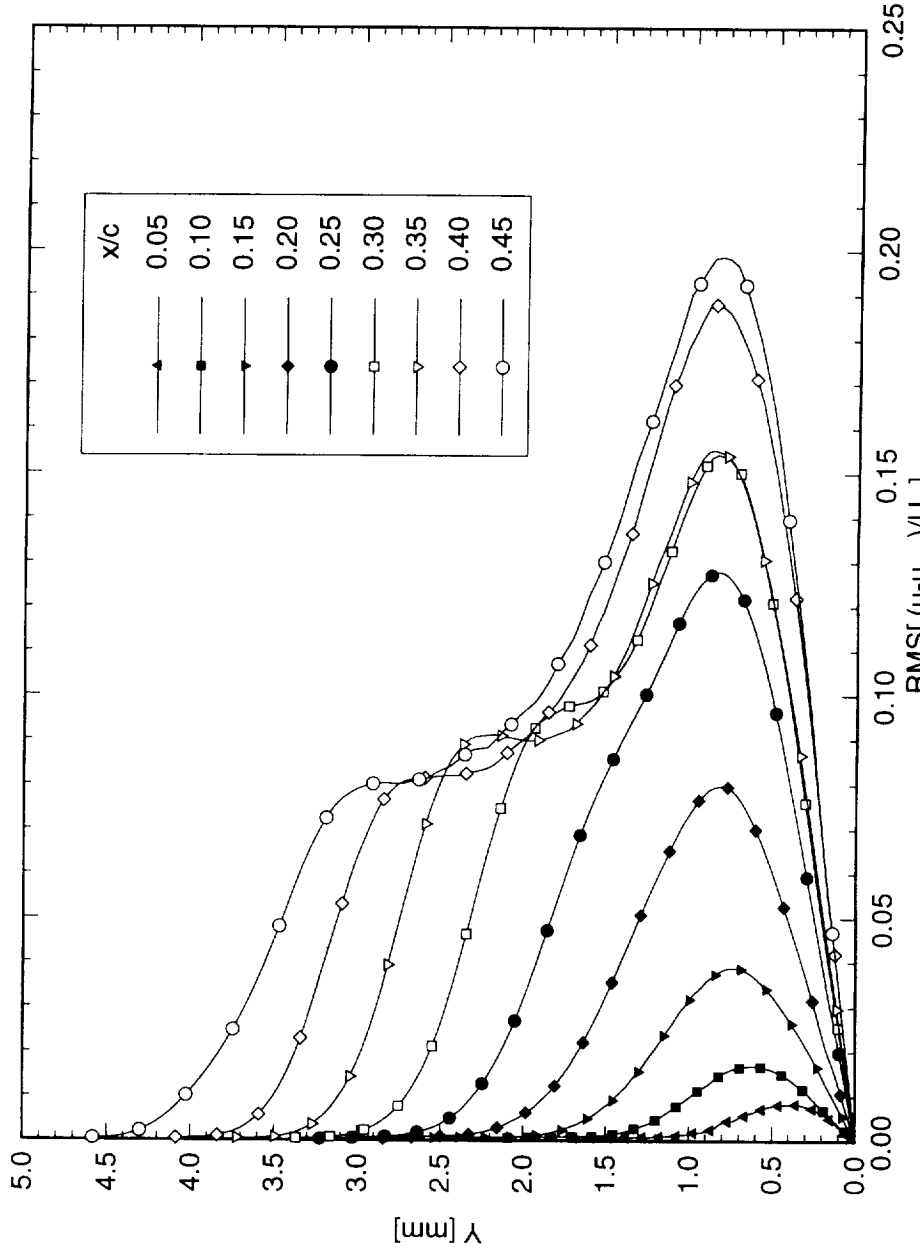

Figure 6.152: Stationary crossflow mode shapes for $Re_c = 2.4 \times 10^6$ and [18|12] roughness. The symbols are simply identifiers and do not represent measurement points.

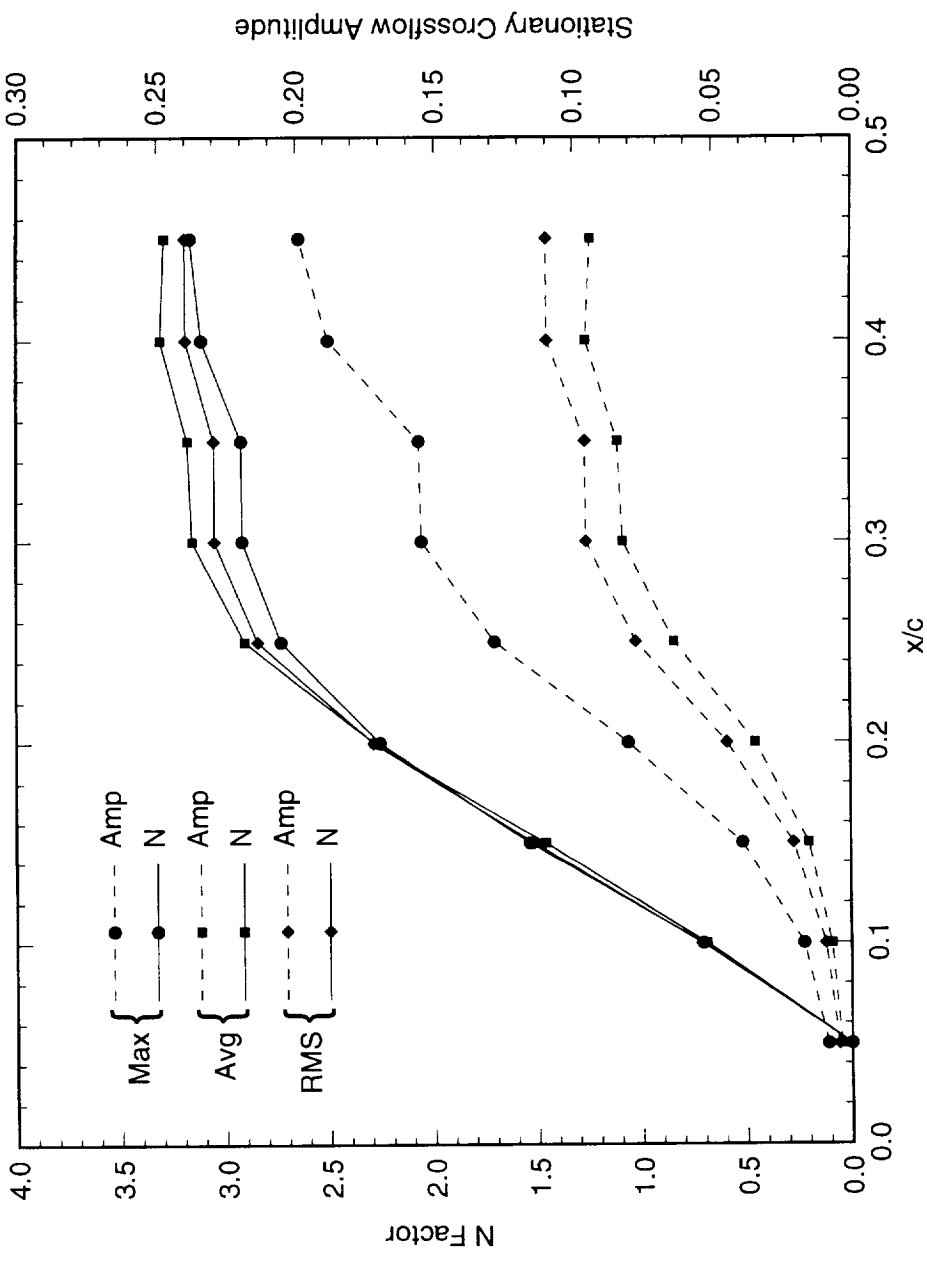

Figure 6.153: Total disturbance amplitude and amplification factor N for $Re_c = 2.4 \times 10^6$ and [18|12] roughness. The reference point for the N-factor calculations is $x/c = 0.05$.

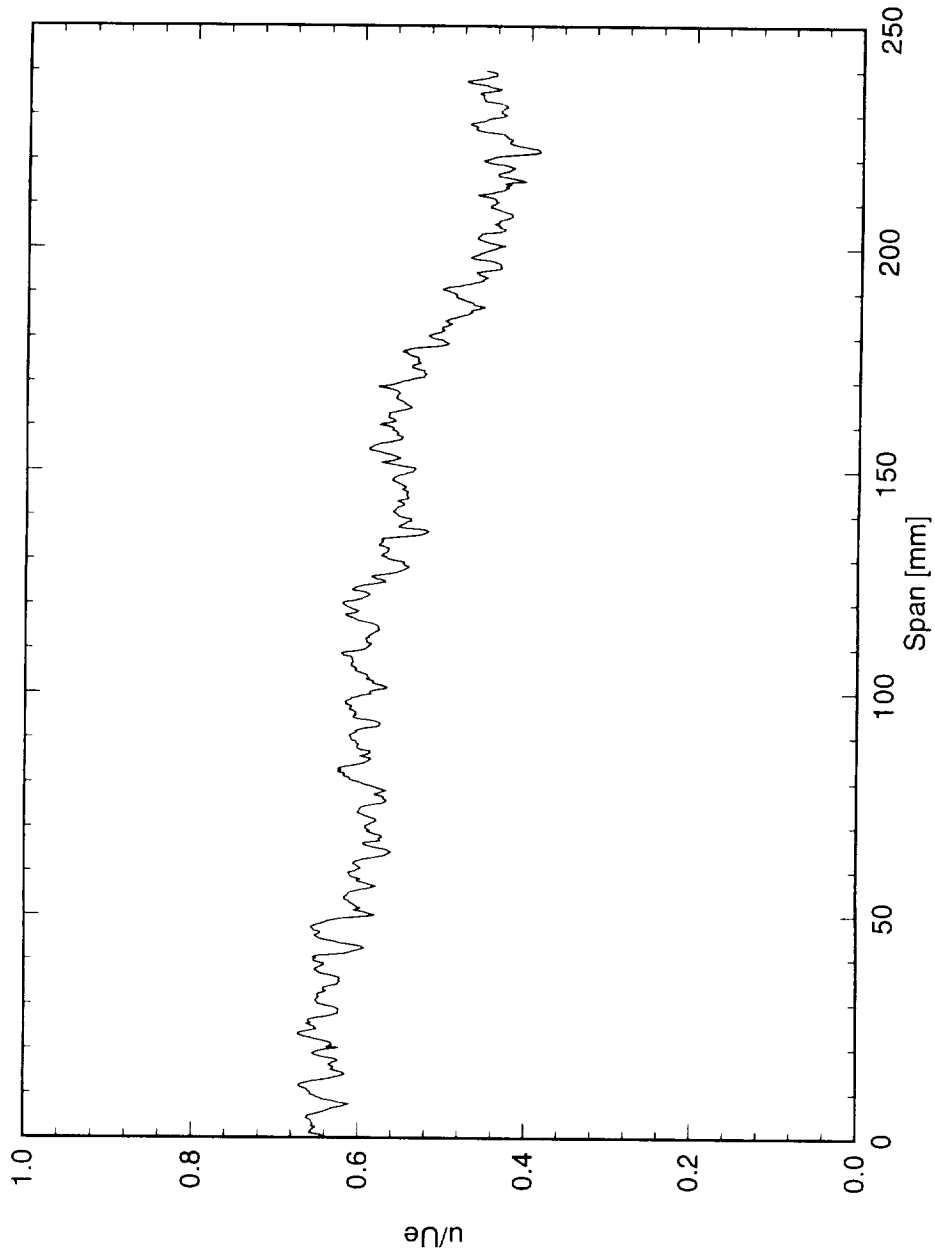

Figure 6.154: Spanwise hot-wire scan at $x/c = 0.05$, $Y = 0.4$ mm. $Re_c = 2.4 \times 10^6$, [18|12] roughness.

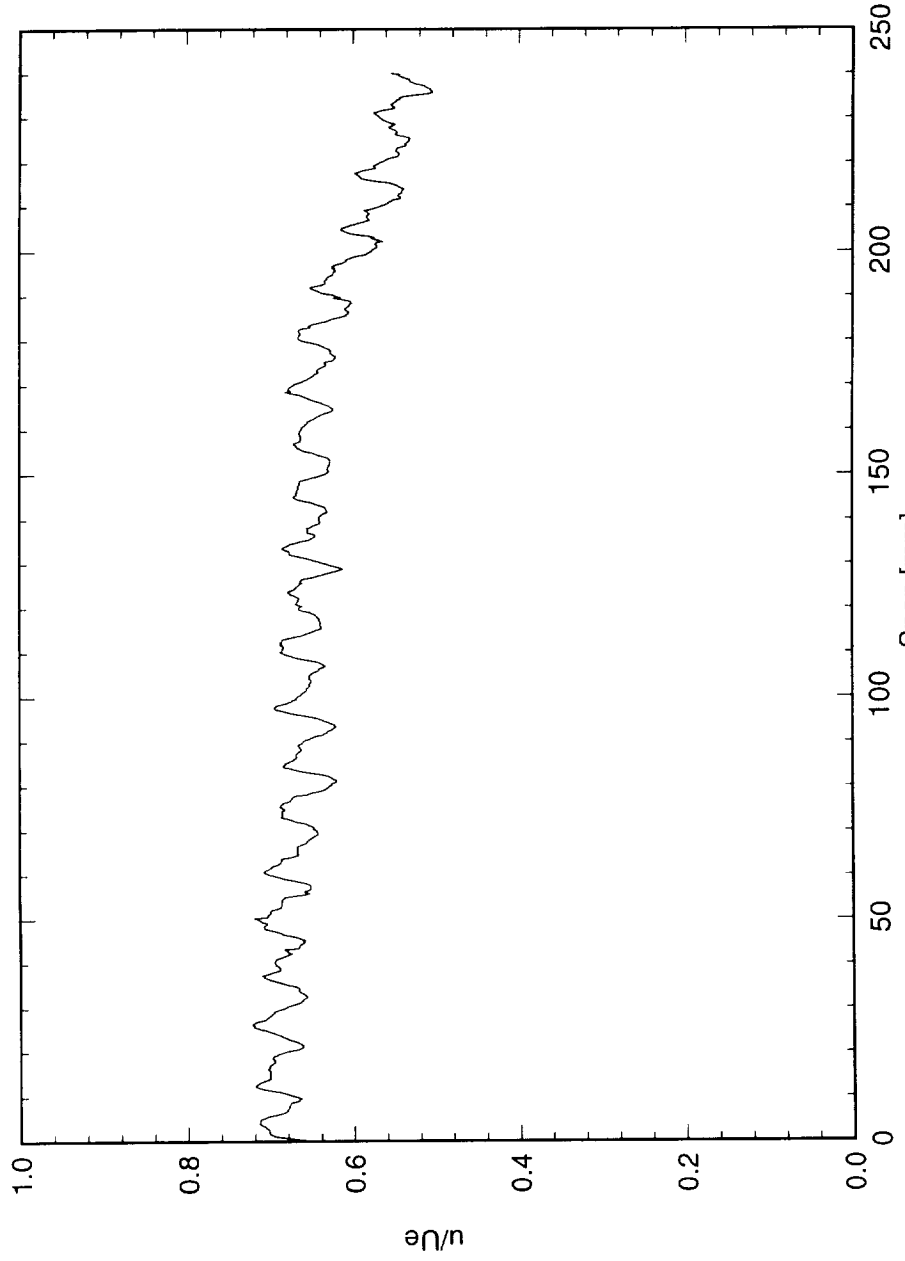

Figure 6.155: Spanwise hot-wire scan at $x/c = 0.10$, $Y = 0.6$ mm. $Re_c = 2.4 \times 10^6$, [18|12] roughness.

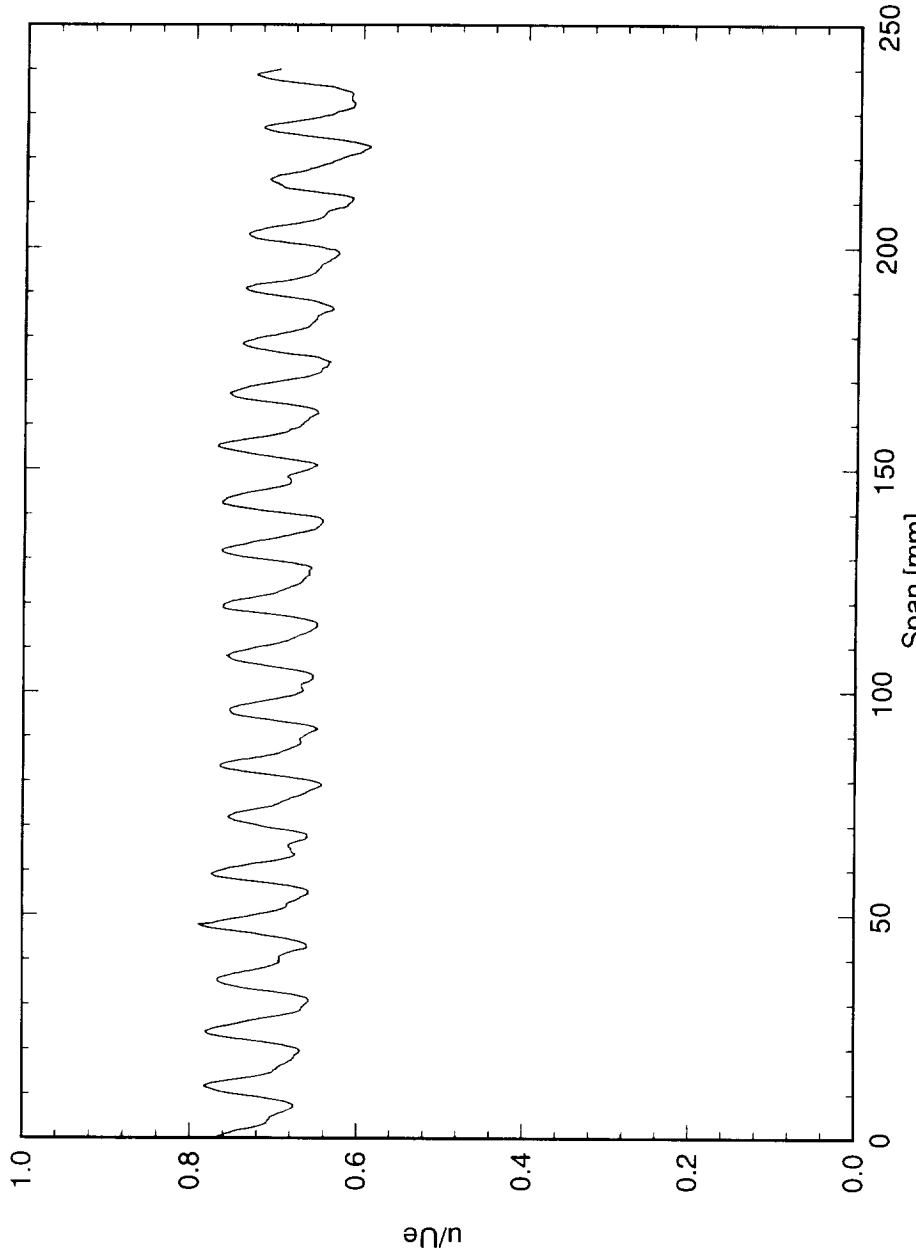

Figure 6.156: Spanwise hot-wire scan at $x/c = 0.15$, $Y = 0.75$ mm. $Re_c = 2.4 \times 10^6$, [18|12] roughness.

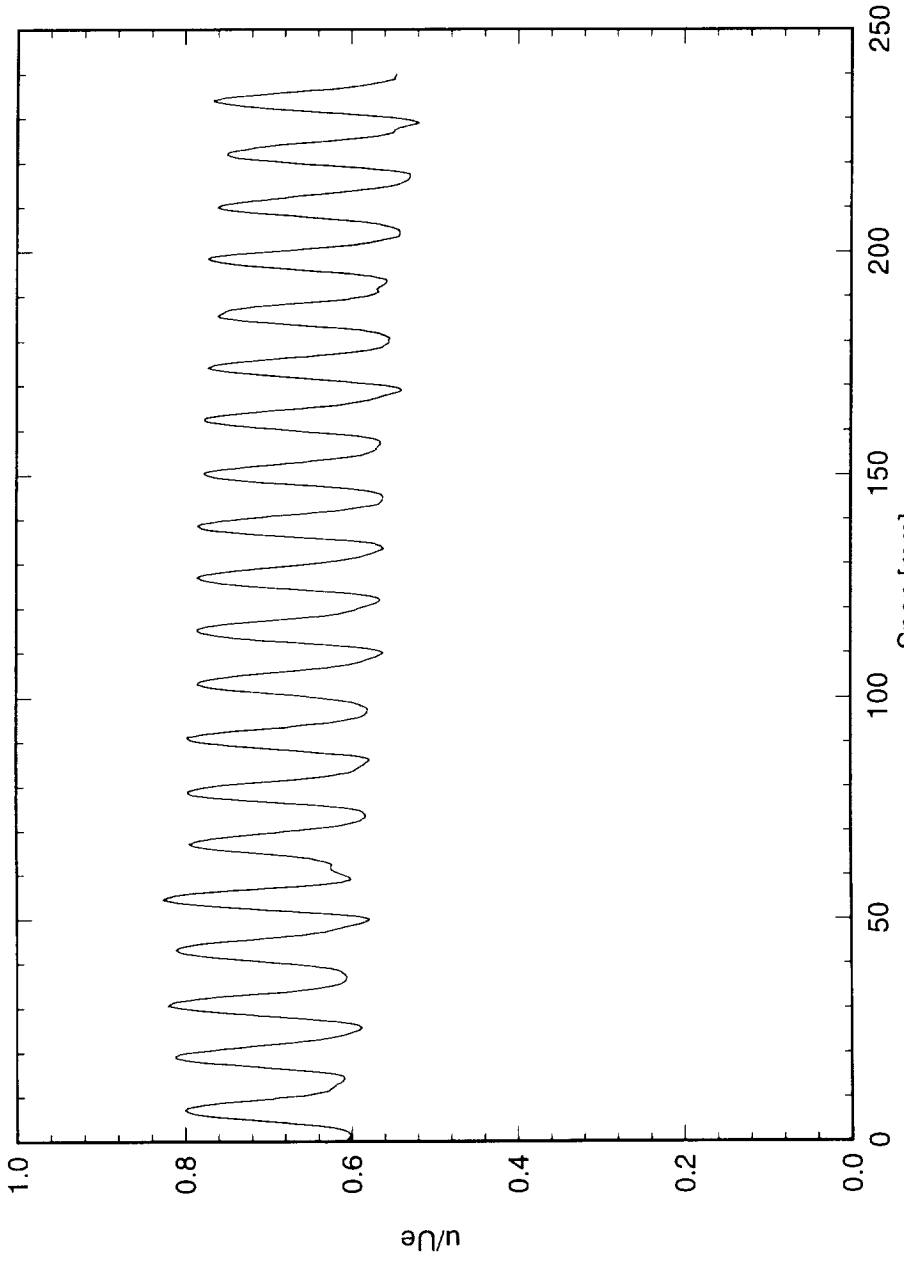

Figure 6.157: Spanwise hot-wire scan at $x/c = 0.20$, $Y = 0.8$ mm. $Re_c = 2.4 \times 10^6$, [18|12] roughness.

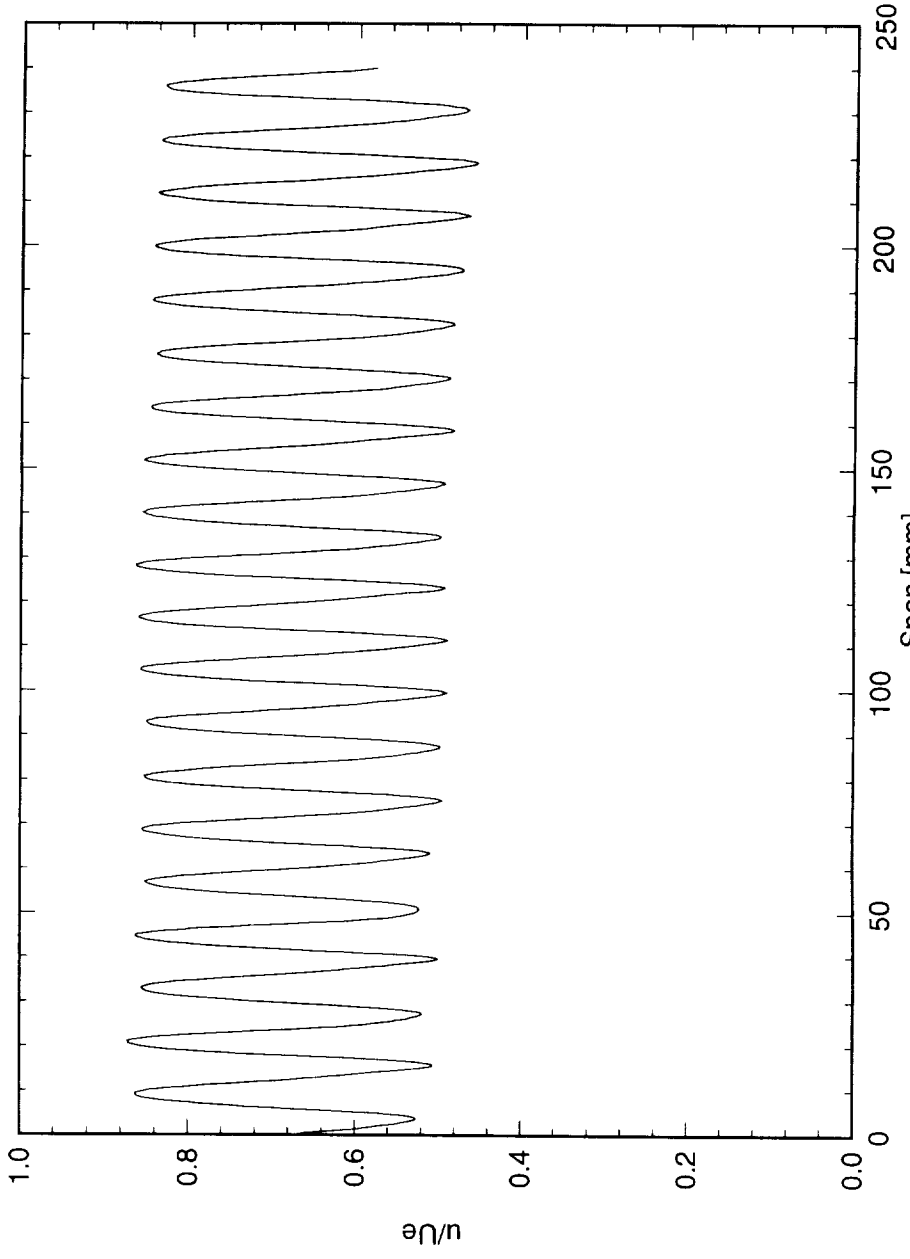

Figure 6.158: Spanwise hot-wire scan at $x/c = 0.25$, $Y = 0.85$ mm. $Re_c = 2.4 \times 10^6$, [18|12] roughness.

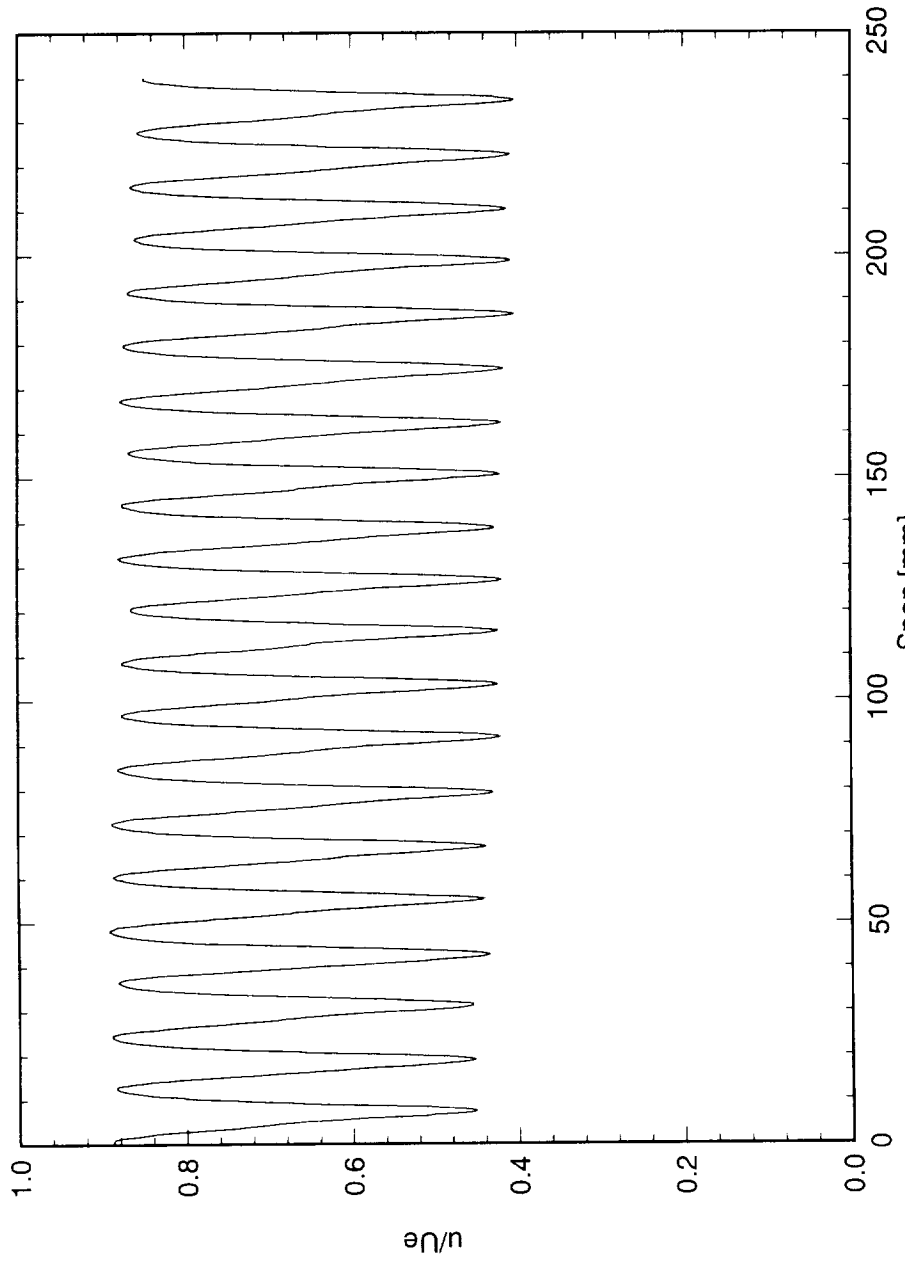

Figure 6.159: Spanwise hot-wire scan at $x/c = 0.30$, $Y = 0.85$ mm. $Re_c = 2.4 \times 10^6$, [18|12] roughness.

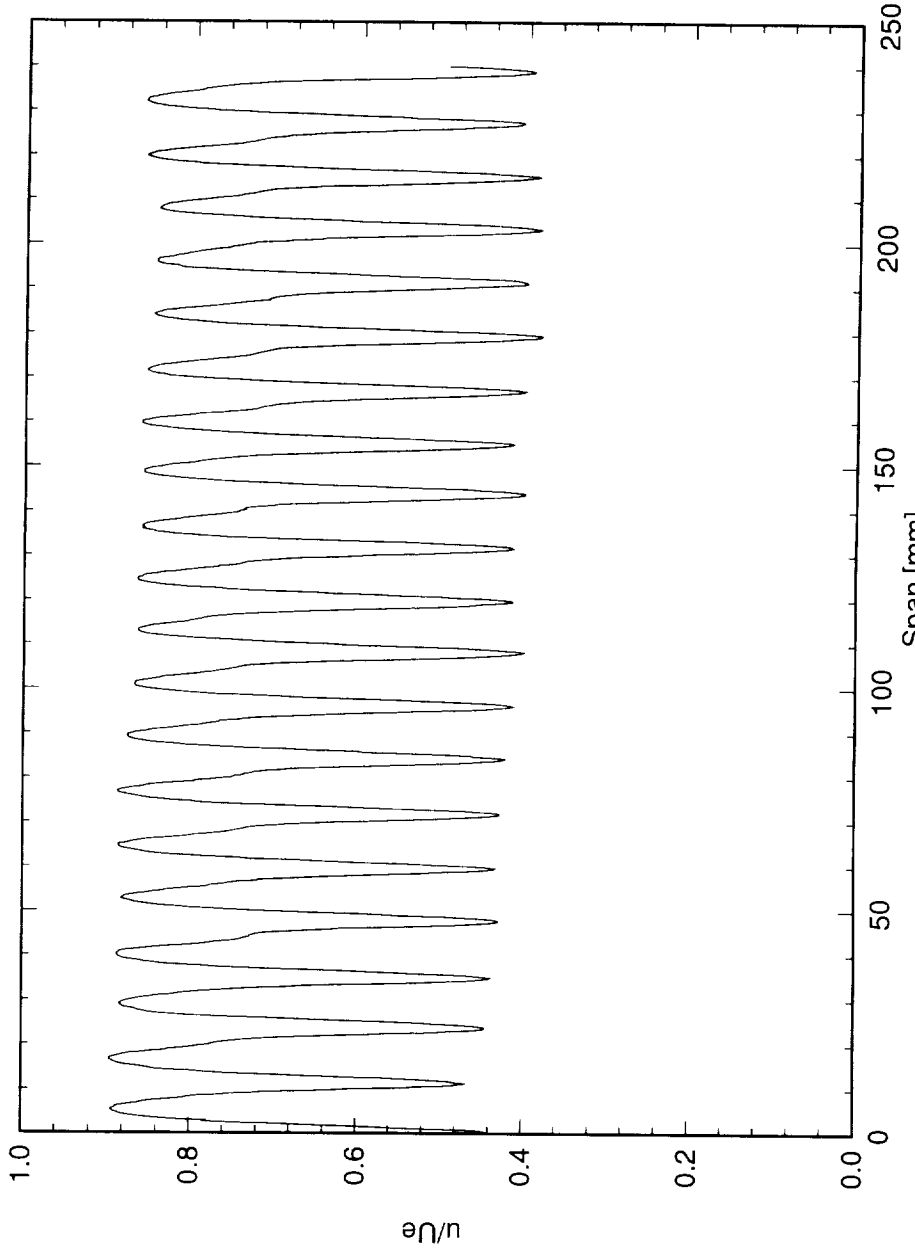

Figure 6.160: Spanwise hot-wire scan at $x/c = 0.35$, $Y' = 0.85$ mm. $Re_c = 2.4 \times 10^6$, [18|12] roughness.

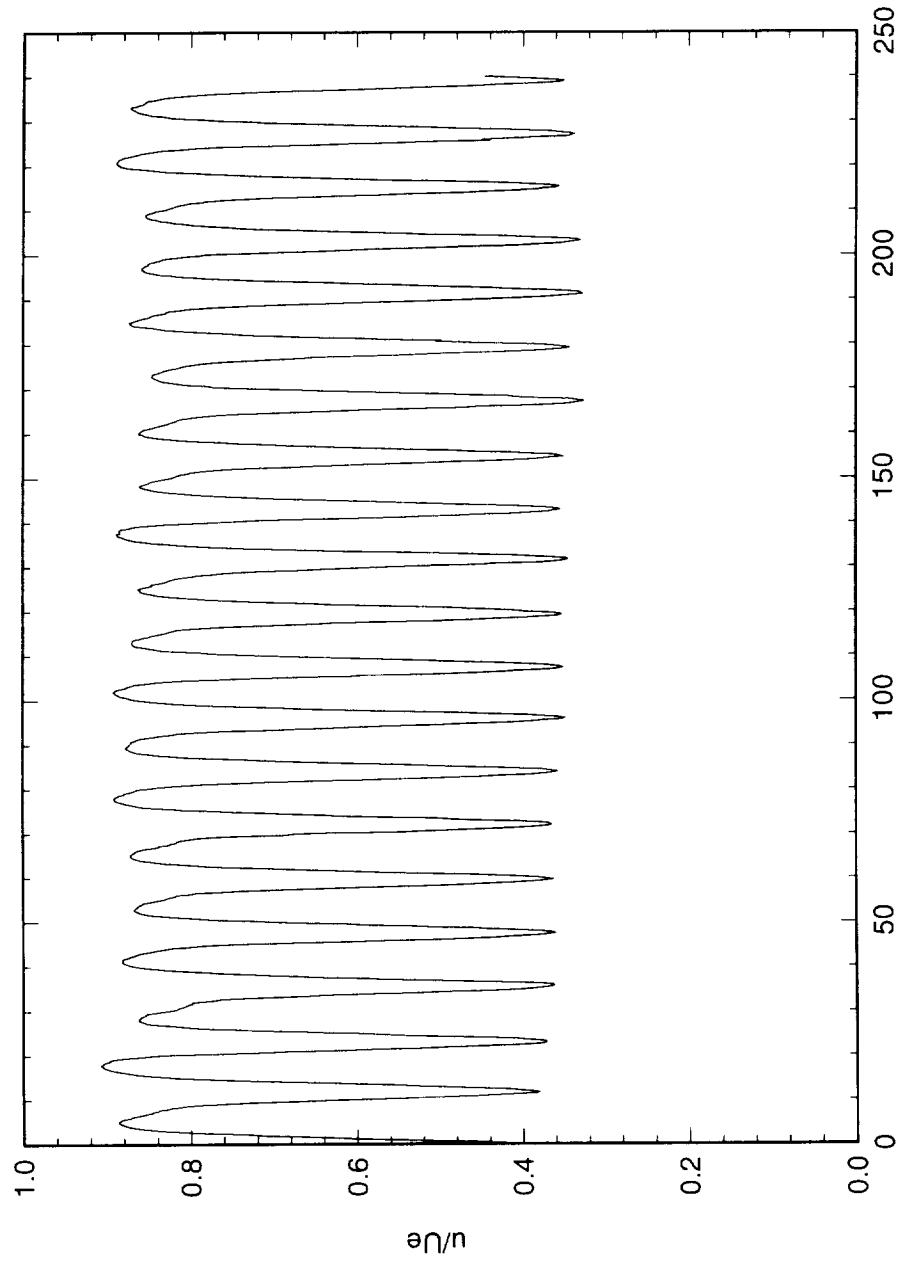

Figure 6.161: Spanwise hot-wire scan at $x/c = 0.40$, $Y = 0.85$ mm. $Re_c = 2.4 \times 10^6$, [18|12] roughness.

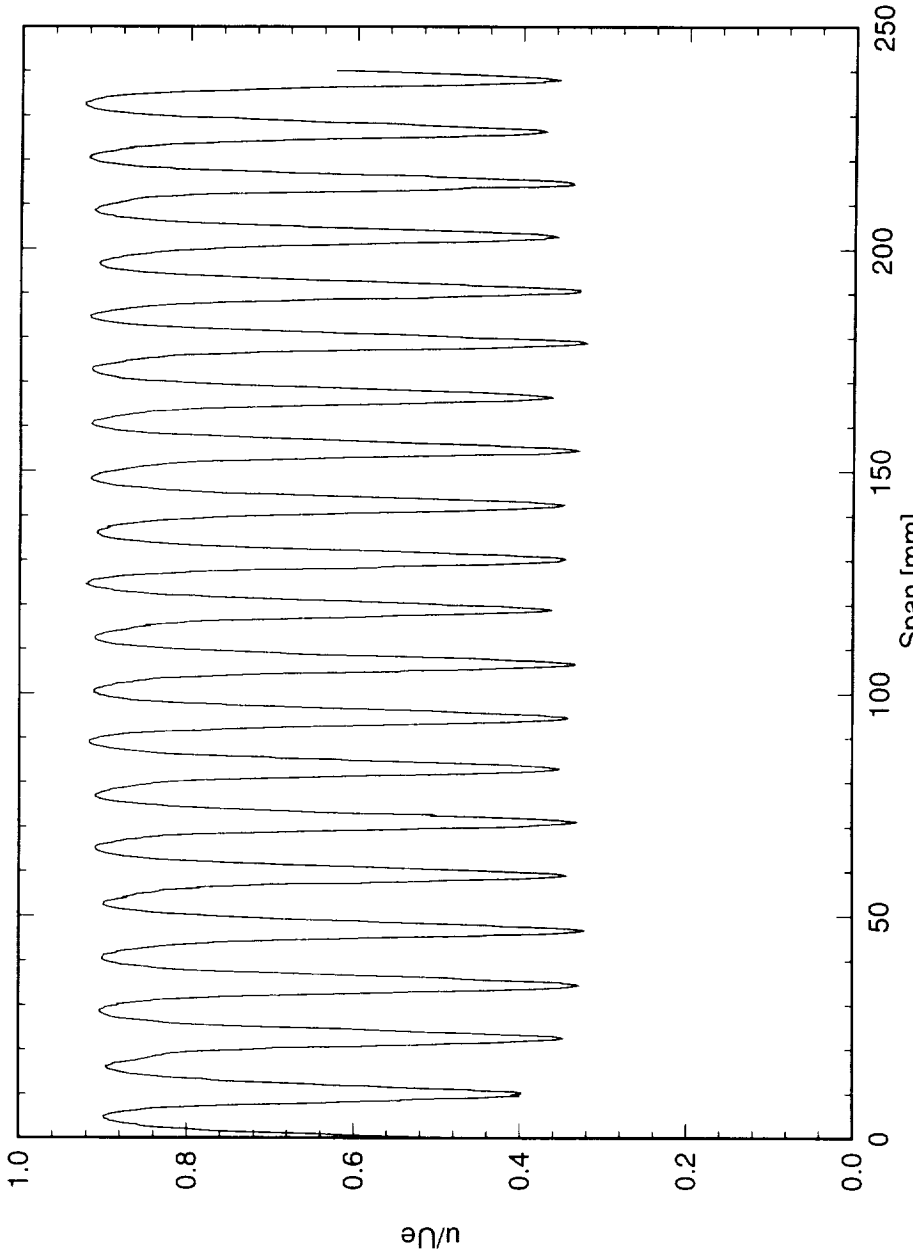

Figure 6.162: Spanwise hot-wire scan at $x/c = 0.45$, $Y = 0.85$ mm. $Re_c = 2.4 \times 10^6$, [18|12] roughness.

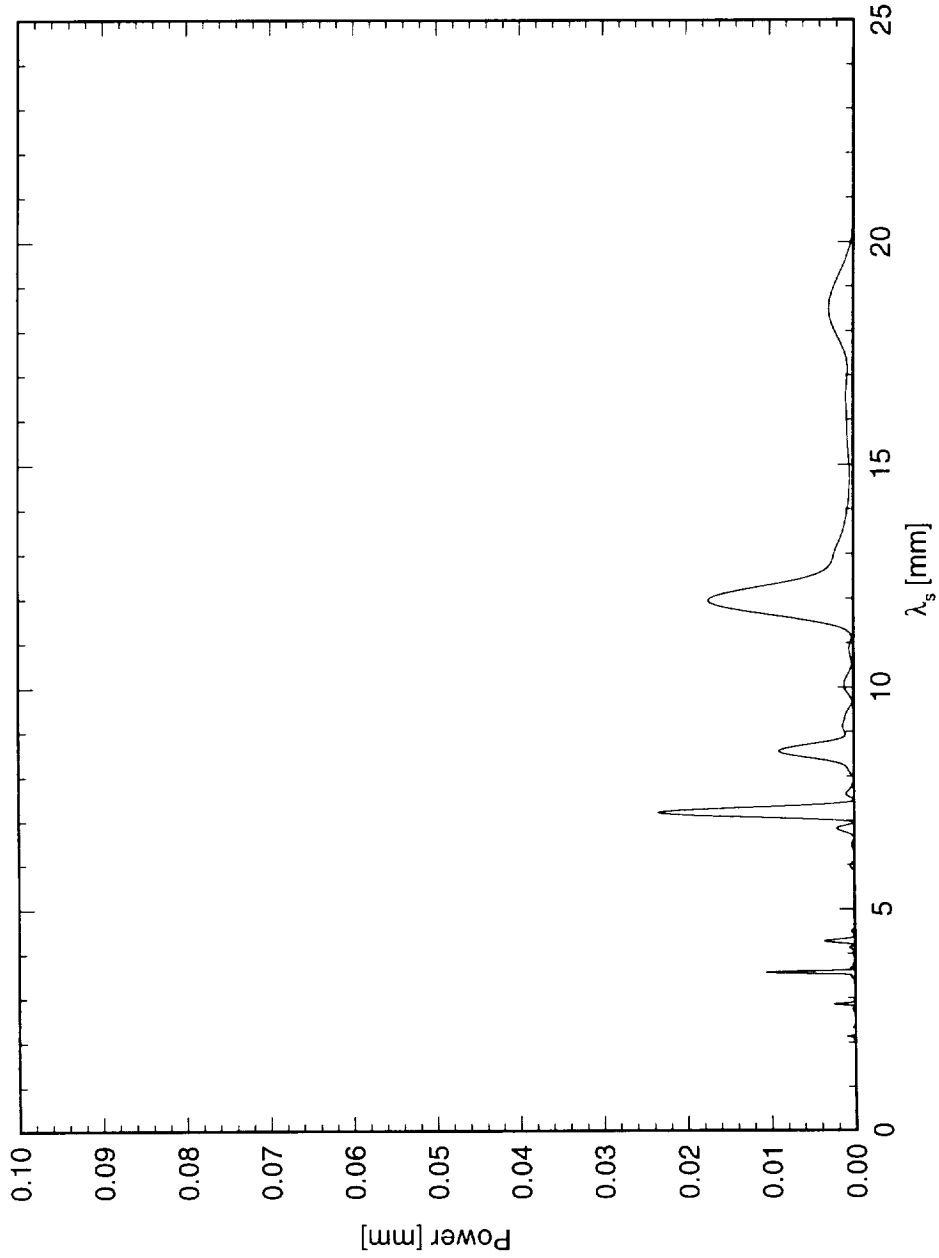

Figure 6.163: Power spectral density of spanwise hot-wire scan at $x/c = 0.05$, $Y = 0.4$ mm. $Re_c = 2.4 \times 10^6$, [18|12] roughness.

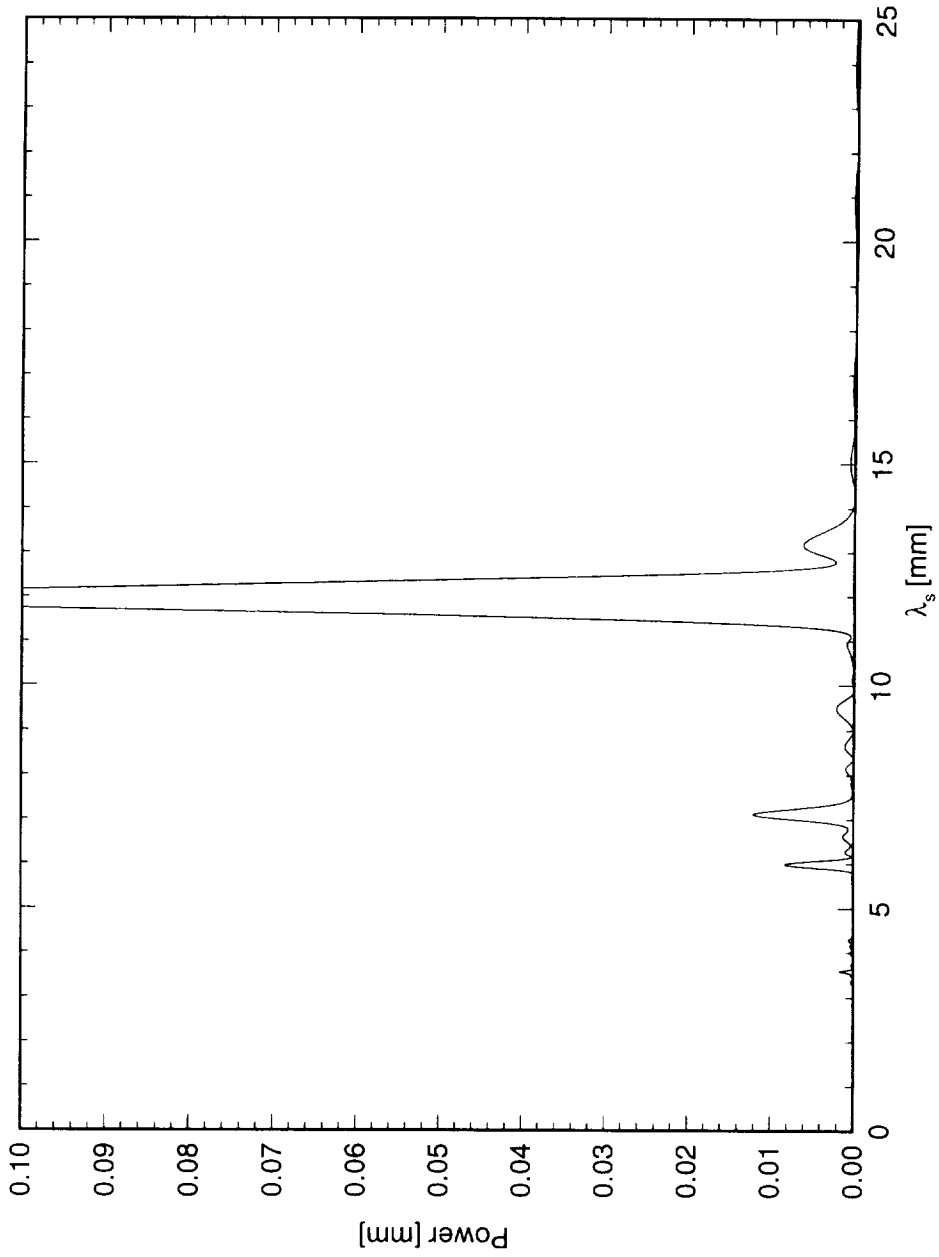

Figure 6.164: Power spectral density of spanwise hot-wire scan at $x/c = 0.10$, $Y = 0.6$ mm. $Re_c = 2.4 \times 10^6$, [18|12] roughness.

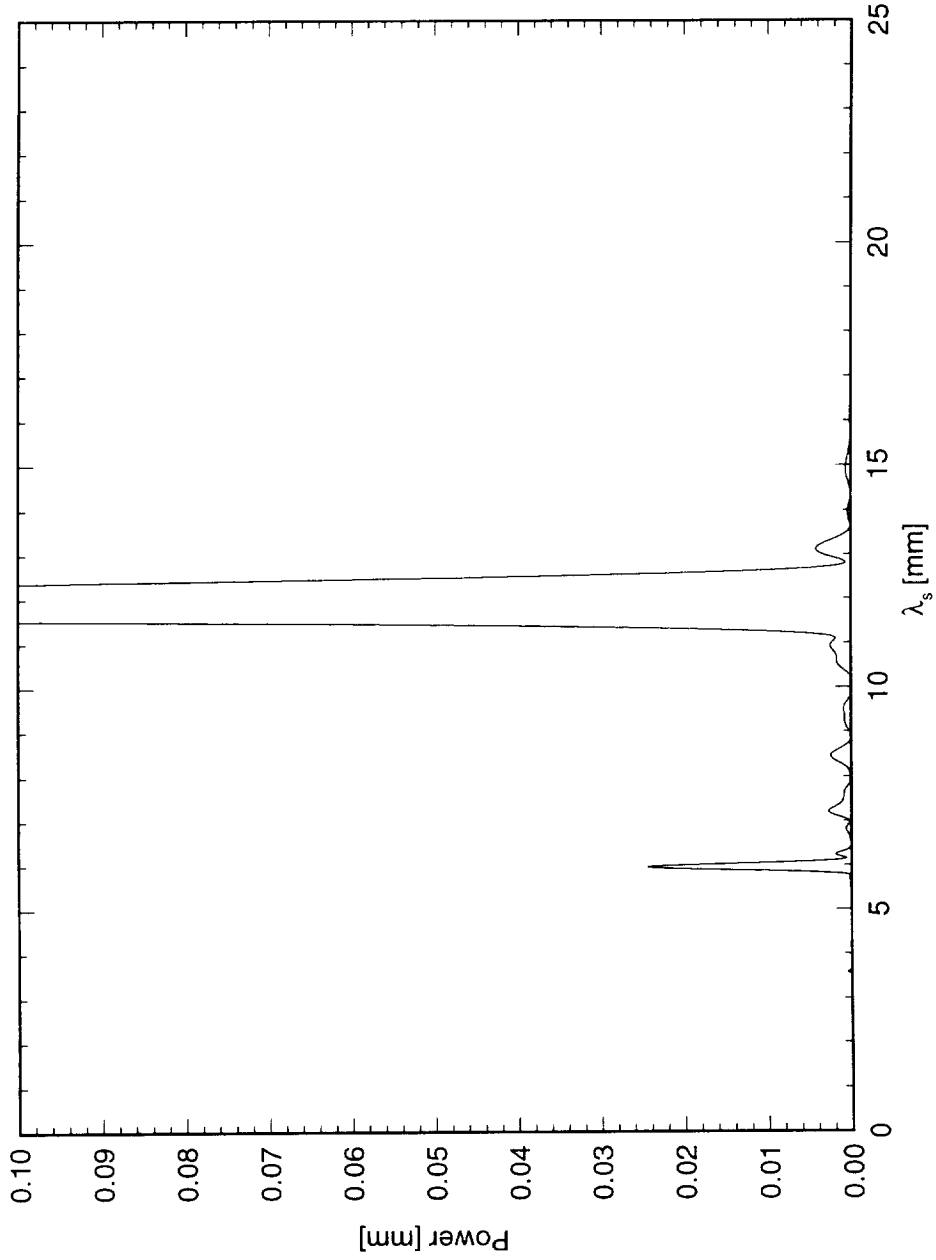

Figure 6.165: Power spectral density of spanwise hot-wire scan at $x/c = 0.15$, $Y = 0.75$ mm. $Re_c = 2.4 \times 10^6$, [18|12] roughness.

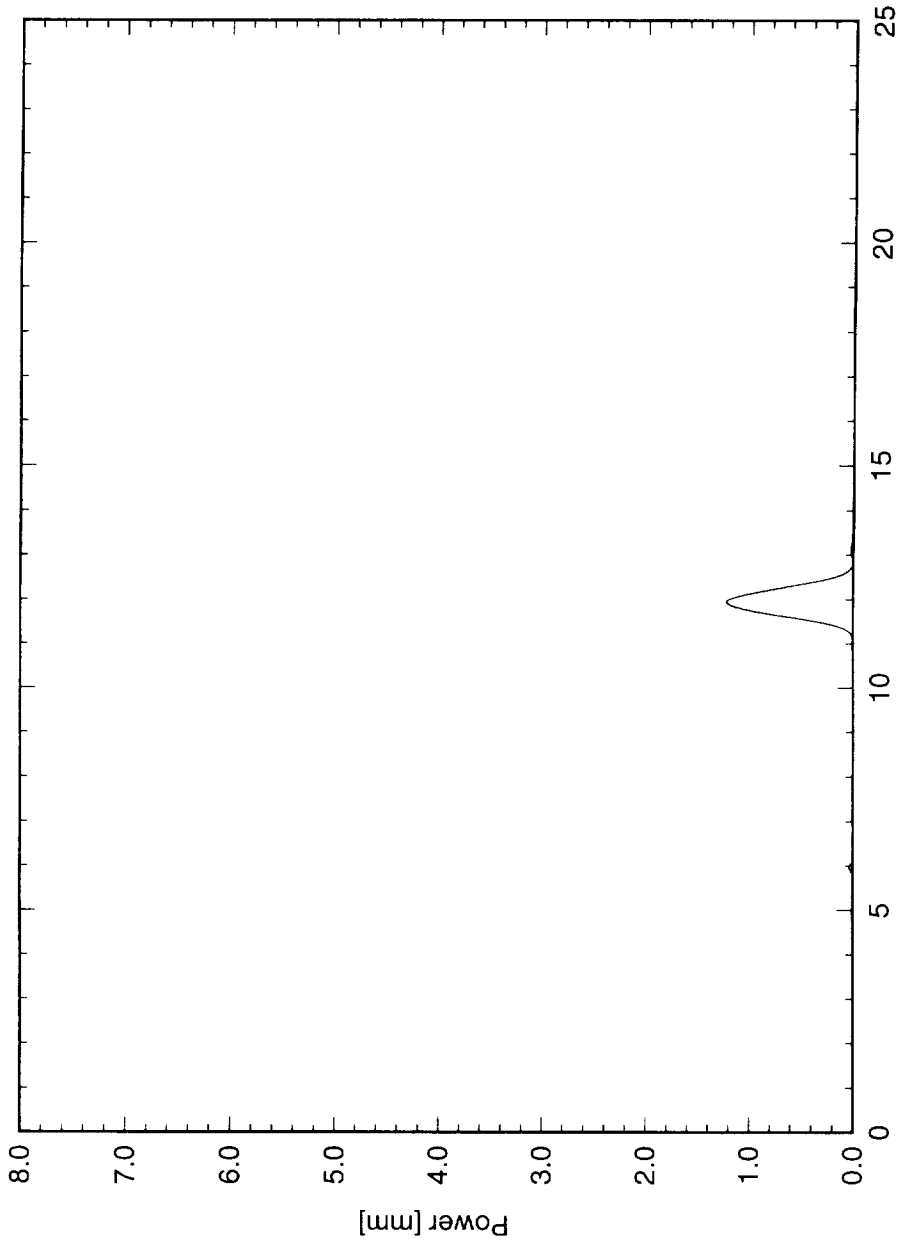

Figure 6.166: Power spectral density of spanwise hot-wire scan at $x/c = 0.20$, $Y = 0.8$ mm. $Re_c = 2.4 \times 10^6$, [18|12] roughness.

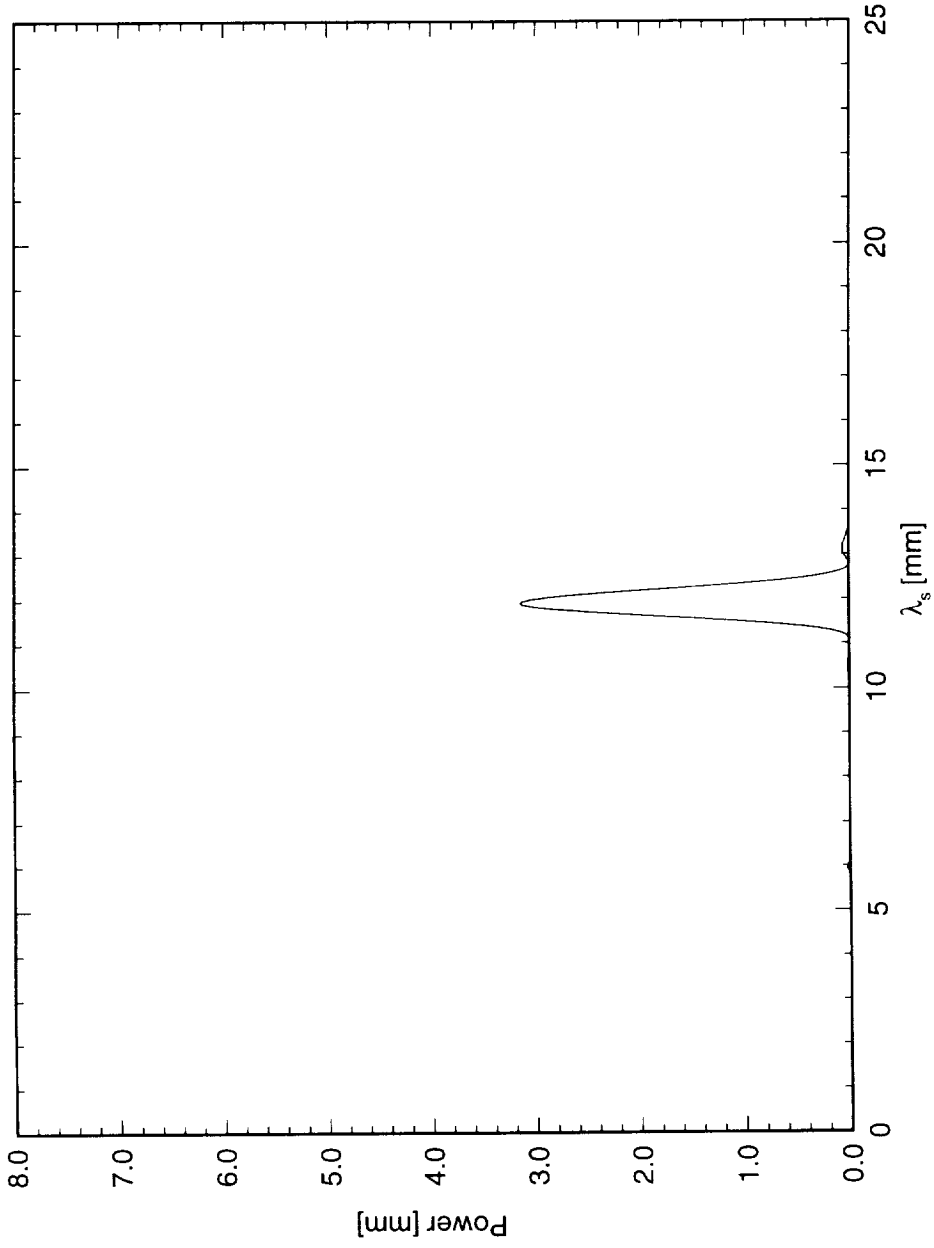

Figure 6.167: Power spectral density of spanwise hot-wire scan at $x/c = 0.25$, $Y = 0.85$ mm. $Re_c = 2.4 \times 10^6$, [18|12] roughness.

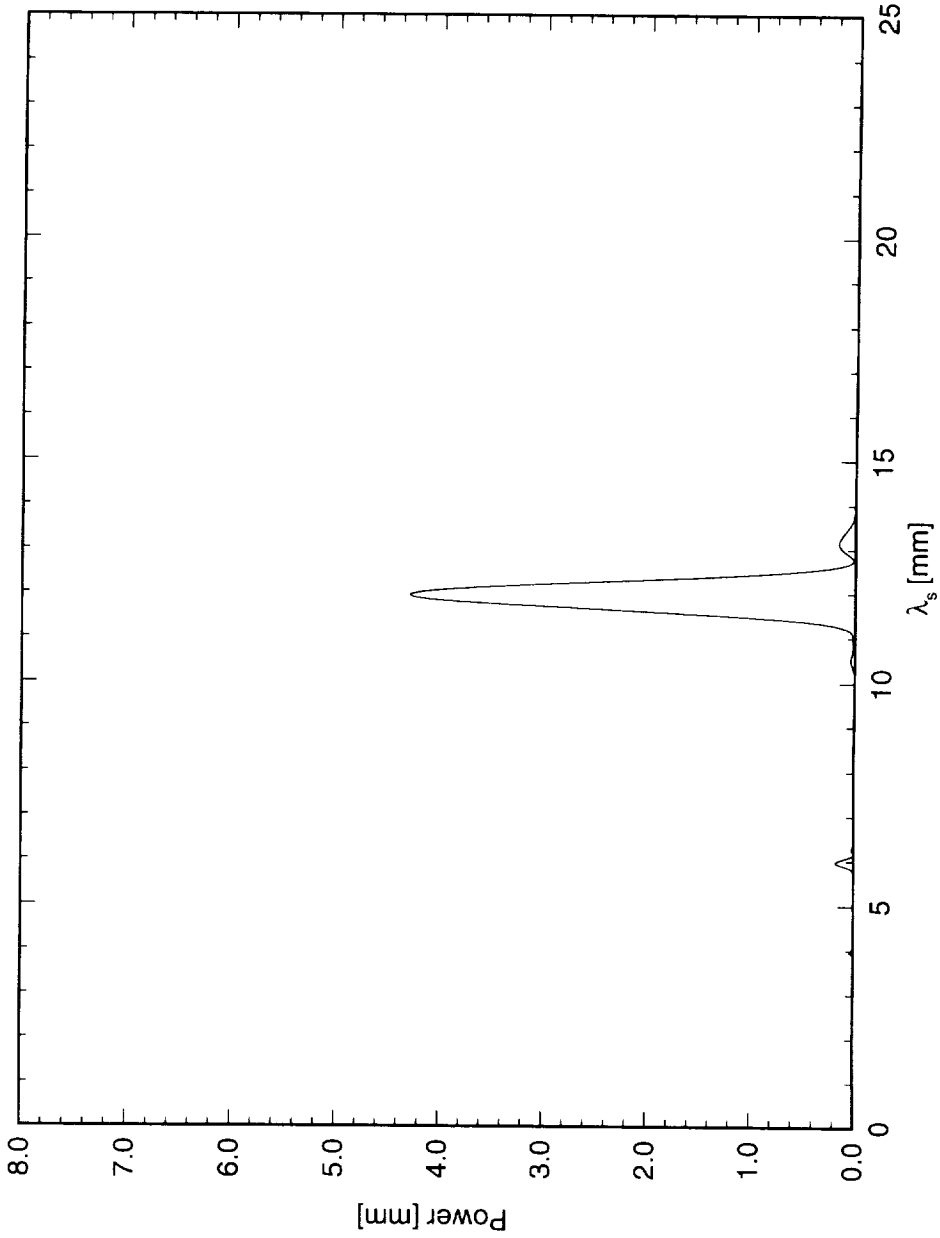

Figure 6.168: Power spectral density of spanwise hot-wire scan at $x/c = 0.30$, $Y = 0.85$ mm. $Re_c = 2.4 \times 10^6$, [18|12] roughness.

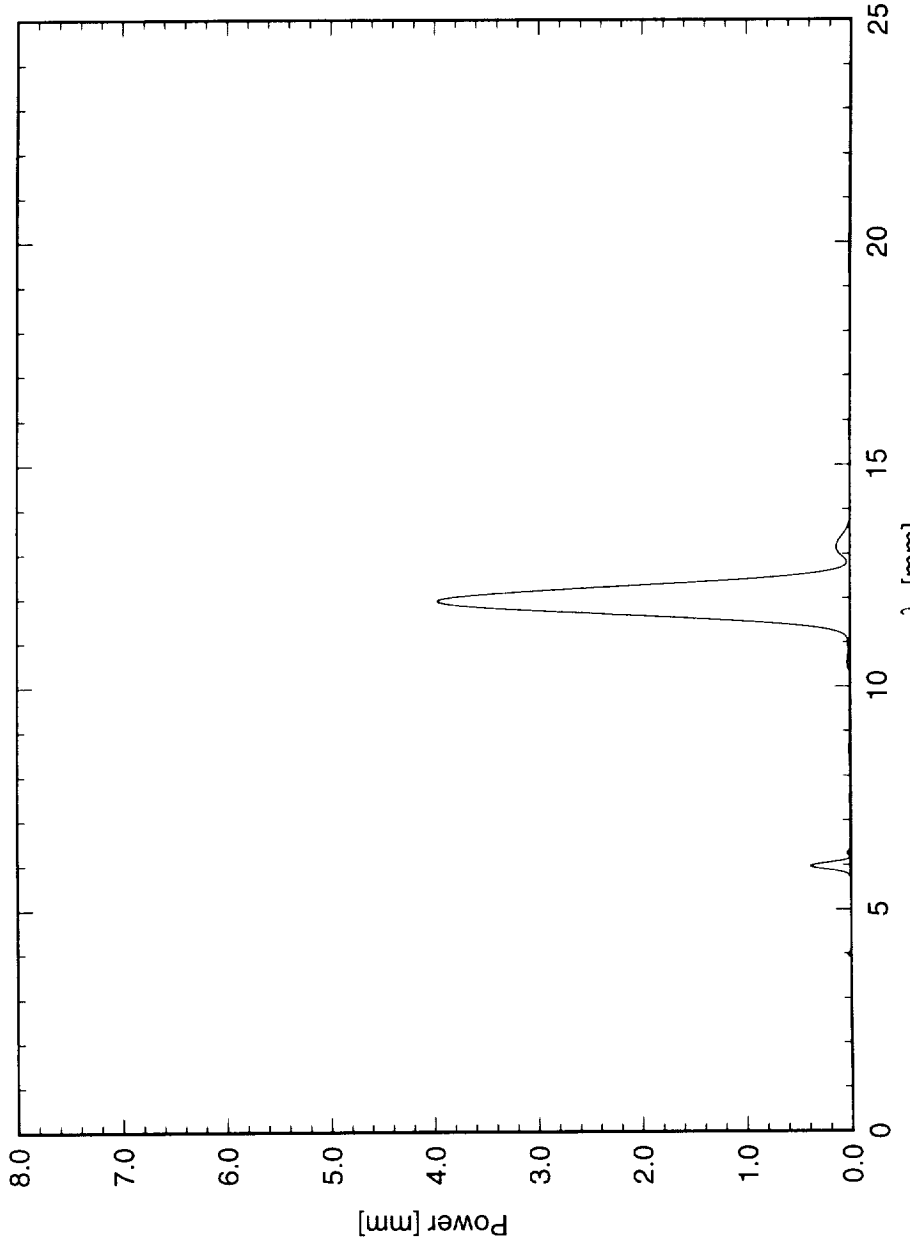

Figure 6.169: Power spectral density of spanwise hot-wire scan at $x/c = 0.35$, $Y = 0.85$ mm. $Re_c = 2.4 \times 10^6$, [18|12] roughness.

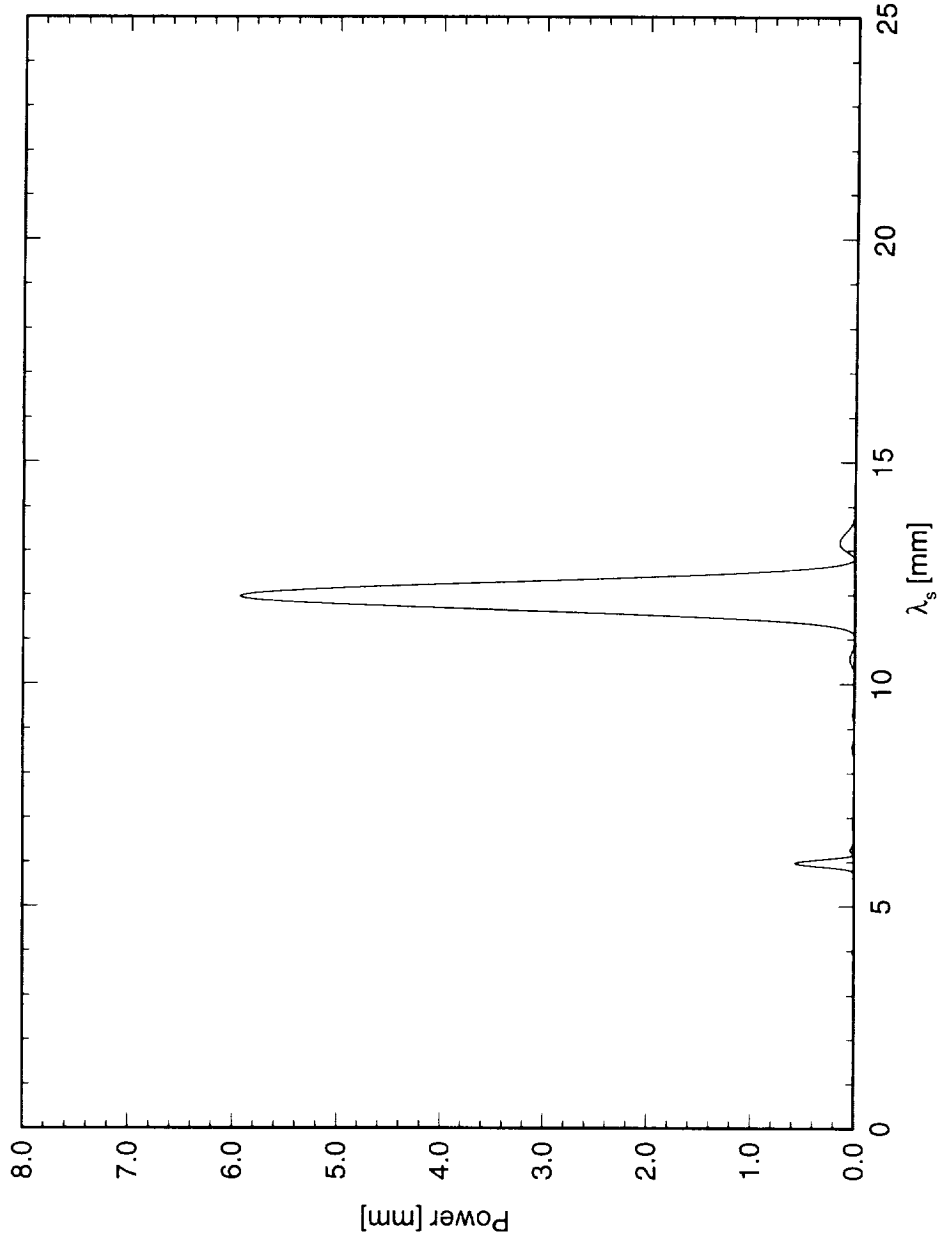

Figure 6.170: Power spectral density of spanwise hot-wire scan at $x/c = 0.40$, $Y = 0.85$ mm. $Re_c = 2.4 \times 10^6$, [18|12] roughness.

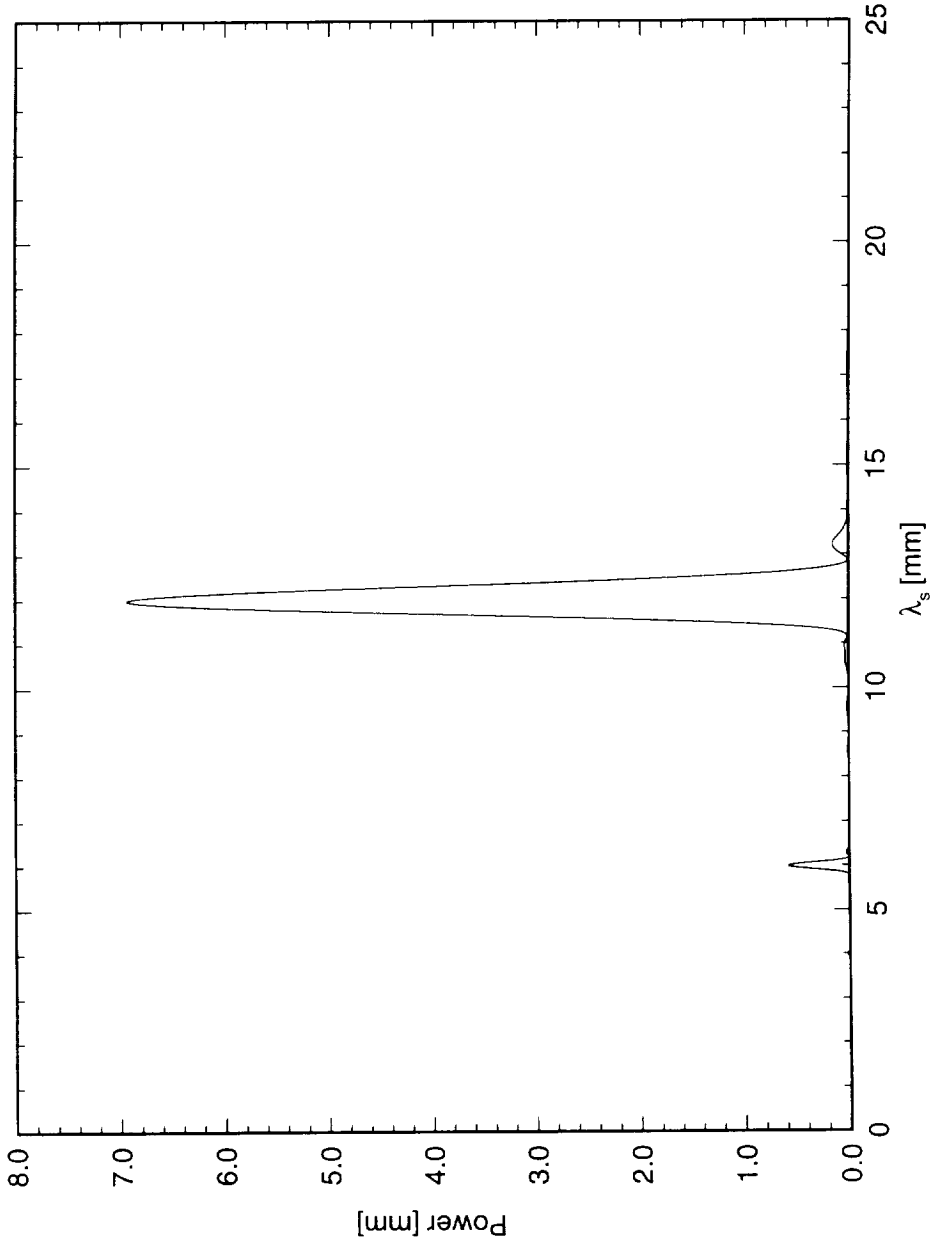

Figure 6.171: Power spectral density of spanwise hot-wire scan at $x/c = 0.45$, $Y = 0.85$ mm. $Re_c = 2.4 \times 10^6$, [18|12] roughness.

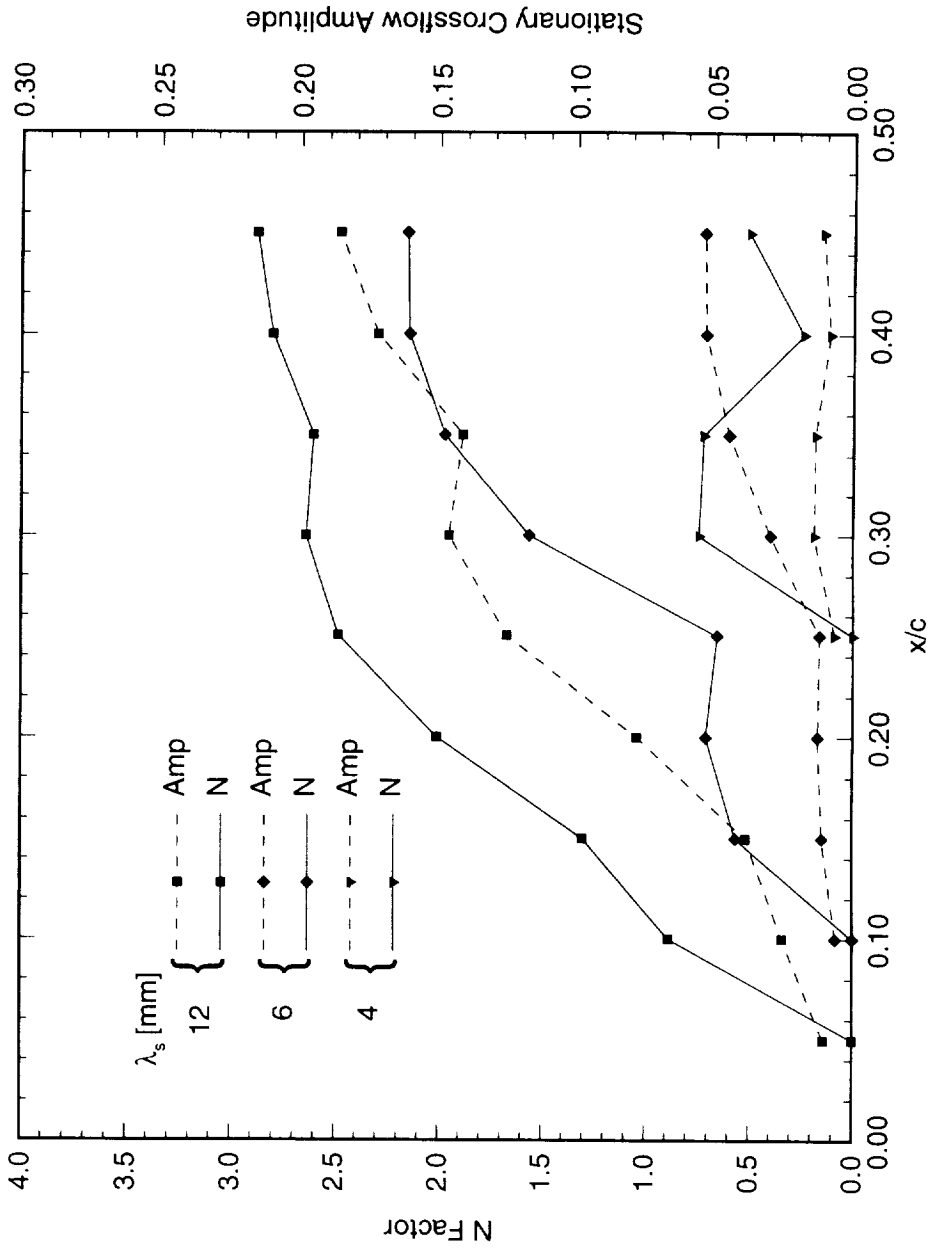

Figure 6.172: Individual-mode disturbance amplitude and amplification factor N for $Re_c = 2.4 \times 10^6$ and [18|12] roughness. N-factors are relative to the point at which the mode is first detected.

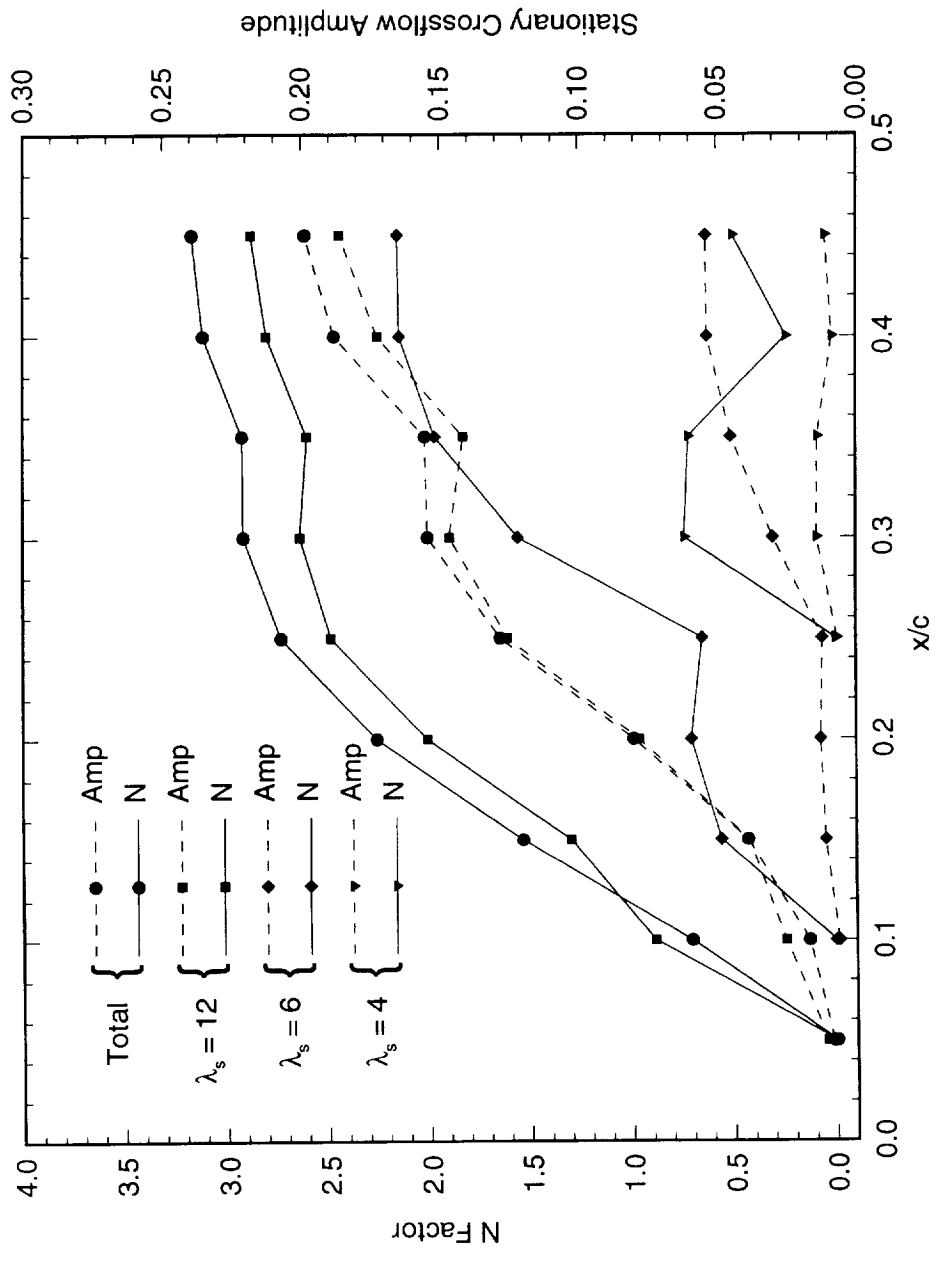

Figure 6.173: Total and individual-mode disturbance amplitude and amplification factor N for $Re_c = 2.4 \times 10^6$ and [18|12] roughness. N-factors are relative to the point at which the disturbance is first detected.

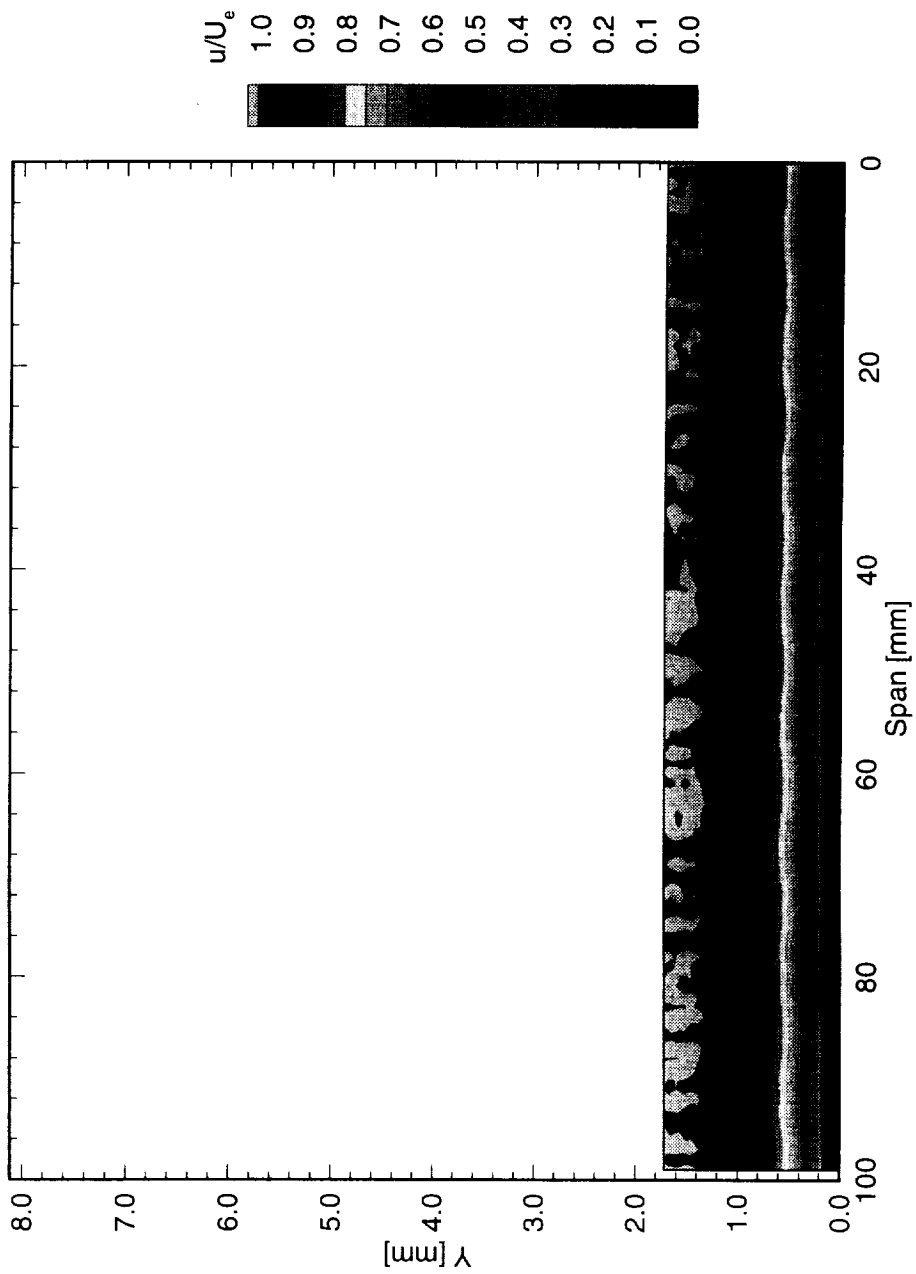

Figure 6.174: Streamwise velocity contours at $x/c = 0.05$. $Re_c = 2.4 \times 10^6$, [48|12] roughness.

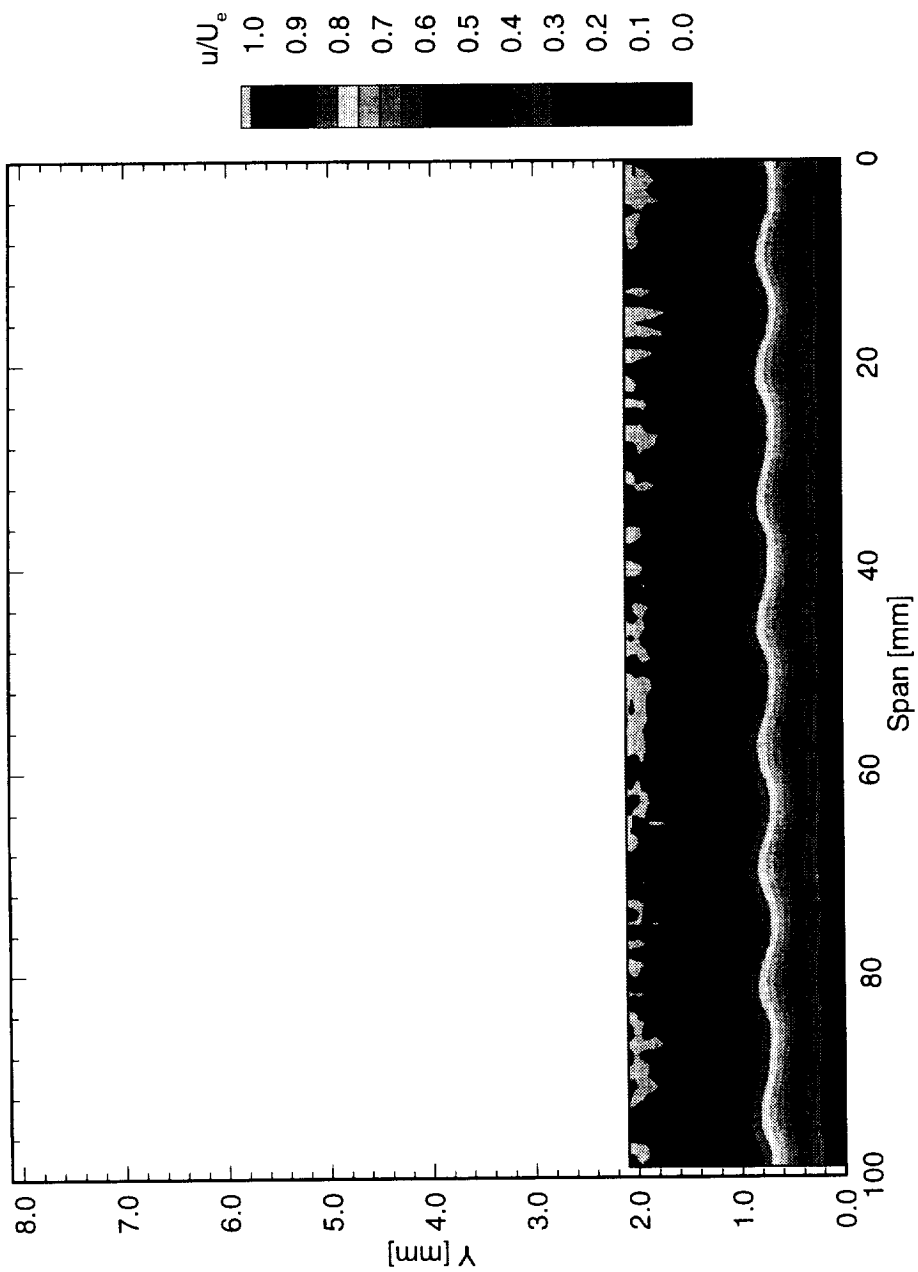

Figure 6.175: Streamwise velocity contours at $x/c = 0.10$. $Re_c = 2.4 \times 10^6$, [48|12] roughness.

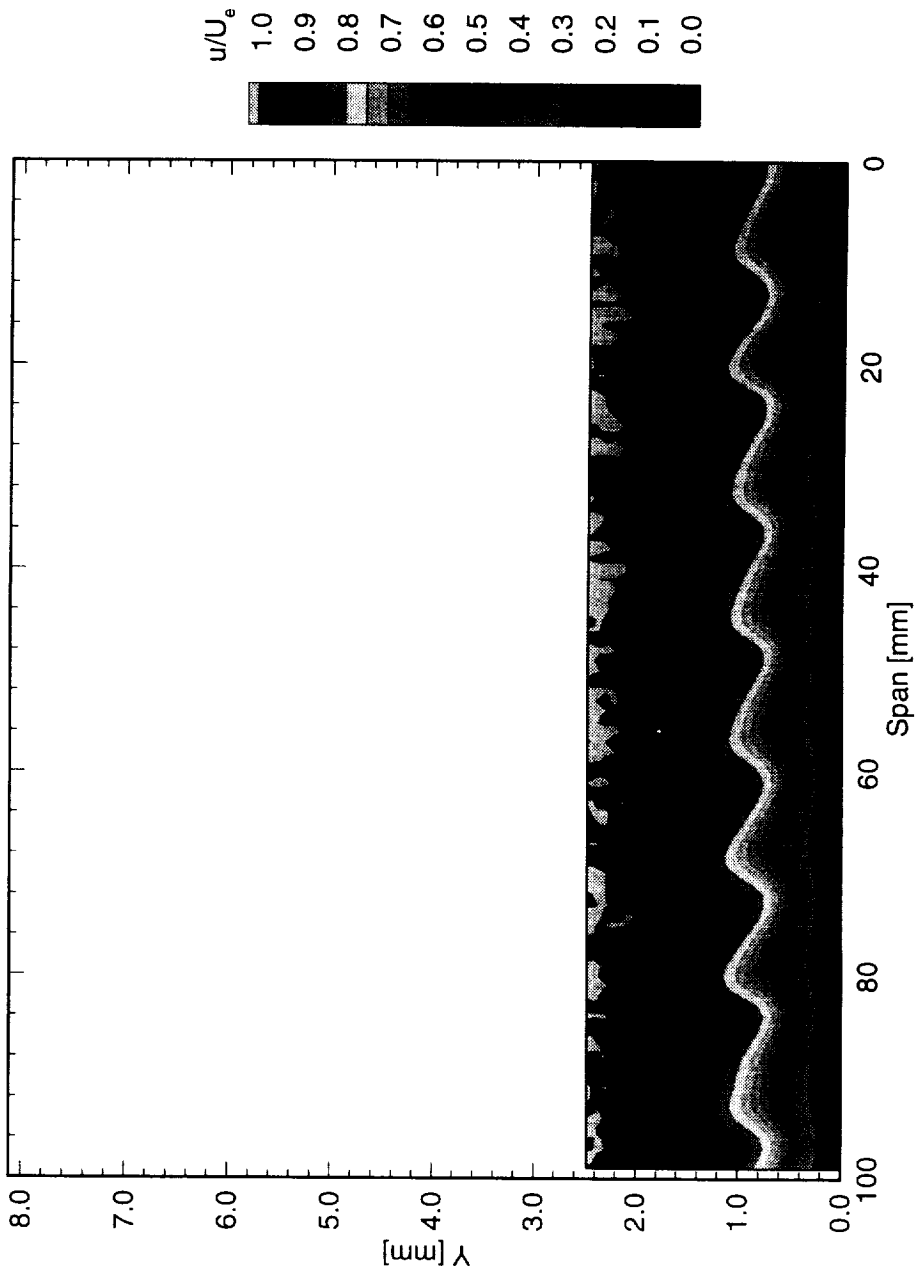

Figure 6.176: Streamwise velocity contours at $x/c = 0.15$. $Re_c = 2.4 \times 10^6$, [48|12] roughness.

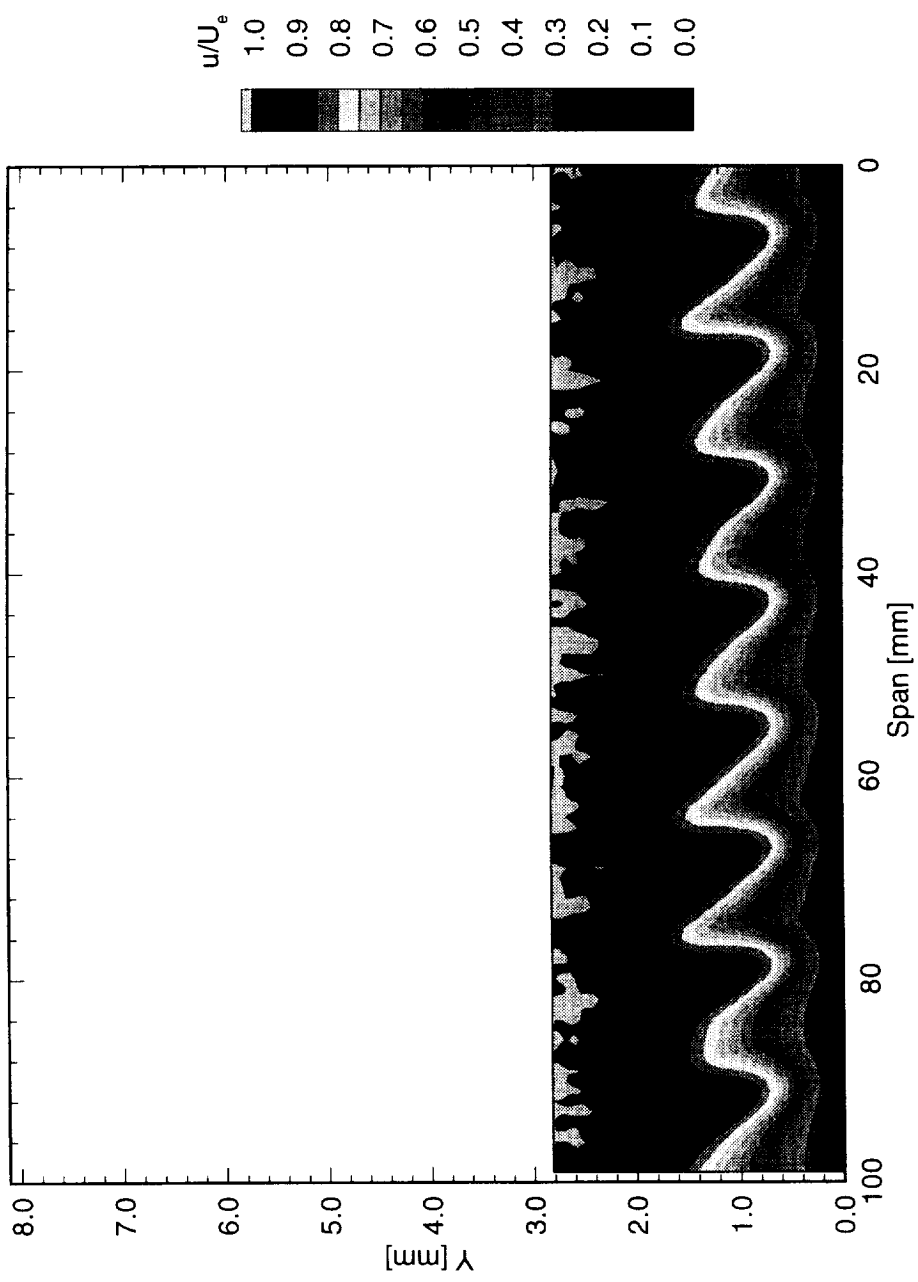

Figure 6.177: Streamwise velocity contours at $x/c = 0.20$. $Re_c = 2.4 \times 10^6$, [48|12] roughness.

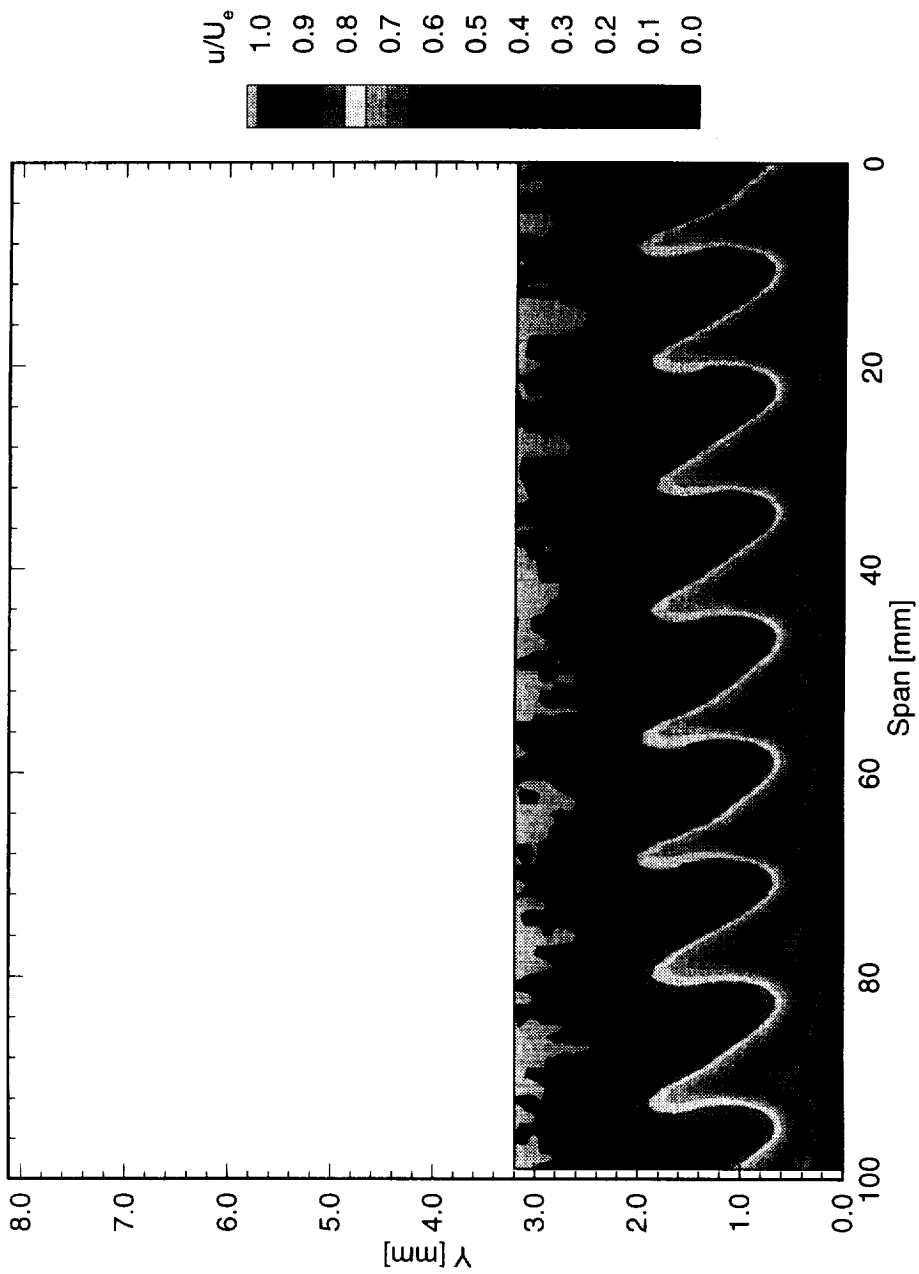

Figure 6.178: Streamwise velocity contours at $x/c = 0.25$. $Re_c = 2.4 \times 10^6$, [48|12] roughness.

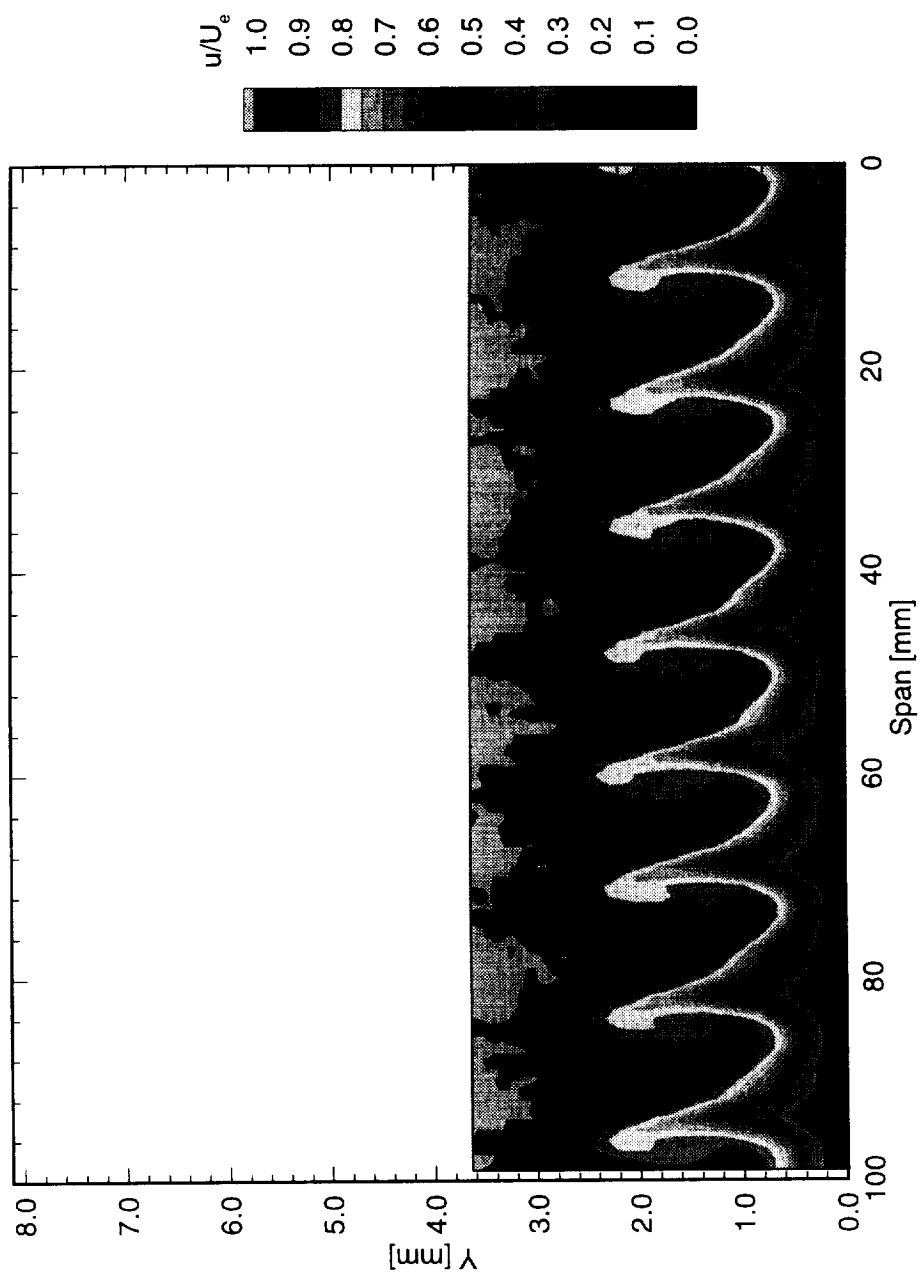

Figure 6.179: Streamwise velocity contours at $x/c = 0.30$. $Re_c = 2.4 \times 10^6$, [48|12] roughness.

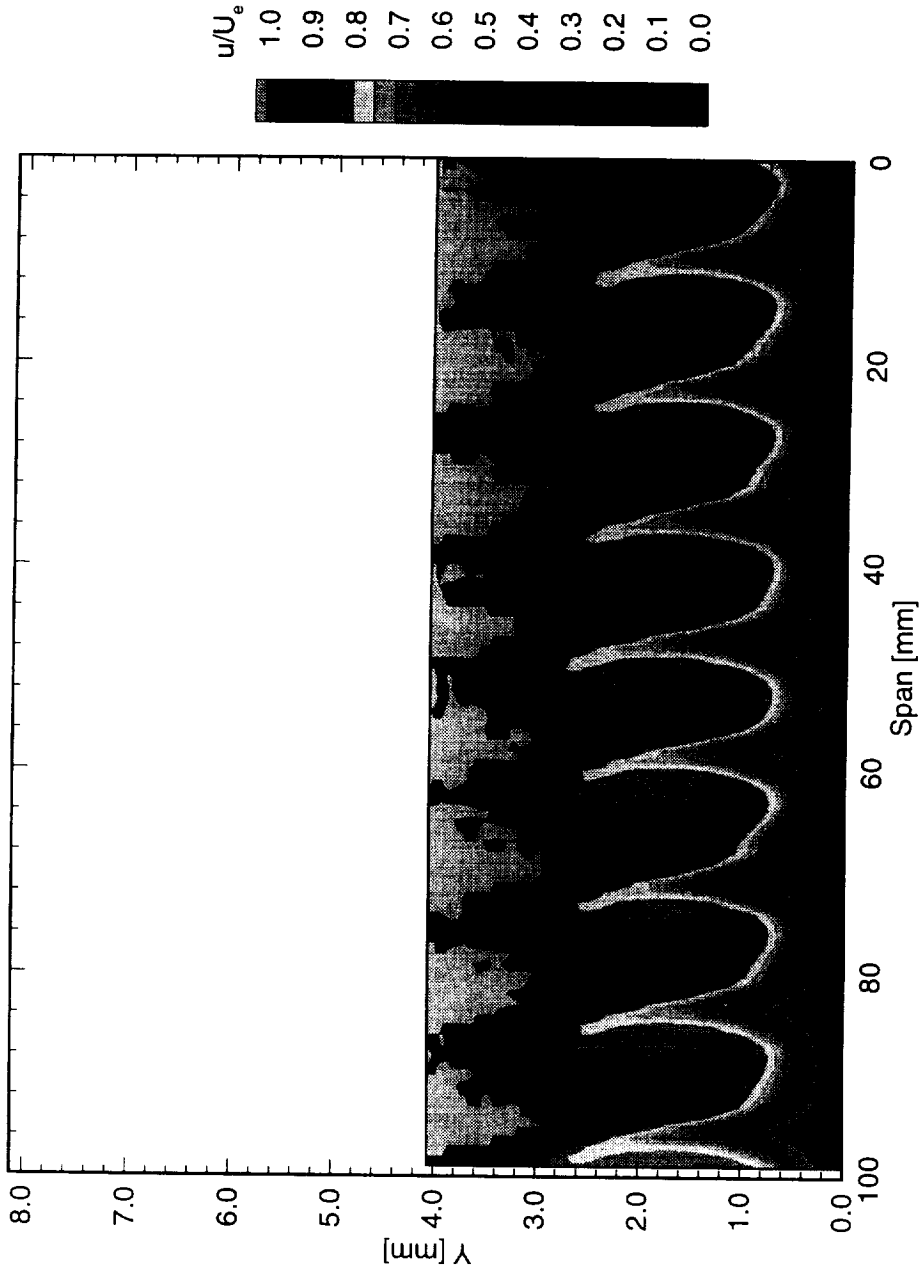

Figure 6.180: Streamwise velocity contours at $x/c = 0.35$. $Re_c = 2.4 \times 10^6$, [48|12] roughness.

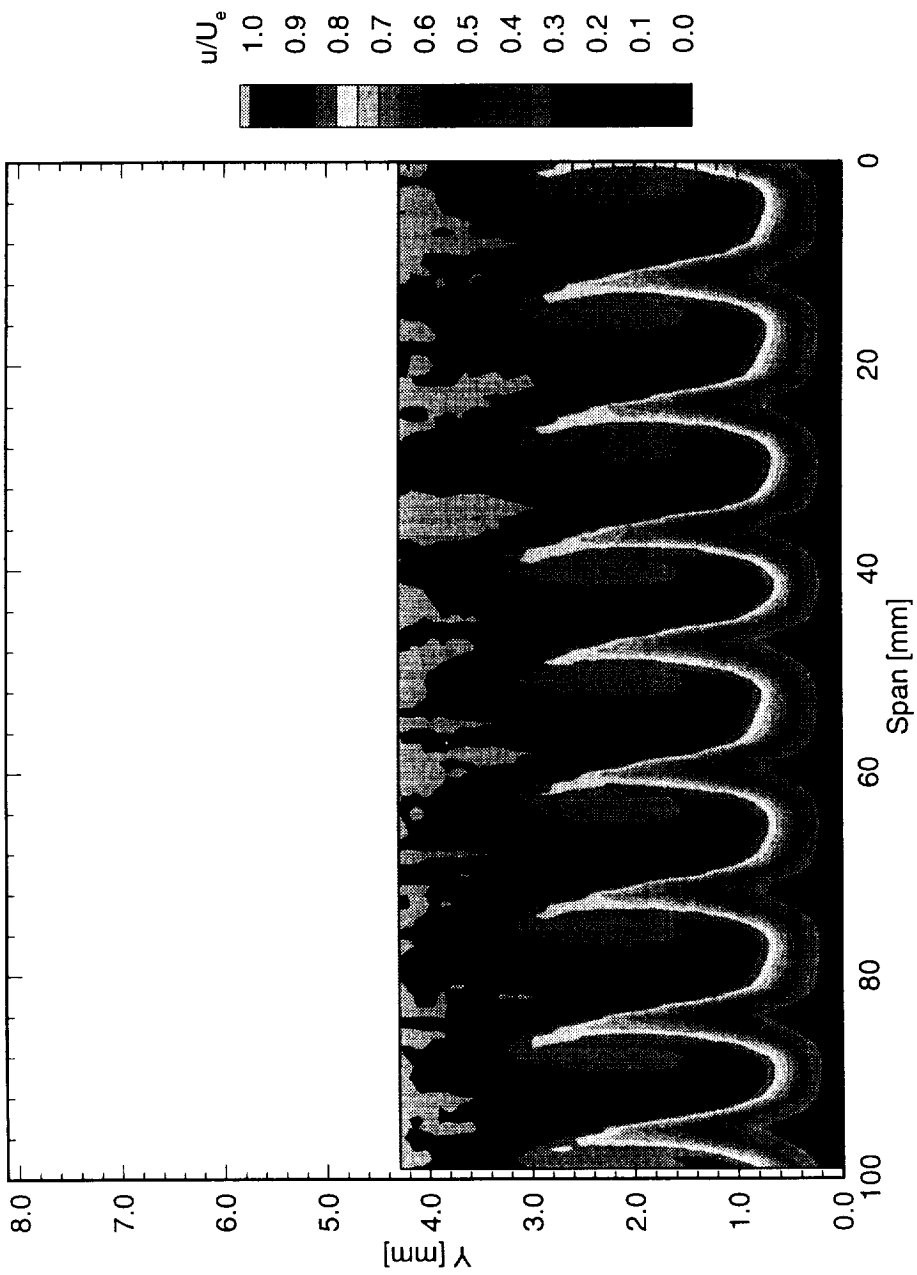

Figure 6.181: Streamwise velocity contours at $x/c = 0.40$. $Re_c = 2.4 \times 10^6$, [48|12] roughness.

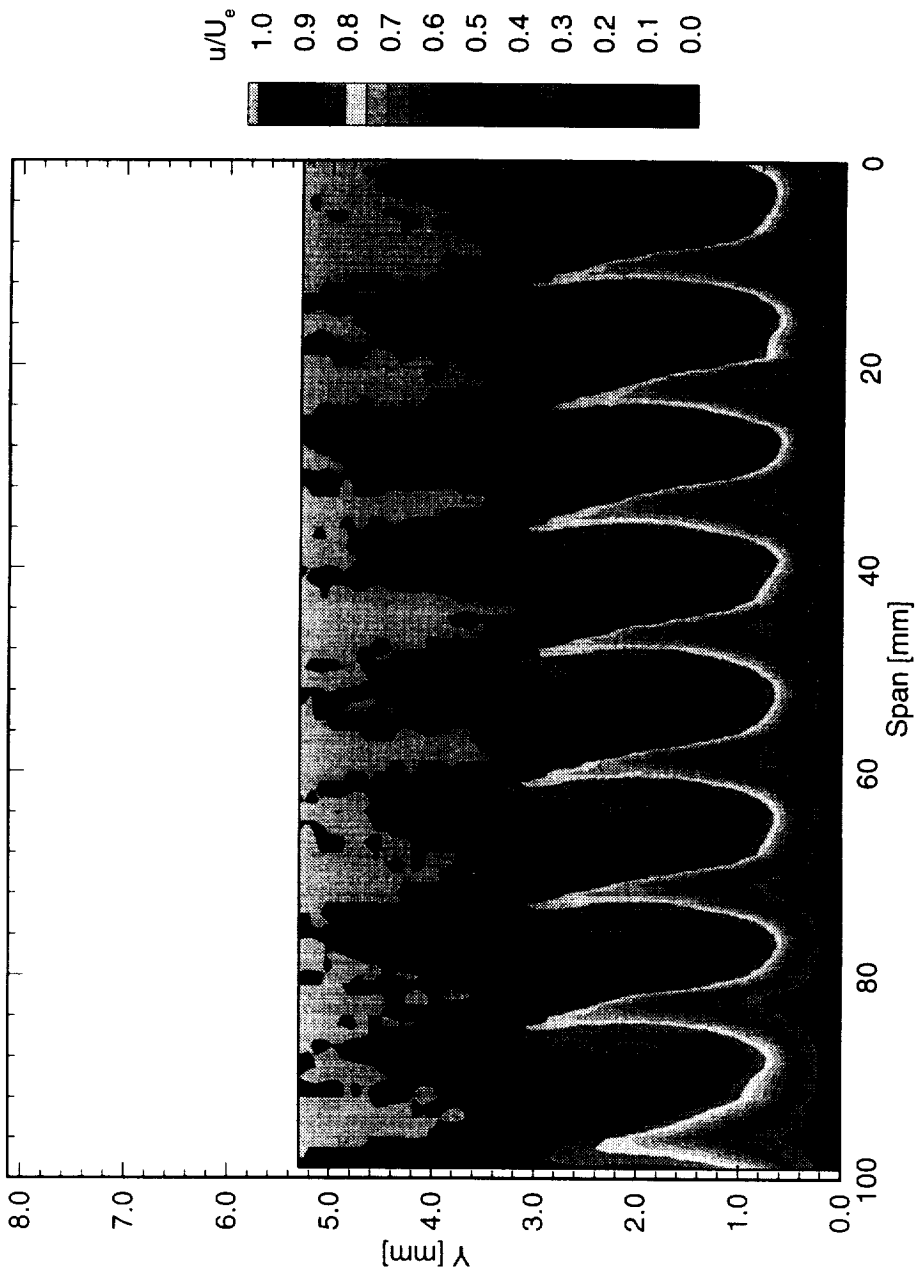

Figure 6.182: Streamwise velocity contours at $x/c = 0.45$. $Re_c = 2.4 \times 10^6$, [48|12] roughness.

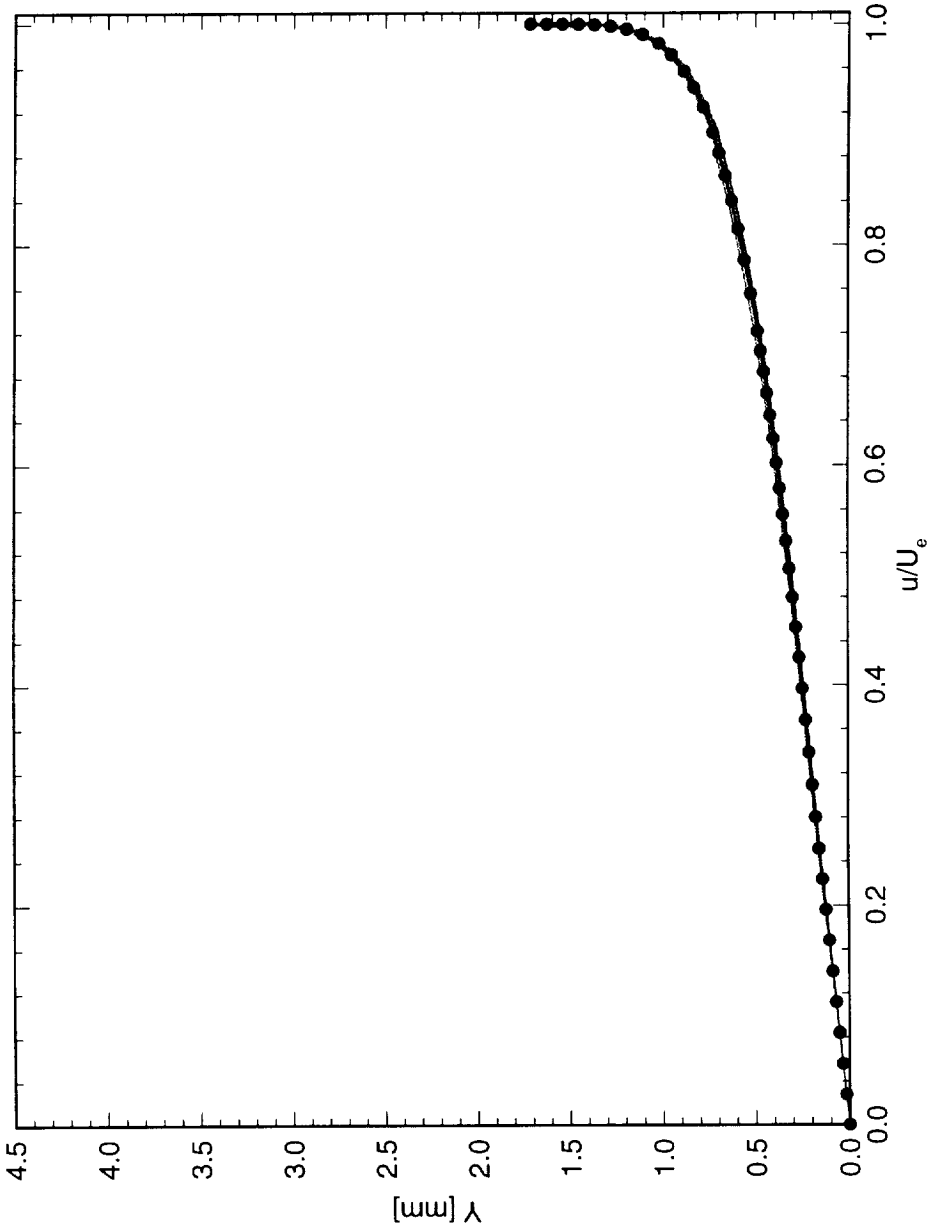

Figure 6.183: Spanwise array of 100 mean-flow boundary-layer profiles covering a span of 99 mm at $x/c = 0.05$. $Re_c = 2.4 \times 10^6$, [48|12] roughness. The dots indicate the mean of the profiles.

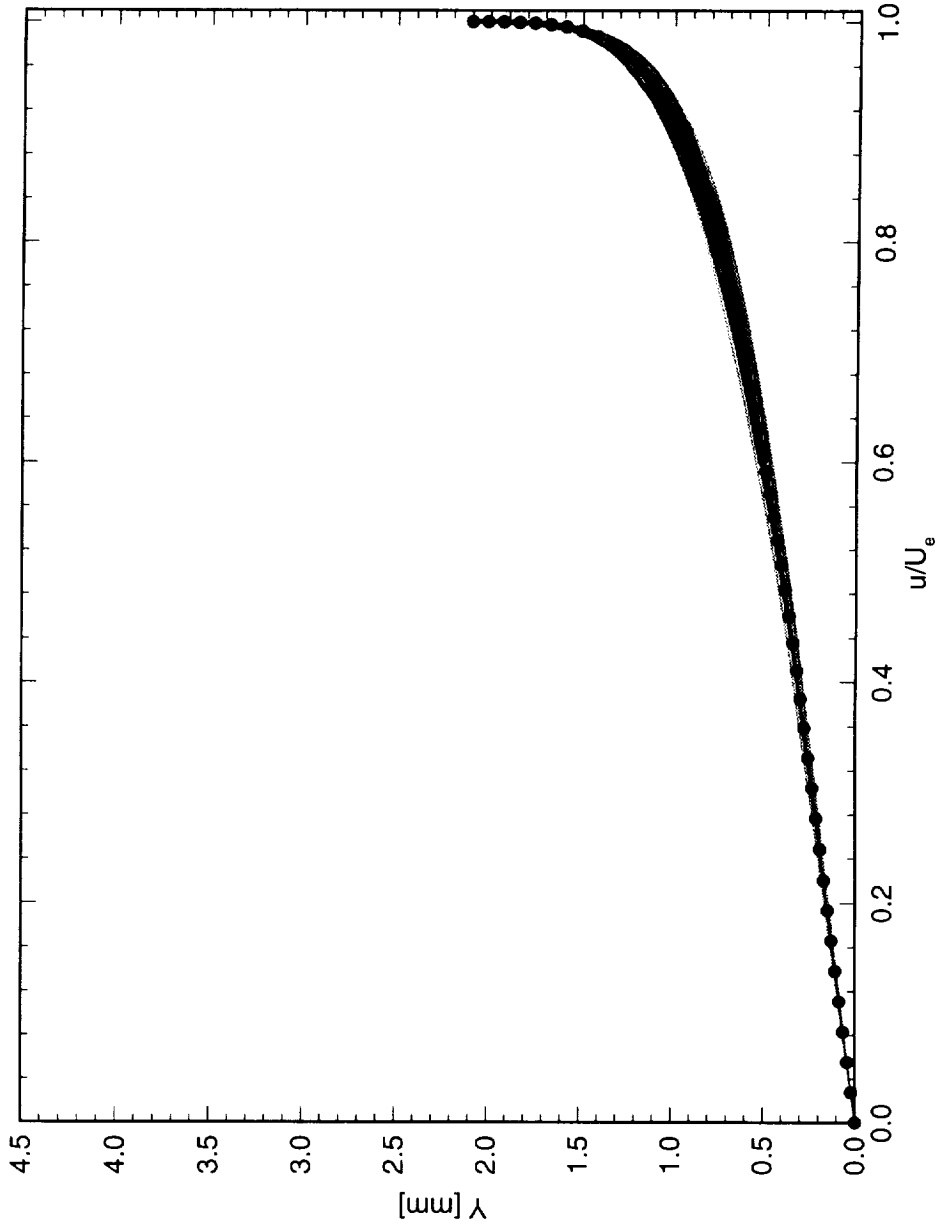

Figure 6.184: Spanwise array of 100 mean-flow boundary-layer profiles covering a span of 99 mm at $x/c = 0.10$. $Re_c = 2.4 \times 10^6$, [48|12] roughness. The dots indicate the mean of the profiles.

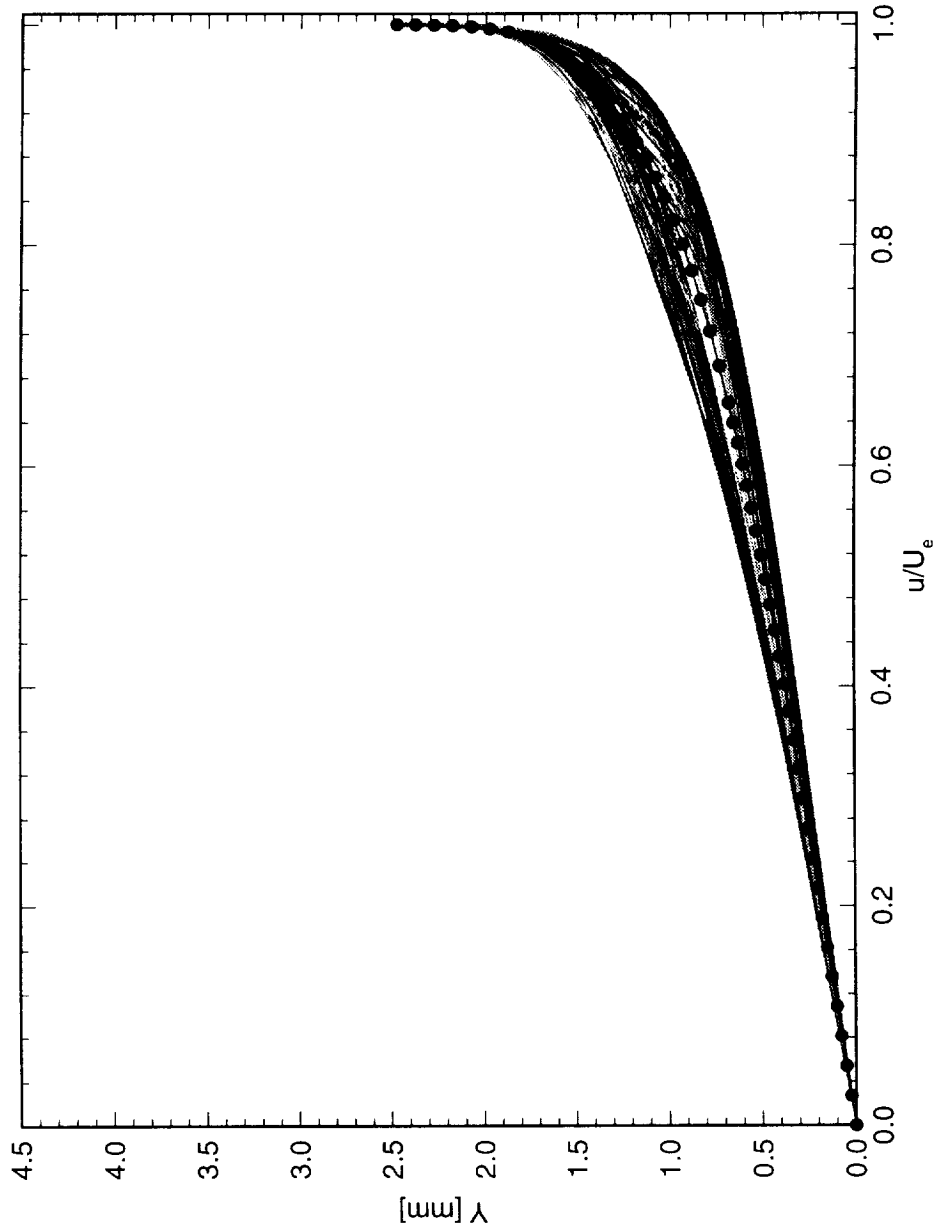

Figure 6.185: Spanwise array of 100 mean-flow boundary-layer profiles covering a span of 99 mm at $x/c = 0.15$. $Re_c = 2.4 \times 10^6$, [48|12] roughness. The dots indicate the mean of the profiles.

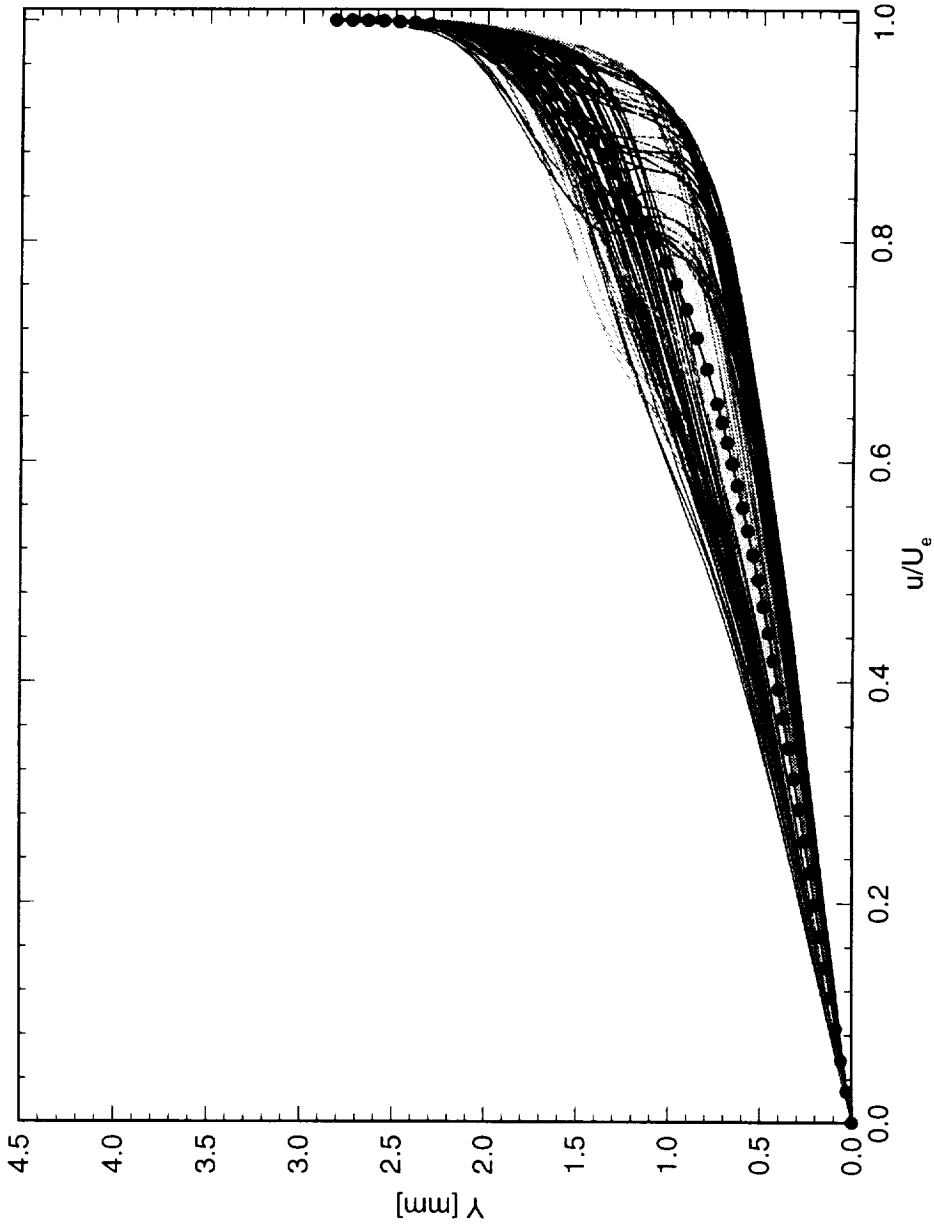

Figure 6.186: Spanwise array of 100 mean-flow boundary-layer profiles covering a span of 99 mm at $x/c = 0.20$. $Re_c = 2.4 \times 10^6$, [48|12] roughness. The dots indicate the mean of the profiles.

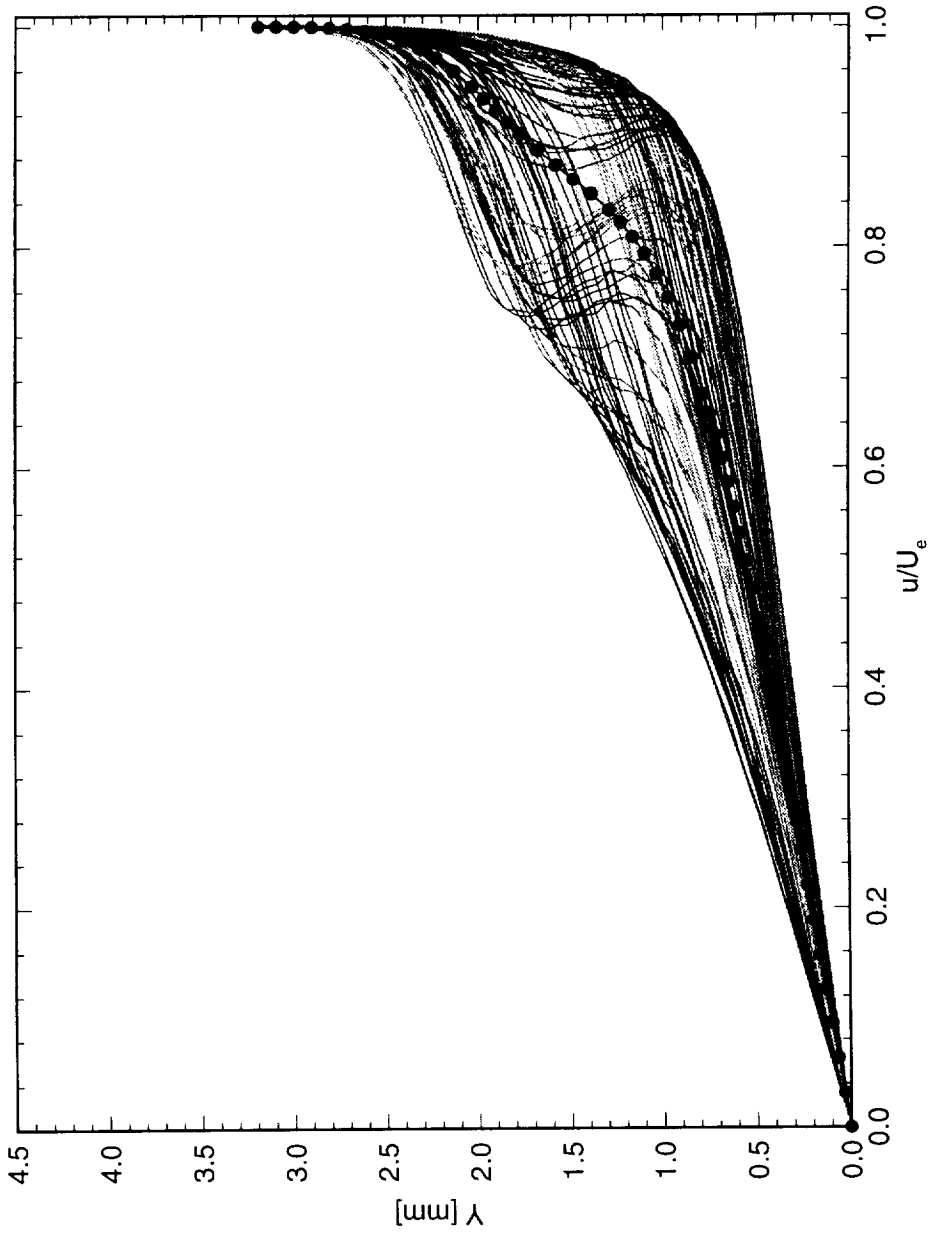

Figure 6.187: Spanwise array of 100 mean-flow boundary-layer profiles covering a span of 99 mm at $x/c = 0.25$. $Re_c = 2.4 \times 10^6$, [48|12] roughness. The dots indicate the mean of the profiles.

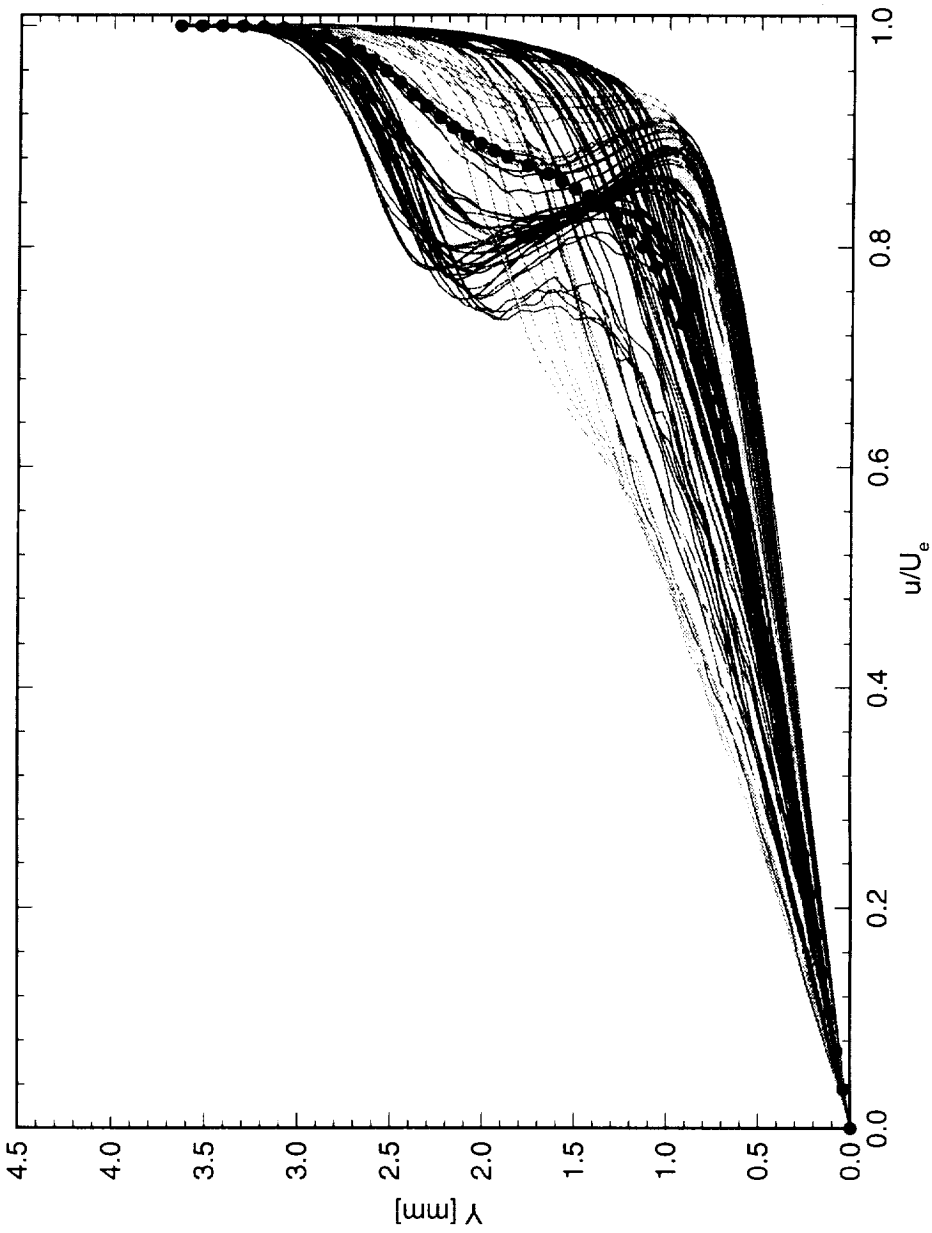

Figure 6.188: Spanwise array of 100 mean-flow boundary-layer profiles covering a span of 99 mm at $x/c = 0.30$. $Re_c = 2.4 \times 10^6$, [48|12] roughness. The dots indicate the mean of the profiles.

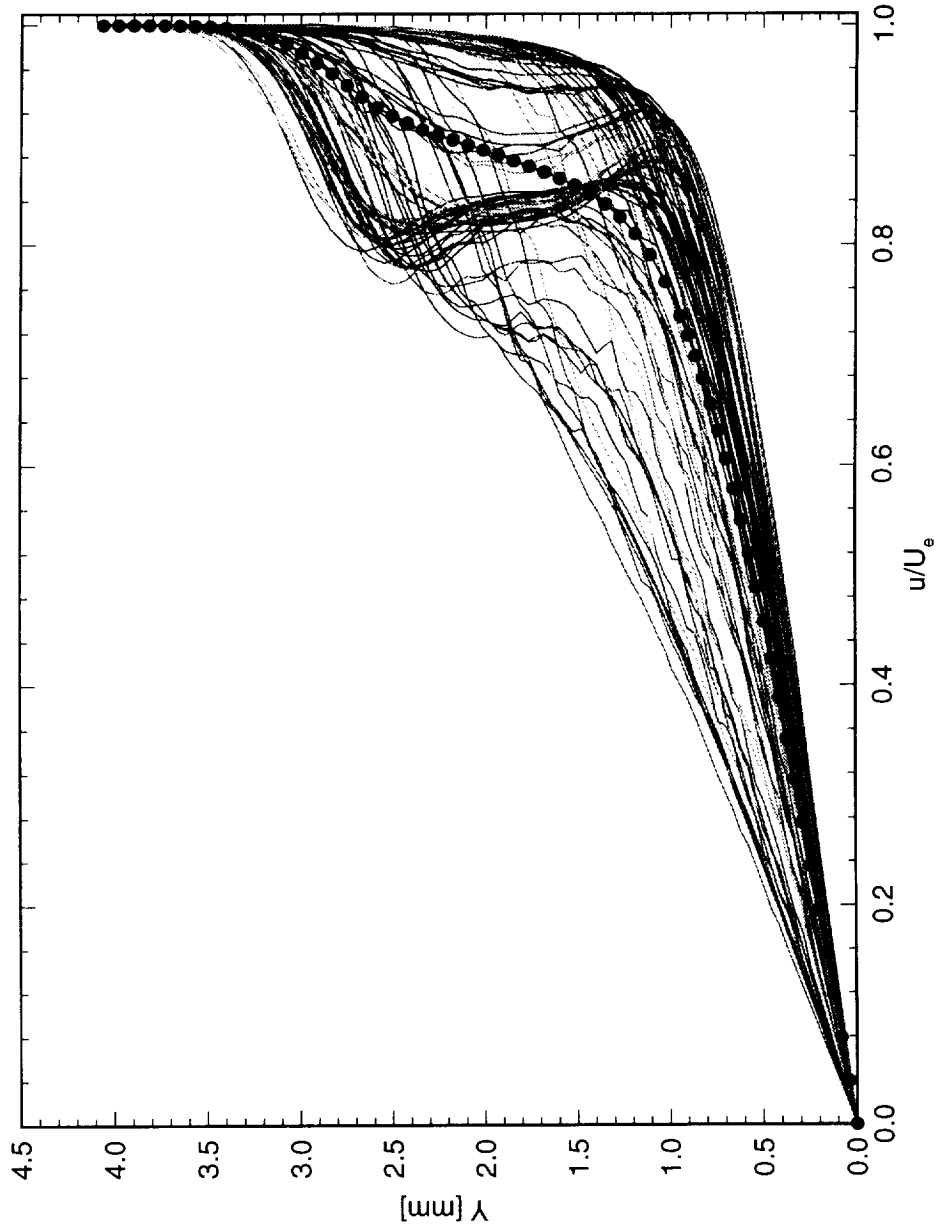

Figure 6.189: Spanwise array of 100 mean-flow boundary-layer profiles covering a span of 99 mm at $x/c = 0.35$. $Re_c = 2.4 \times 10^6$, [48|12] roughness. The dots indicate the mean of the profiles.

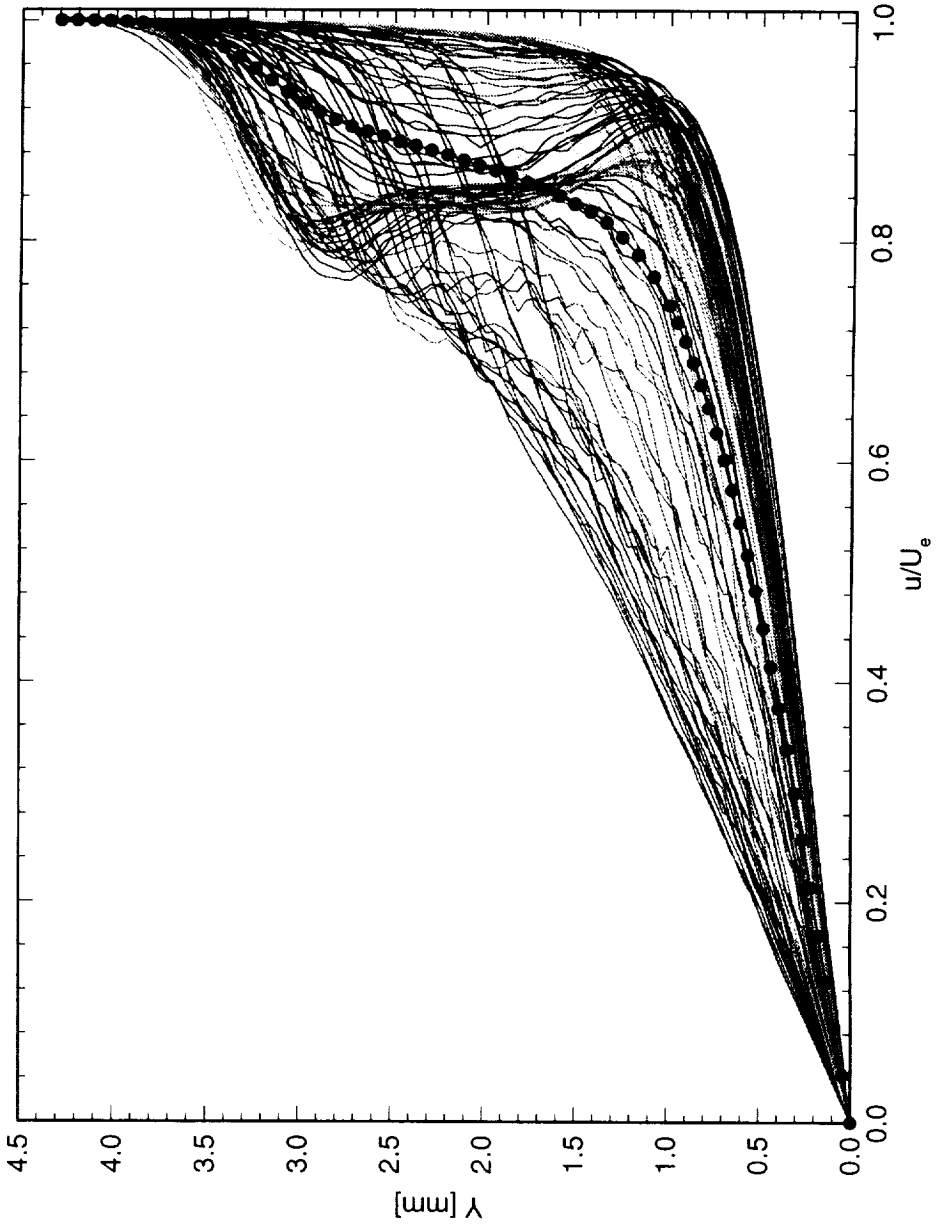

Figure 6.190: Spanwise array of 100 mean-flow boundary-layer profiles covering a span of 99 mm at $x/c = 0.40$. $Re_c = 2.4 \times 10^6$, [48|12] roughness. The dots indicate the mean of the profiles.

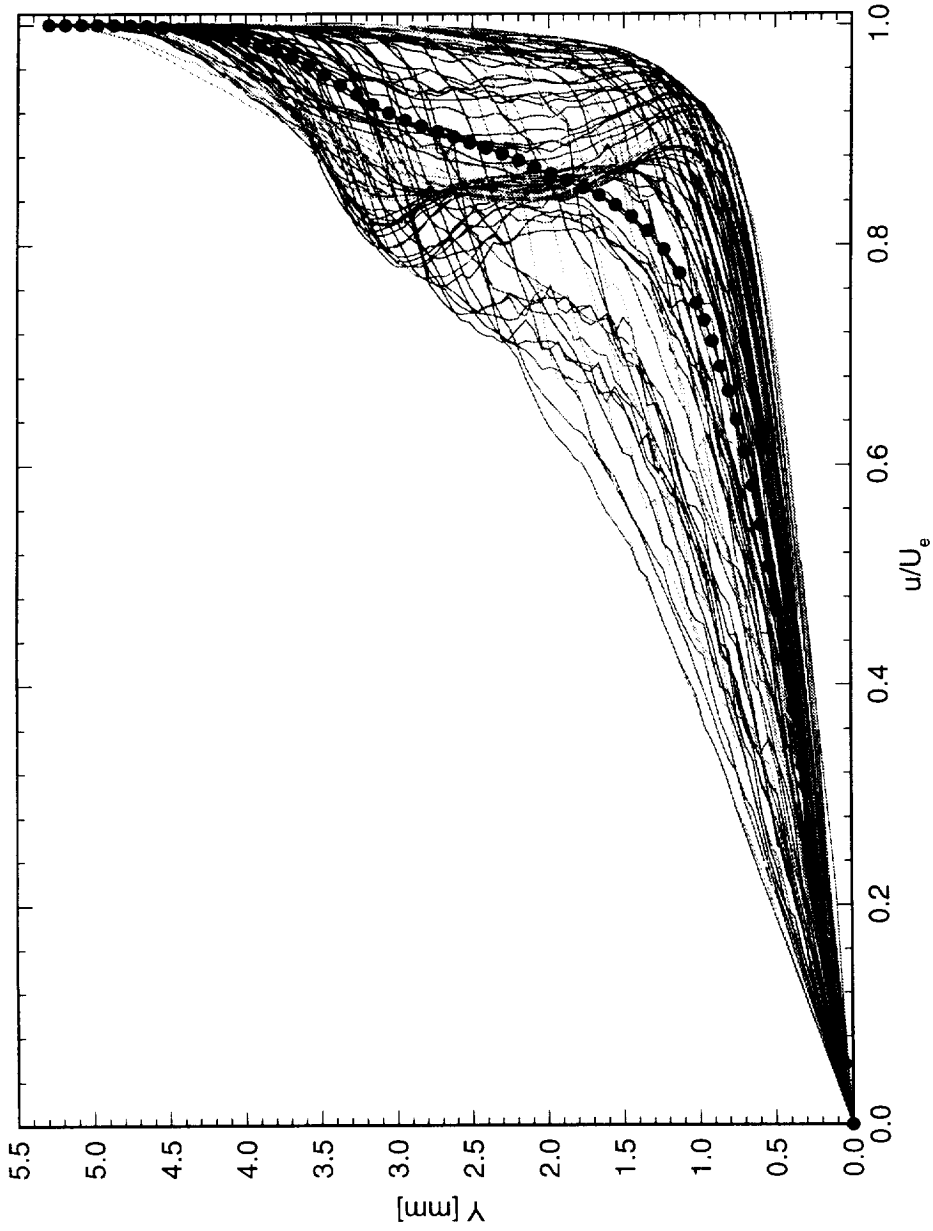

Figure 6.191: Spanwise array of 100 mean-flow boundary-layer profiles covering a span of 99 mm at $x/c = 0.45$. $Re_c = 2.4 \times 10^6$, [48|12] roughness. The dots indicate the mean of the profiles.

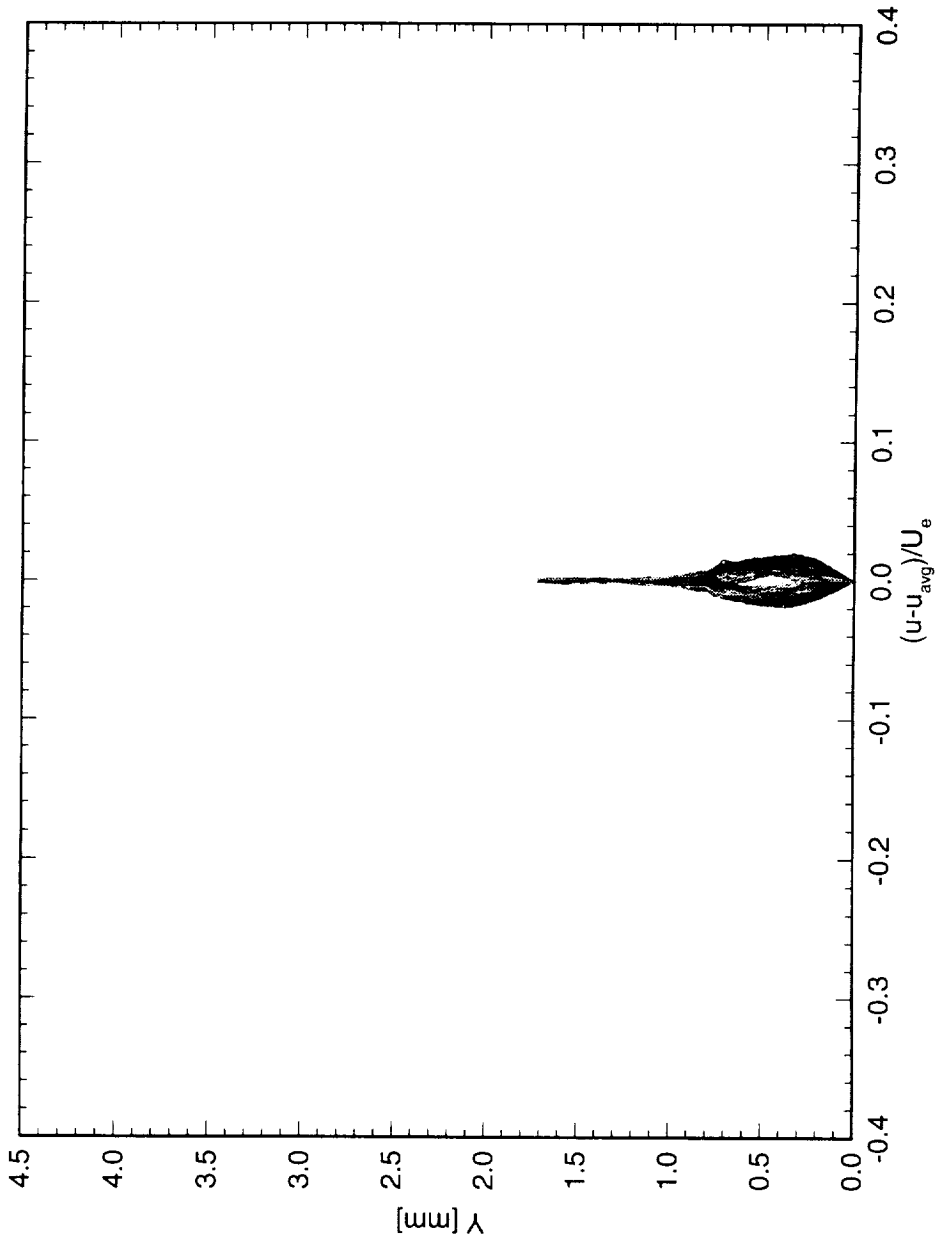

Figure 6.192: Spanwise array of 100 disturbance profiles covering a span of 99 mm at $x/c = 0.05$. $Re_c = 2.4 \times 10^6$, [48|12] roughness.

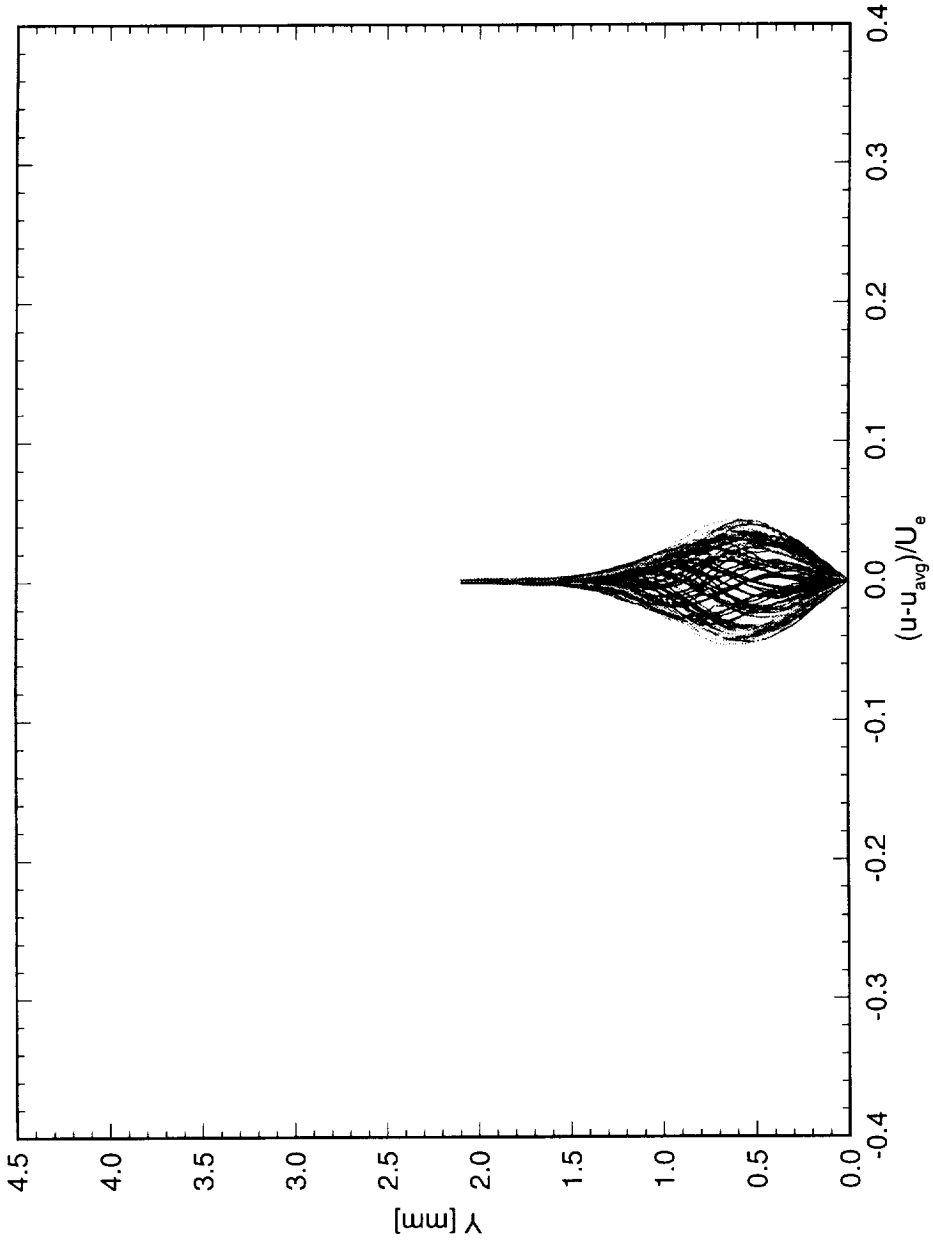

Figure 6.193: Spanwise array of 100 disturbance profiles covering a span of 99 mm at $x/c = 0.10$. $Re_c = 2.4 \times 10^6$, [48|12] roughness.

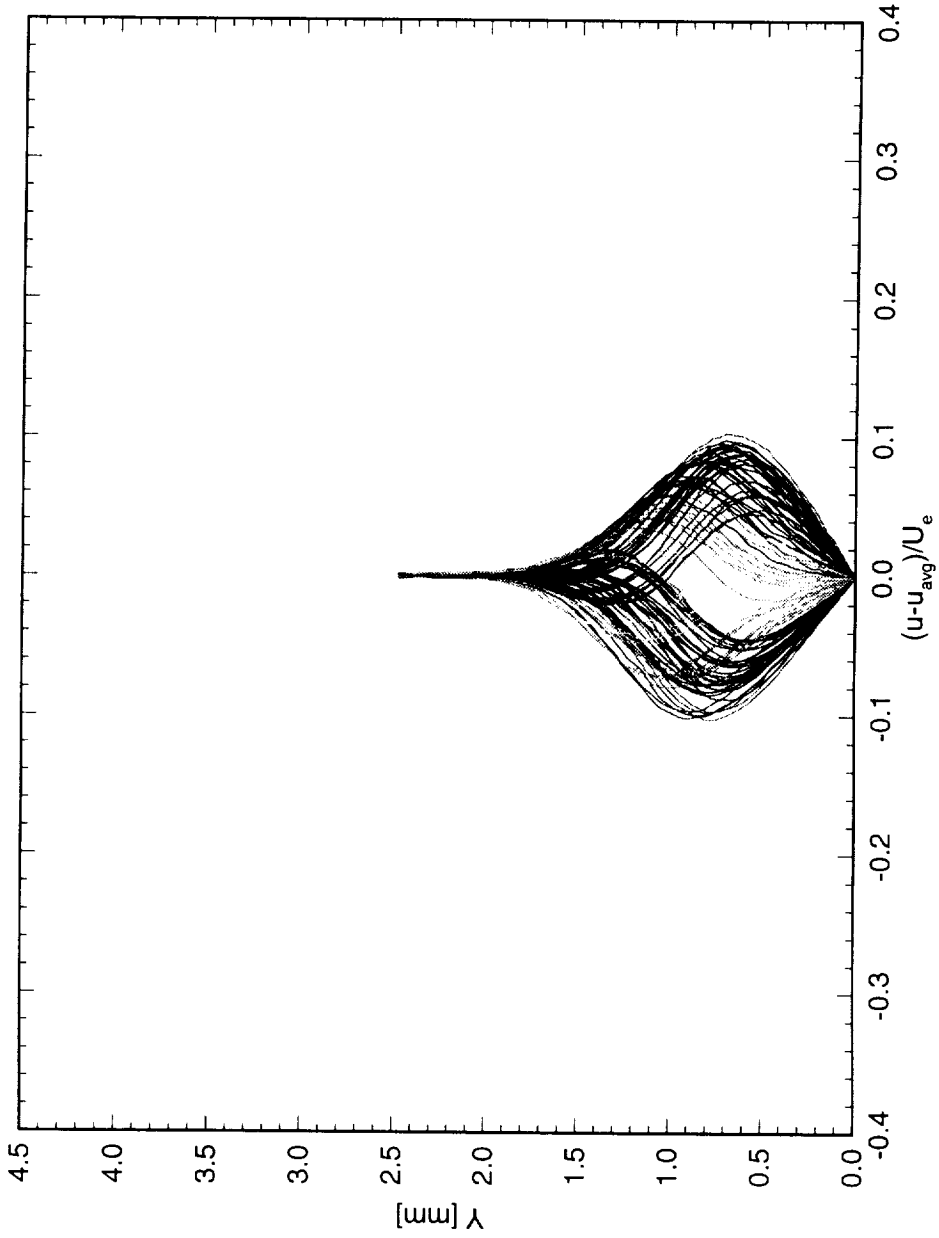

Figure 6.194: Spanwise array of 100 disturbance profiles covering a span of 99 mm at $x/c = 0.15$. $Re_c = 2.4 \times 10^6$, [48|12] roughness.

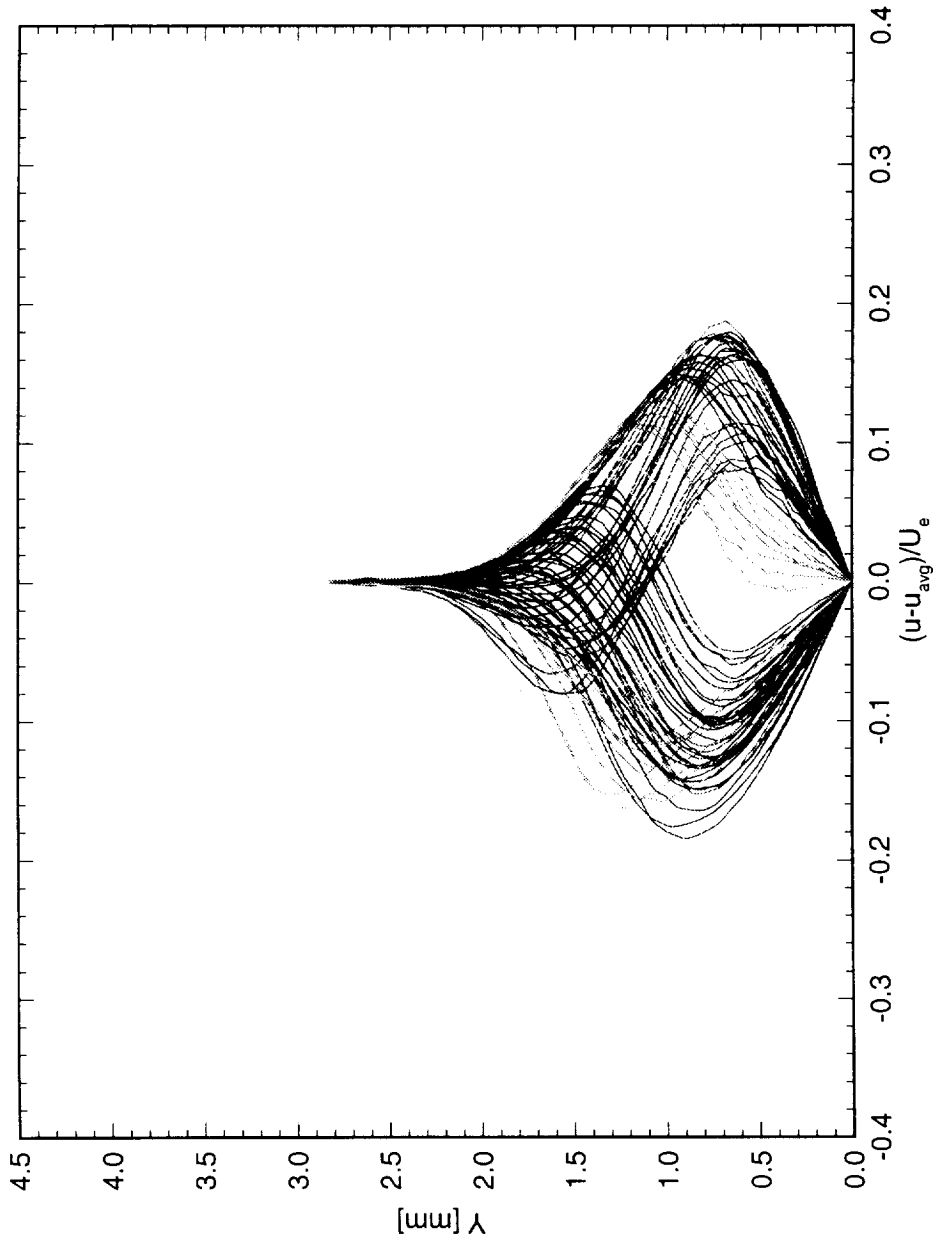

Figure 6.195: Spanwise array of 100 disturbance profiles covering a span of 99 mm at $x/c = 0.20$. $Re_c = 2.4 \times 10^6$, [48|12] roughness.

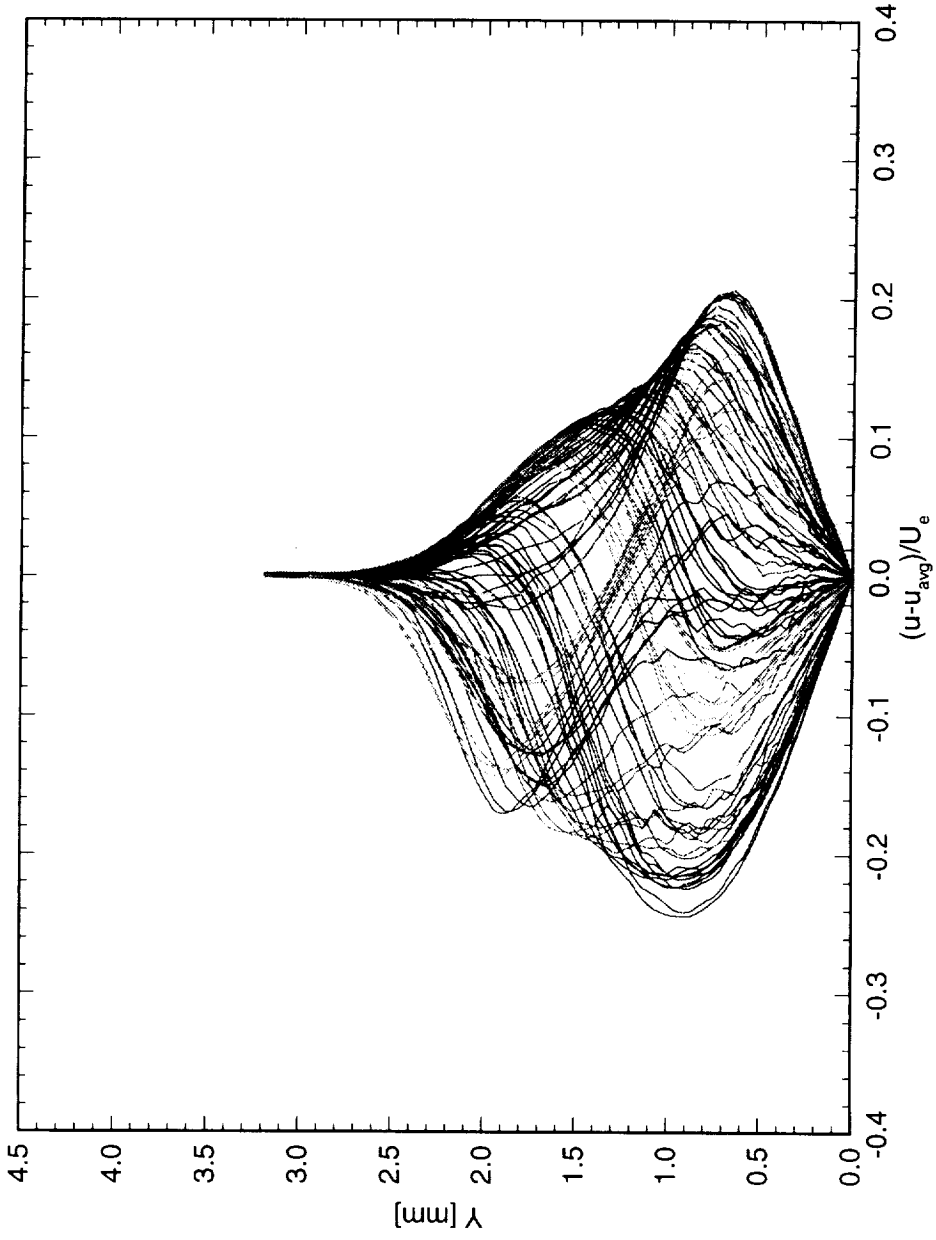

Figure 6.196: Spanwise array of 100 disturbance profiles covering a span of 99 mm at $x/c = 0.25$. $Re_c = 2.4 \times 10^6$. [48|12] roughness.

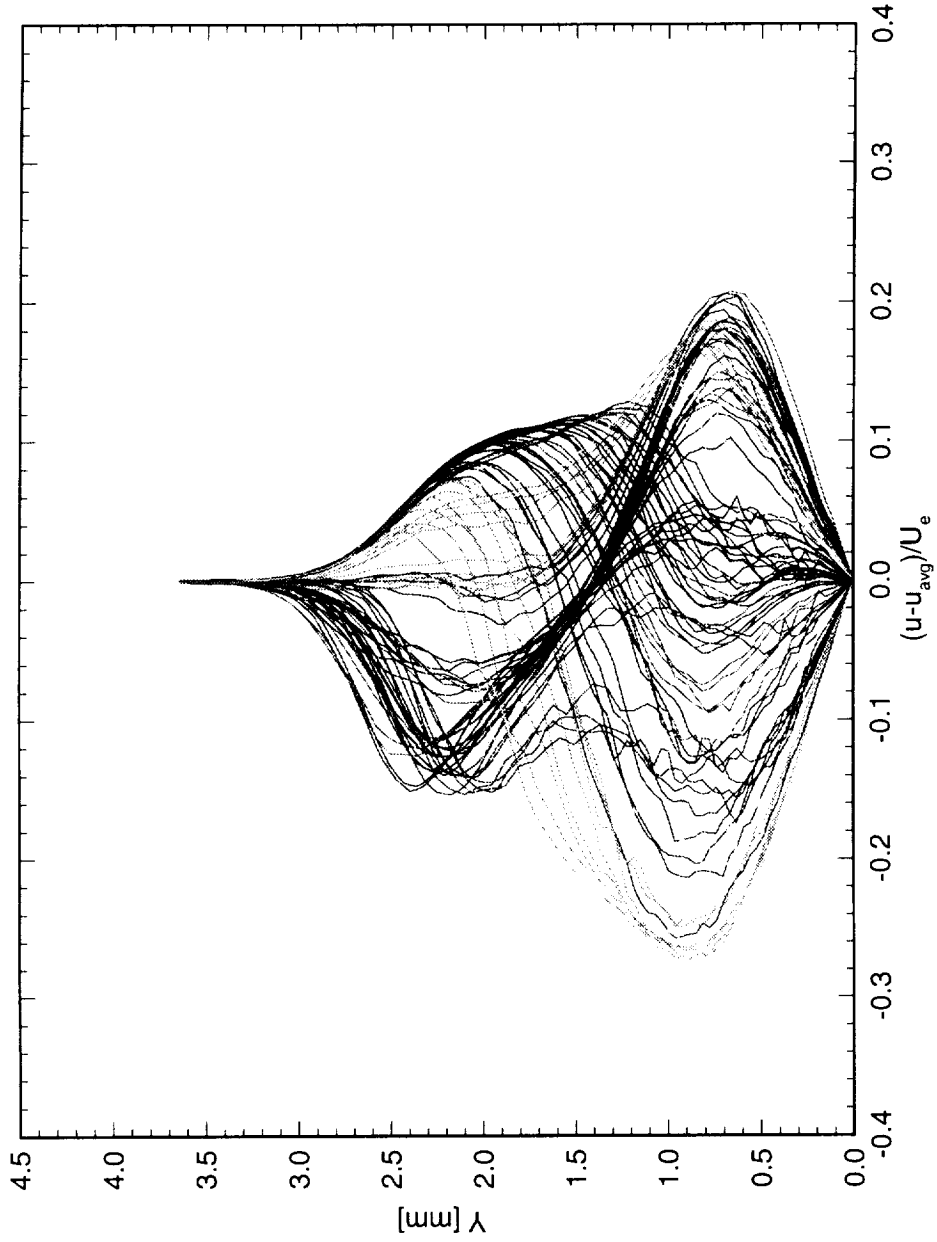

Figure 6.197: Spanwise array of 100 disturbance profiles covering a span of 99 mm at $x/c = 0.30$. $Re_c = 2.4 \times 10^6$, [48|12] roughness.

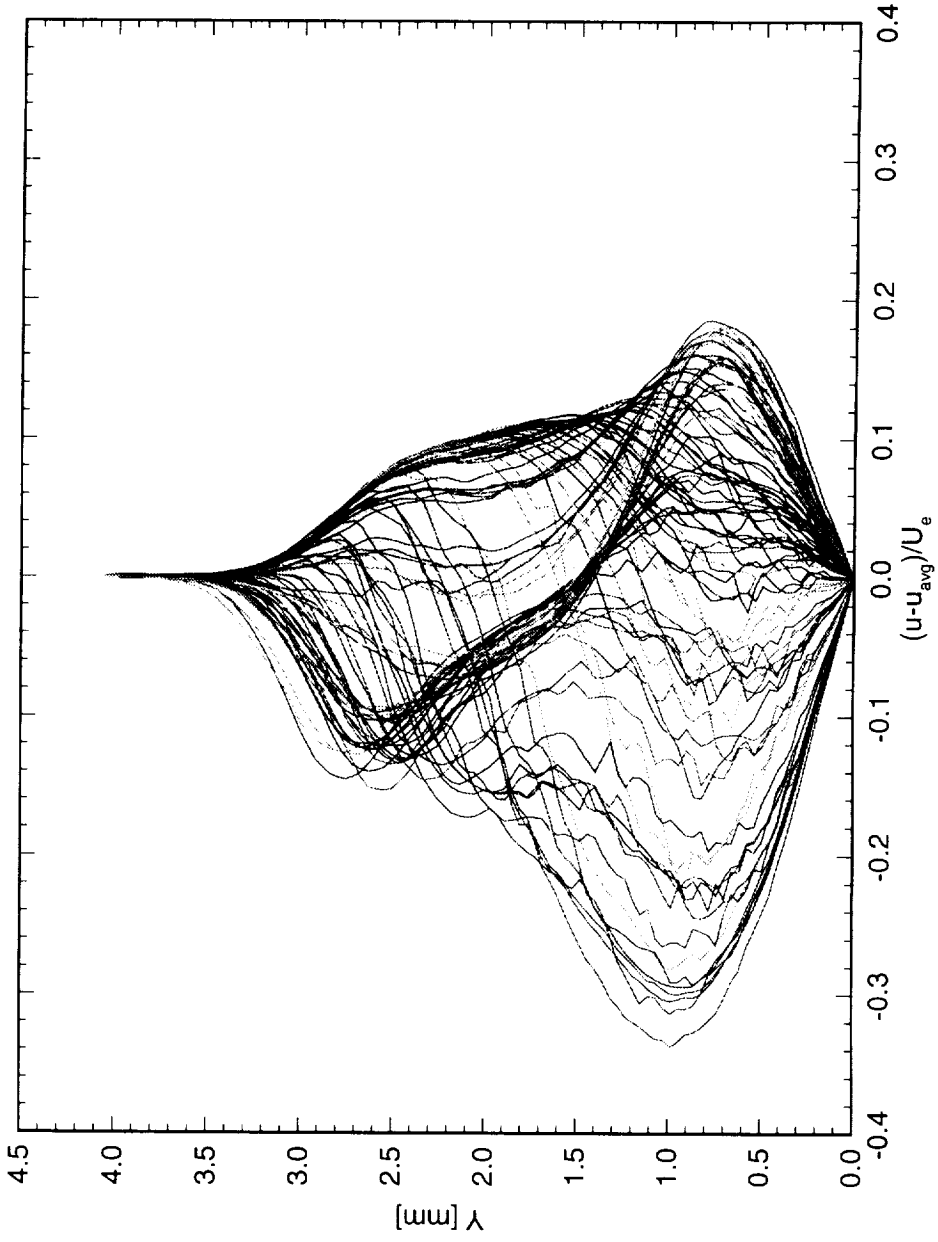

Figure 6.198: Spanwise array of 100 disturbance profiles covering a span of 99 mm at $x/c = 0.35$. $Re_c = 2.4 \times 10^6$, [48|12] roughness.

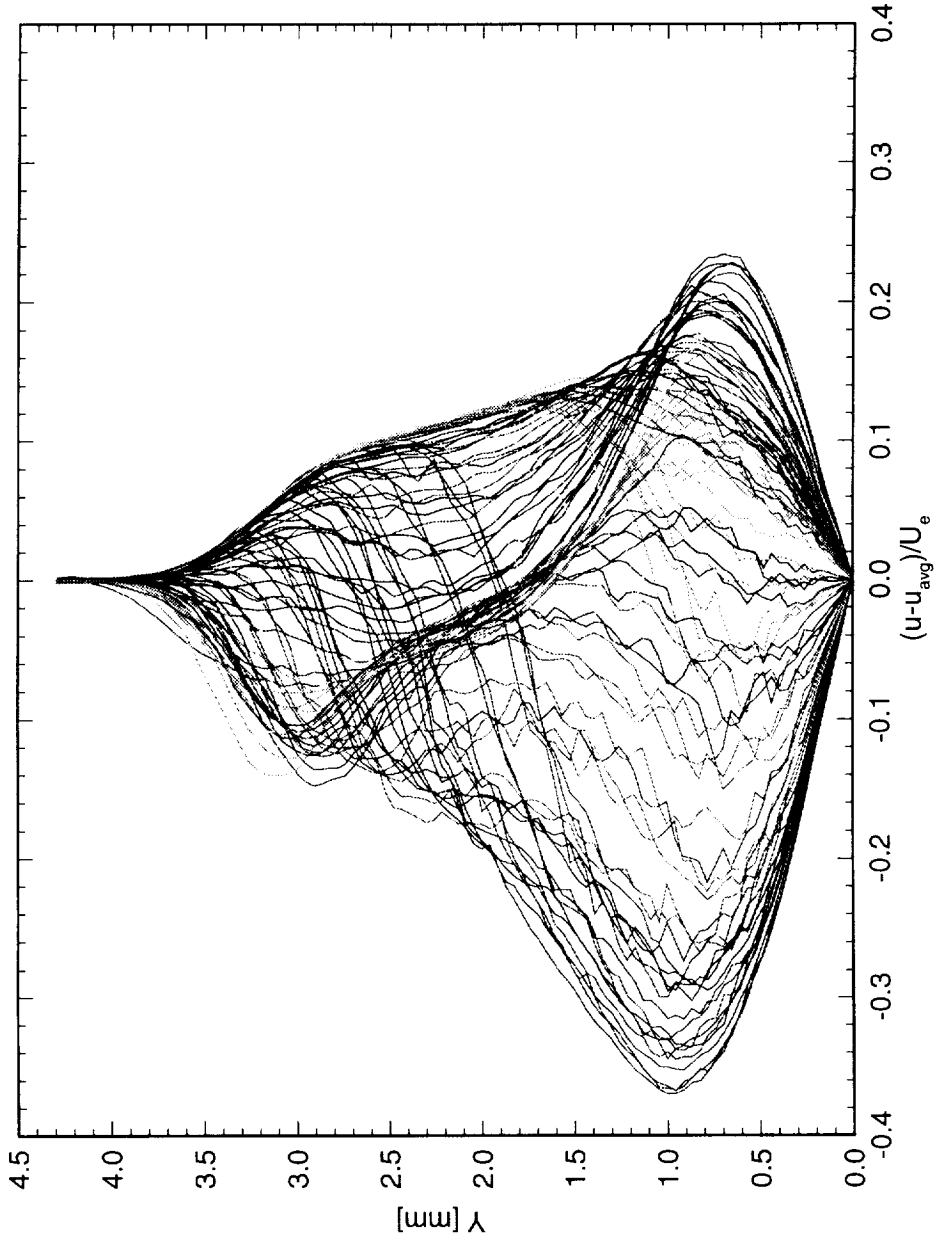

Figure 6.199: Spanwise array of 100 disturbance profiles covering a span of 99 mm at $x/c = 0.40$. $Re_c = 2.4 \times 10^6$, [48|12] roughness.

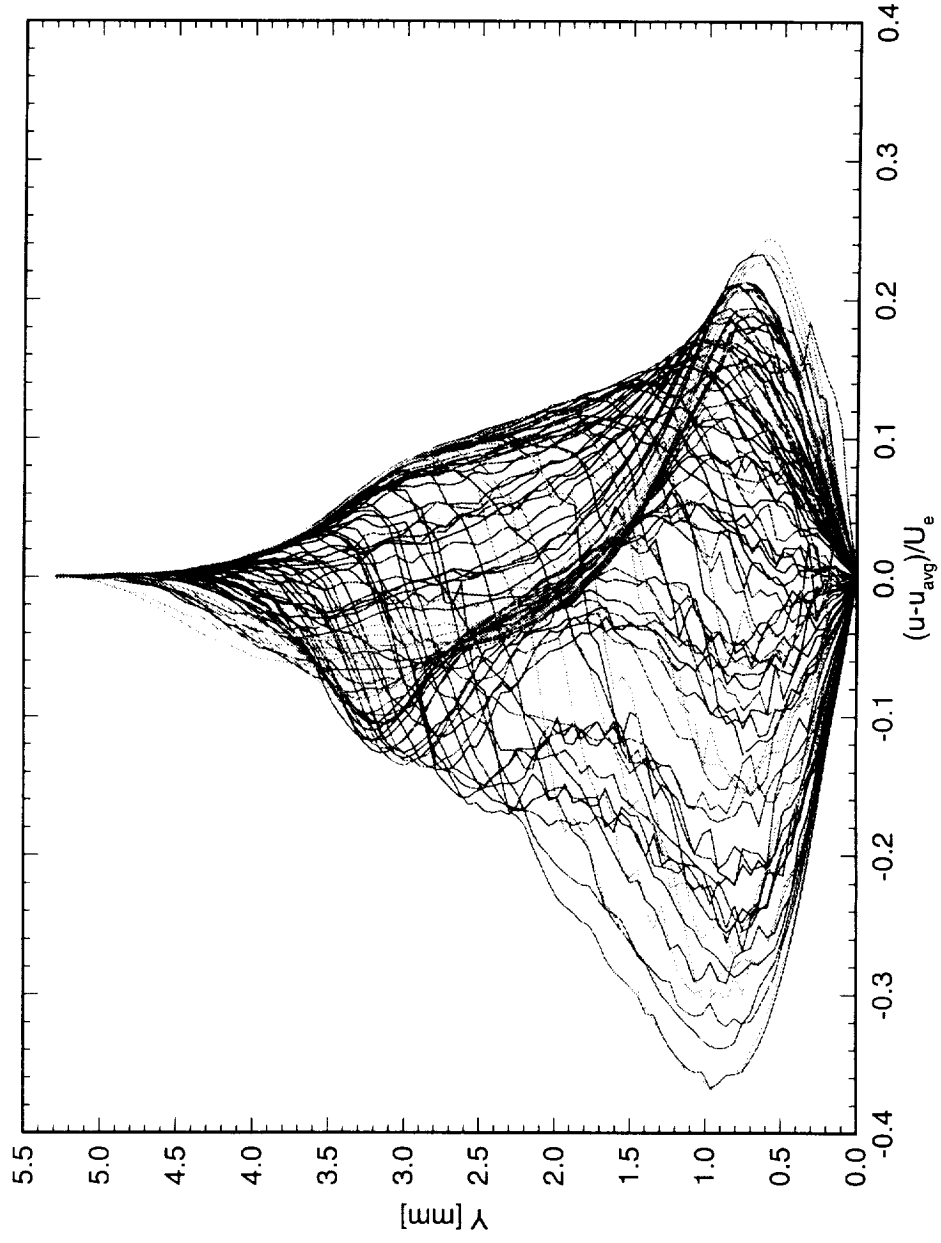

Figure 6.200: Spanwise array of 100 disturbance profiles covering a span of 99 mm at $x/c = 0.45$. $Re_c = 2.4 \times 10^6$, [48|12] roughness.

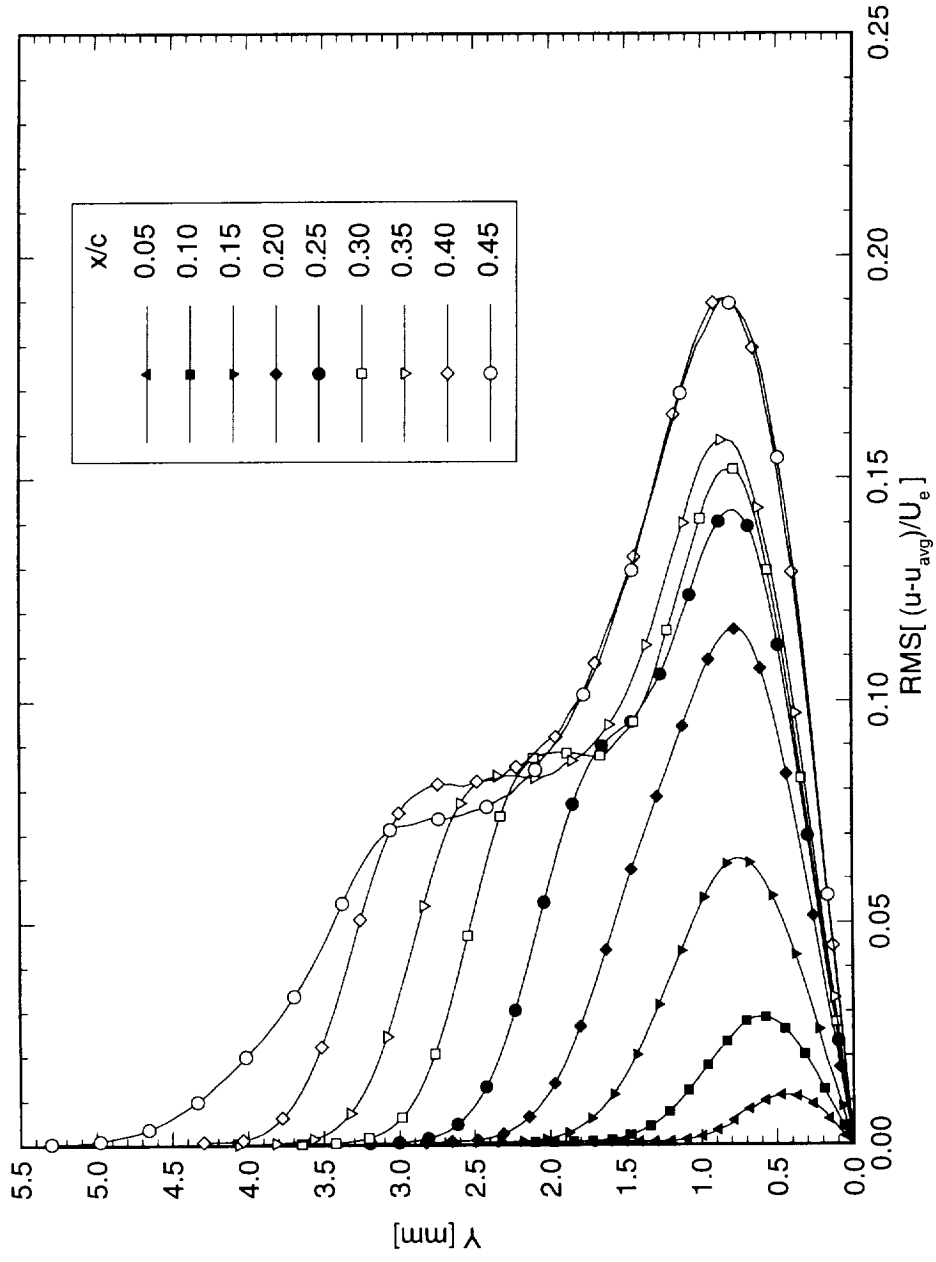

Figure 6.201: Stationary crossflow mode shapes for $Re_c = 2.4 \times 10^6$ and [48|12] roughness. The symbols are simply identifiers and do not represent measurement points.

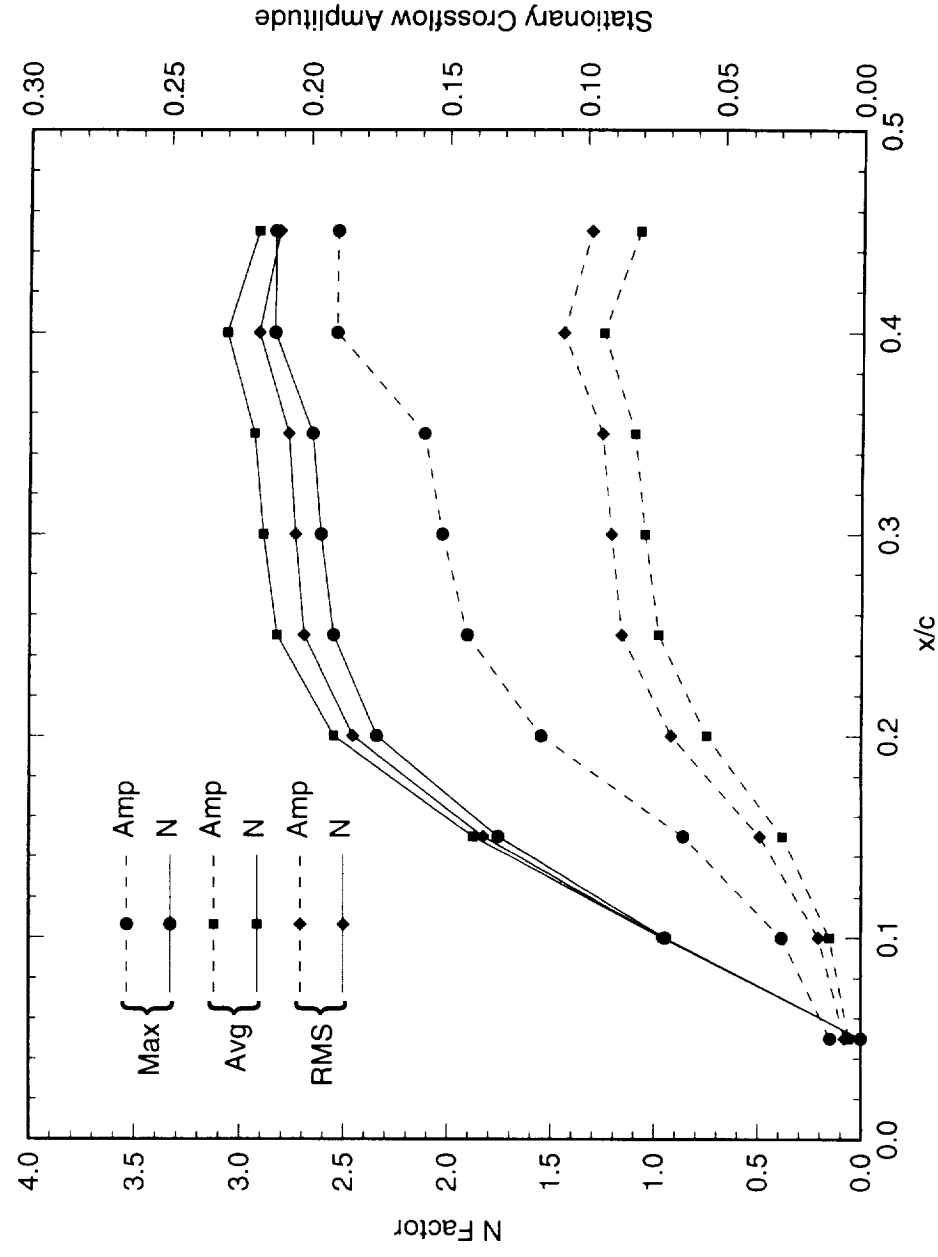

Figure 6.202: Total disturbance amplitude and amplification factor N for $Re_c = 2.4 \times 10^6$ and [48|12] roughness. The reference point for the N-factor calculations is $x/c = 0.05$.

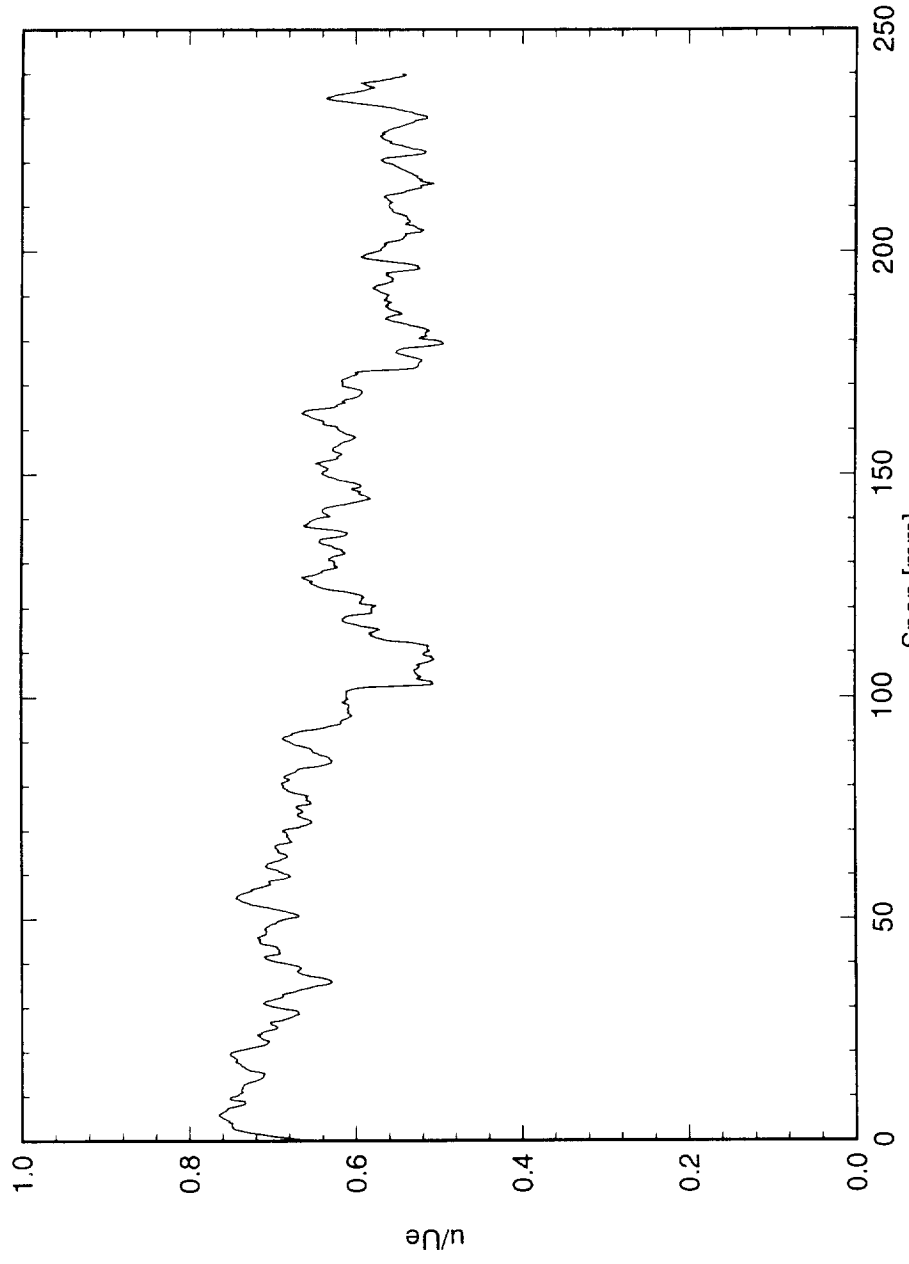

Figure 6.203: Spanwise hot-wire scan at $x/c = 0.05$, $Y = 0.45$ mm. $Re_c = 2.4 \times 10^6$, [48|12] roughness.

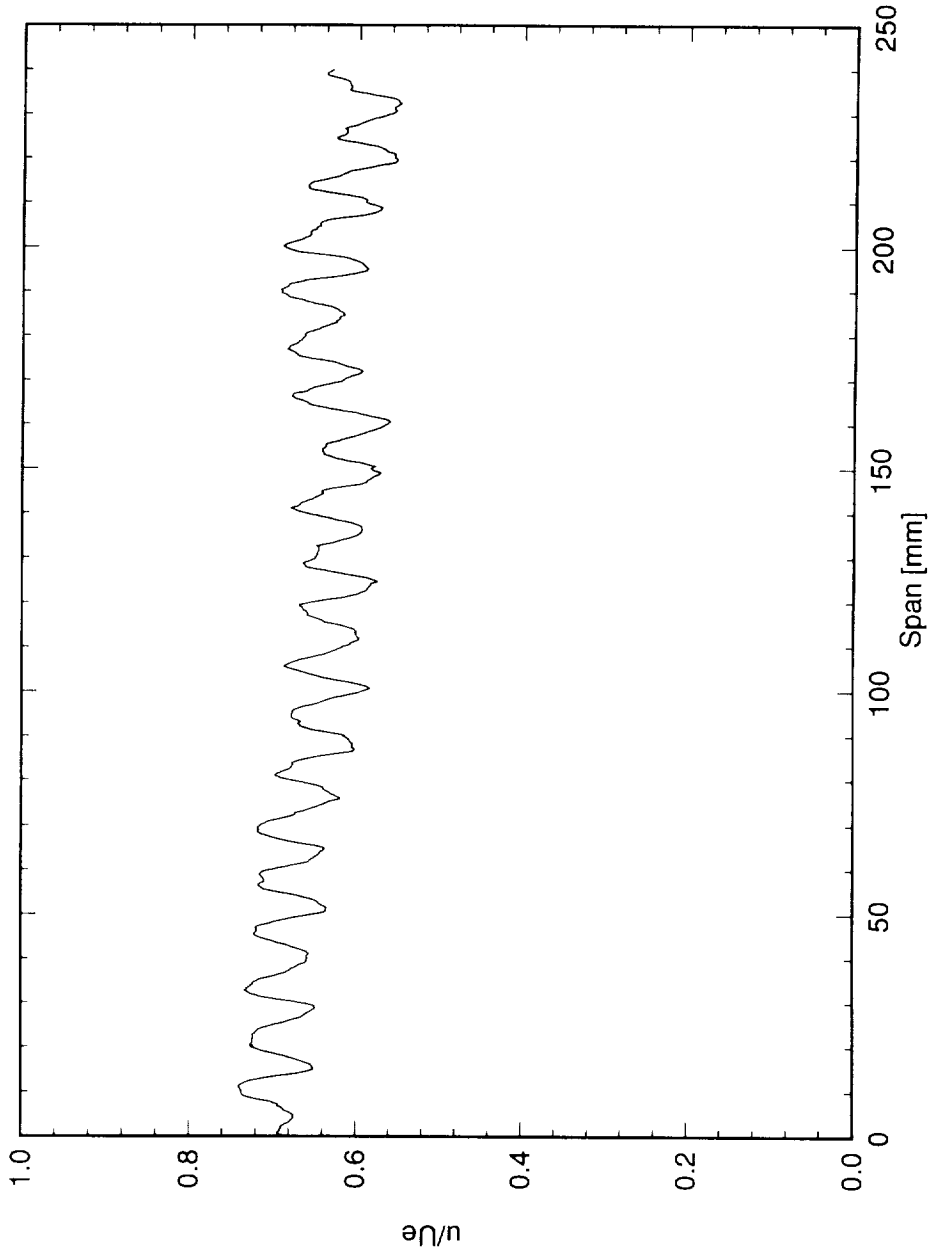

Figure 6.204: Spanwise hot-wire scan at $x/c = 0.10$, $\Upsilon = 0.6$ mm. $Re_c = 2.4 \times 10^6$, [48|12] roughness.

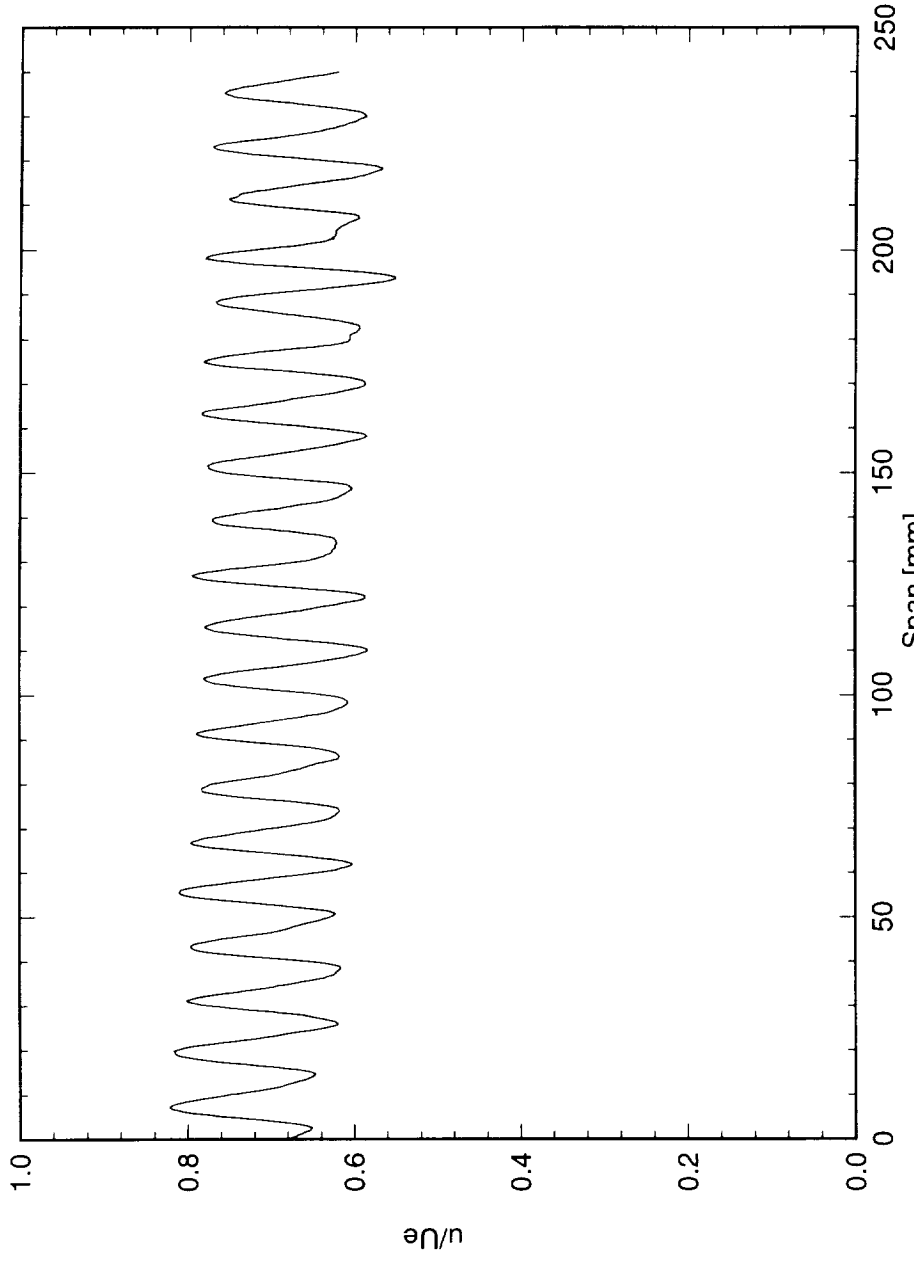

Figure 6.205: Spanwise hot-wire scan at $x/c = 0.15$, $Y = 0.75$ mm. $Re_c = 2.4 \times 10^6$, [48|12] roughness.

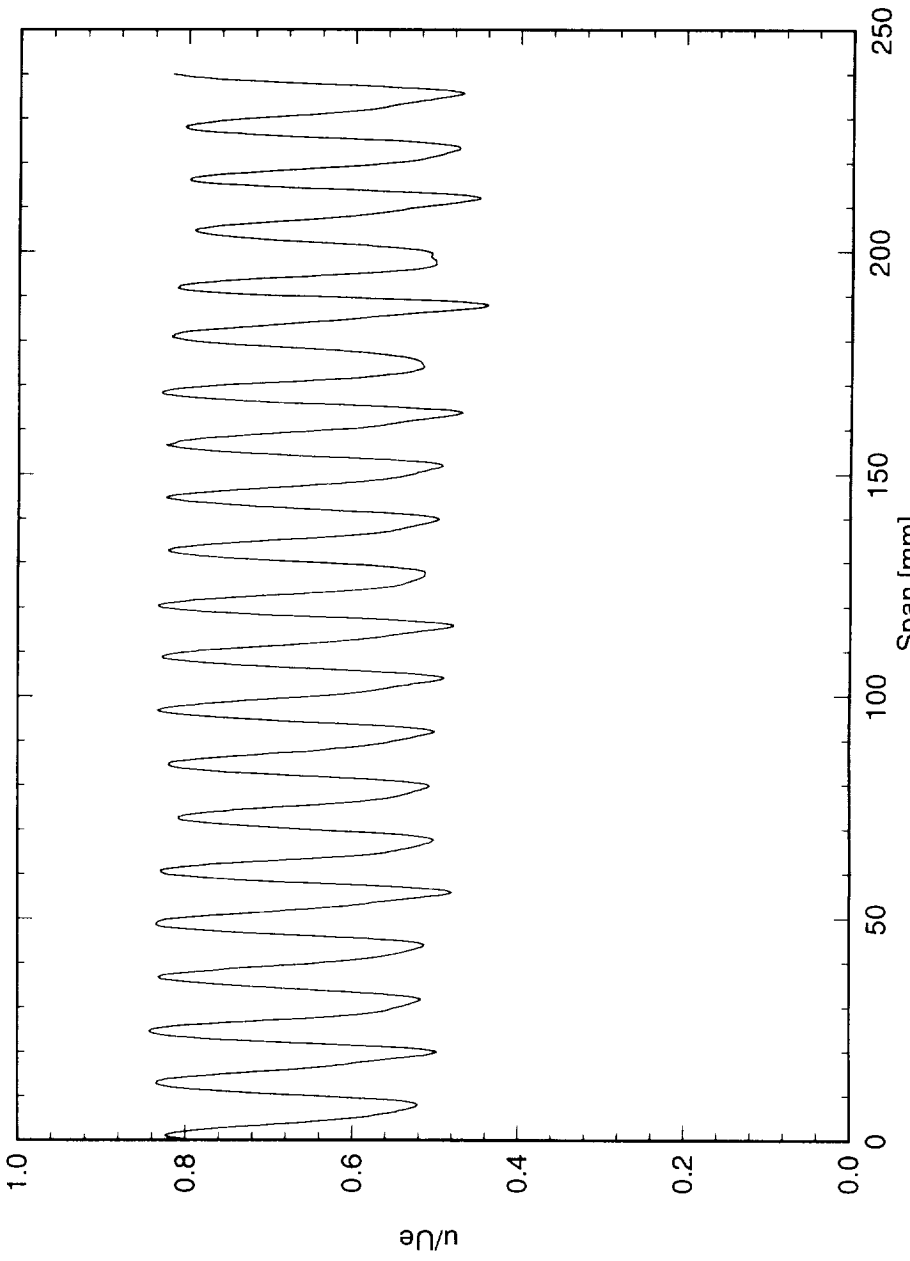

Figure 6.206: Spanwise hot-wire scan at $x/c = 0.20$, $\Upsilon = 0.75$ mm. $Re_c = 2.4 \times 10^6$, [48|12] roughness.

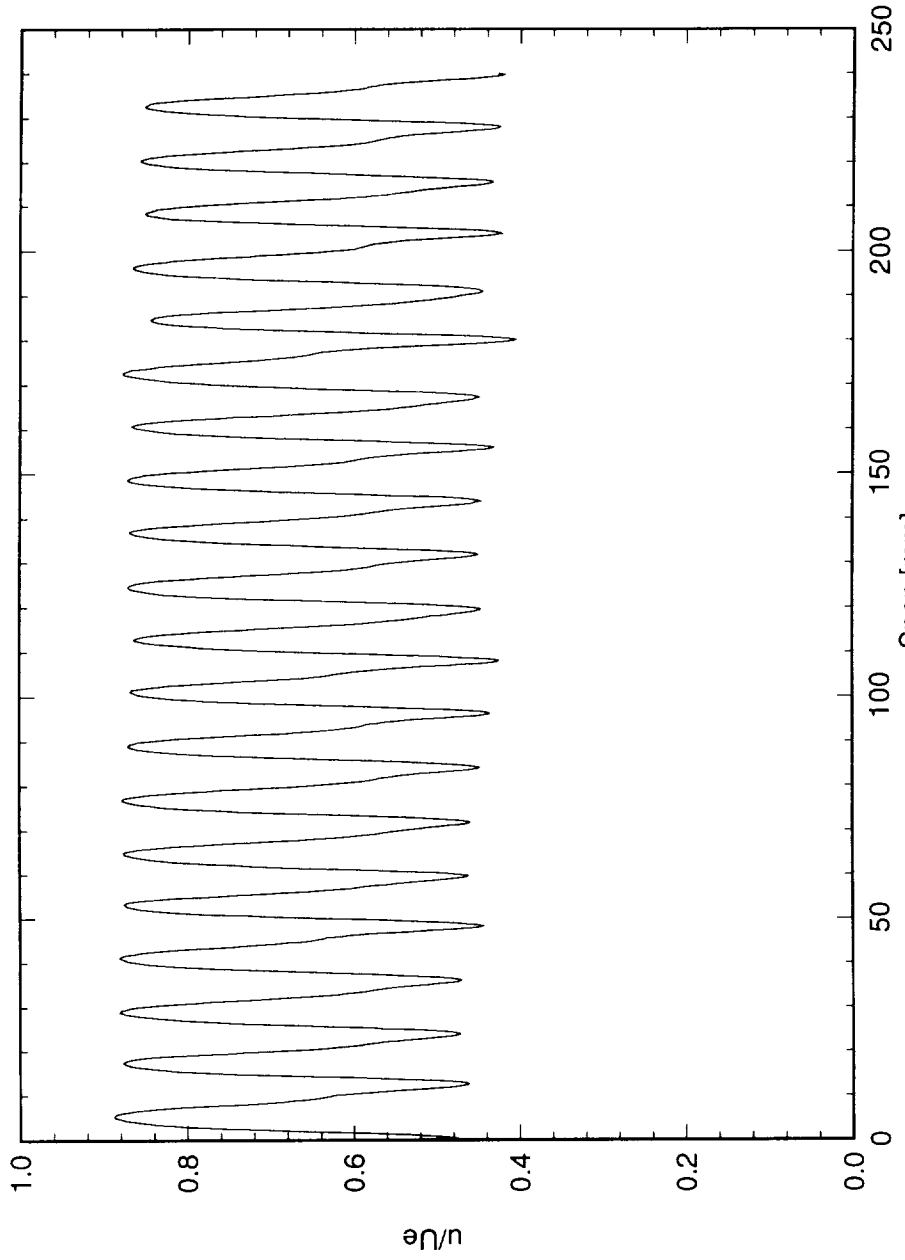

Figure 6.207: Spanwise hot-wire scan at $x/c = 0.25$, $Y = 0.8$ mm. $Re_c = 2.4 \times 10^6$, [48|12] roughness.

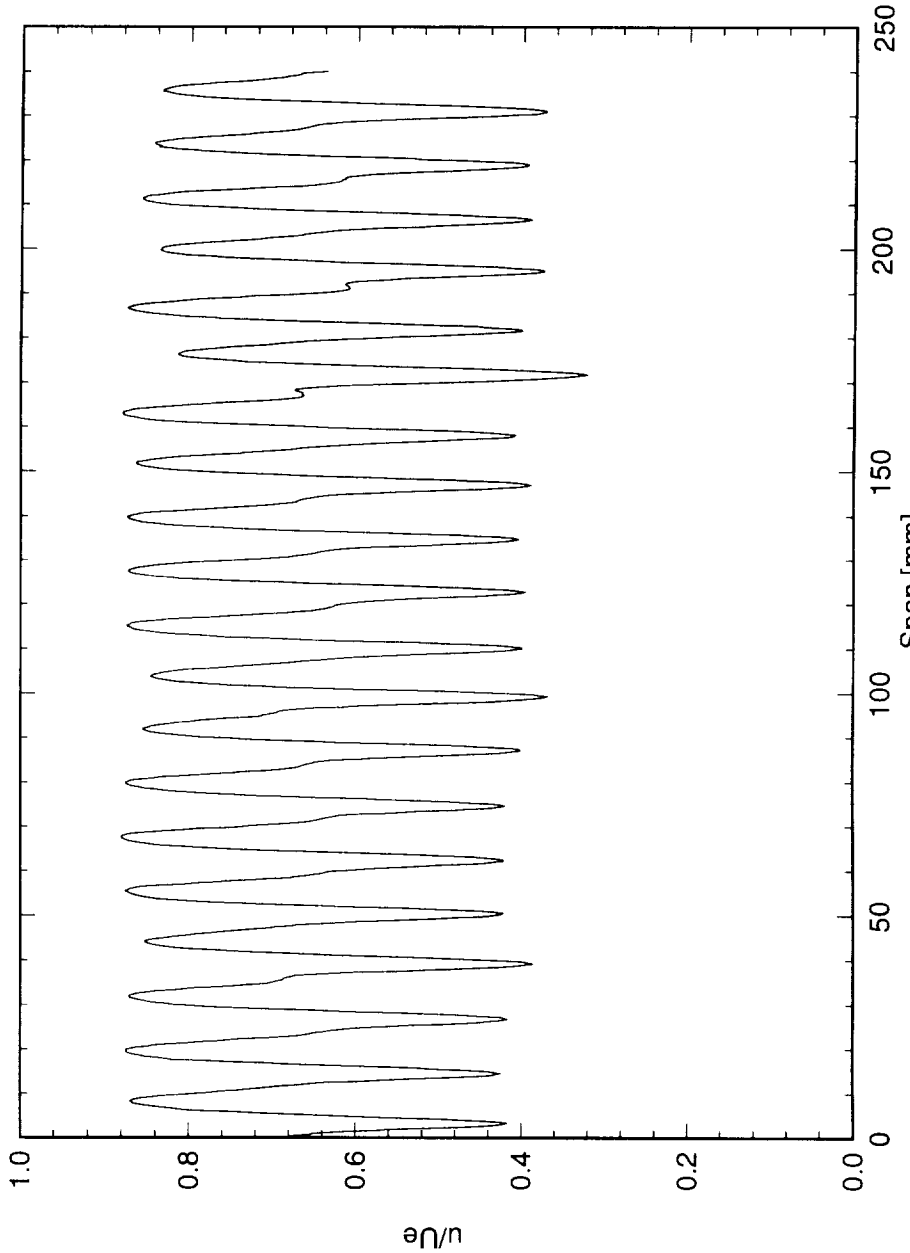

Figure 6.208: Spanwise hot-wire scan at $x/c = 0.30$, $Y = 0.8$ mm. $Re_c = 2.4 \times 10^6$, [48|12] roughness.

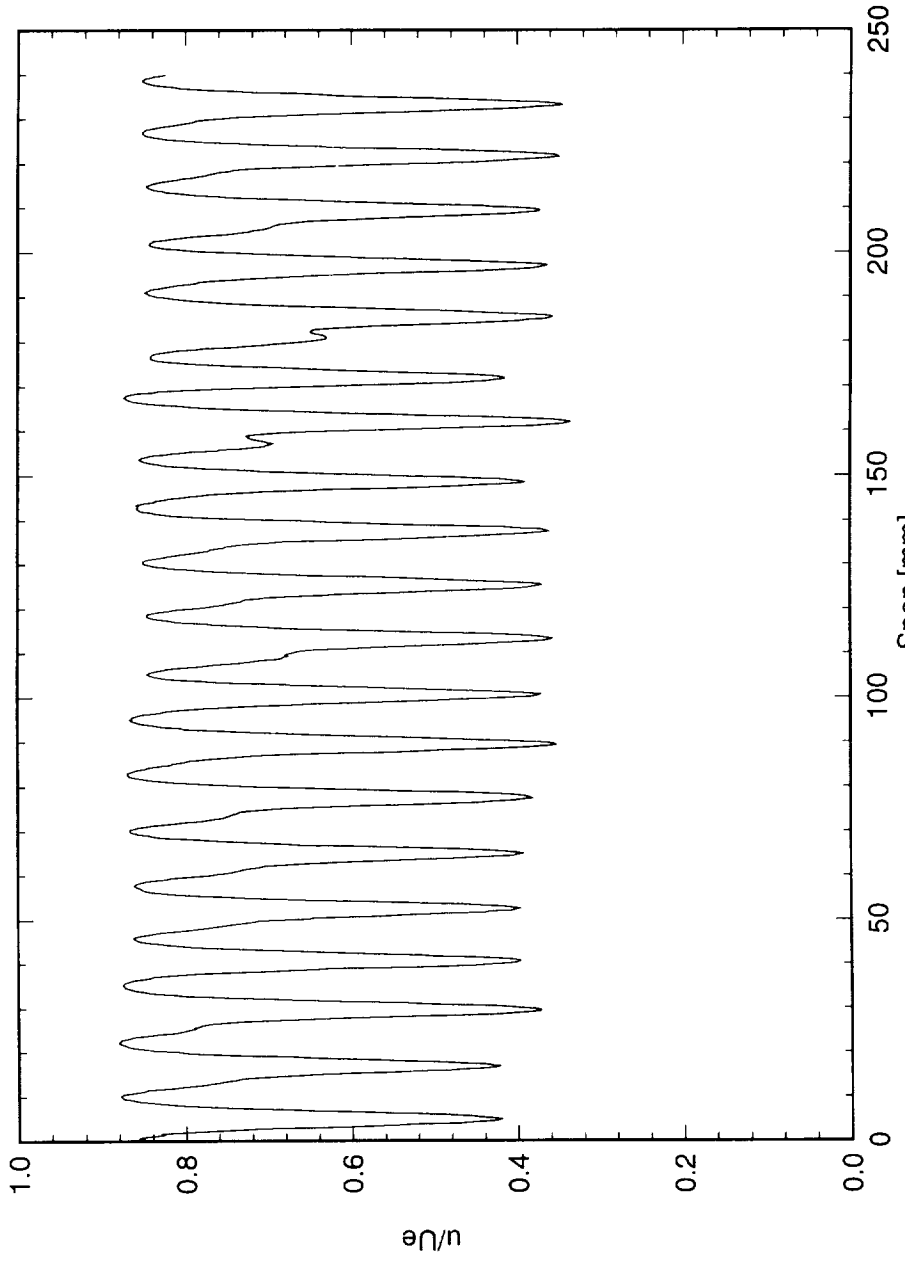

Figure 6.209: Spanwise hot-wire scan at $x/c = 0.35$, $Y = 0.85$ mm. $Re_c = 2.4 \times 10^6$, [48|12] roughness.

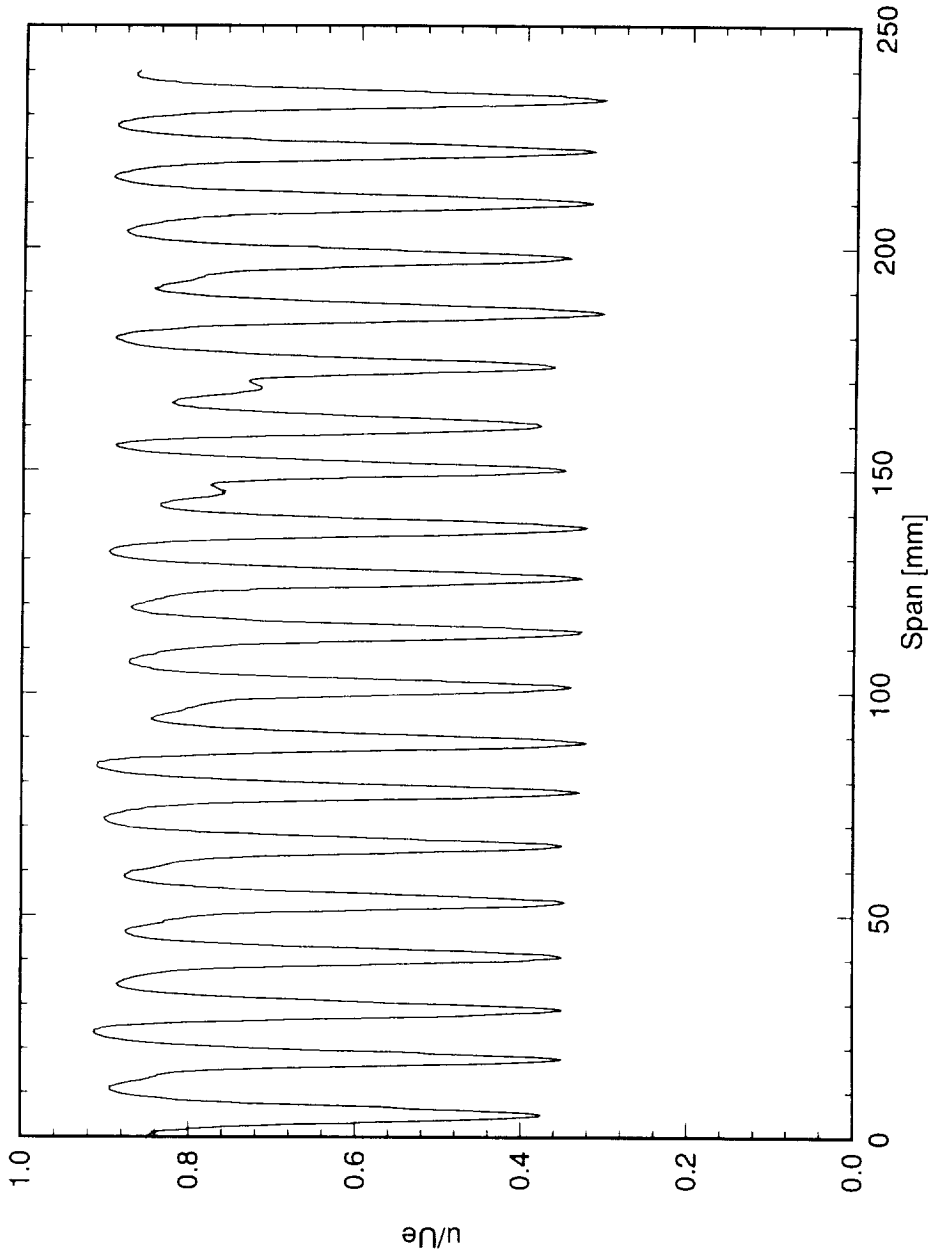

Figure 6.210: Spanwise hot-wire scan at $x/c = 0.40$, $Y = 0.85$ mm. $Re_c = 2.4 \times 10^6$, [48|12] roughness.

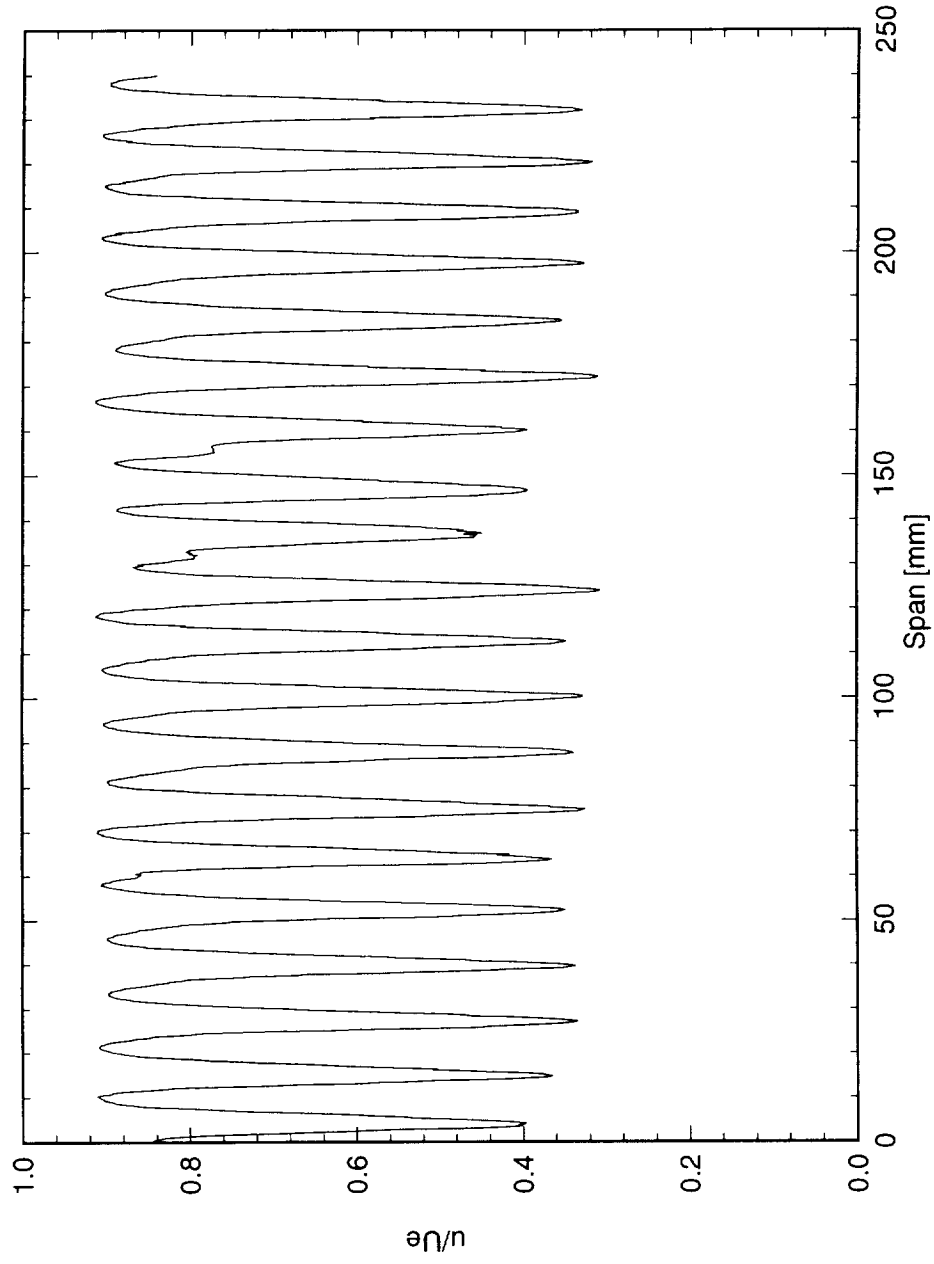

Figure 6.211: Spanwise hot-wire scan at $x/c = 0.45$, $Y = 0.85$ mm. $Re_c = 2.4 \times 10^6$, [48|12] roughness.

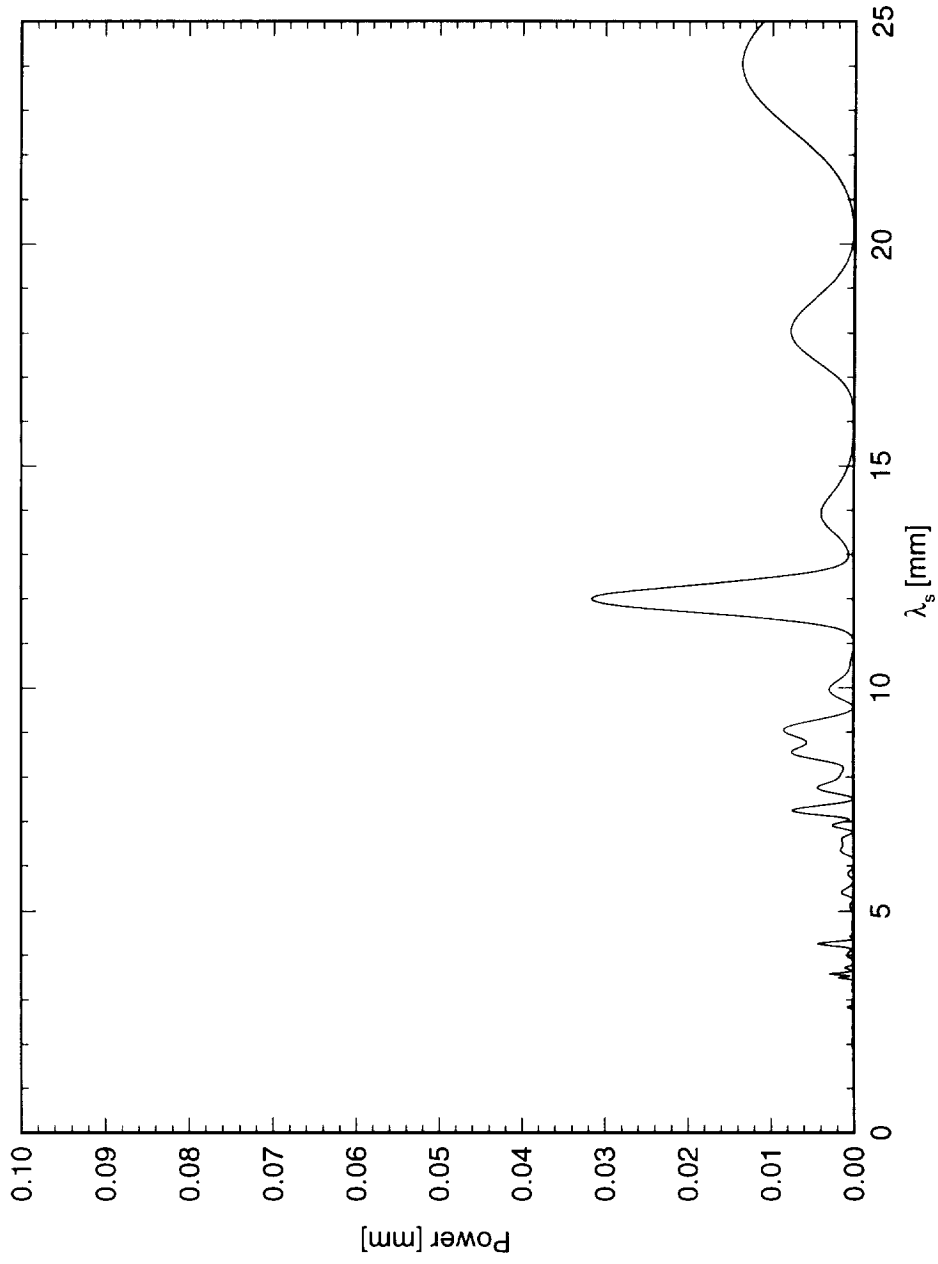

Figure 6.212: Power spectral density of spanwise hot-wire scan at $x/c = 0.05$, $Y = 0.45$ mm. $Re_c = 2.4 \times 10^6$. [48|12] roughness.

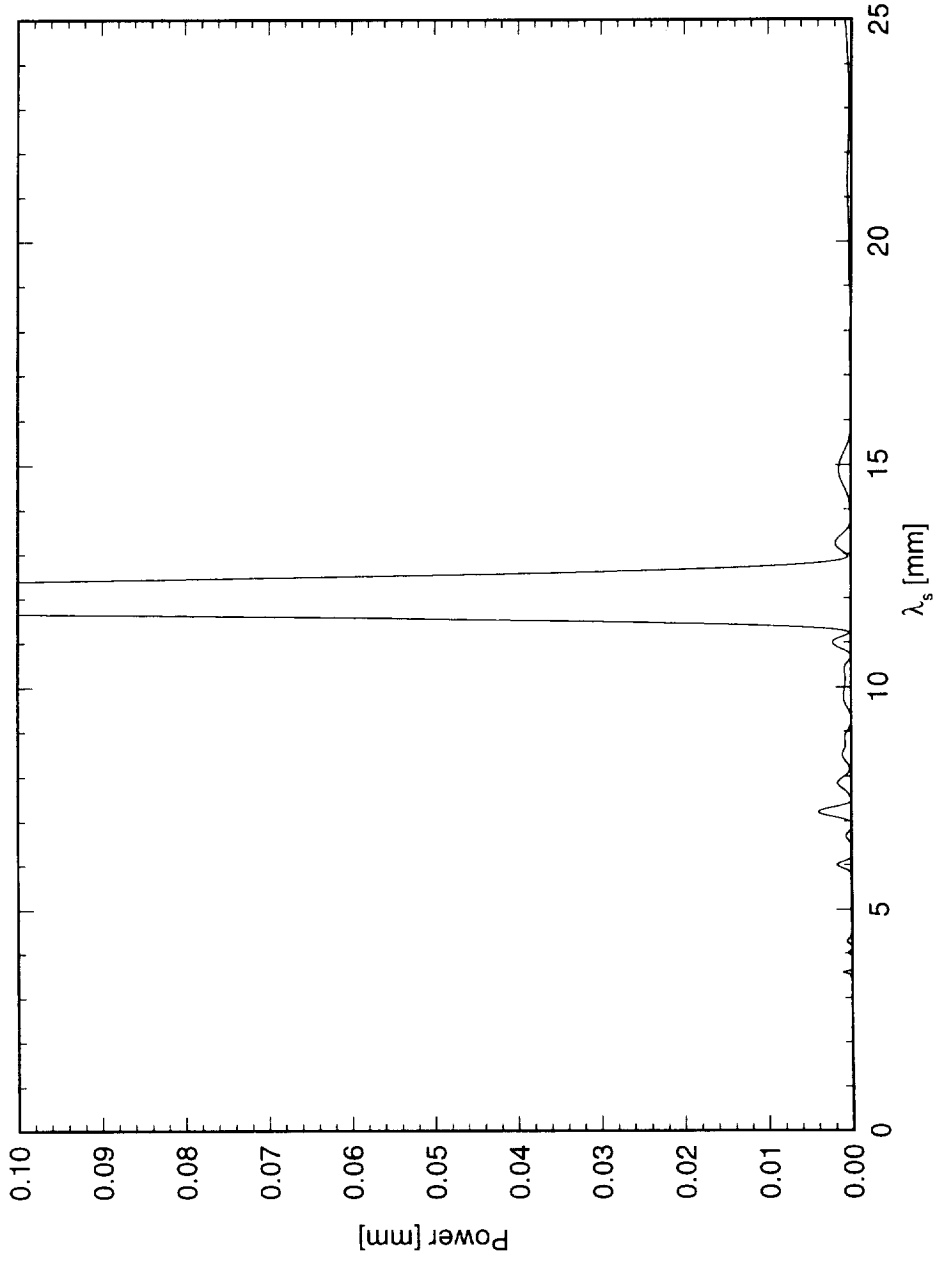

Figure 6.213: Power spectral density of spanwise hot-wire scan at $x/c = 0.10$, $Y = 0.6$ mm. $Re_c = 2.4 \times 10^6$, [48|12] roughness.

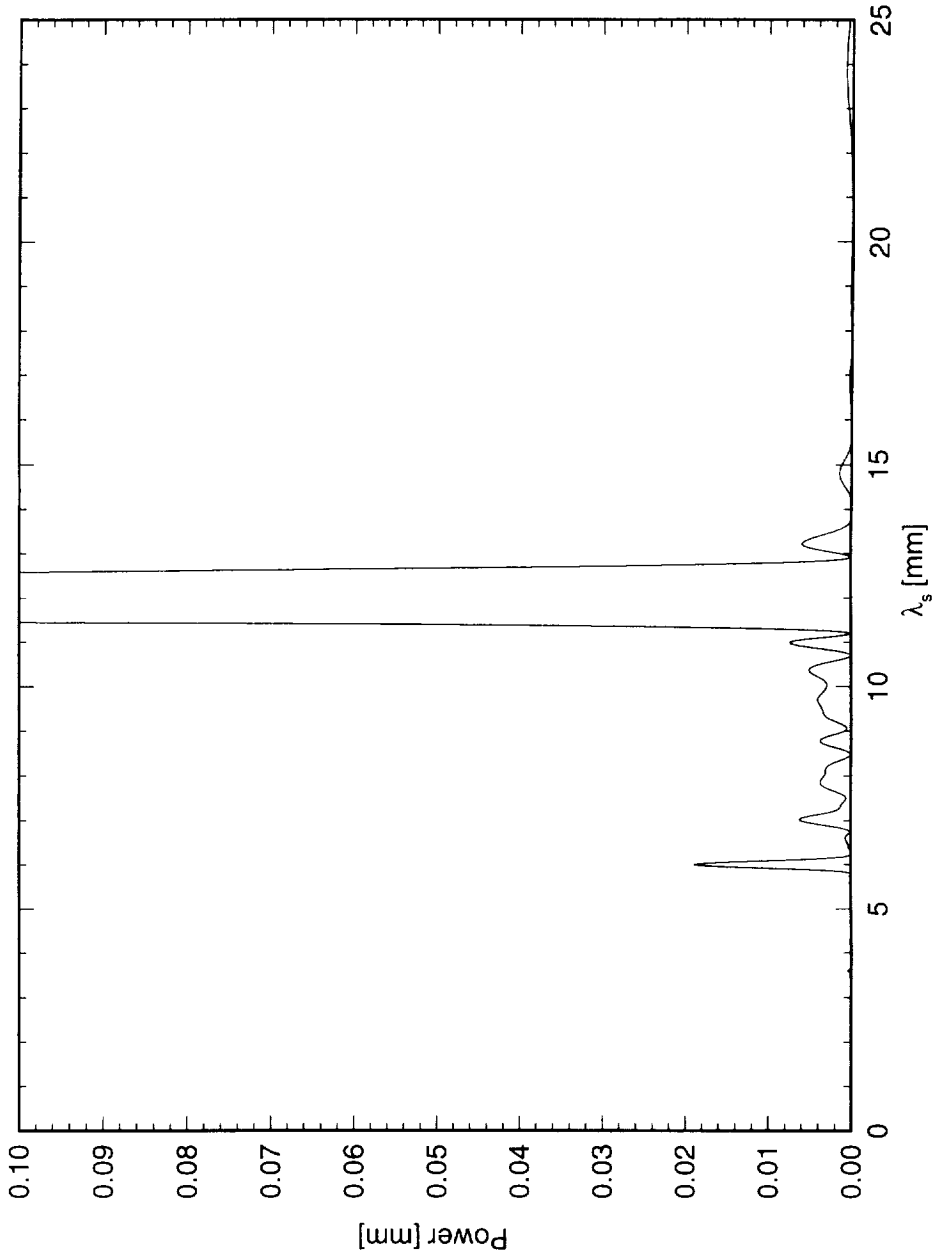

Figure 6.214: Power spectral density of spanwise hot-wire scan at $x/c = 0.15$, $Y = 0.75$ mm. $Re_c = 2.4 \times 10^6$. [48|12] roughness.

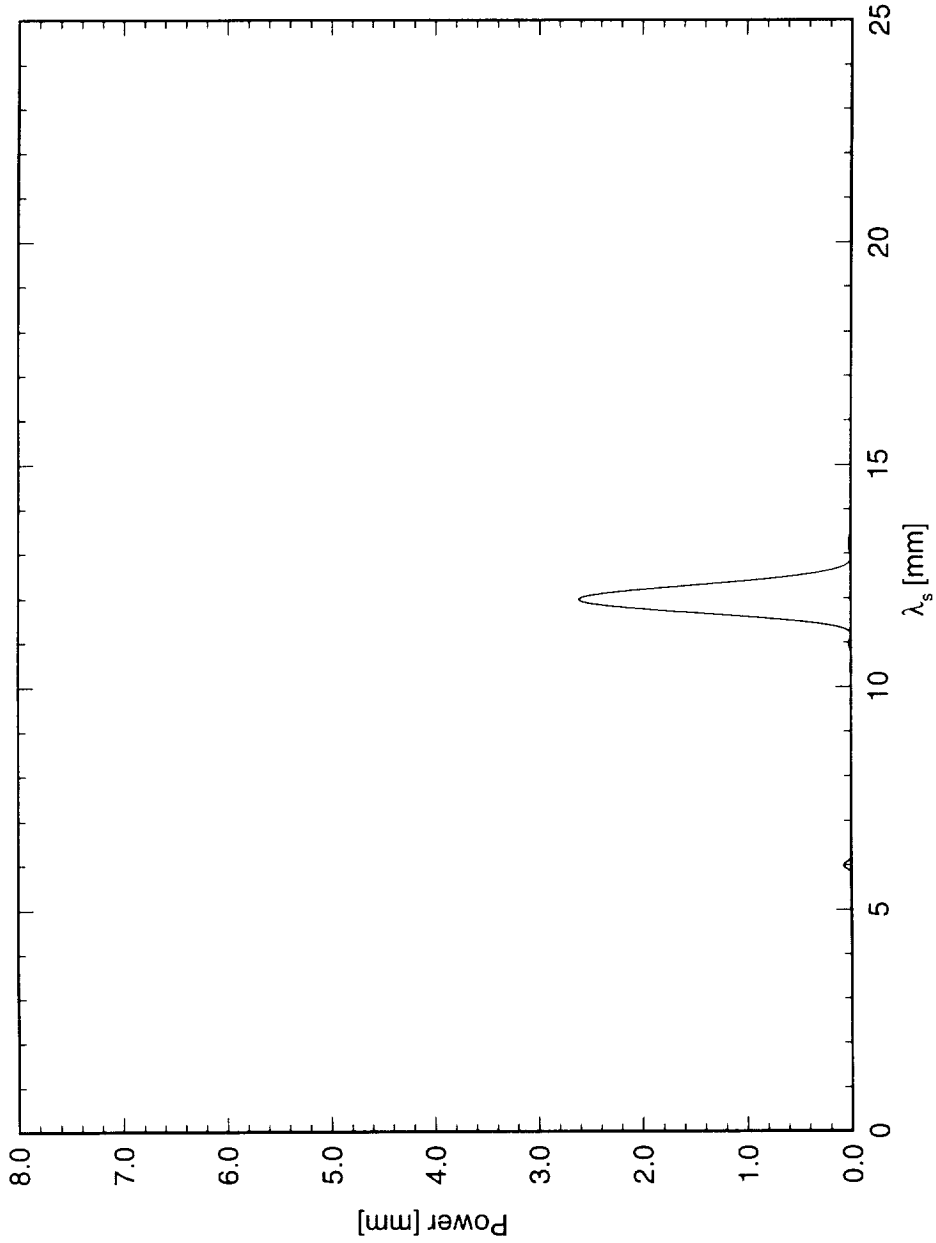

Figure 6.215: Power spectral density of spanwise hot-wire scan at $x/c = 0.20$, $Y = 0.75$ mm. $Re_c = 2.4 \times 10^6$, [48|12] roughness.

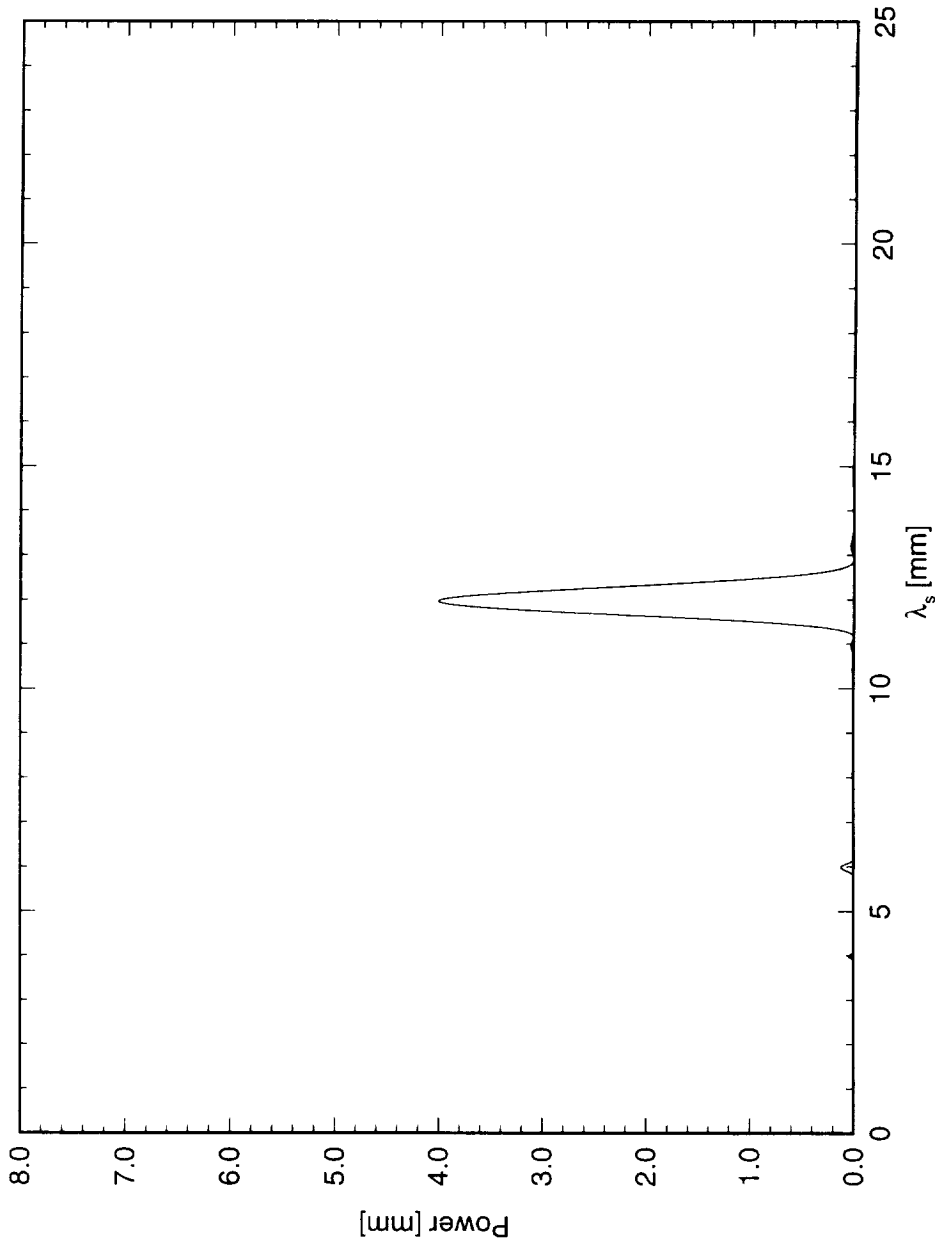

Figure 6.216: Power spectral density of spanwise hot-wire scan at $x/c = 0.25$, $Y = 0.8$ mm. $Re_c = 2.4 \times 10^6$, [48|12] roughness.

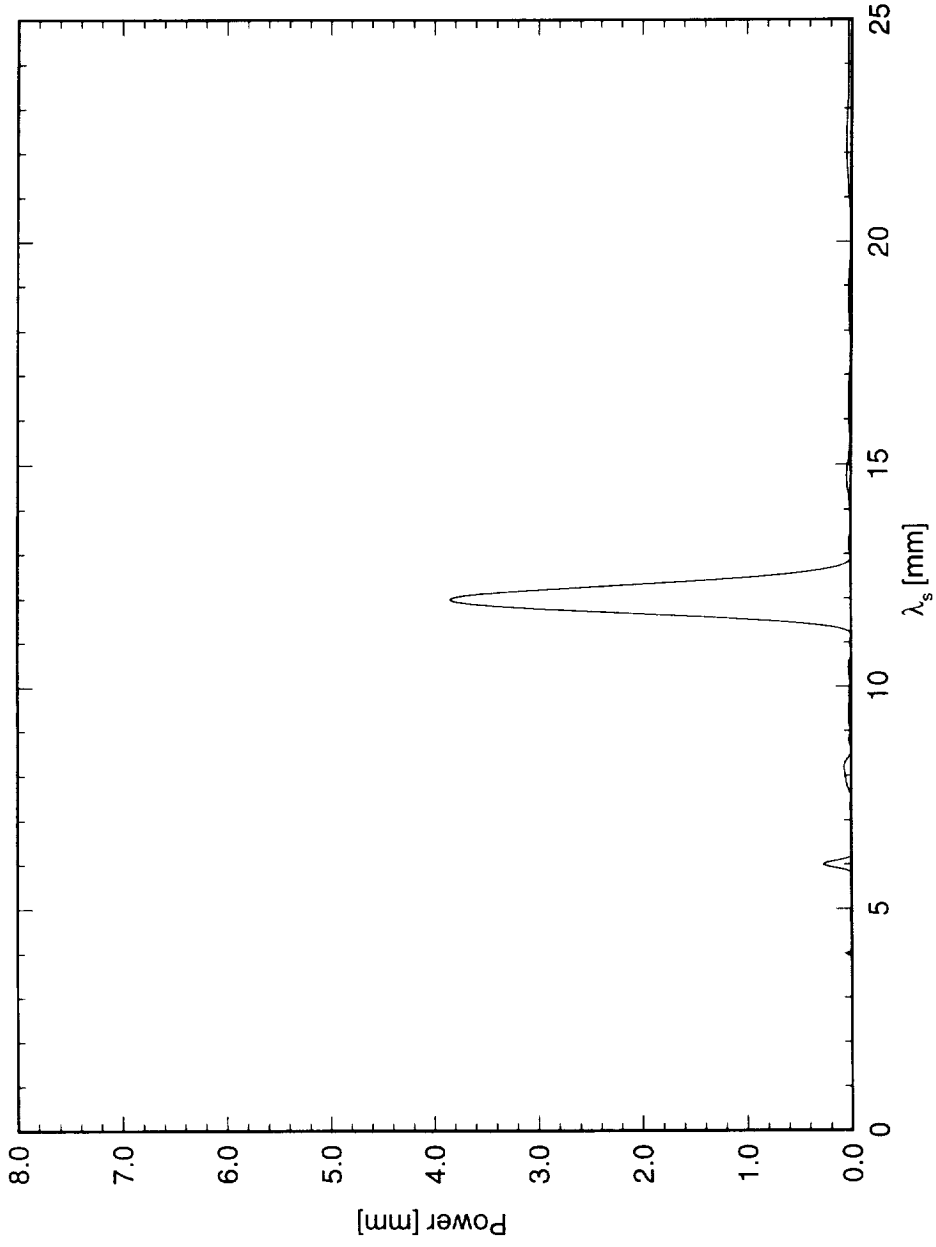

Figure 6.217: Power spectral density of spanwise hot-wire scan at $x/c = 0.30$, $Y = 0.8$ mm. $Re_c = 2.4 \times 10^6$, [48|12] roughness.

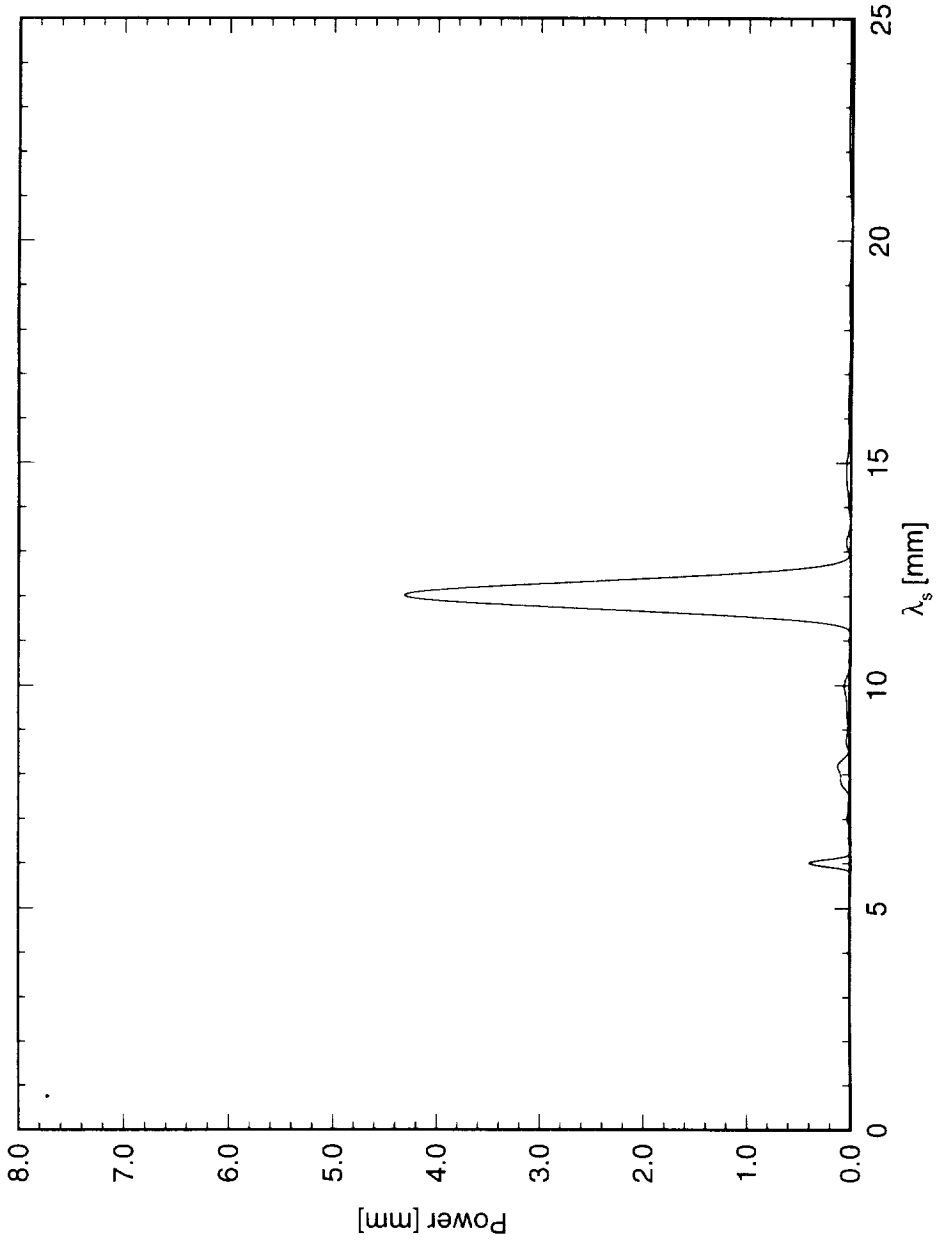

Figure 6.218: Power spectral density of spanwise hot-wire scan at $x/c = 0.35$, $Y = 0.85$ mm. $Re_c = 2.4 \times 10^6$. [48|12] roughness.

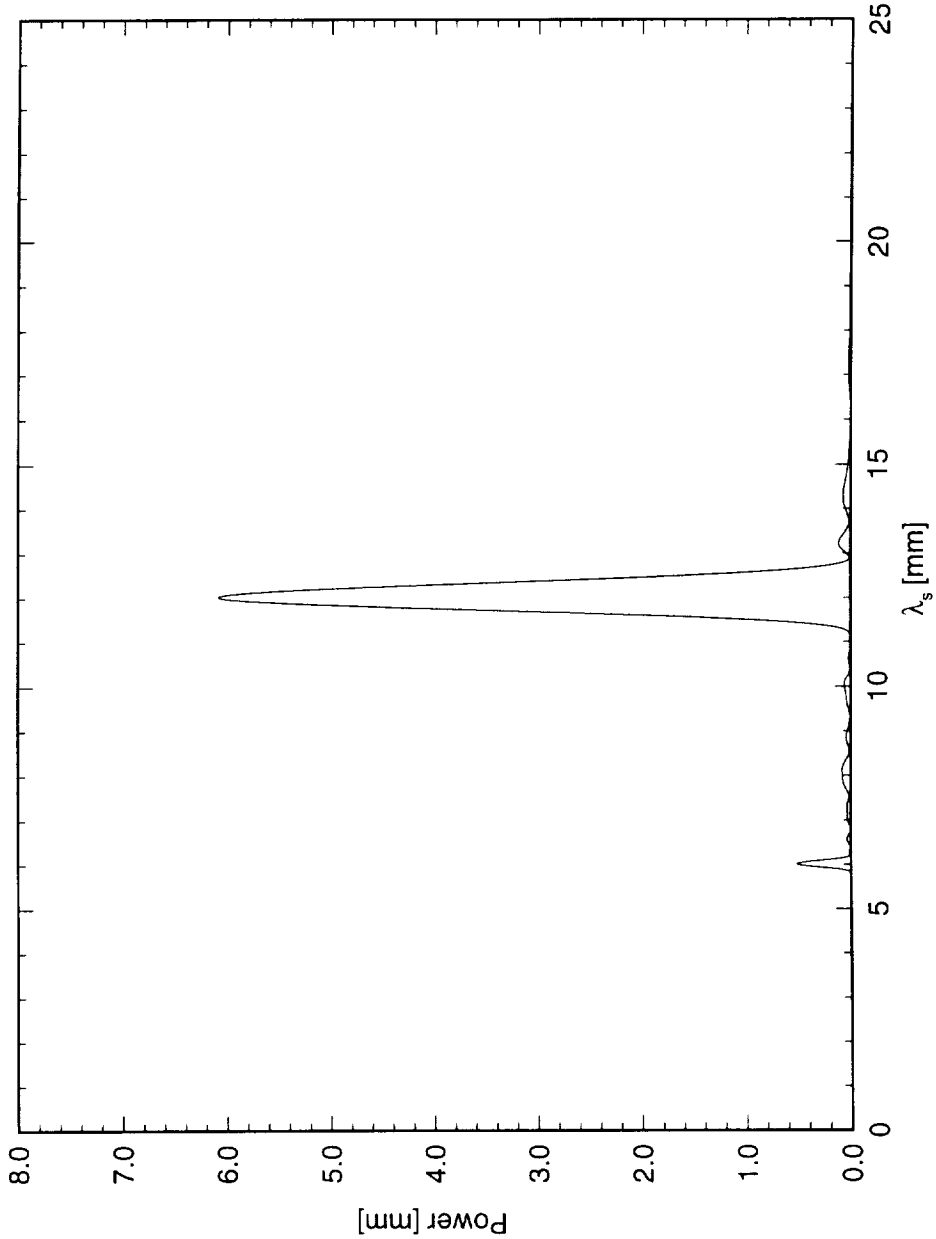

Figure 6.219: Power spectral density of spanwise hot-wire scan at $x/c = 0.40$, $Y = 0.85$ mm. $Re_c = 2.4 \times 10^6$, [48|12] roughness.

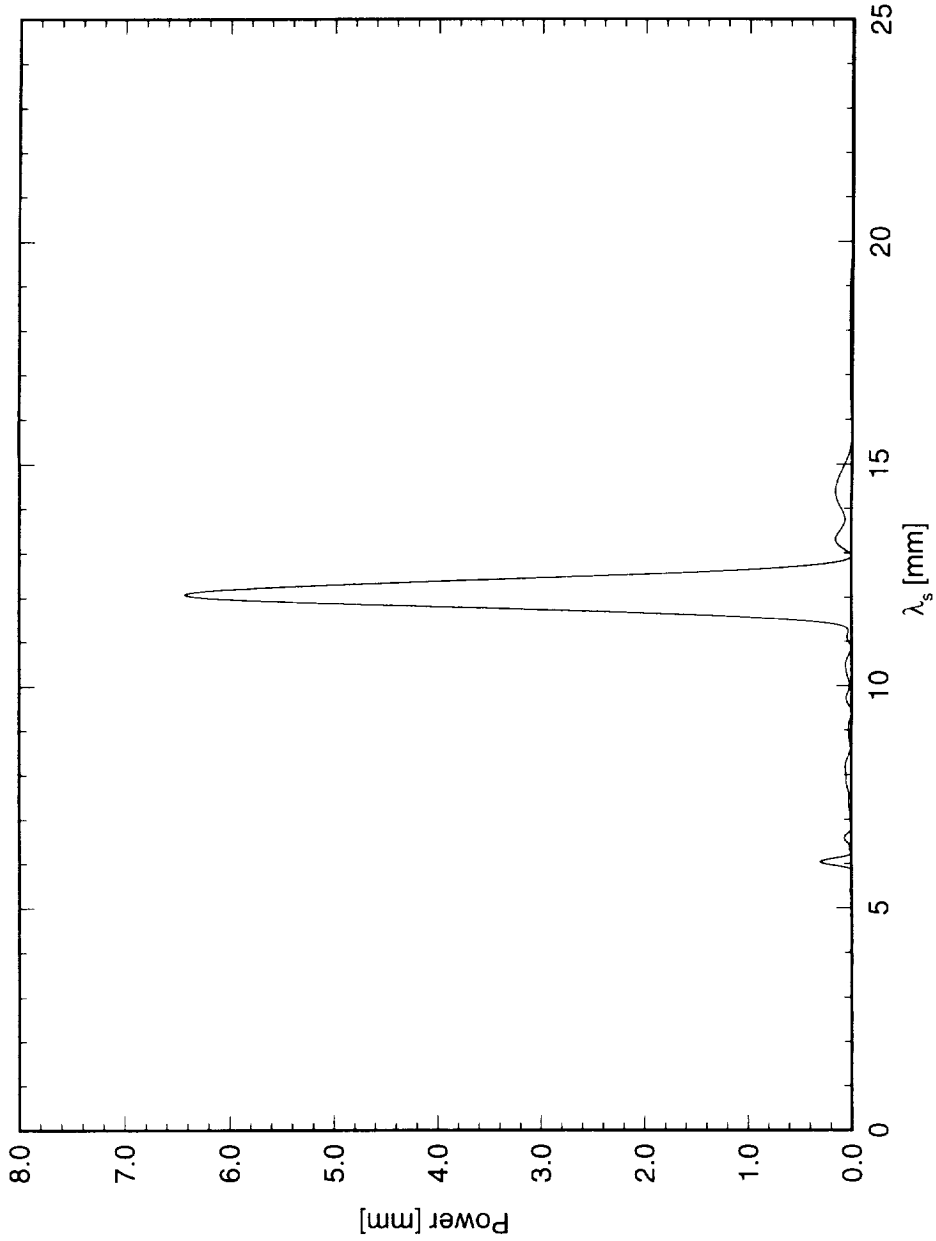

Figure 6.220: Power spectral density of spanwise hot-wire scan at $x/c = 0.45$, $Y = 0.85$ mm. $Re_c = 2.4 \times 10^6$, [48|12] roughness.

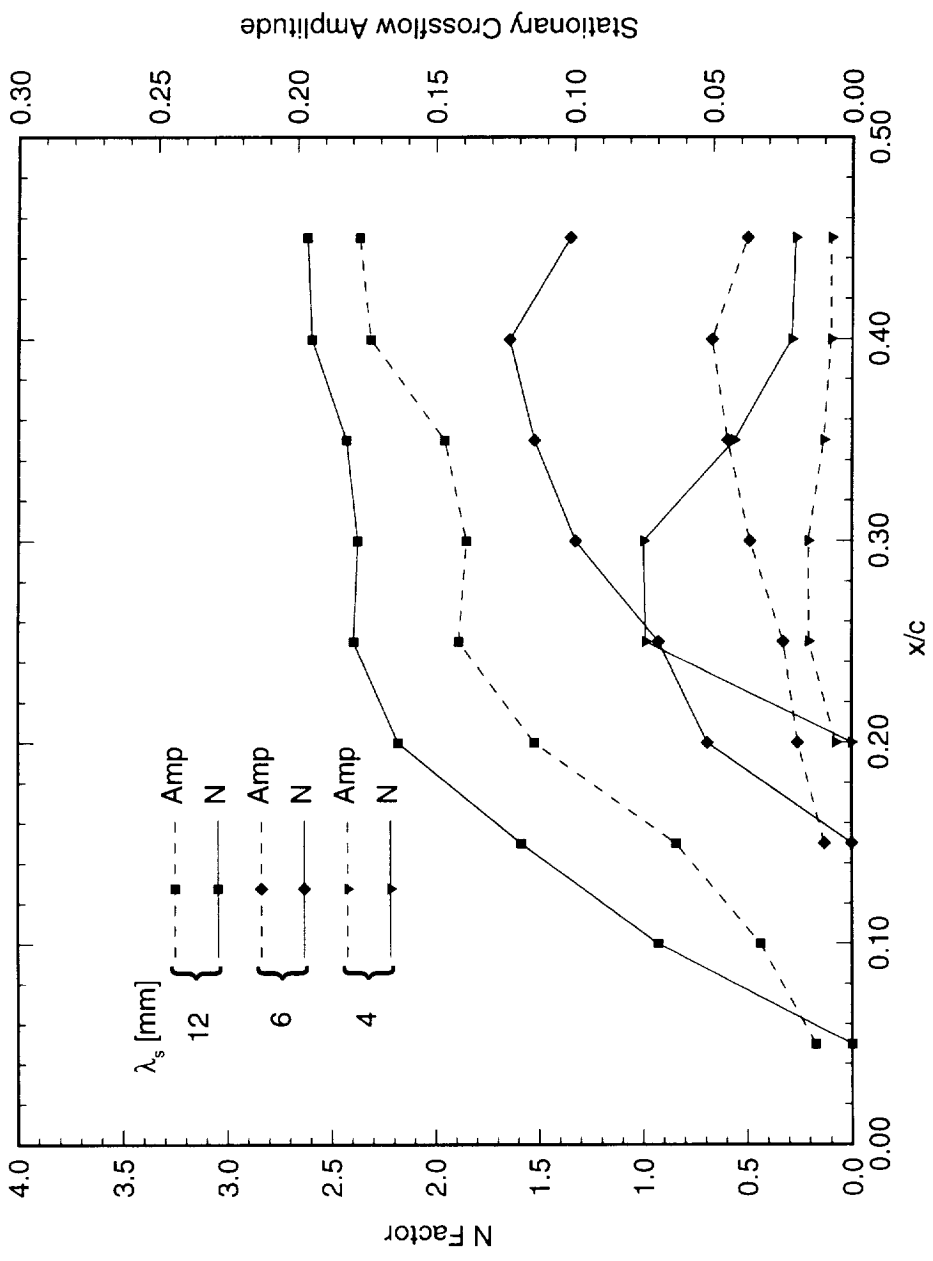

Figure 6.221: Individual-mode disturbance amplitude and amplification factor N for $Re_c = 2.4 \times 10^6$ and [48|12] roughness. N-factors are relative to the point at which the mode is first detected.

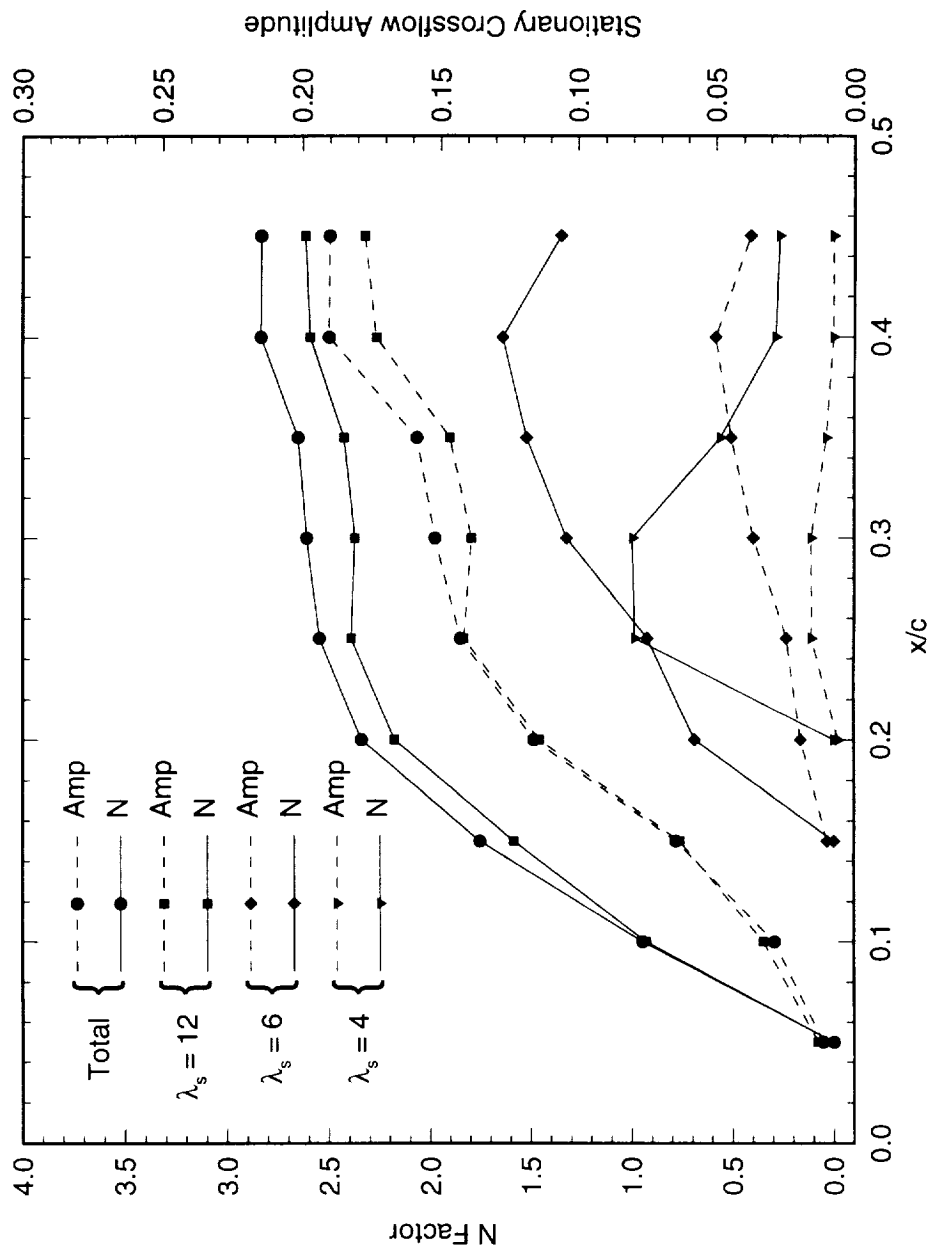

Figure 6.222: Total and individual-mode disturbance amplitude and amplification factor N for $Re_c = 2.4 \times 10^6$ and [48|12] roughness. N-factors are relative to the point at which the disturbance is first detected.

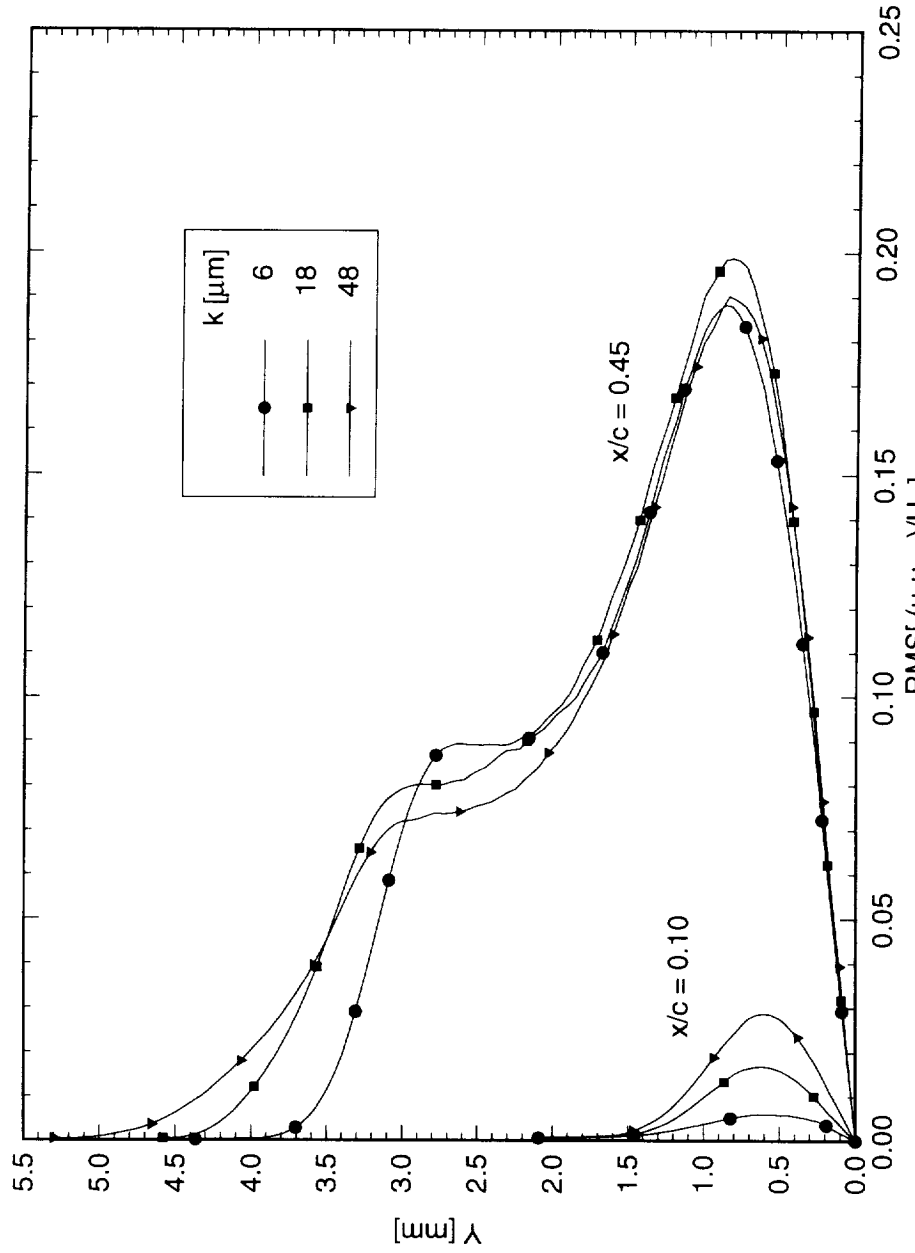

Figure 6.223: Stationary crossflow mode shapes at $x/c = 0.10$ and $x/c = 0.45$ for $Re_c = 2.4 \times 10^6$ and $[k|12]$ roughness. The symbols are simply identifiers and do not represent measurement points.

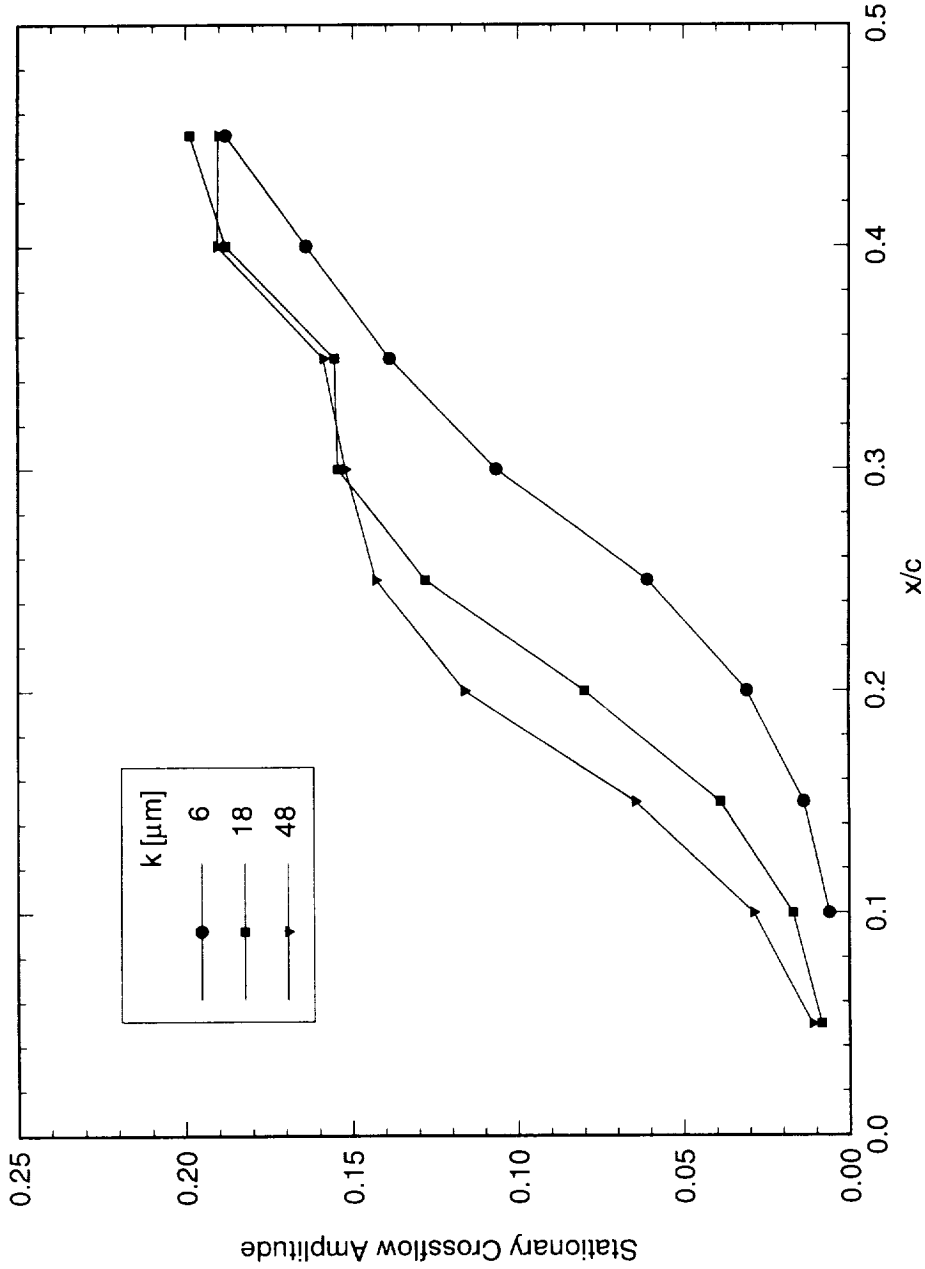

Figure 6.224: Total disturbance amplitude for $Re_c = 2.4 \times 10^6$ and $[k|12]$ roughness. The curves are generated from the maximum of the mode-shape profiles.

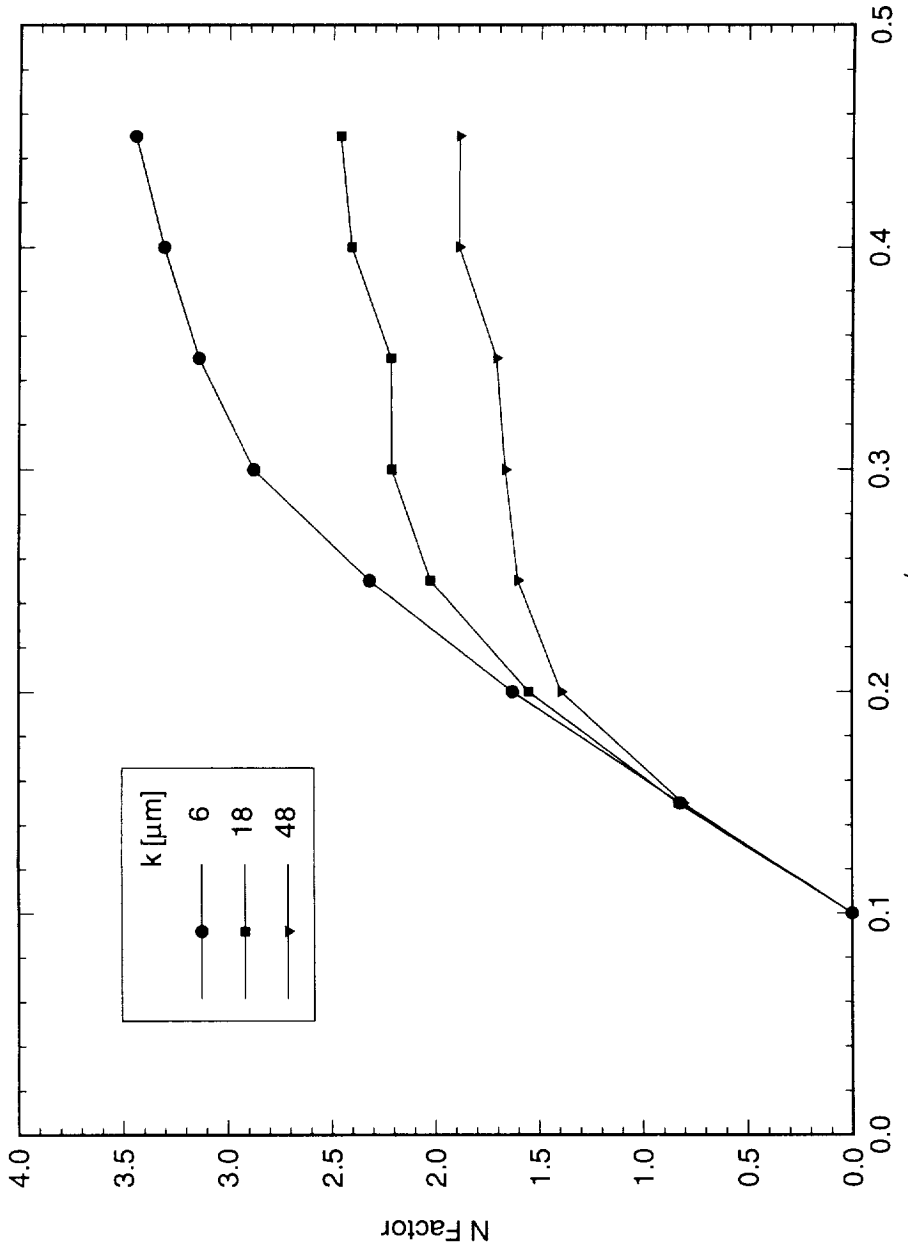

Figure 6.225: Total disturbance amplification factor N for $Re_c = 2.4 \times 10^6$ and $[k|12]$ roughness. The reference point for the N-factor calculations is $x/c = 0.10$.

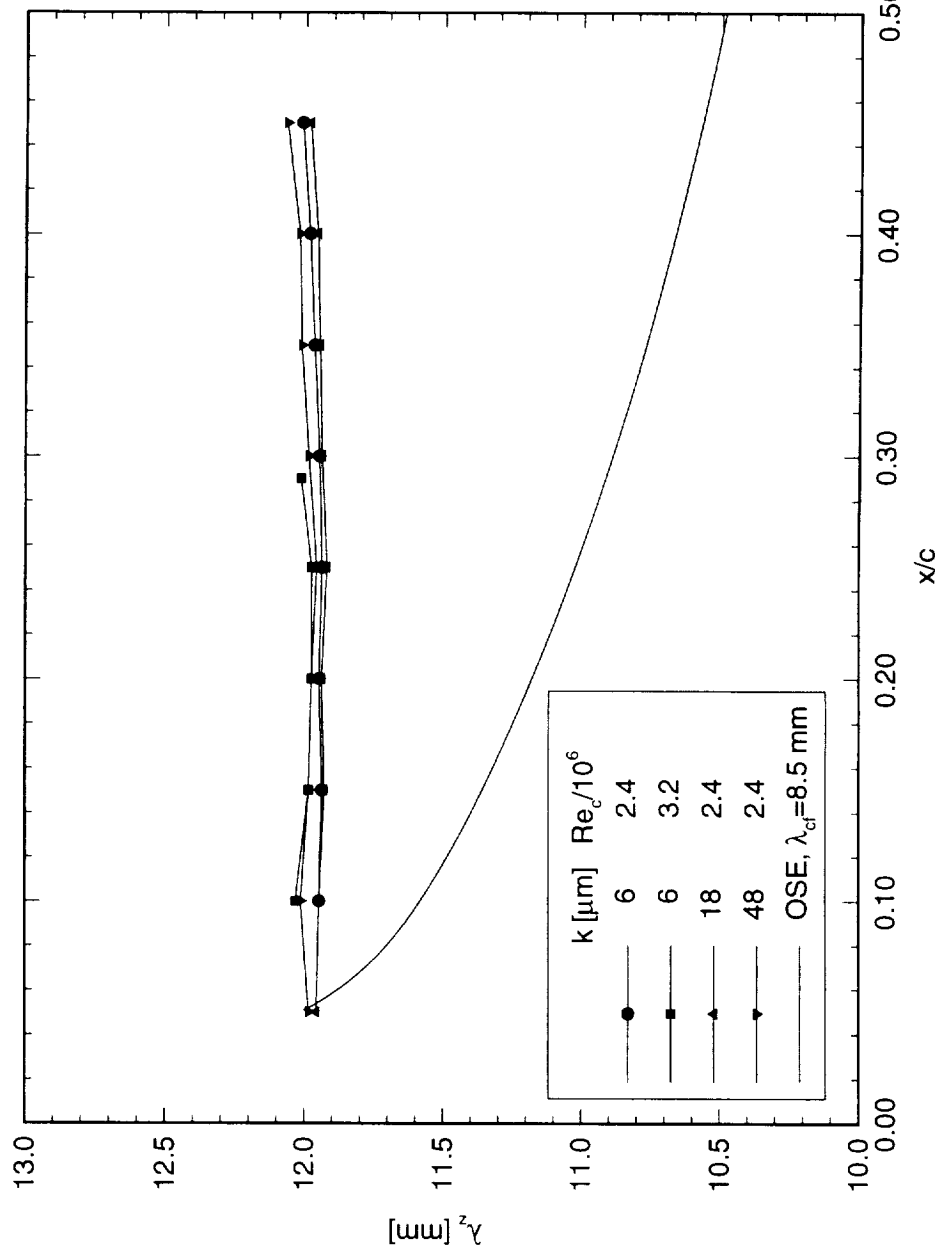

Figure 6.226: Chordwise variation of fundamental crossflow mode wavelength. The experimental data are obtained from the power spectra for all data sets with 12 mm roughness spacing. The linear theory predictions are computed with constant crossflow wavelength.

BIOGRAPHICAL SKETCH

Mark Steven Reibert was born on December 5, 1967 in Phoenix, Arizona. He attended public school in Scottsdale, Arizona, where he graduated first in his class from Coronado High School in 1986. He entered Arizona State University in 1986 on an Arizona Board of Regents Scholarship. Majoring in Aerospace Engineering, Mark was inducted into the Golden Key National Honor Society, the Pi Tau Sigma National Honorary Mechanical Engineering Fraternity, and the Tau Beta Pi National Engineering Honor Society, where he served as Vice President of the Arizona Beta chapter from 1989–1990. He also received the College of Engineering and Applied Sciences Scholastic Excellence Award each year from 1986–1991, when he was awarded the degree of Bachelor of Science in Engineering. Mark continued his studies at Arizona State University, enrolling in the Graduate College to pursue a doctorate in Mechanical Engineering. He received a three-year Office of Naval Research Graduate Fellowship from 1991–1994 and a NASA Graduate Aeronautics Fellowship from 1994–1995. Mark is a member of the American Society for Engineering Education, the American Institute of Aeronautics and Astronautics, and the Aircraft Owners and Pilots Association.